biosensors

Special Issue Reprint

Electrochemical and Fluorescent Biosensors

Novel Strategies, Methods, and Materials

Edited by
Baiqing Yuan, Dong Liu, Lin Liu, Lijun Zhao and Daojun Zhang

mdpi.com/journal/biosensors

MDPI

Electrochemical and Fluorescent Biosensors: Novel Strategies, Methods, and Materials

Electrochemical and Fluorescent Biosensors: Novel Strategies, Methods, and Materials

Editors

Baiqing Yuan
Dong Liu
Lin Liu
Lijun Zhao
Daojun Zhang

MDPI

Basel • Beijing • Wuhan • Barcelona • Belgrade • Novi Sad • Cluj • Manchester

Editors

Baiqing Yuan
School of Chemistry and Materials Science
Ludong University
Yantai
China

Dong Liu
School of Agricultural Engineering
Jiangsu University
Zhenjiang
China

Lin Liu
Henan Province of Key Laboratory of New Optoelectronic Functional Materials
Anyang Normal University
Anyang
China

Lijun Zhao
School of Chemistry & Chemical Engineering
Yantai University
Yantai
China

Daojun Zhang
College of Chemistry and Chemical Engineering
Anyang Normal University
Anyang
China

Editorial Office
MDPI AG
Grosspeteranlage 5
4052 Basel, Switzerland

This is a reprint of articles from the Special Issue published online in the open access journal *Biosensors* (ISSN 2079-6374) (available at: https://www.mdpi.com/journal/biosensors/special_issues/P995FH1NRC).

For citation purposes, cite each article independently as indicated on the article page online and as indicated below:

Lastname, A.A.; Lastname, B.B. Article Title. *Journal Name* **Year**, *Volume Number*, Page Range.

ISBN 978-3-7258-2595-0 (Hbk)
ISBN 978-3-7258-2596-7 (PDF)
doi.org/10.3390/books978-3-7258-2596-7

Contents

About the Editors

Baiqing Yuan

Dr. Yuan earned his Ph.D. in Analytical Chemistry from the Changchun Institute of Applied Chemistry, Chinese Academy of Sciences, in 2010. He is currently a full Professor in the School of Chemistry and Materials Science at Ludong University, with research interests focused on electroanalysis and electrocatalysis. To date, he has published over 70 papers in peer-reviewed journals, which have been cited more than 2000 times.

Dong Liu

Dong Liu obtained his Ph.D. degree in analytical chemistry from Changchun Institute of Applied Chemistry (CIAC), Chinese Academy of Sciences (CAS), in 2013. Currently, he is an associate professor at School of Agricultural Engineering, Jiangsu University, China. His research interests are focused on the synthesis of functional nanomaterials and their applications in analysis and catalysis. He has published more than 60 papers in peer-reviewed journals in e.g., *Analytical Chemistry*, *Biosensors and Bioelectronics*, and *Journal of Hazardous Materials*.

Lin Liu

Lin Liu obtained his Ph.D. in Applied Chemistry from Central South University in 2011.

He is currently a professor at the School of Chemistry and Chemical Engineering, Anyang Normal University. He is mainly engaged in the early diagnosis of major diseases, drug development, and other research work and has published more than 110 SCI papers, as the first author and/or corresponding author, such as *J. Am. Chem. Soc.*, *Green Chem.*, *Chem. Commun.*, *Biosens. Bioelectron.*, *ACS Appl. Mater. Interfaces*, *Electrochem. Commun.*, *Sens. Actuators B: Chem.*, *Electrochem. Acta*, *Analyst*, and other internationally renowned journals.

Lijun Zhao

Lijun Zhao graduated with an M.Sc. degree in Applied Chemistry Major from the Jiangsu University of Science and Technology in 2013, a Ph.D. degree in Analytical Chemistry in 2017. He worked as a postdoctoral researcher at Qingdao Institute of Bioenergy and Process, Chinese Academy of Sciences from 2017 to 2019, and is working in School of Chemistry & Chemical Engineering, Yantai University. His current research interests include Fluorometric Analysis for Biomarkers and Organometallic Catalysis in Hydrogen Transfer, and has published more than 20 papers, applied for more than 5 patents, participated in 7 research projects. He is a member of CCS and a reviewer for different papers in international chemistry and materials journals.

Daojun Zhang

Daojun Zhang obtained his Ph.D. degree in inorganic chemistry from Jilin University in 2011. Currently, he is a full professor at College of Chemistry and Chemical Engineering, Anyang Normal University, China. His research interests are focused on the synthesis of micro-/nano-structured functional materials and their applications in electrocatalysis and devices for energy conversion. He has published more than 100 papers in peer-reviewed journals in e.g., *Inorganic Chemistry*, *Sensors and Actuators B*, *ACS Appl. Energy Mater.*, and *Dalton Trans.*

biosensors

MDPI

Communication

Magnetically Assisted Immobilization-Free Detection of microRNAs Based on the Signal Amplification of Duplex-Specific Nuclease

Gang Liu [1,†], Ming La [2,†], Jiwei Wang [1], Jiawen Liu [1], Yongjun Han [2,*] and Lin Liu [1,*]

[1] College of Chemistry and Chemical Engineering, Anyang Normal University, Anyang 455000, China
[2] School of Chemistry and Environmental Engineering, Pingdingshan University, Pingdingshan 467000, China
* Correspondence: 2773@pdsu.edu.cn (Y.H.); liulin@aynu.edu.cn (L.L.)
† These authors contributed equally to this work.

Abstract: The double specific nuclease (DSN)-based methods for microRNAs (miRNAs) detection usually require the immobilization of DNA probes on a solid surface. However, such strategies have the drawbacks of low hybridization and cleavage efficiency caused by steric hindrance effect and high salt concentration on the solid surface. Herein, we proposed an immobilization-free method for miRNA detection on the basic of DSN-assisted signal amplification. The biotin- and fluorophore-labeled probes were captured by streptavidin-modified magnetic beads through streptavidin–biotin interactions, thus producing a poor fluorescence signal. Once the DNA probes were hybridized with target miRNA in solution to form DNA-miRNA duplexes, DNA stands in the duplexes would be selectively digested by DSN. The released target miRNA could initiate the next hybridization/cleavage recycling in the homogeneous solution, finally resulting in the release of numerous fluorophore-labeled fragments. The released fluorophores remained in solution and emitted strong fluorescence after treatment by the streptavidin-modified magnetic beads. The immobilization-free method achieved the assays of miRNA-21 with a detection limit down to 0.01 pM. It was employed to evaluate the expression levels of miRNA-21 in different cancer cells with satisfactory results.

Keywords: microRNAs; double specific nuclease; magnetic bead; immobilization-free; homogeneous analysis

Citation: Liu, G.; La, M.; Wang, J.; Liu, J.; Han, Y.; Liu, L. Magnetically Assisted Immobilization-Free Detection of microRNAs Based on the Signal Amplification of Duplex-Specific Nuclease. *Biosensors* **2023**, *13*, 699. https://doi.org/10.3390/bios13070699

Received: 26 May 2023
Revised: 15 June 2023
Accepted: 23 June 2023
Published: 30 June 2023

1. Introduction

MicroRNAs (miRNAs) are a group of endogenous, non-coding RNAs that play an important role in physiological and pathological processes. The abnormal expression levels of miRNAs are associated with many human diseases, including cancers and degenerative diseases [1,2]. Therefore, miRNAs have been regarded as the credible biomarkers for early diagnosis and treatment evaluation of diseases. Reverse transcription real-time quantitative polymerase chain reaction (RT-qPCR) is the currently used gold standard method for monitoring the expression levels of miRNAs. The method shows high specificity and sensitivity but requires complex operation procedures, specialized equipment, and a clean experimental environment [3]. Thus, it is meaningful and highly desired to develop a simple and sensitive detection system for the real-time monitoring of the level of miRNAs.

As one of the isothermal amplification strategies for biological analysis, a double specific nuclease (DSN)-based sensing system exhibits the advantages of simple principle, convenient operation, and high specificity [4–7]. DSN can specifically cleave DNA in DNA-DNA or DNA-RNA duplexes but shows no activity toward single-stranded DNA (ssDNA) or double-stranded RNA (dsRNA) [8,9]. The principle of DSN-assisted signal amplification is mainly based on target miRNA recycling. Thus, a few miRNAs could trigger the cleavage of considerable amounts of DNA in DNA-RNA heteroduplexes, leading to the release of a large number of signal molecules, including enzymes, electroactive

molecules, fluorophores, nanoparticles, and nucleotide sequences [10–24]. The concentration of miRNAs can be determined by monitoring the optical or electrical signal change induced by the release of signal molecules. In these methods, signal-labeled capture probes are usually attached onto a solid surface and DSN-based enzymatic reactions happen at the solid–liquid interface. The heterogeneous sensing systems show the advantages of less sample consumption, ultrahigh sensitivity, and excellent selectivity. However, the probe-immobilized methods may cause several drawbacks. First, the steric hindrance effect of the solid surface may affect the configurational freedom of capture probes and prevent interactions between DNA-RNA hybrids and nucleases, thus decreasing the hybridization and cleavage efficiency [25–29]. Second, the high salt concentration on the probe-modified solid surface may limit the activity of nucleases [30,31]. In addition, the immobilization and removal of capture probes require laborious and time-consuming procedures. In contrast to heterogeneous sensing systems, homogeneous assays have the merits of a simple operation and high cleavage efficiency. Although a few DSN-based homogeneous methods have been developed and used for miRNA detection [32,33], they are usually involved in complex procedures, special instruments, and/or the use of additional enzymes or nanomaterials for signal amplification. Thus, it is of importance to develop a simple, sensitive, and high-throughput homogeneous method for the detection of miRNAs with DSN-assisted signal amplification.

Magnetic beads (MBs) have been extensively used for the development of various biosensors for detective applications. Magnetically assisted sensing systems show remarkable advantages in the separation and pre-concentration of targets and high throughput detection of multiple samples [34–37]. Streptavidin (SA) is a homotetramer protein that can bind up to four biotin molecules with a high affinity. Biotin is a commonly used reagent for labeling biomolecules due to its small size and highly selective and stable interaction with SA. Many SA-modified materials, including MB-SA, are commercially available for the collection and immobilization of biotin-labeled proteins or nucleic acids [38]. In this work, we proposed a homogeneous strategy for the detection of miRNAs with DSN-assisted signal amplification. In the absence of target miRNA, the biotinylated fluorescently labeled DNA probes were captured by MB-SA through fast and strong SA-biotin interactions, thus causing a decrease in the fluorescence. In the presence of target miRNA, the capture probes would be digested by DSN, and the released signal molecules in solution showed a high fluorescence. The reaction rate of DSN for the DNA capture probes immobilized on the MB surface and dispersed in solution was investigated. The proposed strategy can be used for the design of various immobilization-free miRNA biosensors by changing the type of signal molecules. Moreover, magnetically assisted sensing systems could be used for the high-throughput detection of multiple miRNAs with different fluorescently labeled sequences.

2. Materials and Methods

2.1. Chemicals and Reagents

DNA, miRNAs, and Trizol reagent were ordered from Sangon Biotech. Co., Ltd. (Shanghai, China). Their sequences are Biotin-TCAACATCAGTCTGATAAGCTA-FAM (Bio-DNA-FAM), UAGCUUAUCAGACUGAUGUUGA (miRNA-21), UAGCUUAUCGGACUGAUGUUGA (single-base mismatch), UUGCUUAUCGGACUGAUCUUGA (three-base mismatch), and GUAAGGCAUCUGACCGAAGGCA (non-complementary). DSN was obtained from Evrogen Joint Stock Company (Moscow, Russia). MB-SA was purchased from Thermo Fisher Scientific (Shanghai, China). Other reagents were of analytical grade and used without further purification. The miRNA samples were prepared freshly using RNase-free ultrapure water. The hybridization and reaction solutions were prepared with TNE buffer (pH 7.4). All aqueous solutions were prepared with ultrapure water treated by a Millipore system.

2.2. Procedures for miRNA Detection

In total, 150 μL of 500 nM DNA probe was mixed with 25 μL of miRNA sample in TNE buffer at 45 °C. After incubation for 10 min, 25 μL of 0.1 U DSN solution was added to the mixture. After reaction for a given time, 10 μL of 10 mg/mL MB-SA suspension was added to the mixed solution and incubated for about 5 min. Under a magnetic force, the supernatant solution was taken out for assays to be conducted. The signals were collected on a Cary Eclipse fluorescence spectrometer (Palo Alto, CA, USA) with an excitation wavelength of 492 nm.

2.3. Assays of miRNAs in Cell Lysates

The cell lysates were extracted from MCF-7 and Hela cells with the procedures detailed in previous reports [39,40]. Briefly, the cells were counted, collected, and washed with phosphate buffer. Then, Trizol reagent was added to extract total RNA according to the manufacturer's protocol. The collected lysates were centrifuged at 10,000 rpm for 15 min and the aqueous supernatants were diluted 10-fold with TNE buffer. Then, 25 μL of the diluted supernatant with additional treatment was added to 150 μL of probe solution for quantification assay. Other procedures for the assays of miRNA in the lysates were the same as those of the standard samples.

3. Results and Discussion

3.1. Detection Principle

The mechanism of the magnetically assisted detection of miRNA is depicted in Scheme 1. The DNA probe labeled with a biotin tag and a fluorophore at two ends (denoted as Bio-DNA-FAM) could hybridize with the target miRNA to form a DNA-miRNA heteroduplex. The DNA strand in the duplex was then selectively digested by DSN. The released miRNA could hybridize with another Bio-DNA-FAM probe and initiate the next cleavage event. In this way, the target miRNA-initiated enzymatic digestion of Bio-DNA-FAM probes by DSN was recycled, leading to the release of numerous FAM-labeled fragments. The released fragments could not be removed by MB-SA under the magnetic force and thus showed a strong fluorescence. In the absence of target miRNA, the Bio-DNA-FAM probe remained intact and would be removed by MB-SA through streptavidin–biotin interaction. In this case, the solution showed weak fluorescence. Therefore, the fluorescence intensity is proportional to the level of target miRNA. Through the signal amplification of DSN, miRNA at a low abundance would be detected. The method should be simple and sensitive since it does not require the pre-immobilization of DNA probe on a solid surface, thus improving the hybridization and cleavage efficiency without the effect of steric hindrance.

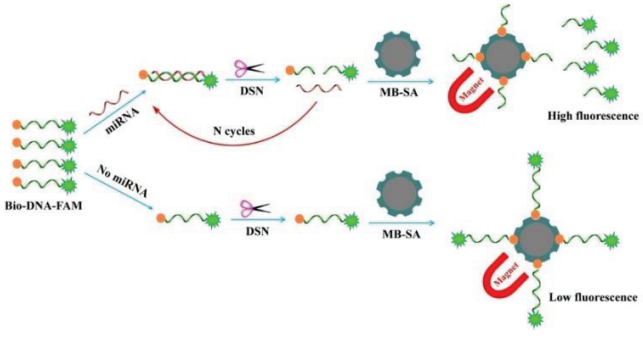

Scheme 1. Schematic representation of the magnetically assisted immobilization-free method for miRNA detection.

3.2. Feasibility of this Method

To probe the feasibility of the method, miRNA-21 was tested as a target model because its expression level is closely related to many cancers. As shown in Figure 1, the Bio-DNA-FAM probe emitted a strong fluorescence at 521 nm (curve a). When it was incubated with MB-SA under magnetic force (curve b), the fluorescence peak disappeared, indicating that the probe could be captured and removed by MB-SA. When the Bio-DNA-FAM probe was mixed with miRNA-21 in the absence of DSN, the fluorescence signal was close to the background value (curve c), indicating that the hybridization of miRNA-21 with Bio-DNA-FAM did not limit the capture of the probe by MB-SA. However, when the DNA-miRNA duplexes were incubated with DSN for a given time and then treated by MB-SA under the magnetic force, the fluorescence signal was intensified greatly (curve d). The result suggested that the Bio-DNA-FAM probes were enzymatically digested by DSN, thus releasing a large number of FAM-labeled fragments into the solution. To study the effect of steric hindrance on the hybridization/cleavage efficiency, the DNA-miRNA duplexes were pre-immobilized onto the MB-SA surface, and then DSN was added to the suspension for enzymatic digestion under the same reaction conditions. As a result, a smaller signal (curve e) was observed in contrast to the immobilization-free strategy (curve d). The result implied that the cleavage efficiency was reduced by the steric hindrance, which is consistent with that in the previous works [27,41]. Thus, our proposal could improve the detection sensitivity without increasing the operation complexity.

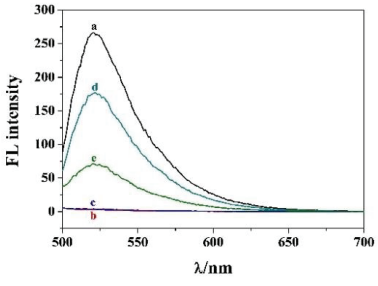

Figure 1. Fluorescence spectra of Bio-DNA-FAM before (curve a) and after (curve b) incubation with MB-SA, as well as the mixture of Bio-DNA-FAM/miRNA-21 (curve c) and Bio-DNA-FAM/miRNA-21/DSN (curve d) after treatment by MB-SA. Curve corresponds to that of incubating the MB-SA-Bio-DNA-FAM conjugates with the mixture of miRNA/DSN. The used concentrations of Bio-DNA-FAM, DSN, and miRNA-21 were 500 nM, 0.1 U, and 100 pM.

3.3. Optimization of Experimental Conditions

To achieve optimum analytical performance, the experimental conditions, such as the probe concentration and cleavage time, were investigated. Because the background signal would be dependent upon the probe concentration, we first measured the fluorescence signals of different concentrations of Bio-DNA-FAM after treatment by MB-SA under a magnetic force. As shown in Figure 2A, when the probe concentration was lower than 500 nM, the fluorescence intensity was negligible. Over the value, the signal began to increase, indicating that the surface of MB-SA was saturated by the probe through the SA-biotin interaction. The abundance of miRNAs in biological samples is extremely low (usually in the range of femtomolar to picomolar), and the background signal can affect the sensitivity of the analytical method. Thus, a low concentration of probe was used in the following trials. When the incubation time for the mixture of DNA/miRNA-21 and DSN was increased, the fluorescence intensity was gradually intensified and began to level off beyond 60 min for 100 pM miRNA-21 (Figure 2B). To attain high sensitivity and save detection time, the samples were incubated for 60 min to achieve hybridization and cleavage recycling.

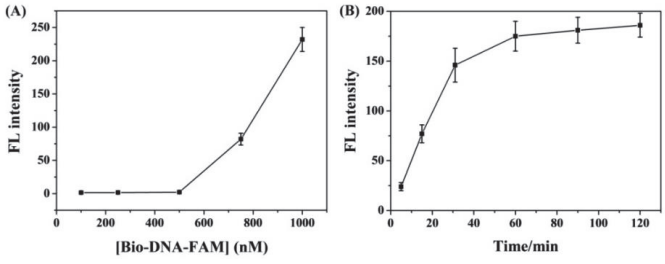

Figure 2. Effect of probe concentration (**A**) and incubation time (**B**) on fluorescence intensity. The concentrations of Bio-DNA-FAM, miRNA-21, and DSN were 500 nM, 100 pM, and 0.1 U, respectively.

3.4. Sensitivity for miRNA-21 Detection

Under the optimal conditions, various concentrations of miRNA-21 were determined to indicate the analytical performance. As shown in Figure 3A, the fluorescence signals were intensified with the increase in the miRNA concentration in the range of 0~100 pM. A good linear relationship was found at the concentration range of 0.01~10 pM (Figure 3B). The linear equation can be expressed as FL = 3.47 + 6.23 [miRNA-21] (pM). The detection limit as the minimum detectable concentration (0.01 pM) [42] is lower than that achieved by other DSN-based fluorescence methods with nanomaterials as the quenchers, including gold nanoparticles, graphene oxide, molybdenum disulfide, and polydopamine-coated magnetic nanoparticles (Table 1). The sensitivity was also comparable to that achieved by DSN plus other signal-amplified techniques [4,6]. The high sensitivity can be attributed to the immobilization-free strategy, the low background signal, and the high hybridization and cleavage efficiency.

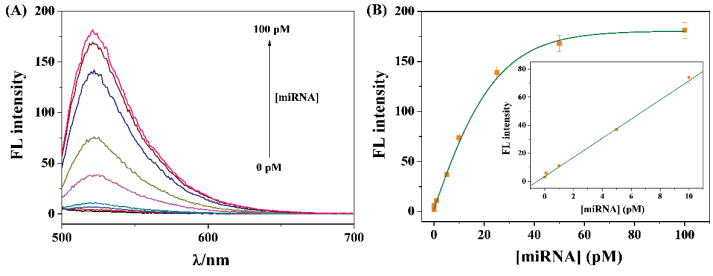

Figure 3. (**A**) Fluorescence spectra for the detection of different concentrations of miRNA-21 (from to bottom to top: 0, 0.01, 0.1, 1, 5, 10, 25, 50, and 100 pM). (**B**) Calibration curve between fluorescence intensity and miRNA-21 concentration. The errors were deduced from three replicate measurements. The inset shows the linear portion of the calibration curve.

Table 1. Analytical performances of DSN-based fluorescence methods for miRNA detection.

Materials/Reporters	Linear Range	Detection Limit	Ref.
AuNPs/dye	5–200 pM	5 pM	[41]
AuNPs/dye	0.1–1000 pM	33.4 fM	[43]
AuNPs/dye	0.1–10 pM	45 fM	[44]
PS@Au/dye	1–1000 pM	50 fM	[45]
MWCNT-AuNCs/dye	0.1–1000 pM	33.4 fM	[46]
GO/dye	0.5–1000 pM	160 fM	[47]
GO/dye	5–40 nM	132 pM	[48]
MoS_2/dye	1–10,000 pM	10 fM	[49]

Table 1. *Cont.*

Materials/Reporters	Linear Range	Detection Limit	Ref.
MoS_2/dye	0.5–50 nM	426 pM	[50]
CCP/dye	10–200 pM	4.6 pM	[51]
PDA-PEI/dye	0.8–50 nM	0.52 nM	[52]
MNPs@PDA/dye	5–5000 pM	0.42 pM	[53]
MB/QDs	0.5–10 pM	0.5 pM	[54]
$Cu_3(PO_4)_2$ NFs/dye	1–100,000 pM	0.23 pM	[55]
MB-SA/dye	0.01–10 pM	0.01 pM	this work

Abbreviations: AuNPs, gold nanoparticles; PS@Au, gold nanoparticle-coated polystyrene microbeads; MWCNT-AuNCs, multi-walled carbon nanotube–gold nanocomposites; GO, graphene oxide; MoS_2, molybdenum disulfide; CCP, cationic conjugated polymer; PDA-PEI, dopamine and polyethyleneimine (PEI) copolymerized nanodots; MNPs@PDA, magnetic nanoparticles coated with polydopamine; MB, magnetic bead; QDs, quantum dots; $Cu_3(PO_4)_2$ NFs, $Cu_3(PO_4)_2$ hybrid nanoflowers.

3.5. Selectivity

To indicate the selectivity of the strategy, a series of miRNA strands were tested, including miRNA-21 and its base-mismatched and non-complementary sequences. As shown in Figure 4, only the target miRNA-21 caused a significant increase in the fluorescence signal. Although the single-based mismatched sequence may hybridize with the probe at room temperature, it did not induce an obvious enhancement in the fluorescence signal. The result should benefit from the high specificity of DSN and the high reaction temperature where the mismatched sequences could not form DNA-RNA duplexes. In addition, the probability and abundance are very low for the existence of the miRNA-21 variant with a single mismatch in the real sample. By labeling the DNA probes with different fluorophores, we believe that the immobilization-free method could be used to simultaneously determine multiple types of miRNAs with a simple operation procedure and high detection throughput.

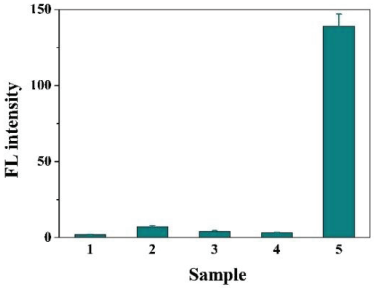

Figure 4. Selectivity of the method. Bar 1, buffer blank; bar 2, single-base mismatch; bar 3, three-base mismatch; bar 4, non-complementary; bar 5, miRNA-21.

3.6. Assays of miRNA-21 in Cellular Lysates

To evaluate the validity of our method for real sample assays, the levels of miRNA-21 extracted from two types of cancer cell lines were determined. As depicted in Figure 5, the signals increased significantly with an increasing concentration of MCF-7 cells, while no obvious change was found for Hela cells even at a concentration higher than 10,000 cells. This indicated that the expression level of miRNA-21 in MCF-7 is higher than that in Hela cells. The result is in agreement with that found by the heterogeneous biosensors [39,40,56,57], indicating that our method can be used to measure the expression levels of miRNA in biological samples. The detectable cell number is higher than that of the heterogeneous assays, which may be attributed to the differences in the used sample volume and the expression level as well as extraction method for miRNA-21. We believe that the sensitivity would be further improved by the signal amplification of enzymes or nanomaterials in combination with the use of a more sensitive fluorescence spectrometer.

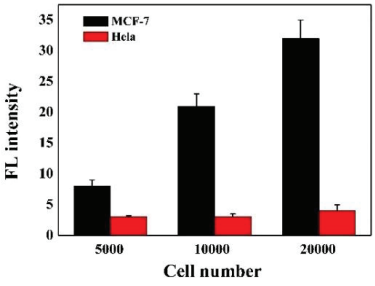

Figure 5. Results for the assays of miRNA-21 in lysates extracted from MCF-7 and Hela cells.

4. Conclusions

In summary, an immobilization-free fluorescence method with DSN-assisted signal amplification was developed for the sensitive detection of miRNAs. The effect of steric hindrance on the hybridization/cleavage efficiency was also investigated. The detection limit of this method is lower than that of other DSN-based fluorescence assays and even comparable to that achieved by multiple signal amplification strategies. It was successfully employed to monitor the expression levels of miRNA-21 in two cancer cell lines. In addition, the strategy does not require the pre-immobilization of a DNA probe on a solid surface for hybridization/cleavage recycling, thus eliminating the effect of steric hindrance and improving the detection efficiency. We believe that the proposal shows great potential for the simultaneous detection of multiple miRNAs by matching the DNA probes with different fluorophores.

Author Contributions: Conceptualization, G.L. and L.L.; methodology, M.L. and Y.H.; investigation, G.L., J.W. and J.L.; writing—original draft preparation, G.L. and M.L.; writing—review and editing, L.L.; project administration, Y.H.; funding acquisition, M.L. and L.L. All authors have read and agreed to the published version of the manuscript.

Funding: This research was funded by the fund project for Young Scholar sponsored by Henan province (2020JS227) and the Program for Innovative Research Team of Science and Technology in the University of Henan Province (21IRTSTHN005).

Institutional Review Board Statement: Not applicable.

Informed Consent Statement: Not applicable.

Data Availability Statement: Not applicable.

Conflicts of Interest: The authors declare no conflict of interest.

References

1. Dong, H.; Lei, J.; Ding, L.; Wen, Y.; Ju, H.; Zhang, X. MicroRNA: Function, detection, and bioanalysis. *Chem. Rev.* **2013**, *113*, 6207–6233. [CrossRef] [PubMed]
2. Imas, J.J.; Zamarreño, C.R.; Zubiate, P.; Sanchez-Martín, L.; Campión, J.; Matías, I.R. Optical biosensors for the detection of Rheumatoid Arthritis (RA) biomarkers: A comprehensive review. *Sensors* **2020**, *20*, 6289. [CrossRef] [PubMed]
3. Chai, H.; Tang, Y.; Miao, P. Tetrahedral DNA supported walking nanomachine for ultrasensitive miRNA detection in cancer cells and serums. *Anal. Chem.* **2022**, *94*, 9975–9980. [CrossRef] [PubMed]
4. Wu, Y.; Cui, S.; Li, Q.; Zhang, R.; Song, Z.; Gao, Y.; Chen, W.; Xing, D. Recent advances in duplex-specific nuclease-based signal amplification strategies for microRNA detection. *Biosens. Bioelectron.* **2020**, *165*, 112449. [CrossRef]
5. Ashraf, G.; Zhong, Z.T.; Asif, M.; Aziz, A.; Iftikhar, T.; Chen, W.; Zhao, Y.D. State-of-the-art fluorescent probes: Duplex-specific nuclease-based strategies for early disease diagnostics. *Biosensors* **2022**, *12*, 1172. [CrossRef]
6. Wu, D.; Yi, X.; Xia, N. Electrochemical biosensors for microRNA detection using duplex-specific nuclease based signal amplification strategies. *Int. J. Electrochem. Sci.* **2020**, *15*, 12136–12148. [CrossRef]
7. Qiu, X.; Liu, X.; Zhang, W.; Zhang, H.; Jiang, T.; Fan, D.; Luo, Y. Dynamic monitoring of microRNA-DNA hybridization using DNAase-triggered signal amplification. *Anal. Chem.* **2015**, *87*, 6303–6310. [CrossRef]
8. Ashraf, G.; Zhong, Z.-T.; Asif, M.; Aziz, A.; Song, L.; Zhang, S.; Liu, B.; Chen, W.; Zhao, Y.-D. Extension of duplex specific nuclease sensing application with RNA aptamer. *Talanta* **2022**, *242*, 123314. [CrossRef]

9. Zhu, J.; Guo, Z.; Cui, J.; Miao, P. Partial collapse of DNA tetrahedron for miRNA assay with duplex-specific nuclease-assisted amplification. *Analyst* **2023**, *148*, 512–515. [CrossRef]
10. Castañeda, A.D.; Brenes, N.J.; Kondajji, A.; Crooks, R.M. Detection of microRNA by electrocatalytic amplification: A general approach for aingle-particle biosensing. *J. Am. Chem. Soc.* **2017**, *139*, 7657–7664. [CrossRef]
11. Yin, B.-C.; Liu, Y.-Q.; Ye, B.-C. One-step, multiplexed fluorescence detection of microRNAs based on duplex-specific nuclease signal amplification. *J. Am. Chem. Soc.* **2012**, *134*, 5064–5067. [CrossRef]
12. Zhou, H.; Yang, C.; Chen, H.; Li, X.; Li, Y.; Fan, X. A simple G-quadruplex molecular beacon-based biosensor for highly selective detection of microRNA. *Biosens. Bioelectron.* **2017**, *87*, 552–557. [CrossRef]
13. Hu, Z.; Chen, J.; Li, W.; Wang, Y.; Li, Y.; Sang, L.; Li, J.; Zhang, Q.; Ibupoto, Z.H.; Yu, C. Label-free fluorescence turn-on detection of microRNA based on duplex-specific nuclease and a perylene probe. *Anal. Chim. Acta* **2015**, *895*, 89–94. [CrossRef]
14. Lu, W.; Chen, Y.; Liu, Z.; Tang, W.; Feng, Q.; Sun, J.; Jiang, X. Quantitative detection of microRNA in one step via next generation magnetic relaxation switch sensing. *ACS Nano* **2016**, *10*, 6685–6692. [CrossRef]
15. Pang, Y.; Wang, C.; Wang, J.; Sun, Z.; Xiao, R.; Wang, S. Fe_3O_4@Ag magnetic nanoparticles for microRNA capture and duplex-specific nuclease signal amplification based SERS detection in cancer cells. *Biosens. Bioelectron.* **2016**, *79*, 574–580. [CrossRef]
16. Li, M.; Xiong, C.; Zheng, Y.; Liang, W.; Yuan, R.; Chai, Y. Ultrasensitive photoelectrochemical biosensor based on DNA tetrahedron as nanocarrier for efficient immobilization of CdTe QDs-methylene blue as signal probe with near-zero background noise. *Anal. Chem.* **2018**, *90*, 8211–8216. [CrossRef]
17. Bai, Y.-Y.; Wu, Z.; Xu, C.-M.; Zhang, L.; Feng, J.; Pang, D.-W.; Zhang, Z.-L. One-to-many single entity electrochemistry biosensing for ultrasensitive detection of microRNA. *Anal. Chem.* **2020**, *92*, 853–858. [CrossRef]
18. Tian, B.; Ma, J.; Qiu, Z.; Zardán Gómez de la Torre, T.; Donolato, M.; Hansen, M.F.; Svedlindh, P.; Strömberg, M. Optomagnetic detection of microRNA based on duplex-specific nuclease-assisted target recycling and multilayer core-satellite magnetic superstructures. *ACS Nano* **2017**, *11*, 1798–1806. [CrossRef]
19. Kim, E.; Howes, P.D.; Crowder, S.W.; Stevens, M.M. Multi-amplified sensing of microRNA by a small DNA fragment-driven enzymatic cascade reaction. *ACS Sens.* **2017**, *2*, 111–118. [CrossRef]
20. Deng, H.; Ren, Y.; Shen, W.; Gao, Z. An ultrasensitive homogeneous chemiluminescent assay for microRNAs. *Chem. Commun.* **2013**, *49*, 9401–9403. [CrossRef]
21. Zhang, J.; Wu, D.; Chen, Q.; Chen, M.; Xia, Y.; Cai, S.; Zhang, X.; Wu, F.; Chen, J. Label-free microRNA detection based on terbium and duplex-specific nuclease assisted target recycling. *Analyst* **2015**, *140*, 5082–5089. [CrossRef] [PubMed]
22. Huang, X.; Xu, Z.; Liu, J.-H.; Yu, B.-Y.; Tian, J. Dual signal amplification for microRNA-21 detection based on duplex-specific nuclease and invertase. *RSC Adv.* **2020**, *10*, 11257–11262. [CrossRef] [PubMed]
23. Li, J.; Tong, Y.; Sun, Z.; Chen, Y.; Wang, Y.; Zhou, L.; Jiang, Y.; Li, P.; Wang, C.; Du, L. A duplex-specific nuclease assisted photoelectrochemical biosensor based on MoS_2@ReS_2/Ti_3C_2 hybrid for ultrasensitive detection of colorectal cancer-related piRNA-31,143. *Acta Biomater.* **2022**, *149*, 287–296. [CrossRef] [PubMed]
24. Shen, W.; Yeo, K.H.; Gao, Z. A simple and highly sensitive fluorescence assay for microRNAs. *Analyst* **2015**, *140*, 1932–1938. [CrossRef] [PubMed]
25. Deng, H.; Shen, W.; Ren, Y.; Gao, Z. A highly sensitive and selective homogenous assay for profiling microRNA expression. *Biosens. Bioelectron.* **2014**, *54*, 650–655. [CrossRef]
26. Fu, C.; Liu, C.; Wang, S.; Luo, F.; Lin, Z.; Chen, G. A signal-on homogeneous electrochemical biosensor for sequence-specific microRNA based on duplex-specific nuclease-assisted target recycling amplification. *Anal. Methods* **2016**, *8*, 7034–7039. [CrossRef]
27. Djebbi, K.; Shi, B.; Weng, T.; Bahri, M.; Elaguech, M.A.; Liu, J.; Tlili, C.; Wang, D. Highly sensitive fluorescence assay for miRNA detection: Investigation of the DNA spacer effect on the DSN enzyme activity toward magnetic-bead-tethered probes. *ACS Omega* **2022**, *7*, 2224–2233. [CrossRef]
28. Zhang, J.; Wu, D.Z.; Cai, S.X.; Chen, M.; Xia, Y.K.; Wu, F.; Chen, J.H. An immobilization-free electrochemical impedance biosensor based on duplex-specific nuclease assisted target recycling for amplified detection of microRNA. *Biosens. Bioelectron.* **2016**, *75*, 452–457. [CrossRef]
29. Chang, J.F.; Wang, X.; Wang, J.; Li, H.Y.; Li, F. Nucleic acid functionalized MOFs-based homogeneous electrochemical biosensor for simultaneous detection of multiple tumor biomarkers. *Anal. Chem.* **2019**, *91*, 3604–3610. [CrossRef]
30. Seferos, D.S.; Prigodich, A.; Giljohann, D.A.; Patel, P.C.; Mirkin, C.A. Polyvalent DNA nanoparticle conjugates stabilize nucleic acids. *Nano Lett.* **2009**, *9*, 308–311. [CrossRef]
31. Prigodich, A.E.; Alhasan, A.H.; Mirkin, C.A. Selective enhancement of nucleases by polyvalent DNA-functionalized gold nanoparticles. *J. Am. Chem. Soc.* **2011**, *133*, 2120–2123. [CrossRef]
32. Zhao, G.; Yan, X.; Zhang, Y.; Deng, J.; Liang, X. Sensitive detection of miRNA and circRNA through DSN enzyme cooperating NEase assisted dual signal amplification. *Anal. Biochem.* **2022**, *654*, 114744. [CrossRef]
33. Ma, F.; Liu, W.J.; Zhang, Q.; Zhang, C.Y. Sensitive detection of microRNAs by duplex specific nuclease-assisted target recycling and pyrene excimer switching. *Chem. Commun.* **2017**, *53*, 10596–10599. [CrossRef]
34. Qi, T.; Song, C.; He, J.; Shen, W.; Kong, D.; Shi, H.; Tan, L.; Pan, R.; Tang, S.; Lee, H.K. Highly sensitive detection of multiple microRNAs by high-performance liquid chromatography coupled with long and short probe-based recycling amplification. *Anal. Chem.* **2020**, *92*, 5033–5040. [CrossRef]

35. Yang, L.M.; Yin, X.H.; An, B.; Li, F. Precise capture and direct quantification of tumor exosomes via highly efficient dual-aptamer recognition-assisted ratiometric immobilization-free electrochemical strategy. *Anal. Chem.* **2021**, *93*, 1709–1716. [CrossRef]
36. Sukla, S.; Mondal, P.; Biswas, S.; Ghosh, S. A rapid and easy-to-perform method of nucleic-acid based dengue virus diagnosis using fluorescence-based molecular beacons. *Biosensors* **2021**, *11*, 479. [CrossRef]
37. Wang, L.; Lin, J. Recent advances on magnetic nanobead based biosensors: From separation to detection. *TrAC-Trend. Anal. Chem.* **2020**, *128*, 115915. [CrossRef]
38. Xia, N.; Sun, T.; Liu, L.; Tian, L.; Sun, Z. Heterogeneous sensing of post-translational modification enzymes by integrating the advantage of homogeneous analysis. *Talanta* **2022**, *237*, 122949. [CrossRef]
39. Liu, L.; Deng, D.; Wu, D.; Hou, W.; Wang, L.; Li, N.; Sun, Z. Duplex-specific nuclease-based electrochemical biosensor for the detection of microRNAs by conversion of homogeneous assay into surface-tethered electrochemical analysis. *Anal. Chim. Acta* **2021**, *1149*, 338199. [CrossRef]
40. Huang, Y.; Sun, T.; Liu, L.; Xia, N.; Zhao, Y.; Yi, X. Surface plasmon resonance biosensor for the detection of miRNAs by combining the advantages of homogeneous reaction and heterogeneous detection. *Talanta* **2021**, *234*, 122622. [CrossRef]
41. Degliangeli, F.; Kshirsagar, P.; Brunetti, V.; Pompa, P.P.; Fiammengo, R. Absolute and direct microRNA quantification using DNA—Gold nanoparticle probes. *J. Am. Chem. Soc.* **2014**, *136*, 2264–2267. [CrossRef] [PubMed]
42. Daniels, J.S.; Pourmand, N. Label-free impedance biosensors: Opportunities and challenges. *Electroanalysis* **2007**, *19*, 1239–1257. [CrossRef] [PubMed]
43. Miao, X.; Cheng, Z.; Ma, H.; Li, Z.; Xue, N.; Wang, P. Label-free platform for microRNA detection based on the fluorescence quenching of positively charged gold nanoparticles to silver nanoclusters. *Anal. Chem.* **2018**, *90*, 1098–1103. [CrossRef] [PubMed]
44. Sun, Z.; Li, J.; Yang, Y.; Tong, Y.; Li, H.; Wang, C.; Du, L.; Jiang, Y. Ratiometric fluorescent biosensor based on self-assembled fluorescent gold nanoparticles and duplex-specific nuclease-assisted signal amplification for sensitive detection of exosomal miRNA. *Bioconjug. Chem.* **2022**, *33*, 1698–1706. [CrossRef]
45. Zhao, Q.; Piao, J.; Peng, W.; Wang, Y.; Zhang, B.; Gong, X.; Chang, J. Simple and sensitive quantification of microRNAs via PS@Au microspheres-based DNA probes and DSN-assisted signal amplification platform. *ACS Appl. Mater. Interfaces* **2018**, *10*, 3324–3332. [CrossRef]
46. Ma, H.; Xue, N.; Li, Z.; Xing, K.; Miao, X. Ultrasensitive detection of miRNA-155 using multi-walled carbon nanotube-gold nanocomposites as a novel fluorescence quenching platform. *Sens. Actuat. B Chem.* **2018**, *266*, 221–227. [CrossRef]
47. Guo, S.; Yang, F.; Zhang, Y.; Ning, Y.; Yao, Q.; Zhang, G.-J. Amplified fluorescence sensing of miRNA by combination of graphene oxide with duplex-specific nuclease. *Anal. Methods* **2014**, *6*, 3598–3603. [CrossRef]
48. Yang, Z.; Qin, L.; Yang, D.; Chen, W.; Qian, Y.; Jin, J. Signal amplification method for miR-205 assay through combining graphene oxide with duplex-specific nuclease. *RSC Adv.* **2019**, *9*, 27341–27346. [CrossRef]
49. Xiao, M.; Man, T.; Zhu, C.; Pei, H.; Shi, J.; Li, L.; Qu, X.; Shen, X.; Li, J. MoS_2 nanoprobe for microRNA quantification based on duplex-specific nuclease signal amplification. *ACS Appl. Mater. Interfaces* **2018**, *10*, 7852–7858. [CrossRef]
50. Gao, Z.; Yuan, H.; Mao, Y.; Ding, L.; Effah, C.Y.; He, S.; He, L.; Liu, L.-E.; Yu, S.; Wang, Y.; et al. In situ detection of plasma exosomal microRNA for lung cancer diagnosis using duplex-specific nuclease and MoS_2 nanosheets. *Analyst* **2021**, *146*, 1924–1931. [CrossRef]
51. Zhou, Y.; Zhang, J.; Zhao, L.; Li, Y.; Chen, H.; Li, S.; Cheng, Y. Visual detection of multiplex microRNAs using cationic conjugated polymer materials. *ACS Appl. Mater. Interfaces* **2016**, *8*, 1520–1526. [CrossRef]
52. Deng, X.; Wu, S.; Zang, S.; Liu, X.; Ma, Y. PDA—PEI-copolymerized nanodots with tailorable fluorescence emission and quenching properties for the sensitive ratiometric fluorescence sensing of miRNA in serum. *Anal. Chem.* **2022**, *94*, 14546–14553. [CrossRef]
53. Sun, Y.; Wang, C.; Tang, L.; Zhang, Y.; Zhang, G.-J. Magnetic-enhanced fluorescence sensing of tumor miRNA by combination of MNPs@PDA with duplex specific nuclease. *RSC Adv.* **2021**, *11*, 2968–2975. [CrossRef]
54. Wang, J.-J.; Zheng, C.; Jiang, Y.-Z.; Zheng, Z.; Lin, M.; Lin, Y.; Zhang, Z.-L.; Wang, H.; Pang, D.-W. One-step monitoring of multiple enterovirus 71 infection-related microRNAs using core-satellite structure of magnetic nanobeads and multicolor quantum dots. *Anal. Chem.* **2020**, *92*, 830–837. [CrossRef]
55. Yan, T.; Zhang, S.; Yang, Y.; Li, Y.; Xu, L. Biomineralizationinspired magnetic nanoflowers for sensitive miRNA detection based on exonuclease assisted target recycling amplification. *Microchim. Acta* **2022**, *189*, 260. [CrossRef]
56. Kaplan, M.; Kilic, T.; Guler, G.; Mandli, J.; Amine, A.; Ozsoz, M. A novel method for sensitive microRNA detection: Electropolymerization based doping. *Biosens. Bioelectron.* **2017**, *92*, 770–778. [CrossRef]
57. Zhang, X.; Yang, Z.; Chang, Y.; Qing, M.; Yuan, R.; Chai, Y. A novel 2D DNA nanoprobe mediated enzyme-free target recycling amplification for ultrasensitive electrochemical detection of microRNA. *Anal. Chem.* **2018**, *90*, 9538–9544. [CrossRef]

biosensors

MDPI

Article

Preparation of a Red−Emitting, Chitosan−Stabilized Copper Nanocluster Composite and Its Application as a Hydrogen Peroxide Detection Probe in the Analysis of Water Samples

Jiaojiao Lu [1], Dawei Wang [1], Xin Li [1], Wei Guo [2,*], Chunyuan Tian [1], Feng Luan [1] and Xuming Zhuang [1,*]

[1] College of Chemistry and Chemical Engineering, Yantai University, Yantai 264005, China
[2] Shandong Dyne Marine Biopharmaceutical Co., Ltd., Weihai 264300, China
* Correspondence: guodawei0298@163.com (W.G.); xmzhuang@iccas.ac.cn (X.Z.)

Abstract: Hydrogen peroxide (H_2O_2) is an important reactive oxygen species that mediates a variety of physiological functions in biological processes, and it is an essential mediator in food, pharmaceutical, and environmental analysis. However, H_2O_2 can be dangerous and toxic at certain concentrations. It is crucial to detect the concentration of H_2O_2 in the environment for human health and environmental protection. Herein, we prepared the red-emitting copper nanoclusters (Cu NCs) by a one-step method, with lipoic acid (LA) and sodium borohydride as protective ligands and reducing agents, respectively, moreover, adding chitosan (CS) to wrap LA−Cu NCs. The as-prepared LA−Cu NCs@CS have stronger fluorescence than LA−Cu NCs. We found that the presence of H_2O_2 causes the fluorescence of LA−Cu NCs@CS to be strongly quenched. Based on this, a fluorescent probe based on LA−Cu NCs@CS was constructed for the detection of H_2O_2 with a limit of detection of 47 nM. The results from this research not only illustrate that the as–developed fluorescent probe exhibits good selectivity and high sensitivity to H_2O_2 in environmental water samples but also propose a novel strategy to prepare red-emitting copper nanoclusters (Cu NCs) by a one-step method.

Keywords: copper nanoclusters; chitosan; aggregation-induced emission; fluorescent probe; hydrogen peroxide

Citation: Lu, J.; Wang, D.; Li, X.; Guo, W.; Tian, C.; Luan, F.; Zhuang, X. Preparation of a Red−Emitting, Chitosan−Stabilized Copper Nanocluster Composite and Its Application as a Hydrogen Peroxide Detection Probe in the Analysis of Water Samples. *Biosensors* **2023**, *13*, 361. https://doi.org/10.3390/bios13030361

Received: 25 January 2023
Revised: 27 February 2023
Accepted: 6 March 2023
Published: 9 March 2023

1. Introduction

Copper nanoclusters (Cu NCs), which have attracted much attention as functionalized green metal nanomaterials, have been widely studied and applied in the fields of fluorescent probes, biosensing, and cell imaging [1–3]. Different from traditional fluorescent materials (such as semiconductor quantum dots, organic dyes, and polymer microspheres), Cu NCs with ultrasmall size endow them with diversified functions, tunable fluorescence, low biological toxicity, and low cost [4–6] also prompt Cu NCs to possess broad application prospects. At present, Cu NCs can be synthesized by many generally adopted methods, such as the chemical reduction method, template method, and electrochemical method [7–9], and the prepared Cu NCs show fluorescence emission that ranges from blue to red light [10]. However, most Cu NCs show blue fluorescent emission with a short emission wavelength and a small Stokes shift. The penetrating ability of the sample is weak, and there is background signal interference, which partly damages biological samples and limits the applicability of Cu NCs as fluorescent probes for highly sensitive detection and biological analysis [11,12]. Therefore, the development of red fluorescent Cu NCs with stable performance and a large Stokes shift has always been the focus of researchers.

Chitosan (CS), a glycosaminoglycan, is a product of partial deacetylation of chitin, with a wide range of sources, and the main biomass sources are fungi, animal bones, and the shells of shrimps and crabs [13–15]. As a multifunctional polymer material, CS has various excellent properties, such as biocompatibility, biodegradability, antibacterial activity, and nontoxicity [16,17], and is regarded as a good applicable raw material in many fields,

such as the food industry, pharmaceutical industry, cosmetics, and biotechnology [18–20]. A valuable feature of CS is that its chemical structure contains many intrinsic oxygen and nitrogen functional groups, which can be used as the starting point for covalent modification or chitosan chain cross-linking. However, the poor solubility limits the further application of CS, and many studies have modified CS to prepare derivatives to improve its solubility. At present, CS can be modified by adjusting the degree of deacetylation and viscosity, introducing hydrophilic groups, and changing the solvent pH (weakly acidic) [21–23]. In addition, CS can self-assemble and combine with nanomaterials such as graphene and metal nanomaterials [24,25] through covalent bonds and hydrogen bonds, which not only expands the application of CS but also provides functionalized properties.

The proposal of the aggregation-induced emission (AIE) effect fundamentally solved the problem of luminescence quenching caused by aggregation in solution, and the majority of researchers have performed much work on AIE [26–28]. The AIE enhancement effect is also an effective means for many metal nanoclusters to enhance fluorescence. In the aggregated state, intramolecular movement is restricted, which increases the coplanarity of the fluorescent molecules and contributes to fluorescence emission [29]. Several past studies [30–32] have shown that metal clusters can also produce AIE. Combined with these studies and our experimental results, we reasonably believe that the reason for the fluorescence of LA−Cu NCs@CS is related to the AIE effect of Cu NCs. After the coating of LA−Cu NCs with chitosan, the connection between Cu NCs and its ligand is closer, to produce AIE and emit strong red fluorescence. In this study, with lipoic acid (LA) as the ligand and sodium borohydride ($NaBH_4$) as the reducing agent, LA−protected Cu NCs (LA−Cu NCs) were synthesized by a one-step method. The prepared LA−Cu NCs showed red fluorescence emission, but the stability was poor, the yield was low, and the NCs were difficult to separate and purify (Scheme 1). After adding CS, the dispersed LA−Cu NCs showed a state of aggregation, and the fluorescence intensity was increased by four times, showing AIE enhancement characteristics. Based on this, LA−Cu NCs@CS nanocomposites were prepared, and their related properties were explored. Finally, a fluorescent probe was constructed to realize the selective and sensitive detection of H_2O_2 in environmental water samples, and the limit of detection (LOD) was 47 nM in the detection range of 0.2–128 μM.

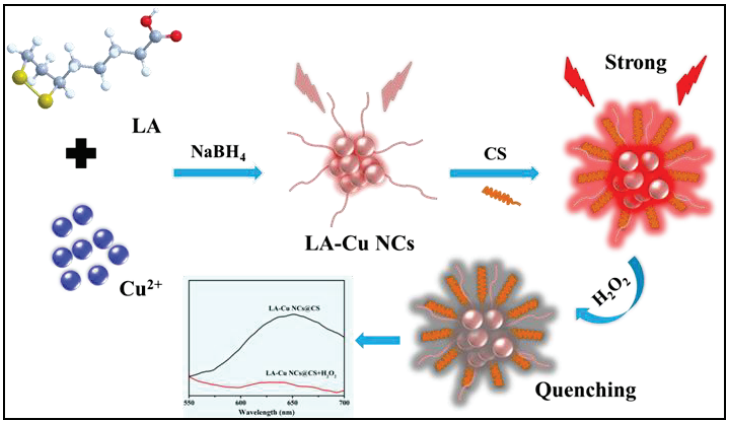

Scheme 1. The preparation of the LA−Cu NCs@CS nanocomposite and the detection principle of H_2O_2.

2. Materials and Methods

2.1. Materials

Lipoic acid (LA) and chitosan (CS) were purchased from Aladdin Reagent Co., Ltd. (Shanghai, China). Sodium borohydride ($NaBH_4$) was obtained from Kelon Chemical Reagent Co., Ltd. (Chengdu, China). Copper nitrate trihydrate ($Cu(NO_3)_2 \bullet 3H_2O$), anhy-

drous ethanol, and acetic acid were purchased from Sinopharm Chemical Reagent Co., Ltd. (Shanghai, China). Hydrogen peroxide (H_2O_2) was purchased from Beilian Fine Chemicals Development Co., Ltd. (Tianjin, China). Different metal−ionic (Ag^+, Al^{3+}, Cd^{2+}, Cr^{2+}, Cu^{2+}, Eu^{3+}, Fe^{2+}, Fe^{3+}, Hg^{2+}, Mn^{2+}, Ni^{2+}, Pb^{2+}, and Zn^{2+}) and anionic (F^- Cl^-, Br^-, I^-, S^{2-}, NO_2^{2-}, $S_2O_3^{2-}$, SO_4^{2-}, Ac^-, $[Fe(CN)_6]^{3-}$, CO_3^{2-}, and PO_4^{3-}) solutions were prepared by their respective crystal salts with the same concentration (32 μM). The tap water and lake water samples were randomly taken from the local tap water and Sanyuan Lake of Yantai University. All experimental water in this study was produced from a UPT−II−10T ultrapure water purifier (18.2 MΩ•cm). All chemical reagents were not further purified unless otherwise specified.

2.2. Apparatus

Scanning electron microscope (TEM) images were taken through a TSM-7900F electron microscope (JEOL Ltd., Tokyo, Japan). Transmission electron microscopy (TEM) and High resolution transmission electron microscope (HRTEM) images were taken through a JEM−2010 transmis XCsion electron microscope with an accelerating voltage of 200 kV (JEOL Ltd., Tokyo, Japan). Ultraviolet-visible absorption (UV-Vis) spectroscopy was obtained by a PerkinElmer Lambda 365 spectrometer (Shimfusa, Japan) with a wavelength interval of 5 nm. Fourier transform infrared (FT−IR) spectroscopy was performed using a Nicolet 5700 FT−IR spectrometer (Thermo Fisher Scientific, Waltham, MA, USA). X-ray photoelectron spectroscopy (XPS) was carried out using a Thermo ESCALAB−250 (Thermo Fisher Scient-ific, Waltham, MA, USA). The fluorescent spectrum was measured by an F−2700 spectrophotometer (Hitachi, Japan). Energy dispersive X-ray spectrometry (EDS) and EDS mapping elemental analysis were measured by an Ultim Extreme detector (Oxford Instruments Technology, Shanghai, China).

2.3. Synthesis of Nanocomposites

2.3.1. Preparation of LA−Cu NCs

Seventy−two milligrams (0.35 mmol) of LA and 14 mg (0.37 mmol) of $NaBH_4$ were accurately weighed into 16 mL ultrapure water and stirred thoroughly for 5 min at room temperature. Then, 700 μL of 25 mM $Cu(NO_3)_2$•$3H_2O$ was added to the above-mixed solution, and the color of the solution gradually changed from colorless to yellow-brown. After that, the dissolved oxygen in the mixed solution was pumped out with a vacuum pump, and then high-purity nitrogen was injected. The step was repeated three times to ensure that the oxygen was completely removed. Finally, the above-mixed solution was stirred and reacted for 6 h in an ice water bath (5–10 °C) to obtain a clear yellow-brown LA−Cu NC solution, which exhibited weak red fluorescence under 365 nm UV light. The prepared LA−Cu NC solution was stored at 4 °C for subsequent use.

2.3.2. Preparation of LA−Cu NCs@CS

The operation was to add 1.6 mL 1 mg/mL CS−1% acetic acid solution (ratio of CuNCs and CS solutions = 10:1 *v/v*) to the preprepared LA−Cu NC solution, and there was a clear yellow precipitate in the solution. After vigorously stirring for 30 min at room temperature, a large amount of aggregated precipitate was generated, which emitted obvious red fluorescence under irradiation with 365 nm UV light. After that, the same volume of absolute ethanol was added to the above-mixed solution, and ultrasonic treatment was performed for 5 min to uniformly disperse the yellow precipitate. Then, the mixture was centrifuged at 8000 rpm for 8 min, washed three times with anhydrous ethanol, and dried in a rotary evaporator at 50 °C for 1 h. The yellow powder obtained was the pure product of LA−Cu NCs@CS, which was stored at 4 °C for future use.

2.4. Construction of Fluorescent Probe Based on LA−Cu NCs@CS

First, an anhydrous ethanol solution of LA−Cu NCs@CS (2 mg mL^{-1}, pH = 7.40) was prepared, and then a series of H_2O_2 aqueous solutions with different concentrations (0.8, 2,

8, 16, 32, 64 and 128 μM) were added to 1 mL of LA−Cu NCs@CS solution. After reacting at room temperature for 5 min, the fluorescence emission spectrum was measured with fluorescence spectrophotometry. As the concentration of H_2O_2 increased, the intensity of the fluorescence spectrum showed a gradually decreasing trend, a linear curve was drawn, and a linear regression equation was obtained by fitting, which was a model of the fluorescent probe.

In addition, under optimized conditions, different methodological verifications of the fluorescent probe were also carried out. Selectivity: Explore the interference of different cations and anions on the fluorescence of LA−Cu NCs@CS; Stability: the fluorescence intensity changes of LA−Cu NCs@CS within a certain time; Reproducibility: Three parallel experiments were performed to verify that the LA−Cu NCs@CS fluorescent probe has a good response to H_2O_2.

2.5. Detection of H_2O_2 Using LA−Cu NCs@CS

To investigate the performance of the fluorescent probe in actual detection, different actual water samples were analyzed. After filtering the tap water and lake water samples with a 0.22 μm filter membrane, the fluorescent probe was used to test the tap water and lake water samples to find no H_2O_2, and then the spiked recovery method was used for H_2O_2 determination. Three groups of H_2O_2 spiked solutions of different concentrations (0.8, 8, 32 μM) were added to the treated tap water and lake water samples, and the fluorescence emission spectrum was tested after incubating at room temperature for 5 min. Three experiments were performed in parallel, and the relative standard deviation (RSD) was calculated. The measured fluorescence intensity value was substituted into the constructed linear regression equation to calculate the final spiked recovery rate.

3. Results and Discussion

3.1. Morphology of LA−Cu NCs and LA−Cu NCs@CS

Figure 1 demonstrates the morphology and nanometer size of the prepared LA−Cu NCs and LA−Cu NCs@CS by TEM and HRTEM. LA−Cu NCs showed spherical dispersion in shape with an average size of 3.1 nm (Figures 1A and S2). In the presence of CS, LA−Cu NCs appeared to aggregate in an aqueous solution, which was also confirmed by TEM. LA−Cu NCs@CS did show an aggregate state in Figure 1B. The HRTEM image (Figure 1C) showed that the single crystal lattice of LA−Cu NCs@CS was approximately 0.33 nm (3.3 Å), which corresponded to the 102 planes of Cu [30], and the average size was 3.5 nm (Figure 1D). The characterization of the morphology above showed that the successful combination of CS and LA−Cu NCs, the formation of an aggregated state, and the size distribution had not changed significantly.

3.2. Optical Performance Analysis

As shown in Figure 2A, the UV-vis spectra showed that synthesized LA−Cu NCs had a broad absorption shoulder at 250~300 nm; LA−Cu NCs@CS had a strong and broad absorption peak at approximately 300 nm. The change in the spectrum proved that the encapsulation of the LA−Cu NCs by CS caused variation in the molecular structure of the light−absorbing group, which led to a shift in the absorption peak. In the FT−IR spectra (Figure 2B), the infrared peak at 515 cm^{-1} in the curve (a) was located in the disulfide bond (−S−S−) in LA. Under alkalinity and the reduction of $NaBH_4$, the −S−S− in LA−Cu NCs was broken and bonded with the reduced Cu^{2+} to form a −S−Cu bond and the characteristic peak position was at 2509 cm^{-1} (curve c). The infrared peaks at 1060 cm^{-1}, 1066 cm^{-1}, and 3439 cm^{-1} in curve (b) were the C−O and C−O−C stretching vibration peaks and the characteristic peaks of amino ($-NH_2$) in CS, respectively. When LA−Cu NCs were encapsulated by CS, the peak position of −S−Cu (2368 cm^{-1}) was redshifted under the influence of the electron−donating group ($-NH_2$, −OH) in CS (curve d), and the infrared peak positions of other groups were unchanged.

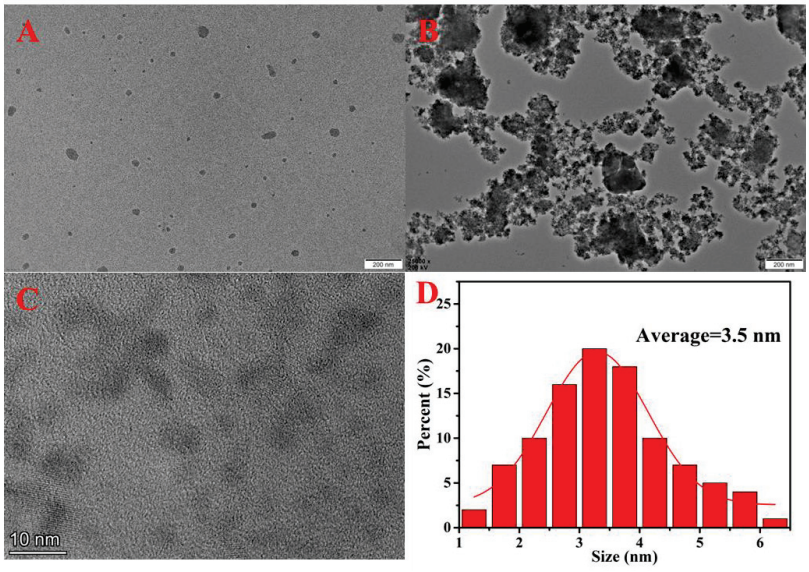

Figure 1. The TEM images of (**A**) LA−Cu NCs, (**B**) LA−Cu NCs@CS, (**C**) HRTEM image of LA−Cu NCs@CS, The diameter distributions histogram of (**D**) LA−Cu NCs@CS.

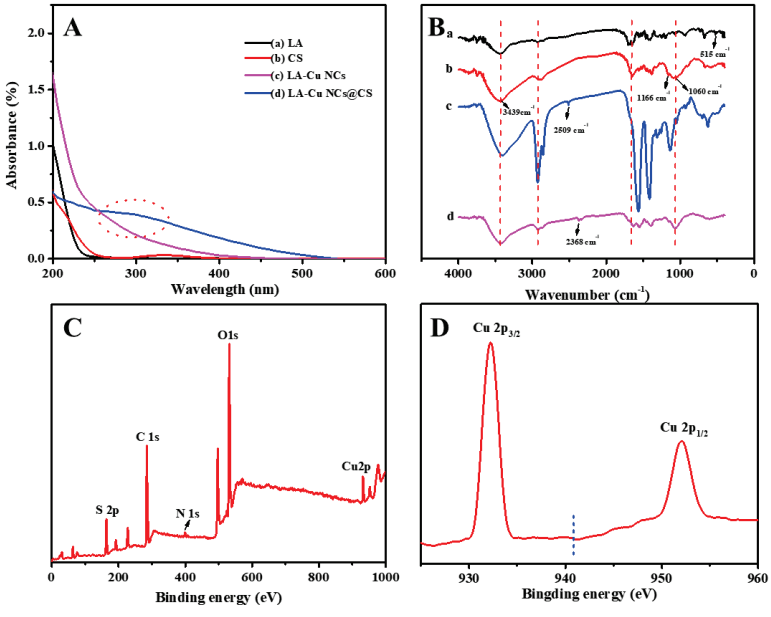

Figure 2. (**A**)The UV−vis and (**B**) FT−IR spectra of LA (a), CS (b) LA−Cu NCs (c) and LA−Cu NCs@CS (d), XPS spectra of (**C**) LA−Cu NCs@CS and (**D**) Cu 2p region.

XPS was employed to perform chemical element and valence analysis. The XPS total spectrum showed that there were five peaks of C 1 s, N 1 s, O 1 s, S 2p, and Cu 2p under the corresponding binding energy, corresponding to the existence of C, N, O, S, and Cu elements in LA−Cu NCs@CS (Figure 2C), which was consistent with expectations. In the Cu 2p spectrum (Figure 2D), the characteristic peaks at 932.2 eV and 952.3 eV were

attributed to Cu 2p3/2 and Cu 2p1/2 of Cu(0), respectively. In addition, there was no obvious absorption peak at 943.5 eV, which indicated that Cu(II) in LA−Cu NCs@CS was almost nonexistent and had been completely reduced. The difference in binding energy between Cu(0) and Cu(I) was only approximately 0.1 eV, indicating that the valence state of Cu in LA−Cu NCs@CS may be 0 or +1 [33]. In addition, the EDS spectrum clearly shows the inclusion of C, N, O, S, and Cu elements (Figure S1), which was consistent with the XPS spectrum test result, and the mapping element distribution of the characteristic elements of N, O, S, and Cu was also very uniform. In addition, EDS Mapping analysis of LA−Cu NCs@CS was performed to further verify the successful synthesis of the materials. As shown in Figure S1, the characteristic spectra of Cu, N, S and other elements can be seen from the figure, indicating that the elements in LA−Cu NCs@CS are closely combined.

As shown in Figure 3A, under different excitation wavelengths (350–440 nm), LA−Cu NCs@CS had the maximum fluorescence emission when the excitation wavelength was 400 nm. At the optimal excitation wavelength, the excitation and emission spectra of LA−Cu NCs and LA−Cu NCs@CS showed that the fluorescence emission intensity of LA−Cu NCs was relatively weak, and the fluorescence intensity became approximately four times that of the original after adding CS (Figure 3B). After CS encapsulated LA−Cu NCs to form LA−Cu NCs@CS, it triggered the aggregation of fluorophores and increased the fluorescence intensity. Figure 3C shows the fluorescence decay spectrum of LA−Cu NCs, whose fluorescence lifetime was 77.94 ns, as calculated by the weighted average method [34]. After adding CS, the fluorescence lifetime calculated by the same method was 58.03 ns (Figure 3D), which was less than that without CS. This result indicated that the presence of CS can enhance the fluorescence intensity of LA−Cu NCs.

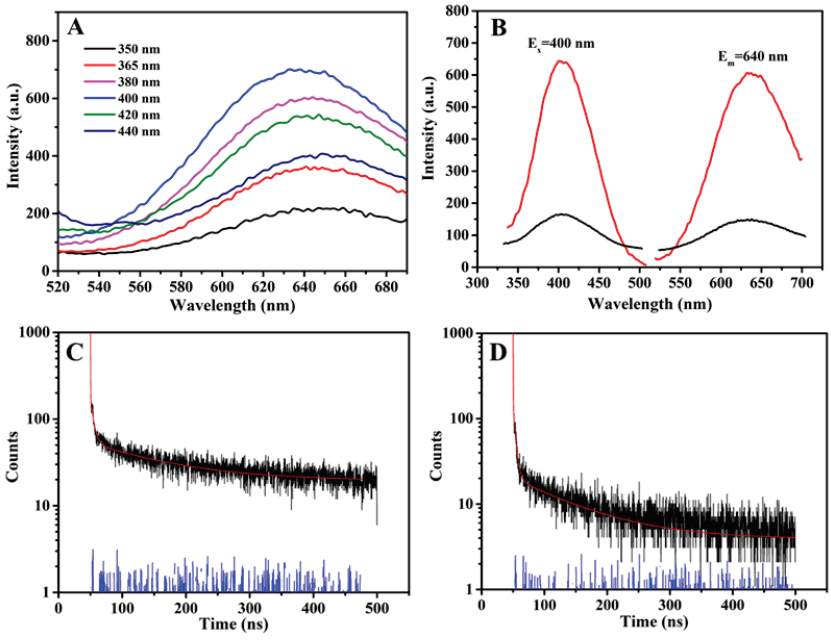

Figure 3. (**A**) Emission spectra of LA−Cu NCs@CS with different excitation wavelengths (**B**) Excitation and emission spectra of LA−Cu NCs (black line) and LA−Cu NCs@CS (red line). Time−resolved fluorescent decay spectra of (**C**) LA−Cu NCs and (**D**) LA−Cu NCs@CS.

3.3. Optimization of Conditions

During the synthesis process, the effects of different reaction conditions on the fluorescence performance of LA−Cu NCs@CS were determined, including the ratio of raw materials, reaction time, pH, and reaction temperature. Figure 4A shows the fluorescence

emission intensity of the different molar ratios of LA and Cu^{2+} (1:1, 5:1, 10:1, 20:1, and 30:1) and the volume ratios (1:1, 5:1, 10:1, 20:1, and 30:1) of the total volume of the LA−Cu NC solution under excitation at 400 nm. As the ratio of LA increased, the fluorescence intensity gradually increased, reaching a maximum of 20:1. At the same time, the fluorescence intensity was the largest when the ratio of the total volume of the LA−Cu NC solution to the volume of the CS solution was 10:1. The appropriate reaction time was not only conducive to the benign growth of LA−Cu NCs@CS molecules but could also avoid the excessive growth of the reaction time that would affect the fluorescence performance. The fluorescence emission intensity at different reaction times in Figure 4B shows that the fluorescence intensity was the maximum at 6 h, which was the time for the final reaction to prepare LA−Cu NCs@CS. The initial pH value of the synthesized LA−Cu NCs@CS was 4.14. When the pH was adjusted by adding 1 M NaOH, it was found that the fluorescence intensity changed little at pH 4–6, and the fluorescence intensity decreased significantly when the pH value was greater than 6 (Figure 4C), which indicated that the weakly acidic environment (pH = 4–6) was suitable for the synthesis of LA−Cu NCs@CS. The effect of reaction temperature on fluorescence was also further optimized. As shown in Figure 4D, as the reaction temperature increased, the fluorescence intensity decreased greatly, which demonstrated that low temperature was more suitable for the synthesis of LA−Cu NCs@CS, and the final preparation of LA−Cu NCs@CS was carried out in an ice bath environment (5–10 °C).

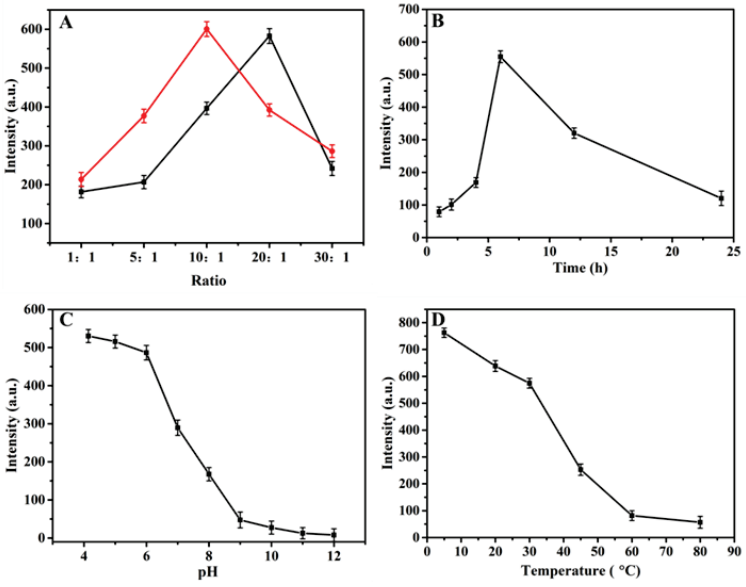

Figure 4. Optimization results of (**A**) the molar ratio of LA and Cu^{2+} (black line) and the ratio of LA−Cu NCs solution volume to CS (red line), (**B**) reaction time (25 °C), (**C**) pH value and (**D**) reaction temperature (reaction time: 6 h).

3.4. Fluorescence Response of LA−Cu NCs@CS in the Presence of H_2O_2

H_2O_2 is an important and abundant reactive oxygen species in organisms that play an important role in maintaining the physiological balance of cells in the body, and H_2O_2 has a wide range of applications in the food, environment, pharmaceutical, and textile industries. However, excessive discharge of sewage and waste liquid containing a large amount of H_2O_2 will cause harm to the environment and water resources. At present, the analysis and monitoring of H_2O_2 have always been the focus of related research. In this study, it is found that the presence of H_2O_2 will cause the fluorescence of the LA−Cu NCs@CS solution to

be significantly reduced. Therefore, the construction of a probe based on LA−Cu NCs@CS will show good prospects in the detection of H_2O_2.

Figure 5A and Table S1 show the changes in fluorescence intensity after adding a series of concentrations (0.2, 0.8, 2, 8, 16, 32, 64, and 128 μM) of H_2O_2 to LA−Cu NCs@CS for 5 min at room temperature. With increasing H_2O_2 concentration, the fluorescence intensity of LA−Cu NCs@CS showed a declining trend, and the greater the H_2O_2 concentration, the higher the fluorescence quenching degree. Figure 5B shows the linear relationship between the H_2O_2 concentration and LA−Cu NCs@CS fluorescence intensity ratio $((F_0 - F)/F_0)$. Where F_0 and F are the fluorescence intensities of the LA−Cu NCs@CS solution without H_2O_2 and with different concentrations of H_2O_2, respectively. There was a good linear relationship between LA−Cu NCs@CS and the fluorescence intensity ratio. The linear equation was $(F_0 - F)/F_0 = 0.00378C + 0.00578$ ($R^2 = 0.9941$), where C is the H_2O_2 concentration. The LOD of the probe for the H_2O_2 response was 47 nM (S/N = 3). In addition, to reflect the good detection performance of this method for H_2O_2, the detection of H_2O_2 by different methods was compared with the methods mentioned in this study. As shown in Table 1, compared with other nanomaterials [35–39], this method had a lower LOD for H_2O_2 detection. The above results showed that the fluorescent probe based on LA−Cu NCs@CS had a good performance and could achieve sensitive detection of H_2O_2. Moreover, this result was obtained by using three different hydrogen peroxide probes on the same day, which also proved that the probe had little difference in the detection performance of hydrogen peroxide during the day with acceptable RSD (2.21%).

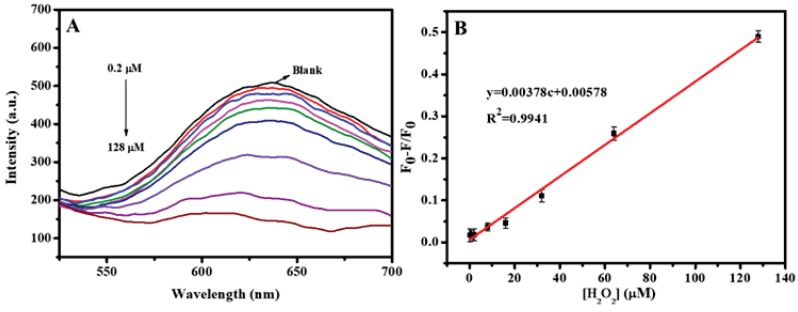

Figure 5. (**A**) The emission spectra of LA−Cu NCs@CS with increasing H_2O_2 concentration (**B**) Linear relationship between H_2O_2 concentration and LA−Cu NCs@CS FL quenching.

Table 1. Comparison of different nanomaterials for H_2O_2 detection.

Nanomaterial	Linear Range/μM	Detection Limit/μM	Ref.
carbon quantum dots	0.5~50	0.2	[35]
gold nanoclusters capped by hemoglobin	0.5~700	0.21	[36]
Fe, N−incorporated carbon nanotubes	0.1~100	0.068	[37]
naphthalene backbone and a boric acid ester	1~250	0.7	[38]
sulfonated porphyrin	1~8	0.32	[39]
LA−Cu NCs@CS	0.2~128	0.047	This work

3.5. Stability and Selectivity

Stability and selectivity experiments were performed separately to evaluate the applicability of the probe based on LA−Cu NCs@CS. Figure 6A shows the fluorescence intensity changes of LA−Cu NCs and LA−Cu NCs@CS prepared under the same conditions at

different periods after storage at room temperature for approximately five days. In the first 20 h, the fluorescence intensity of LA−Cu NCs (red line) was reduced by approximately half, and the fluorescence intensity of LA−Cu NCs@CS (black line) decreased slowly within 20 h. Even after 128 h, the fluorescence intensity was also greater than the initial value of LA−Cu NCs. From this point of view, after adding CS to LA−Cu NCs, CS might have a certain stabilizing and protective effect on LA−Cu NC molecules, and the electron−donating groups (−NH_2 and −OH) contained in CS were also beneficial to the fluorescence emission of LA−Cu NCs. It is worth noting that the difference in inner−day fluorescence intensity is slightly larger, and the relevant RSDs are between 3.77% and 4.84%. In addition, the red fluorescence intensity of the powder products of LA−Cu NCs@CS was much higher than that of LA−Cu NCs (inset a) under ultraviolet light. It is worth noting that the fluorescence intensity of the LA−Cu NCs@CS powder product under ultraviolet light hardly changed after storage for 2 months (inset b). Therefore, the addition of CS to LA−Cu NCs not only enhanced the fluorescence but also improved the stability, which provided a guarantee for practical applications.

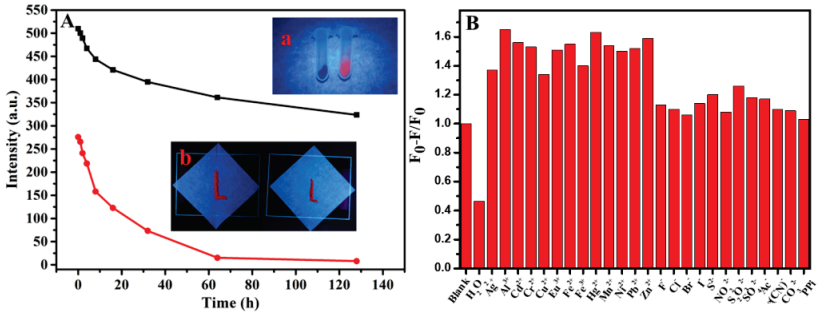

Figure 6. (**A**) The stability test of LA−Cu NCs (lower, red line) and LA−Cu NCs@CS (upper, black line), Insert: (a) Photos of the solid powder products of LA−Cu NCs (left) and LA−Cu NCs@CS (right) under UV light; (b) The photos of LA−Cu NCs@CS powder under UV light before (left) and after (right) two months. (**B**) Fluorescence responses of the fluorescence probe towards H_2O_2 and various metal ions.

Under optimized conditions, the interference of different metal ions and anions with the same concentration (32 μM) on the response of the LA−Cu NCs@CS system to H_2O_2 was explored separately. Figure 6B shows that only the fluorescence response of H_2O_2 had a significant change, and different metal ions and anions had almost no effect on the H_2O_2 probe test process, which indicated that the fluorescent probe based on LA−Cu NCs@CS had good anti-interference ability for H_2O_2 detection.

3.6. Actual Detection of H_2O_2

To verify the feasibility of the prepared fluorescent probe for H_2O_2 detection, we tested tap water and lake water samples and the presence of H_2O_2 was not detected. Then, the recovery rate was calculated using the spiked recovery method. First, the tap water and lake water were filtered with 0.22 μm membranes, and then the filtered tap water and lake water were used to prepare H_2O_2 with different concentrations (0.8, 8, and 32 μM) as the spiked samples. Finally, the linear equation of $(F_0–F)/F_0$ and H_2O_2 concentration was employed for the calculation of the final recovery rate. The spiked experiment was performed three times in parallel, and the results are shown in Table 2. The recovery rate of tap water was 95.88–98.44%, the recovery rate of lake water was 94.38–102.5%, and the total RSD ranged from 2.9% to 4.5%.

Table 2. Detection of H_2O_2 in actual water samples. (n = 3).

Samples	Added (μM)	Found (μM)	Recovery (%)	RSD (%)
Tap water	0	0	-	-
	0.80	0.767	95.88	3.6
	8.00	7.860	98.25	4.5
	32.0	31.50	98.44	3.7
Lake water	0	0	-	-
	0.80	0.755	94.38	2.9
	8.00	7.650	95.62	3.5
	32.0	32.80	102.5	3.4

Accordingly, the fluorescent probe based on LA−Cu NCs@CS had good sensitivity and selectivity, which opened up a new path for the analysis and monitoring of H_2O_2 in actual environmental water samples.

4. Conclusions

In summary, we report a novel method that is used to construct a probe for detecting H_2O_2. The as-synthesized LA−Cu NCs@CS had good nanomorphology and superior luminescence properties. The linear range of the method was from 0.2 μM to 128 μM, and the limit of detection was 47 nM. In addition, this probe exhibits strong anti-interference ability in water samples with excellent selectivity and reproducibility. Furthermore, the synthesis of LA−Cu NCs@CS was simple and environmentally friendly, inexpensive, and served as a reference for the quantitative analysis of H_2O_2 in natural water and other water samples.

Supplementary Materials: The following supporting information can be downloaded at: https://www.mdpi.com/article/10.3390/bios13030361/s1, Figure S1: The EDS image of LA−CuNCs@CS; Figure S2: The diameter distribution histogram of LA−Cu NCs.; Table S1: The corresponding fluorescence intensity under different concentrations of H_2O_2 from Figure 5A. Equation (S1): The equation to calculate the LOD.

Author Contributions: Conceptualization, J.L. and D.W.; methodology, J.L., D.W. and X.L.; software, X.L., F.L., C.T. and X.Z.; validation, J.L., D.W., X.L. and X.Z.; formal analysis, J.L., C.T. and D.W.; investigation, J.L., D.W. and X.L.; resources, W.G., F.L. and X.Z.; writing—original draft preparation, J.L., D.W. and X.L.; writing—review and editing, W.G., C.T., F.L. and X.Z. All authors have read and agreed to the published version of the manuscript.

Funding: This work was financially supported by the National Natural Science Foundation of China (21778047), and Natural Science Foundation of Shandong Province (ZR2021MB024).

Institutional Review Board Statement: Not applicable.

Informed Consent Statement: Not applicable.

Data Availability Statement: Not applicable.

Conflicts of Interest: The authors declare no conflict of interest.

References

1. Benavides, J.; Quijada-Garrido, I.; García, O. The synthesis of switch-off fluorescent waterstable copper nanocluster Hg^{2+} sensors via a simple one-pot approach by an in situ metal reduction strategy in the presence of a thiolated polymer ligand template. *Nanoscale* **2020**, *12*, 944–955. [CrossRef] [PubMed]
2. Wang, Z.G.; Shi, Y.; Yang, X.M.; Xiong, Y.; Li, Y.X.; Chen, B.K.; Lai, W.F.; Rogach, A.L. Water-soluble biocompatible copolymer hypromellose grafted chitosan able to load exogenous agents and copper nanoclusters with aggregation-induced emission. *Adv. Funct. Mater.* **2018**, *28*, 1802848. [CrossRef]
3. Liu, X.; Astruc, D. Atomically precise copper nanoclusters and their applications. *Coord. Chem. Rev.* **2018**, *359*, 112–126. [CrossRef]
4. Hu, X.; Liu, X.D.; Zhang, X.D.; Chai, H.X.; Huang, Y.M. One-pot synthesis of the CuNCs/ZIF−8 nanocomposites for sensitively detecting H_2O_2 and screening of oxidase activity. *Biosens. Bioelectron.* **2018**, *105*, 65–70. [CrossRef]

5. Zhang, D.D.; Hu, J.; Yang, X.Y.; Wu, Y.X.; Su, W.M.; Zhang, C.Y. Target-initiated synthesis of fluorescent copper nanoparticles for the sensitive and label-free detection of bleomycin. *Nanoscale* **2018**, *10*, 11134–11142. [CrossRef]
6. Lai, W.F.; Wong, W.T.; Rogach, A.L. Development of copper nanoclusters for in vitro and in vivo theranostic applications. *Adv. Mater.* **2020**, *32*, 1906872. [CrossRef]
7. Wei, W.T.; Lu, Y.Z.; Chen, W.; Chen, S.W. One-pot synthesis, photoluminescence, and electrocatalytic properties of subnanometer-sized copper clusters. *J. Am. Chem. Soc.* **2011**, *133*, 2060–2063. [CrossRef]
8. Ye, T.; Li, C.Y.; Su, C.; Ji, X.H.; Zheng, J.; Tinnefeld, P.; He, Z.K. Enzymatic polymerization of poly(thymine) for the synthesis of copper nanoparticles with tunable size and their application in enzyme sensing. *Chem. Commun.* **2015**, *51*, 8644–8647. [CrossRef]
9. Vilar−Vidal, N.; Blanco, M.C.; López-Quintela, M.A.; Rivas, J.; Serra, C. Electrochemical synthesis of very stable photoluminescent copper clusters. *J. Phys. Chem. C* **2010**, *114*, 15924–15930. [CrossRef]
10. Guo, Y.M.; Cao, F.P.; Lei, X.L.; Mang, L.H.; Cheng, S.J.; Song, J.T. Fluorescent copper nanoparticles: Recent advances in synthesis and applications for sensing metal ions. *Nanoscale* **2016**, *8*, 4852–4863. [CrossRef]
11. Zhao, T.; He, X.W.; Li, W.Y.; Zhang, Y.K. Transferrin−directed preparation of red−emitting copper nanoclusters for targeted imaging of transferrin receptor over-expressed cancer cells. *J. Mater. Chem. B* **2015**, *3*, 2388–2394. [CrossRef] [PubMed]
12. Aparna, R.S.; Anjali Devi, J.S.; Anjana, R.R.; Nebu, J.; George, S. Zn(II) ion modulated red emitting copper nanocluster probe for the fluorescence turn on sensing of RDX. *Sens. Actuators B Chem.* **2019**, *291*, 298–305. [CrossRef]
13. Sahariah, P.; Másson, M. Antimicrobial chitosan and chitosan derivatives: A review of the structure-activity relationship. *Biomacromolecules* **2017**, *18*, 3846–3868. [CrossRef]
14. Khoushab, F.; Yamabhai, M. Chitin research revisited. *Mar. Drugs* **2010**, *8*, 1988–2012. [CrossRef] [PubMed]
15. Younes, I.; Rinaudo, M. Chitin and chitosan preparation from marine sources. Structure, properties and applications. *Mar. Drugs* **2015**, *13*, 1133–1174. [CrossRef] [PubMed]
16. Kumar, M.N.; Muzzarelli, R.A.; Muzzarelli, C.; Sashiwa, H.; Domb, A.J. Chitosan chemistry and pharmaceutical perspectives. *Chem. Rev.* **2004**, *104*, 6017–6084. [CrossRef] [PubMed]
17. Jaafari, J.; Barzanouni, H.; Mazloomi, S.; Farahani, N.A.A.; Sharafi, K.; Soleimani, P.; Haghighat, G.A. Effective adsorptive removal of reactive dyes by magnetic chitosan nanoparticles: Kinetic, isothermal studies and response surface methodology. *Int. J. Biol. Macromol.* **2020**, *164*, 344–355. [CrossRef]
18. Wang, H.X.; Qain, J.; Ding, F.Y. Emerging chitosan-based films for food packaging applications. *J. Agric. Food Chem.* **2018**, *66*, 395–413. [CrossRef]
19. Liu, Y.; Yu, Z.L.; Zhang, Y.M.; Guo, D.S.; Liu, Y.P. Supramolecular architectures of β-cyclodextrin-modified chitosan and pyrene derivatives mediated by carbon nanotubes and their DNA condensation. *J. Am. Chem. Soc.* **2008**, *130*, 10431–10439. [CrossRef]
20. Mahanta, A.K.; Maiti, P. Injectable hydrogel through hydrophobic grafting on chitosan for controlled drug delivery. *ACS Appl. Bio. Mater.* **2019**, *2*, 5415–5426. [CrossRef]
21. Sajomsang, W. Synthetic methods and applications of chitosan containing pyridylmethyl moiety and its quaternized derivatives: A review. *Carbohydr. Polym.* **2010**, *80*, 631–647. [CrossRef]
22. Dowling, M.B.; Kumar, R.; Keibler, M.A.; Hess, J.R.; Bochicchio, G.V.; Raghavan, S.R. A self-assembling hydrophobically modified chitosan capable of reversible hemostatic action. *Biomaterials* **2011**, *32*, 3351–3357. [CrossRef] [PubMed]
23. Bakshi, P.S.; Selvakumar, D.; Kadirvelu, K.; Kumar, N.S. Comparative study on antimicrobial activity and biocompatibility of N−selective chitosan derivatives. *React. Funct. Polym.* **2018**, *124*, 149–155. [CrossRef]
24. Liang, Y.P.; Zhao, X.; Hu, T.L.; Han, Y.; Guo, B.L. Mussel−inspired, antibacterial, conductive, antioxidant, injectable composite hydrogel wound dressing to promote the regeneration of infected skin. *J. Colloid Interface Sci.* **2019**, *556*, 514–528. [CrossRef]
25. Pan, J.; Zhang, Z.; Zhan, Z.Y.; Xiong, Y.F.; Wang, Y.F.; Cao, K.Y.; Chen, Y.J. In situ generation of silver nanoparticles and nanocomposite films based on electrodeposition of carboxylated chitosan. *Carbohydr. Polym.* **2020**, *242*, 116391. [CrossRef]
26. Gao, T.; Huang, X.Y.; Huang, S.; Dong, J.; Yuan, K.; Feng, X.P.; Liu, T.T.; Yu, K.Q.; Zeng, W.B. Sensitive water-soluble fluorescent probe based on umpolung and aggregation-induced emission strategies for selective detection of Hg^{2+} in living cells and zebrafish. *J. Agric. Food Chem.* **2019**, *67*, 2377–2383. [CrossRef]
27. Li, J.; Wang, J.X.; Li, H.X.; Song, N.; Wang, D.; Tang, B.Z. Supramolecular materials based on AIE luminogens (AIEgens): Construction and applications. *Chem. Soc. Rev.* **2020**, *49*, 1144–1172. [CrossRef]
28. Mei, J.; Leung, N.L.C.; Kwok, R.T.K.; Lam, J.W.Y.; Tang, B.Z. Aggregation-induced emission: Together we shine, united we soar! *Chem. Rev.* **2015**, *115*, 11718–11940. [CrossRef]
29. Hong, Y.N.; Lam, J.W.Y.; Tang, B.Z. Aggregation-induced emission. *Chem. Soc. Rev.* **2011**, *40*, 5361–5388. [CrossRef]
30. Goswami, N.; Yao, Q.; Luo, Z.; Li, J.; Chen, T.; Xie, J. Luminescent Metal Nanoclusters with Aggregation-Induced Emission. *J. Phys. Chem. Lett.* **2016**, *7*, 6, 962–975. [CrossRef]
31. Wu, Z.; Liu, J.; Gao, Y.; Liu, H.; Li, T.; Zou, H.; Wang, Z.; Zhang, K.; Wang, Y.; Zhang, H.; et al. Assembly-Induced Enhancement of Cu Nanoclusters Luminescence with Mechanochromic Property. *J. Am. Chem. Soc.* **2015**, *137*, 12906–12913. [CrossRef]
32. Hu, X.; Mao, X.X.; Zhang, X.D.; Huang, Y.M. One-step synthesis of orange fluorescent copper nanoclusters forsensitive and selective sensing of Al^{3+} ions in food samples. *Sens. Actuators B Chem.* **2017**, *247*, 312–318. [CrossRef]
33. Lin, L.Y.; Hu, Y.F.; Zhang, L.L.; Huang, Y.; Zhao, S.L. Photoluminescence light-up detection of zinc ion and imaging in living cells based on the aggregation induced emission enhancement of glutathionecapped copper nanoclusters. *Biosens. Bioelectron.* **2017**, *94*, 523–529. [CrossRef] [PubMed]

34. Tu, X.J.; Chen, W.B.; Guo, X.Q. Facile one-pot synthesis of near-infrared luminescent gold nanoparticles for sensing copper (II). *Nanotechnology* **2011**, *22*, 095701. [CrossRef] [PubMed]
35. Zhang, Y.M.; Yang, X.J.; Gao, Z.Q. In situ polymerization of aniline on carbon quantum dots: A new platform for ultrasensitive detection of glucose and hydrogen peroxide. *RSC Adv.* **2015**, *5*, 21675–21680. [CrossRef]
36. Molaabasi, F.; Hosseinkhani, S.; Moosavi-Movahedi, A.A.; Shamsipur, M. Hydrogen peroxide sensitive hemoglobin-capped gold nanoclusters as a fluorescence enhancing sensor for the label-free detection of glucose. *RSC Adv.* **2015**, *5*, 33123–33135. [CrossRef]
37. Zhang, R.Z.; He, S.J.; Zhang, C.M.; Chen, W. Three-dimensional Fe− and N-incorporated carbon structures as peroxidase mimics for fluorescence detection of hydrogen peroxide and glucose. *J. Mater. Chem. B* **2015**, *3*, 4146–4154. [CrossRef]
38. Ma, Q.J.; Li, X.; Zhang, J.; Zhu, X.Y.; Zhou, L.Y.; Liu, H.W. A novel two-photon fluorescent probe for the selective detection of hydrogen peroxide based on a naphthalene derivative. *Anal. Methods* **2017**, *9*, 4558–4565. [CrossRef]
39. Huan, Y.F.; Fei, Q.; Shan, H.Y.; Wang, B.J.; Hu, H.; Feng, G.D. A novel water-soluble sulfonated porphyrin fluorescence sensor for sensitive assays of H_2O_2 and glucose. *Analyst* **2015**, *140*, 1655–1661. [CrossRef]

biosensors

MDPI

Article

Insights into the Mechanism of Bipolar Electrodeposition of Au Films and Its Application in Visual Detection of Prostate Specific Antigens

Daoyuan Zhao [1], Yujing Liu [2], Hong Jiang [2], Haijian Yang [1], Huihui Yu [1], Jingtang Qiao [1], Zhiwen Li [1], Bing Jin [1,*] and Meisheng Wu [1,*]

[1] Department of Chemistry, College of Sciences, Nanjing Agricultural University, 1 Weigang, Nanjing 210095, China
[2] College of Life Sciences, Nanjing Agricultural University, 1 Weigang, Nanjing 210095, China
* Correspondence: jinbing@njau.edu.cn (B.J.); wumeisheng@njau.edu.cn (M.W.)

Abstract: Au particles are commonly used for deposition on the surface of a bipolar electrode (BPE) in order to amplify electrochemical and electrochemiluminescence (ECL) signal because of their excellent conductivity, biocompatibility, and large surface area. In this work, a closed BPE device was fabricated and Au particles were deposited on the two poles of a BPE via bipolar deposition. Results indicated that the electrochemical stability of Au film on the anode part of the BPE and the reduction of $AuCl_4^-$ to Au on the cathode part of the BPE depended on the conductivity of the solution. The prepared Au–Au BPE exhibited a remarkable amplification effect on the ECL signal. Then, a specific sensing interface was constructed on one pole of the BPE for the visual detection of prostate-specific antigens (PSA) based on sandwich-type immunoreactions between primary PSA antibodies (Ab_1) on the electrode surface, PSA, and SiO_2 nanoparticles labeled secondary PSA antibodies (SiO_2-Ab_2). The designed biosensor exhibited a good linear relationship for the ECL detection of PSA in the range of 1×10^{-6} to 1×10^{-10} g/mL with a correlation coefficient of 0.9866; the limit of detection (LOD) was 1.5×10^{-11} g/mL. Additionally, the biosensor can realize the electrochemical imaging of PSA by regulating the electrochemical oxidation of the Au anode with the immunoreactions on the cathode part of BPE. Therefore, the small, portable and highly sensitive biosensors have great potential for on-site detection.

Keywords: bipolar electrode; ECL imaging; electrochemical imaging; electrochemical dissolution; biosensor

Citation: Zhao, D.; Liu, Y.; Jiang, H.; Yang, H.; Yu, H.; Qiao, J.; Li, Z.; Jin, B.; Wu, M. Insights into the Mechanism of Bipolar Electrodeposition of Au Films and Its Application in Visual Detection of Prostate Specific Antigens. *Biosensors* **2023**, *13*, 158. https://doi.org/10.3390/bios13020158

Received: 14 December 2022
Revised: 11 January 2023
Accepted: 16 January 2023
Published: 19 January 2023

1. Introduction

Bipolar electrochemistry devices, as a newly emerging analytical approach, have attracted significant attention because of their easy fabrication, high sensitivity, low production cost, etc. [1–6]. A bipolar electrode is a conductor situated in solution; it has no direct electrical connection with an external power source. When an electric field is applied to the solution, a potential difference is generated between the conductor and the solution on its surface. Therefore, one end of the conductor becomes the anode, and the other end becomes the cathode, namely bipolar electrodes (BPEs). According to the current flow path, BPE devices can be divided into open BPEs and closed BPEs [7,8]. In closed BPEs, the anode and the cathode of the BPE are immersed into two electrochemical cells which enable the specific modifications of one pole of the BPE and avoid the chemical interference between the two solutions.

In recent years, visualized detection of the current changes in BPEs using imaging technology has attracted great attention [9–12]. For example, Liu et al. constructed a multicolor electrochemiluminescence (ECL)-BPE device for visualized sensing of Salmonella typhimurium [13]. Cheng has developed a novel ratiometric ECL-BPE device for miRNA-21 measurement by introducing mesoporous silica nanoparticles (NPs) at the cathode of the

BPE as a molecular gating system to amplify the cathodic ECL signal [14]. To achieve a visual readout of target, it is essential to integrate signal amplification strategies into the BPE system.

Since the only way that the current can pass through the two electrochemical cells in closed BPE devices is by BPE, many efforts have been made to improve the electrochemical signal at the anode of BPEs, such as changing the electrochemical reactions that occur at the cathode of BPEs [11] and introducing electroactive species and catalysts on the cathode of BPEs [15–17] to increase the current [18], catalyze the redox reactions of the BPEs [19], and decrease the onset voltage for driving the redox reactions occurring at BPEs [20,21]. For example, Xu and coworkers have developed an enhancement strategy to detect prostate-specific antigen (PSA) through a BPE-ECL approach [22]. By immobilizing the thionine@ SiO_2 NPs at a BPE's cathode and the Au nanoparticles at its anode through DNA hybridization, the ECL signal was improved approximately five-fold compared with that of a bare indium tin oxide (ITO) electrode.

Besides the above catalysts, Au NPs are extensively used in BPE devices due to their good electrical conductivity, high catalytic activity, and large specific surface area [5,16,23,24]. For example, Ge and coworkers have constructed an Au BPE by growing an Au NPs layer in situ on the surfaces of cellulose fibers to improve the BPE's conductivity [23]. In addition, they constructed a biosensing interface with AuPd NPs tags at the cathode of the bipolar electrode which can catalyze a H_2O_2 reduction reaction, causing significant enhancement of the ECL signal at the anode. The designed biosensor enables the measurement of miRNA-155 in the range of 1 pM–10 μM, with a detection limit of 0.67 pM. Ding's group introduced patchy gold coated Fe_3O_4 hybrid nanoparticles on Au NPs-modified cathode in immunoreaction [24]. The biosensor achieved sensitive detection of carcinoembryonic antigen (CEA) with a low detection limit of 0.03 pg/mL. However, little attention has been paid to improve the sensitivity of BPE-ECL device by modifying Au NPs on both poles of BPE. This is because Au NPs on the anode of BPE may undergo electrochemical oxidation under high voltage, thereby reducing the stability and reproducibility of the BPE. Therefore, improving the stability of the gold film in the BPE system is one of the challenges in further improving the sensitivity of BPE systems.

Inspired by these, we designed a portable ECL-BPE device and attempted to fabricate a Au (cathode)-Au (anode) BPE through bipolar deposition. The oxidation conditions of the Au anode and the deposition conditions of the Au particles on the cathode of the BPE were studied in detail by adjusting the solution in the anodic reservoir. The amplification effect and the reproducibility of the prepared BPE were evaluated by ECL imaging. Then, a sandwich-type immunointerface was constructed on the cathode of the BPE by using SiO_2-Ab_2 as the recognition probe. In the presence of PSA, SiO_2-Ab_2 was bound to electrode surface, leading to an inhibited ECL signal at the anode of the BPE due to the increased resistance. Additionally, the PSA could be visualized using the electrochemical imaging method based on the resistance-modulated oxidation of the Au film on the anode.

2. Materials and Methods

2.1. Reagents

Chloroauric acid ($HAuCl_4$), N-(3-(Dimethylamino)propyl)-N′-ethylcarbodiimide hydrochloride (EDC), N-hydroxysuccinimide (NHS), and $Ru(bpy)_3^{2+}$ were purchased from Sinopharm Chemical Reagent Company (Shanghai, China). L-Cysteine was purchased from Sinopharm chemical reagent company (Shanghai, China). Total prostate-specific antigen (PSA) and PSA antibodies were purchased from Linc-Bio Science (Shanghai, China). SiO_2 nanoparticles modified with KH550 (20 nm) were purchased from Nanjing Xianfeng Nano Co. (Nanjing, China). A 10 mM PBS buffer solution (pH 7.4) was purchased from KeyGEN Bio-Technology Co., Ltd. (Taixing, China). Sylgard 184 (including a polydimethylsiloxane (PDMS) monomer and curing agent) was purchased from Dow Corning (Midland, MI, USA). Graphite paper (GP) was purchased from Jing Long TeTan Co., Ltd. (Beijing, China).

2.2. Instruments

The voltage applied on the driving electrodes was supplied by a CHI 660E electrochemical workstation (Shanghai Chenhua instrument, Shanghai, China). A MS23 CCD camera was used to capture images and movies (Guangzhou Mingmei Technology Co., Ltd., Guangzhou, China). The conductivity meter used (DDS-307A) was purchased from INESA Scientific Instrument Co., Ltd., Shanghai, China.

2.3. Bipolar Deposition

A closed BPE device was designed by placing graphite paper (GP, length of 2 cm, width of 1 cm) on a flat PDMS slice and then covering it with two layers of PDMS slices (Scheme S1). Two holes were punched in each PDMS slice as reservoirs. The diameter of holes on the second PDMS slice was 3 mm, with a gap of 2 mm. The diameter of the holes on the top layer was 7 mm, with a gap of 1 mm. After that, two Pt wires were placed on the top of the second PDMS slice and connected with CHI 660E to perform the bipolar deposition of Au.

Bipolar deposition of Au particles at the two poles of BPE was carried out in two steps. First, 100 μL of 5 mM $HAuCl_4$ was introduced into the right reservoir and 100 μL of PBS (10 mM, pH 7.4) was added into the left reservoir. A constant voltage of 4.5 V was applied for 300 s, using an amperometric i-t curve technique. After finishing the deposition, the solutions were removed and the GP was washed with water three times. Second, the direction of the electric field was reversed. The left reservoir was filled with 5 mM $HAuCl_4$ and the right reservoir was filled with different solutions such as water, various concentrations of PBS, KCl, HCl, and $HAuCl_4$. A constant voltage of 4.5 V was applied for 300 s. Movies and images were taken by a CCD camera at the same time. In order to study the mechanism, a linear sweep voltage (LSV) from 0 to 5.5 V at a scan rate of 0.005 V/s was applied to the driving electrodes. Images were taken every 1 min and when the current exhibited remarkable change.

2.4. Fabricating of Specific Sensing Interface for PSA Assay

The left pole of GP BPE was first modified with Au particles by adding 100 μL of 5 mM $HAuCl_4$ in the left reservoir, PBS in the left reservoir and a constant voltage of 4.5 V for 300 s. Then, the right pole of the BPE was modified with Au particles by applying 4.5 V for 200 s, and the two reservoirs were filled with 5 mM $HAuCl_4$. The left reservoir was filled with 0.175 M L-cysteine at room temperature for 10 h. Then, the carboxyl group at the Au surface was activated by the mixture solution of 7.0 mg/mL EDC and 21.0 mg/mL NHS. After rinsing with PBS, 20 μL of primary PSA antibody (Ab_1) was introduced and incubated at 4 °C overnight. Then, 0.2% BSA was added to block the unreacted sites on Au NPs at 37 °C for 1 h in order to avoid non-specific adsorption. The modified electrode was then incubated with different concentrations of PSA. After washing with PBS, 20 μL of SiO_2-modified secondary PSA antibody (SiO_2-Ab_2) was introduced and reacted at 37 °C for 1 h. Finally, the electrode was washed with PBS, and a sandwich immunocomplex was formed at the right pole of BPE.

2.5. ECL Imaging

The left reservoir was filled with 50 mM H_2O_2 (PBS) and the right reservoir was filled with the mixture solution of 10 mM $Ru(bpy)_3^{2+}$ and 100 mM 2-(Dibutylamino) ethanol (DBAE). A constant voltage of 3.5 V was applied and the ECL images were captured by the CCD camera. The exposure time was 7 s.

2.6. Electrochemical Imaging

For the visual assay of PSA based on the oxidative electrodissolution of the Au anode, the left reservoir was filled with 100 μL of 50 mM H_2O_2 (PBS) and the right reservoir was filled with 100 μL of PBS. The external voltage was set at 3.0 V to drive the dissolution of Au film in the right reservoir.

3. Results and Discussion

3.1. Bipolar Deposition of Au on Two Poles of BPE

In our study, both ends of a graphite paper (anode and cathode) were exposed to different solutions; this can effectively avoid the chemical interference of the solutions. Through this configuration, different interfaces can be constructed on the anode and cathode of the device. For example, a signal amplification unit can be constructed at one end, and a sensing interface can be constructed at the other end for the specific detection of target substances. Gold was electrodeposited on both ends of the bipolar electrode by two-step electrodeposition. First, Au particles were deposited on one end of the electrode by bipolar electrodeposition. Then, the direction of the applied electric field was changed, and Au particles were deposited at the other end. At the same time, the factors affecting the electrochemical stability of gold films and the electrodeposition of gold were investigated. Finally, the Au (cathode)-Au (anode) bipolar electrode was used for the visualization of prostate-specific antigen (PSA).

The detailed construction process of the closed bipolar electrode device was described as the following. Two Pt wires were placed on the top of the middle PDMS slice and were connected to a power source. We plated Au particles at the GP surface in the right reservoir, under voltages ranging from 3.0 to 5.5 V, by filling reservoir-1 (anode) with 10 mM PBS, and reservoir-2 (cathode) with $HAuCl_4$ (Figure 1A). The reduction of $HAuCl_4$ at the BPE cathode in reservoir-2 was coupled with the oxidation of H_2O at the BPE anode in reservoir-1. Figure 1B shows that the GP color (in reservoir-2) gradually turned yellow with the increase in external voltage. However, the left reservoir's GP was damaged (as pointed out by the red arrow) when the voltage was 5.5 V. Additionally, a lot of bubbles could be observed escaping from the Au surface due to the reduction of H^+, when the voltage was 5.0 V, which resulted in the formation of a porous Au film. Therefore, 4.5 V was chosen as the optimal voltage for the bipolar deposition of Au.

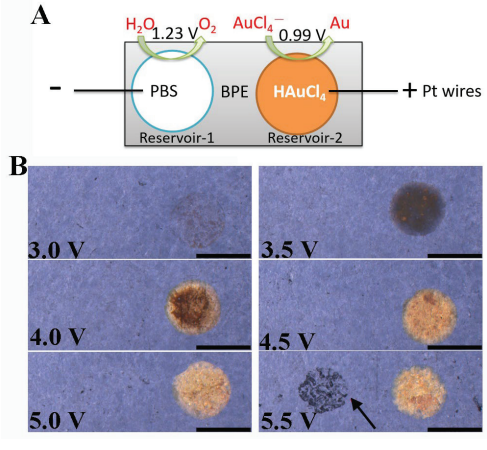

Figure 1. Bipolar electrodeposition of Au particles on one pole of the GP BPE. (**A**) Schematic representation of bipolar deposition of Au on one pole of GP BPE. (**B**) Optical images of Au film obtained under various external voltages from 3.0 to 5.5 V for 300 s. The concentration of $HAuCl_4$ was 5 mM. The black arrow indicates the corrosion of GP in the right reservoir; the scale bar represents 3 mm.

After washing the prepared Au-modified BPE with water, we reversed the direction of the electric field and exchanged the solutions in these two reservoirs for the deposition of Au film on the left GP surface. We applied 4.5 V to the driving electrodes for 5 min. Figure 2A and Video S1 (×5 frame rate) show that Au particles were produced in the left reservoir with a lot of bubbles, indicating that both $AuCl_4^-$ and H^+ were reduced at

the BPE cathode (see Figure 2B for the reactions). For the anodic pole (right), water was oxidized before the Au film, because the voltage needed to drive the oxidation of water is lower than that of the Au film (Figure 2B). However, the results of Figure 2A revealed that the Au film was promptly decomposed, it disappeared within 93 s (Video S1). Once the Au completely disappeared, the current was significantly decreased and then reached a steady state (Figure S1, curve a, in Supplementary Material). This result suggested that 4.5 V was too high. We then decreased the external voltage to 3.0 V (Figure 2A). Unfortunately, the Au film was dissolved again. Additionally, the speed of Au particles' disappearance and the number of bubbles produced at the cathode's surface also decreased.

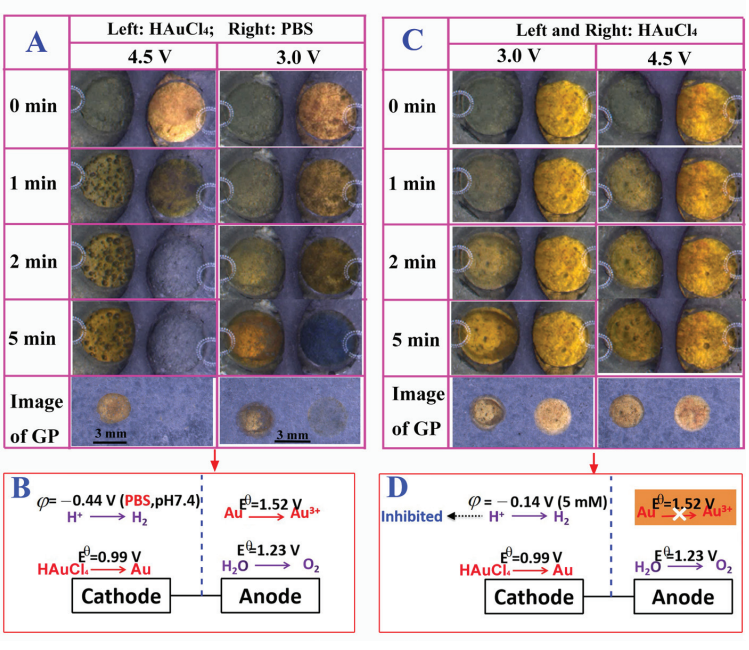

Figure 2. Deposition of Au particles on GP in the left reservoir. GP in the right reservoir was pre-modified with Au particles under 4.5 V for 300 s through bipolar deposition. (**A**) The left reservoir was filled with 5 mM $HAuCl_4$, and the right reservoir was filled with 10 mM PBS. (**B**) Redox reactions occurred at the two poles of the BPE in (**A**). (**C**) Both reservoirs were filled with 5 mM $HAuCl_4$. (**D**) Redox reactions occurred at the two poles of the BPE in (**C**). The deposition time was 300 s.

The above results showed that it is difficult to electrodeposit Au particles on both ends of the bipolar electrode. However, in the previous work, we successfully adopted a two-step bipolar electrodeposition method to electrodeposit gold and platinum on its two ends, using carbon spheres as the BPE [25]. Compared with the current method, an open system was used in previous work wherein both the anode and cathode of the BPE were immersed in the same solution for electrodeposition. In the current work, the end of the BPE that needed to be gold-plated was immersed in $HAuCl_4$, and the anode of the BPE that did not need to be gold-plated was immersed in PBS. To understand whether the solution had an impact on the BPE's electrochemical reactions, we replaced the PBS in the right reservoir (anode) with $HAuCl_4$ during the second bipolar deposition process (Figure 2C). To our surprise, the Au film in the right reservoir showed no significant change, and bright yellow Au could be observed on the GP surface in the left reservoir (cathode) after 2 min. Even when a high voltage was applied (4.5 V) (Figure 2C, Video S2, ×10 frame rate), the Au film at the right reservoir (anode) still maintained its original color, and the Au deposition rate in the left reservoir (cathode) increased. By comparing the videos (Videos S1 and S2)

and images (Figure 2A,C) captured at 4.5 V, it was found that a lower number of bubbles were produced on the cathodic BPE filled with $HAuCl_4$ than those filled with PBS. This difference indicated that the reduction of protons at the cathode and the oxidation of Au at the BPE anode were greatly inhibited (Figure 2D) when PBS was replaced with $HAuCl_4$. In this case, the fact that only water could be oxidized at the BPE anode suggested that the voltage at both the BPE poles was decreased insufficiently to drive the oxidation of Au at the anode. Furthermore, the amperometric i–t curve obtained from electrodes exposed to $HAuCl_4$ was very stable after approximately 40 s (curve b in Figure S1), which was different from that obtained from the electrode exposed to PBS (curve a in Figure S1).

We speculated that the factors that influence the deposition procedure included the pH and the conductivity of the solution. To verify our speculation and understand the influence of these factors on the electrochemical reaction on BPE, we replaced the right liquid reservoir with a series of different candidate solutions to carry out the next experiment. $HAuCl_4$ solution was used in the left reservoir in the experiment. To investigate the effect of pH, the second-step electrodeposition was performed by using HCl solution (acidic) and KCl solution (neutral) at the right reservoir. Figure 3 shows the images of Au deposition in the second step captured before (0 min) and after (5 min). When the right reservoir was filled with either HCl or KCl solution, the colors of the Au film exhibited no significant change (at both 0 and 5 min), and Au was successfully deposited on the left GP surface (Figure 3). The result suggested that the oxidation of Au observed previously was not caused by the pH value.

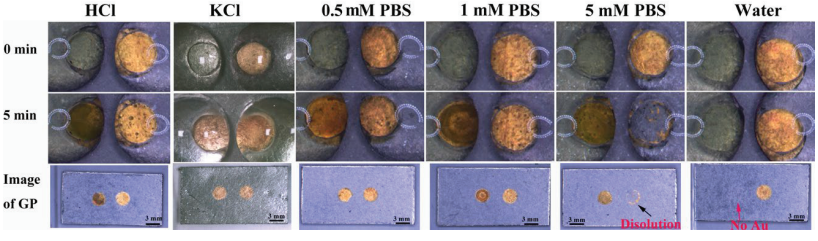

Figure 3. Deposition of Au at the cathode in the left reservoir. The anode was pre-deposited with Au at 4.5 V for 300 s. The left reservoirs were filled with 5 mM $HAuCl_4$. The right reservoir was filled with 5 mM HCl and 5 mM KCl, respectively. The right reservoir was filled with ultra-pure water and different concentrations of PBS. Solutions were prepared with ultra-pure water unless otherwise specified.

Different concentrations of PBS solutions were used to study the effect of solution conductivity on the electrochemical reaction on the bipolar electrodes (Table S1). The right reservoir was filled with water, 0.5 mM PBS, 1 mM PBS, and 5 mM PBS. The left reservoir was filled with a 5 mM $HAuCl_4$ solution. As shown in Figure 3, Au was deposited on the left GP without any significant change from the right reservoir's Au film when 0.5 and 1 mM PBS were used. However, the Au film in the right reservoir decomposed when the PBS concentration was increased to 5 mM. When the right reservoir was filled with ultrapure water, no obvious change was observed on the graphite paper electrodes at the left and right ends, suggesting that the electrochemical oxidation of gold did not occur at the BPE anode, and the reduction of $HAuCl_4$ did not occur at the cathode. In summary, the electrochemical reactions on bipolar electrodes are mainly affected by the conductivity of the solution.

3.2. Mechanism of Au Film Dissolution in BPE Device

To further investigate the dissolution and formation of Au at the BPE's two poles, a linear sweep voltage (LSV, Figure 4A), from 0 to 5.5 V was applied to the driving electrodes during the second Au deposition, and a low scan rate of 0.005 V/s was used to decrease the speed of the electrochemical reactions, including the oxidization speed of Au particles at

the anode of the BPE and the reduction speed of $AuCl_4^-$ at the cathode of the BPE. With a decreased concentration of PBS, the electrical conductivity was clearly decreased (Table S1), leading to a decreased current flowing across the BPE (Figure 4A), and a high $iR_{solution}$ which cannot be ignored. The voltage on the BPE (ΔE_{BPE}, Equation (1)) decreased accordingly, and an enhanced external voltage was needed to trigger the BPE's electrochemical reactions.

$$\Delta E_{external} = iR_{solution} + \Delta E_{BPE} + \Delta E_{sys} \quad (1)$$

where $\Delta E_{external}$ is the voltage applied to the driving electrodes, iR (ΔE_{BPE}) refers to the voltage applied at the BPE's two poles, and i stands for the current flowing through the BPE. ΔE_{sys} denotes the voltage losses in this device.

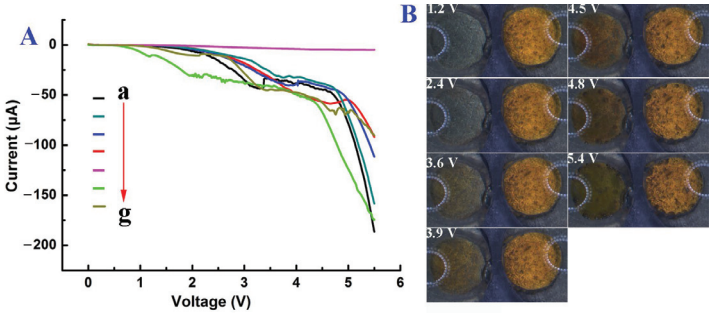

Figure 4. (**A**) LSV curves recorded during the second-step deposition of Au. The currents were obtained by filling the right reservoir with different solutions: 10 mM PBS (a), 5 mM PBS (b), 1 mM PBS (c), 0.5 mM PBS (d), water (e), 5 mM $HAuCl_4$ (f), and 5 mM HCl (g). The left reservoir was filled with 5 mM $HAuCl_4$. (**B**) Optical images were recorded during the second deposition of Au under linear sweep voltage. Both reservoirs were filled with 5 mM $HAuCl_4$. The applied voltage was changed from 0 to 5.5 V at a scan rate of 0.005 V/s.

As discussed above, when the right reservoir was filled with a poor conductive solution (i.e., water), no obvious change was observed at either pole of BPE (Figure S2) and an ultra-low current was obtained (Figure 4A, curve e). If the right reservoir contained 10 mM PBS (i.e., an excellent conductive solution), the Au film started to dissolve when the voltage reached 2.9 V (Figure S3). Subsequently, the rate of dissolution increased, and most of the Au film was dissolved when the voltage was 3.4 V, leading to a sharp decrease in current (Figure 4A, curve a). The rate of Au particles' deposition at the cathode increased along with the increase in voltage. When the voltage was further increased to 4.8 V, the GP in the right reservoir began to degrade. A small number of bubbles started to appear at the cathode's surface when the voltage was approximately 5.2 V. A large number of bubbles at the cathode's surface appeared when a constant voltage of 4.5 V was applied for 1 min (Figure 2A). This suggested that the formation of Au particles at the cathode could significantly catalyze the reduction of H^+ at its surface. As the concentration of PBS was increased, the onset voltage for the deposition of Au on the GP in the left reservoir was decreased from 4.2 to 3.9 V (Figure S4). Moreover, the dissolution of the Au anode in the right reservoir was inhibited.

When the right reservoir was filled with $HAuCl_4$, which is less conductive than 5 mM PBS (Table S1), the current was the highest at the lowest external voltage (around 0.5 V, Figure 4A, green line). A small amount of Au could be seen on GP in the left reservoir when the voltage was 2.4 V (Figure 4B), which is a much lower voltage than that for all the other solutions. This result illustrated that the BPE's electrochemical reactions not only depended on the solution's conductivity but also changed with the reactions that happened on the driving electrodes, which could enhance the current flowing through the electric circuit. The Au film in the right reservoir remained intact except for several bubbles being

produced. Similar results were observed when $HAuCl_4$ was replaced with 5 mM HCl. Figure S4 shows that the minimum voltage for driving the deposition of Au was about 3.3 V when the Au anode was immersed in HCl, which was lower than that in the diluted PBS solution (4.2 to 3.9 V), but was higher than that in the solution of 5 mM $HAuCl_4$ (2.4 V, Figure S3) even though these solutions have similar conductivity (Table S1). This was because both the protons and $AuCl_4^-$ could be reduced at the driving electrodes in the right reservoir, leading to an enhanced current flowing through the BPE (Figure 4A). As a result, the voltage drop across the BPE increased, and a low external voltage could be applied to drive the redox reactions on the BPE. Therefore, the unwanted decomposition of the Au film at the BPE anode could be avoided by adjusting the conductivity of the solution and controlling the electrochemical reactions at the driving electrode.

3.3. Characterization of Au–Au BPE

Figure S5 displays the scanning electronic microscopy (SEM) images of Au film obtained under optimal conditions by filling the two reservoirs with $HAuCl_4$ for bipolar deposition of Au film. Figure S5A showed that the graphite paper (GP) had a relatively smooth surface. After the first-step deposition of Au, the GP was coated with a high density of Au layer (Figure S5B). In the second-step deposition of Au, a highly dense Au layer could also be observed on GP surface (Figure S5C). The crystal structure of Au film was analyzed by XRD (Figure S6). Both Au-1/GP and Au-2/GP showed a new obvious peak at 2θ of 38.12° compared to that of GP, corresponding to the Au [111] plane [26].

The remarkable signal amplification effect of the modified BPE was then studied by immersing the Au film anode in $Ru(bpy)_3^{2+}$/DBAE solution and the Au film cathode in H_2O_2 (PBS). As shown in Figure 5A, three different BPEs, including a bipolar electrode with two poles without gold plating (BPE-1, a and b), a bipolar electrode with one pole plated with gold (BPE-2, c and d), and a bipolar electrode with two poles plated with gold (BPE-3, e and f), were used in the experiment. BPE-1 and BPE-2 were used as control electrodes. When the voltage was 3.0 V, ECL signal could only be observed on BPE-3. With the further increase in voltage to 3.5 V, the brightest ECL signal could be observed on BPE-3, indicating a high amplification effect of Au particles on the ECL signal. Additionally, Figure S7 shows the stability of ECL signal on BPE-3 under different voltages from 2.5 to 4.0 V. A stable and strong ECL intensity could be obtained when the voltage was 3.5 V. The reproducibility and stability of the prepared BPE was evaluated by recording the ECL signals on three different batches of electrodes. Each electrode was measured three times (Figure S8). The relative standard deviation (RSD) values obtained on each electrode in three consecutive measurements were 2.1%, 1.8%, and 1.3%, respectively. The RSD value on these three Au-modified (cathode)-Au-modified (anode) GP BPEs was 3.5%, indicating the good repeatability and reproducibility of the prepared BPEs. Furthermore, after three consecutive measurements, there was no significant change to the anode surface of the BPE (Figure S9). All these results showed that the prepared BPEs have good stable and signal-amplifying characteristics which are promising for sensitive ECL detection.

3.4. ECL Imaging of PSA

The prepared BPE device was then used for ECL detection of prostate-specific antigen (PSA) concentration based on the sandwich immunoassay. First, a primary PSA antibody was constructed at the cathode surface of Au–Au-modified GP BPE. In the presence of PSA, silica nanoparticles labeled secondary PSA-antibodies (Ab_2-SiO_2) (TEM image in Figure S10A, ca. 20 nm) could be captured, and formed sandwich immunocomplexes at the Au anode surface, resulting in the enhanced resistance of electrode and a quenched ECL signal. The resistance change in the presence of PSA was characterized by an electrochemical impedance spectroscopy (EIS) (Figure S10B). The resistance of bare GP was about 1600 Ω (curve a). After the deposition of Au film and the modification of primary antibody, the resistance decreased significantly (curve b) due to the excellent conductivity of Au film. When PSA was introduced, the resistance was increased (curve c). With the

further combination of Ab_2-SiO_2, the resistance was increased again (curve d), indicating the successful formation of a sandwich structure on the electrode surface.

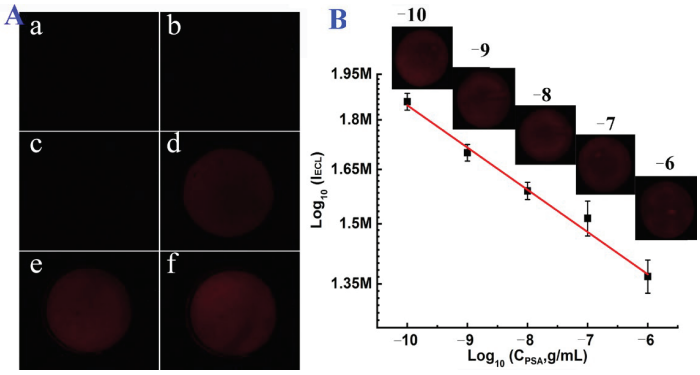

Figure 5. (**A**) ECL images obtained at bare (cathode)-bare (anode) GP BPE (BPE-1, a and b), bare (cathode)-Au-modified (anode) GP BPE (BPE-2, c and d), and Au-modified (cathode)-Au-modified (anode) GP BPE (BPE-3, e and f). The voltage applied in a, c, e was 3.0 V. The voltage applied in b, d, and f was 3.5 V. Images were obtained after applying voltages for 110 s. (**B**) Calibration curve for PSA detection. The deposition time of Au in the second process was 100 s. The concentration of PSA was 10^{-10}, 10^{-9}, 10^{-8}, 10^{-7}, and 10^{-6} g/mL.

Figure 5B is the calibration curve of the prepared electrode for the detection of PSA at the anode of BPE. A good linear relationship was observed between the ECL intensity and the logarithmic PSA concentration from 1×10^{-10} to 1×10^{-6} g/mL, with a correlation coefficient of 0.9866. The linear equation is lg $I_{ECL} = -0.0322$ lgC (g/mL) + 5.944. The limit of detection (LOD) and quantification (LOQ) was calculated to be 1.5×10^{-11} and 1.0×10^{-10} g/mL based on 3 σ/s and 10 σ/s, respectively. Here, σ and s are the standard deviation of the blank signal and the slope of the calibration curve. Compared with other PSA biosensors based on imaging strategies [27–30], the ECL biosensor developed in this work displayed a wider linear range and a high sensitivity for imaging of PSA (Table S2).

The selectivity of the designed biosensor was then evaluated in the presence of interfering proteins such as thrombin and BSA. Figure S11 exhibited that the ECL signal obtained in the presence of those two proteins was similar to the blank sample, which demonstrated the biosensor has good specificity and anti-interference ability.

3.5. Electrochemical Imaging of PSA

Alternatively, the electrodissolution of Au film at the anode of the BPE provided a novel way to visualize reactions at the cathode of Au/BPE. Here, the primary PSA antibody (Ab_1) was labeled at the cathode of the BPE. Figure 6A shows that the Au anode was dissolved completely within 50 s and without modification. Upon the combination of the primary PSA antibody (Ab_1) at its surface (Figure 6B), the oxidative dissolution time of the Au anode was prolonged slightly. After the specific formation of a sandwich immunocomplex in the presence of 10 (Figure 6C) and 100 ng/mL PSA (Figure 6D), the dissolution of the Au anode was inhibited, apparently due to the increased resistance of the Au cathode (Figure S10B). The Au film was partially dissolved, even when the voltage was applied for 100 s (Figure 6D). The change in RGB value could be used for the quantitative measurement of PSA concentration based on the dissolution of Au film. The visual readout of the dissolution of the Au anode provides a good way to observe the sensing reactions at the BPE cathode.

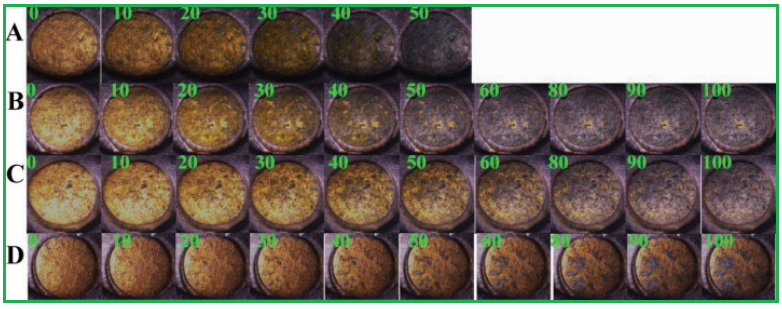

Figure 6. Dissolution of Au film at the anode of the BPE when the cathode of the GP BPE was modified with Au (**A**), Ab_1/Au (**B**), SiO_2-Ab_2/PSA (10 ng/mL)/Ab_1/Au (**C**), and SiO_2-Ab_2/PSA (100 ng/mL)/Ab_1/Au (**D**). The external voltage was 3.0 V.

4. Conclusions

In conclusion, we studied the mechanism of electrochemical oxidation of Au particles on the anode surface of a BPE. Additionally, the factors that affect the electrodeposition of Au particles at both ends of a BPE were also studied. The electrochemical oxidation of Au film on BPE anode is affected by many factors, including solution conductivity and pH value. The Au BPE device prepared by this method showed a good signal amplification effect and can emit a strong visible red-light emission signal in ECL reagent. The biosensor constructed by this method has good signal stability and a wide linear range for the detection of tumor markers (PSA). Because the detection platform is simple to prepare and the signal can be collected by taking photos, it could be extended to the measurement of various targets by coupling different recognition probes on the electrode surface.

Supplementary Materials: The following supporting information can be downloaded at: https://www.mdpi.com/article/10.3390/bios13020158/s1. Video S1: Deposition of Au at the cathode of bare GP (cathode)—Au particles modified GP (anode). Video S2: Deposition of Au at the cathode of bare GP (cathode)—Au particles modified GP (anode). Scheme S1: Close bipolar deposition device. Figure S1: Amperometric i-t plots. Figure S2: Effect of water on the dissolution and deposition of Au particles. Figure S3: Effect of 10 mM PBS on the dissolution and deposition of Au. Figure S4: Effects of HCl and different concentrations of PBS on the dissolution and deposition of Au. Figure S5: SEM images of (A) GP, (B) Au-1 film modified GP, and (C) Au-2 film modified GP. Figure S6: XRD patterns of GP substrate, Au-1 film modified GP (Au-1/GP), and Au-2 film modified GP (Au-2/GP). Figure S7: ECL signal obtained on the prepared BPE modified with Au particles at both poles. Figure S8: Reproducibility and stability of the prepared Au modified BPE in ECL measurement. Figure S9: Optical images of Au modified BPE after three consecutive detections. Figure S10: TEM image of SiO_2 NPs and EIS of different biomolecules modified Au electrodes. Figure S11: Selectivity of the designed biosensor towards thrombin and BSA. Table S1: Electrical conductivity of solutions. Table S2: Performance of the proposed biosensor compared with other biosensors

Author Contributions: Conceptualization, D.Z. and M.W.; methodology, M.W., B.J. and Y.L.; software, M.W., H.Y. (Haijian Yang); validation, M.W., J.Q. and D.Z.; formal analysis, B.J.; investigation, M.W.; resources, M.W.; data curation, D.Z., H.J., H.Y. (Huihui Yu), J.Q. and Z.L.; writing—M.W.; writing—review and editing, M.W. and B.J.; visualization, B.J.; supervision, M.W.; project administration, M.W.; funding acquisition, M.W. All authors have read and agreed to the published version of the manuscript.

Funding: This research was funded by National Natural Science Foundation of China (No. 21675087), Qinglan Project of Jiangsu Province of China, and the Fundamental Research Funds for the Central Universities, Nanjing Agricultural University (Grant No. XUEKEN2022033).

Institutional Review Board Statement: Not applicable.

Informed Consent Statement: Not applicable.

Data Availability Statement: Not applicable.

Conflicts of Interest: The authors declare no conflict of interest.

References

1. Jin, L.; Qiao, J.; Chen, J.; Xu, N.; Wu, M. Combination of area controllable sensing surface and bipolar electrode-electrochemiluminescence approach for the detection of tetracycline. *Talanta* **2020**, *208*, 120404. [CrossRef] [PubMed]
2. Rafatmah, E.; Hemmateenejad, B. Colorimetric and visual determination of hydrogen peroxide and glucose by applying paper-based closed bipolar electrochemistry. *Microchim. Acta* **2019**, *186*, 684. [CrossRef] [PubMed]
3. Tian, Z.; Mi, L.; Wu, Y.; Shao, F.; Zou, M.; Zhou, Z.; Liu, S. Visual Electrofluorochromic Detection of Cancer Cell Surface Glycoprotein on a Closed Bipolar Electrode Chip. *Anal. Chem.* **2019**, *91*, 7902–7910. [CrossRef] [PubMed]
4. Li, X.; Qin, X.; Tian, Z.; Wang, K.; Xia, X.; Wu, Y.; Liu, S. Gold Nanowires Array-Based Closed Bipolar Nanoelectrode System for Electrochemiluminescence Detection of α-Fetoprotein on Cell Surface. *Anal. Chem.* **2022**, *94*, 7350–7357. [CrossRef] [PubMed]
5. Zhang, N.; Gao, H.; Xu, C.-H.; Cheng, Y.; Chen, H.-Y.; Xu, J.-J. An Efficient Electrochemiluminescence Enhancement Strategy on Bipolar Electrode for Bioanalysis. *Anal. Chem.* **2019**, *91*, 12553–12559. [CrossRef]
6. Zhang, X.; Lazenby, R.A.; Wu, Y.; White, R.J. Electrochromic, Closed-Bipolar Electrodes Employing Aptamer-Based Recognition for Direct Colorimetric Sensing Visualization. *Anal. Chem.* **2019**, *91*, 11467–11473. [CrossRef]
7. Fiorani, A.; Irkham; Valenti, G.; Paolucci, F.; Einaga, Y. Electrogenerated Chemiluminescence with Peroxydisulfate as a Coreactant Using Boron Doped Diamond Electrodes. *Anal. Chem.* **2018**, *90*, 12959–12963. [CrossRef]
8. Chow, K.-F.; Chang, B.-Y.; Zaccheo, B.A.; Mavre, F.; Crooks, R.M. A Sensing Platform Based on Electrodissolution of a Ag Bipolar Electrode. *J. Am. Chem. Soc.* **2010**, *132*, 9228–9229. [CrossRef]
9. Liu, Y.; Zhang, N.; Pan, J.-B.; Song, J.; Zhao, W.; Chen, H.-Y.; Xu, J.J. Bipolar Electrode Array for Multiplexed Detection of Prostate Cancer Biomarkers. *Anal. Chem.* **2022**, *94*, 3005–3012. [CrossRef]
10. Du, F.; Dong, Z.; Guan, Y.; Zeid, A.M.; Ma, D.; Feng, J.; Yang, D.; Xu, G. Single-Electrode Electrochemical System for the Visual and High-Throughput Electrochemiluminescence Immunoassay. *Anal. Chem.* **2022**, *94*, 2189–2194. [CrossRef]
11. Zhao, J.; Chen, C.-X.; Zhu, J.-W.; Zong, H.-L.; Hu, Y.-H.; Wang, Y.-Z. Ultrasensitive and Visual Electrochemiluminescence Ratiometry Based on a Constant Resistor-Integrated Bipolar Electrode for MicroRNA Detection. *Anal. Chem.* **2022**, *94*, 4303–4310. [CrossRef]
12. Wang, X.; Yuan, W.; Sun, Z.; Liu, F.; Wang, D. Ultrasensitive multicolor electrochromic sensor built on closed bipolar electrode: Application in the visual detection of Pseudomonas aeruginosa. *Food Chem.* **2023**, *403*, 134240. [CrossRef]
13. Luo, Y.; Lv, F.; Wang, M.; Lu, L.; Liu, Y.; Xiong, X. A multicolor electrochemiluminescence device based on closed bipolar electrode for rapid visual screening of Salmonella typhimurium. *Sens. Actuators B Chem.* **2021**, *349*, 130761. [CrossRef]
14. Yang, X.-Y.; Wang, Y.-Z.; Wang, L.-L.; Zhu, J.W.; Zhao, J.; Zong, H.-L.; Chen, C.X. Bipolar electrode ratiometric electrochemiluminescence biosensing analysis based on boron nitride quantum dots and biological release system. *Biosens. Bioelectron.* **2021**, *191*, 113393. [CrossRef]
15. Motaghi, H.; Ziyaee, S.; Mehrgardi, M.A.; Kajani, A.A.; Bordbar, A.-K. Electrochemiluminescence detection of human breast cancer cells using aptamer modified bipolar electrode mounted into 3D printed microchannel. *Biosens. Bioelectron.* **2018**, *118*, 217–223. [CrossRef]
16. Lu, H.-J.; Zhao, W.; Xu, J.-J.; Chen, H.-Y. Visual electrochemiluminescence ratiometry on bipolar electrode for bioanalysis. *Biosens. Bioelectron.* **2018**, *102*, 624–630. [CrossRef]
17. Zhang, X.; Ding, S.-N. Graphite paper-based bipolar electrode electrochemiluminescence sensing platform. *Biosens. Bioelectron.* **2017**, *94*, 47–55. [CrossRef]
18. Xiong, X.; Li, Y.; Yuan, W.; Lu, Y.; Xiong, X.; Li, Y.; Chen, X.; Liu, Y. Screen printed bipolar electrode for sensitive electrochemiluminescence detection of aflatoxin B1 in agricultural products. *Biosens. Bioelectron.* **2020**, *150*, 111873. [CrossRef]
19. Wang, D.; Liang, Y.; Su, Y.; Shang, Q.; Zhang, C. Sensitivity enhancement of cloth-based closed bipolar electrochemiluminescence glucose sensor via electrode decoration with chitosan/multi-walled carbon nanotubes/graphene quantum dots-gold nanoparticles. *Biosens. Bioelectron.* **2019**, *130*, 55–64. [CrossRef]
20. Zhang, X.; Chen, C.; Li, J.; Zhang, L.; Wang, E. New Insight into a Microfluidic-Based Bipolar System for an Electrochemiluminescence Sensing Platform. *Anal. Chem.* **2013**, *85*, 5335–5339. [CrossRef]
21. Chang, B.-Y.; Chow, K.-F.; Crooks, J.A.; Mavré, F.; Crooks, R.M. Two-channel microelectrochemical bipolar electrode sensor array. *Analyst* **2012**, *137*, 2827–2833. [CrossRef] [PubMed]
22. Shi, H.-W.; Zhao, W.; Liu, Z.; Liu, X.-C.; Wu, M.-S.; Xu, J.-J.; Chen, H.Y. Joint enhancement strategy applied in ECL biosensor based on closed bipolar electrodes for the detection of PSA. *Talanta* **2016**, *154*, 169–174. [CrossRef] [PubMed]
23. Wang, F.; Fu, C.; Huang, C.; Li, N.; Wang, Y.; Ge, S.; Yu, J. Paper-based closed Au-Bipolar electrode electrochemiluminescence sensing platform for the detection of miRNA-155. *Biosens. Bioelectron.* **2019**, *150*, 111917. [CrossRef] [PubMed]
24. Zhang, X.; Bao, N.; Luo, X.; Ding, S.-N. Patchy gold coated Fe_3O_4 nanospheres with enhanced catalytic activity applied for paper-based bipolar electrode-electrochemiluminescence aptasensors. *Biosens. Bioelectron.* **2018**, *114*, 44–51. [CrossRef] [PubMed]
25. Wu, M.; Koizumi, Y.; Nishiyama, H.; Tomita, I.; Inagi, S. Buoyant force-induced continuous floating and sinking of Janus micromotors. *RSC Adv.* **2018**, *8*, 33331–33337. [CrossRef]

26. Navaee, A.; Salimi, A. FAD-based glucose dehydrogenase immobilized on thionine/AuNPs frameworks grafted on amino-CNTs: Development of high power glucose biofuel cell and biosensor. *J. Electroanal. Chem.* **2018**, *815*, 105–113. [CrossRef]
27. Cao, J.-T.; Wang, Y.-L.; Zhang, J.-J.; Dong, Y.-X.; Liu, F.-R.; Ren, S.-W.; Liu, Y.-M. Immuno-Electrochemiluminescent Imaging of a Single Cell Based on Functional Nanoprobes of Heterogeneous $Ru(bpy)_3^{2+}$@SiO_2/Au Nanoparticles. *Anal. Chem.* **2018**, *90*, 10334–10339. [CrossRef]
28. Shayesteh, O.H.; Ghavami, R. A novel label-free colorimetric aptasensor for sensitive determination of PSA biomarker using gold nanoparticles and a cationic polymer in human serum. *Spectrochim. Acta Part A Mol. Biomol. Spectrosc.* **2020**, *226*, 117644. [CrossRef]
29. Lei, Q.; Wang, Y.; Dong, W.; Sun, H.; Lv, J.; Li, H. Self-powered electrochromic sensing for visual determination of PSA in serum using PB as an indicator. *J. Electroanal. Chem.* **2019**, *839*, 108–115. [CrossRef]
30. Lv, S.; Zhang, K.; Tang, D. A new visual immunoassay for prostate-specific antigen using near-infrared excited CuxS nanocrystals and imaging on a smartphone. *Analyst* **2019**, *144*, 3716–3720. [CrossRef]

biosensors

MDPI

Communication

Surface Plasmon Resonance-Based Gold-Coated Hollow-Core Negative Curvature Optical Fiber Sensor

J. Divya and S. Selvendran *

School of Electronics Engineering (SENSE), Vellore Institute of Technology, Chennai 600127, Tamil Nadu, India
* Correspondence: selvendran.s@vit.ac.in or selvendrans21@gmail.com

Abstract: The hollow-core fiber-based sensor has garnered high interest due to its simple structure and low transmission loss. A new hollow-core negative-curvature fiber (HC-NCF) sensor based on the surface plasmon resonance (SPR) technique is proposed in this work. The cladding region is composed of six circular silica tubes and two elliptical silica tubes to reduce fabrication complexity. Chemically stable gold is used as a plasmonic material on the inner wall of the sensor structure to induce the SPR effect. The proposed sensor detects a minor variation in the refractive indices (RIs) of the analyte placed in the hollow core. Numerical investigations are carried out using the finite element method (FEM). Through the optimization of structural parameters, the maximum wavelength sensitivity of 6000 nm/RIU and the highest resolution of 2.5×10^{-5} RIU are achieved in the RI range of 1.31 to 1.36. In addition, an improved figure of merit (FOM) of 2000 RIU^{-1} for Y-polarization and 857.1 RIU^{-1} for X-polarization is obtained. Because of its simple structure, high sensitivity, high FOM, and low transmission loss, the proposed sensor can be used as a temperature sensor, a chemical sensor, and a biosensor.

Keywords: photonic crystal fibers; hollow core; negative curvature; surface plasmon resonance; gold; sensitivity

Citation: Divya, J.; Selvendran, S. Surface Plasmon Resonance-Based Gold-Coated Hollow-Core Negative Curvature Optical Fiber Sensor. *Biosensors* **2023**, *13*, 148. https://doi.org/10.3390/bios13020148

Received: 2 December 2022
Revised: 5 January 2023
Accepted: 6 January 2023
Published: 17 January 2023

1. Introduction

In recent years, the optical fiber has emerged as a feasible option for sensing applications because of its small size, precision, remote sensing, and high sensitivity [1]. There are numerous versions of optical fibers, including single-mode fibers [2], multimode fibers [3], and micro- and nanostructured fibers [4]. Different types of sensing approaches are used in an optical fiber, including Bragg gratings, long-period gratings, interferometers, surface plasmon resonance (SPR), and fluorescence [5]. Yang et al., developed a long-period fiber grating (LPFG) sensor for the rapid detection of Staphylococcus aureus bacteria. Bacterial adhesion and sensitivity are enhanced by poly-electrolyte coatings. This sensor has obtained a sensitivity of 0.478 ± 0.005 nm/log (colony-forming unit/mL) at a short detection time of 30 min [6]. Ivanov et al., proposed a thin-core optical fiber sensor coated with polymer monolayers. When the layer thickness increased, the resonance frequency shifted, and this structure has been used as a chemical sensor to measure the pH level [7].

The SPR-based optical fiber sensing approach is more feasible than other conventional prism-based sensing methods due to their small size, real-time sensing, high sensitivity, and high accuracy [8,9]. A surface plasmon is produced when guided light of a specific wavelength interacts with a metal surface. As a result, the core develops a leaky mode that transfers the partial energy from core mode to plasmon mode. That particular wavelength is called the resonance wavelength, and this state is known as the phase-matching condition [10]. This SPR technique detects the minute RI variation near the metal surface. Different types of metallic coatings are used in SPR-based sensors. In optical-fiber-based sensors, noble metals are coated on the lateral surface of the fiber to realize the SPR effect [11], while in nanostructured fibers, metallic arrays are developed in the fiber tip, which enhances the sensor performance by improving the light–matter interaction [12].

The performance of the sensor is strongly influenced by the SPR effect when plasmonic materials are used. In general, the SPR effect is induced by coating or filling the sensor structure with noble metals. Gold [13] and silver [14] are the two common noble metals that are most frequently used in SPR sensors because of their sharp resonance peak, low material loss, and excellent sensitivity. Many researchers prefer gold over silver due to its higher chemical stability and biocompatibility. The two basic types of sensing techniques that can be used to find RI variations are internal and external sensing techniques. In the external sensing method, the analyte is placed on the outer surface of the sensor structure, which leads high transmission loss. To overcome this issue, the internal sensing method is used, in which the analyte is infiltered inside a hollow-core fiber, and this method reduces transmission loss and improves sensitivity by having light pass through the hollow core.

The photonic crystal fiber (PCF) is another form of optical fiber. Unlike conventional fibers, the PCF has unique properties, such as a flexible structure, strong nonlinearity, high birefringence, low transmission loss, and control sensing [15]. The limitations of conventional fiber sensors are overcome by combining PCFs with SPR techniques. Compactness and performance tuning using structural parameters of the PCF are the key benefits of SPR-based PCF sensors [16]. Depending on the guiding mechanism, the PCF has been categorized into two major types: solid-core PCF and hollow-core PCF. In solid-core fibers, light is guided by a total internal reflection method and the hollow-core fiber (HCF) drives the light inside the air core using the photonic bandgap method [17].

In an HCF, lights are guided inside the hollow core, which reduces transmission loss, which provides better accuracy and a wide transmission band [18]. In an HCF, the central air core is encased by air tubes of varying wall thicknesses. Momota et al. designed a circular-lattice hollow-core SPR-based refractive index sensor in which silver was used as a plasmonic material to induce the SPR effect, and it was placed on the outer surface of the structure. The highest wavelength sensitivity of 4200 nm/RIU was obtained for analyte RI value ranges between 1.33 and 1.37 [19]. Nazeri et al., developed a hollow-core photonic crystal fiber sensor for gas detection. This sensor obtained a maximum wavelength sensitivity of 4629 nm/RIU for the RI range of 1.0000347–1.000436 [20].

Hollow-core negative-curvature fibers (HC-NCFs) are another form of HCFs with a simple cladding region consisting of a single layer of circular or elliptical air tubes [21]. In HC-NCFs, the surface normal to the boundary is in the opposite direction from the core, which minimizes the coupling between core and cladding, which results in minimal transmission loss [22]. This type of fiber is used in remote sensing, chemical applications [23], and biosensing applications [24]. The HC-NCF has many advantages over the HCF, which include low transmission loss, a simple structure, and a large bandwidth.

Qiu et al., proposed a hollow-core negative-curvature fiber based on the surface plasmon resonance method for refractive index sensing. The cladding region was composed of eight circular silica tubes, two of which were filled with gold to produce the SPR effect. The optimum wavelength sensitivity of 5700 nm/RIU was achieved for analytes with RI values between 1.2 and 1.34 [25].

In this paper, a new HC-NCF sensor based on the SPR technique is proposed. A minimal number of silica tubes, such as six circular and two elliptical silica tubes, were preferred in the cladding region, which minimized fabrication complexity. Gold was used as a plasmonic material to realize the SPR effect. The proposed sensor is capable of detecting the RI variation in the substance present in the hollow-core region. Numerical analyses were carried out using the finite element method (FEM) in the frequency domain, and the confinement loss obtained for the proposed SPR sensor was 279.69 dB/cm and 376.83 dB/cm for X-polarization and Y-polarization, respectively. For the RI range of 1.31 to 1.36, a measured wavelength sensitivity of 6000 nm/RIU and a resolution of 2.5×10^{-5} RIU were obtained by the optimization of structural parameters. The proposed sensor can be used as a temperature sensor, a chemical sensor, a biosensor, and a gas sensor due to its simple structure, high sensitivity, high FOM, and low transmission loss.

2. Materials and Methods

The graphical representation of the proposed SPR-based HC-NCF sensor structure is illustrated in Figure 1a. The cladding region was composed of six circular silica tubes and two elliptical silica tubes to reduce fabrication complexity. A higher birefringence was generated by using elliptical tubes; their sensing capabilities outperform those of circular ones [26]. This birefringence concept facilitates the fiber to function as a polarization filter. The analyte was filled in that structure, and it was used as a sensor to realize the resonance shift of X- and Y-polarization in different wavelengths. To generate birefringence, circular silica tubes with two different diameters, such as d1 of 3.4 μm and d2 of 1 μm, and an elliptical silica tube with major (a) and minor (b) axis diameters of 3.4 μm and 2.8 μm were used. The significant birefringence of the core separates the X- and Y-polarized modes [27]. For all circular and elliptical silica tubes, the same 0.1 μm thickness (t_{silica}) was maintained. A 0.2-μm-thick (t_{gold}) gold layer was coated on the inner wall of the structure to induce the SPR effect, because gold is chemically balanced and biocompatible. The outer diameter of the sensor structure was 9.8 μm, with a 0.1 μm thickness. The length of the fiber sensor was taken as 1 mm, because in photonics, the coupling length between two modes is below 6 mm [28]. The fabrication of HC-NCFs is similar to that of conventional PCFs. The two-stage stack-and-draw technique [29] was used to fabricate the proposed sensor. In the first stage, capillaries and spacing elements were stacked into a small jacket tube to create a preform, which was then pulled into canes. The second stage preform was made by inserting the cane into a large tube with an outer diameter of 9.8 μm. Different gas pressures were used in the preform to obtain a different size of hollow tubes. After assembling the fiber framework, a 0.2-μm-thick layer of gold was deposited on the inner wall of the fiber using the electroless plating technique [30] or the high-pressure chemical vapor deposition method [31]. The analyte was injected into the sensor using an infiltration method [32].

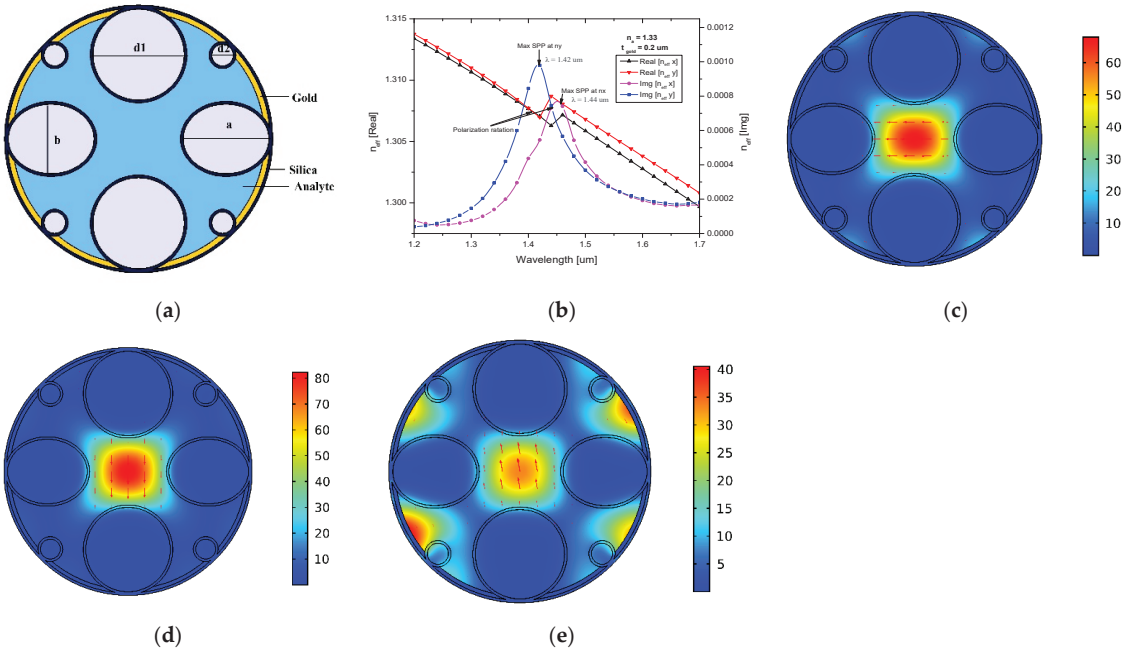

Figure 1. (**a**) Graphical representation of the proposed HC-NCF sensor. (**b**) Dispersion relations of the core-guided mode as a function of wavelength. Electric field distribution of (**c**) X-polarized mode, (**d**) Y-polarized mode, and (**e**) plasmon mode.

Numerical analyses were carried out using the finite element method (FEM) in the frequency domain. The amount of energy reflected was further decreased by applying a scattering boundary condition to the outer surface of the structure.

The dispersion relationship between the real and the imaginary part of the effective mode index (neff) with respect to the wavelength is shown in Figure 1b. The effective index of the real part decreased when the wavelength increased. A sharp drop in the real part of X- and Y-polarization indicates that light in the core mode is coupled to the plasmon mode. The resonance peak is the point at which the effective index of imaginary value reaches its highest value. Y-polarization reached its resonance peak at a wavelength of 1.42 μm, whereas X-polarization was minimal at this time, which shows that only Y-polarization propagated at this time, while X-polarization diminished. X-polarization reached its maximum at 1.44 μm; however, Y-polarization was attenuated in this situation. Figure 1c–e represents the electric field distribution of the X-polarized mode, the Y-polarized mode, and the plasmon mode, where incident light was guided via the core. The maximum amount of energy was transferred from core mode to plasmon mode when the phase-matching condition was achieved.

The proposed HC-NCF sensor was made up of pure silica, and the RI of pure silica was obtained using the Sellmeier equation [10]:

$$n(\lambda)^2 = 1 + \frac{A_1\lambda^2}{\lambda^2 - \lambda_1^2} + \frac{A_2\lambda^2}{\lambda^2 - \lambda_2^2} + \frac{A_3\lambda^2}{\lambda^2 - \lambda_3^2} \quad (1)$$

where A_1 = 0.6961663, A_2 = 0.4079426, A_3 = 0.897479, λ_1 = 0.068404, λ_2 = 0.1162414, and λ_3 = 9.896161 are the Sellmeier constants and λ is the operating wavelength.

The Drude model was used to estimate the wavelength-dependent dispersion phenomenon of gold [10] and is expressed by

$$\varepsilon = 1 - \frac{{\omega_p}^2}{\omega^2 + i\omega\Gamma_P} \quad (2)$$

where the plasma frequency ω_P = 9.06 eV and the damping rate Γ_P = 0.07 eV.

The confinement loss refers the amount of light that leaks when light is guided in the core region [33]. The following equation is used to calculate the confinement loss:

$$\text{Confinement loss} = 8.686 \times \frac{2\Pi}{\lambda} \times \text{Im}(n_{\text{eff}}) \times 10^4 (\text{dB/cm}), \quad (3)$$

where Im (n_{eff}) is the imaginary part of the effective mode index and λ is the operating wavelength.

3. Results

The performance if the proposed SPR-based HC-NCF sensor was evaluated by optimizing geometrical parameters, such as the gold layer thickness and the diameter of the circular and elliptical silica tubes. The sensor's performance was enhanced when these parameters were optimized. The impact of each parameter was investigated by individually varying it, while maintaining the other structural elements constant, and a constant RI value of 1.33 was used for the analyte throughout the optimization procedure.

The gold layer thickness, as well as the resonance wavelength, had a substantial impact on the sensor's performance. The effects of various gold layer thicknesses, including 0.15 μm, 0.2 μm, and 0.25 μm, were analyzed, Figure 2a,b shows the confinement loss spectrum for X-polarization and Y-polarization. The resonance peak shifted to shorter wavelengths when the gold layer thickness increased. The best sensitivity was obtained by using the strongest resonance peak, which could be seen at a thickness of 0.2 μm. The effectiveness of a sensor is dependent on its sensitivity. The following expression can be used to calculate the sensor's wavelength sensitivity [10]:

$$s_\lambda = \frac{\Delta\lambda_{Peak}}{\Delta n_a} \text{ (nm/RIU)} \quad (4)$$

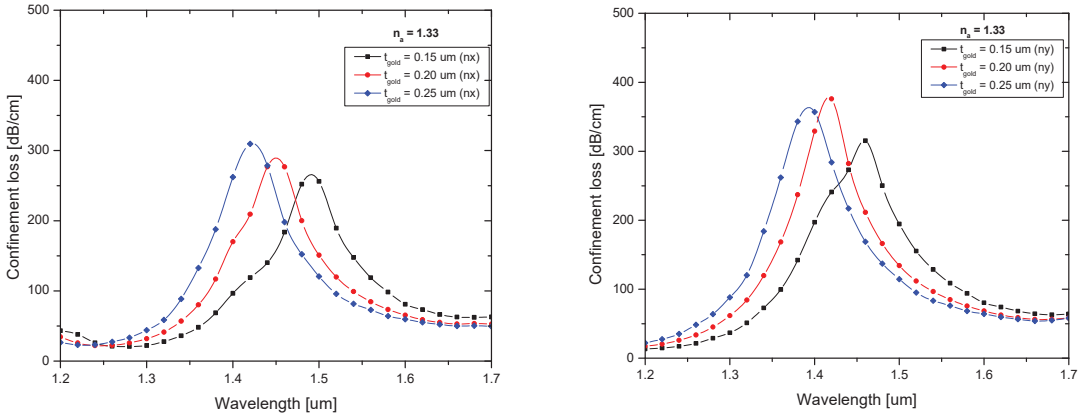

(**a**) (**b**)

Figure 2. Confinement loss characteristics for different gold layer thicknesses for (**a**) X-polarization and (**b**) Y-polarization.

The circular and elliptical silica tube diameter plays a vital role in the sensor's sensing performance because these silica tubes create the path between core and analyte. In the cladding region, elliptical as well as circular silica tubes combine to form an anisotropic shape. An anisotropic shape provides a strong negative curvature and a node-free anti-resonance element [34], and this structure also enhances sensor performance. Figure 3a,b depicts the loss spectrum for different values of d1 for X-polarization and Y-polarization. The core effective area decreased as the silica tube radius increased, which in turn decreased the core strength. This shows that as the silica tube diameter increases, the resonance peak shifts to longer wavelengths. At a diameter of 3.4 µm, a sharp peak was obtained for both polarizations and was used for further analysis.

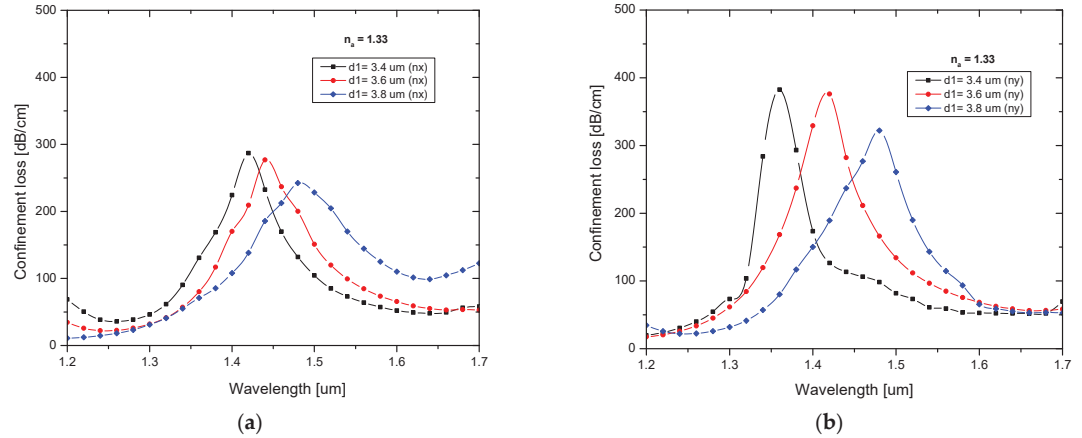

(**a**) (**b**)

Figure 3. Confinement loss characteristics for different values of d1 for (**a**) X-polarization and (**b**) Y-polarization.

The loss spectrum for various major and minor axes of the elliptical tube for X-polarization and Y-polarization is shown in Figure 4a,b. The core effective area decreased as the elliptical tube's major axis increased, which in turn decreased the core strength. This shows that as the elliptical tube major and minor axes increase, the resonance peak shifts to longer wavelengths. A sharp loss peak was observed for both polarizations at 3.4 μm for the major and 2.8 μm for the minor axis.

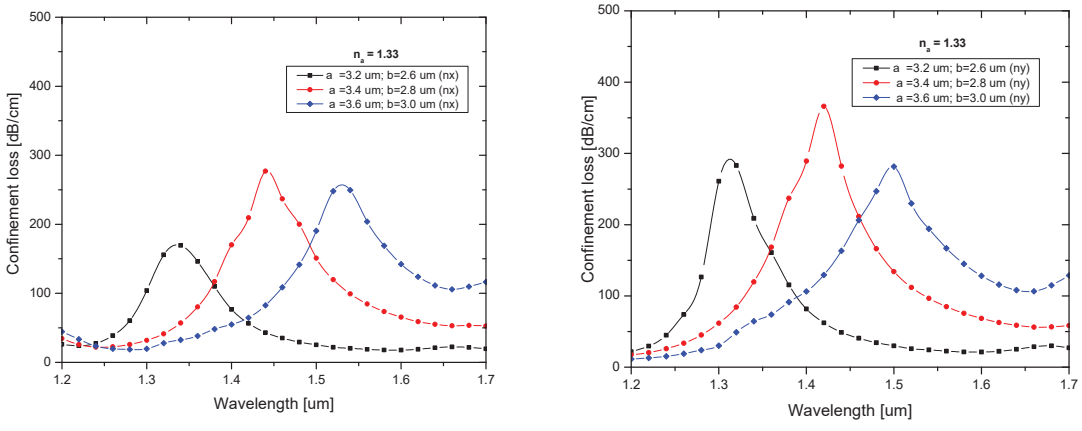

(**a**) (**b**)

Figure 4. Confinement loss characteristics of different major and minor axes for (**a**) X-polarization and (**b**) Y-polarization.

To evaluate the proposed sensor, the confinement loss properties of various analytes, which had a range of 1.31 to 1.36 with a step value of 0.01, were analyzed. Figure 5a,b depicts the loss spectrum for various analyte RI values for X-polarization and Y-polarization.

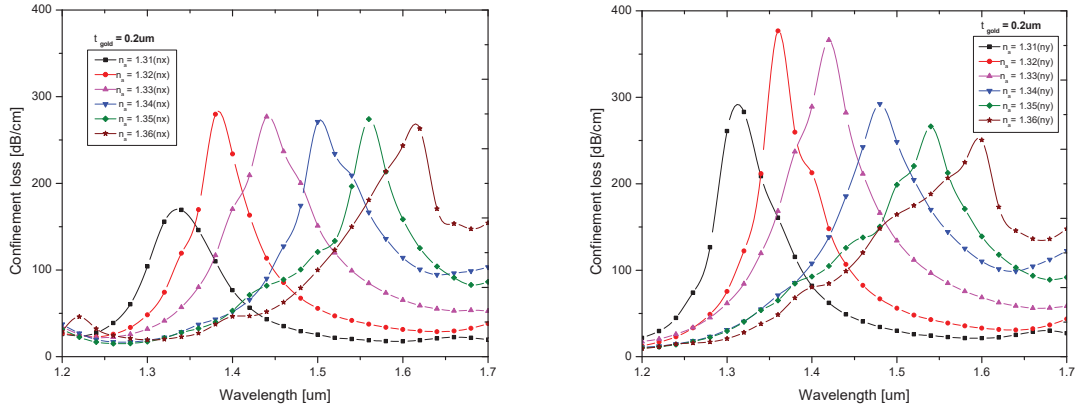

(**a**) (**b**)

Figure 5. Confinement loss characteristics with respect to wavelength for RI ranges of 1.31–1.36 for (**a**) X-polarization and (**b**) Y-polarization.

As shown in Figure 5a,b, the resonance peak moved to longer wavelengths as the RI value increased. For various RI values, Y-polarization also exhibited greater confinement loss. The maximum confinement loss of 376.83 dB/cm was found for an analyte RI value of 1.32 at a resonance wavelength of 1.36 μm. In contrast to Y-polarization, X-polarization

experienced less confinement loss. The maximum confinement loss of 279.69 dB/cm was observed at a resonance wavelength 1.38 µm, where the RI value was 1.32. Table 1 shows the performance analysis results of the proposed sensor for different analyte RI values for X- and Y-polarization.

The proposed sensor's resolution was a measurement of its capacity to identify even the slightest fluctuations in the analyte RI. The following expression can be used to calculate the resolution of the sensor [10]:

$$\text{Resolution} = \Delta n_a \times \frac{\Delta\lambda_{min}}{\Delta\lambda_{Peak}} \text{ (RIU)} \quad (5)$$

where $\Delta\lambda_{min}$ represents the minimum spectral resolution, and this was taken as 0.1 nm. $\Delta\lambda_{peak}$ is the peak wavelength shift, and Δn_a is the change of the analyte RI. The highest resolution measured using this sensor was 2.5×10^{-5} RIU.

The figure of merit (FOM) is another significant sensor characteristic. This is a wavelength-dependent parameter, and it is defined as the ratio between the sensitivity and the full width half maximum (FWHM), which was obtained from the following equation [10]:

$$\text{FOM} = \frac{S\ (\text{nm/RIU})}{FWHM\ (\text{nm})}\ (\text{RIU}^{-1}) \quad (6)$$

Table 1. Sensitivity analysis for different analyte RI values.

Refractive Index	X-Polarization				Y-Polarization				Refractive Index Resolution (RIU)	Sensitivity (nm/RIU)
	Resonance Wavelength (µm)	Confinement Loss (dB/cm)	FWHM (nm)	FOM (RIU^{-1})	Resonance Wavelength (µm)	Confinement Loss (dB/cm)	FWHM (nm)	FOM (RIU^{-1})		
1.31	1.34	169.34	12	-	1.32	283.07	04	-	2.5×10^{-5}	-
1.32	1.38	279.69	05	800	1.36	376.83	02	2000	1.67×10^{-5}	4000
1.33	1.44	276.90	09	666.7	1.42	366.07	03	2000	1.67×10^{-5}	6000
1.34	1.5	270.94	08	750	1.48	292.27	05	1200	1.67×10^{-5}	6000
1.35	1.56	274.13	07	857	1.54	266.36	05	1200	1.67×10^{-5}	6000
1.36	1.62	262.97	09	666.7	1.6	250.58	07	857.1	-	6000

The sensitivity of the proposed sensor for X- and Y-polarization is depicted in Figure 6. It shows that a maximal sensitivity of 6000 nm/RIU was obtained in the RI range of 1.31 to 1.36. The proposed sensor performed better than those described in the recent literature. Table 2 shows a performance comparison between the proposed sensor and the most recent publications.

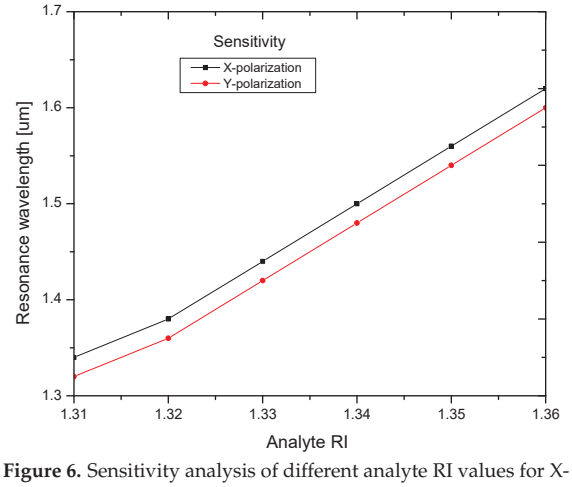

Figure 6. Sensitivity analysis of different analyte RI values for X- and Y-polarization.

Table 2. Comparative study of the sensor's performance and sensors in other recent published work.

Ref.	Structures	Material Used	Sensitivity (nm/RIU)	RI Range
[19]	Hollow-core PCF	Silver	4200	1.33–1.37
[20]	Hollow-core PCF	-	4629	1.000034–1.000449
[25]	Hollow-core NCF	Gold	5700	1.2–1.34
[35]	Hollow-core graded-index fiber	Silver	4350	1.38–1.49
[36]	Hollow-core micro-structured fiber	-	3000	1.325–1.36
[37]	Negative-curvature HC fiber	-	4411	1.33–1.39
Proposed work	Hollow-core NCF	Gold	6000	1.31–1.36

Comparing the obtained result with experimentally investigated HCF-based sensors, the proposed sensor performed better than previously reported sensors in terms of sensitivity, FOM, resolution, and confinement loss [38,39].

4. Conclusions

A new SPR-based hollow-core negative-curvature fiber (HC-NCF) sensor was proposed. The cladding region was formed by six circular silica tubes and two elliptical silica tubes to reduce fabrication complexity. Both elliptical and circular silica tubes were combined to generate an anisotropic shape, which outperformed an isotropic sensor in terms of performance. A high birefringence was created using two different sizes of circular silica tubes. Chemically stable gold was used as a plasmonic material on the inner wall of the sensor structure to induce the SPR effect. The proposed sensor detected the minor variation in the RI of the analytes placed in the hollow core. Numerical analyses were carried out using the FEM in the frequency domain, and the confinement loss obtained for the proposed SPR sensor was 279.69 dB/cm for X-polarization and 376.83 dB/cm for Y-polarization. The highest resolution of 2.5×10^{-5} RIU and the maximum wavelength sensitivity of 6000 nm/RIU were accomplished in the RI range of 1.31 to 1.36 through the optimization of structural parameters. In addition, a FOM value of 2000 RIU^{-1} for Y-polarization and 857.1 RIU^{-1} for X-polarization was realized. Due to high confinement loss and FOM, Y-polarization was used for better performance of the proposed sensor. Because of its simple structure, high sensitivity, high FOM, and low transmission loss, this sensor can be used as a temperature sensor, a chemical sensor, and a biosensor.

Author Contributions: Conceptualization, J.D. and S.S.; methodology, J.D.; writing—original draft preparation, J.D.; writing—review and editing, S.S.; supervision, S.S. All authors have read and agreed to the published version of the manuscript.

Funding: This research received no external funding.

Institutional Review Board Statement: Not applicable.

Informed Consent Statement: Not applicable.

Data Availability Statement: Not applicable.

Acknowledgments: The authors thankfully acknowledge the financial support rendered by the leadership and management of Vellore Institute of Technology Chennai under its research promotion scheme.

Conflicts of Interest: The authors declare no conflict of interest.

References

1. Luo, W.; Liu, B.; Liu, J.; Wu, T.; Liu, Q.; Wang, M.Y.; Wu, Q. Tapered side-polished micro fibre sensor for high sensitivity hCG detection. *IEEE Sens. J.* **2022**, *22*, 7727–7733. [CrossRef]
2. Mohammed, H.A.; Rashid, S.A.; Abu Bakar, M.H.; Ahmad Anas, S.B.; Mahdi, M.A.; Yaacob, M.H. Fabrication and characterizations of a novel etched-tapered single mode optical fiber ammonia sensors integrating PANI/GNF nanocomposite. *Sens. Actuators B Chem.* **2019**, *287*, 71–77. [CrossRef]

3. Huong, V.T.; Phuong, N.T.T.; Tai, N.T.; An, N.T.; Lam, V.D.; Manh, D.H.; Tran, N.H.T. Gold nanoparticles modified a multimode clad-free fiber for ultrasensitive detection of bovine serum albumin. *J. Nanomater.* **2021**, *2021*, 5530709. [CrossRef]
4. Kim, D.M.; Park, J.S.; Jung, S.W.; Yeom, J.; Yoo, S.M. Biosensing applications using nanostructure-based localized surface plasmon resonance sensors. *Sensors* **2021**, *21*, 3191. [CrossRef] [PubMed]
5. Elsherif, M.; Salih, A.E.; Muñoz, M.G.; Alam, F.; AlQattan, B.; Antonysamy, D.S.; Butt, H. Optical fiber sensors: Working principle, applications, and limitations. *Adv. Photonics Res.* **2022**, *3*, 2100371. [CrossRef]
6. Yang, F.; Chang, T.L.; Liu, T.; Wu, D.; Du, H.; Liang, J.; Tian, F. Label-free detection of *Staphylococcus aureus* bacteria using long-period fiber gratings with functional polyelectrolyte coatings. *Biosens. Bioelectron.* **2019**, *133*, 147–153. [CrossRef]
7. Ivanov, O.V.; Yang, F.; Tian, F.; Du, H. Thin-core fiber structures with overlays for sensing applications. *Opt. Express* **2017**, *25*, 31197. [CrossRef]
8. Islam, M.R.; Iftekher, A.N.M.; Hasan, K.R.; Nayen, M.J.; Islam, S.B. Dual-polarized highly sensitive surface-plasmon-resonance-based chemical and biomolecular sensor. *Appl. Opt.* **2020**, *59*, 3296–3305. [CrossRef]
9. Islam, M.R.; Khan, M.M.I.; Al Rafid, R.; Mehjabin, F.; Rashid, M.S.; Chowdhury, J.A.; Islam, M. Trigonal cluster-based ultra-sensitive surface plasmon resonance sensor for multipurpose sensing. *Sens. Bio-Sens. Res.* **2022**, *35*, 100477. [CrossRef]
10. Ayyanar, N.; Sreekanth, K.V.; Raja, G.T.; Rajan, M.S.M. Photonic crystal fiber-based reconfigurable biosensor using phase change material. *IEEE Trans. Nanobiosci.* **2021**, *20*, 338–344. [CrossRef]
11. Zhao, Y.; Tong, R.J.; Xia, F.; Peng, Y. Current status of optical fiber biosensor based on surface plasmon resonance. *Biosens. Bioelectron.* **2019**, *142*, 111505. [CrossRef] [PubMed]
12. Wang, Q.; Wang, L. Lab-on-fiber: Plasmonic nano-arrays for sensing. *Nanoscale* **2020**, *12*, 7485–7499. [CrossRef] [PubMed]
13. Islam, M.R.; Iftekher, A.N.M.; Hasan, K.R.; Nayen, M.; Islam, S.B.; Hossain, A.; Tahsin, T. Design and numerical analysis of a gold-coated photonic crystal fiber based refractive index sensor. *Opt. Quantum Electron.* **2021**, *53*, 1–18. [CrossRef]
14. Kumar, D.; Sharma, M.; Singh, V. Surface plasmon resonance implemented silver thin film PCF sensor with multiple–hole microstructure for wide ranged refractive index detection. *Mater. Today: Proc.* **2022**, *62*, 6590–6595. [CrossRef]
15. Yang, T.; Zhang, L.; Shi, Y.; Liu, S.; Dong, Y. A highly birefringent photonic crystal fiber for terahertz spectroscopic chemical sensing. *Sensors* **2021**, *21*, 1799. [CrossRef] [PubMed]
16. Sharma, A.K.; Pandey, A.K.; Kaur, B. A Review of advancements (2007–2017) in plasmonics-based optical fiber sensors. *Opt. Fiber Technol.* **2018**, *43*, 20–34. [CrossRef]
17. Yu, R.; Chen, Y.; Shui, L.; Xiao, L. Hollow-core photonic crystal fiber gas sensing. *Sensors* **2020**, *20*, 2996. [CrossRef]
18. Liu, C.; Fu, H.; Lv, Y.; Yi, Z.; Lin, J.; Lv, J.; Chu, P.K. $HE_{1,1}$ mode-excited surface plasmon resonance for refractive index sensing by photonic crystal fibers with high sensitivity and long detection distance. *Optik* **2022**, *265*, 169471. [CrossRef]
19. Momota, M.R.; Hasan, M.R. Hollow-core silver coated photonic crystal fiber plasmonic sensor. *Opt. Mater.* **2018**, *76*, 287–294. [CrossRef]
20. Nazeri, K.; Ahmed, F.; Ahsani, V.; Joe, H.-E.; Bradley, C.; Toyserkani, E.; Jun, M.B.G. Hollow-Core Photonic Crystal Fiber Mach–Zehnder Interferometer for Gas Sensing. *Sensors* **2020**, *20*, 2807. [CrossRef]
21. Kolyadin, A.N.; Alagashev, G.K.; Pryamikov, A.D.; Mouradian, L.; Zeytunyan, A.; Toneyan, H.; Bufetov, I.A. Negative curvature hollow-core fibers: Dispersion properties and femtosecond pulse delivery. *Phys. Procedia* **2015**, *73*, 59–66. [CrossRef]
22. Debord, B.; Alharbi, M.; Bradley, T.; Fourcade-Dutin, C.; Wang, Y.Y.; Vincetti, L.; Benabid, F. Hypocycloid-shaped hollow-core photonic crystal fiber part I: Arc curvature effect on confinement loss. *Opt. Express* **2013**, *21*, 28597. [CrossRef] [PubMed]
23. Hossain, S.; Mollah, A.; Hosain, K.; Ankan, I.M. THz spectroscopic sensing of liquid chemicals using hollow-core anti-resonant fiber. *OSA Contin.* **2021**, *4*, 621. [CrossRef]
24. Khozeymeh, F.; Melli, F.; Capodaglio, S.; Corradini, R.; Benabid, F.; Vincetti, L.; Cucinotta, A. Hollow-core fiber-based biosensor: A platform for lab-in-fiber optical biosensors for DNA detection. *Sensors* **2022**, *22*, 5144. [CrossRef]
25. Qiu, S.; Yuan, J.; Zhou, X.; Li, F.; Wang, Q.; Qu, Y.; Yan, B.; Wu, Q.; Wang, K.; Sang, X.; et al. Hollow-core negative curvature fiber with high birefringence for low refractive index sensing based on surface plasmon resonance effect. *Sensors* **2020**, *20*, 6539. [CrossRef] [PubMed]
26. Chao, C.-T.C.; Kooh, M.R.R.; Chau, Y.-F.C.; Thotagamuge, R. Susceptible plasmonic photonic crystal fiber sensor with elliptical air holes and external-flat gold-coated surface. *Photonics* **2022**, *9*, 916. [CrossRef]
27. Liu, Q.; Li, S.; Chen, H. Two kinds of polarization filter based on photonic crystal fiber with nanoscale gold film. *IEEE Photonics J.* **2015**, *7*, 1–11. [CrossRef]
28. Selvendran, S.; Raja, A.S.; Yogalakshmi, S. A highly sensitive surface plasmon resonance biosensor using photonic crystal fiber filled with gold nanowire encircled by silicon lining. *Optik* **2018**, *156*, 112–120. [CrossRef]
29. Jasion, G.T.; Hayes, J.R.; Wheeler, N.V.; Chen, Y.; Bradley, T.D.; Richardson, D.J.; Poletti, F. Fabrication of tubular anti-resonant hollow core fibers: Modelling, draw dynamics and process optimization. *Opt. Express* **2019**, *27*, 20567. [CrossRef] [PubMed]
30. Takeyasu, N.; Tanaka, T.; Kawata, S. Metal deposition deep into microstructure by electroless plating. *Jpn. J. Appl. Phys.* **2005**, *44*, 1134–1137. [CrossRef]
31. Akowuah, K.; Gorman, T.; Ademgil, H.; Haxha, S.; Robinson, G.K.; Oliver, J.V. Numerical analysis of a photonic crystal fiber for biosensing applications. *IEEE J. Quantum Electron.* **2012**, *48*, 1403–1410. [CrossRef]
32. Maji, P.S.; Roy Chaudhuri, P. A New design for all-normal near zero dispersion photonic crystal fiber with selective liquid infiltration for broadband supercontinuum generation at 1.55 μm. *J. Photonics* **2014**, *2014*, 1–9. [CrossRef]

33. Islam, M.R.; Jamil, M.A.; Ahsan, S.A.H.; Khan, M.M.I.; Mehjabin, F.; Chowdhury, J.A.; Islam, M. Highly birefringent gold-coated SPR sensor with extremely enhanced amplitude and wavelength sensitivity. *Eur. Phys. J. Plus* **2021**, *136*, 238. [CrossRef]
34. Habib, M.S.; Bang, O.; Bache, M. Low-loss single-mode hollow-core fiber with anisotropic anti-resonant elements. *Opt. Express* **2016**, *24*, 8429. [CrossRef]
35. Nasirifar, R.; Danaie, M.; Dideban, A. Hollow-core graded index optical fiber refractive index sensor based on surface plasmon resonance. *Opt. Quantum Electron.* **2020**, *52*, 1–23. [CrossRef]
36. Ermatov, T.; Noskov, R.E.; Machnev, A.A.; Gnusov, I.; Atkin, V.; Lazareva, E.N.; Gorin, D.A. Multispectral sensing of biological liquids with hollow-core microstructured optical fibres. *Light Sci. Appl.* **2020**, *9*, 173. [CrossRef] [PubMed]
37. Stawska, H.I.; Popenda, M.A. Refractive index sensors based on long-period grating in a negative curvature hollow-core fiber. *Sensors* **2021**, *21*, 1803. [CrossRef] [PubMed]
38. Sultana, J.; Islam, M.S.; Cordeiro, C.M.; Habib, M.S.; Dinovitser, A.; Kaushik, M.; Abbott, D. Hollow core inhibited coupled antiresonant terahertz fiber: A numerical and experimental study. *IEEE Trans. Terahertz Sci. Technol.* **2021**, *11*, 245–260. [CrossRef]
39. Habib, M.; Anower, M.; AlGhamdi, A.; Faragallah, O.S.; Eid, M.; Rashed, A.N.Z. Efficient way for detection of alcohols using hollow core photonic crystal fiber sensor. *Opt. Rev.* **2021**, *28*, 383–392. [CrossRef]

biosensors

MDPI

Article

Fast and Ultrasensitive Electrochemical Detection for Antiviral Drug Tenofovir Disoproxil Fumarate in Biological Matrices

Jingyun Xiao [1,2,3], Shuting Shi [1], Liangyuan Yao [2,*], Jinxia Feng [1], Jinsong Zuo [1] and Quanguo He [1,2,3,*]

[1] School of Life Science and Chemistry, Hunan University of Technology, Zhuzhou 412007, China
[2] Hunan Qianjin Xiangjiang Pharmaceutical Joint Stock Co., Ltd., Zhuzhou 412001, China
[3] Geriatric Rehabilitation Department, Zhuzhou People's Hospital, Zhuzhou 421007, China
* Correspondence: yly733@163.com (L.Y.); hequanguo@hut.edu.cn (Q.H.); Tel.: +86-731-2218-3426 (Q.H.); Fax: 86-731-2218-3426 (Q.H.)

Abstract: Tenofovir disoproxil fumarate (TDF) is an antiretroviral medication with significant curative effects, so its quantitative detection is important for human health. At present, there are few studies on the detection of TDF by electrochemical sensors. This work can be a supplement to the electrochemical detection of TDF. Moreover, bare electrodes are susceptible to pollution, and have high overvoltage and low sensitivity, so it is crucial to find a suitable electrode material. In this work, zirconium oxide (ZrO_2) that has a certain selectivity to phosphoric acid groups was synthesized by a hydrothermal method with zirconyl chloride octahydrate as the precursor. A composite modified glassy carbon electrode for zirconium oxide-chitosan-multiwalled carbon nanotubes (ZrO_2-CS-MWCNTs/GCE) was used for the first time to detect the TDF, and achieved rapid, sensitive detection of TDF with a detection limit of sub-micron content. The ZrO_2-CS-MWCNTs composite was created using sonication of a mixture of ZrO_2 and CS-MWCNTs solution. The composite was characterized using scanning electron microscopy (SEM) and cyclic voltammetry (CV). Electrochemical analysis was performed using differential pulse voltammetry (DPV). Compared with single-material electrodes, the ZrO_2-CS-MWCNTs/GCE significantly improves the electrochemical sensing of TDF due to the synergistic effect of the composite. Under optimal conditions, the proposed method has achieved good results in linear range (0.3~30 μM; 30~100 μM) and detection limit (0.0625 μM). Moreover, the sensor has the merits of simple preparation, good reproducibility and good repeatability. The ZrO_2-CS-MWCNTs/GCE has been applied to the determination of TDF in serum and urine, and it may be helpful for potential applications of other substances with similar structures.

Keywords: Tenofovir disoproxil fumarate; zirconium oxide; multiwalled carbon nanotubes; differential pulse voltammetry; biological samples

Citation: Xiao, J.; Shi, S.; Yao, L.; Feng, J.; Zuo, J.; He, Q. Fast and Ultrasensitive Electrochemical Detection for Antiviral Drug Tenofovir Disoproxil Fumarate in Biological Matrices. *Biosensors* **2022**, *12*, 1123. https://doi.org/10.3390/bios12121123

Received: 11 October 2022
Accepted: 29 November 2022
Published: 3 December 2022

Publisher's Note: MDPI stays neutral with regard to jurisdictional claims in published maps and institutional affiliations.

1. Introduction

Acquired Immune Deficiency Syndrome (AIDS) and hepatitis B can cause a series of physical and mental health problems, about which the global community has become increasingly concerned. AIDS is caused by human immunodeficiency virus (HIV), which mainly causes damage to CD4 T cells [1], affecting the human immune system and causing the human body to become infected with other diseases or even die, due to the loss of resistance to diseases. Hepatitis B is one of the most dangerous forms of hepatitis. It is a disease caused by hepatitis B virus (HBV) and can cause damage to liver tissue [2]. Antiretroviral drugs are used in the treatment of retroviral infection. They can effectively treat HIV and HBV, and according to their molecular mechanism and drug resistance distribution, they are divided into six types: nucleoside reverse transcriptase inhibitors (NRTIs), non-nucleoside reverse transcriptase inhibitors (NNRTIs), integrase inhibitors, protease inhibitors (PIs), fusion inhibitors, and coreceptor antagonists [3]. One of the NRTIs, Tenofovir disoproxil fumarate (TDF, trade name Viread®) was researched and

developed by Gilead Sciences, Inc. Its International Union of Pure and Applied Chemistry (IUPAC) name is Bis{[(isopropoxycarbonyl)oxy]methyl}({[(2R)-1-(6-amino-9H-purin-9-yl)-2-propanyl]oxy}methyl) phosphonate fumarate. TDF has been approved by the Food and Drug Administration (FDA) for the treatment of AIDS and hepatitis B, and it appears in the list of essential drugs of the World Health Organization (WHO) [4]. TDF is a precursor of Tenofovir (TFV). The oral bioavailability of TFV is low, while that of TDF is greatly improved [5]. At the same time, compared with other mainstream NRTIs, TDF has the advantages of reducing the rate of development of drug resistance, longer half-life and fewer side effects [6]. The possibility of drug resistance of TDF is very low [7]. These characteristics make TDF more popular in the treatment of HIV and HBV. After oral administration of TDF, it is first metabolized into TFV in vivo. Next, this is phosphorylated into the active metabolite Tenofovir bisphosphate under the action of cell kinase. After this, it actively inhibits virus activity, thus acting as a treatment. After 3 days of administration, TDF is excreted in vivo through glomerular filtration and the active tubular transport system, such that about 70%~80% of it is excreted in urine. At the same time, TDF does not need to be taken on an empty stomach; on the contrary, it can have improved bioavailability when it is consumed with high-fat food [8]. However, long-term use of TDF may lead to nephrotoxicity [9] and halisteresis [10]. Therefore, it is of great significance for individualized drug delivery, rational drug use, and precision medicine to quantitatively detect the content of TDF.

Nowadays, several analytical techniques for detection TDF have been reported upon, including spectrophotography [11–13], ultraviolet spectrophotometry [14,15], liquid chromatography tandem mass spectrometry [16], reversed-phase high-performance liquid chromatography [17], ultra-high efficiency supercritical fluid chromatography [18], high-performance thin layer chromatography [19], and so on. Although these traditional methods have been widely used and these technologies are mature, they often need large-scale precision instruments, and the pretreatment process is often complex. In this case, electrochemical methods are being gradually developed. Electrochemical analysis is used to determine the different oxidation states of an element in solution. This technique is more advantageous for analyzing the active components of drugs with extremely low detection limits. It also allows the determination of the mechanisms of a given drug, through the study of its electrochemical behavior. This method is not affected by excipients. This means that electrochemical detection can be directly used to detect drugs, with the advantages of speed, high sensitivity, low cost, and miniaturization [20,21]. In addition to modifying the electrode to detect substances [22], electrochemistry is also used in photocatalysis [23], disease screening and diagnosis [24,25], real-time monitoring of living cells [26], brain electrodes [27,28], and so on. At present, only one document on the use of a bare electrode has been reported on, for the electrochemical detection of TDF [29]. However, the bare electrode is easily polluted and interfered with, and has the disadvantages of high overvoltage and low sensitivity [30], so it is important to modify the electrode. Materials used for the surface modification of glassy carbon electrodes (GCEs) for electrochemical sensors mainly include carbon-based nanomaterials (such as carbon nanotubes and graphene), metal nanoparticles, metal oxide nanoparticles, and polymer materials. The materials used for electrochemical sensors should have good conductivity and selectivity to given drug molecules [31]. Therefore, it is necessary to choose suitable electrode materials to design a sensitive, cheap and effective electrochemical method, to determine TDF.

Metal oxide nanostructures are an ideal class of sensing materials [32–37], because of their large surface-to-volume ratio, high electroactive surface area, and good electrical conductivity [38]. These characteristics lead to their widespread use in electrochemical detection. They are usually used in combination with conductive support materials, to improve their electrochemical properties. At the same time, metal oxides have the advantages of rich sources and low cost. They have been extensively used in the preparation of electrochemical sensors and successfully used to analyze a variety of substances [23,39–47], such as biological small molecules, food additives, pesticides [48] and drugs. Zirconium

oxide (ZrO_2) is an inorganic oxide crystal with thermal stability, chemical inertia and avirulence. Additionally, it has a strong affinity for the phosphonic part. It was originally studied for use in the detection of enriched phosphopeptides, captured phosphoprotein and organophosphorus pesticides [49]. It has potential applications in catalysis, solid oxide fuel cells, sensors and nuclear radiation shielding materials [50,51]. At present, the methods of synthesizing zirconium oxide include the sol–gel method, precipitation method, solvothermal synthesis, hydrothermal synthesis, etc. [52]. The synthesized pure zirconium oxide has three crystal forms: monoclinic phase (m-ZrO_2), tetragonal phase (t-ZrO_2) and cubic phase (c-ZrO_2) [53]. Zirconium oxide has been used in an electrochemical sensor and biosensor [54]. ReddyPrasad et al. added zirconyl chloride octahydrate ($ZrOCl_2$) and C-dots to chitosan solution, obtained a C-dots/ZrO_2 nanocomposite modified electrode by ultrasound and electrodeposition, and successfully applied it in the detection of Parathion in rice samples [49]. Chen et al. prepared an alveolated zirconium oxide with a chitosan modified electrode for electrochemical detection of the antituberculosis drug Rifampicin, and achieved good results. It has been applied to biological samples such as human serum and urine [55]. Tan and Wu used zirconium chloride and alcohol to synthesize zirconium oxide for an oxygen molecular sensor and achieved good results [56]. It can be seen that zirconium oxide can be used as electrode modification material.

Multiwalled carbon nanotubes (MWCNTs) have the properties of large specific surface area, strong adsorption capacity, strong conductivity and strong catalytic properties [57], and they can be used to construct high-performance sensors. Although carbon materials have many advantages, they lack selectivity to target molecules when used alone in sensing devices [58]. In practical applications, MWCNTs are often combined with other materials to enhance selectivity. Chitosan (CS) is deacetylated from natural chitin. It not only has hydrophilic and hydrophobic groups, but also -NH_2 and -OH groups. It has been reported that a chitosan modified electrode can be used to detect various substances [2,57,59], and it can promote the even and steady dispersion of MWCNTs [2]. Drawing on the idea of using composites, metal and carbon matrix composites are developed, in order to obtain good selectivity and excellent thermal and electrical properties. Therefore, in this work, zirconium oxide-chitosan-multiwalled carbon nanotubes composites were prepared to detect TDF.

A ZrO_2-CS-MWCNTs mixture was evenly modified onto the smooth surface of a glassy carbon electrode (GCE) using the drop coating method, to get a modified electrode (ZrO_2-CS-MWCNTs/GCE). The electrochemical properties of the ZrO2-CS-MWCNTs/GCE were studied using cyclic voltammetry (CV) and differential pulse voltammetry (DPV). The sensor shows good selectivity, repeatability, reproducibility and low detection limit. In addition, the prepared electrochemical sensor was used to detect chemicals in serum and urine, with satisfactory results.

2. Materials and Methods

2.1. Materials

Tenofovir disoproxil fumarate was provided by Hunan Qianjin Xiangjiang Pharmaceutical Joint Stock Co., Ltd. (Zhuzhou, China); zirconium oxychloride octahydrate, MWCNTs, and sodium acetate trihydrate were purchased from Aladdin Biochemical Technology Co., Ltd. (Shanghai, China); chitosan, sodium hydroxide, glycerol and glacial acetic acid were purchased from Sinopharm Chemical Reagent Co., Ltd. (Shanghai, China). Other reagents used in the laboratory were analytically pure and can be used directly, without purification. All solutions were prepared with deionized water (resistivity is 18.2 MΩ·cm).

The preparation method was to weigh 0.0636 g of TDF and dissolve it in deionized water, then dilute it with water in a 100 mL brown volumetric flask to prepare a stock solution, and keep it away from light. A solution of 1 M acetic acid and 1 M sodium acetate solution was mixed to prepare an acetic acid-sodium acetate buffer as the supporting solution of the working solution.

2.2. Apparatus

Every electrochemical measurement was performed using a CHI660E electrochemical workstation (Shanghai Chenhua Instruments Co., Ltd., Shanghai, China). The pH of the solution was measured using a digital PHS-3C pH meter (Shanghai Leici Instrument Factory, Shanghai, China). The morphologies of nano-materials were characterized using a scanning electron microscope (SEM, ZEISS Sigma 300, Jena, Germany) and an energy dispersion spectrometer (EDS) attached to the SEM. The crystal structures of the nanomaterials were characterized using X-ray diffraction (XRD, Rigaku Smart Lab SE, Tokyo, Japan).

2.3. Preparation of ZrO_2

ZrO_2 was synthesized using a hydrothermal method. 1.289 g zirconium oxychloride octahydrate was turned into a 4 mM zirconium oxychloride octahydrate solution with deionized water, and then added to the 8 mM glycerol solution. At this time, their molar ratio was 1:2. Then they were mixed evenly with a magnetic stirrer, and 0.2 M sodium hydroxide solution was added to adjust the solution to pH = 9. When the solution presented as a white emulsion, the mixture was transferred to a 100 mL stainless steel autoclave and reacted at 180 °C for 18 h, after which it was cooled at room temperature. The obtained white precipitate was centrifuged and washed with water and ethanol multiple times, and finally dried in a vacuum at 60 °C for 3 h to obtain zirconium oxide nanoparticles.

2.4. Preparation of ZrO_2-CS-MWCNTs Composite Dispersion

To prepare the composite dispersion, 1 mg ZrO_2 and 1 mg MWCNTs were scattered in 2 mL acetic acid solution (2% *v*/*v*) containing 1 mg CS. Ultrasonication was performed for 1 h to obtain a uniform dispersion. Used as a dispersant, 2% acetic acid can easily dissolve CS.

2.5. Fabrication of Modified Electrode

Firstly, the bare electrode was thoroughly polished on suede with 1.0, 0.3 and 0.05 μM aluminum oxide (Al_2O_3) slurries in that order. After each polishing process, the electrode was washed with ethanol and deionized water in turn, until a mirror-like surface was formed. Finally, the GCE was dried under an infrared lamp. In order to prepare the TDF electrochemical sensor (ZrO_2-CS-MWCNTs/GCE), ZrO_2-CS-MWCNTs composite dispersion was carefully dropped on the electrode surface. After the electrode was dried under an infrared lamp, the sensor we prepared was obtained. The fabrication process of the modified electrode is displayed in Figure S1. Similarly, ZrO_2/GCE and CS-MWCNTs/GCE were also fabricated in accordance with the above process.

2.6. Electrochemical Detection of TDF

All electrochemical measurements in this work were carried out on a CHI660E electrochemical workstation including a conventional three-electrode system. ZrO_2-CS-MWCNTs/GCE was used as the working electrode, a platinum wire electrode was used as the auxiliary electrode, and a saturated calomel electrode (SCE) was used as the reference electrode in this system. Cyclic voltammetry (CV) was used for characterization in a solution of 5 mM potassium ferricyanide, 5 mM potassium ferrocyanide and 0.1 M potassium chloride. The performance, optimization of measurement conditions, selectivity, repeatability, reproducibility and stability of TDF on ZrO_2-CS-MWCNTs/GCE were tested using differential pulse voltammetry (DPV). Before each experiment, the newly prepared electrode needed to be activated and have dust removed by scanning 20 cycles using CV in 1 M acetic acid–sodium acetate buffer solution. Next, the treated electrode was inserted into the working solution of TDF that had been diluted with acetic acid-sodium acetate buffer solution, and stirred continuously for 90 s at the potential of 0.2 V. Then the TDF was measured by the DPV at the scanning rate of 0.1 V/s within the potential range of 1.0 V~1.5 V. For DPV, the potential pulse amplitude is 0.05 V, potential pulse width is 0.05 s, data sampling width is 0.0167 s, and potential pulse period is 0.2 s. After every

measurement, stirring and using the electrochemical workstation were suspended. After this, under the condition of constant potential of −1 V, the corresponding potential of 30 s was applied in the detection solution to prevent electrode passivation. Each electrochemical measurement was carried out at room temperature.

2.7. Sample Preparation

In this experiment, serum and urine were used as the actual samples. The blood of a drug-free human was acquired from the local hospital, and the urine was from the laboratory staff. First, 1 mL of blood and an appropriate amount of TDF stock solution were centrifuged for 30 min with 4000 rpm at room temperature. Next, 0.9 mL of 15% (*w*/*v*) zinc sulfate solution–acetonitrile (50/40, *v*/*v*) was added to remove protein from the blood sample [60]. The supernatant was collected, and then acetic acid-sodium acetate buffer was added to make the supernatant and buffer reach a constant volume of 10 mL to prepare the serum sample containing TDF of the required concentration. Additionally, 1 mL of urine and an appropriate amount of TDF stock solution were centrifuged for 30 min with 4000 rpm. The collected supernatant was diluted to 10 mL with acetic acid-sodium acetate buffer to prepare a urine sample containing TDF of the required concentration. Both were detected using the standard addition method.

3. Results and Discussion

3.1. Crystal Phase and Morphology Characterization

The crystal structures of the ZrO_2, CS-MWCNTs and ZrO_2-CS-MWCNTs composites were studied using XRD. As shown in Figure 1, CS-MWCNTs showed an obvious peak at $2\theta = 26°$, which was consistent with the reported typical diffraction peaks of MWCNTs [61]. It can also clearly be seen from Figure 1 that the diffraction peaks appeared at $2\theta = 30.12°$, 34.96°, 50.22°, 59.74°, 62.68°, 73.94°, 81.76° and 84.40°, which corresponded to the (111), (200), (220), (311), (222), (400), (331) and (430) crystal planes of ZrO_2. These peak positions were compared with the diffraction peak of a c-ZrO_2 standard card (JCPDS, No. 49-1642), which indicated that the ZrO_2 synthesized by us was of cubic phase structure. In the XRD pattern of the ZrO_2-CS-MWCNTs composite, not only the characteristic diffraction peak of CS-MWCNTs, but also the characteristic diffraction peak of ZrO_2 can be observed; this was the first indication that the composite had been successfully prepared.

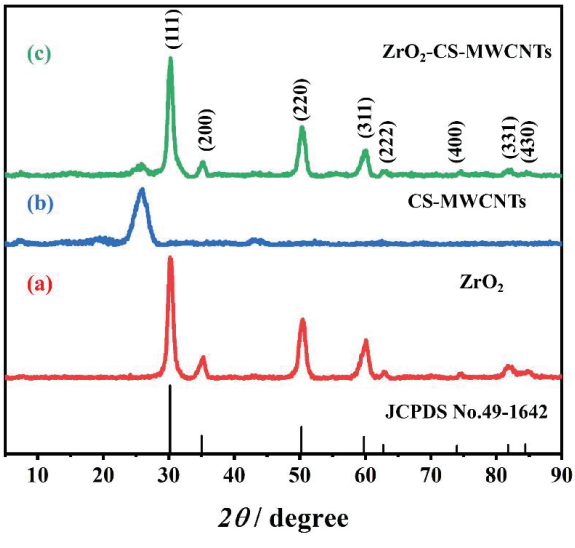

Figure 1. The X-ray diffraction (XRD) patterns of ZrO_2 (**a**), CS-MWCNTs (**b**) and ZrO_2-CS-MWCNTs composites (**c**).

The morphologies of the ZrO_2, CS-MWCNTs and ZrO_2-CS-MWCNTs composites were characterized using SEM, as shown in Figure 2. It can be observed in Figure 2a that ZrO_2 had a small spherical shape with relatively uniform particles. In Figure 2b, CS-MWCNTs showed tubular structure. Figure 2c,d illustrates the morphologies of ZrO_2-CS-MWCNTs composites at different magnification. These SEM images showed that a dense covering of spherical ZrO_2 was present on the surface of CS-MWCNTs; this phenomenon may be caused by the particle size difference between the them. At the same time, they form a honeycomb shape, which is conducive to the attachment of the target detection object.

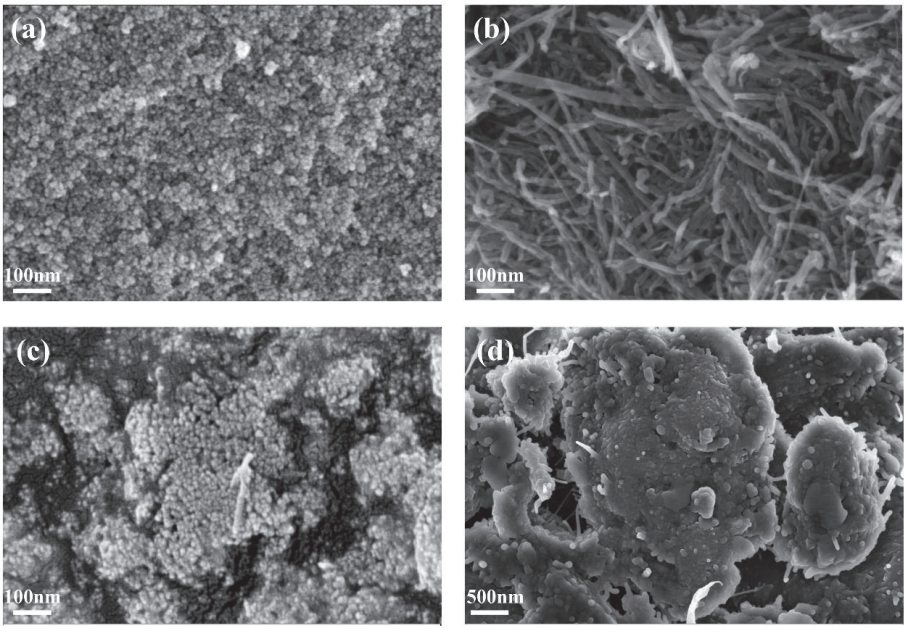

Figure 2. Scanning electron microscope (SEM) images of the ZrO_2 (**a**), CS-MWCNTs (**b**) and ZrO_2-CS-MWCNTs composites (**c**,**d**).

Figure S2a shows the EDS of the ZrO_2-CS-MWCNTs composites. The peaks of carbon (C), nitrogen (N), oxygen (O) and zirconium (Zr) can be observed in EDS. Their contents in the composite were 54.27%, 5.59%, 15.62% and 24.52%, respectively, and their atomic ratios were 73.32%, 6.48%, 15.84% and 4.36%, respectively. The mass ratio of oxygen to zirconium in the composite was about 0.64:1, which is greater than the theoretical ratio of zirconium dioxide 0.35:1, and the atomic ratio is about 3.6:1, which is greater than the theoretical ratio of zirconium dioxide of 2:1. This may be due to the presence of oxygen in chitosan and air. Combined with the XRD analysis of the composites, the results further confirmed that ZrO_2-CS-MWCNTs composites had been successfully prepared. Figure S2c–f shows the element mapping of the designated area of ZrO_2-CS-MWCNTs composites (Figure S2b), which more clearly shows the distribution of carbon, nitrogen, oxygen and zirconium in the ZrO_2-CS-MWCNTs composites. It was found that they are evenly distributed in the composites, further indicating that the composite has been successfully prepared.

3.2. Electrochemical Characterization

GCE, ZrO_2/GCE, CS-MWCNTs/GCE and ZrO_2-CS-MWCNTs/GCE were immersed in a potassium ferricyanide–potassium ferrocyanide solution (5 mM), containing 0.1 M potassium chloride, and CV characterization was performed at a scanning speed of 0.1 V/s in the potential range of −0.2~0.6 V (Figure 3a). The current of oxidation peak (I_{pa}) and

reduction peak (I_{pc}) on GCE was 108.4 μA and 109.9 μA, respectively. On ZrO_2/GCE, the redox peaks of $[Fe(CN)_6]^{3-/4-}$ were slightly reduced; these were 69.32 μA and 69.07 μA, respectively. This may be due to the thin conductivity of ZrO_2. On CS-MWCNTs/GCE, the currents of I_{pa} and I_{pc} were 113.8 μA and 125.6 μA, respectively. The values of these currents are slightly higher than those of GCE, due to the excellent conductivity and catalytic performance of multiwalled carbon nanotubes. Compared with other electrodes, ZrO_2-CS-MWCNTs/GCE showed the largest redox peaks; the values of these currents were 177.3 μA and 172.1 μA, respectively. This may be due to the synergistic effect of ZrO_2 and multiwalled carbon nanotubes, which improves the performance of the sensor. The surface active areas of these electrodes are calculated according to the Randles–Ševčík formula [62]:

$$I_p = \left(2.69 \times 10^5\right) n^{3/2} D^{1/2} v^{1/2} AC \quad (1)$$

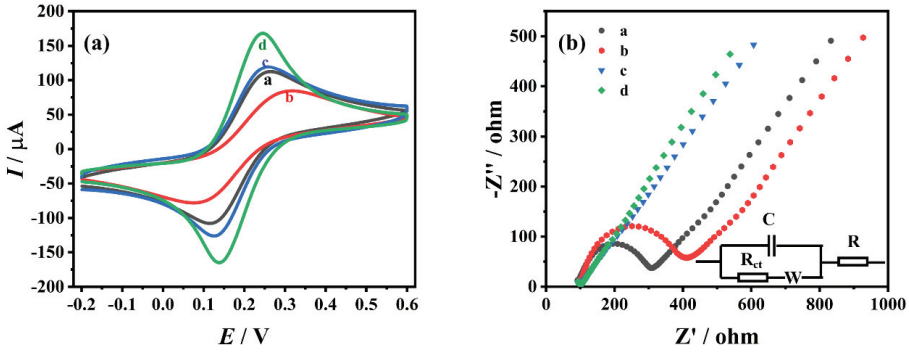

Figure 3. Cyclic voltammetry (CV) diagrams (**a**) and Nyquist plots (**b**) obtained on different electrodes in a solution of 5 mM $K_3[Fe(CN)_6]^{3-/4-}$ and 0.1 M KCl (a: GCE, b: ZrO_2/GCE, c: CS−MWCNTs/GCE, d: ZrO_2−CS−MWCNTs/GCE).

In the Randles–Ševčík formula, I_p is the peak current of $K_3[Fe(CN)_6]$ (A), n is the number of electrons transmitted, A is the surface active area (cm^2), D is the diffusion coefficient of $K_3[Fe(CN)_6]$ (7.6×10^{-6} cm^2s^{-1}), v is the scanning rate (V/s), and C is the concentration of $K_3[Fe(CN)_6]$ (mol/cm^3). The calculated effective areas of GCE, ZrO_2/GCE, CS-MWCNTs/GCE and ZrO_2-CS-MWCNTs/GCE are 0.092 cm^2, 0.059 cm^2, 0.097 cm^2 and 0.151 cm^2, respectively. The results show that the ZrO_2-CS-MWCNTs composites notably improved the effective area value of the glassy carbon electrode.

Electrochemical impedance spectroscopy (EIS) is an effective method to characterize electronic heterogeneity at the solution/electrode interface. Figure 3b shows the Nyquist diagrams of GCE, ZrO_2/GCE, CS-MWCNTs/GCE and ZrO_2-CS-MWCNTs/GCE in potassium ferricyanide–potassium ferrocyanide solution (5 mM) containing 0.1 M potassium chloride. The figure includes the semicircular part of the high-frequency region and the linear part of the low-frequency region. The electron transfer resistance (R_{ct}) of the electrode is equal to the semicircle diameter of the high-frequency region of the Nyquist diagram. This resistance regulates the electron transport kinetics of the redox probe on the electrode surface. Two obvious semicircles can be seen in GCE and ZrO_2/GCE, and the semicircle diameter of ZrO_2/GCE is larger than that of GCE, indicating that the impedance of ZrO_2/GCE is larger than that of GCE, which may be due to the poor conductivity of ZrO_2. In CS-MWCNTs/GCE and ZrO_2-CS-MWCNTs/GCE, it can be seen that the curves obtained in the high-frequency region are almost straight lines, which indicates that their impedance is significantly reduced. The R_{ct} values of GCE, ZrO_2/GCE, CS-MWCNTs/GCE and ZrO_2-CS-MWCNTs/GCE are 210.4 Ω, 294.0 Ω, 35.23 Ω and 19.32 Ω, respectively. The impedance of ZrO_2-CS-MWCNTs/GCE is the lowest, indicating that the combination of

ZrO_2 and CS-MWCNTs has a synergistic effect and is more conducive to the electrochemical reaction. This result is consistent with the CV characterization results.

3.3. Electrochemical Behavior of TDF on Different Electrodes

The electrochemical behaviors of different electrodes in 10^{-4} M TDF solution (acetic acid–sodium acetate buffer solution at pH 4.5) were investigated by DPV, as shown in Figure S3. It was found that the peak current of TDF is the smallest on ZrO_2/GCE, while it is the largest on ZrO_2-CS-MWCNTs/GCE, at more than eight times that of TDF on the bare electrode. This shows that the synergistic effect of ZrO_2 and CS-MWCNTs enhances the electrocatalysis effect, which increases the electrochemical response of TDF.

3.4. Effect of pH

The effect of the pH value of buffer solution on the peak current of 10^{-4} M TDF on ZrO_2-CS-MWCNTs/GCE was studied using DPV. Figure 4a shows the corresponding DPV diagrams of 10^{-4} M TDF in the pH range of 3.5 to 6.5. It can be clearly seen that when the value of pH is 4.5, the maximum oxidation peak current of TDF can be obtained (Figure 4b), and when the pH value increases, the oxidation peak potential gradually moves negatively (Figure 4c), and the linear regression equation is: E_p (V) = −0.04931 pH + 1.489 (R^2 = 0.9936). The oxidation reaction of TDF on the surface of ZrO_2-CS-MWCNTs/GCE is a process with same number of protons and electrons because the slope of E_p-pH is close to the theoretical value [63] of −0.0590 V/pH.

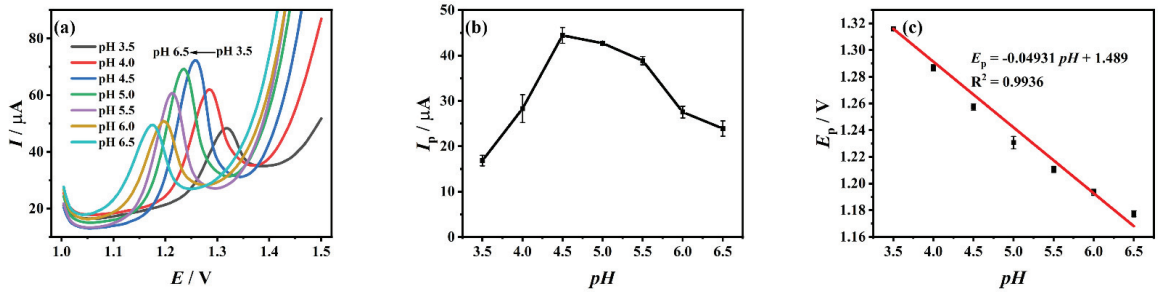

Figure 4. Differential pulse voltammetry (DPV) diagrams (**a**), current response (**b**) and the relationship diagram between peak potential and pH (**c**) of Tenofovir disoproxil fumarate (TDF) on ZrO_2−CS−MWCNTs/GCE at different pH values.

3.5. Effect of Scan Rate

In this work, the effect of the scanning rate on the oxidation of 10^{-4} M TDF on the modified electrode was studied and compared using CV. Figure 5a shows the CV diagrams of TDF in a certain scanning rate range (0.03 V/s~0.24 V/s). It can be seen that the oxidation reaction of TDF on ZrO_2-CS-MWCNTs/GCE is irreversible. As illustrated in Figure 5b,c, the linear regression equation of $v^{1/2}$ and peak current can be expressed as: I_p (μA) = 325.2 $v^{1/2}$ − 24.18 (R^2 = 0.9993); the linear regression equation of log$v$ and logI_p can be expressed as: logI_p = 0.6444 log$v$ + 2.531 (R^2 = 0.9921). The slope of log$v$ and logI_p is 0.6444, between 0.5 and 1, and there is a linear relationship between I_p and $v^{1/2}$, indicating that the oxidation reaction of TDF on ZrO_2-CS-MWCNTs/GCE is a mixed control process, dominated by diffusion. Simultaneously, it can be concluded from Figure 5d that the peak potential of TDF is directly proportional to ln$v$, and the linear regression equation is expressed as: E_p (V) = 0.03111 ln$v$ + 1.417 (R^2 = 0.9906). In accordance with the Laviron equation [64]:

$$E_p = E^0 + (RT/\alpha nF)\ln\left(RTk^0/\alpha nF\right) + (RT/\alpha nF)\ln v \quad (2)$$

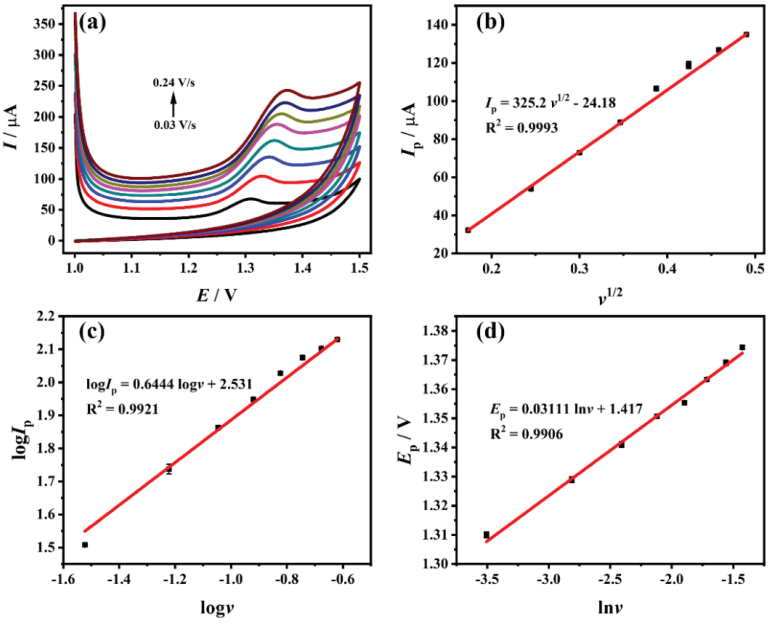

Figure 5. (**a**) CV diagrams of TDF on ZrO_2−CS−MWCNTs/GCE at different scan rates (0.03 V/s ~ 0.24 V/s); (**b**) the plot of the peak current versus $v^{1/2}$; (**c**) the plot of logI_p versus log$v$; (**d**) the plot of the peak potential versus ln$v$.

For the Laviron equation, E_p, E^0, v, α, k^0, n, T, F and R respectively represent the peak potential (V), the formal potential (V), the scanning rate (V/s), the charge transfer coefficient, the standard heterogeneous velocity rate constant, the number of electron transfers, temperature in Kelvin (K), the Faraday constant (96,480 C/mol) and the molar gas constant (8.314 J/mol·K). Because the reaction of TDF on ZrO_2-CS-MWCNTs/GCE is irreversible, it can be known that α = 0.5 [55]. It is calculated that n = 1.652, so TDF is an oxidation reaction involving two electrons on ZrO_2-CS-MWCNTs/GCE. Combined with the conclusion obtained from the pH, it can be seen that the electrochemical oxidation of TDF on the electrode is a two-electron and two-proton transfer process. According to the existing reports on the oxidation mechanism of TFV (of which TDF is a precursor) [65,66], it can be speculated that the oxidation mechanism of TDF on ZrO_2-CS-MWCNTs/GCE is as shown in Figure S4.

3.6. Effects of Deposition Conditions and Dropping Amount of ZrO_2-CS-MWCNTs Composites

The effects of deposition time, deposition potential, and dropping amount of ZrO_2-CS-MWCNTs composites on the electrochemical activity of 10^{-4} M TDF on ZrO_2-CS-MWCNTs/GCE were analyzed using DPV. As shown in Figure S5a, the peak current first increases and then decreases with the increase of deposition time from 30~210 s, and reaches the maximum at 90 s. This may be because the supersaturated adsorption of TDF on the electrode surface leads to the passivation of ZrO_2-CS-MWCNTs/GCE, which hinders the transfer of electrons and reduces the activity of the electrode. Therefore, 90 s is selected as the deposition time. As shown in Figure S5b, the deposition potential is between 0.0~1.0 V, the degree of TDF adsorbed on the electrode gradually increases, the peak current also first increases and then decreases, and reaches a maximum at 0.2 V. At this point, the TDF is fully adsorbed. With the growth of deposition potential, the background current also grows, which has a certain impact on the electrochemical response of TDF. Therefore, 0.2 V is selected as the optimum deposition potential. The film thickness of electrode modification material will also affect the determination of TDF. In the range of 1~9 μL, the effects of

different dropping amounts of ZrO_2-CS-MWCNTs composites on the TDF oxidation peak current were studied (Figure S5c). Between 1 and 5 μL, the peak current increases with the increase of the dropping amount. When the dropping amount exceeds 5 μL, the peak current decreases with further increases in dropping amount; this may be because the film thickness hinders the transmission of electrons. Therefore, 5 μL is selected as the best dropping amount. To sum up, the optimal detection conditions for the electrochemical detection of TDF with the modified electrode are a deposition time of 90 s, a deposition potential of 0.2 V, and a dropping amount of 5 μL.

3.7. Standard Curve and Detection Limit

Under the optimal detection conditions, DPV was used for the detection of different concentrations (0.3 μM~100 μM) of TDF, as shown in Figure 6a. Within this range, the oxidation peak current increases linearly with the increase of TDF concentration (Figure 6b, its specific data are in Table S1), and the linear regression equations are I_p (μA) = 1.079 c (μM) + 0.2354 (R^2 = 0.9904) (0.3 μM~30 μM) and I_p (μA) = 0.2989 c (μM) + 21.34 (R^2 = 0.9924) (30 μM~100 μM). The standard errors for estimated parameters of linear regressions for the peak current and TDF concentration can be calculated by the Formula (3):

$$\sigma_{est} = \sqrt{\sum (Y - Y')^2 / (N - K)} \quad (3)$$

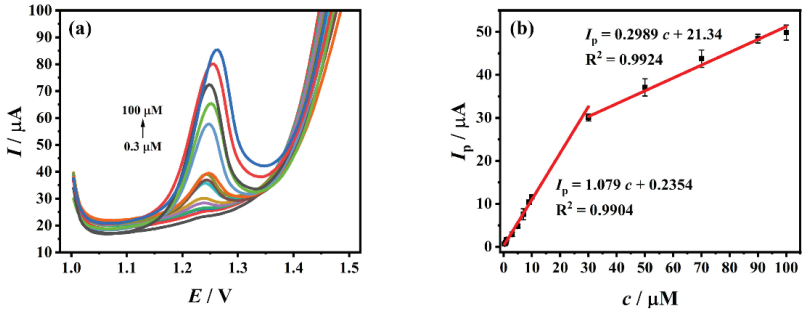

Figure 6. (**a**) DPV diagrams of different concentrations of TDF (0.3 μM~100 μM); (**b**) the linear relationship between the peak current and TDF concentration in the range of 0.3 μM~30 μM and 30 μM~100 μM.

In Formula (3), σ_{est} is the standard error of the estimate, Y is an actual value, Y' is a predicted value, and N is the number of pairs of value, K is the number of parameters. These values of standard errors for estimated parameters of linear regressions for I_p and TDF concentration can be calculated to 0.9479 and 1.280 respectively. It can be seen that the approximation error between the estimator and its true value is smaller.

When the signal-to-noise ratio was 3 (S/N = 3), the limit of detection (LOD) was estimated using the Formula (4) [21]:

$$\mathrm{LOD} = 3\,\mathrm{s/m} \quad (4)$$

In Formula (4), s is the standard deviation of 5 blank signals and equals to 0.02248 μA, m is the slope of the calibration line within the corresponding range and equals to 1.079 μA/μM. The LOD is accordingly calculated as 0.0625 μM. The TDF electrochemical sensor prepared in this work is compared with other detection methods. The results are shown in Table 1. The detection limit is one of the important indicators to judge the sensitivity of a method. The lower the detection limit, the better the sensitivity of the method. Compared with other traditional methods, ZrO_2-CS-MWCNTs/GCE, as an electrochemical method, is faster and more sensitive. Although spectrophotometry uses acid triphenylmethane dye as a material to make TDF complexed with dye ion pairs [11], the linear range

and detection limit of the current work are still superior to this method. Compared with the existing electrochemical methods, although TDF has certain electrochemical activity that can be directly detected with bare electrodes, ZrO_2-CS-MWCNTs/GCE overcomes the shortcomings of direct detection with bare electrodes, and shows a wider range of linearity and lower limit of detection. The results show that the sensor has good sensitivity.

Table 1. Comparison of various Tenofovir disoproxil fumarate (TDF) determination methods.

Method	Material	Linear Range (μM)	Detection Limit (μM)	Reference
Spectrophotometry	Acid triphenylmethane dye	6.29~62.9	0.692	[11]
Ultraviolet spectrophotometry	/	7.87~62.9	0.804	[15]
[a] RP-HPLC	/	236~708	4.75	[67]
First order derivative spectrophotometry	/	7.87~62.9	1.03	[15]
[b] AdSDPV	GCE	0.6~60	0.102	[29]
[c] AdSSWV	GCE	0.6~60	0.0839	[29]
[d] DPV	ZrO_2-CS-MWCNTs/GCE	0.3~30; 30~100	0.0625	This work

[a] RP-HPLC: reversed-phase high performance liquid chromatogram. [b] AdSDPV: adsorptive stripping differential pulse voltammetry. [c] AdSSWV: adsorptive stripping square wave voltammetry. [d] DPV: differential pulse voltammetry.

3.8. Selectivity

In order to investigate the anti-interference of ZrO_2-CS-MWCNTs/GCE, under the best conditions, potential interfering substances in body fluids and products were added to 10^{-4} M TDF solution. As shown in Figure S6, within ±5% of the allowable relative error, 100 times amounts of Fe^{3+}, Cu^{2+}, K^+, Zn^{2+} and Na^+ did not significantly interfere with the electrochemical response of TDF on ZrO_2-CS-MWCNTs/GCE, and 10 times amounts of glucose, L-glutamic acid, dopamine hydrochloride, citric acid, uric acid and Fumaric acid also did not interfere with the electrochemical response of TDF. The results show that the sensor has good anti-interference properties for the analysis of TDF, which makes the detection of TDF in actual samples feasible. It can therefore be used for the detection and analysis of complex samples.

3.9. Repeatability, Reproducibility and Stability

The indicators for evaluating the reliability and accuracy of the electrode also include repeatability, reproducibility and stability. These indicators of ZrO_2-CS-MWCNTs/GCE were studied through DPV in 10^{-4} M TDF working solution, which provided a basis for demonstrating the reliability and accuracy of this method. On a ZrO_2-CS-MWCNTs/GCE, the peak currents were recorded for five consecutive times (Figure S7a). The relative standard deviation (RSD) of these measured peak currents is 4.94%, implying that the ZrO_2-CS-MWCNTs/GCE has good repeatability in TDF determination. In addition, five different ZrO_2-CS-MWCNTs/GCEs were obtained through the same preparation process to research the reproducibility. The peak currents of different electrodes under the same conditions are shown in Figure S7b. The RSD of these measured peak currents is 4.60%, which means that the ZrO_2-CS-MWCNTs/GCE shows good reproducibility in TDF determination. Two ZrO_2-CS-MWCNTs/GCEs were prepared in the same way and reused for five days. It was found that the peak currents of ZrO_2-CS-MWCNTs/GCE remained 92.23% and 93.15%, respectively (Figure S7c), indicating that the modified electrode has good stability.

3.10. Sample Detection

Tenofovir plasmatic concentration has a high predictive value in monitoring the prevention of HIV infection by TDF, and different concentrations have different protection rates against HIV [68]. In addition, the monitoring of plasmatic and urinary drug concentrations

of TDF has a certain reference value for the clinical treatment of CHB patients [69]. It can be seen that the treatment effect on HIV and CHB patients can be predicted by measuring the concentration of TDF in serum and urine. In order to study the feasibility of using ZrO_2-CS-MWCNTs/GCEs to detect the content of TDF in actual situations, human serum and urine were taken as actual samples and tested by the method of standard addition and recovery. Under optimal conditions, the results are shown in Table 2 (specific urine and serum measurement data are shown in Table S2, and the histogram of their related I_p and c is shown in Figure S8), which also contains the use of traditional methods to detect the recoveries of TDF products, and the use of electrochemical methods to detect the recoveries of TDF and TFV (the key intermediate of TDF [70]). Compared with the recovery of TDF tablets determined by RP-HPLC ((99.57% ± 0.09)~(101.42% ± 0.08)) [17], the recovery of TDF tablets determined by UV-vis spectrophotometry (99.45%~100.4%) [14] and the recovery of TDF tablets determined by AdSDPV (100.35%) and AdSSWV (100.50%) [29], the serum recovery (96.13%~99.70%) and urine recovery (95.87%~101.0%) measured by ZrO_2-CS-MWCNTs/GCE were consistent. Meanwhile, the recoveries of TFV in the electrochemically detected drugs, using AdSSWV (101.33%) and SWV (95.8% or 101.9%) were also consistent with those in this work. The results show that the electrode can be used for the determination of TDF in actual samples, which is similar to the results obtained from the intermediates and products, and has good feasibility.

Table 2. Recovery of TDF in actual samples.

Sample	Method	Measured/μM	Added/μM	Detected/μM	RSD/%	Recovery/%	Reference
TDF tablets	[a] RP-HPLC	3.147	1.574	4.743	0.17	101.42 ± 0.08	[17]
		3.147	3.147	6.323	0.25	100.89 ± 0.07	
		3.147	4.721	7.849	0.31	99.57 ± 0.09	
TDF tablets	[b] UV-Vis	9.441	4.721	/	0.54	100.21	[14]
		9.441	9.441	/	0.94	100.4	
		9.441	14.16	/	0.54	99.45	
TDF tables	[c] AdSDPV	/	/	/	1.69	100.35	[29]
	[d] AdSSWV	/	/	/	1.50	100.50	
TFV in pharmaceutical dosage form	AdSSWV	/	/	/	1.36	101.33	[65]
TFV in Viread	[e] SWV	/	/	/	/	95.8	[71]
TFV in Tenofovir disoproxil Teva		/	/	/	/	101.9	
serum 1	[f] DPV	[g] ND	5	4.881	2.91	97.62	This work
		ND	10	9.689	2.38	96.89	
		ND	15	14.42	4.84	96.13	
serum 2		ND	5	4.985	2.01	99.70	
		ND	10	9.810	4.58	98.10	
		ND	15	14.68	2.42	97.87	
urine 1		ND	5	4.862	1.32	97.24	
		ND	10	9.587	2.59	95.87	
		ND	15	14.55	4.96	97.00	
urine 2		ND	5	4.851	0.196	97.02	
		ND	10	9.791	2.11	97.91	
		ND	15	15.15	1.21	101.0	

[a] RP-HPLC: reversed-phase high performance liquid chromatogram. [b] UV-Vis: ultraviolet and visible spectrophotometry. [c] AdSDPV: adsorptive stripping differential pulse voltammetry. [d] AdSSWV: adsorptive stripping square wave voltammetry. [e] SWV: square wave voltammetry. [f] DPV: differential pulse voltammetry. [g] ND: not detected.

4. Conclusions

In this work, cubic zirconium oxide was synthesized using the hydrothermal method, and based on this, a new fast and ultrasensitive electrochemical method for the determination of TDF, based on ZrO_2-CS-MWCNTs/GCE, was studied. The prepared ZrO_2-CS-MWCNTs composites were characterized using XRD, SEM and EDS. The results showed

that under the optimum experimental conditions, ZrO_2-CS-MWCNTs composites have good electrochemical activity for TDF determination. The ranges of 0.3 μM~30 μM and 0.3 μM~100 μM show good linear correlation with the oxidation current of TDF, and the detection limit reaches 0.0625 μM. In addition, ZrO_2-CS-MWCNTs/GCE has good selectivity, repeatability, reproducibility and stability for TDF. The sensor can be used in the determination of TDF in serum and urine, with good recovery. The electrochemical sensor is a simple and fast method for TDF detection.

Supplementary Materials: The following supporting information can be downloaded at: https://www.mdpi.com/article/10.3390/bios12121123/s1, Figure S1: Scheme of ZrO_2-CS-MWCNTs/GCE preparation and detection of Tenofovir disoproxil fumarate (TDF); Figure S2: The energy dispersion spectrometer (EDS) spectrum of ZrO_2-CS-MWCNTs composites (a); Element mappings of carbon, nitrogen, oxygen and zirconium (c–f) in designated area (b) of ZrO_2-CS-MWCNTs composites; Figure S3: Differential pulse voltammetry (DPV) diagrams of 10^{-4} M TDF on different electrodes (a: GCE, b: ZrO_2/GCE, c: CS-MWCNTs/GCE, d: ZrO_2-CS-MWCNTs/GCE); Figure S4: The possible oxidation mechanism of TDF; Figure S5: Effects of deposition time (a), deposition potential (b) and dropping amount (c) on oxidation peak current of 10^{-4} M TDF on ZrO_2-CS-MWCNTs/GCE; Figure S6: Inorganic (a) and organic (b) interference experiments of TDF detected by ZrO_2-CS-MWCNTs/GCE; Figure S7: Repeatability (a), reproducibility (b) and stability (c) of ZrO_2-CS-MWCNTs/GCE; Figure S8: Peak current of TDF with different concentrations in the actual sample (n = 3); Table S1: Specific peak current of TDF concentration range 0.3 μM~100 μM; Table S2: Recovery of TDF and peak currents of experiments in actual samples (n = 3).

Author Contributions: J.X.: conceptualization, methodology, investigation, data curation, writing—original draft. L.Y.: funding acquisition, methodology, investigation. J.F.: methodology, formal analysis. S.S.: formal analysis, supervision. J.Z.: formal analysis, supervision. Q.H.: conceptualization, methodology, supervision, funding acquisition, final writing and revision. All authors have read and agreed to the published version of the manuscript.

Funding: The authors gratefully acknowledge the financial support of the Special Project of 2022 Social Development and Transformation of Scientific and Technological Achievements (NO.51318), Zhuzhou Municipal Science and Technology Bureau (2020, NO.30 and 2021, NO.44), Doctoral Program Construction of Hunan University of Technology, Postgraduates Innovation Fund of HUT, Hunan Provincial Natural Science Foundation (2018JJ34) and Project of Science and Technology Department of Hunan Province (18A273, 2021JJ50035).

Institutional Review Board Statement: After the review of the ethics committee of the hospital, the research plan and other materials submitted by this project conform to the medical ethics principles and the requirements of the Helsinki Declaration. The research design has a scientific basis, and does not bring unnecessary risk to the subjects. The method of extraction of the urine, blood and biological fluid of the subjects is standardized, which gives maximum protection to the safety and privacy of the subjects. There is no harm to the environment, and the experiment conforms to the ethical standards of experimental research. Agree to submit papers generated by the project.

Informed Consent Statement: Not applicable.

Data Availability Statement: Not applicable.

Acknowledgments: We sincerely express our thanks to all participants for this study.

Conflicts of Interest: The authors declare that they have no competing interests.

References

1. Douek, D.C.; Roederer, M.; Koup, R.A. Emerging concepts in the immunopathogenesis of AIDS. *Annu. Rev. Med.* **2009**, *60*, 471–484. [CrossRef] [PubMed]
2. Dorraji, P.S.; Noori, M.; Fotouhi, L. Voltammetric determination of Adefovir dipivoxil by using a nanocomposite prepared from molecularly imprinted poly(o-phenylenediamine), multi-walled carbon nanotubes and carbon nitride. *Microchim. Acta* **2019**, *186*, 2–9. [CrossRef] [PubMed]
3. Arts, E.J.; Hazuda, D.J. HIV-1 antiretroviral drug therapy. *Cold Spring Harb. Perspect. Med.* **2012**, *2*, a007161. [CrossRef] [PubMed]
4. Wu, C.J.; You, J.Z.; Wang, X.J. Thermal decomposition mechanism of tenofovir disoproxil fumarate. *J. Therm. Anal. Calorim.* **2018**, *132*, 471–482. [CrossRef]

5. Watkins, M.E.; Wring, S.; Randolph, R.; Park, S.; Powell, K.; Lutz, L.; Nowakowski, M.; Ramabhadran, R.; Domanico, P.L. Development of a novel formulation that improves preclinical bioavailability of Tenofovir disoproxil fumarate. *J. Pharm. Sci.* **2017**, *106*, 906–919. [CrossRef]
6. Riley, D.L.; Walwyn, D.R.; Edlin, C.D. An improved process for the preparation of Tenofovir disoproxil fumarate. *Org. Process Res. Dev.* **2016**, *20*, 742–750. [CrossRef]
7. Yuen, M.F.; Lai, C.L. Treatment of chronic hepatitis B: Evolution over two decades. *J. Gastroenterol. Hepatol.* **2011**, *26*, 138–143. [CrossRef]
8. Chapman, T.M.; McGavin, J.K.; Noble, S. Tenofovir disoproxil fumarate. *Drugs* **2003**, *63*, 1597–1608. [CrossRef]
9. Monteiro, N.; Branco, M.; Peres, S.; Borges, F.; Mansinho, K. The impact of Tenofovir disoproxil fumarate on kidney function: Four-year data from the HIV-infected outpatient cohort. *J. Int. AIDS Soc.* **2014**, *17*, 19565. [CrossRef]
10. Grant, P.M.; Cotter, A.G. Tenofovir and bone health. *Curr. Opin. HIV AIDS* **2016**, *11*, 326–332. [CrossRef]
11. Susmitha, K.; Thirumalachary, M.; Singh, T.C.; Venkateshwarlu, G. Extractive spectrophotometric determination of Tenofovir disoproxil fumarate using acidic triphenylmethane dyes. *ISRN Spectrosc.* **2014**, *2014*, 856760. [CrossRef]
12. Venkatesan, S.; Kannappan, N. Simultaneous spectrophotometric method for determination of Emtricitabine and Tenofovir disoproxil fumarate in three-component tablet formulation containing Rilpivirine Hydrochloride. *Int. Sch. Res. Not.* **2014**, *2014*, 541727. [CrossRef] [PubMed]
13. Onah, J.O.; Ajima, U. Spectrophotometric determination of Tenofovir disoproxil fumarate after complexation with ammonium molybdate and picric acid. *Int. J. Drug Dev. Res.* **2011**, *3*, 199–204.
14. Choudhari, V.P.; Parekar, S.R.; Chate, S.G.; Bharande, P.D.; Singh, R.R.; Kuchekar, B.S. Development and validation of UV-visible spectrophotometric baseline manipulation method for simultaneous quantitation of Tenofovir disoproxil fumarate and Emtricitabine in pharmaceutical dosage form. *J. Spectrosc.* **2013**, *1*, 146580. [CrossRef]
15. Shirkhedkar Atul, A.; Bhirud Charushila, H.; Surana Sanjay, J. Application of UV-spectrophotometric methods for estimation of Tenofovir disoproxil fumarate in tablets. *Pak. J. Pharm. Sci.* **2009**, *22*, 27–29.
16. Nye, L.C.; Gray, N.; McClure, M.; Boffit, M.; Holmes, E.; Plumb, R.S.; Wilson, I.D. Identification of a novel human circulating metabolite of Tenofovir disoproxil fumarate with LC-MS/MS. *Bioanalysis* **2015**, *7*, 643–652. [CrossRef] [PubMed]
17. Bhavsar, D.S.; Patel, B.N.; Patel, C.N. RP-HPLC method for simultaneous estimation of Tenofovir disoproxil fumarate, Lamivudine, and Efavirenz in combined tablet dosage form. *Pharm. Methods* **2012**, *3*, 73–78. [CrossRef] [PubMed]
18. Kurmi, M.; Jayaraman, K.; Natarajan, S.; Kumar, G.S.; Bhutani, H.; Bajpai, L. Rapid and efficient chiral method development for Lamivudine and Tenofovir disoproxil fumarate fixed dose combination using ultra-high performance supercritical fluid chromatography: A design of experiment approach. *J. Chromatogr. A* **2020**, *1625*, 461257. [CrossRef]
19. Bhirud, C.H.; Hiremath, S.N. Indicating high performance thin layer chromatography determination of Tenofovir disoproxil fumarate in bulk and tablet dosage form. *Int. J. Chem. Anal. Sci.* **2014**, *5*, 1–5.
20. Ozkan, S.A.; Uslu, B. From mercury to nanosensors: Past, present and the future perspective of electrochemistry in pharmaceutical and biomedical analysis. *J. Pharm. Biomed. Anal.* **2016**, *130*, 126–140. [CrossRef]
21. Wu, Y.; Deng, P.; Tian, Y.; Feng, J.; Xiao, J.; Li, J.; Liu, J.; Li, G.; He, Q. Simultaneous and sensitive determination of ascorbic acid, dopamine and uric acid via an electrochemical sensor based on PVP-graphene composite. *J. Nanobiotechnol.* **2020**, *18*, 112. [CrossRef] [PubMed]
22. Pérez-Fernández, B.; Escosura-Muñiz, A. Electrochemical biosensors based on nanomaterials for aflatoxins detection: A review (2015–2021). *Anal. Chim. Acta* **2022**, *1212*, 339658. [CrossRef] [PubMed]
23. Li, G.; Zhong, P.; Ye, Y.; Wan, X.; Cai, Z.; Yang, S.; Xia, Y.; Li, Q.; Liu, J.; He, Q. A highly sensitive and stable dopamine sensor using shuttle-like α-Fe_2O_3 nanoparticles/electro-reduced graphene oxide composites. *J. Electrochem. Soc.* **2019**, *166*, B1552–B1561. [CrossRef]
24. Wang, T.-T.; Huang, X.-F.; Huang, H.; Luo, P.; Qing, L.-S. Nanomaterial-based optical- and electrochemical-biosensors for urine glucose detection: A comprehensive review. *Adv. Sens. Energy Mater.* **2022**, *1*, 100016. [CrossRef]
25. Muthumariappan, A.; Sakthivel, K.; Chen, S.M.; Chen, T.W.; Mani, G.; Lou, B.S. Effects of annealing temperature on crystal structure and glucose sensing properties of cuprous oxide. *Sensors Actuators B Chem.* **2018**, *266*, 655–663. [CrossRef]
26. Arul, P.; Huang, S.T.; Mani, V.; Huang, C.H. Gold-silver bimetallic alloy nanoparticles in a covalent organic framework for real-time monitoring of hydrogen peroxide from live cells. *ACS Appl. Nano Mater.* **2022**, *5*, 6340–6351. [CrossRef]
27. Liu, J.; Ma, N.; Wu, W.; He, Q. Recent progress on photocatalytic heterostructures with full solar spectral responses. *Chem. Eng. J.* **2020**, *393*, 124719. [CrossRef]
28. Li, G.; Wu, J.; Xia, Y.; Wu, Y.; Tian, Y.; Liu, J.; Chen, D.; He, Q. Towards emerging EEG applications: A novel printable flexible Ag/AgCl dry electrode array for robust recording of EEG signals at forehead sites. *J. Neural Eng.* **2020**, *17*, 026001. [CrossRef]
29. Ozcelikay, G.; Dogan-Topal, B.; Ozkan, S.A. Electrochemical characteristics of Tenofovir and its determination in dosage form by electroanalytical methods. *Rev. Roum. Chim* **2017**, *62*, 569–578.
30. Sakthinathan, S.; Kubendhiran, S.; Chen, S.M.; Govindasamy, M.; Al-Hemaid, F.M.A.; Ajmal Ali, M.; Tamizhdurai, P.; Sivasanker, S. Metallated porphyrin noncovalent interaction with reduced graphene oxide-modified electrode for amperometric detection of environmental pollutant hydrazine. *Appl. Organomet. Chem.* **2017**, *31*, e3703. [CrossRef]

31. Rajaji, U.; Ms, R.; Al-Kahtani, A.A.; Chen, C.P.; Juang, R.S.; Liu, T.Y. Electrocatalytic oxidation and amperometric determination of sulfasalazine using bimetal oxide nanoparticles-decorated graphene oxide composite modified glassy carbon electrode at neutral pH. *Mikrochim. Acta* **2022**, *189*, 409. [CrossRef] [PubMed]
32. Gao, C.; Guo, Z.; Liu, J.H.; Huang, X.J. The new age of carbon nanotubes: An updated review of functionalized carbon nanotubes in electrochemical sensors. *Nanoscale* **2012**, *4*, 1940–1948. [CrossRef]
33. He, Q.; Liu, J.; Liu, X.; Xia, Y.; Li, G.; Deng, P.; Chen, D. Novel electrochemical sensors based on cuprous oxide-electrochemically reduced graphene oxide nanocomposites modified electrode toward sensitive detection of sunset yellow. *Molecules* **2018**, *23*, 2130. [CrossRef]
34. Zhou, S.; Deng, Z.; Wu, Z.; Xie, M.; Tian, Y.; Wu, Y.; Liu, J.; Li, G.; He, Q. Ta_2O_5/rGO nanocomposite modified electrodes for detection of tryptophan through electrochemical route. *Nanomaterials* **2019**, *9*, 811. [CrossRef] [PubMed]
35. He, Q.; Liu, J.; Xia, Y.; Tuo, D.; Deng, P.; Tian, Y.; Wu, Y.; Li, G.; Chen, D. Rapid and sensitive voltammetric detection of Rhodamine B in chili-containing foodstuffs using MnO_2 nanorods/electro-reduced graphene oxide composite. *J. Electrochem. Soc.* **2019**, *166*, B805–B813. [CrossRef]
36. Irfan, M.F.; Qurashi, A.; Alam, M.W. Metal oxide nanostructures and nanocomposites for selective catalytic reduction of NOx: A review. *Arab. J. Sci. Eng.* **2010**, *35*, 79–92.
37. Alam, M.W.; Al Qahtani, H.S.; Souayeh, B.; Ahmed, W.; Albalawi, H.; Farhan, M.; Abuzir, A.; Naeem, S. Novel copper-zinc-manganese ternary metal oxide nanocomposite as heterogeneous catalyst for glucose sensor and antibacterial activity. *Antioxidants* **2022**, *11*, 1064. [CrossRef]
38. Arul, P.; Huang, S.T.; Mani, V.; Huang, C.H. Graphene quantum dots-based nanocomposite for electrocatalytic application of L-cysteine in whole blood and live cells. *Electrochim. Acta* **2022**, *428*, 140937. [CrossRef]
39. Wang, M.; Chen, K.; Liu, J.; He, Q.; Li, G.; Li, F. Efficiently enhancing electrocatalytic activity of α-MnO_2 nanorods/N-doped ketjenblack carbon for oxygen reduction reaction and oxygen evolution reaction using facile regulated hydrothermal treatment. *Catalysts* **2018**, *8*, 138. [CrossRef]
40. Chen, K.; Wang, M.; Li, G.; He, Q.; Liu, J.; Li, F. Spherical α-MnO_2 supported on N-KB as efficient electrocatalyst for oxygen reduction in Al-air battery. *Materials.* **2018**, *11*, 601. [CrossRef]
41. Ding, Z.; Deng, P.; Wu, Y.; Tian, Y.; Li, G.; Liu, J.; He, Q. A novel modified electrode for detection of the food colorant sunset yellow based on nanohybrid of MnO_2 nanorods-decorated electrochemically reduced graphene oxide. *Molecules* **2019**, *24*, 1178. [CrossRef]
42. He, Q.; Li, G.; Liu, X.; Liu, J.; Deng, P.; Chen, D. Morphologically tunable MnO_2 nanoparticles fabrication, modelling and their influences on electrochemical sensing performance toward dopamine. *Catalysts* **2018**, *8*, 323. [CrossRef]
43. Ning, J.; He, Q.; Luo, X.; Wang, M.; Liu, D.; Wang, J.; Liu, J.; Li, G. Rapid and sensitive determination of vanillin based on a glassy carbon electrode modified with Cu_2O-electrochemically reduced graphene oxide nanocomposite film. *Sensors* **2018**, *18*, 2762. [CrossRef] [PubMed]
44. Tian, Y.; Deng, P.; Wu, Y.; Liu, J.; Li, J.; Li, G.; He, Q. High sensitive voltammetric sensor for nanomolarity vanillin detection in food samples via manganese dioxide nanowires hybridized electrode. *Microchem. J.* **2020**, *157*, 104885. [CrossRef]
45. Tian, Y.; Deng, P.; Wu, Y.; Li, J.; Liu, J.; Li, G.; He, Q. MnO_2 nanowires-decorated reduced graphene oxide modified glassy carbon electrode for sensitive determination of Bisphenol A. *J. Electrochem. Soc.* **2020**, *167*, 046514. [CrossRef]
46. Wu, Y.; Deng, P.; Tian, Y.; Magesa, F.; Liu, J.; Li, G.; He, Q. Construction of effective electrochemical sensor for the determination of quinoline yellow based on different morphologies of manganese dioxide functionalized graphene. *J. Food Compos. Anal.* **2019**, *84*, 103280. [CrossRef]
47. Wei, Y.; Yao, L.; Wu, Y.; Liu, X.; Feng, J.; Ding, J.; Li, K.; He, Q. Ultrasensitive electrochemical detection for nanomolarity Acyclovir at ferrous molybdate nanorods and graphene oxide composited glassy carbon electrode. *Colloids Surf. A Physicochem. Eng. Asp.* **2022**, *641*, 128601. [CrossRef]
48. Govindasamy, M.; Sakthinathan, S.; Chen, S.M.; Chiu, T.W.; Sathiyan, A.; Merlin, J.P. Reduced graphene oxide supported cobalt bipyridyl complex for sensitive detection of methyl parathion in fruits and vegetables. *Electroanalysis* **2017**, *29*, 1950–1960. [CrossRef]
49. ReddyPrasad, P.; Naidoo, E.B.; Sreedhar, N.Y. Electrochemical preparation of a novel type of C-dots/ZrO_2 nanocomposite onto glassy carbon electrode for detection of organophosphorus pesticide. *Arab. J. Chem.* **2019**, *12*, 2300–2309. [CrossRef]
50. Wang, K.; Morris, M.A.; Holmes, J.D.; Yu, J.; Xu, R. Thermally stable nanocrystallised mesoporous zirconia thin films. *Microporous Mesoporous Mater.* **2009**, *117*, 161–164. [CrossRef]
51. Liu, J.; Lu, Z.; Chen, Z.; Rimoldi, M.; Howarth, A.J.; Chen, H.; Alayoglu, S.; Snurr, R.Q.; Farha, O.K.; Hupp, J.T. Ammonia capture within zirconium metal−organic frameworks: Reversible and irreversible uptake. *ACS Appl. Mater. Interfaces.* **2021**, *13*, 20081–20093. [CrossRef] [PubMed]
52. Avila-Orta, C.; Cabello-Alvarado, C.; Andrade, M. Zirconium dioxide: Synthesis alternatives and biomedical applications. *CienciaUAT* **2019**, *14*, 18–30. [CrossRef]
53. Dercz, G.; Prusik, K.; Pająk, L. X-ray and SEM studies on zirconia powders. *J. Achiev. Mater. Manuf. Eng.* **2008**, *31*, 408–414.
54. Teymourian, H.; Salimi, A.; Firoozi, S.; Korani, A.; Soltanian, S. One-pot hydrothermal synthesis of zirconium dioxide nanoparticles decorated reduced graphene oxide composite as high performance electrochemical sensing and biosensing platform. *Electrochim. Acta* **2014**, *143*, 196–206. [CrossRef]

55. Chen, T.W.; Sivasamy Vasantha, A.; Chen, S.M.; Al Farraj, D.A.; Soliman Elshikh, M.; Alkufeidy, R.M.; Al Khulaifi, M.M. Sonochemical synthesis and fabrication of honeycomb like zirconium dioxide with chitosan modified electrode for sensitive electrochemical determination of anti-tuberculosis (TB) drug. *Ultrason. Sonochem.* **2019**, *59*, 104718. [CrossRef]
56. Tan, G.L.; Wu, X.J. Electronic conductivity of a ZrO_2 thin film as an oxygen sensor. *Thin Solid Films* **1998**, *330*, 59–61. [CrossRef]
57. Wu, Y.; Deng, P.; Tian, Y.; Ding, Z.; Li, G.; Liu, J.; Zuberi, Z.; He, Q. Rapid recognition and determination of tryptophan by carbon nanotubes and molecularly imprinted polymer-modified glassy carbon electrode. *Bioelectrochemistry* **2020**, *131*, 107393. [CrossRef]
58. Naveen, M.H.; Gurudatt, N.G.; Shim, Y.-B. Applications of conducting polymer composites to electrochemical sensors: A review. *Appl. Mater. Today* **2017**, *9*, 419–433. [CrossRef]
59. Deng, P.; Fei, J.; Feng, Y. Sensitive voltammetric determination of tryptophan using an acetylene black paste electrode modified with a Schiff's base derivative of chitosan. *Analyst* **2011**, *136*, 5211–5217. [CrossRef]
60. Suh, J.H.; Lee, Y.Y.; Lee, H.J.; Kang, M.; Hur, Y.; Lee, S.N.; Yang, D.H.; Han, S.B. Dispersive liquid-liquid microextraction based on solidification of floating organic droplets followed by high performance liquid chromatography for the determination of duloxetine in human plasma. *J. Pharm. Biomed. Anal.* **2013**, *75*, 214–219. [CrossRef]
61. Singh, D.K.; Iyer, P.K.; Giri, P.K. Diameter dependence of interwall separation and strain in multiwalled carbon nanotubes probed by X-ray diffraction and Raman scattering studies. *Diam. Relat. Mater.* **2010**, *19*, 1281–1288. [CrossRef]
62. Feng, J.; Deng, P.; Xiao, J.; Li, J.; Tian, Y.; Wu, Y.; Liu, J.; Li, G.; He, Q. New voltammetric method for determination of tyrosine in foodstuffs using an oxygen-functionalized multi-walled carbon nanotubes modified acetylene black paste electrode. *J. Food Compos. Anal.* **2020**, *96*, 103708. [CrossRef]
63. Wu, Y.; Li, G.; Tian, Y.; Feng, J.; Xiao, J.; Liu, J.; Liu, X.; He, Q. Electropolymerization of molecularly imprinted polypyrrole film on multiwalled carbon nanotube surface for highly selective and stable determination of carcinogenic amaranth. *J. Electroanal. Chem.* **2021**, *895*, 115494. [CrossRef]
64. Deng, P.; Xiao, J.; Feng, J.; Tian, Y.; Wu, Y.; Li, J.; He, Q. Highly sensitive electrochemical sensor for tyrosine detection using a sub-millimeter electrode. *Microchem. J.* **2021**, *165*, 106106. [CrossRef]
65. Ozcelikay, G.; Dogan-Topal, B.; Ozkan, S.A. An electrochemical sensor based on silver nanoparticles-benzalkonium chloride for the voltammetric determination of antiviral drug Tenofovir. *Electroanalysis* **2018**, *30*, 943–954. [CrossRef]
66. Festinger, N.; Spilarewicz-Stanek, K.; Borowczyk, K.; Guziejewski, D.; Smarzewska, S. Highly sensitive determination of Tenofovir in pharmaceutical formulations and patients urine—Comparative electroanalytical studies using different sensing methods. *Molecules* **2022**, *27*, 1992. [CrossRef]
67. Godasu, S.K.; Sreenivas, S.A. Determination of simultaneous estimation HPLC method for Elvitegravir, Tenofovir disoproxil fumarate, Emtricitabine and cobicistat it's pure and tablet form. *Der Pharma Chem.* **2018**, *10*, 158–165.
68. Donnell, D.; Baeten, J.M.; Bumpus, N.N.; Brantley, J.; Bangsberg, D.R.; Haberer, J.E.; Mujugira, A.; Mugo, N.; Ndase, P.; Hendrix, C.; et al. HIV protective efficacy and correlates of tenofovir blood concentrations in a clinical trial of PrEP for HIV prevention. *J. Acquir. Immune Defic. Syndr.* **2014**, *66*, 340–348. [CrossRef]
69. Boglione, L.; Benedetto, I.D.; Dodaro, V.; Chiecchio, M.; Nicolò, A.D.; Perri, G.D.; D'Avolio, A. Role of plasmatic and urinary concentration of Tenofovir disoproxil fumarate in a cohort of patients affected by chronic hepatitis B. *Arch. Virol.* **2021**, *167*, 1669–1674. [CrossRef]
70. Chavakula, R.; Mutyala, N.; Chennupati, S. Industrially viable synthesis of Tenofovir a key intermediate of Tenofovir disoproxil fumarate and related impurities. *OCAIJ* **2012**, *8*, 432–436.
71. Morawska, K.; Popławski, T.; Ciesielski, W.; Smarzewska, S. Electrochemical and spectroscopic studies of the interaction of antiviral drug Tenofovir with single and double stranded DNA. *Bioelectrochemistry* **2018**, *123*, 227–232. [CrossRef] [PubMed]

biosensors

MDPI

Article

Spectroelectrochemical Enzyme Sensor System for Acetaldehyde Detection in Wine

David Ibáñez *, María Begoña González-García, David Hernández-Santos and Pablo Fanjul-Bolado

Metrohm DropSens S.L., Vivero de Ciencias de la Salud, C/Colegio Santo Domingo de Guzmán s/n, 33010 Oviedo (Asturias), Spain
* Correspondence: david.ibanez@metrohm.com

Abstract: A new spectroelectrochemical two-enzyme sensor system has been developed for the detection of acetaldehyde in wine. A combination of spectroscopy and electrochemistry improves the analytical features of the electrochemical sensor because the optical information collected with this system is only associated with acetaldehyde and avoids the interferents also present in wines as polyphenols. Spectroelectrochemical detection is achieved by the analysis of the optical properties of the $K_3[Fe(CN)_6]/K_4[Fe(CN)_6]$ redox couple involved in the enzymatic process: aldehyde dehydrogenase catalyzes the aldehyde oxidation using β-nicotinamide adenine dinucleotide hydrate (NAD^+) as a cofactor and, simultaneously, diaphorase reoxidizes the NADH formed in the first enzymatic process due to the presence of $K_3[Fe(CN)_6]$. An analysis of the characteristic UV-vis bands of $K_3[Fe(CN)_6]$ at 310 and 420 nm allows the detection of acetaldehyde, since absorption bands are only related to the oxidation of this substrate, and avoids the contribution of other interferents.

Keywords: spectroelectrochemistry; acetaldehyde; aldehyde dehydrogenase; diaphorase; screen-printed electrodes (SPEs)

Citation: Ibáñez, D.; González-García, M.B.; Hernández-Santos, D.; Fanjul-Bolado, P. Spectroelectrochemical Enzyme Sensor System for Acetaldehyde Detection in Wine. *Biosensors* **2022**, *12*, 1032. https://doi.org/10.3390/bios12111032

Received: 17 October 2022
Accepted: 14 November 2022
Published: 17 November 2022

1. Introduction

Acetaldehyde (AA) is a basic compound present in certain alcoholic beverages such as wine. It is mainly produced through two processes, through the oxidation of ethanol by the action of the enzyme alcohol dehydrogenase, and also during the fermentation process by the decarboxylation of pyruvate by the enzyme pyruvate decarboxylase. Both reactions can take place throughout the wine production process, with the quantity of aldehyde produced in these processes being important. AA is currently an indicator of wine quality despite being used to control its biological aging, since it has a negative impact on the wine's aroma when it is present in high concentrations. Furthermore, due to its toxic effects, it plays a crucial role in alcohol intoxication [1,2]. Concentration of AA in wine depends on many important factors [3,4], such as, its rapid reaction with sulfur dioxide, the grape variety, the manufacturing process, fermentation time, alcoholic strength, etc. Quantification of AA in alcoholic beverages is traditionally carried out using chemical methods based on the distillation of AA with bisulfite [5,6], colorimetry [7], chromatography [8,9] or enzymatic methods [1,10]. However, these methods show several drawbacks such as a derivatization step due to its high volatility, the necessity of weak interactions to improve the sensitivity, their susceptibility to environmental interferences, the need to decolorize, filter, or degas samples before assay, tedious and long (more than 2 h) protocols for the preparation of the sample, high costs, etc.

The development of new methods for fast and easy AA detection as well as to avoid complicated instrumentation and long and complex procedures is still required. A combination of enzymatic systems with electrochemistry provides new devices for the easy and quick detection of aldehyde compounds [11–13]. Particularly, AA detection is based on the enzymatic system formed by the combinative work of aldehyde dehydrogenase

(ALDH) and diaphorase (DP) (Figure 1). ALDH catalyzes the oxidation of aldehydes to carboxylic acids using NAD^+ as a cofactor, and particularly, AA is oxidized to acetate. At the same time, DP reoxidizes the NADH previously generated during the ALDH reaction and reduces $K_3[Fe(CN)_6]$ to $K_4[Fe(CN)_6]$. The enzymatic system is completed with the electrochemical oxidation of $K_4[Fe(CN)_6]$, previously generated to $K_3[Fe(CN)_6]$.

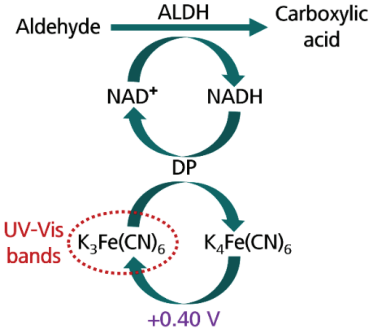

Figure 1. Enzymatic system formed by aldehyde dehydrogenase (ALDH), diaphorase (DP), β-nicotinamide adenine dinucleotide hydrate (NAD^+), and $K_3[Fe(CN)_6]$ which catalyzes the aldehyde oxidation to carboxylic acid.

A combination of electrochemical sensors and spectroscopy has been scarcely used due to the traditional instrumental limitations of spectroelectrochemical techniques. Fortunately, the development of new setups and commercial instruments [14] enables the spectroelectrochemical detection of a variety of analytes [15,16] due to UV-vis spectroelectrochemistry and joins the advantages of electrochemistry and UV-vis spectroscopy. In a single experiment, spectroelectrochemistry provides two signals of different natures, which is a very powerful feature to obtain valuable information about the system being studied. In this enzymatic system, electrochemistry produces the oxidation of $K_4[Fe(CN)_6]$, previously generated during the enzymatic process, to $K_3[Fe(CN)_6]$. The simultaneous optical monitorization takes the advantage of the optical properties of the $K_4[Fe(CN)_6]/K_3[Fe(CN)_6]$ redox couple, allowing the quick and easy detection of AA. Furthermore, the autovalidated character of this technique provides valuable information in a single experiment [17,18]. Although the number of spectroelectrochemical sensors is increasing due to the advantages of this hybrid technique [19–23], enzymatic systems are rarely analyzed using spectroelectrochemical techniques.

In the present work, the usefulness of the proposed enzymatic sensor system is demonstrated for the spectroelectrochemical detection of AA. To the best of our knowledge, this is the first time that a disposable sensor combines UV-vis spectroelectrochemistry with the enzymatic system previously described, providing excellent results.

2. Materials and Methods

2.1. Reagents and Instrumentation

Aldehyde dehydrogenase, potassium activated from baker's yeast (*S. cerevisiae*) (ALDH, EC 1.2.1.5), diaphorase from clostridium kluyveri (DP, EC 1.8.1.4), β-nicotinamide adenine dinucleotide hydrate (NAD^+), bovine serum albumin (BSA), potassium ferricyanide ($K_3[Fe(CN)_6]$), polyvinylpolypyrrolidone (PVPP), and acetaldehyde (AA) were purchased from Merck (Sigma–Aldrich, Madrid, Spain). All chemicals were analytical grade. Aqueous solutions were prepared using ultrapure water (Direct-Q^{TM} 5 system, Millipore, Spain).

Screen-printed carbon electrodes (DRP-110, Metrohm DropSens, Oviedo, Spain) were used to perform the electrochemical experiments, while spectroelectrochemical measurements were carried out with screen-printed gold electrodes (DRP-220AT, Metrohm DropSens, Spain) in order to favor the reflection of the light on the electrode surface. The elec-

tronic systems consisted of a flat ceramic card with a circular carbon or gold working electrode (WE, 4 mm diameter), a carbon or gold counter electrode (CE), and a silver pseudoreference electrode (RE). Electrochemical measurements were performed at room temperature using a multichannel bipotentiostat, galvanostat, and impedance analyzer μStat-i Multi16 controlled using DropView 8400 M v.1.01 software in combination with an eight-channel connector and specific connectors for SPEs (DRP-4MMHCAST8 and DRP-CASTDIR respectively, Metrohm DropSens, Oviedo, Spain). Spectroelectrochemical measurements were performed with SPELEC instrument (Metrohm DropSens, Oviedo, Spain) controlled using DropView SPELEC software in combination with a bifurcated reflection probe (DRP-RPROBE-VIS-UV, Metrohm DropSens, Oviedo, Spain), and a reflection cell (DRP-REFLECELL, Metrohm DropSens, Oviedo, Spain) for working in a near-normal reflection configuration.

A fluorometric assay kit (Sigma–Aldrich, Madrid, Spain) was used to determine the concentration of acetaldehyde in white and rosé wines. Fluorometric experiments were carried out using the 532 nm laser of SPELECRAMAN532 instrument (Metrohm DropSens, Oviedo, Spain) as an excitation source, while the fluorescence signal was acquired with SPELEC.

2.2. Methods

2.2.1. Electrochemical and Spectroelectrochemical Detection of Acetaldehyde

Electrochemical detection was performed with a drop of 60 μL on the screen-printed electrode (SPE), ensuring that the solution covers WE, RE, and CE, using chronoamperometry at +0.40 V for 60 s.

Spectroelectrochemical detection was also carried out using chronoamperometry applying +0.40 V for 300 s. In order to favor the increase of the absorption bands and their better definition, longer times were required for the spectroelectrochemical detection than for the electrochemical one. In addition, 100 μL of solution was used to ensure the spectroelectrochemical cell was filled and bubbles did not remain inside of the device. Light reflected onto the electrode surface was collected using an integration time of 1 s. UV-vis spectra were simultaneously recorded with the electrochemical measurements. According to the experimental time of the spectroelectrochemical experiments (300 s) and the integration time selected (1 s), 300 spectra were recorded during the whole measurement.

2.2.2. Preparation of Wine Samples

Two Spanish wines, Cariñena white wine and Jerez rosé wine, were tested. The samples were not treated before taking the electrochemical and spectroelectrochemical measurements, and were only diluted in a 0.1 M phosphate + 0.1 M KCl buffer solution (pH 8). Calibration plots of wine dilutions were represented in terms where, for example, the value of 0.1 corresponded to the dilution of 1 mL of wine to 10 mL (1:10), 0.25 corresponded to a dilution of 2.5 mL of wine to 10 mL (2.5:10), etc. For fluorometric tests, white and rosé wine samples were diluted 100 times in ultrapure water.

2.2.3. Determination of Enzyme Activities and Michaelis Constants

Enzyme activity of ALDH and DP, expressed in U (μmole of substrate transformed per minute and per mg of protein), has been calculated using spectroscopic methods [10] in previous work [24]. Briefly, ALDH activity was measured following the rate of reduction of NAD^+ using spectroscopic monitoring for 3 min of the band at 340 nm, which was associated with NADH. DP activity was measured following the rate of reduction of $K_3[Fe(CN)_6]$ by the analysis of the band at 420 nm for 3 min. Spectroscopic determination was performed in transmission configuration considering Lambert–Beer's law ($A = \varepsilon \times b \times C$) and the calculated activities of ALDH and DP were 0.26 U/mg and 5.93 U/mg, respectively.

In addition, Michaelis constants for NAD^+ and AA were also calculated in previous work by the fitting of the amperometric data to the Lineweaver-Burk model [24]. The calculated K_M of NAD^+ and AA were 0.101 mM and 0.907 mM, respectively.

3. Results

3.1. Electrochemical Detection of Acetaldehyde

Preliminary assays were considered to establish the initial experimental conditions. Electrochemical detection of AA was performed in 0.07 U/mL ALDH, 0.07 U/mL DP, 1 mM NAD^+, 1 mM $K_3[Fe(CN)_6]$, and 0.1% BSA in 0.1 M phosphate + 0.1 M KCl buffer solution (pH 8) applying +0.40 V for 60 s (electrochemical data are shown in Figure S1). Under these experimental conditions, Figure 2 shows the calibration plot obtained from 1×10^{-5} M to 5×10^{-4} M AA. As can be observed, the results fit the equation y = 1.816 + 0.0592 for this concentration range. In addition, the high correlation coefficient value (R^2 = 0.999) and very low error bars ensures good adjustment and reproducibility.

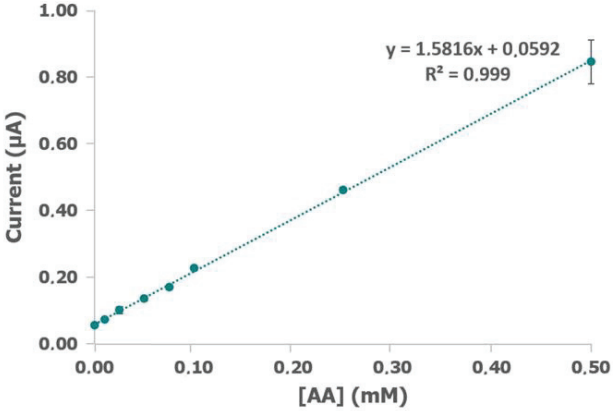

Figure 2. Calibration plot of current obtained after applying +0.40 V for 60 s with different concentrations of acetaldehyde (AA) and 0.07 U/mL ALDH, 0.07 U/mL DP, 1 mM NAD^+, 1 mM $K_3[Fe(CN)_6]$, and 0.1% bovine serum albumin (BSA) in 0.1 M phosphate and 0.1 M KCl buffer solution (pH 8).

In order to obtain a wider concentration range, different concentrations of ALDH and DP were evaluated. The ratio between ALDH and DP is a crucial parameter because the lack of activity of one of them could hamper the reliability of the electrochemical measurements [13]. According to previous works [12,13,24], ratio ALDH/DP = 1 remains constant and both concentrations were modified in the same way. Different amounts of enzymes were evaluated, but the best results shown in Figure 3 were obtained working in in 0.14 U/mL ALDH, 0.14 U/mL DP, 1 mM NAD^+, 1 mM $K_3[Fe(CN)_6]$, and 0.1% BSA in 0.1 M phosphate + 0.1 M KCl buffer solution (pH 8) (electrochemical data are shown in Figure S2). A higher concentration of ALDH and DP did not improve the electrochemical results. The calibration curve showed a higher slope than the value obtained under the previous conditions (Figure 2), a wider concentration range (from 5×10^{-6} M to 2.5×10^{-4} M), and maintained a good adjustment (R^2 = 0.999) and reproducibility.

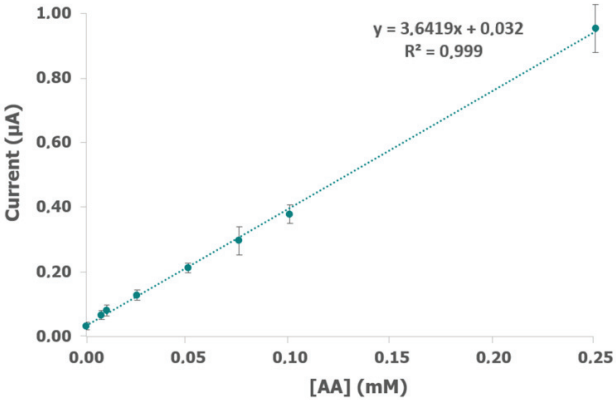

Figure 3. Calibration plot of AA obtained after applying +0.40 V for 60 s with different concentrations of acetaldehyde (AA) and 0.14 U/mL ALDH, 0.14 U/mL DP, 1 mM NAD^+, 1 mM $K_3[Fe(CN)_6]$, and 0.1% BSA in 0.1 M phosphate and 0.1 M KCl buffer solution (pH 8).

Table 1 summarizes the experimental conditions and the electrochemical results in the detection of AA. According to the linear range of AA, 0.14 U/mL ALDH and 0.14 U/mL DP were selected to continue with the development of the new enzymatic device.

Table 1. Experimental conditions for the electrochemical detection of acetaldehyde.

Electrochemical Technique	Potential	Time	ALDH	DP	NAD^+	$K_3[Fe(CN)_6]$	BSA	AA Linear Range
Chronoamperometry	+0.40 V	60 s	0.07 U/mL	0.07 U/mL	1 mM	1 mM	0.1%	1×10^{-5}–5×10^{-4} M
Chronoamperometry	+0.40 V	60 s	0.14 U/mL	0.14 U/mL	1 mM	1 mM	0.1%	5×10^{-6}–2.5×10^{-4} M

However, apart from AA there were more components in wine samples that could interfere in the electrochemical detection, for instance, polyphenols. Initially, calibration curves with different dilutions of rosé and white wines in buffer solution were carried out (green dots in Figure 4a,b, respectively) (electrochemical data are shown in Figure S3a,b). As can be observed, dilutions from 0.05 to 0.5 for rosé wine and 0.1 to 1 (no dilution) for white wine fit a linear curve. In addition, the same experiments were performed without a NAD^+ cofactor in the sample (orange dots in Figure 4a,b) to remove the contribution of AA to the current. In this way, these measurements provide the electrochemical signal associated with other components but not with AA because the enzymatic reaction did not take place. Similar slopes were obtained working without NAD^+, and the interferents contribution is clearly demonstrated since the electrochemical current was closer than the response obtained with NAD^+. The average of the current difference observed with and without NAD^+ was 0.29 µA and 0.19 µA for rosé and white wine, respectively.

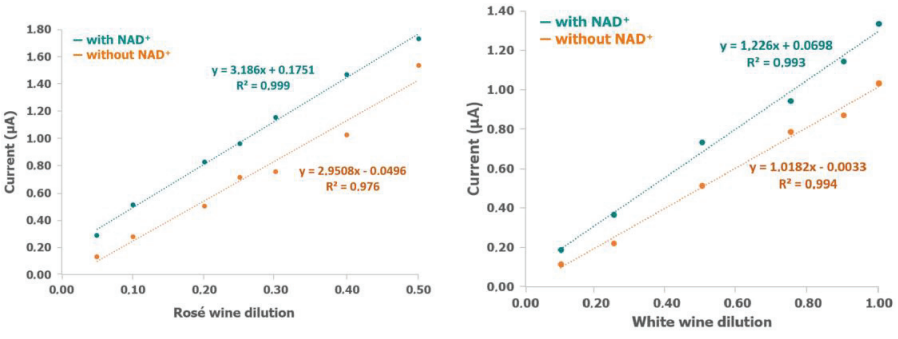

(**a**) (**b**)

Figure 4. Calibration plot of (**a**) rosé and (**b**) white wines obtained after applying +0.40 V for 60 s with different dilutions of wine and 0.14 U/mL ALDH, 0.14 U/mL DP, with (green dots) and without (orange dots) 1 mM NAD^+, 1 mM $K_3[Fe(CN)_6]$, and 0.1% BSA in 0.1 M phosphate and 0.1 M KCl buffer solution (pH 8).

Other parameters involved in the detection of AA were optimized to minimize the contribution of the interferents. Particularly, lower potential + 0.20 V was applied to carry out the AA calibration with and without NAD^+. As was expected, the current value obtained was lower than when applying +0.40 V, but the contribution of the interferents in the electrochemical signal did not decrease when NAD^+ was not added in the system (data not shown). A significant alternative to remove the phenolic compounds in wines consists of their treatment with polyvinylpolypyrrolidone (PVPP) [25–27]. Accordingly, 25 mL of each wine was mixed with 0.5 g of PVPP, the mixture was stirred for at least 5 min and then filtered before being used [28,29]. After this protocol, the samples were decolored due to the fact that PVPP absorbs most polyphenol present in wines. The electrochemical calibration of decolored rosé and white wines was performed under the same experimental conditions as those shown in Figure 4 (0.14 U/mL ALDH, 0.14 U/mL DP, 1 mM NAD^+, 1 mM $K_3[Fe(CN)_6]$, and 0.1% BSA in 0.1 M phosphate and 0.1 M KCl buffer solution). Although PVPP is useful to decrease the amount of phenolic compounds, the electrochemical results (data not shown) do not display good reproducibility and the accurate quantification of AA cannot be achieved. According to the results obtained, the electrochemical detection of AA based on the enzymatic ALDH/DP sensor systems seems complicated and alternative methodologies must be developed.

3.2. Spectroelectrochemical Detection of Acetaldehyde

Spectroscopic detection simultaneously performed with the electrochemical oxidation is an interesting methodology based on the optical properties of the enzymatic system employed, particularly those related to the $K_3[Fe(CN)_6]/K_4[Fe(CN)_6]$ redox couple. $K_3[Fe(CN)_6]$ shows two characteristic UV-vis bands at 310 and 420 nm [30], while $K_4[Fe(CN)_6]$ does not show an absorption signal. The main advantage with respect to electrochemical detection is that $K_3[Fe(CN)_6]/K_4[Fe(CN)_6]$ conversion is only related to AA and not to polyphenols or other interferents present in wine samples. In order to ensure the removal of this contribution, gallic acid was considered as representative polyphenol and its optical properties were analyzed. Gallic acid only shows one band at 280 nm, which does not interfere with $K_3[Fe(CN)_6]$ bands. An additional advantage of spectroelectrochemical analysis is that the pretreatment of wine samples is not required.

UV-vis spectroelectrochemistry was carried out, applying +0.40 V for 300 s instead of 60 s to favor the enhancement of the optical signal. The electrochemical reaction (chronoamperogram shown in Figure 5a) produces the oxidation to $K_3[Fe(CN)_6]$ while their characteristic bands are simultaneously detected (Figure 5b) during the whole measurement. Figure 5b shows the evolution of the spectroelectrochemical signal in 0.6 mM AA during

300 s. The spectrum of the initial solution, which corresponds to the $K_4[Fe(CN)_6]$ generated during the enzymatic reaction, was taken as a reference (blue line in Figure 5b). As Figure 5b shows, absorbance of UV-vis bands of $K_3[Fe(CN)_6]$ increases during the oxidation process of $K_4[Fe(CN)_6]$. In order to demonstrate that the observed signal corresponds to the oxidation process previously explained, the optical monitoring of the enzymatic reaction (10 min) without potential, was carried out. As can be observed in Figure S4, the absorbance decreases during the enzymatic reaction because the initial $K_3[Fe(CN)_6]$ present in solution is reduced to $K_4[Fe(CN)_6]$ which does not absorb in the UV-vis region.

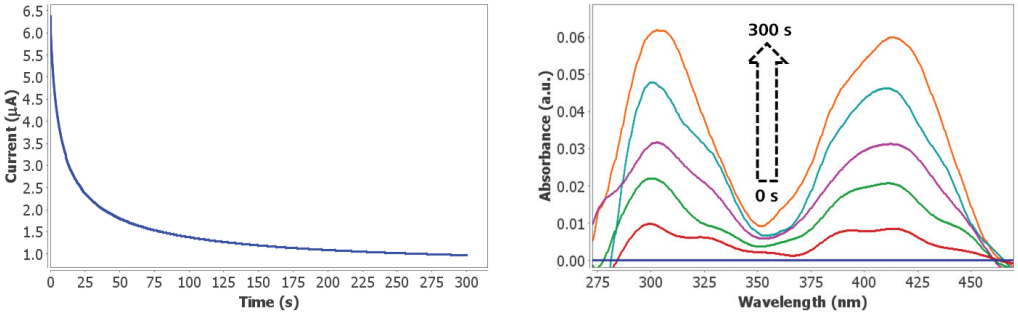

Figure 5. (**a**) Chronoamperometry and (**b**) UV-vis spectra recorded in 0.6 mM AA, 0.14 U/mL ALDH, 0.14 U/mL DP, 1 mM NAD^+, 1 mM $K_3[Fe(CN)_6]$, and 0.1% BSA in 0.1 M phosphate and 0.1 M KCl buffer solution (pH 8). Potential of +0.40 V was applied for 300 s.

Different concentrations of AA were evaluated in 0.14 U/mL ALDH, 0.14 U/mL DP, 1 mM NAD^+, 1 mM $K_3[Fe(CN)_6]$, and 0.1% BSA in 0.1 M phosphate and 0.1 M KCl buffer solution. Figure S5 displays the spectrum obtained after 300 s with different concentrations of AA. The calibration curve done with the absorbance at 420 nm after 300 s (Figure 6) from 0.1 to 0.7 mM AA fits the equation y = 0.993x + 0.0014. The high correlation coefficient value (R^2 = 0.996) ensures the good adjustment and the usefulness and sensitivity of the spectroelectrochemical method for the detection of AA in this concentration range. Furthermore, good reproducibility is demonstrated with the small error bars.

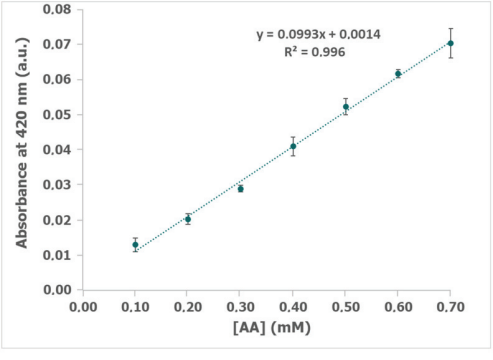

Figure 6. A calibration plot of absorbance at 420 nm obtained after applying +0.40 V for 300 s with different concentrations of acetaldehyde (AA) (0.1–0.7 mM) and 0.14 U/mL ALDH, 0.14 U/mL DP, 1 mM NAD^+, 1 mM $K_3[Fe(CN)_6]$, and 0.1% BSA in 0.1 M phosphate and 0.1 M KCl buffer solution (pH 8).

Once the AA calibration was obtained, wine samples were measured. Different dilutions of white and rosé wines were tested, allowing us to optimize the dilution factor for each type of wine. In the case of white wine, the most reproducible results which fit the calibration range were obtained with the sample 1:2 diluted, while rosé wine must be 1:4 diluted to optimize the spectroelectrochemical results. Applying these dilution factors to the wine samples, the mixture with the other reagents was achieved. After 10 min of enzymatic reaction, the spectroelectrochemical detection was performed applying +0.40 V for 300 s and UV-vis spectra were simultaneously recorded. For white wine, absorbance at 420 nm was 0.0212 +/− 0.0012 a.u. (n = 3), while for rosé wine it was 0.0287 +/− 0.0025 a.u. (n = 3). Quantification of AA was easily calculated extracting the AA concentration from the calibration curve (y = 0.993x + 0.0014, Figure 6) and considering the dilution factor for each type of wine, but also the dilution of the wine sample in the mixture with the other reagents. The concentration of AA was calculated, obtaining 1.99 mM (87.56 mg/L) in white wine and 5.51 mM (242.44 mg/L) in rosé wine. In addition, an RSD of 5.79% and 8.84% were obtained for white and rosé wine, respectively. As was previously explained, the variability in the concentration of AA present in wines is very high, since it not only depends on the type of wine (white, rosé, etc.), but also on many other factors, with certain wines able to have a concentration of up to 700 mg/L [3]. As is reported in literature, a concentration of AA in Cariñena white wine, calculated using gas chromatography–mass spectrometry, is 87.2–87.9 mg/L [31]. In terms of Jerez rosé wine, the characteristic concentration in this kind of wine is 220–380 mg/L [32]. Hence, the experimental results obtained in this work agree with the data reported in the literature using other methods, demonstrating the usefulness of the spectroelectrochemical enzymatic system.

To validate the spectroelectrochemical method, a commercial assay kit was used to determine the AA concentration in wine samples. According to the protocol, white and rosé wines were evaluated using fluorometric tests after 30 min of incubation, obtaining 2.13 ± 0.05 mM (93.72 ± 2.2 mg/L) and 5.41 ± 0.16 mM (238.04 ± 7.4 mg/L), respectively. Hence, the spectroelectrochemical results obtained with the enzyme sensor system not only agree with those reported in literature, but also with the value calculated with a commercial kit designed for that purpose (Table 2).

Table 2. Comparison among several methods for the determination of acetaldehyde in Cariñena and Jerez wines.

Detection Technique	Cariñena White Wine (mg/L)	Jerez Rosé Wine (mg/L)
GC-MS	87.2–87.9 [31]	220–380 [32]
Fluorometry	93.72 (this work)	238.04 (this work)
Spectroelectrochemistry	87.56 (this work)	242.44 (this work)

4. Conclusions

In summary, a new spectroelectrochemical enzymatic sensor has been developed in this work. A combination of electrochemistry and UV-vis spectroscopy in a single experiment allows us to improve the analytical features that both techniques have separately. The new device is based on the joint action of ALDH and DP, which produce the oxidation of AA to acetate, but also generate $K_4[Fe(CN)_6]$ during the enzymatic reactions. The $K_4[Fe(CN)_6]/K_3[Fe(CN)_6]$ redox couple has interesting optical properties, $K_3[Fe(CN)_6]$ has two absorption bands, while $K_4[Fe(CN)_6]$ does not have any. The spectroscopic signal obtained in the spectroelectrochemical measurements only displays the two absorption bands of $K_3[Fe(CN)_6]$, and additional bands related to the interferents also present in wines are not detected. In that way, it avoids the pretreatment of the samples to remove the contribution of other compounds as polyphenols, simplifies the detection protocol, and saves time and cost. Furthermore, the easy spectroelectrochemical monitoring of the oxidation of $K_4[Fe(CN)_6]$ to $K_3[Fe(CN)_6]$ allows the quantification of AA. Two different wines have been evaluated in this work and, as the pretreatment was very easy, they only required an initial dilution, white wine was diluted 1:2 and rosé wine 1:4. The calibration

curve with absorbance at 420 nm vs. the AA concentration, allowed the quantification of aldehyde, being 1.99 mM or 87.66 mg/L in white wine and 5.51 mM or 242.57 mg/L in rosé wine. The spectroelectrochemical results agree with the literature as well as with those obtained with a commercial kit, and in this way, this spectroelectrochemical enzymatic sensor opens new possibilities in the detection of acetaldehyde in the wine industry.

Supplementary Materials: The following are available online at https://www.mdpi.com/article/10.3390/bios12111032/s1, Figures S1 and S2: Chronoamperograms obtained applying +0.40 V for 60 s with different concentrations of AA, ALDH, DP, NAD^+, $K_3[Fe(CN)_6]$ and BSA in phosphate and KCl buffer solution (pH 8). Figure S3: Chronoamperograms obtained applying +0.40 V for 60 s with different dilutions of rosé and white wines, ALDH, DP, NAD^+, $K_3[Fe(CN)_6]$ and BSA in phosphate and KCl buffer solution (pH 8). Figure S4: UV-vis spectra recorded during the enzymatic reaction (10 min) in AA, ALDH, DP, NAD^+, $K_3[Fe(CN)_6]$ and BSA in phosphate and KCl buffer solution (pH 8). Figure S5: UV-vis spectra obtained after applying +0.40 V for 300 s with different concentrations of AA, ALDH, DP, NAD^+, $K_3[Fe(CN)_6]$ and BSA in phosphate and KCl buffer solution (pH 8).

Author Contributions: Conceptualization, D.I.; methodology, D.I. and M.B.G.-G.; investigation D.I. and M.B.G.-G.; writing—original draft preparation, D.I.; writing—review and editing M.B.G.-G., D.H.-S., and P.F.-B.; project administration P.F.-B.; supervision, D.H.-S. and P.F.-B. All authors have read and agreed to the published version of the manuscript.

Funding: This research was funded by ENZ4IFACES (IDE/2020/000017) project funding by IDEPA and the European Regional Development Funds under the ERA-NET framework.

Institutional Review Board Statement: Not applicable.

Informed Consent Statement: Not applicable.

Conflicts of Interest: The authors declare no conflict of interest.

References

1. Noguer, T.; Marty, J.L. Reagentless Sensors for Acetaldehyde. *Anal. Lett.* **1997**, *30*, 1069–1080. [CrossRef]
2. Avramescu, A.; Noguer, T.; Avramescu, M.; Marty, J.L. Screen-Printed Biosensors for the Control of Wine Quality Based on Lactate and Acetaldehyde Determination. *Anal. Chim. Acta* **2002**, *458*, 203–213. [CrossRef]
3. Arias-Pérez, I.; Sáenz-Navajas, M.P.; De-la-Fuente-Blanco, A.; Ferreira, V.; Escudero, A. Insights on the Role of Acetaldehyde and Other Aldehydes in the Odour and Tactile Nasal Perception of Red Wine. *Food Chem.* **2021**, *361*, 130081. [CrossRef] [PubMed]
4. Liu, S.Q.; Pilone, G.J. An Overview of Formation and Roles of Acetaldehyde in Winemaking with Emphasis on Microbiological Implications. *Int. J. Food Sci. Technol.* **2000**, *35*, 49–61. [CrossRef]
5. Jeong, H.S.; Chung, H.; Song, S.H.; Kim, C.I.; Lee, J.G.; Kim, Y.S. Validation and Determination of the Contents of Acetaldehyde and Formaldehyde in Foods. *Toxicol. Res.* **2015**, *31*, 273–278. [CrossRef]
6. Parkinson, A.E.; Wagner, E.C. Estimation of Aldehydes by the Bisulfite Method: An Improved Procedure. *Ind. Eng. Chem.-Anal. Ed.* **1934**, *6*, 433–436. [CrossRef]
7. Li, Z.; Fang, M.; LaGasse, M.K.; Askim, J.R.; Suslick, K.S. Colorimetric Recognition of Aldehydes and Ketones. *Angew. Chem.* **2017**, *129*, 9992–9995. [CrossRef]
8. Miyake, T.; Shibamoto, T. Quantitative Analysis of Acetaldehyde in Foods and Beverages. *J. Agric. Food Chem.* **1993**, *41*, 1968–1970. [CrossRef]
9. Guan, X.; Rubin, E.; Anni, H. An Optimized Method for the Measurement of Acetaldehyde by High-Performance Liquid Chromatography. *Alcohol. Clin. Exp. Res.* **2012**, *36*, 398–405. [CrossRef]
10. Noguer, T.; Marty, J.L. An Amperometric Bienzyme Electrode for Acetaldehyde Detection. *Enzyme Microb. Technol.* **1995**, *17*, 453–456. [CrossRef]
11. Marty, J.L.; Mionetto, N.; Noguer, T.; Ortega, F.; Roux, C. Enzyme Sensors for the Detection of Pesticides. *Biosens. Bioelectron.* **1993**, *8*, 273–280. [CrossRef]
12. Noguer, T.; Gradinaru, A.; Ciucu, A.; Marty, J.L. A New Disposable Biosensor for the Accurate and Sensitive Detection of Ethylenebis(Dithiocarbamate) Fungicides. *Anal. Lett.* **1999**, *32*, 1723–1738. [CrossRef]
13. Noguer, T.; Marty, J.L. High Sensitive Bienzymic Sensor for the Detection of Dithiocarbamate Fungicides. *Anal. Chim. Acta* **1997**, *347*, 63–70. [CrossRef]
14. Navarro, C.; Begoña, M.; García, G.; Hernández, D.; Aranzazu, M.; Colina, A.; Fanjul-Bolado, P. Electrochemistry Aqueous UV–VIS Spectroelectrochemical Study of the Voltammetric Reduction of Graphene Oxide on Screen-Printed Carbon Electrodes. *Electrochem. Commun.* **2016**, *64*, 65–68. [CrossRef]

15. Garoz-Ruiz, J.; Perales-Rondon, J.V.; Heras, A.; Colina, A. Spectroelectrochemical Sensing: Current Trends and Challenges. *Electroanalysis* **2019**, *31*, 1254–1278. [CrossRef]
16. Hernandez, S.; Perales-Rondon, J.V.; Arnaiz, A.; Perez-Estebanez, M.; Gomez, E.; Colina, A.; Heras, A. Determination of Nicotinamide in a Multivitamin Complex by Electrochemical-Surface Enhanced Raman Spectroscopy. *J. Electroanal. Chem.* **2020**, *879*, 114743. [CrossRef]
17. González-Diéguez, N.; Colina, A.; López-Palacios, J.; Heras, A. Spectroelectrochemistry at Screen-Printed Electrodes: Determination of Dopamine. *Anal. Chem.* **2012**, *84*, 9146–9153. [CrossRef]
18. Hernandez, S.; Perales-Rondon, J.V.; Heras, A.; Colina, A. Determination of Uric Acid in Synthetic Urine by Using Electrochemical Surface Oxidation Enhanced Raman Scattering. *Anal. Chim. Acta* **2019**, *1085*, 61–67. [CrossRef]
19. El-Said, W.A.; Kim, T.H.; Chung, Y.H.; Choi, J.W. Fabrication of New Single Cell Chip to Monitor Intracellular and Extracellular Redox State Based on Spectroelectrochemical Method. *Biomaterials* **2015**, *40*, 80–87. [CrossRef]
20. Lynk, T.P.; Clarke, O.J.R.; Kesavan, N.; Brosseau, C.L. Development of a Sustainable Plasmon-Enhanced Spectroelectrochemical Sensor Using Avocado Pit (*Persea americana*) Extract. *Sens. Actuators B Chem.* **2018**, *257*, 270–277. [CrossRef]
21. Cannan, S.; Douglas Macklam, I.; Unwin, P.R. Three-Dimensional Imaging of Proton Gradients at Microelectrode Surfaces Using Confocal Laser Scanning Microscopy. *Electrochem. Commun.* **2002**, *4*, 886–892. [CrossRef]
22. Imai, K.; Okazaki, T.; Hata, N.; Taguchi, S.; Sugawara, K.; Kuramitz, H. Simultaneous Multiselective Spectroelectrochemical Fiber-Optic Sensor: Demonstration of the Concept Using Methylene Blue and Ferrocyanide. *Anal. Chem.* **2015**, *87*, 2375–2382. [CrossRef] [PubMed]
23. Wilson, R.; Schiffrin, D.J.; Luff, B.J.; Wilkinson, J.S. Optoelectrochemical Sensor for Lead Based on Electrochemically Assisted Solvent Extraction. *Sens. Actuators B Chem.* **2000**, *63*, 115–121. [CrossRef]
24. Ibáñez, D.; Izquierdo-Bote, D.; González-García, M.B.; Hernández-Santos, D.; Fanjul-Bolado, P. Development of a New Screen-Printed Transducer for the Electrochemical Detection of Thiram. *Chemosensors* **2021**, *9*, 303. [CrossRef]
25. Bilko, M.; Gunko, S.; Babych, I.; Naumenko, O.; Mukoid, R.; Ischenko, M.; Doboniy, I.; Danylenko, S.; Bovkun, A.; Stotska, O. Investigation of the Appearance and Elimination of Pinking Coloration in White Wines. *East.-Eur. J. Enterp. Technol.* **2022**, *1*, 56–62. [CrossRef]
26. Nel, A.P.; du Toit, W.J.; van Jaarsveld, F.P. Pinking in White Wines—A Review. *S. Afr. J. Enol. Vitic.* **2020**, *41*, 151–157. [CrossRef]
27. Gil, M.; Avila-Salas, F.; Santos, L.S.; Iturmendi, N.; Moine, V.; Cheynier, V.; Saucier, C. Rosé Wine Fining Using Polyvinylpolypyrrolidone: Colorimetry, Targeted Polyphenomics, and Molecular Dynamics Simulations. *J. Agric. Food Chem.* **2017**, *65*, 10591–10597. [CrossRef]
28. Shin, K.S.; Lee, J.H. Acetaldehyde Contents and Quality Characteristics of Commercial Alcoholic Beverages. *Food Sci. Biotechnol.* **2019**, *28*, 1027–1036. [CrossRef]
29. Grassin, C.; Dubourdieu, D. Quantitative Determination of Botrytis Laccase in Musts and Wines by the Syringaldazine Test. *J. Sci. Food Agric.* **1989**, *48*, 369–376. [CrossRef]
30. Schroll, C.A.; Chatterjee, S.; Heineman, W.R.; Bryan, S.A. Semi-Infinite Linear Diffusion Spectroelectrochemistry on an Aqueous Micro-Drop. *Anal. Chem.* **2011**, *83*, 4214–4219. [CrossRef]
31. Escudero, A.; Asensio, E.; Cacho, J.; Ferreira, V. Sensory and Chemical Changes of Young White Wines Stored under Oxygen. An Assessment of the Role Played by Aldehydes and Some Other Important Odorants. *Food Chem.* **2002**, *77*, 325–331. [CrossRef]
32. Ribéreau-Gayon, P.; Dubourdieu, D.; Donèche, B.; Lonvaud, A. *Handbook of Enology: The Microbiology of Wine and Vinifications*; John Wiley & Sons, Ltd.: Chichester, UK, 2006; Volume 1, ISBN 0470010347.

biosensors

MDPI

Review

Fluorescent Sensing Platforms for Detecting and Imaging the Biomarkers of Alzheimer's Disease

Xingyun Liu [1], Yibiao Liu [2,3,*] and Qiong Liu [3,4]

[1] Department of Chemistry, College of Chemistry and Environmental Engineering, Shenzhen University, Shenzhen 518060, China; liuxingyunfairy20@163.com
[2] Longgang District Central Hospital of Shenzhen, Shenzhen 518116, China
[3] Shenzhen-Hong Kong Institute of Brain Science, Shenzhen Fundamental Research Institutions, Shenzhen 518055, China
[4] Shenzhen Key Laboratory of Marine Biotechnology and Ecology, College of Life Sciences and Oceanography, Shenzhen University, Shenzhen 518055, China
* Correspondence: liuyibiao12345@126.com

Abstract: Alzheimer's disease (AD) is an irreversible neurodegenerative disease with clinical symptoms of memory loss and cognitive impairment. Currently, no effective drug or therapeutic method is available for curing this disease. The major strategy used is to identify and block AD at its initial stage. Thus, early diagnosis is very important for intervention of the disease and assessment of drug efficacy. The gold standards of clinical diagnosis include the measurement of AD biomarkers in cerebrospinal fluid and positron emission tomography imaging of the brain for amyloid-β (Aβ) deposits. However, these methods are difficult to apply to the general screening of a large aging population because of their high cost, radioactivity and inaccessibility. Comparatively, blood sample detection is less invasive and more accessible for the diagnosis of AD. Hence, a variety of assays based on fluorescence analysis, surface-enhanced Raman scattering, electrochemistry, etc., were developed for the detection of AD biomarkers in blood. These methods play significant roles in recognizing asymptomatic AD and predicting the course of the disease. In a clinical setting, the combination of blood biomarker detection with brain imaging may enhance the accuracy of early diagnosis. Fluorescence-sensing techniques can be used not only to detect the levels of biomarkers in blood but also to image biomarkers in the brain in real time due to their low toxicity, high sensitivity and good biocompatibility. In this review, we summarize the newly developed fluorescent sensing platforms and their application in detecting and imaging biomarkers of AD, such as Aβ and tau in the last five years, and discuss their prospects for clinical applications.

Keywords: Alzheimer's disease; biomarkers; diagnosis

Citation: Liu, X.; Liu, Y.; Liu, Q. Fluorescent Sensing Platforms for Detecting and Imaging the Biomarkers of Alzheimer's Disease. *Biosensors* **2023**, *13*, 515. https://doi.org/10.3390/bios13050515

Received: 30 March 2023
Revised: 22 April 2023
Accepted: 28 April 2023
Published: 30 April 2023

1. Introduction

Alzheimer's disease (AD) is a common neurodegenerative disease accompanied by the clinical features of memory loss and cognitive decline [1]. Approximately 34 million people worldwide are suffering from this disease at present. With the rising aging population, more than 131 million people are expected to be affected by this disease by 2050, resulting in a huge burden to individuals and society [1,2]. So far, the pathogenesis of the disease has not been revealed clearly, and there are no effective measures for the treatment in clinical settings. Early diagnosis and intervention are still the only measures to prevent the disease. Amyloid plaques formed by extracellular Aβ peptide precipitation and neurofibrillary tangles (NFTs) formed by intracellular tau protein aggregation are the main pathological features of AD in the brain [3], whose levels in the cerebrospinal fluid (CSF) have been used as the gold standards for neuropathological diagnosis of AD. Alteration in Aβ and tau levels in CSF and plasma may appear many years before symptoms. Tracking these

changes in biomarkers is very important to identify asymptomatic AD, and thus, predict the progression of the pathological process.

According to the report by the National Institute on Aging-Alzheimer's Association (NIA-AA) in 2018 [1,3,4], the quantitative detection of AD biomarkers, including Aβ40 and Aβ42 peptides and phosphorylated and total tau proteins, in CSF was established as the diagnostic criteria for identifying probable AD patients. However, these methods based on CSF biomarkers are not applicable for physical examination of the public due to their invasiveness during sample collection via lumbar puncture. Research showed that biomarkers in CSF can access the blood due to damage to the blood–brain barrier (BBB) in AD [5–9]. In the blood, a low level of Aβ42 and high levels of total and phosphorylated tau proteins indicate damage and degeneration of neurons in the brain [10], and the contents of these biomarkers are altered with the process of AD development. Therefore, detecting readily available blood biomarkers (e.g., Aβ42 peptides, phosphorylated tau proteins and total tau proteins) is becoming a promising strategy for AD diagnosis. In clinical settings, the currently available and practical methods for AD diagnosis are the rating scale tests and brain imaging, including positron emission tomography (PET) [11], single-photon emission computed tomography (SPECT) [12–15] and magnetic resonance imaging (MRI). However, the rating scale tests are highly dependent on the judgment of doctors, with high subjectivity and inaccuracy. Brain imaging with the above investment is comparably accurate, but the expensive instruments and radioactive tracer for PET block their application in physical examinations and population screening [16,17]. For example, PET detection uses the accumulation of ^{11}C or ^{18}F isotopes in the metabolism of radionuclides in the human body to reflect the metabolic activities of life. However, the half-lives of ^{11}C and ^{18}F are relatively short at 20 and 110 min, respectively, and they are quickly metabolized in the body [18].

The combination of blood biomarker detection with neuroimaging in the brain could be an effective strategy to enhance the accuracy of early diagnosis. With the rapid progress of sensing techniques, fluorescent methods are used not only to detect the levels of biomarkers in blood but also to instantly image them in the brain based on the low toxicity, high sensitivity and good biocompatibility of fluorescent agents and the excellent sensing performance and accessibility of the technology platform. However, for the detection of a trace amount of samples, such as a drop of blood, the fluorescence signal is weak, and thus, the detection sensitivity needs to be improved, leading to the optical signal detection equipment needing to be much more complex and expensive, which limits its application [19]. At present, a single-molecular array (Simoa) based on the principle of immunofluorescence became a mature technology from Quanterix company that can measure AD blood biomarkers at femtomolar concentrations. As shown in Figure 1, the ultra-high sensitivity of Simoa mainly relies on its femtoliter-sized reaction system to reduce the background noise. This technology requires expensive equipment for the measurement, which is a typical example of using a large-scale detection system to achieve an ultra-sensitive measurement [20]. In contrast to the published articles on the targeting of amyloid aggregates using photoactive probes [21], the targeting of AD using small molecule near-infrared fluorescence probes [22] was discussed. In this review, we excluded the fluorescence methods considering their high cost and restrictions regarding equipment. We focused on the newly developed enhanced fluorescent sensing platforms for their application in detecting AD blood biomarkers, such as Aβ, tau, BACE1 and APOE4. Moreover, the imaging of Aβ plaques and tau tangles in the brain based on fluorescent sensing platforms is also summarized. In brief, this review first overviews some AD biomarkers in the blood from the last five years and then introduces enhanced fluorescence-sensing platforms for detecting them, with further applications in imaging Aβ plaques and NFTs in the brain. The prospects and challenges of those platforms are also discussed in terms of research directions and clinical applications.

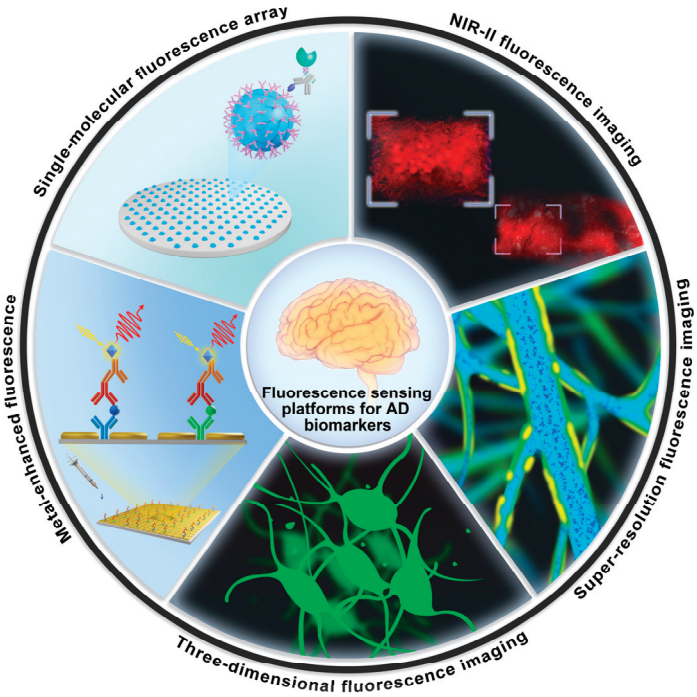

Figure 1. Schematic illustration of enhanced fluorescence-sensing platforms for detecting trace-level AD blood biomarkers and imaging AD features in the brain.

2. Biomarkers for AD Diagnosis

Compared with cerebrospinal fluid sampling via a lumbar puncture and other invasive methods, using blood as a non-invasive method to detect AD biomarkers has attracted great attention. AD occurs over a long period with various biomarkers, such as Aβ, tau, APOE, BACE1 and microRNAs, showing up in the blood. The main pathological features of AD are senile plaques, which are mainly formed by the aggregation of Aβ and neurofibrillary tangles (NFTs) formed by the hyperphosphorylation of tau (P-tau), with both of these leading to the death of neurons [23,24]. Therefore, Aβ (including Aβ monomers, oligomers and plaques) [17,25,26] and tau (including total tau proteins and phosphorylated tau proteins) [9,20,27] are generally regarded as the two most important types of AD biomarkers in blood. In addition, other blood biomarkers were also reported, such as the specific microRNAs [28], BACE1 [29,30] APOE [31–34] and metal ions [35,36].

Many studies showed that the level of Aβ protein begins to change 10–15 years before clinical manifestation [25]. As the major component of senile plaques, Aβ is derived from amyloid precursor protein (APP). APP metabolism is mediated by three hydrolases, i.e., α-, β- and γ-secretases. Aβ is produced by APP cleavage sequentially through β- and γ-secretases. Polypeptides Aβ40 and Aβ42 containing 40 and 42 amino acids, respectively, are the two most important isoforms [26]. Normally, the production and clearance of Aβ peptides should be balanced, but in AD patients, increased production and decreased clearance of Aβ lead to abnormal extracellular accumulation of Aβ40 and Aβ42 peptides. Since the concentration of Aβ40 in CFS is ten times that of Aβ42, the concentration of Aβ40 does not change significantly during the process of AD, and the ratio of Aβ42/Aβ40 is more accurate than that of a single indicator [37]. The abnormally aggregated Aβ42 monomer self-assembles into soluble Aβ oligomers, which then form fibrils and plaques that eventually lead to tau pathology and subsequent neuronal dysfunction [38]. Soluble

Aβ oligomers are the main toxic substances and are more specifically involved in neuronal death and cognitive impairment than insoluble fibrils [38,39].

Tau proteins play physiological roles in stabilizing microtubules, reducing the dissociation of tubulin molecules and inducing microtubules to form bundles. There are six isoforms of tau proteins containing 352, 381, 383, 410, 412 and 441 amino acids [40]. In the case of full-length tau, which contains 441 amino acids, there are a total of 85 possible phosphorylation sites that regulate the binding of tau to microtubules to keep them stable [41]. In healthy people, a tau protein contains 2–3 phosphate groups, while in AD patients, tau is abnormally hyperphosphorylated and can contain 5–9 phosphate groups per protein. Hyperphosphorylation of tau reduces the binding affinity between tau and microtubules and grabs other microtubule-associated proteins (MAPs) from microtubules, which leads to the formation of NFTs and ultimately results in microtubule depolymerization and impaired neuronal function [42].

In addition, APOE, BACE1 and some microRNAs are used to analyze the pathology of AD. Apolipoprotein E (APOE) is a major lipid transporter in the brain, with three main isoforms (APOE2, APOE3 and APOE4) [31]. The APOE4 allele is one of the most important genetic risk factors [43]. APOE4 heterozygous carriers have a 2–3 times higher risk of AD than noncarriers, while homozygous individuals have a 12 times higher risk of AD than noncarriers [31,44]. APOE2 carriers have a protective effect compared with APOE3 and APOE4 carriers [45]. Although the exact mechanism of how APOE4 mediates AD pathology is still unclear, APOE4 was accepted in clinical settings as a biomarker to distinguish AD candidates and healthy controls. BACE1 (i.e., β-secretase) is an aspartic acid protease that mediates the cleavage of APP to release Aβ. Therefore, the reduction in BACE1 can effectively reduce the overproduction of Aβ [46]. Studies showed that BACE1 inhibitors effectively reduce excessive production and abnormal accumulation of Aβ [47]. MicroRNAs are small endogenous noncoding RNAs [48]. Some microRNAs are regulatory factors used to regulate the expression of APP and the production and clearance of Aβ during their formation. MicroRNAs are very stable in blood, plasma and CSF, and are gradually becoming biomarkers for the detection of AD [49]. For example, Arun Richard Chandrasekaran et al. [50] developed AD-related miR-107 native assays, achieving ultrasensitive detection of miR-107 without amplification or labeling. The metabolism of human cells produces reactive nitrogen species (RNS) and reactive oxygen species (ROS). ROS has a dual role in the body. Overactivity of ROS will play a destructive role in accelerating human aging and cell damage [51]. The content of ROS in AD patients is higher than that in normal people. $ONOO^-$ is a combination product of superoxide and nitric oxide, which is an active substance that causes great harm via oxidative stress. Wang et al. [52] designed a peroxynitrite ($ONOO^-$)-activated near-infrared probe, namely, Rd-DPA3, whose detection limit of $ONOO^-$ was 3.4 nM, which is higher than that of other ROS. In this study, the structure and lipophilicity of the probe scaffold were adjusted to improve the ability of the current probe to cross the weak blood–brain barrier and realize the monitoring of $ONOO^-$ in vivo.

3. Enhanced Fluorescence-Sensing Platforms for the Detection of AD Blood Biomarkers

As mentioned above, AD blood biomarkers are important for early diagnosis, predicting the stage of disease and monitoring drug effects [9,10]. Compared with CSF sampling using a lumbar puncture and other invasive methods, blood detection has attracted great attention. However, blood-analysis methods also have certain limitations, such as very low levels of pathological proteins transferring from the brain to the blood and a wide range of interfering proteins. Therefore, there is an urgent need for ultrasensitive, stable and repeatable methods to detect AD biomarkers in blood [53]. The fluorescence detection technique was previously tried for detecting AD blood biomarkers, which exhibited some advantages, including high sensitivity, simple operation and fast detection speed compared with traditional protein analytical methods. However, the fluorescence signal is very weak

when the concentration of the target analyte is low. To obtain higher sensitivity, there are generally two strategies. One is to use large detection equipment to identify weak signals, and the other is to amplify weak fluorescence signals. Under physiological conditions, the concentration of AD blood biomarkers is only in the order of pg/mL, which is beyond the detection limit of ordinary fluorescence detection methods [19]. Considering the complexity and high cost of large-scale instruments, here we mainly summarize the application and advance of enhanced fluorescence-sensing platforms in the detection of AD biomarkers in blood, including Aβ, tau, metal ions and microRNA.

3.1. Amyloid-β Peptide

The Aβ peptide is a classical biomarker of AD in its early stage. It includes multiple forms, such as Aβ40, Aβ42, Aβ oligomers and Aβ fibers. To improve the sensitivity of fluorescence detection, Chen et al. [54] constructed an enhanced fluorescence platform for the ultrasensitive detection of Aβ40 and Aβ42 based on gold nanoislands. The research procedures included the screening of Aβ antibody, optimizing the conditions and adjusting the program to realize near-infrared fluorescence enhancement of a plasmonic gold nanochip. The detection limit of this method reached 0.1 pg/mL. As shown in Figure 2A, the plasmonic gold nanochip surface contains a gold nanoisland layer with nonuniform gap separation. The gold nanoislands provide a powerful surface plasmon resonance enhancement, which, in turn, significantly increases the fluorescence signal.

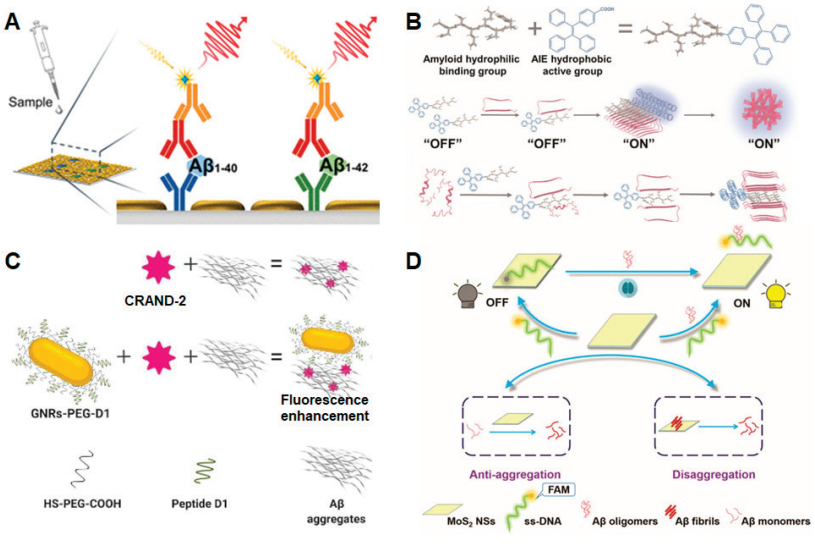

Figure 2. Schematic diagrams of four enhanced fluorescence-sensing platforms. (**A**) Enhanced fluorescence-sensing platform based on plasmonic gold nanoislands for the detection of Aβ40 and Aβ42. Copyright (2021) ACS publications [54]. (**B**) Design of an amyloid-AIE fluorescence molecule and the principle of detecting amyloid proteins. Copyright (2022) Wiley [55]. (**C**) Enhanced fluorescence sensor based on gold nanorods for Aβ aggregates. Copyright (2020) MDPI [56]. (**D**) Fluorescence-sensing platform based on MoS_2 nanosheets for monitoring Aβ oligomers. Copyright (2020) RSC publications [57].

Tang et al. [55] conjugated a hydrophilic peptide GNNQQNY (G7) with the hydrophobic AIE fluorescent molecule triphyenylvinyl benzoic acid (TBA) to form a G7-TBA molecule for the multifunctional detection and regulation of Aβ (Figure 2B). As an Aβ probe G7-TBA solves the problems of poor water solubility and low permeability of traditional AIE molecules. The hydrophilic peptide of G7, i.e., GNNQQNY, is a short fragment of the yeast prion protein Sup35 with a binding motif to interact with Aβ and human islet amyloid

polypeptide (hIAPP) in type II diabetes. According to the AIE luminescence mechanism, the G7-TBA probe has low fluorescence in an Aβ monomer state and high fluorescence in an aggregated state. The G7-TBA probe showed a higher affinity for amyloid aggregates than the commercial ThT and amyloid aggregates.

Francisco Morales-Zavala et al. [56] combined CRANAD-2 with functionalized gold nanorods (GNRs) to significantly improve the fluorescence signals of CRANAD-2 for Aβ aggregates (see Figure 2C). The detection method consists of two parts: CRANAD-2 fluorescent probe and GNRs. The CRANAD-2 probe is a curcumin analog that has a high affinity for insoluble amyloid aggregates, such as Aβ fibrils (K_d = 38 nM); however, its low quantum yield (20%) makes the probe difficult to detect [58], and this limited the application of the probe in detecting amyloid aggregates in AD. The surface of the gold nanorods was modified with HS-PEG-OMe and HS-PEG-COOH, and then coupled with a peptide with selective recognition of Aβ aggregates (please refer to the author's article) [59]. The functionalized GNRs enhance the fluorescence signal of the CRANAD-2 probe and target Aβ aggregates that are impossible to be detected using CRANAD-2 alone. This method can be used for the detection of amyloid in vivo, and it provides a more reliable way for the fluorescence imaging of AD pathology.

Lingna Kong et al. [57] combined fluorescent dye-labeled single-stranded DNA (ssDNA) with molybdenum disulfide nanosheets (MoS_2 NSs) and realized the detection of Aβ oligomers with a detection limit of 3.1 nM (Figure 2D). The fluorescence group FAM, which specifically recognizes Aβ oligomers, was labeled on single-stranded DNA and then coupled with MoS_2 NSs. At this time, fluorescence quenching is caused by the action of van der Waals forces. After the addition of an Aβ oligomer, a hybrid structure was formed between the Aβ oligomer and ssDNA, resulting in the stripping of fluorescent dye-labeled single-stranded DNA from the molybdenum disulfide nanosheet and fluorescence recovery. By adding different concentration gradients of Aβ oligomers and measuring different fluorescence signals, the ultra-low concentration of Aβ oligomers was detected. In addition, the team also found that MoS_2 NSs can inhibit Aβ aggregation and degrade the formed Aβ fibrils.

3.2. Tau

Tau protein plays an important role in stabilizing microtubules; however, its hyperphosphorylation destabilizes microtubules and leads to the pathogenesis of AD. Total tau and phosphorylated tau in CSF have been widely accepted in clinical settings as the key biomarkers of AD. With the advances in analytical techniques, the phosphorylated tau at amino acid positions 181 (p-tau181) and 217 (p-tau217) are also considered the biomarkers of AD in blood.

Yao et al. [60] developed a non-enzyme-linked secondary antibody to recognize proteins and an enzyme substrate to generate optical signals, which greatly reduced the operation steps for tau detection and improved the experimental accuracy (Figure 3A). The team adsorbed anti-human tau antibodies onto graphene oxide (GO) surfaces to provide specific binding sites for tau. The tau protein, which binds to the binding site, is added to a buffer containing antibody-conjugated GO, followed by the addition of standard fluorescein isothiocyanate-labeled tau (tau-FITC). The GO surface is both a nanoscale binding platform and an energy acceptor, which quenches the fluorescence of tau-FITC that is close to and adsorbed to the graphene surface, while those that are not close to the graphene surface emit fluorescence. The number of binding sites for modified GO is limited, where the more tau protein that is adsorbed, the less tau-FITC that is adsorbed and the stronger the fluorescence signal generated by free tau-FITC in the solution. Therefore, the fluorescence intensity can be controlled by the tau protein concentration, and the tau protein can be detected according to the changes before and after fluorescence.

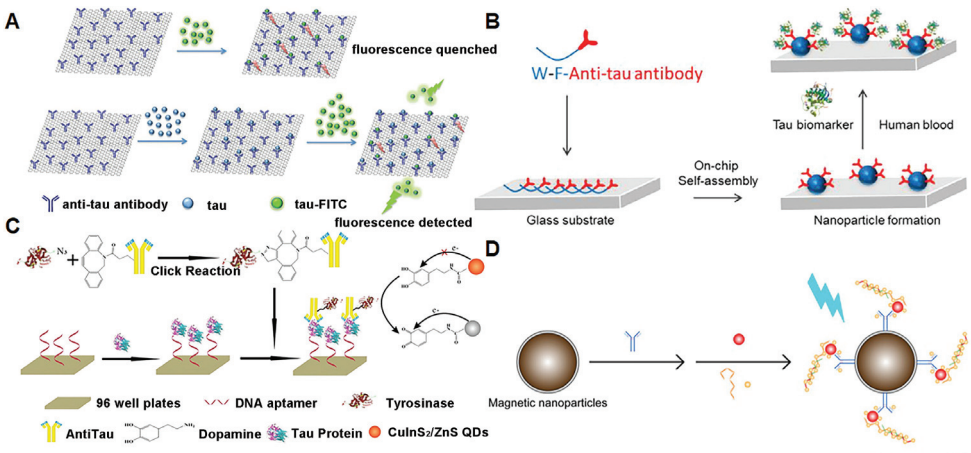

Figure 3. Fluorescence-sensing platforms for the detection of tau proteins. (**A**) Fluorescence quenching based on graphene oxide for detecting the tau protein. Copyright (2018) RSC publications [60]. (**B**) Anti-tau arrays on chip for detecting tau protein in the blood. Copyright (2021) Elsevier [61]. (**C**) The fluorescence immunoassay based on $CuInS_2$/ZnS quantum dots for the detection of tau protein. Copyright (2019) Springer [62]. (**D**) Fluorescence-sensing platform based on magnetic nanoparticles for detecting AD biomarkers. Copyright (2019) Ivyspring International Publisher [63].

Sun et al. [61] developed fluorescent peptide nanoparticle (f-PNPs) arrays to simultaneously detect multiple signals of AD blood biomarkers (Figure 3B). Tryptophane-phenylalanine (WF) dipeptide is an effective self-assembly sequence that induces the formation of f-PNPs arrays on glass substrates. The f-PNPs arrays are modified by anti-tau antibodies to target serum tau protein. This method not only shows a high signal-to-noise ratio for AD diagnosis but also detects multiple signals simultaneously, such as tau protein concentration and aggregation stages.

Zhang et al. [62] established a redox-mediated fluorescent immunoassay for the detection of tau protein based on dopamine (DA)-functionalized $CuInS_2$/ZnS quantum dots (Figure 3C). DA is modified on the surface of $CuInS_2$/ZnS quantum dots via amide reactions. A biotin-modified aptamer, tau protein and TRY-anti-tau were sequentially added to the 96-hole polystyrene plate coated with avidin. Tyrosinase (TYR) is an oxidase that catalyzes dopamine oxidation. After washing off the excess TRY-anti-tau, $CuInS_2$/ZnS-DA quantum dots were added. Under the catalysis of TYR, the DA in $CuInS_2$/ZnS-DA is partially oxidized to dopamino quinone, which can be used as a quenching agent of $CuInS_2$/ZnS quantum dots, triggering fluorescence quenching. By modifying TYR, the sensitivity of the fluorescence-sensing platform was improved to a detection limit of 9.3 pM and a linear range of 10 pM~200 nM.

Chan et al. [63] developed an ultrasensitive multiple assay using a hybrid antibody-aptamer immunoassay, and then amplified the target signal via DNA amplification technology, with a sensitivity down to the femtomolar level (Figure 3D). For example, the simultaneous detection and recognition of p-tau181 and tau441 can be achieved using two different morphometric magnetic probes with detection limits of 3.6 fM and 4.3 fM, respectively. This method uses fewer samples, does not require pre-labeled antibodies and can distinguish protein isomerism.

3.3. Other Biomarkers in the Blood

In addition to the most important Aβ and tau biomarkers, there are some other AD biomarkers in the blood, such as microRNA, metal ions, APOE and BACE1. We also summarize the fluorescence-sensing platform for detecting these AD blood biomarkers.

Specific miRNAs in the blood are biomarkers for the early diagnosis of AD, and the detection procedure is minimally invasive and painless. Zhang et al. [64] developed a method that combines acoustic-aggregation-induced particles with fluorescence enhancement, providing a new strategy for the detection of the AD biomarker miRNA (Figure 4A). Briefly, carboxyfluorescein (FAM)-modified DNA probes were coupled with carboxyl-functionalized polystyrene particles. The DNA probes on fluorescein-labeled particles were complementary to the miRNAs and base-paired with them to form double-stranded structures. DNA exonuclease was then introduced to cut the unhybridized DNA probe to release FAM, and the double-stranded structure with bases complementary to the miRNA was protected. When the ultrasound is turned off, the particles modified by the FAM-labeled DNA probe are in a dispersed state, and the fluorescence signal is weak. However, when the ultrasound is turned on, driven by sound waves with a frequency of 530 kHz and a voltage of 500 mV, the particles modified by the FAM-labeled DNA probes will move and gather in the center of the chip, and strong fluorescence can be detected at this time. The research group verified miRNA-101 with a detection limit of 5 fM.

Studies showed that Cu^{2+} is involved in the regulation of Aβ fibril assembly and neurotoxicity. Cysteine plays the role of redox signaling in AD, and thus, the detection of Cu^{2+} and cysteine is essential for the study of the pathology of AD [65]. In 2021, Niu et al. [32] developed a label-free fluorescent probe to continuously detect the levels of cysteine and Cu^{2+}. As shown in Figure 4B, under alkaline conditions, gold nanoclusters (AuNCs) were prepared using the reaction of $HAuCl_4$ with bovine serum protein (BSA-AuNCs). The electron transition of BSA-AuNCs molecular orbitals produced fluorescence signals. When cysteine was added, it filled the gap on the BSA-AuNCs surface and reacted with BSA-AuNCs, resulting in a significantly enhanced fluorescence signal. With the addition of Cu^{2+}, cysteine is oxidized and the Au-S bond between cysteine and BSA-AuNCs is destroyed. Cu^{2+} will also interact with tryptophan in BSA, which will destroy the stability of BSA-AuNCs and lead to fluorescence quenching. The detection limit of Cu^{2+} in AD mice was 0.1465 μM.

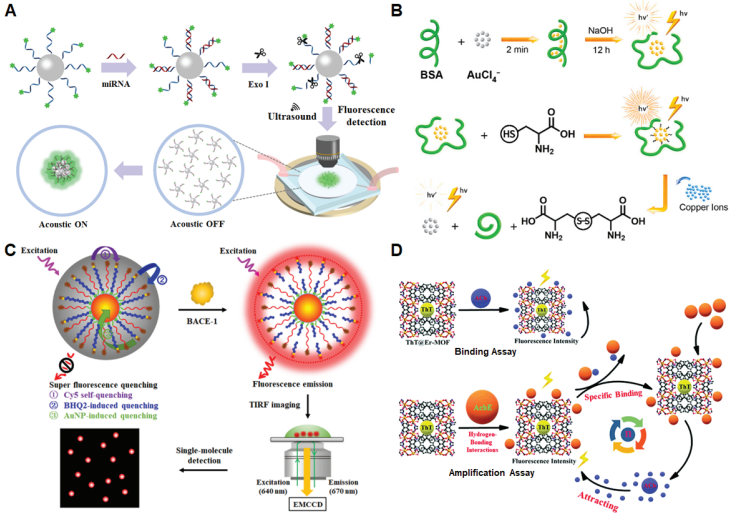

Figure 4. Fluorescence-sensing platforms for the detection of microRNA, metal ions and pathological enzymes of AD. (**A**) Fluorescence enhancement based on acoustic aggregation for detecting miRNA. Copyright (2021) Elsevier [64]. (**B**) Fluorescence switch for the detection of Cu^{2+}. Copyright (2021) Elsevier [35]. (**C**) Fluorescence nanosensors based on the self-assembly of superquenched AuNPs for the detection of BACE-1. Copyright (2021) ACS publications [66]. (**D**) Fluorescence-sensing platform based on ThT@Er-MOF for AChE detection. Copyright (2020) RSC publications [67].

Zhang et al. [66] constructed a self-assembly superhardened gold nanoparticle (AuNP) nanosensor to detect and image BACE-1 instantaneously in living cells (Figure 4C). The nanoprobes consist of three parts: multiple fluorophore-labeled peptide probes, an assistant DNA containing a black hole quencher 2 (BHQ2) and AuNPs. The fluorescein-labeled peptide probes and BHQ2-labeled DNA probes assist with self-assembly on the surface of AuNPs, resulting in superfluorescence quenching. When BACE1 is added, this enzyme catalyzed the cleavage of the fluorophore-labeled peptide probes to release abundant fluorophores. The fluorophores signal can be displayed directly using single-molecular imaging. This enhanced fluorescent sensor has the advantages of high efficiency, low detection limit and good stability. The quenching efficiency of the self-assembly process is up to 98.37% and the background fluorescence is close to zero. Combined with the single molecule detection technique, the sensor can sensitively detect BACE1 with a detection limit of 26.48 pM. This nanoprobe can also be used to instantaneously image endogenous BACE1 in living cells.

Ding et al. [67] introduced the fluorescent dye thioflavin (ThT) into the three-dimensional material Er-MOF (a novel metal–organic framework $[Er(L)(DMF)_{1.27}]_n$) to construct a ratiometric fluorescence sensor based on ThT@Er-MOF. The ThT@Er-MOF sensor successfully achieved ultrasensitive detection of AD biomarkers, such as presenilin 1 (PS1), Aβ and acetylcholine (ACh), with three different detection strategies. Mutation in the PS1 gene leads to the pathology of AD [68]. ACh is a neurotransmitter that can be degraded by acetylcholinesterase (AchE), which is considered one of the biomarkers of AD [69]. Figure 4D introduces two different ACh detection processes based on the ThT@Er-MOF-modified fluorescence-sensing platform.

There were many valuable studies on enhanced fluorescence-sensing platforms for detecting AD blood biomarkers. Detailed information about each biomarker and the analytical performance, including the limit of detection (LOD) is shown in Table 1.

Table 1. Fluorescence-sensing platforms based on nanomaterials for detecting AD blood biomarkers.

Nanomaterials	Biomarkers	LOD	Clinical Samples	References
Cu-BTC/Tb	Aβ40	0.3 nM	Human blood	[70]
3D hydrogel	Aβ	0.5 pM	Human serum	[71]
pGOLD	Aβ	0.1 pg/mL	Human blood	[54]
H-USM/BHQ-1	Aβ oligomers	28.4 pg/mL	/	[72]
AuNP-RAMRA	Aβ oligomers	22.3 pM	AD mice	[73]
ThT@Er-MOF	AchE	0.03226 nM	/	[67]
L-MOF	Aβ oligomers	0.4 pg/mL	Human serum	[74]
LMOF/Apt-Au	Aβ oligomers	0.3 pM	Human serum	[75]
CDs@Eu/GMP	Aβ	0.17 nM	Brain tissue of rat	[76]
MoS_2 NSs	Aβ oligomers	3.1 nM	Brain tissue of AD mice	[57]
FAM-AptAβ@PBNPs	Aβ oligomers	1.0 nM	Human CSF	[77]
$CuInS_2$/ZnS quantum dots	Tau protein	9.3 pM	Human serum	[62]
GO	Tau protein	0.14 nM	Human samples	[60]
WS_2 nanosheet	BACE1	66 pM	Rat CSF	[46]
GQD-CM	APOE4	18.6 pg/mL	Human plasma	[78]
AuNPs	BACE-1	26.48 pM	/	[66]
PS nanoparticle	miRNA-101	5 fM	Human serum	[64]
GOX-SYBR	miRNA-137, miRNA-142	82 nM	Human serum	[79]
WS_2 nanosheets	miR-29a	745 pM	Human serum	[80]
BSA-AuNCs	Cu^{2+}	0.1465 μM	Mice sample	[35]

4. Fluorescence-Sensing Platforms for Imaging AD Biomarkers in the Brain

The detection of AD biomarkers in blood has the advantages of less invasiveness, lower cost and faster response time. However, currently, its accuracy is not good enough for clinical diagnosis. The combination of blood biomarkers' detection with brain imaging analysis can greatly improve the accuracy of diagnosis. Enhanced fluorescence-sensing techniques also show important value in brain imaging in addition to their advantage in detecting trace amounts of AD biomarkers in blood. This section mainly reviews the appli-

cation of fluorescence-sensing technology in high-resolution imaging of AD biomarkers in the brain.

Real-time imaging plays an important role in tracing the distribution and alteration of neuronal development and disease processes, as well as the efficiency of drug treatment in living animals. Wang et al. [81] developed a PBAE-PLGA-Ag_2S-RA-SiSOX9 (PPAR-SiSOX9) (PBAE: poly(beta- amino esters), PLGA: poly(D,L-lactide-co-glycolide)) nanoformulation with high gene/drug deliverability to neural stem cells (NSCs). After co-transfection with the lentivirus-carrying neprilysin (NEP) gene, the multifunctional NSCs were then transplanted into mouse brains with the guidance of second near-infrared (NIR-II) imaging. The therapeutic potential of NSCs that clear Aβ plaques and regenerate nerve cells through NEP expression were investigated following the treatment. For accurate stereotactic transplantation, fluorescence imaging based on Ag_2S quantum dots (QDs) was used in real time. As shown in Figure 5A, the NIR-II imaging based on Ag_2S QDs can be used to monitor the whole process.

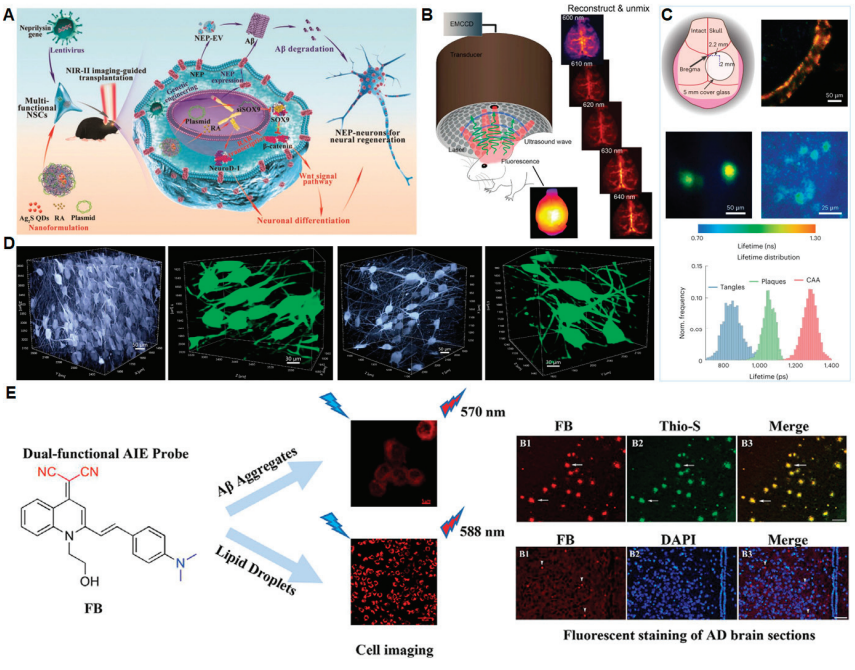

Figure 5. Fluorescence-sensing platforms for imaging AD biomarkers in the brain. (**A**) The schematic of a multifunctional PPAR-SiSOX9 nanoformulation for the treatment and imaging of AD. Copyright (2021) Wiley [81]. (**B**) The hybrid epifluorescence–vMSOT system for tau mapping. Copyright (2022) Springer [82]. (**C**) Intact skull imaging for Aβ plaques and NFTs. Copyright (2023) Springer Nature [83]. (**D**) High-resolution 3D crops of NA neurons according to the spatiotemporal three-dimensional imaging. Copyright (2022) Springer [84]. (**E**) Dual-functional AIE probe for imaging Aβ aggregates and lipid droplets (FB: a quinoline derivative). Copyright (2020) Elsevier [85].

High-resolution imaging of whole-brain scale tau deposits is of great significance. Patrick et al. developed a non-invasive tau-targeted probe and imaged tau deposits in the whole mouse brain using a multi-spectral optoacoustic tomography (vMSOT) system, fluorescence imaging setup and data analysis [83]. Figure 5B shows the hybrid fluorescent–vMSOT system that was established for tau mapping across the entire mouse brain. This high-resolution imaging platform is of great significance for studying tau spreading and clearance and evaluating the therapeutic effect of tau-targeting drugs.

Hak Soo Choi et al. [83] reported a NIR heptamethine fluorophore ZW800-1C with a peak excitation of 753 nm and emission of 772 nm in the NIR window. This NIR fluorescent probe can combine with Aβ and tau simultaneously and can be used as a multifunctional probe for AD imaging in vivo. The probe can be applied to image the intact skull. As shown in Figure 5C, both plaques and NFTs can be imaged using the intact skull. In addition, the NIR fluorescent probe can cross the BBB, which is very important for imaging encephalopathy. Abris Gilvesy et al. studied the spatiotemporal characterization of the process of cellular tau pathology in the human locus coeruleus using 3D imaging. This study addressed the relationship between the locus coeruleus cell structure in the 3D view and tau cytoskeletal pathology and the possible transmission mode of disease-associated tau (Figure 5D) [84].

Yan et al. [86] designed two quinoline-based AIE probes to perform high-resolution imaging of Aβ plaques and lipid droplets at the cellular level and in the brain (Figure 5E). It would be helpful to specify what the probe is enhancing fluorescence of, such as "the Aβ plaques". To target lipid droplets, the research team introduced a fat-soluble substance to the probe, which facilitates its penetration of the blood–brain barrier. The detection limit reached 26.9 nM. With further development, this high-resolution imaging probe has great promise for AD clinical diagnosis.

5. Conclusions and Prospects

Alzheimer's disease poses a serious threat to cognitive function and quality of life in affected individuals. Its pathogenic factors are very complex. Aβ aggregation, tau hyperphosphorylation, neuroinflammation and even intestine flora change were all reported to be associated with AD; however, its pathogenesis remains unclear [1,86,87]. Therefore, early detection and intervention are still the only measures to prevent this disease. The enhanced fluorescence-sensing platform is a technique to improve the sensitivity of fluorescence detection through the plasma resonance effect on the basis of classical fluorescence analysis. A large number of studies showed that trace amounts of AD biomarkers in blood can be detected well by fluorescence enhancement technology, such as Aβ40, Aβ42, T-tau and P-tau. Furthermore, fluorescence-sensing platforms also provide great potential in high-resolution, three-dimensional and living biological imaging. A combination of blood biomarkers detection and brain imaging can significantly improve the accuracy of distinguishing AD patients at different stages, including subjective cognitive decline (SCD), mild cognitive impairment (MCI) and dementia. As an easy method and readily available instrument, fluorescence enhancement platforms provide a promising future in the application of AD diagnosis, mainly including the following three aspects:

(1) Application of novel composite nanomaterials. The accuracy and sensitivity of the analytical method can be significantly improved via the development of special structures and biocompatible nanomaterials combined with fluorescence enhancement technology.
(2) In-depth application of near-infrared fluorescence probes. The biggest defect of fluorescence detection is the decrease in resolution with the increase in fluorescence emission depth, and thus, only the outer surface of the brain can be identified. Furthermore, the fluorescence wavelength is below 550 nm, and some biological substances themselves also fluoresce in this range, which interferes with the detection of organisms in vivo [12,13,15]. With the advent of near-infrared fluorescence imaging, the above problems are gradually solved. The wavelength range of NIR fluorescence imaging is between 700 nm and 2500 nm, which greatly enhances the penetration depth and reduces the interference of biomaterials themselves [88].
(3) Simultaneous detection of different forms of aggregates. For example, Aβ has many aggregation forms, and the current method still utilizes the single detection of only one form. Simultaneous detection of different aggregation forms can not only reduce the cost but also save time and samples, leading to the method being simple, fast and sensitive for the trace analysis of AD biomarkers.

In summary, we believe enhanced fluorescence techniques may be the most promising diagnostic technology for detecting AD blood biomarkers. Although the accuracy of diagnosing AD based on blood biomarkers still needs to be improved, it is the least harmful diagnostic method for patients. Currently, fluorescent detection is still limited to being used by professionals. An integrated, miniaturized testing equipment may be the ultimate layman's product. As the aging population grows, non-invasive enhanced fluorescence techniques for both blood detection and brain imaging provide great potential for the early diagnosis of AD in clinical settings.

Author Contributions: Writing—original draft preparation, X.L. and Y.L.; writing—review and editing, Y.L. and Q.L.; supervision, Q.L.; funding acquisition, Y.L. and Q.L. All authors have read and agreed to the published version of the manuscript.

Funding: This work was jointly supported by the National Key Research and Development Program of China #2018YFE0118900, the Shenzhen Science and Technology Innovation Committee (grant no. JCYJ20220530153811027, JCYJ20200109110001818), Longgang District Medical and health science and technology project (grant no. LGKCYLWS2021000003), Shenzhen-Hong Kong Institute of Brain Science-Shenzhen Fundamental Research Institutions (2023SHIBS0003).

Institutional Review Board Statement: Not applicable.

Informed Consent Statement: Not applicable.

Data Availability Statement: Not applicable.

Conflicts of Interest: The authors declare no conflict of interest.

References

1. Scheltens, P.; De Strooper, B.; Kivipelto, M.; Holstege, H.; Chételat, G.; Teunissen, C.E.; Cummings, J.; van der Flier, W.M. Alzheimer's disease. *Lancet* **2021**, *397*, 1577–1590. [CrossRef] [PubMed]
2. 2022 Alzheimer's disease facts and figures. *Alzheimers Dement.* **2022**, *18*, 700–789. [CrossRef] [PubMed]
3. Scheltens, P.; Blennow, K.; Breteler, M.M.B.; de Strooper, B.; Frisoni, G.B.; Salloway, S.; Van der Flier, W.M. Alzheimer's disease. *Lancet* **2016**, *388*, 505–517. [CrossRef] [PubMed]
4. Ossenkoppele, R.; Pichet Binette, A.; Groot, C.; Smith, R.; Strandberg, O.; Palmqvist, S.; Stomrud, E.; Tideman, P.; Ohlsson, T.; Jögi, J.; et al. Amyloid-beta and tau PET scans predict clinical progression in cognitively unimpaired people. *Nat. Med.* **2022**, *28*, 2267–2268.
5. Sebastian, P.; Shorena, J.; Yakeel, T.Q.; Henrik, Z.; Francisco, L.; Erik, S.; Yi, S.; Yinghua, C.; Geidy, E.S.; Antoine, L.; et al. Discriminative Accuracy of Plasma Phospho-tau217 for Alzheimer Disease vs Other Neurodegenerative Disorders. *JAMA* **2020**, *324*, 772–781.
6. Nakamura, A.; Kaneko, N.; Villemagne, V.L.; Kato, T.; Doecke, J.; Dore, V.; Fowler, C.; Li, Q.X.; Martins, R.; Rowe, C.; et al. High performance plasma amyloid-beta biomarkers for Alzheimer's disease. *Nature* **2018**, *554*, 249–254. [CrossRef]
7. Janelidze, S.; Mattsson, N.; Palmqvist, S.; Smith, R.; Beach, T.G.; Serrano, G.E.; Chai, X.; Proctor, N.K.; Eichenlaub, U.; Zetterberg, H.; et al. Plasma P-tau181 in Alzheimer's disease: Relationship to other biomarkers, differential diagnosis, neuropathology and longitudinal progression to Alzheimer's dementia. *Nat. Med.* **2020**, *26*, 379–386. [CrossRef]
8. Frank, B.; Ally, M.; Brekke, B.; Zetterberg, H.; Blennow, K.; Sugarman, M.A.; Ashton, N.J.; Karikari, T.K.; Tripodis, Y.; Martin, B.; et al. Plasma p-tau181 shows stronger network association to Alzheimer's disease dementia than neurofilament light and total tau. *Alzheimers Dement.* **2021**, *18*, 1523–1536. [CrossRef]
9. Thijssen, E.H.; La Joie, R.; Strom, A.; Fonseca, C.; Iaccarino, L.; Wolf, A.; Spina, S.; Allen, I.E.; Cobigo, Y.; Heuer, H.; et al. Plasma phosphorylated tau 217 and phosphorylated tau 181 as biomarkers in Alzheimer's disease and frontotemporal lobar degeneration: A retrospective diagnostic performance study. *Lancet Neurol.* **2021**, *20*, 739–752. [CrossRef]
10. Moscoso, A.; Karikari, T.K.; Grothe, M.J.; Ashton, N.J.; Lantero-Rodriguez, J.; Snellman, A.; Zetterberg, H.; Blennow, K.; Scholl, M. CSF biomarkers and plasma p-tau181 as predictors of longitudinal tau accumulation: Implications for clinical trial design. *Alzheimers Dement.* **2022**, *18*, 2614–2626. [CrossRef]
11. Yeo, S.K.; Shepelytskyi, Y.; Grynko, V.; Albert, M.S. Molecular Imaging of Fluorinated Probes for Tau Protein and Amyloid-β Detection. *Molecules* **2020**, *25*, 3413. [CrossRef]
12. Xu, M.Y.; Li, R.H.; Li, X.; Lv, G.L.; Li, S.P.; Sun, A.Y.; Zhou, Y.F.; Yi, T. NIR fluorescent probes with good water-solubility for detection of amyloid beta aggregates in Alzheimer's disease. *J. Mater. Chem. B* **2019**, *7*, 5535–5540. [CrossRef]
13. Si, G.F.; Zhou, S.J.; Xu, G.Y.; Wang, J.F.; Wu, B.X.; Zhou, S.S. A curcumin-based NIR fluorescence probe for detection of amyloid-beta (A beta) plaques in Alzheimer's disease. *Dyes Pigments* **2019**, *163*, 509–515. [CrossRef]

14. Sato, T.; Hotsumi, M.; Makabe, K.; Konno, H. Design, synthesis and evaluation of curcumin-based fluorescent probes to detect A beta fibrils. *Bioorg. Med. Chem. Lett.* **2018**, *28*, 3520–3525. [CrossRef]
15. Rajasekhar, K.; Narayanaswamy, N.; Murugan, N.A.; Viccaro, K.; Lee, H.G.; Shah, K.; Govindaraju, T. A beta plaque-selective NIR fluorescence probe to differentiate Alzheimer's disease from tauopathies. *Biosens. Bioelectron.* **2017**, *98*, 54–61. [CrossRef]
16. Peng, C.; Wang, X.; Li, Y.; Li, H.W.; Wong, M.S. Versatile fluorescent probes for near-infrared imaging of amyloid-beta species in Alzheimer's disease mouse model. *J. Mater. Chem. B* **2019**, *7*, 1986–1995. [CrossRef]
17. DeTure, M.A.; Dickson, D.W. The neuropathological diagnosis of Alzheimer's disease. *Mol. Neurodegener.* **2019**, *14*, 32. [CrossRef]
18. Jiang, M.; Wang, X.-Y.; Wang, X.-B. Advances in Detection Methods of β-Amyloid Protein. *Chin. J. Anal. Chem.* **2018**, *46*, 1339–1349. [CrossRef]
19. Semeniak, D.; Cruz, D.F.; Chilkoti, A.; Mikkelsen, M.H. Plasmonic Fluorescence Enhancement in Diagnostics for Clinical Tests at Point-of-Care: A Review of Recent Technologies. *Adv. Mater.* **2022**, e2107986. [CrossRef]
20. Hu, S.; Yang, C.; Luo, H. Current trends in blood biomarker detection and imaging for Alzheimer's disease. *Biosens. Bioelectron.* **2022**, *210*, 114278. [CrossRef]
21. Aliyan, A.; Cook, N.P.; Marti, A.A. Interrogating Amyloid Aggregates using Fluorescent Probes. *Chem. Rev.* **2019**, *119*, 11819–11856. [CrossRef] [PubMed]
22. Liu, Y.; Zhuang, D.; Wang, J.; Huang, H.; Li, R.; Wu, C.; Deng, Y.; Hu, G.; Guo, B. Recent advances in small molecular near-infrared fluorescence probes for a targeted diagnosis of the Alzheimer disease. *Analyst* **2022**, *147*, 4701–4723. [CrossRef] [PubMed]
23. Lane, C.A.; Hardy, J.; Schott, J.M. Alzheimer's disease. *Eur. J. Neurol.* **2018**, *25*, 59–70. [CrossRef] [PubMed]
24. Hardy, J.; Selkoe, D.J. The Amyloid Hypothesis of Alzheimer's Disease: Progress and Problems on the Road to Therapeutics. *Science* **2002**, *297*, 353–356. [CrossRef] [PubMed]
25. Morris, G.P.; Clark, I.A.; Vissel, B. Questions concerning the role of amyloid-beta in the definition, aetiology and diagnosis of Alzheimer's disease. *Acta Neuropathol.* **2018**, *136*, 663–689. [CrossRef]
26. Lee, S.J.C.; Nam, E.; Lee, H.J.; Savelieff, M.G.; Lim, M.H. Towards an understanding of amyloid-β oligomers: Characterization, toxicity mechanisms, and inhibitors. *Chem. Soc. Rev.* **2017**, *46*, 310–323. [CrossRef]
27. Zamanian, J.; Khoshbin, Z.; Abnous, K.; Taghdisi, S.M.; Hosseinzadeh, H.; Danesh, N.M. Current progress in aptamer-based sensing tools for ultra-low level monitoring of Alzheimer's disease biomarkers. *Biosens. Bioelectron.* **2022**, *197*, 113789. [CrossRef]
28. Wang, M.; Qin, L.; Tang, B. MicroRNAs in Alzheimer's Disease. *Front. Genet.* **2019**, *10*, 153. [CrossRef]
29. Ge, L.H.; Liu, Z.C.; Tian, Y. A novel two-photon ratiometric fluorescent probe for imaging and sensing of BACE1 in different regions of AD mouse brain. *Chem. Sci.* **2020**, *11*, 2215–2224. [CrossRef]
30. Singh, N.; Benoit, M.R.; Zhou, J.; Das, B.; Davila-Velderrain, J.; Kellis, M.; Tsai, L.-H.; Hu, X.; Yan, R. BACE-1 inhibition facilitates the transition from homeostatic microglia to DAM-1. *Sci. Adv.* **2022**, *8*, eabo1286. [CrossRef]
31. Roberts, J.A.; Varma, V.R.; An, Y.; Varma, S.; Candia, J.; Fantoni, G.; Tiwari, V.; Anerillas, C.; Williamson, A.; Saito, A.; et al. A brain proteomic signature of incipient Alzheimer's disease in young APOE ε4 carriers identifies novel drug targets. *Sci. Adv.* **2021**, *7*, eabi8178. [CrossRef]
32. Liu, Y.; Xu, L.-P.; Wang, S.; Yang, W.; Wen, Y.; Zhang, X. An ultrasensitive electrochemical immunosensor for apolipoprotein E4 based on fractal nanostructures and enzyme amplification. *Biosens. Bioelectron.* **2015**, *71*, 396–400. [CrossRef]
33. Singh, N.A.; Tosakulwong, N.; Graff-Radford, J.; Machulda, M.M.; Pham, N.T.T.; Sintini, I.; Weigand, S.D.; Schwarz, C.G.; Senjem, M.L.; Carrasquillo, M.M.; et al. APOE epsilon4 influences medial temporal atrophy and tau deposition in atypical Alzheimer's disease. *Alzheimers Dement.* **2022**, *19*, 784–796. [CrossRef]
34. Mahan, T.E.; Wang, C.; Bao, X.; Choudhury, A.; Ulrich, J.D.; Holtzman, D.M. Selective reduction of astrocyte apoE3 and apoE4 strongly reduces Aβ accumulation and plaque-related pathology in a mouse model of amyloidosis. *Mol. Neurodegener.* **2022**, *17*, 13. [CrossRef]
35. Niu, Y.X.; Ding, T.; Liu, J.M.; Zhang, G.L.; Tong, L.L.; Cheng, X.F.; Yang, Y.M.; Chen, Z.Z.; Tang, B. Fluorescence switch of gold nanoclusters stabilized with bovine serum albumin for efficient and sensitive detection of cysteine and copper ion in mice with Alzheimer 's disease. *Talanta* **2021**, *223*, 121745. [CrossRef]
36. Yao, Y.S.; Li, W.H.; Han, Q.Q.; Lv, G.L.; Li, C.X.; Sun, A.Y. A Pyridyl Zn (II) Chelate for the Fluorescent Detection of A beta Fibrils. *Z. Anorg. Allg. Chem.* **2022**, *648*, e202200070. [CrossRef]
37. Guo, Y.X.; Hu, Z.Y.; Wang, Z.H. Recent Advances in the Application Peptide and Peptoid in Diagnosis Biomarkers of Alzheimer's Disease in Blood. *Front. Mol. Neurosci.* **2021**, *14*, 778955. [CrossRef]
38. Panza, F.; Lozupone, M.; Logroscino, G.; Imbimbo, B.P. A critical appraisal of amyloid-β-targeting therapies for Alzheimer disease. *Nat. Rev. Neurol.* **2019**, *15*, 73–88. [CrossRef]
39. Yang, H.L.; Fang, S.Q.; Tang, Y.W.; Wang, C.; Luo, H.; Qu, L.L.; Zhao, J.H.; Shi, C.J.; Yin, F.C.; Wang, X.B.; et al. A hemicyanine derivative for near-infrared imaging of beta-amyloid plaques in Alzheimer's disease. *Eur. J. Med. Chem.* **2019**, *179*, 736–743. [CrossRef]
40. Lim, J.; Kim, S.; Oh, S.J.; Han, S.M.; Moon, S.Y.; Kang, B.; Seo, S.B.; Jang, S.; Son, S.U.; Jung, J.; et al. miRNA sensing hydrogels capable of self-signal amplification for early diagnosis of Alzheimer's disease. *Biosens. Bioelectron.* **2022**, *209*, 114279. [CrossRef]
41. Kim, K.; Lee, C.H.; Park, C.B. Chemical sensing platforms for detecting trace-level Alzheimer's core biomarkers. *Chem. Soc. Rev.* **2020**, *49*, 5446–5472. [CrossRef] [PubMed]

42. Alonso, A.C.; Zaidi, T.; Grundke-Iqbal, I.; Iqbal, K. Role of abnormally phosphorylated tau in the breakdown of microtubules in Alzheimer disease. *Proc. Natl. Acad. Sci. USA* **1994**, *91*, 5562–5566. [CrossRef] [PubMed]
43. Safieh, M.; Korczyn, A.D.; Michaelson, D.M. ApoE4: An emerging therapeutic target for Alzheimer's disease. *BMC Med.* **2019**, *17*, 64. [CrossRef]
44. Woo, N.; Kim, S.K.; Sun, Y.; Kang, S.H. Enhanced capillary electrophoretic screening of Alzheimer based on direct apolipoprotein E genotyping and one-step multiplex PCR. *J. Chromatogr. B Anal. Technol. Biomed. Life Sci.* **2018**, *1072*, 290–299. [CrossRef]
45. Theendakara, V.; Peters-Libeu, C.A.; Bredesen, D.E.; Rao, R.V. Transcriptional Effects of ApoE4: Relevance to Alzheimer's Disease. *Mol. Neurobiol.* **2018**, *55*, 5243–5254. [CrossRef] [PubMed]
46. Zuo, X.W.; Dai, H.X.; Zhang, H.G.; Liu, J.J.; Ma, S.D.; Chen, X.G. A peptide-WS2 nanosheet based biosensing platform for determination of beta-secretase and screening of its inhibitors. *Analyst* **2018**, *143*, 4585–4591. [CrossRef]
47. Das, B.; Yan, R. Role of BACE1 in Alzheimer's synaptic function. *Transl. Neurodegener.* **2017**, *6*, 23. [CrossRef]
48. Kou, X.; Chen, D.; Chen, N. The Regulation of microRNAs in Alzheimer's Disease. *Front. Neurol.* **2020**, *11*, 288. [CrossRef]
49. Sheinerman, K.S.; Toledo, J.B.; Tsivinsky, V.G.; Irwin, D.; Grossman, M.; Weintraub, D.; Hurtig, H.I.; Chen-Plotkin, A.; Wolk, D.A.; McCluskey, L.F.; et al. Circulating brain-enriched microRNAs as novel biomarkers for detection and differentiation of neurodegenerative diseases. *Alzheimers Res. Ther.* **2017**, *9*, 89. [CrossRef]
50. Chandrasekaran, A.R.; Halvorsen, K. DNA-Based Smart Reagent for Detecting Alzheimer's Associated MicroRNAs. *ACS Sens.* **2021**, *6*, 3176–3181. [CrossRef]
51. Jiao, C.; Liu, Y.; Lu, W.; Zhang, P.; Wang, Y. Molecular Fluorescence Probe for Detecting Reactive Nitrogen/Reactive Oxygen. *Chin. J. Org. Chem.* **2019**, *39*, 591–616. [CrossRef]
52. Wang, P.; Yu, L.; Gong, J.; Xiong, J.; Zi, S.; Xie, H.; Zhang, F.; Mao, Z.; Liu, Z.; Kim, J.S. An Activity-Based Fluorescent Probe for Imaging Fluctuations of Peroxynitrite ($ONOO^-$) in the Alzheimer's Disease Brain. *Angew. Chem. Int. Ed. Engl.* **2022**, *61*, e202206894.
53. Oyarzun, M.P.; Tapia-Arellano, A.; Cabrera, P.; Jara-Guajardo, P.; Kogan, M.J. Plasmonic Nanoparticles as Optical Sensing Probes for the Detection of Alzheimer's Disease. *Sensors* **2021**, *21*, 2067. [CrossRef]
54. Han, H.F.; Yen, H.C.; Wu, H.C.; Tan, H.Y.; Xu, W.; Jiang, H.S.; Tsai, P.J.; Qian, K.; Wu, Y.C.; Chen, C.C. Ultrasensitive Detection of Alzheimer's Amyloids on a Plasmonic-Gold Platform. *ACS Appl. Mater. Interfaces* **2021**, *13*, 57036–57042. [CrossRef]
55. Tang, Y.; Zhang, D.; Gong, X.; Zheng, J. Dual-Functional, Multi-Targeting GNNQQNY-AIE Conjugates as Amyloid Probes and Amyloid Modulators via Amyloid Cross-Seeding Principle. *Adv. Funct. Mater.* **2022**, *32*, 2208022. [CrossRef]
56. Jara-Guajardo, P.; Cabrera, P.; Celis, F.; Soler, M.; Berlanga, I.; Parra-Munoz, N.; Acosta, G.; Albericio, F.; Guzman, F.; Campos, M.; et al. Gold Nanoparticles Mediate Improved Detection of beta-amyloid Aggregates by Fluorescence. *Nanomaterials* **2020**, *10*, 690. [CrossRef]
57. Kong, L.N.; Zhou, X.G.; Shi, G.Y.; Yu, Y.Y. Molybdenum disulfide nanosheets-based fluorescent "off-to-on" probe for targeted monitoring and inhibition of beta-amyloid oligomers. *Analyst* **2020**, *145*, 6369–6377. [CrossRef]
58. Ran, C.; Xu, X.; Raymond, S.B.; Ferrara, B.J.; Neal, K.; Bacskai, B.J.; Medarova, Z.; Moore, A. Design, Synthesis, and Testing of Difluoroboron-Derivatized Curcumins as Near-Infrared Probes for in Vivo Detection of Amyloid-β Deposits. *J. Am. Chem. Soc.* **2009**, *131*, 15257–15261. [CrossRef]
59. Nikoobakht, B.; El-Sayed, M.A. Preparation and Growth Mechanism of Gold Nanorods (NRs) Using Seed-Mediated Growth Method. *Chem. Mater.* **2003**, *15*, 1957–1962. [CrossRef]
60. Huang, A.; Zhang, L.N.; Li, W.W.; Ma, Z.Y.; Shuo, S.; Yao, T.M. Controlled fluorescence quenching by antibody-conjugated graphene oxide to measure tau protein. *R. Soc. Open Sci.* **2018**, *5*, 171808. [CrossRef]
61. Leming, S.; Yang, L.; Yuerong, W.; Dingchang, L. Blood-based Alzheimer's disease diagnosis using fluorescent peptide nanoparticle arrays. *Chin. Chem. Lett.* **2021**, *33*, 1946–1950.
62. Chen, L.; Lin, J.W.; Yi, J.Q.; Weng, Q.H.; Zhou, Y.; Han, Z.Z.; Li, C.Y.; Chen, J.H.; Zhang, Q. A tyrosinase-induced fluorescence immunoassay for detection of tau protein using dopamine-functionalized CuInS2/ZnS quantum dots. *Anal. Bioanal. Chem.* **2019**, *411*, 5277–5285. [CrossRef] [PubMed]
63. Chan, H.N.; Xu, D.; Ho, S.L.; He, D.; Wong, M.S.; Li, H.W. Highly sensitive quantification of Alzheimer's disease biomarkers by aptamer-assisted amplification. *Theranostics* **2019**, *9*, 2939–2949. [CrossRef] [PubMed]
64. Sun, Y.; Luo, Y.; Xu, T.L.; Cheng, G.Z.; Cai, H.; Zhang, X.J. Acoustic aggregation-induced separation for enhanced fluorescence detection of Alzheimer's biomarker. *Talanta* **2021**, *233*, 122517. [CrossRef] [PubMed]
65. Lee, J.-S.; Ulmann, P.A.; Han, M.S.; Mirkin, C.A. A DNA-gold nanoparticle-based colorimetric competition assay for the detection of cysteine. *Nano Lett.* **2008**, *8*, 529–533. [CrossRef]
66. Ma, F.; Wang, Q.; Xu, Q.F.; Zhang, C.Y. Self-Assembly of Superquenched Gold Nanoparticle Nanosensors for Lighting up BACE-1 in Live Cells. *Anal. Chem.* **2021**, *93*, 15124–15132. [CrossRef]
67. Wang, X.Z.; Du, J.; Xiao, N.N.; Zhang, Y.; Fei, L.; LaCoste, J.D.; Huang, Z.; Wang, Q.; Wang, X.R.; Ding, B. Driving force to detect Alzheimer's disease biomarkers: Application of a thioflavine T@Er-MOF ratiometric fluorescent sensor for smart detection of presenilin 1, amyloid beta-protein and acetylcholine. *Analyst* **2020**, *145*, 4646–4663. [CrossRef]
68. Frederiksen, H.R.; Holst, B.; Mau-Holzmann, U.A.; Freude, K.; Schmid, B. Generation of two isogenic iPSC lines with either a heterozygous or a homozygous E280A mutation in the PSEN1 gene. *Stem Cell Res.* **2019**, *35*, 101403. [CrossRef]

69. Albishri, H.M.; Abd El-Hady, D. Hyphenation of enzyme/graphene oxide-ionic liquid/glassy carbon biosensors with anodic differential pulse stripping voltammetry for reliable determination of choline and acetylcholine in human serum. *Talanta* **2019**, *200*, 107–114. [CrossRef]
70. Liu, X.W.; Li, X.; Xu, S.L.; Guo, S.J.; Xue, Q.W.; Wang, H.S. Efficient ratiometric fluorescence probe based on dual-emission luminescent lanthanide coordination polymer for amyloid beta-peptide detection. *Sens. Actuator B Chem.* **2022**, *352*, 131052. [CrossRef]
71. Hamd-Ghadareh, S.; Salimi, A.; Parsa, S.; Mowla, S.J. Development of three-dimensional semi-solid hydrogel matrices for ratiometric fluorescence sensing of Amyloid beta peptide and imaging in SH-SY5 cells: Improvement of point of care diagnosis of Alzheimer's disease biomarker. *Biosens. Bioelectron.* **2022**, *199*, 113895. [CrossRef]
72. Fang, W.K.; Liu, L.; Zhang, L.L.; Liu, D.; Liu, Y.; Tang, H.W. Detection of Amyloid beta Oligomers by a Fluorescence Ratio Strategy Based on Optically Trapped Highly Doped Upconversion Nanoparticles-SiO2@Metal-Organic Framework Microspheres. *Anal. Chem.* **2021**, *93*, 12447–12455. [CrossRef]
73. Yin, Y.M.; Chen, G.F.; Gong, L.; Ge, K.Z.; Pan, W.Z.; Li, N.; Machuki, J.O.; Yu, Y.Y.; Geng, D.Q.; Dong, H.F.; et al. DNAzyme-Powered Three-Dimensional DNA Walker Nanoprobe for Detection Amyloid beta-Peptide Oligomer in Living Cells and in Vivo. *Anal. Chem.* **2020**, *92*, 9247–9256. [CrossRef]
74. Ren, H.X.; Zhong, Q.L.; Miao, Y.B.; Wen, X.W.; Wu, G.Y.; Wang, H.L.; Zhang, Y. A label-free reusable aptasensor for Alzheimer's disease. *Microchim. Acta* **2020**, *187*, 515. [CrossRef]
75. Ren, H.X.; Miao, Y.B.; Zhang, Y.D. An aptamer based fluorometric assay for amyloid-beta oligomers using a metal-organic framework of type Ru@MIL-101(Al) and enzyme-assisted recycling. *Microchim. Acta* **2020**, *187*, 514. [CrossRef]
76. Liu, C.; Lu, D.; You, X.; Shi, G.; Deng, J.; Zhou, T. Carbon dots sensitized lanthanide infinite coordination polymer nanoparticles: Towards ratiometric fluorescent sensing of cerebrospinal Aβ monomer as a biomarker for Alzheimer's disease. *Anal. Chim. Acta* **2020**, *1105*, 147–154. [CrossRef]
77. Chen, W.; Gao, G.; Jin, Y.; Deng, C. A facile biosensor for Aβ40O based on fluorescence quenching of prussian blue nanoparticles. *Talanta* **2020**, *216*, 120930. [CrossRef]
78. Mars, A.; Hamami, M.; Bechnak, L.; Patra, D.; Raouafi, N. Curcumin-graphene quantum dots for dual mode sensing platform: Electrochemical and fluorescence detection of APOe4, responsible of Alzheimer's disease. *Anal. Chim. Acta* **2018**, *1036*, 141–146. [CrossRef]
79. Rahaie, M.; Noroozi, S.K. A nanobiosensor based on graphene oxide and DNA binding dye for multi-microRNAs detection. *Biosci. Rep.* **2019**, *39*, BSR20181404. [CrossRef]
80. Kim, H.I.; Yim, D.; Jeon, S.J.; Kang, T.W.; Hwang, I.J.; Lee, S.; Yang, J.K.; Ju, J.M.; So, Y.; Kim, J.H. Modulation of oligonucleotide-binding dynamics on WS2 nanosheet interfaces for detection of Alzheimer's disease biomarkers. *Biosens. Bioelectron.* **2020**, *165*, 112401. [CrossRef]
81. Huang, D.; Cao, Y.; Yang, X.; Liu, Y.; Zhang, Y.; Li, C.; Chen, G.; Wang, Q. A Nanoformulation-Mediated Multifunctional Stem Cell Therapy with Improved Beta-Amyloid Clearance and Neural Regeneration for Alzheimer's Disease. *Adv. Mater.* **2021**, *33*, 2006357. [CrossRef] [PubMed]
82. Vagenknecht, P.; Luzgin, A.; Ono, M.; Ji, B.; Higuchi, M.; Noain, D.; Maschio, C.A.; Sobek, J.; Chen, Z.; Konietzko, U.; et al. Non-invasive imaging of tau-targeted probe uptake by whole brain multi-spectral optoacoustic tomography. *Eur. J. Nucl. Med. Mol. Imaging* **2022**, *49*, 2137–2152. [CrossRef] [PubMed]
83. Hou, S.S.; Yang, J.; Lee, J.H.; Kwon, Y.; Calvo-Rodriguez, M.; Bao, K.; Ahn, S.; Kashiwagi, S.; Kumar, A.T.N.; Bacskai, B.J.; et al. Near-infrared fluorescence lifetime imaging of amyloid-β aggregates and tau fibrils through the intact skull of mice. *Nat. Biomed. Eng.* **2023**, *7*, 270–280. [CrossRef] [PubMed]
84. Gilvesy, A.; Husen, E.; Magloczky, Z.; Mihaly, O.; Hortobágyi, T.; Kanatani, S.; Heinsen, H.; Renier, N.; Hökfelt, T.; Mulder, J.; et al. Spatiotemporal characterization of cellular tau pathology in the human locus coeruleus–pericoerulear complex by three-dimensional imaging. *Acta Neuropathol.* **2022**, *144*, 651–676. [CrossRef]
85. Wang, Y.X.; Qiu, Y.T.; Sun, A.Y.; Xiong, Y.H.; Tan, H.Y.; Shi, Y.Q.; Yu, P.; Roy, G.; Zhang, L.; Yan, J.W. Dual-functional AIE fluorescent probes for imaging beta-amyloid plaques and lipid droplets. *Anal. Chim. Acta* **2020**, *1133*, 109–118. [CrossRef]
86. Yujun, H.; Yong, W.; Sofie, L.; Beimeng, Y.; Yue, W.; Stephanie, C.; Mark, P.M.; Deborah, L.C.; Vilhelm, A.B. NAD+ supplementation reduces neuroinflammation and cell senescence in a transgenic mouse model of Alzheimer's disease via cGAS-STING [Neuroscience]. *Proc. Natl. Acad. Sci. USA* **2021**, *24*, 3.
87. Hokari, R.; Tomioka, A. The role of lymphatics in intestinal inflammation. *Inflamm. Regen.* **2021**, *41*, 25. [CrossRef]
88. Yang, J.; Zeng, F.; Ge, Y.; Peng, K.; Li, X.; Li, Y.; Xu, Y. Development of Near-Infrared Fluorescent Probes for Use in Alzheimer's Disease Diagnosis. *Bioconjug. Chem.* **2020**, *31*, 2–15. [CrossRef]

biosensors

MDPI

Review

Biosensors Based on the Binding Events of Nitrilotriacetic Acid–Metal Complexes

Lin Zhu, Yong Chang, Yingying Li, Mingyi Qiao and Lin Liu *

College of Chemistry and Chemical Engineering, Anyang Normal University, Anyang 455000, China; zhulin1231989@aynu.edu.cn (L.Z.); yongchang_swudc@163.com (Y.C.); liyingying2362@163.com (Y.L.); qiaomingyi2003@163.com (M.Q.)
* Correspondence: liulin@aynu.edu.cn

Abstract: Molecular immobilization and recognition are two key events for the development of biosensors. The general ways for the immobilization and recognition of biomolecules include covalent coupling reactions and non-covalent interactions of antigen–antibody, aptamer–target, glycan–lectin, avidin–biotin and boronic acid–diol. Tetradentate nitrilotriacetic acid (NTA) is one of the most common commercial ligands for chelating metal ions. The NTA–metal complexes show high and specific affinity toward hexahistidine tags. Such metal complexes have been widely utilized in protein separation and immobilization for diagnostic applications since most of commercialized proteins have been integrated with hexahistidine tags by synthetic or recombinant techniques. This review focused on the development of biosensors with NTA–metal complexes as the binding units, mainly including surface plasmon resonance, electrochemistry, fluorescence, colorimetry, surface-enhanced Raman scattering spectroscopy, chemiluminescence and so on.

Keywords: nitrilotriacetic acid; metal complexes; molecular recognition; biosensors

1. Introduction

The immobilization of biomolecules onto solid supports (e.g., electrodes, chips, quartz and substrates) or functional units (e.g., dyes, enzymes and nanomaterials) is of great importance for implementing bioassays [1,2]. A desired methodology for bioreceptor immobilization should ensure the following terms: (i) a proper orientation and uniform distribution to promise target accessibility, recognition and detectability; (ii) stability and robustness to allow flow-through assays or sequential measurement cycles; and (iii) antifouling capabilities to lower nonspecific interactions and reduce false positive signals [3]. Currently, versatile immobilization strategies have been reported, including physical adsorption based on electrostatic and hydrophobic interactions, direct chemical adsorption based on the gold–thiol binding, chemical cross-linking to functional monolayers and affinity-or linker-mediated immobilization [4,5]. The selection of an appropriate immobilization approach is dependent on the physicochemical and chemical properties of solid interfaces and target proteins as well as the intended usage scenario. For example, surface-accessible active functional groups of exposed amino acid residues, such as an amine group in lysine residue and thiol group in cysteine residue, can be utilized as the anchoring points through covalent coupling onto a pretreated solid surface [6–9]. Despite the high simplicity and stability, covalent binding may lead to the random orientation of biomolecules and the follow-up conformational change, thus decreasing the activity of bioreceptor and the partial or complete loss of its binding ability toward the target. Thus, site-specific immobilization strategies based on specific recognitions or affinity ligands are peculiarly attractive for the construction of biosensors. Typically, biotinylated antibodies have been well tethered to the avidin-modified layers via the strong avidin–biotin interactions [10–12].

Citation: Zhu, L.; Chang, Y.; Li, Y.; Qiao, M.; Liu, L. Biosensors Based on the Binding Events of Nitrilotriacetic Acid–Metal Complexes. *Biosensors* **2023**, *13*, 507. https://doi.org/10.3390/bios13050507

Received: 25 March 2023
Revised: 21 April 2023
Accepted: 24 April 2023
Published: 28 April 2023

However, the chemical modification of proteins may result in the decline inactivity and the presence of multiple siteson proteins may cause their uncontrollable orientation.

The immobilized metal ion affinity chromatography (IMAC) principle is based on the relatively strong interaction between transition metal cations (e.g., Cu^{2+}, Ni^{2+}, Zn^{2+} and Co^{2+}) and accessible metal-binding amino acid residues (e.g., cysteine, histidine and tryptophan) [13–15]. It is originally applied to the purification of proteins containing histidine residues on the surface with the equal strength of "bio-specific" interactions. A multitude of metal-chelating ligands with different denticities have been fixed on the solid support matrixes changed from agarose gels to rigid silica particles. In this process, the ligands act as Lewis bases to bind divalent transition metal ions, such as tridentate iminodiacetic acid, tetradentate nitrilotriacetic acid (NTA) and pentadentatetris(carboxymethyl)ethylene diamine [16,17]. The entrapped metal ions serve as Lewis acids and the remained unoccupied coordination sites can further ligate to the imidazole moieties of hexahistidine (His_6) tags. As coordination-bonding-based artificial receptors, the ligands exhibit different IMAC protein separation efficiencies based on the number and conformation of chelation sites [18,19]. Among them, the tetradentate ligand of NTA can be chelated with bivalent transition metal cations (e.g., Cu^{2+}, Ni^{2+}, Zn^{2+} and Co^{2+}) to form a hexagonal complex and two unoccupied coordination sites remain for the further ligation to the imidazole moieties of His_6 tag. Nowadays, NTA-based IMAC is one of the most promising approaches for reversible and controlled protein immobilization [3,20].

Some characteristic groups of biomolecules can be used as the anchor sites or affinity tags for the coupling of them onto the transducer surfaces with preserving activity [21]. As one of the smallest and most commonly used affinity elements, His_6 tag can be readily fused to the N- or C-terminal of a synthetic peptide or recombinant protein without influence on the target-binding activity [22]. Moreover, the immobilized His_6-tagged proteins can be easily displaced by competing coordinators (e.g., ethylenediaminetetraacetic acid (EDTA) or imidazole) under mild conditions, realizing the elution of targets and the regeneration of solid surfaces and materials [23,24]. Furthermore, histidine-rich proteins with unusually high histidine contents can also interact with NTA–metal complexes [25,26]. The dysregulation of these proteins has been associated with several diseases, including liver cirrhosis, cancer, asthma and pulmonary disease [27,28]. Wright's group has reported a series of novel works for *Plasmodium falciparum* histidine-rich protein 2 (*pf*HRP-II) extraction and detection using NTA–metal complexes [29–31]. Thus, the broad arrays of chelators modified on various materials, including NTA, polydopamine, 1-acetato-4-benzyl-triazacyclononane and chitosan, have been popularly used to extract and immobilize biomolecules from real samples while retaining bioactivity for further research [32–39]. Currently, countless NTA-functionalized molecules and materials are commercially available for protein immobilization and site-specific labeling, including fluorescent dyes, lipids, antibodies, peptides, magnetic beads and gold nanoparticles [40]. Considering their great potential, the applications of NTA–metal complexes in different fields have been summarized in several reviews [41–44]. For instance, Wieneke et al. reviewed the development of multivalent chelators for in vivo protein labeling [45]. You et al. summarized the progress of multivalent chelators for spatially and temporally controlled protein functionalization [46]. López-Laguna et al. provided comprehensive insights on the emerging biotechnology of histidine-rich peptides [47]. However, no systematic reviews currently focus on the advancement of biosensors with NTA–metal complexes as the binding units. To maintain the theme of this review, herein, we summarized the current developments of biosensors based on the binding events of NTA–metal complexes. We classified the developments of such biosensors according to the detection techniques, including surface plasmon resonance (SPR), electrochemistry, fluorescence, colorimetry, surface-enhanced Raman scattering spectroscopy (SERS), chemiluminescence and so on. Moreover, future challenges and research trends for NTA–metal complexes-based bioassays are briefly discussed.

2. NTA–Metal Complexes−Based Biosensors

There are several important factors for the modulation of the binding affinity and the constant between NTA–metal complexes and biomolecules. The choice of the NTA–metal-based system for a particular application is critical for the efficient immobilization and detection of biomolecules [48]. The reversible character is favorable for protein purification and a higher affinity interaction is desired in the case of protein labeling in vitro and in live cells. The length, number and position of His_6 tag may influence the purification and immobilization of recombinant proteins [49–51]. In this aspect, Knechtet al. investigated the binding properties between several different series of oligohistidines as well as mixed oligohistidines/oligoalanines and Ni^{2+}–NTA by SPR experiments [52]. The results suggested that His_6 tag possessed an equilibrium dissociation constant (K_D) of 14 ± 1 nM, and the highest affinity of the peptides and two His residues separated by either one or four residues are the preferred binding motifs. Although a longer histidine tag (e.g., His_8 or His_{10}) can achieve higher purity efficiency, it may cause the inhibition of protein functions and require a higher concentration of imidazole to elute. In addition, Madoz-Gúrpide et al. suggested that the orientation of enzyme ferredoxin/$NADP^+$ reductase on the surface of NTA–Cu^{2+} complexes-functionalized electrode could be tuned by adjusting the position of a histidine pair (His–X_3–His) in α-helices [53]. Schröper et al. investigated the effect of His_6 tag-based affinity-binding strategy on the immobilization of redox protein horse heart cytc on the gold electrode surface [54]. It was found that cytc with C-terminal His tag exhibited the strongest redox signal due to the proximity between the His_6 tag and the intramolecular electron transfer pathway. Moreover, Khan et al. found that double-His_6 tags separated by an 11-amino acid spacer exhibited at least one order of magnitude stronger binding affinity to Ni–NTA-modified surfaces, compared with the single-His_6 tag or two single-His_6 tags at both the N- and C-terminals [55].

An individual metal–NTA–His_6 complex shows relatively low stability and affinity ($K_D = 1 \times 10^{-5}$ M) [56]. The binding stability can be enhanced by increasing the surface density of NTA [57,58]. Multivalent chelators such as di- (2.7×10^{-7} M), tri- (2×10^{-7} M) or tetra-NTA (4×10^{-8} M) derivatives have also been designed to achieve a high density of chelators as binding sites, thus enhancing the NTA-based surface stability [59–63]. For instance, Lata et al. demonstrated that an increasing number of NTA moieties could lead to a substantial increase in binding stability, achieving a subnanomolar affinity [64]. You et al. reported the application of multivalent chelators for high-affinity and spatially and temporally controlled the recognition and functionalization of His_6-tagged proteins [46]. Moreover, other irreversible covalent interactions were combined with the reversible coordination interaction, including photochemical reaction, amine coupling reaction and epoxide chemistry [65–69]. However, these approaches typically require complicated synthetic processes and lack high specificity.

The chelators exhibit a different affinity for bivalent metal ions ($Cu^{2+} > Ni^{2+} > Zn^{2+} \geq Co^{2+}$) and distinctive specificity ($Co^{2+} > Zn^{2+} > Ni^{2+} > Cu^{2+}$) toward His_6-tagged proteins, which may affect their utilization in practical applications [70,71]. Compared with the carboxyl self-assembled monomer (SAM), that of Ni–NTA can pattern His_6-tagged biomolecules in a higher immobilization capacity and binding activity, improving the detection sensitivity [72]. However, the sensing surface may suffer from slow and continuous dissociation of immobilized biomolecules due to the low affinity and stability between the His-tagged biomolecules and NTA mediated by Ni^{2+} and other metal ions [73]. Moreover, low pH, reductants and chelators, such as EDTA and imidazole in matrices, may quickly disturb the NTA–metal complexes. Cu^{2+} shows the greatest affinity, which can be used to isolate low abundant proteins from crude lysates, followed by other purification steps. In addition, the conversion of bivalent metal ions to different metal oxidation states is one of the alternative strategies to address those shortcomings and maintain the benefits of His_6-tagged protein immobilization [74]. For example, Spatz's group developed the Co^{3+}-mediated, stable and kinetically inert interaction between His_6 tag and NTA for a permanent, oriented and specific protein immobilization [75,76]. In this strategy, the formation constant of exchange-

inert Co^{3+} complexes is higher than that of conventional Co^{2+} and Ni^{2+} complexes, which is resistant toward competitive chelators and washing off over time.

In case of the NTA–Ni^{2+}–His_6 tag system, the stability constants of four complexes should be considered, including Ni^{2+}/His_6-tagged protein, Ni^{2+}/NTA ($K_D = 1.8 \times 10^{-11}$ M), Ni^{2+}/imidazole ($K_D = 9.8 \times 10^{-4}$ M) and Ni^{2+}/EDTA ($K_D = 4 \times 10^{-19}$ M) [52]. Taking advantage of the differences between the adjustable dissociation constants, the captured His_6-tagged proteins can be eluted by imidazole under mild conditions, resulting in Ni^{2+} ions to remain bound to NTA. In the context of protein purification, the addition of imidazole can improve the selectivity of NTA–metal complexes toward His_6-tagged proteins. Based on the differences between the dissociation constants of Ni^{2+}/EDTA and Ni^{2+}/NTA, the surface can be regenerated by completely removing Ni^{2+} ions with EDTA and then followed by repeatedly loading the chelators with Ni^{2+} ions [52]. The regeneration of sensing surfaces can make the ligand density similar with that for the incubation or injection of each analyte, which is helpful for the conventional analysis [77].

The compatibility of NTA with chemical conjugation protocols can enable versatile and efficient surface chemistries for the robust and reproducible immobilization of His_6-tailed biomolecules on different solid surfaces and nanomaterials. SAMs of NTA–metal chelators can endow the interface with desired properties. At present, various strategies have been reported to modify the interface with NTA–metal chelators for the deposition of His_6-tagged biomolecules [78–80]. For example, NTA moieties can be functionalized with different alkyl thiols to form metal-chelating layers on gold electrodes [81–83]. However, the synthesis of the alkane thiol chelators was complicated and the formed monolayer was less well-ordered. To overcome these difficulties, NTA modified with an amino group can be covalently tethered onto the carboxyl-terminated SAM preformed on the electrode through the 1-(3-dimethylaminopropyl)-3-ethylcarbodiimide (EDC)/N-hydroxysuccinimide (NHS)-activated amine coupling reaction [58,84,85]. In addition, Haddour et al. reported that the pyrrole monomer modified with NTA could be electrochemically polymerized into a conductive poly(pyrrole)-NTA film for the reversible oriented immobilization of His_6-tagged proteins [86]. NTA conjugated with pyrene can attach onto carbon-based nanomaterials (e.g., carbon nanotubes and graphene) deposited on the interface via π-stacking interactions between pyrene derivatives and the materials, which could be reinforced by electropolymerization [87–90].

2.1. SPR Biosensors

SPR technique can determine the binding affinity and kinetics between ligands and receptors, which has been widely used in the monitoring of various biological recognition events in real time. The rational fabrication of biorecognition interface is responsible for the reliability and accuracy of SPR assays [91]. Among various immobilization strategies, NTA–metal complex-aided approach can facilitate the immobilization of His_6-tagged bioreceptors on SPR platform in a site-specific and oriented manner [92–95]. For example, thiol-functionalized NTA can be tethered on the gold-based SPR chip [96]. However, the oxygen sensitivity of thiol species may cause the degradation of the chemisorbed SAM during storage. For this consideration, NTA could be coupled to polymer brushes which were pre-immobilized on the chips for the construction of protein-resistant interfaces [97,98].

His_6-tagged biomolecules can be immobilized on NTA-functionalized chips for the sensitive and accurate investigation of the interaction between bioreceptor and analyte [99,100]. The integration of single-layer graphene with gold chip can improve the sensitivity of SPR biosensors. Singh et al. developed a SPR immunosensor by growing graphene on the chip surface through chemical vapor deposition, which is different from that of graphene oxide, reduced graphene oxide (rGO) or grapheme decorated metal nanoparticle-based platforms (Figure 1A) [101]. In this study, graphene was modified with the film of ploypyrrole-NTA or pyrene-NTA, followed by the immobilization of biotinylated cholera toxin as the bioreceptor unit via the effective

NTA–Cu^{2+}/biotin system for antibody detection. The result demonstrated that the ultrathin functional layer formed by the π-stacking interaction of pyrene-NTA and the subsequent electropolymer achieved the best detection performance (Table 1). With the similar immobilization system, Yuan et al. reported SPR-based DNA assays using an NTA–Cu^{2+}-covered graphene-modified chip to immobilize a biotinylated DNA capture probe, in which the enzymatic catalysis was integrated into SPR assay for signal amplification (Figure 1B) [102]. In this study, nickel-chelated pyrene-NTA was tethered onto the rGO-modified chip to immobilize biotin-labeled capture DNA. After the hybridization between capture DNA, target DNA and reporter DNA, HRP-tagged reporters could catalyze the conversion of aniline into polyaniline precipitation, resulting in great signal amplification via the mass-effect. However, the gradual dissociation of His_6-tagged proteins may result in an unstable baseline, adversely influencing the accurate analysis.

To increase the binding stability, Wang et al. reported the SPR detection of small molecule binding events by integrating the His_6–Ni^{2+} coordination and the amine coupling reaction to covalently affix His_6-tagged proteins [103,104]. Although proteins exhibit amore uniform orientation and a higher density through this immobilization approach, the chip surface would not be regenerated due to the covalent linkage. Double- or triple-His_6 residues could be added into the sequence of proteins for enhancing the attachment [55,105,106]. However, the increased cost and complexity in expressing proteins with double- or triple-His_6 residues will present a disagreeable problem. To overcome this shortcoming, trisNTA-functionalized polymers, such as poly-L-lysine graftpoly(ethyleneglycol) polymer and dextran, were utilized to stably yet reversibly bind His_6-tagged or biotin-labeled proteins for the investigation of different protein bindings and interactions [107–112]. With a trisNTA–Ni^{2+}-covered chip, Liu et al. developed a SPR biosensor for the detection of biomarkers in body fluids (Figure 1C) [113]. It was found that the His_6-tagged proteins attached on the chip surface could be readily regenerated by changing the pH of EDTA solution. Alternatively, Spatz's group reported a novel surface functionalization strategy by using Co^{3+} ion as the mediator between NTA and His_6-tagged protein [76,114]. In this approach, Co^{2+} ion in the complex was oxidized to Co^{3+} in situ by H_2O_2. Compared with Co^{2+} and Ni^{2+} complexes, Co^{3+} complexes exhibit exchange-inert property, higher association and lower dissociation rate constant under the similar coordination environments [114]. Thus, Co^{3+} complexes have been employed to immobilize His_6-tagged proteins for bioassays, such as QCM, biolayer interferometry and fluorescent assays [99,115–119]. Notably, Lammertyn's group used NTA–Co^{3+}-modified surface to design fiber optic (FO)-SPR biosensors (Figure 1D) [70]. The analytical performances, including immobilization efficiency, surface coverage, reproducibility, stability and specificity, were investigated with plasminogen activator inhibitor-1 (PAI-1) as the model example. His_6-tagged anti-PAI-1 antibody fragment (scFv-33H1F7) was used as the receptor and anti-PAI-1 monoclonal antibody (MA-31C9)-modified AuNPs were used as the recognition elements for signal amplification.

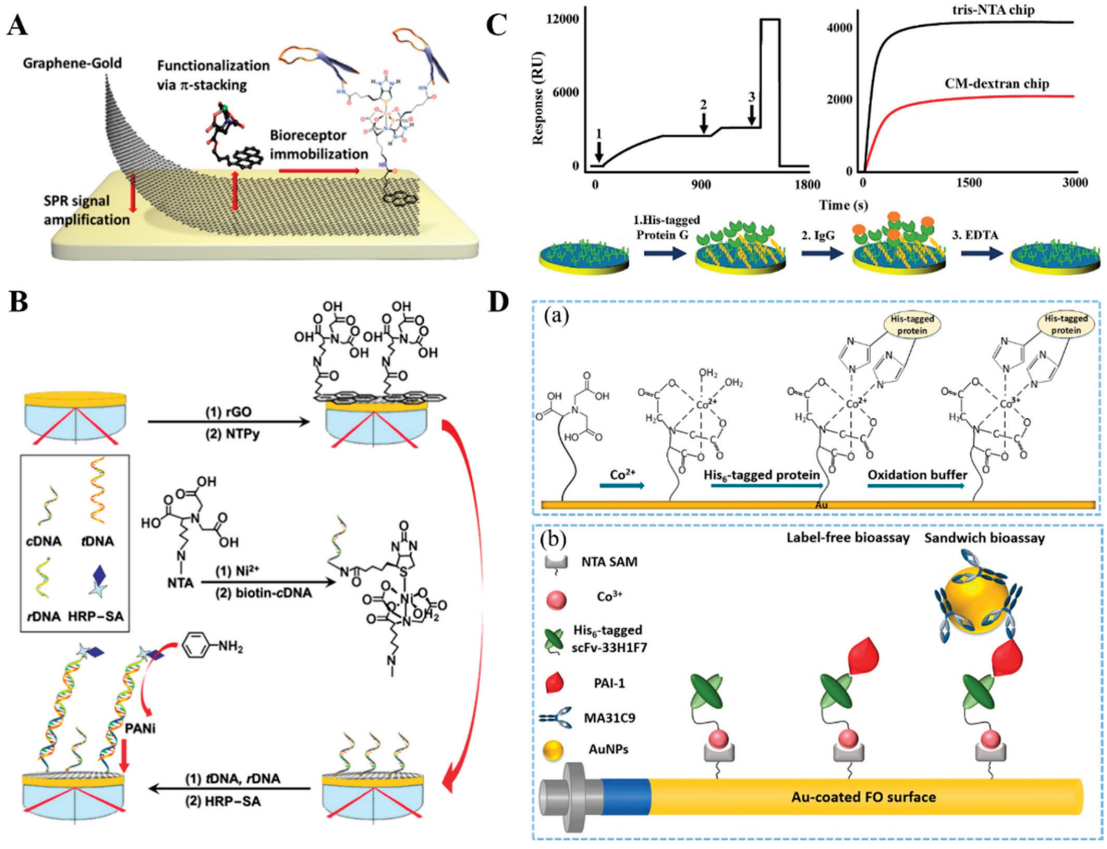

Figure 1. (**A**) Schematic illustration of the functionalization of the graphene layer via π-stacking of pyrene-NTA followed by electropolymerization for the reinforcement of the layer [101]. Copyright 2015 American Chemical Society. (**B**) Schematic illustration of the noncovalent functionalization of rGO for sensitizing SPR-based DNA sensing synergistically with biocatalytic polymerization [102]. Copyright 2017 Elsevier. (**C**) Schematic illustration of trisNTA-based rapid and regenerable SPR determinations of biomarker concentration and biomolecular interaction [113]. Copyright 2021Elsevier. (**D**) Schematic illustration of (**a**) the immobilization steps of His_6-tagged protein on Au-coated surface by Co^{3+}–NTA strategy and (**b**) FO-SPR based bioassay of PAI-1 using Co^{3+}–NTA for bioreceptor immobilization [70]. Copyright 2020 American Chemical Society.

2.2. Electrochemical Biosensors

Electrochemical biosensors can measure the target concentration by monitoring the change of current, potential, conductance or impedance at a solid electrode [120,121]. The electrode modifiers can significantly affect the performances of electrochemical biosensors. The assembly of redox enzymes in a proper alignment is particularly critical for the realization of fast electron transfer between the electrode surface and the redox center of enzyme, retaining the catalytic and regulatory property of protein [122–124]. The SAMs of NTA–metal chelators on the electrode surface can allow for the well-controlled and reversible immobilization of a wide range of His_6-tagged enzymes via the specific affinity binding, including horseradish peroxidase (HRP), alkaline phosphatase (ALP), laccase and glucose oxidase and nitrate reductase [125–130]. For instance, Blankespoor et al. fabricated a dense monolayer of NTA–Cu^{2+} complexes on the surface of a carbon electrode for the immobilization of His_6-tagged HRP and realized the electrochemical reduction of H_2O_2

in the presence of an artificial redox mediator [131]. Wang et al. reported the immobilization of superoxide dismutase (SOD) on the NTA–Ni^{2+}-modified electrode for the in vivo detection of $O_2^{\bullet -}$ in a rat brain, demonstrating that the direct electron transfer of SOD was greatly enhanced by the NTA–Ni^{2+} complexes (Table 1) [132]. Conzuelo et al. reported the competitive detection of β-lactam antibiotics using an NTA–Co^{2+}-modified electrode to immobilize the recombinant bacterial penicillin binding protein (PBP) (Figure 2A) [133]. In this study, HRP-labeled specific tracer (PENG-HRP) was used as the signal label for the competitive binding and hydroquinone (HQ) was used as the redox mediator for the catalytic oxidation of H_2O_2.

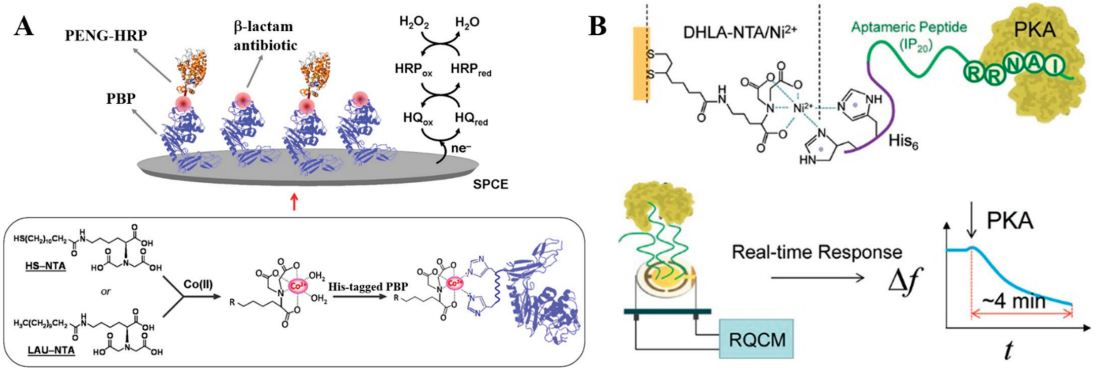

Figure 2. (**A**) Schematic illustration of the development of the affinity biosensor involved in the immobilization of the recombinant His_6-tagged PBP by using Co^{2+}−NTA-modified SPCEs [133]. Copyright 2013 American Chemical Society. (**B**) Schematic illustration of the aptameric peptide (IP_{20})−PKA conjugate as a sensing platform to monitor kinase [134]. Copyright 2012 American Chemical Society.

Aptamers including DNA/RNA and peptide possess several intrinsic properties, such as excellent structure flexibility, high specificity and affinity, good target diversity and ease of synthesis. The immobilization of His_6-tagged aptamers on an NTA–metal complex-modified electrode can produce a highly oriented aptamer assembly to prevent the nonspecific adsorption [135]. Cosnier's group utilized poly(pyrrole-NTA) film to immobilize His_6-tagged aptamer in the presence of Cu^{2+} ions for a label-free impedimetric detection of thrombin and bisphenol-A, respectively [136,137]. Quartz crystal microbalance (QCM) is a simple and direct electrochemical method to study molecular interactions. Xu et al. reported the QCM-based detection of protein kinase A (PKA) with a His_6-tagged peptide inhibitor of IP_{20} as the aptamer-mimicking biorecognition element, in which the aptameric peptide was immobilized on the NTA–Ni^{2+}-covered quartz electrode (Figure 2B) [134]. The kinase concentration could be sensitively determined based on the frequency response of the QCM crystal. In addition, Zaitouna et al. developed an electrochemical biosensor for Ara h 2 antibody detection using the NTA–Ni^{2+} SAM to immobilize the His_6-tagged and methylene blue (MB)-labeled peptide [138]. The detection performance of NTA–Ni^{2+}SAM-based assay was better than that of the biosensor based on the conventional immobilization with a thiolated peptide.

Aside from His_6 tag, biotinylated biomolecules can bind with NTA–metal complexes because three potential binding sites (carboxylate, thioether and ureido groups) of biotin can coordinate with a bivalent metal cation in the NTA chelate [88,139]. For this view, Bauret al. reported the immobilization of biotinylated GOx and polyphenol oxidase on the Cu^{2+}-chelated poly(pyrrole-NTA) film for the amperometric detection of glucose and catechol, respectively [140]. Meanwhile, Palomar et al. developed an impedimetric immunosensor for the determination of an anticholera toxin antibody by the immobilization of biotin-labeled cholera toxin B subunit on the Cu^{2+}-chelated poly(pyrrole-NTA) [141].

The coordinated metal ions in an NTA complex can also bind specifically to phosphorylated biomolecules. Gao et al. reported an electrochemical assay for sphingosine kinase 1 (SphK1) detection using NTA–Fe^{3+} complex to recognize phosphorylated lipids on liposomes [142]. As presented in Figure 3A, liposome was used to embed a substrate of SphK1 in lipid layer through hydrophobic interaction and encapsulate electroactive MB molecules. After the catalytic reaction on the membrane, the reacted liposomes were captured by the NTA–Fe^{3+} complex-modified sensing electrode, and the abundant MB molecules in liposome could generate a strong electrochemical signal, thus reflecting the kinase activity.

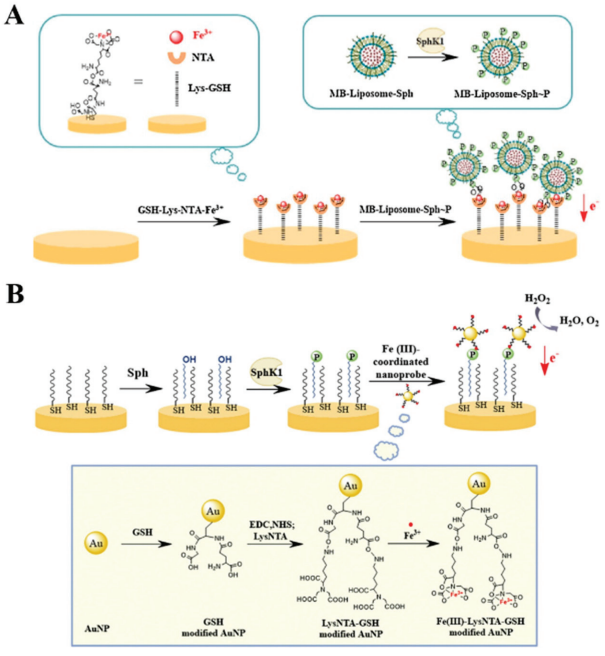

Figure 3. (**A**) Schematic illustration of the principle and fabrication procedures for lipid kinase activity based on liposome-assisted electrochemical assay [142]. Copyright 2017 Elsevier. (**B**) Schematic illustration of SphK1 activity assay based on the bifunctional NTA–Fe^{3+} complex-modified AuNPs [143]. Copyright 2016 Elsevier.

SAM of NTA assembled on the electrode can coordinate with metal ions for electrochemical detection by stripping voltammetry. For instance, Kerekovic et al. investigated the copper(II) binding capacity of an NTA-modified gold electrode via adsorption transfer stripping voltammetry [144]. The results showed that Cu^{2+} ions in the chelates could be directly determined by adsorption transfer stripping voltammetry without an electrochemical accumulation step. Meanwhile, Sasaki et al. developed an electrical assay for the on-site detection of Cu^{2+} ions based on the SAMs of NTA-modified organic thin-film transistor [145]. The coordination of Cu^{2+} ions with NTA could induce the potential shift of the extended-gate, generating an observed change in the drain current. Moreover, Fe^{3+} in the chelating condition retains the ability to catalyze the electrochemical redox of H_2O_2. Gu et al. reported a bifunctional NTA–Fe^{3+} complex-based nanoprobe for the electrochemical detection of SphK1 activity [143]. As displayed in Figure 3B, gold nanoparticles (AuNPs) were employed to carry NTA–Fe^{3+} complexes to recognize phosphorylated sites of substrates. Then, multiple NTA–Fe^{3+} complexes and AuNPs catalyzed the decomposition of H_2O_2, largely amplifying the catalytic amperometric response.

2.3. Fluorescence Biosensors

Fluorescence assays are the most commonly used optical methods to determine molecular interaction, mobility and conformational change. NTA moieties have been linked to peptide substrates or modified with fluorescent units for fluorescent bioassays and bioimaging [146–149]. For example, Kim et al. used NTA–Ni^{2+} complex-modified tetramethylrhodamine (TMR)-doped SiO_2nanoparticles to label a bacterial lysate containing estrogen receptor R ligand binding domain [150]. SiO_2 NPs could improve the sensitivity and limit the fluorescence quenching of dyes by external nickel ions.

Magnetic nanoparticles (MNPs) or magnetic beads (MBs) can be facilely manipulated with an extra magnetic field. They have been widely used in protein/peptide isolation after modification with NTA–metal complexes. Thus, NTA–metal–coated MBs or MNPs have been employed to separate fluorescently labeled peptides from a homogeneous solution (Table 1), leading to the change of fluorescence intensity. For example, Wang et al. reported a label-free fluorescent method for the detection of thrombin activity based on a His_6-tagged recombinant green fluorescence protein (EGFP) and Ni^{2+}–NTA-coated MNPs [151]. As shown in Figure 4A, EGFP with a thrombin cleavage site and a His_6 tag at the N-terminal could be enzymatically cleaved by thrombin, thus resulting in the release of His_6 tag with the inability to attach NTA–Ni^{2+}-coated MNPs. After magnetic separation, the fluorescence intensity of EGFP in the solution is positively related to the activity of thrombin. However, the high cost, large size and pH sensitivity may limit the application of the method for protease assays. In addition, Tan et al. developed a fluorometric method for the detection of protein kinase activity based on the adsorption between NTA–Zr^{4+} MNPs and phosphorylated peptides [152]. As shown in Figure 4B, the fluorescein isothiocyanate (FITC)-conjugated substrate peptide was phosphorylated by protein kinase. The phosphorylated product could adsorb on the surface of NTA–Zr^{4+} MNPs via the chelation of Zr^{4+} and phosphate. After magnetic separation, the fluorescence intensity of the solution evidently decreased, which was indicative of the activity of protein kinase.

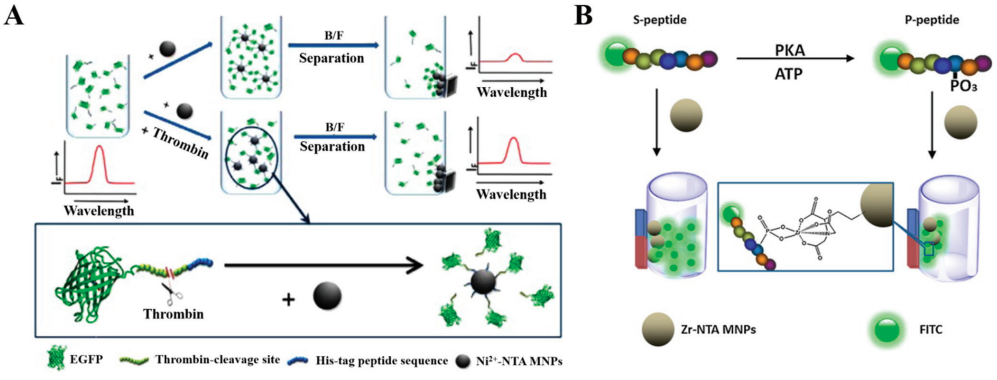

Figure 4. (**A**) Schematic illustration of the strategy using Ni^{2+}–NTA MNPs and the recombinant EGFP to detect the activity of thrombin [151]. Copyright 2013 Elsevier. (**B**) Schematic illustration of the fluorescence kinase activity assay based on Zr–NTA MNPs enrichment [152]. Copyright 2013 Elsevier.

Organic fluorophores have been extensively used to label proteins in vivo through different chemically and biologically labeling techniques without changing the structure and disrupting the normal function of proteins. NTA has been used as a chemical recognition unit to modify fluorescent probes for labeling His_6-tagged proteins or peptides at a specific site via reversible metallochelate coupling of metal ion and His_6 tag. A few organic dyes have been conjugated with NTA complexes to label His_6 tags, such as fluorescein, perylene and Atto488 [56,153–157]. Typically, Glymenaki et al. synthesized three different porphyrin−NTA dyads and successfully employed them to label different His_6-containing peptides [158]. Lata et al. modified different fluorophores with trisNTA groups

for the selective labeling of proteins in cell lysates and on the surface of living cells [159]. Gatterdam et al. prepared several NTA-based multivalent chelators with linear, cyclic and dendritic scaffolds, respectively, and compared their performances on the labeling of cellular His_6-tagged proteins [160]. The results demonstrated that the cyclic trisNTA chelator exhibited the highest affinity and kinetic stability. Furthermore, Uchinomiya et al. reported a site-specific covalent labeling of His_{10}-tagged proteins [161]. In this study, the interaction between His-tag and NTA–Ni^{2+} facilitated the nucleophilic reaction between ahistidine residue in His_{10} tag and the electrophilic tosyl group in the NTA–Ni^{2+} probe by the proximity effect. Different from the probes that merely labeled proteins, dye–NTA conjugates designed by Margulies and coworkers could monitor the change on protein surface by altering the intensity or wavelength of emission upon binding [162–164]. Peri-Naor et al. used the DNA probe modified with both His tag and boronic acid group to develop targeted, pattern-generating and protein surface sensors (Figure 5A) [165]. The method can be used to discriminate between the distinct glycoform populations and identify the glycosylation states of therapeutic proteins.

The poor ability of NTA-based fluorescent probes to penetrate cell membrane may significantly limit the applications in the study of intracellular proteins and subcellular organelles. To facilitate the identification of proteins in living cells, Wieneke et al. designed a cell-penetrating multivalent *tris*NTA chelator of carrier complexes to label protein of interest (POI) based on the cell-penetrating peptide (CPP) [166]. As shown in Figure 5B, Ni^{2+}-loaded and fluorophore-modified *tris*NTA could bind to His_6-tagged HIV TAT_{49-57}. After being delivered into the cytosol and nucleus, the *tris*NTA preferentially interacted with His_{10}–POI, thus resulting in the release of the carrier peptide. In addition, Zhang et al. synthesized a Nap-G/Biotin/ANA-FFpYGK-NTA–Ni^{2+} probe consisting of an NTA–Ni^{2+} group, a self-assembling peptide FFpY and a hydrophobic group [167]. After the hydrolysis is catalyzed by ALP, the product could self-assemble into nanofibers and enter the cells with an increased efficiency to label His_6-tagged proteins.

In single-molecule fluorescence imaging, it is important to improve the photostability of fluorophores by using solution additives/photostabilizers or directly conjugating the photostabilizer to the fluorophores, leading to the quenching of photodegradation-involved transient intermediates. It has been documented that Ni^{2+} ion is an efficient photostabilizing agent through a physical route to quench the triplet excited state of some fluorophores [168,169]. For example, Glembockyte et al. designed a *tris*NTA Alexa647 fluorophore as a self-healing dye for single molecule fluorescence imaging [170]. As illustrated in Figure 5C, four different Alexa647-labeled *tris*NTA probes were synthesized with various length and rigidity of linkers. After the complexation of three Ni^{2+} ions, the photostability of Alexa647 was significantly enhanced due to the closer proximity between Ni^{2+}ions and fluorophores. Moreover, *tris*NTA in the fluorophores also acted as a handle to specifically label His_6-tagged POI for single-molecule imaging.

Transition-metal ions with paramagnetic nature can quench the fluorescence of molecules and nanomaterials with a distance-dependence property [171,172]. Ahn et al. reported the label-free, single-protein detection based on a near-infrared fluorescent NTA–Ni^{2+} complex-modified single-walled carbon nanotube (SWNT) [173]. As shown in Figure 5D, when the His_6-tagged proteins were bound to the complex, the fluorescence intensity was reduced due to the decrease in the intermolecular distance between Ni^{2+} and SWNT. After the addition of target protein (antiHis_6-tag antibody), the fluorescence signal increased based on the analyte–protein interaction. Based on this platform, Ahn et al. investigated glycan–lectin binding for glycan profiling [174].

NTA chelator can also be used to immobilize drugs and biomolecules on the surface of nanomaterials for targeting delivery. For instance, the *tris*NTA-modified graphene oxide has been used to load His_{10}-tagged EGFP for the delivery of drugs into cells [175]. Morales et al. developed a light-activated genome editing platform by monitoring the release of enzymes from hollow gold nanoshell (HGN) nanocarriers [176]. As shown in

Figure 6, Crerecombinase, a protein fusion with a TAT internalization peptide segment, was tested. The protein was immobilized on the HGN modified with NTA-labeled dsDNA in the presence of Cu^{2+}. A red fluorescence was observed after the release of Crerecombinase.

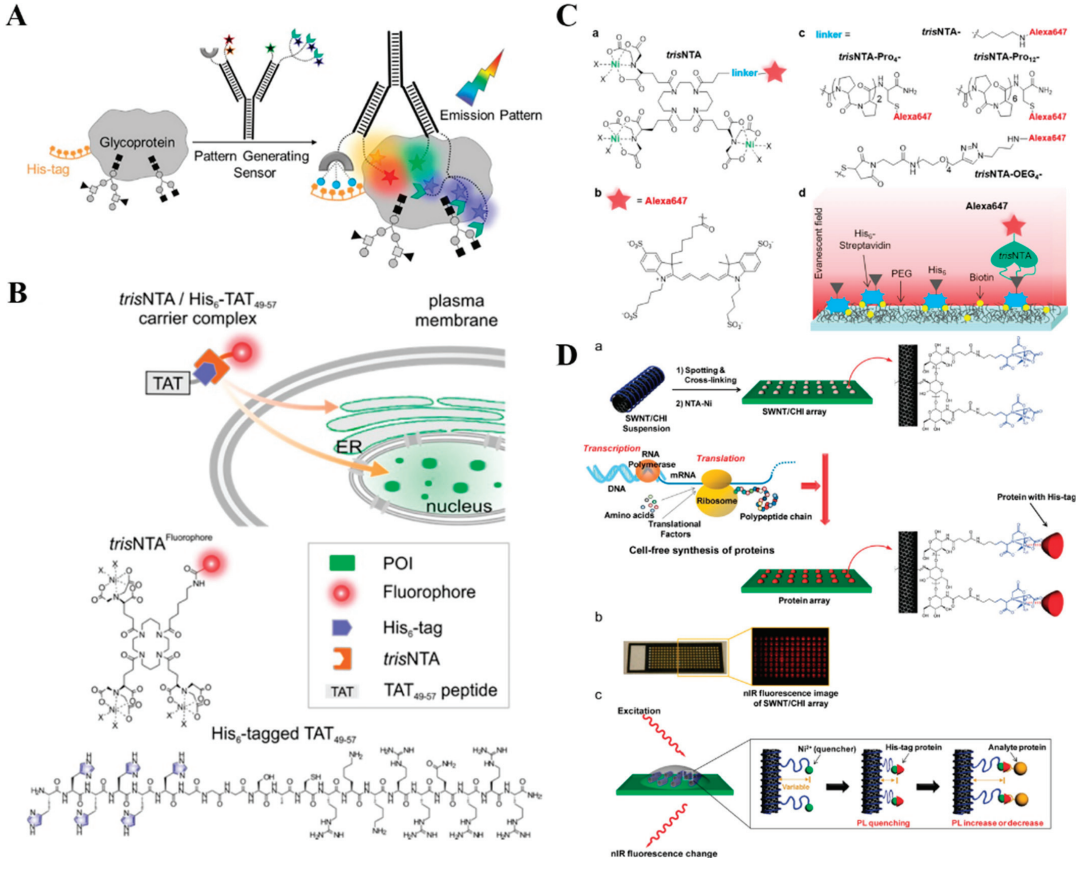

Figure 5. (**A**) Schematic illustration of glycoform differentiation by a targeted, self-assembled, pattern-generating protein surface sensor [165]. Copyright 2020 American Chemical Society. (**B**) Schematic illustration of live-cell labeling of His-tagged proteins in distinct cellular compartments using a cell-penetrating noncovalent *tris*NTA carrier complex formed by fluorescent trisNTA and His_6-tagged TAT_{49-57} [166]. Copyright 2018 American Chemical Society. (**C**) Schematic illustration of: (**a**) the structure of *tris*NTA construct, (**b**) structure of Alexa647, (**c**) structure of the linkers used for *tris*NTA–Alexa647; *tris*NTA–Pro12-Alexa647; *tris*NTA–Pro4-Alexa647 and *tris*NTA–OEG_4-Alexa647 constructs. (**d**) Schematic illustration of the single-molecule experiment used to evaluate the photostability of *tris*NTA constructs [170]. Copyright 2018 American Chemical Society. (**D**) Schematic of a label-free protein array based on fluorescent NTA–Ni^{2+} complex-modified SWNT [173]. (**a**) Array fabrication using SWNT/CHI and in situ generation of individually addressed capture proteins using cell-free protein synthesis for label-free optical detection of protein interactions. A SWNT/CHI suspension is spotted on glass and functionalized with Ni-NTA to bind His-tag-containing capture proteins. Cell-free extract and PCR amplified DNA coding for each protein were added to each spot for protein expression and in situ immobilization. (**b**) Optical and NIR fluorescence image of the SWNT/CHI array. (**c**) Signal transduction mechanism for label-free detection of protein-protein interactions: a NIR fluorescence change from the SWNT occurs when the distance between the Ni2þ quencher and SWNT is altered upon analyte protein binding. Copyright 2011 American Chemical Society.

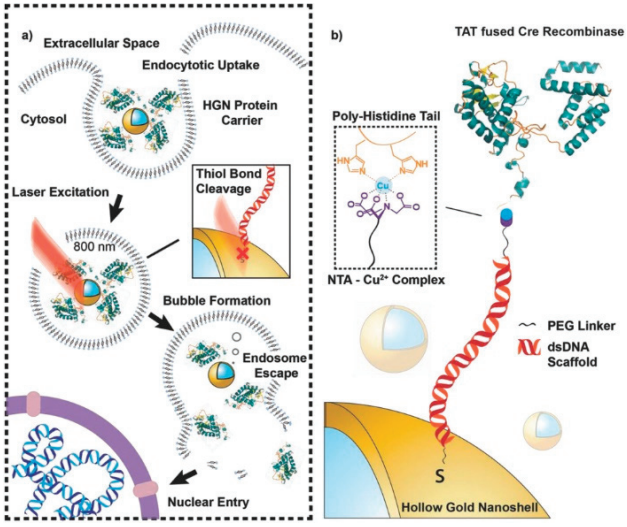

Figure 6. Schematic of (**a**) a light-activated delivery of gene editing enzymes, such as Cre recombinase by HGN-mediated release by NIR laser irradiation and (**b**) assembly of a TAT peptide fusion of Cre-erecombinase on HGN surfaces by a modular handle based on the affinity of polyhistidine tags to a NTA–metal complex presented by a double-stranded DNA scaffold [176]. Copyright 2018 WILEY-VCH.

2.4. Colorimetric Assays

Colorimetric assays have attracted intensive attention due to their low cost and high simplicity. Such methods do not require expensive or sophisticated instrumentation because the color change can be read by the naked eye. Enzymes can efficiently catalyze various chromogenic reactions for colorimetric assays [177,178]. For example, a phosphotriesterase (PTE) trimer can hydrolyze the substrate organophosphate paraoxon to produce faint yellow *p*-nitrophenol. However, the stability and activity of enzymes are not sufficient for usage in the development of portable sensing devices. Medintz's group demonstrated that the stability and activity of PTE were obviously enhanced when it was adsorbed onto NTA–Ni^{2+} complex-modified AuNPs [179]. For this view, they developed a colorimetric method for the detection of organophosphates with PTE–NTA–Ni^{2+}-AuNPs [180].

Peptide-based colorimetric assays have been widely developed to evaluate different protease activities. The signal reporter-modified His_6-tagged peptide can be immobilized on the solid surface or nanoparticles (Table 1). In the presence of target protease, peptide was enzymatically hydrolyzed and the release of signal reporter would result in the change of solution color. Moss et al. designed an enzyme-based amplification system for the colorimetric detection of proteases [181]. HRP-conjugated His_6-tagged substrate peptides were attached onto NTA–Ni^{2+}–modified MBs. In the presence of target enzymes matrix metalloproteinase 2 or disintegrin and metalloproteinase 8, the peptide was cleaved to release HRP into solution. After magnetic separation, HRP in the unreacted peptide on the MBs was quantified by a standard HRP color assay with 3,3′,5,5′-tetramethylbenzidine (TMB) and H_2O_2 as the substrates. However, the high cost and complicated cross-linking procedures of the enzyme-conjugated substances may limit the applications of the colorimetric assays.

To enhance the sensitivity of colorimetric methods, nanomaterials can be used as the carriers to load signal molecules in a high loading efficiency. Under the external stimulus, such as pH, light and surfactants, signal molecules will be rapidly released, generating a significant colorimetric response for signal amplification. For this consideration, Gao et al. reported an integrated magneto-colorimetric method for the assay of lipid kinase (SphK1) activity using NTA-modified MNPs and TMB-loaded liposomes [182]. As shown in Figure 7A, lipid substrates anchored on liposomes were phosphorylated by

SphK1. NTA–Fe^{3+}–MNPs could specifically bind to the phosphate sites on liposomes. After magnetic separation, TMB molecules were released from the liposomes and then oxidized by H_2O_2 under the catalysis of NTA–MNPs, producing a colorimetric signal for the visual detection of SphK1 activity.

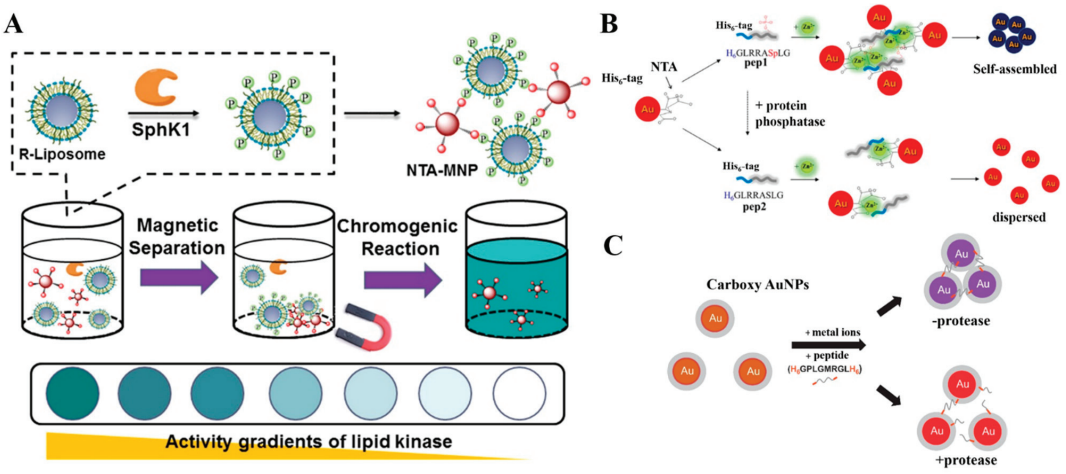

Figure 7. (**A**) Schematic illustration of the principle and assay procedures of the magneto-colorimetric assay for SphK1 activity [182]. Copyright 2018 American Chemical Society. (**B**) Schematic illustration of colorimetric assay for protein phosphatase activity based on AuNPs and His_6-tagged phosphopeptides in the presence of Zn^{2+} [183]. Copyright 2015 American Chemical Society. (**C**) Schematic illustration of the colorimetric assay for protease activity based on metal-induced self-assembly of AuNPs [184]. Copyright 2013 Elsevier.

The aggregation/disaggregation of AuNPs can result in a detectable color change due to the surface plasmon coupling. Based on this unique property, several colorimetric assays based on AuNPs and NTA–metal complexes have been reported for clinical diagnosis and environmental protection [31,185,186]. For example, Lee et al. reported the AuNPs-based colorimetric assay of protein phosphatase activity through Zn^{2+}–phosphate interaction (Figure 7B) [183]. The His_6-tagged peptide substrates could bind to NTA–Ni^{2+}-covered AuNPs by specific coordination. After phosphorylation, the peptide could trigger the aggregation of AuNPs in the presence of Zn^{2+} ions. In addition, Kim et al. found that the carboxy AuNPs could adsorb metal ions such as Ni^{2+} through metal-affinity coordination [184]. As illustrated in Figure 7C, peptide labeled with His_6 tags at both ends could trigger the aggregation of Ni^{2+}-adsorbed carboxy AuNPs. Cleavage of the peptide into two segments by protease (matrix metalloproteinase) prevented the aggregation of AuNPs. Swartz et al. developed a colorimetric sensor for the detection of histidine-rich proteins based on NTA–Ni^{2+}-functionalized AuNPs and AgNPs [187]. In this work, *pf*HRP-II with multiple repeats of AHH and AHHAAD exhibited high affinity toward NTA–Ni^{2+} and could induce the aggregation of NTA–Ni^{2+}-functionalized AuNPs in a concentration-and pH-dependent manner. Additionally, AuNPs can catalyze the silver deposition on the nanoparticle surface. Based on this catalytic ability, Cheng et al. reported a scanometric strategy for the determination of matrix metalloproteinases using His_6-tagged peptide-AuNPs [188]. The metalloproteinases could cleave the specific substrate peptide to release AuNPs from the NTA–Ni^{2+}-modified chips. The greyscale signal from the silver enhancement decreased with the reduction of the amount of bound AuNPs.

2.5. Others

2.5.1. SERS

SERS can provide the molecular fingerprint information for sensitive chemical andbiological detection. However, most of biomolecules only produce weak SERS response due to

their small Raman cross-section and low polarizability. To enhance the sensitivity, silver and gold nanoparticles could be used as the substrates to amplify the SERS signal. NTA–metal complexes modified on the substrate can act as the recognition elements to capture targets from complex samples. The captured target in proximal to the substrate surface would offer a Raman signal. For example, catechol can bind to Fe^{3+} ions with exceptional stability via the coordination interaction. Kaya et al. used NTA–Fe^{3+} complex-modified AgNPs as the substrate for the SERS detection of dopamine in the presence of ascorbic acid [189]. The formed NTA–Fe^{3+}–dopamine complexes caused the signal enhancement. In addition, Cao et al. reported the sensitive SERS determination of catecholamine by using NTA–Fe^{3+} complexes-modified polyvinylpyrrolidone-capped AuNPs as the substrates [190]. Li et al. prepared NTA–Ni^{2+} complex-modified AuNPs active substrate to capture histamine via the formation of NTA–Ni^{2+}–histamine complex for histamine detection [191].

2.5.2. Chemiluminescence

Chemiluminescence signal can be generated by a redox reaction in which the electronically excited species from a chemical reaction return to the ground state. Based on this principle, Han et al. developed a chemiluminescence immunosensor for the detection of allergen-specific IgE (sIgE) by immobilizing the His_6-tagged allergens to the NTA-modified MNPs [192]. As shown in Figure 8, NTA was conjugated to the surface of Fe_3O_4@SiO_2 through the amidation reaction and the recombinant His_6-tagged Can f 1 (rCan f1), which was then adsorbed onto the Fe_3O_4@SiO_2-NTA surface in the presence of Ni^{2+} ions. Next, sIgE in sera from allergic patients specifically captured by Fe_3O_4@SiO_2-NTA@rCan f1 was labeled with HRP-modified anti-IgE. After the magnetic separation, HRP on MNPs surface-catalyzed the chemiluminescence reaction, achieving the quantitative detection of sIgEs.

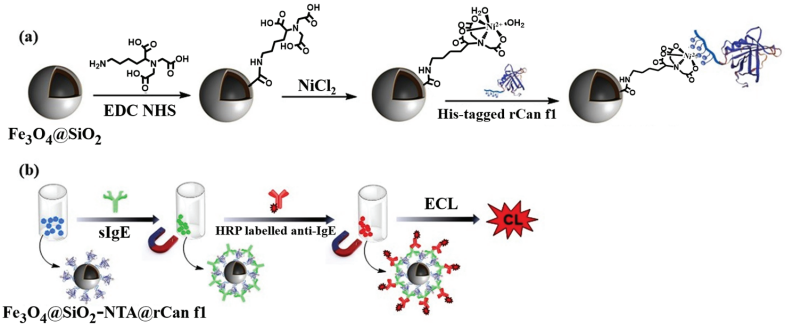

Figure 8. Schematic illustration of (**a**) the synthetic route of Fe_3O_4@SiO_2-NTA and immobilization of rCan f1 via Ni–NTA and His-tag interaction, and (**b**) the immunosensor Fe_3O_4@SiO_2-NTA@rCan f1 for quantitative detection of sIgE in real samples [192]. Copyright 2020 Elsevier.

2.5.3. Immunochromatic Rapid Diagnostic Tests (RDTs)

RDTs show the advantages of easy operation, wide applicability, rapid response and low cost [193]. Wright's group used NTA–Ni^{2+}-coated MBs to concentrate the malarial biomarker of histidine-rich protein II (*pf*HRP-II) for enhancing test performances [194]. To realize the detection of low level of infection by multiantigen RDTs, they further developed a magnetically assisted multiplex biomarker enrichment strategy [195]. As shown in Figure 9, the antibodies were first modified with His_6 tags by maleimide-thiol interaction and then captured by NTA–Ni^{2+}-coated magnetic beads. The captured antibody–antigen conjugates could be magnetically purified, concentrated, and then released into a RDT-compatible volume for assay.

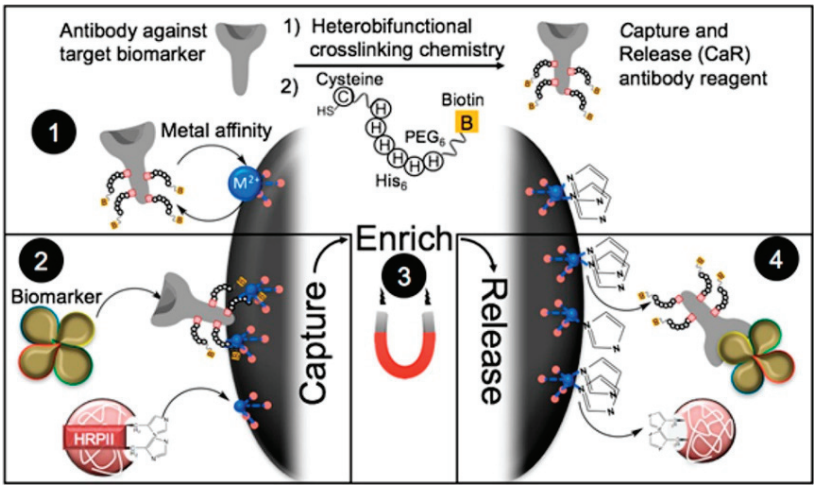

Figure 9. Schematic illustration of conjugation strategy and operation principle for the pLDH and HRPII biomarker enrichment strategy [195]. Copyright 2017 American Chemical Society.

Particles in an evaporating colloidal drop can migrate onto the drop's edge to form a ring on the underlying substrate, which has been widely exploited in the analytical science called as the coffee-ring effect [196]. Wright's group reported an RDT for the detection of poly-L-histidine (PLH) as a *pf*HRP-II biomimic based on the biomarker-mediated disruption of coffee-ring formation [197]. In this work, *pf*HRP-II promoted the cross-linking between NTA–Ni^{2+}-functionalized magnetic particles and indictor particles with red fluorescence. The conjugates were then pulled to the center under a magnetic field. Meanwhile, the indictor particles with green fluorescence were transported to the edge. However, in the absence of *pf*HRP-II, the colocation of both indicator particles at the edge led to a ring with yellow emission with no center signal. However, this method exhibited the shortcomings of low sensitivity, the requirement of an extra magnetic field and a high background signal. To solve those problems, Wright's group developed a platform for recombinant HRP-II detection using NTA–Ni^{2+} complex-modified gold-plated polystyrene microspheres (AuPS) and NTA–Ni^{2+} complex-functionalized glass [198]. During the coffee ring formation, the conjugate of recombinant HRP-II and AuPS particles moved to the drop edge by binding to the NTA–Ni^{2+} complex-functionalized glass. The non-specific materials could be washed away from the surface.

Table 1. Biosensors based on the binding events of NTA–metal complexes.

Detection Techniques	Substrate	Biorecognition Elements	Metal Ions	Target	Linear Range	LOD	Ref.
SPR	NTA-modified gold-coated fiber-optic probe	His_6-tagged scFv-33H1F7	Co^{3+}	PAI-1	3.125~400 ng/mL	0.20 ng/mL	[70]
	Polypyrrole-NTA-modified graphene-gold chip	BiotinylatedCT cholera toxin	Cu^{2+}	Anti-CT	4×10^{-3}~4 ng/mL	4 pg/mL	[101]
	TrisNTA-modified chip	His_6-tagged S1 protein	Ni^{2+}	Anti-SARS-CoV-2 antibody	0.5~96 μg/mL	57 ng/mL	[111]
	TrisNTA-modified chip	His_6-tagged protein G	Ni^{2+}	IgG	0.5~20 μg/mL	47 ng/mL	[113]
	NTA-modified gold-coated fiber-optic probe	His_6-tagged ADAMTS13	Co^{3+}	Anti-ADAMTS13 autoantibodies	1.56~100 ng/mL	0.24 ng/mL	[116]
	NTA-modified electrode	His_6-tagged receptor	Cu^{2+}	Amyloid-beta$_{16-23}$	1×10^{-3}~1 μM	1.43 nM	[82]

Table 1. *Cont.*

Detection Techniques	Substrate	Biorecognition Elements	Metal Ions	Target	Linear Range	LOD	Ref.
EC	NTA-modified gold electrode	NTA–Cu^{2+}	Cu^{2+}	Lipopolysaccharide	1×10^{-4}~0.1 ng/mL	0.1 pg/mL	[84]
	NTA-modified carbon electrode	His_6-tagged SOD	Ni^{2+}	$O_2^{\bullet-}$	0.1~100 μM	21 nM	[132]
	NTA-modified SPCEs	His_6-tagged PBP	Co^{2+}	Ampicillin	1.3~9.9 ng/mL	0.7 ng/mL	[133]
	NTA-modified Au-coated quartz electrode	His_6-tagged peptide	Ni^{2+}	PKA	0.64~22.33 mU/μL	0.061 mU/μL	[134]
	Polypyrrole-NTA-modified electrode	NH_2–His_5-DNA	Cu^{2+}	HIV DNA	1×10^{-6}~10 nM	1 fM	[135]
	Polypyrrole-NTA-modified electrode	His_5-modified aptamer	Cu^{2+}	Thrombin	4.7×10^{-3}~0.5 nM	4.4 pM	[136]
	Polypyrrole-NTA-modified electrode	His_5-modified aptamer	Cu^{2+}	Bisphenol A	1×10^{-5}~1μM	10 pM	[137]
	NTA-modified gold electrode	His_6-tagged Ara h 2	Ni^{2+}	Ara h 2 antibody	1~10 pM	1 pM	[138]
	Polypyrrole /NTA-modified electrode	Biotinylated CT B Subunit	Cu^{2+}	Anti-CT	1×10^{-7}~10 μg/mL	0.1 pg/mL	[141]
	NTA-modified gold electrode	NTA		Cu^{2+}	0.4~100 μM	10 nM	[144]
	NTA-modified thin-film transistor	NTA		Cu^{2+}	0~15 μM	0.51 μM	[145]
FL	Zr–NTA-modified MNPs	EGFP	Ni^{2+}	thrombin	3×10^{-4}~5×10^{-2} U/mL	0.3 mU/mL	[151]
	Zr–NTA-modified MNPs	FITC-labeled peptide	Zr^{4+}	PKA	0~1 U/μL	0.5 mU/μL	[152]
Color	Carboxy AuNPs	Dual His_6-tagged peptide	Ni^{2+}	MMP-7	3~52 nM	10 nM	[184]
	NTA-modified chip	His_6-tagged peptide	Ni^{2+}	MMP-7	0.1~100 ng/mL	97 pg/mL	[188]
SERS	NTA-modified AgNPs	NTA–Fe^{3+}	Fe^{3+}	Dopamine	0.5~4 nM	60 pM	[189]
	NTA-modified AuNPs	NTA–Fe^{3+}	Fe^{3+}	Dopamine, norepinephrine and epinephrine	0.556~10 μM; 0.125~10 μM; 0.2~9.09 μM	Notreported	[190]
	NTA-modified AgNPs	NTA–Ni^{2+}	Ni^{2+}	Histamine	1~100 μM	1 μM	[191]
CL	Fe_3O_4@SiO_2-NTA	His_6-taggedCan f 1	Ni^{2+}	SpecifcIgE	2.52~10.02 ng/mL	0.35 ng/mL	[192]

Abbreviation: EC, electrochemistry; FL, fluorescence; CL, chemiluminescence; CT, cholera toxin; PKA, protein kinase A; Ara h2, *Arachishypogaea*2; SOD, superoxide dismutase; SPCEs, screen-printed carbon electrodes; PBP, penicillin binding protein; MNPs, magnetic nanoparticles; FITC, fluorescein isothiocyanate; recombinant-enhanced green fluorescence protein; MMP-7, matrix metalloproteinase-7; AuNPs, gold nanoparticles; AgNPs, silver nanoparticles.

3. Conclusions

NTA–metal complexes were initially developed as coordination-bonding-based artificial receptors for protein purification. Their pleiotropic merits have facilitated their expanded applications recently as functional and structural agents in multidisciplinary research such as protein engineering, synthetic chemistry and biological analysis. The noncovalent, specific and strong interaction between NTA–metal complexes and His_6 tags enabled the site-specific and reversible immobilization or labeling of biomolecules, which is helpful to fabricate versatile optical and electrochemical biosensors, especially for point-of-care tests in low-resource settings. For example, NTA–metal complex-functionalized materials, such as cellulose membranes and MBs, have been successfully used to enrich the biomarker concentration for sample preparation, resulting in the enhanced sensitivity of diagnostics. NTA–metal complexes-based affinity techniques provide site-specific, controllable and reversible approaches to immobilize biorecognition elements on detection platforms or nanomaterials under mild conditions without decreasing their functional activities. Moreover, NTA–metal complexes conjugated with other functional species can be used to label His_6-tagged proteins, and their unique optical, catalytic, electrochemical and magnetic properties have endowed them with signal generation ability in diagnostics.

Despite the successful applications in different research fields, there are still some important challenges to be resolved. For example, the cytotoxicity of NTA–metal-His_6 tags and their influence on the structure, function and stability of proteins should be carefully investigated even though the site-specific modification of proteins by NTA derivatives have already been widely used for living-cell and single-molecule imaging. In addition, the insufficient fouling resistance ability should be improved when the biosensors are used

for the assays of undiluted blood plasma samples. NTA–metal complexes can be coupled with other strategies for signal amplification, such as DNA techniques and enzymes. We believe that the integration of NTA–metal complexes with modern analytical techniques would result in a remarkable boost for the design and implementation of powerful and novel biosensors.

Author Contributions: Conceptualization, L.Z.; writing—original draft preparation, L.Z., Y.C., Y.L. and M.Q.; writing—review and editing, L.L.; project administration, L.L.; funding acquisition, L.Z. and L.L. All authors have read and agreed to the published version of the manuscript.

Funding: This research was funded by the Science and Technology Research Project of Henan Province (212102210037) and the Program for Innovative Research Team of Science and Technology in the University of Henan Province (21IRTSTHN005).

Data Availability Statement: Not applicable.

Conflicts of Interest: The authors declare no conflict of interest.

References

1. Wong, L.S.; Khan, F.; Micklefield, J. Selective covalent protein immobilization: Strategies and applications. *Chem. Rev.* **2009**, *109*, 4025–4053. [CrossRef]
2. Trilling, A.K.; Beekwilder, J.; Zuilhof, H. Antibody orientation on biosensor surfaces: A minireview. *Analyst* **2013**, *138*, 1619–1627. [CrossRef] [PubMed]
3. Steen Redeker, E.; Ta, D.T.; Cortens, D.; Billen, B.; Guedens, W.; Adriaensens, P. Protein engineering for directed immobilization. *Bioconjug. Chem.* **2013**, *24*, 1761–1777. [CrossRef]
4. Samanta, D.; Sarkar, A. Immobilization of bio-macromolecules on self-assembled monolayers: Methods and sensor applications. *Chem. Soc. Rev.* **2011**, *40*, 2567–2592. [CrossRef]
5. Li, Y.; Zhang, J.W.; Huang, X.R.; Wang, T.H. Construction and direct electrochemistry of orientation controlled laccase electrode. *Biochem. Biophys. Res. Commun.* **2014**, *446*, 201–205. [CrossRef]
6. Kim, E.S.; Shim, C.K.; Lee, J.W.; Park, J.W.; Choi, K.Y. Synergistic effect of orientation and lateral spacing of protein g on an on-chip immunoassay. *Analyst* **2012**, *137*, 2421–2430. [CrossRef] [PubMed]
7. Karyakin, A.A.; Presnova, G.V.; Rubtsova, M.Y.; Egorov, A.M. Oriented immobilization of antibodies onto the gold surfaces via their native thiol groups. *Anal. Chem.* **2000**, *72*, 3805–3811. [CrossRef]
8. Della Ventura, B.; Schiavo, L.; Altucci, C.; Esposito, R.; Velotta, R. Light assisted antibody immobilization for bio-sensing. *Biomed. Opt. Express.* **2011**, *2*, 3223–3231. [CrossRef] [PubMed]
9. Song, S.; Li, N.; Bai, L.; Gai, P.; Li, F. Photo-assisted robust anti-interference self-powered biosensing of MicroRNA based on Pt-s bonds and the inorganic-organic hybridization strategy. *Anal. Chem.* **2022**, *94*, 1654–1660. [CrossRef]
10. Guesdon, J.L.; Ternynck, T.; Avrameas, S. The use of avidin-biotin interaction in immunoenzymatic techniques. *J. Histochem. Cytochem.* **2017**, *27*, 1131–1139. [CrossRef]
11. Yu, C.C.; Kuo, Y.Y.; Liang, C.F.; Chien, W.T.; Wu, H.T.; Chang, T.C.; Jan, F.D.; Lin, C.C. Site-specific immobilization of enzymes on magnetic nanoparticles and their use in organic synthesis. *Bioconjug. Chem.* **2012**, *23*, 714–724. [CrossRef]
12. Holland-Nell, K.; Beck-Sickinger, A.G. Specifically immobilised aldo/keto reductase akr1a1 shows a dramatic increase in activity relative to the randomly immobilised enzyme. *Chembiochem* **2007**, *8*, 1071–1076. [CrossRef]
13. Cheung, R.C.; Wong, J.H.; Ng, T.B. Immobilized metal ion affinity chromatography: A review on its applications. *Appl. Microbiol. Biotechnol.* **2012**, *96*, 1411–1420. [CrossRef] [PubMed]
14. Arnold, F.H. Metal-affinity separations: A new dimension in protein processing. *Nat. Biotechnol.* **1991**, *9*, 151–156. [CrossRef] [PubMed]
15. Block, H.; Maertens, B.; Spriestersbach, A.; Brinker, N.; Kubicek, J.; Fabis, R.; Labahn, J.; Schäfer, F. Immobilized-metal affinity chromatography (imac): A review. *Methods Enzymol.* **2009**, *463*, 439–473.
16. Gaberc-Porekar, V.; Menart, V. Perspectives of immobilized-metal affinity chromatography. *J. Biochem. Biophys. Methods* **2001**, *49*, 335–360. [CrossRef] [PubMed]
17. Xu, J.J.; Ambrosini, S.; Tamahkar, E.; Rossi, C.; Haupt, K.; Tse Sum Bui, B. Toward a universal method for preparing molecularly imprinted polymer nanoparticles with antibody-like affinity for proteins. *Biomacromolecules* **2016**, *17*, 345–353. [CrossRef]
18. Hochuli, E.; Dobeli, H.; Schacher, A. New metal chelate adsorbent selective for proteins and peptides containing neighbouring histidine residues. *J. Chromatogr.* **1987**, *411*, 177–184. [CrossRef]
19. Ruan, M.; Nicolas, I.; Baudy-Floèh, M. New building blocks or dendritic pseudopeptides for metal chelating. *Springerplus* **2016**, *5*, 55–61. [CrossRef]
20. Hsieh, Y.L.; Chen, C.W.; Lin, W.H.; Li, B.R. Construction of the nickel oxide nanocoral structure on microscope slides for total self-assembly-oriented probe immobilization and signal enhancement. *ACS Appl. Bio Mater.* **2020**, *3*, 3304–3312. [CrossRef]

21. Hall, E.A.H.; Chen, S.; Chun, J.; Du, Y.; Zhao, Z.Y. A molecular biology approach to protein coupling at a biosensor interface. *TrAC-Trend. Anal. Chem.* **2016**, *79*, 247–256. [CrossRef]
22. Zeng, X.Q.; Shen, Z.H.; Mernaugh, R. Recombinant antibodies and their use in biosensors. *Anal. Bioanal. Chem.* **2012**, *402*, 3027–3038. [CrossRef] [PubMed]
23. Bellare, M.; Kadambar, V.K.; Bollella, P.; Gamella, M.; Katz, E.; Melman, A. Electrochemical signal-triggered release of biomolecules functionalized with His-tag units. *Electroanalysis* **2019**, *31*, 2274–2282. [CrossRef]
24. Wang, W.; Wang, D.I.; Li, Z. Facile fabrication of recyclable and active nanobiocatalyst: Purification and immobilization of enzyme in one pot with Ni-NTA functionalized magnetic nanoparticle. *Chem. Commun.* **2011**, *47*, 8115–8117. [CrossRef]
25. Bauer, W.S.; Kimmel, D.W.; Adams, N.M.; Gibson, L.E.; Scherr, T.F.; Richardson, K.A.; Conrad, J.A.; Matakala, H.K.; Haselton, F.R.; Wright, D.W. Magnetically-enabled biomarker extraction and delivery system: Towards integrated ASSURED diagnostic tools. *Analyst* **2017**, *142*, 1569–1580. [CrossRef] [PubMed]
26. Rowinska-Zyrek, M.; Witkowska, D.; Potocki, S.; Remelli, M.; Kozlowski, H. His-rich sequences—Is plagiarism from nature a good idea? *New J. Chem.* **2013**, *37*, 58–70. [CrossRef]
27. Jones, A.L.; Hulett, M.D.; Parish, C.R. Histidine-rich glycoprotein: A novel adaptor protein in plasma that modulates the immune, vascular and coagulation systems. *Immunol. Cell Biol.* **2005**, *83*, 106–118. [CrossRef]
28. Sahal, D.; Kannan, R.; Sinha, A.; Babbarwal, V.; Gnana Prakash, B.; Singh, G.; Chauhan, V.S. Specific and instantaneous one-step chemodetection of histidine-rich proteins by pauly's stain. *Anal. Biochem.* **2002**, *308*, 405–408. [CrossRef]
29. Davis, K.M.; Gibson, L.E.; Haselton, F.R.; Wright, D.W. Simple sample processing enhances malaria rapid diagnostic test performance. *Analyst* **2014**, *139*, 3026–3031. [CrossRef]
30. Ricks, K.M.; Adams, N.M.; Scherr, T.F.; Haselton, F.R.; Wright, D.W. Direct transfer of hrpii-magnetic bead complexes to malaria rapid diagnostic tests significantly improves test sensitivity. *Malar. J.* **2016**, *15*, 399–406. [CrossRef]
31. Kantor, A.G.; Markwalter, C.F.; Nourani, A.; Wright, D.W. An antibody-free dual-biomarker rapid enrichment workflow (andrew) improves the sensitivity of malaria rapid diagnostic tests. *Anal. Biochem.* **2021**, *612*, 114020–114026. [CrossRef] [PubMed]
32. Liu, T.H.; Huang, Y.T.; Cheng, H.W.; Chen, Y.W.; Lee, C.H.; Hsu, Y.D.; Pan, R.L.; Tseng, F.G. Single molecule take-and-place technique for positioning a membrane protein on a lipid bilayer. *J. Phys. Chem. C* **2015**, *119*, 21184–21190. [CrossRef]
33. Kitai, T.; Watanabe, Y.; Toyoshima, Y.Y.; Kobayashi, T.; Murayama, T.; Sakaue, H.; Suzuki, H.; Takahagi, T. Simple method of synthesizing nickel–nitrilotriacetic acid gold nanoparticles with a narrow size distribution for protein labeling. *Jpn. J. Appl. Phys.* **2011**, *50*, 095002–095006. [CrossRef]
34. Schmid, E.L.; Keller, T.A.; Dienes, Z.; Vogel, H. Reversible oriented surface immobilization of functional proteins on oxide surfaces. *Anal. Chem.* **1997**, *69*, 1979–1985. [CrossRef]
35. Wasserberg, D.; Cabanas-Danes, J.; Prangsma, J.; O'Mahony, S.; Cazade, P.A.; Tromp, E.; Blum, C.; Thompson, D.; Huskens, J.; Subramaniam, V.; et al. Controlling protein surface orientation by strategic placement of oligo-histidine tags. *ACS Nano* **2017**, *11*, 9068–9083. [CrossRef]
36. Hainfeld, J.F.; Liu, W.; Halsey, C.M.; Freimuth, P.; Powell, R.D. Ni-NTA-gold clusters target His-tagged proteins. *J. Struct. Biol.* **1999**, *127*, 185–198. [CrossRef] [PubMed]
37. Yang, J.B.; Ni, K.F.; Wei, D.Z.; Ren, Y.H. One-step purification and immobilization of his-tagged protein via ni2+-functionalized Fe_3O_4@polydopamine magnetic nanoparticles. *Biotechnol. Bioproc. Eng.* **2015**, *20*, 901–907. [CrossRef]
38. Johnson, D.L.; Martin, L.L. Controlling protein orientation at interfaces using histidine tags: An alternative to Ni/NTA. *J. Am. Chem. Soc.* **2005**, *127*, 2018–2019. [CrossRef]
39. Ravikumar, R.; Chen, L.H.; Jayaraman, P.; Poh, C.L.; Chan, C.C. Chitosan-nickel film based interferometric optical fiber sensor for label-free detection of histidine tagged proteins. *Biosens. Bioelectron.* **2018**, *99*, 578–585. [CrossRef]
40. Schmitt, L.; Dietrich, C.; Tampé, R. Synthesis and characterization of chelator-lipids for reversible immobilization of engineered proteins at self-assembled lipid interfaces. *J. Am. Chem. Soc.* **2002**, *116*, 8485–8491. [CrossRef]
41. You, C.J.; Bhagawati, M.; Brecht, A.; Piehler, J. Affinity capturing for targeting proteins into micro and nanostructures. *Anal. Bioanal. Chem.* **2009**, *393*, 1563–1570. [CrossRef] [PubMed]
42. Markwalter, C.F.; Kantor, A.G.; Moore, C.P.; Richardson, K.A.; Wright, D.W. Inorganic complexes and metal-based nanomaterials for infectious disease diagnostics. *Chem. Rev.* **2019**, *119*, 1456–1518. [CrossRef]
43. Soler, M.; Lechuga, L.M. Biochemistry strategies for label-free optical sensor biofunctionalization: Advances towards real applicability. *Anal. Bioanal. Chem.* **2022**, *414*, 5071–5085. [CrossRef]
44. Mu, B.; Zhang, J.Q.; McNicholas, T.P.; Reuel, N.F.; Kruss, S.; Strano, M.S. Recent advances in molecular recognition based on nanoengineered platforms. *Acc. Chem. Res.* **2014**, *47*, 979–988. [CrossRef]
45. Wieneke, R.; Tampe, R. Multivalent chelators for in vivo protein labeling. *Angew. Chem. Int. Ed.* **2019**, *58*, 8278–8290. [CrossRef] [PubMed]
46. You, C.J.; Piehler, J. Multivalent chelators for spatially and temporally controlled protein functionalization. *Anal. Bioanal. Chem.* **2014**, *406*, 3345–3357. [CrossRef]
47. López-Laguna, H.; Voltà-Durán, E.; Parladé, E.; Villaverde, A.; Vázquez, E.; Unzueta, U. Insights on the emerging biotechnology of histidine-rich peptides. *Biotechnol. Adv.* **2022**, *54*, 107817–107831. [CrossRef]

48. Bauer, W.S.; Richardson, K.A.; Adams, N.M.; Ricks, K.M.; Gasperino, D.J.; Ghionea, S.J.; Rosen, M.; Nichols, K.P.; Weigl, B.H.; Haselton, F.R.; et al. Rapid concentration and elution of malarial antigen histidine-rich protein II using solid phase Zn(II) resin in a simple flow-through pipette tip format. *Biomicrofluidics* **2017**, *11*, 034115–034130. [CrossRef] [PubMed]
49. Hochuli, E.; Bannwarth, W.; Döbeli, H.; Gentz, R.; Stüber, D. Genetic approach to facilitate purification of recombinant proteins with a novel metal chelate adsorbent. *Nat. Biotechnol.* **1988**, *6*, 1321–1325. [CrossRef]
50. Suh, J.K.; Poulsen, L.L.; Ziegler, D.M.; Robertus, J.D. Molecular cloning and kinetic characterization of a flavin-containing monooxygenase from saccharomyces cerevisiae. *Arch. Biochem. Biophys.* **1996**, *336*, 268–274. [CrossRef]
51. Giusti, F.; Kessler, P.; Hansen, R.W.; Della Pia, E.A.; Le Bon, C.; Mourier, G.; Popot, J.L.; Martinez, K.L.; Zoonens, M. Synthesis of a polyhistidine-bearing amphipol and its use for immobilizing membrane proteins. *Biomacromolecules* **2015**, *16*, 3751–3761. [CrossRef]
52. Knecht, S.; Ricklin, D.; Eberle, A.N.; Ernst, B. Oligohis-tags: Mechanisms of binding to Ni^{2+}-NTA surfaces. *J. Mol. Recognit.* **2009**, *22*, 270–279. [CrossRef] [PubMed]
53. Madoz-Gúrpide, J.; Abad, J.M.; Fernández-Recio, J.; Vélez, M.; Vázquez, L.; Gómez-Moreno, C.; Fernández, V.M. Modulation of electroenzymatic nadph oxidation through oriented immobilization of ferredoxin: $NANP^+$ reductase onto modified gold electrodes. *J. Am. Chem. Soc.* **2000**, *122*, 9808–9817. [CrossRef]
54. Schroper, F.; Baumann, A.; Offenhausser, A.; Mayer, D. Direct electrochemistry of novel affinity-tag immobilized recombinant horse heart cytochrome c. *Biosens. Bioelectron.* **2012**, *34*, 171–177. [CrossRef]
55. Khan, F.; He, M.Y.; Taussig, M.J. Double-hexahistidine tag with high-affinity binding for protein immobilization, purification, and detection on ni-nitrilotriacetic acid surfaces. *Anal. Chem.* **2006**, *78*, 3072–3079. [CrossRef] [PubMed]
56. Kapanidis, A.N.; Ebright, Y.W.; Ebright, R.H. Site-specific incorporation of fluorescent probes into protein: Hexahistidine-tag-mediated fluorescent labeling with $(Ni^{2+}$:nitrilotriacetic acid$)_n$-fluorochrome conjugates. *J. Am. Chem. Soc.* **2001**, *123*, 12123–12125. [CrossRef]
57. Gershon, P.D.; Khilko, S. Stable chelating linkage for reversible immobilization of oligohistidine tagged proteins in the biacore surface plasmon resonance detector. *J. Immunol. Methods* **1995**, *183*, 65–76. [CrossRef]
58. Le, T.T.; Wilde, C.P.; Grossman, N.; Cass, A.E. A simple method for controlled immobilization of proteins on modified SAMs. *Phys. Chem. Chem. Phys.* **2011**, *13*, 5271–5278. [CrossRef]
59. Tinazli, A.; Tang, J.; Valiokas, R.; Picuric, S.; Lata, S.; Piehler, J.; Liedberg, B.; Tampe, R. High-affinity chelator thiols for switchable and oriented immobilization of histidine-tagged proteins: A generic platform for protein chip technologies. *Chem. Eur. J.* **2005**, *11*, 5249–5259. [CrossRef]
60. Lata, S.; Piehler, J. Stable and functional immobilization of histidine-tagged proteins via multivalent chelator headgroups on a molecular poly(ethylene glycol) brush. *Anal. Chem.* **2005**, *77*, 1096–1105. [CrossRef]
61. Knezevic, J.; Langer, A.; Hampel, P.A.; Kaiser, W.; Strasser, R.; Rant, U. Quantitation of affinity, avidity, and binding kinetics of protein analytes with a dynamically switchable biosurface. *J. Am. Chem. Soc.* **2012**, *134*, 15225–15228. [CrossRef] [PubMed]
62. Huang, Z.H.; Hwang, P.; Watson, D.S.; Cao, L.M.; Szoka, F.C., Jr. Tris-nitrilotriacetic acids of subnanomolar affinity toward hexahistidine tagged molecules. *Bioconjug. Chem.* **2009**, *20*, 1667–1672. [CrossRef] [PubMed]
63. Huang, Z.H.; Park, J.I.; Watson, D.S.; Hwang, P.; Szoka, F.C., Jr. Facile synthesis of multivalent nitrilotriacetic acid (NTA) and NTA conjugates for analytical and drug delivery applications. *Bioconjug. Chem.* **2006**, *17*, 1592–1600. [CrossRef] [PubMed]
64. Lata, S.; Reichel, A.; Brock, R.; Tampe, R.; Piehler, J. High-affinity adaptors for switchable recognition of histidine-tagged proteins. *J. Am. Chem. Soc.* **2005**, *127*, 10205–10215. [CrossRef] [PubMed]
65. Meredith, G.D.; Wu, H.Y.; Allbritton, N.L. Targeted protein functionalization using His-tags. *Bioconjug. Chem.* **2004**, *15*, 969–982. [CrossRef]
66. Hintersteiner, M.; Weidemann, T.; Kimmerlin, T.; Filiz, N.; Buehler, C.; Auer, M. Covalent fluorescence labeling of His-tagged proteins on the surface of living cells. *Chembiochem* **2008**, *9*, 1391–1395. [CrossRef]
67. Willard, F.S.; Siderovski, D.P. Covalent immobilization of histidine-tagged proteins for surface plasmon resonance. *Anal. Biochem.* **2006**, *353*, 147–149. [CrossRef]
68. Chevalier, S.; Cuestas-Ayllon, C.; Grazu, V.; Luna, M.; Feracci, H.; de la Fuente, J.M. Creating biomimetic surfaces through covalent and oriented binding of proteins. *Langmuir* **2010**, *26*, 14707–14715. [CrossRef]
69. Mateo, C.; Fernández-Lorente, G.; Cortés, E.; Garcia, J.L.; Fernández-Lafuente, R.; Guisan, J.M. One-step purification, covalent immobilization, and additional stabilization of poly-His-tagged proteins using novel heterofunctional chelate-epoxy supports. *Biotechnol. Bioeng.* **2001**, *76*, 269–276. [CrossRef]
70. Qu, J.H.; Horta, S.; Delport, F.; Sillen, M.; Geukens, N.; Sun, D.W.; Vanhoorelbeke, K.; Declerck, P.; Lammertyn, J.; Spasic, D. Expanding a portfolio of (FO-) SPR surface chemistries with the Co(III)-NTA oriented immobilization of His_6-tagged bioreceptors for applications in complex matrices. *ACS Sens.* **2020**, *5*, 960–969. [CrossRef]
71. Mehlenbacher, M.R.; Bou-Abdallah, F.; Liu, X.X.; Melman, A. Calorimetric studies of ternary complexes of Ni(II) and Cu(II) nitrilotriacetic acid and N-acetyloligohistidines. *Inorg. Chim. Acta* **2015**, *437*, 152–158. [CrossRef]
72. Li, X.M.; Song, S.Y.; Pei, Y.X.; Dong, H.; Aastrup, T.; Pei, Z.C. Oriented and reversible immobilization of His-tagged proteins on two- and three-dimensional surfaces for study of protein–protein interactions by a qcm biosensor. *Sens. Actuat. B Chem.* **2016**, *224*, 814–822. [CrossRef]

73. Clow, F.; Fraser, J.D.; Proft, T. Immobilization of proteins to biacore sensor chips using Staphylococcus aureus sortase A. *Biotechnol. Lett.* **2008**, *30*, 1603–1607. [CrossRef]
74. Pellis, A.; Vastano, M.; Quartinello, F.; Herrero Acero, E.; Guebitz, G.M. His-tag immobilization of cutinase 1 from thermobifida cellulosilytica for solvent-free synthesis of polyesters. *Biotechnol. J.* **2017**, *12*, 1700322–1700327. [CrossRef] [PubMed]
75. Wegner, S.V.; Spatz, J.P. Cobalt(III) as a stable and inert mediator ion between NTA and his6-tagged proteins. *Angew. Chem. Int. Ed.* **2013**, *52*, 7593–7596. [CrossRef]
76. Wegner, S.V.; Schenk, F.C.; Spatz, J.P. Cobalt(III)-mediated permanent and stable immobilization of histidine-tagged proteins on NTA-functionalized surfaces. *Chem. Eur. J.* **2016**, *22*, 3156–3162. [CrossRef]
77. Tang, Y.J.; Mernaugh, R.; Zeng, X.Q. Nonregeneration protocol for surface plasmon resonance: Study of high-affinity interaction with high-density biosensors. *Anal. Chem.* **2006**, *78*, 1841–1848. [CrossRef]
78. Lori, J.A.; Morrin, A.; Killard, A.J.; Smyth, M.R. Development and characterization of nickel-NTA-polyaniline modified electrodes. *Electroanalysis* **2006**, *18*, 77–81. [CrossRef]
79. Kang, E.; Park, J.W.; McClellan, S.J.; Kim, J.M.; Holland, D.P.; Lee, G.U.; Franses, E.I.; Park, K.; Thompson, D.H. Specific adsorption of histidine-tagged proteins on silica surfaces modified with Ni^{2+}/NTA-derivatized poly(ethylene glycol). *Langmuir* **2007**, *23*, 6281–6288. [CrossRef]
80. Ley, C.; Holtmann, D.; Mangold, K.M.; Schrader, J. Immobilization of histidine-tagged proteins on electrodes. *Colloids Surf. B* **2011**, *88*, 539–551. [CrossRef]
81. Tinazli, A.; Piehler, J.; Beuttler, M.; Guckenberger, R.; Tampé, R. Native protein nanolithography that can write, read and erase. *Nat. Nanotechnol.* **2007**, *2*, 220–225. [CrossRef] [PubMed]
82. Zborowska, M.; Sulima, M.; Marszałek, I.; Wysłouch-Cieszyńska, A.; Radecka, H.; Radecki, J. Nitrilotriacetic acid–copper(II) monolayer deposited on a gold electrode for the immobilization of histidine tagged v domain of receptor for advanced glycation end products–the basis of amyloid–beta peptide sensing. *Anal. Lett.* **2014**, *47*, 1375–1391. [CrossRef]
83. Cheng, F.; Gamble, L.J.; Castner, D.G. XPS, tof-sims, NEXAFS, and SPR characterization of nitrilotriacetic acid-terminated self-assembled monolayers for controllable immobilization of proteins. *Anal. Chem.* **2008**, *80*, 2564–2573. [CrossRef] [PubMed]
84. Cho, M.; Chun, L.; Lin, M.; Choe, W.; Nam, J.; Lee, Y. Sensitive electrochemical sensor for detection of lipopolysaccharide on metal complex immobilized gold electrode. *Sens. Actuat. B Chem.* **2012**, *174*, 490–494. [CrossRef]
85. Tran, Q.T.; de Sanoit, J.; Pierre, S.; Arnault, J.-C.; Bergonzo, P. Diamond electrodes for trace alpha pollutant sequestration via covalent grafting of nitrilotriacetic acid (NTA) ligand. *Electrochim. Acta* **2014**, *136*, 430–434. [CrossRef]
86. Haddour, N.; Cosnier, S.; Gondran, C. Electrogeneration of a poly(pyrrole)-NTA chelator film for a reversible oriented immobilization of histidine-tagged proteins. *J. Am. Chem. Soc.* **2005**, *127*, 5752–5753. [CrossRef] [PubMed]
87. Holzinger, M.; Baur, J.; Haddad, R.; Wang, X.; Cosnier, S. Multiple functionalization of single-walled carbon nanotubes by dip coating. *Chem. Commun.* **2011**, *47*, 2450–2452. [CrossRef]
88. Singh, M.; Holzinger, M.; Biloivan, O.; Cosnier, S. 3D-nanostructured scaffold electrodes based on single-walled carbon nanotubes and nanodiamonds for high performance biosensors. *Carbon* **2013**, *61*, 349–356. [CrossRef]
89. Osella, S.; Kiliszek, M.; Harputlu, E.; Unlu, C.G.; Ocakoglu, K.; Kargul, J.; Trzaskowski, B. Controlling the charge transfer flow at the graphene/pyrene–nitrilotriacetic acid interface. *J. Mater. Chem. C* **2018**, *6*, 5046–5054. [CrossRef]
90. Jorde, L.; Li, Z.H.; Pöppelwerth, A.; Piehler, J.; You, C.J.; Meyer, C. Biofunctionalization of carbon nanotubes for reversible site-specific protein immobilization. *J. Appl. Phys.* **2021**, *129*, 094302–094311. [CrossRef]
91. Mauriz, E.; García-Fernández, M.C.; Lechuga, L.M. Towards the design of universal immunosurfaces for SPR-based assays: A review. *TrAC-Trend. Anal. Chem.* **2016**, *79*, 191–198. [CrossRef]
92. Pfeifer, P.; Aldinger, U.; Schwotzer, G.; Diekmann, S.; Steinrücke, P. Real time sensing of specific molecular binding using surface plasmon resonance spectroscopy. *Sens. Actuat. B Chem.* **1999**, *54*, 166–175. [CrossRef]
93. Boonen, A.; Singh, A.K.; Hout, A.V.; Das, K.; Loy, T.V.; Noppen, S.; Schols, D. Development of a novel SPR assay to study cxcr4-ligand interactions. *Biosensors* **2020**, *10*, 150. [CrossRef] [PubMed]
94. Maalouli, N.; Gouget-Laemmel, A.C.; Pinchemel, B.; Bouazaoui, M.; Chazalviel, J.N.; Ozanam, F.; Yang, Y.K.; Burkhard, P.; Boukherroub, R.; Szunerits, S. Development of a metal-chelated plasmonic interface for the linking of His-peptides with a droplet-based surface plasmon resonance read-off scheme. *Langmuir* **2011**, *27*, 5498–5505. [CrossRef]
95. Wegner, G.J.; Lee, H.J.; Marriott, G.; Corn, R.M. Fabrication of histidine-tagged fusion protein arrays for surface plasmon resonance imaging studies of protein-protein and protein-DNA interactions. *Anal. Chem.* **2003**, *75*, 4740–4746. [CrossRef]
96. Sigal, G.B.; Bamdad, C.; Barberis, A.; Strominger, J.; Whitesides, G.M. A self-assembled monolayer for the binding and study of histidine-tagged proteins by surface plasmon resonance. *Anal. Chem.* **1996**, *68*, 490–497. [CrossRef]
97. Gautrot, J.E.; Huck, W.T.; Welch, M.; Ramstedt, M. Protein-resistant NTA-functionalized polymer brushes for selective and stable immobilization of histidine-tagged proteins. *ACS Appl. Mater. Interfaces* **2010**, *2*, 193–202. [CrossRef]
98. Schartner, J.; Hoeck, N.; Guldenhaupt, J.; Mavarani, L.; Nabers, A.; Gerwert, K.; Kotting, C. Chemical functionalization of germanium with dextran brushes for immobilization of proteins revealed by attenuated total reflection fourier transform infrared difference spectroscopy. *Anal. Chem.* **2015**, *87*, 7467–7475. [CrossRef]
99. Qu, J.H.; Leirs, K.; Escudero, R.; Strmsek, Z.; Jerala, R.; Spasic, D.; Lammertyn, J. Novel regeneration approach for creating reusable FO-SPR probes with NTA surface chemistry. *Nanomaterials* **2021**, *11*, 186. [CrossRef] [PubMed]

100. Yi, X.Y.; Hao, Y.Q.; Xia, N.; Wang, J.X.; Quintero, M.; Li, D.; Zhou, F.M. Sensitive and continuous screening of inhibitors of beta-site amyloid precursor protein cleaving enzyme 1 (BACE1) at single SPR chips. *Anal. Chem.* **2013**, *85*, 3660–3666. [CrossRef]
101. Singh, M.; Holzinger, M.; Tabrizian, M.; Winters, S.; Berner, N.C.; Cosnier, S.; Duesberg, G.S. Noncovalently functionalized monolayer graphene for sensitivity enhancement of surface plasmon resonance immunosensors. *J. Am. Chem. Soc.* **2015**, *137*, 2800–2803. [CrossRef]
102. Yuan, P.X.; Deng, S.Y.; Yao, C.G.; Wan, Y.; Cosnier, S.; Shan, D. Polymerization amplified SPR-DNA assay on noncovalently functionalized graphene. *Biosens. Bioelectron.* **2017**, *89*, 319–325. [CrossRef] [PubMed]
103. Wang, X.Y.; Liu, Q.H.; Tan, X.F.; Liu, L.Y.; Zhou, F.M. Covalent affixation of histidine-tagged proteins tethered onto Ni-nitrilotriacetic acid sensors for enhanced surface plasmon resonance detection of small molecule drugs and kinetic studies of antibody/antigen interactions. *Analyst* **2019**, *144*, 587–593. [CrossRef] [PubMed]
104. Wang, X.Y.; Zhou, F.M. Dual-valve and counter-flow surface plasmon resonance. *Anal. Chem.* **2018**, *90*, 4972–4977. [CrossRef] [PubMed]
105. Nieba, L.; Nieba-Axmann, S.E.; Persson, A.; Hamalainen, M.; Edebratt, F.; Hansson, A.; Lidholm, J.; Magnusson, K.; Karlsson, A.F.; Pluckthun, A. Biacore analysis of histidine-tagged proteins using a chelating NTA sensor chip. *Anal. Biochem.* **1997**, *252*, 217–228. [CrossRef] [PubMed]
106. Fischer, M.; Leech, A.P.; Hubbard, R.E. Comparative assessment of different histidine-tags for immobilization of protein onto surface plasmon resonance sensorchips. *Anal. Chem.* **2011**, *83*, 1800–1807. [CrossRef]
107. Liu, J.; Spulber, M.; Wu, D.; Talom, R.M.; Palivan, C.G.; Meier, W. Poly(N-isopropylacrylamide-co-tris-nitrilotriacetic acid acrylamide) for a combined study of molecular recognition and spatial constraints in protein binding and interactions. *J. Am. Chem. Soc.* **2014**, *136*, 12607–12614. [CrossRef]
108. Tanner, P.; Ezhevskaya, M.; Nehring, R.; Van Doorslaer, S.; Meier, W.; Palivan, C. Specific his_6-tag attachment to metal-functionalized polymersomes relies on molecular recognition. *J. Phys. Chem. B* **2012**, *116*, 10113–10124. [CrossRef]
109. Rakickas, T.; Gavutis, M.; Reichel, A.; Piehler, J.; Liedberg, B.; Valiokas, R. Protein-protein interactions in reversibly assembled nanopatterns. *Nano Lett.* **2008**, *8*, 3369–3375. [CrossRef]
110. Bhagawati, M.; You, C.J.; Piehler, J. Quantitative real-time imaging of protein-protein interactions by LSPR detection with micropatterned gold nanoparticles. *Anal. Chem.* **2013**, *85*, 9564–9571. [CrossRef]
111. Jiang, M.; Dong, T.B.; Han, C.W.; Liu, L.Y.; Zhang, T.T.; Kang, Q.; Wang, P.C.; Zhou, F.M. Regenerable and high-throughput surface plasmon resonance assay for rapid screening of anti-SARS-CoV-2 antibody in serum samples. *Anal. Chim. Acta.* **2022**, *1208*, 339830–339838. [CrossRef] [PubMed]
112. Reichel, A.; Schaible, D.; Al Furoukh, N.; Cohen, M.; Schreiber, G.; Piehler, J. Noncovalent, site-specific biotinylation of histidine-tagged proteins. *Anal. Chem.* **2007**, *79*, 8590–8600. [CrossRef] [PubMed]
113. Liu, L.Y.; Han, C.W.; Jiang, M.; Zhang, T.T.; Kang, Q.; Wang, X.Y.; Wang, P.C.; Zhou, F.M. Rapid and regenerable surface plasmon resonance determinations of biomarker concentration and biomolecular interaction based on tris-nitrilotriacetic acid chips. *Anal. Chim. Acta.* **2021**, *1170*, 338625–338633. [CrossRef] [PubMed]
114. Pires, M.M.; Chmielewski, J. Self-assembly of collagen peptides into microflorettes via metal coordination. *J. Am. Chem. Soc.* **2009**, *131*, 2706–2712. [CrossRef] [PubMed]
115. Xu, L.; Cao, H.Y.; Huang, C.D.; Jia, L.Y. Oriented immobilization and quantitative analysis simultaneously realized in sandwich immunoassay via His-tagged nanobody. *Molecules* **2019**, *24*, 1890. [CrossRef]
116. Horta, S.; Qu, J.H.; Dekimpe, C.; Bonnez, Q.; Vandenbulcke, A.; Tellier, E.; Kaplanski, G.; Delport, F.; Geukens, N.; Lammertyn, J.; et al. Co(III)-NTA mediated antigen immobilization on a fiber optic-SPR biosensor for detection of autoantibodies in autoimmune diseases: Application in immune-mediated thrombotic thrombocytopenic purpura. *Anal. Chem.* **2020**, *92*, 13880–13887. [CrossRef]
117. Auer, S.; Azizi, L.; Faschinger, F.; Blazevic, V.; Vesikari, T.; Gruber, H.J.; Hytönen, V.P. Stable immobilisation of His-tagged proteins on BLI biosensor surface using cobalt. *Sens. Actuat. B Chem.* **2017**, *243*, 104–113. [CrossRef]
118. Qu, J.H.; Leirs, K.; Maes, W.; Imbrechts, M.; Callewaert, N.; Lagrou, K.; Geukens, N.; Lammertyn, J.; Spasic, D. Innovative FO-SPR label-free strategy for detecting anti-rbd antibodies in COVID-19 patient serum and whole blood. *ACS Sens.* **2022**, *7*, 477–487. [CrossRef]
119. Qu, J.H.; Peeters, B.; Delport, F.; Vanhoorelbeke, K.; Lammertyn, J.; Spasic, D. Gold nanoparticle enhanced multiplexed biosensing on a fiber optic surface plasmon resonance probe. *Biosens. Bioelectron.* **2021**, *192*, 113549–113557. [CrossRef]
120. Yang, L.; Yin, X.; An, B.; Li, F. Precise capture and direct quantification of tumor exosomes via a highly efficient dual-aptamer recognition-assisted ratiometric immobilization-free electrochemical strategy. *Anal. Chem.* **2021**, *93*, 1709–1716. [CrossRef]
121. Lu, L.; Su, H.; Li, F. Ultrasensitive homogeneous electrochemical detection of transcription factor by coupled isothermal cleavage reaction and cycling amplification based on Exonuclease III. *Anal. Chem.* **2017**, *89*, 8328–8334. [CrossRef] [PubMed]
122. Ataka, K.; Giess, F.; Knoll, W.; Naumann, R.; Haber-Pohlmeier, S.; Richter, B.; Heberle, J. Oriented attachment and membrane reconstitution of His-tagged cytochrome c oxidase to a gold electrode: In situ monitoring by surface-enhanced infrared absorption spectroscopy. *J. Am. Chem. Soc.* **2004**, *126*, 16199–16206. [CrossRef]
123. Aghamiri, Z.S.; Mohsennia, M.; Rafiee-Pour, H.A. Immobilization of cytochrome c and its application as electrochemical biosensors. *Talanta* **2018**, *176*, 195–207. [CrossRef] [PubMed]

124. Akram, M.S.; Ur Rehman, J.; Hall, E.A. Engineered proteins for bioelectrochemistry. *Annu. Rev. Anal. Chem.* **2014**, *7*, 257–274. [CrossRef]
125. Maly, J.; Di Meo, C.; De Francesco, M.; Masci, A.; Masojidek, J.; Sugiura, M.; Volpe, A.; Pilloton, R. Reversible immobilization of engineered molecules by Ni-NTA chelators. *Bioelectrochemistry* **2004**, *63*, 271–275. [CrossRef] [PubMed]
126. Maly, J.; Ilie, M.; Foglietti, V.; Cianci, E.; Minotti, A.; Nardi, L.; Masci, A.; Vastarella, W.; Pilloton, R. Continuous flow micro-cell for electrochemical addressing of engineered bio-molecules. *Sens. Actuat. B Chem.* **2005**, *111–112*, 317–322. [CrossRef]
127. Balland, V.; Hureau, C.; Cusano, A.M.; Liu, Y.; Tron, T.; Limoges, B. Oriented immobilization of a fully active monolayer of histidine-tagged recombinant laccase on modified gold electrodes. *Chem. Eur. J.* **2008**, *14*, 7186–7192. [CrossRef]
128. Demin, S.; Hall, E.A. Breaking the barrier to fast electron transfer. *Bioelectrochemistry* **2009**, *76*, 19–27. [CrossRef]
129. Campbell, W.H.; Henig, J.; Plumeré, N. Affinity binding via zinc(II) for controlled orientation and electrochemistry of histidine-tagged nitrate reductase in self-assembled monolayers. *Bioelectrochemistry* **2013**, *93*, 46–50. [CrossRef]
130. Vallina-Garcia, R.; del Mar Garcia-Suarez, M.; Fernandez-Abedul, M.T.; Mendez, F.J.; Costa-Garcia, A. Oriented immobilisation of anti-pneumolysin fab through a histidine tag for electrochemical immunosensors. *Biosens. Bioelectron.* **2007**, *23*, 210–217. [CrossRef]
131. Blankespoor, R.; Limoges, B.; Schollhorn, B.; Syssa-Magalé, J.L.; Yazidi, D. Dense monolayers of metal-chelating ligands covalently attached to carbon electrodes electrochemically and their useful application in affinity binding of histidine-tagged proteins. *Langmuir* **2005**, *21*, 3362–3375. [CrossRef]
132. Wang, Z.; Liu, D.; Gu, H.; Zhu, A.W.; Tian, Y.; Shi, G.Y. NTA-modified carbon electrode as a general relaying substrate to facilitate electron transfer of SOD: Application to in vivo monitoring of O^{2-} in a rat brain. *Biosens. Bioelectron.* **2013**, *43*, 101–107. [CrossRef]
133. Conzuelo, F.; Gamella, M.; Campuzano, S.; Martinez-Ruiz, P.; Esteban-Torres, M.; de las Rivas, B.; Reviejo, A.J.; Munoz, R.; Pingarron, J.M. Integrated amperometric affinity biosensors using Co^{2+}-tetradentate nitrilotriacetic acid modified disposable carbon electrodes: Application to the determination of beta-lactam antibiotics. *Anal. Chem.* **2013**, *85*, 3246–3254. [CrossRef] [PubMed]
134. Xu, X.H.; Zhou, J.; Liu, X.; Nie, Z.; Qing, M.; Guo, M.L.; Yao, S.Z. Aptameric peptide for one-step detection of protein kinase. *Anal. Chem.* **2012**, *84*, 4746–4753. [CrossRef] [PubMed]
135. Baur, J.; Gondran, C.; Holzinger, M.; Defrancq, E.; Perrot, H.; Cosnier, S. Label-free femtomolar detection of target DNA by impedimetric DNA sensor based on poly(pyrrole-nitrilotriacetic acid) film. *Anal. Chem.* **2010**, *82*, 1066–1072. [CrossRef] [PubMed]
136. Xu, H.; Gorgy, K.; Gondran, C.; Le Goff, A.; Spinelli, N.; Lopez, C.; Defrancq, E.; Cosnier, S. Label-free impedimetric thrombin sensor based on poly(pyrrole-nitrilotriacetic acid)-aptamer film. *Biosens. Bioelectron.* **2013**, *41*, 90–95. [CrossRef]
137. Kazane, I.; Gorgy, K.; Gondran, C.; Spinelli, N.; Zazoua, A.; Defrancq, E.; Cosnier, S. Highly sensitive bisphenol-a electrochemical aptasensor based on poly(pyrrole-nitrilotriacetic acid)-aptamer film. *Anal. Chem.* **2016**, *88*, 7268–7273. [CrossRef]
138. Zaitouna, A.J.; Lai, R.Y. An electrochemical peptide-based Ara h 2 antibody sensor fabricated on a nickel(II)-nitriloacetic acid self-assembled monolayer using a His-tagged peptide. *Anal. Chim. Acta.* **2014**, *828*, 85–91. [CrossRef]
139. Griesser, R.; Sigel, H.; Wright, L.D.; McCormick, D.B. Interactions of metal ions with biotin and biotin derivatives. Complexing and hydrogen-bond formation of the ureido group. *Biochemistry* **1973**, *12*, 1917–1922. [CrossRef] [PubMed]
140. Baur, J.; Holzinger, M.; Gondran, C.; Cosnier, S. Immobilization of biotinylated biomolecules onto electropolymerized poly(pyrrole-nitrilotriacetic acid)–Cu^{2+} film. *Electrochem. Commun.* **2010**, *12*, 1287–1290. [CrossRef]
141. Palomar, Q.; Gondran, C.; Holzinger, M.; Marks, R.; Cosnier, S. Controlled carbon nanotube layers for impedimetric immunosensors: High performance label free detection and quantification of anti-cholera toxin antibody. *Biosens. Bioelectron.* **2017**, *97*, 177–183. [CrossRef] [PubMed]
142. Gao, T.; Gu, S.; Mu, C.; Zhang, M.; Yang, J.; Liu, P.; Li, G. Electrochemical assay of lipid kinase activity facilitated by liposomes. *Electrochim. Acta* **2017**, *252*, 362–367. [CrossRef]
143. Gu, S.; Gao, T.; Yang, Y.; Zhi, J.; Li, J.; Xiang, Y.; Wang, K.; Yang, J. A bifunctional Fe(III)-coordinated nanoprobe for electrochemical detection of sphingosine kinase 1 activity. *Electrochem. Commun.* **2016**, *72*, 104–108. [CrossRef]
144. Kerekovic, I.; Milardovic, S.; Palcic, M.; Grabaric, Z. Characterization of cysteamine self assembled on gold functionalized with nitrilotriacetic acid and evaluation of copper(II) binding capacity with adsorption transfer stripping voltammetry. *J. Electroanal. Chem.* **2014**, *724*, 103–110. [CrossRef]
145. Sasaki, Y.; Minami, T.; Minamiki, T.; Tokito, S. An organic transistor-based electrical assay for copper(ii) in water. *Electrochemistry* **2017**, *85*, 775–778. [CrossRef]
146. Yang, W.C.; Swartz, J.R. A filter microplate assay for quantitative analysis of DNA binding proteins using fluorescent DNA. *Anal. Biochem.* **2011**, *415*, 168–174. [CrossRef]
147. Kim, S.H.; Ge, P.; Katzenellenbogen, J.A. A new quinoline sensitizer-centered lanthanide chelate and its use for protein labling on Ni-NTA beads for TR LRET assays. *Chem. Commun.* **2009**, *45*, 183–185. [CrossRef]
148. Li, N.; Yi, L.; He, Z.; Zhang, W.; Li, H.; Lin, J.M. A DNA-directed covalent conjugation fluorescence probe for in vitro detection of functional matrix metalloproteinases. *Analyst* **2017**, *142*, 634–640. [CrossRef]
149. Chao, A.L.; Jiang, N.; Yang, Y.; Li, H.Y.; Sun, H.Z. A Ni-NTA-based red fluorescence probe for protein labelling in live cells. *J. Mater. Chem. B* **2017**, *5*, 1166–1173. [CrossRef]

150. Kim, S.H.; Jeyakumar, M.; Katzenellenbogen, J.A. Dual-mode fluorophore-doped nickel nitrilotriacetic acid-modified silica nanoparticles combine histidine-tagged protein purification with site-specific fluorophore labeling. *J. Am. Chem. Soc.* **2007**, *129*, 13254–13264. [CrossRef]
151. Wang, M.; Lei, C.Y.; Nie, Z.; Guo, M.L.; Huang, Y.; Yao, S.Z. Label-free fluorescent detection of thrombin activity based on a recombinant enhanced green fluorescence protein and nickel ions immobilized nitrilotriacetic acid-coated magnetic nanoparticles. *Talanta* **2013**, *116*, 468–473. [CrossRef]
152. Tan, P.L.; Lei, C.Y.; Liu, X.; Qing, M.; Nie, Z.; Guo, M.L.; Huang, Y.; Yao, S.Z. Fluorescent detection of protein kinase based on zirconium ions-immobilized magnetic nanoparticles. *Anal. Chim. Acta.* **2013**, *780*, 89–94. [CrossRef]
153. Goldsmith, C.R.; Jaworski, J.; Sheng, M.; Lippard, S.J. Selective labeling of extracellular proteins containing polyhistidine sequences by a fluorescein-nitrilotriacetic acid conjugate. *J. Am. Chem. Soc.* **2006**, *128*, 418–419. [CrossRef]
154. Peneva, K.; Mihov, G.; Herrmann, A.; Zarrabi, N.; Borsch, M.; Duncan, T.M.; Mullen, K. Exploiting the nitrilotriacetic acid moiety for biolabeling with ultrastable perylene dyes. *J. Am. Chem. Soc.* **2008**, *130*, 5398–5399. [CrossRef]
155. Guignet, E.G.; Hovius, R.; Vogel, H. Reversible site-selective labeling of membrane proteins in live cells. *Nat. Biotechnol.* **2004**, *22*, 440–444. [CrossRef]
156. Thai, H.B.; Yu, J.K.; Park, Y.J.; Ahn, D.R. A dual-responsive pH-sensor and its potential as a universal probe for assays of pH-changing enzymes. *Analyst* **2015**, *140*, 2804–2809. [CrossRef]
157. Zhao, C.X.; Hellman, L.M.; Zhan, X.; Bowman, W.S.; Whiteheart, S.W.; Fried, M.G. Hexahistidine-tag-specific optical probes for analyses of proteins and their interactions. *Anal. Biochem.* **2010**, *399*, 237–245. [CrossRef]
158. Glymenaki, E.; Kandyli, M.; Apostolidou, C.P.; Kokotidou, C.; Charalambidis, G.; Nikoloudakis, E.; Panagiotakis, S.; Koutserinaki, E.; Klontza, V.; Michail, P.; et al. Design and synthesis of porphyrin-nitrilotriacetic acid dyads with potential applications in peptide labeling through metallochelate coupling. *ACS Omega* **2022**, *7*, 1803–1818. [CrossRef]
159. Lata, S.; Gavutis, M.; Tampe, R.; Piehler, J. Specific and stable fluorescence labeling of histidine-tagged proteins for dissecting multi-protein complex formation. *J. Am. Chem. Soc.* **2006**, *128*, 2365–2372. [CrossRef]
160. Gatterdam, K.; Joest, E.F.; Gatterdam, V.; Tampé, R. The scaffold design of trivalent chelator heads dictates affinity and stability for labeling His-tagged proteins in vitro and in cells. *Angew. Chem. Int. Ed.* **2018**, *57*, 12395–12399. [CrossRef]
161. Uchinomiya, S.H.; Nonaka, H.; Fujishima, S.H.; Tsukiji, S.; Ojida, A.; Hamachi, I. Site-specific covalent labeling of His-tag fused proteins with a reactive Ni(II)-NTA probe. *Chem. Commun.* **2009**, *59*, 5880–5882. [CrossRef]
162. Hatai, J.; Prasad, P.K.; Lahav-Mankovski, N.; Oppenheimer-Low, N.; Unger, T.; Sirkis, Y.F.; Dadosh, T.; Motiei, L.; Margulies, D. Assessing changes in the expression levels of cell surface proteins with a turn-on fluorescent molecular probe. *Chem. Commun.* **2021**, *57*, 1875–1878. [CrossRef]
163. Selvakumar, K.; Motiei, L.; Margulies, D. Enzyme-artificial enzyme interactions as a means for discriminating among structurally similar isozymes. *J. Am. Chem. Soc.* **2015**, *137*, 4892–4895. [CrossRef]
164. Nissinkorn, Y.; Lahav-Mankovski, N.; Rabinkov, A.; Albeck, S.; Motiei, L.; Margulies, D. Sensing protein surfaces with targeted fluorescent receptors. *Chem. Eur. J.* **2015**, *21*, 15981–15987. [CrossRef]
165. Peri-Naor, R.; Pode, Z.; Lahav-Mankovski, N.; Rabinkov, A.; Motiei, L.; Margulies, D. Glycoform differentiation by a targeted, self-assembled, pattern-generating protein surface sensor. *J. Am. Chem. Soc.* **2020**, *142*, 15790–15798. [CrossRef]
166. Wieneke, R.; Laboria, N.; Rajan, M.; Kollmannsperger, A.; Natale, F.; Cardoso, M.C.; Tampe, R. Live-cell targeting of his-tagged proteins by multivalent N-nitrilotriacetic acid carrier complexes. *J. Am. Chem. Soc.* **2014**, *136*, 13975–13978. [CrossRef]
167. Zhang, L.S.; Yin, Y.L.; Wang, L.; Xia, Y.; Ryu, S.; Xi, Z.; Li, L.Y.; Zhang, Z.S. Self-assembling nitrilotriacetic acid nanofibers for tracking and enriching His-tagged proteins in living cells. *J. Mater. Chem. B* **2021**, *9*, 80–84. [CrossRef]
168. Glembockyte, V.; Lincoln, R.; Cosa, G. Cy3 photoprotection mediated by Ni^{2+} for extended single-molecule imaging: Old tricks for new techniques. *J. Am. Chem. Soc.* **2015**, *137*, 1116–1122. [CrossRef]
169. Glembockyte, V.; Lin, J.; Cosa, G. Improving the photostability of red- and green-emissive single-molecule fluorophores via Ni^{2+} mediated excited triplet-state quenching. *J. Phys. Chem. B* **2016**, *120*, 11923–11929. [CrossRef]
170. Glembockyte, V.; Wieneke, R.; Gatterdam, K.; Gidi, Y.; Tampé, R.; Cosa, G. Tris -N-nitrilotriacetic acid fluorophore as a self-healing dye for single-molecule fluorescence imaging. *J. Am. Chem. Soc.* **2018**, *140*, 11006–11012. [CrossRef]
171. Brege, J.J.; Gallaway, C.; Barron, A.R. Fluorescence quenching of single-walled carbon nanotubes with transition-metal ions. *J. Phys. Chem. C* **2009**, *113*, 4270–4276. [CrossRef]
172. Hendler-Neumark, A.; Bisker, G. Fluorescent single-walled carbon nanotubes for protein detection. *Sensors* **2019**, *19*, 5403. [CrossRef]
173. Ahn, J.H.; Kim, J.H.; Reuel, N.F.; Barone, P.W.; Boghossian, A.A.; Zhang, J.; Yoon, H.; Chang, A.C.; Hilmer, A.J.; Strano, M.S. Label-free, single protein detection on a near-infrared fluorescent single-walled carbon nanotube/protein microarray fabricated by cell-free synthesis. *Nano Lett.* **2011**, *11*, 2743–2752. [CrossRef]
174. Reuel, N.F.; Ahn, J.H.; Kim, J.H.; Zhang, J.Q.; Boghossian, A.A.; Mahal, L.K.; Strano, M.S. Transduction of glycan-lectin binding using near-infrared fluorescent single-walled carbon nanotubes for glycan profiling. *J. Am. Chem. Soc.* **2011**, *133*, 17923–17933. [CrossRef]
175. Jana, B.; Mondal, G.; Biswas, A.; Chakraborty, I.; Saha, A.; Kurkute, P.; Ghosh, S. Dual functionalized graphene oxide serves as a carrier for delivering oligohistidine- and biotin-tagged biomolecules into cells. *Macromol. Biosci.* **2013**, *13*, 1478–1484. [CrossRef]

176. Morales, D.P.; Morgan, E.N.; McAdams, M.; Chron, A.B.; Shin, J.E.; Zasadzinski, J.A.; Reich, N.O. Light-triggered genome editing: Cre recombinase mediated gene editing with near-infrared light. *Small* **2018**, *14*, e1800543–e1800550. [CrossRef]
177. Lan, W.S.; Chen, G.P.; Cui, F.; Tan, F.; Liu, R.; Yushupujiang, M. Development of a novel optical biosensor for detection of organophosphorus pesticides based on methyl parathion hydrolase immobilized by metal-chelate affinity. *Sensors* **2012**, *12*, 8477–8490. [CrossRef]
178. Chen, Y.Y.; Lian, H.T.; Liu, B.; Liu, G.M.; Wei, X.F. Ni-NTA resin-based multiplexed origami device for highly efficient sensing of allergen-specific IgE. *Sens. Actuat. B Chem.* **2023**, *385*, 133674–133684. [CrossRef]
179. Breger, J.C.; Oh, E.; Susumu, K.; Klein, W.P.; Walper, S.A.; Ancona, M.G.; Medintz, I.L. Nanoparticle size influences localized enzymatic enhancement-a case study with phosphotriesterase. *Bioconjug. Chem.* **2019**, *30*, 2060–2074. [CrossRef]
180. Hondred, J.A.; Breger, J.C.; Garland, N.T.; Oh, E.; Susumu, K.; Walper, S.A.; Medintz, I.L.; Claussen, J.C. Enhanced enzymatic activity from phosphotriesterase trimer gold nanoparticle bioconjugates for pesticide detection. *Analyst* **2017**, *142*, 3261–3271. [CrossRef]
181. Moss, M.L.; Koller, G.; Bartsch, J.W.; Rakow, S.; Schlomann, U.; Rasmussen, F.H. A colorimetric-based amplification system for proteinases including MMP2 and ADAM8. *Anal. Biochem.* **2015**, *484*, 75–81. [CrossRef] [PubMed]
182. Gao, T.; Mu, C.L.; Shi, H.; Shi, L.; Mao, X.X.; Li, G.X. Embedding capture-magneto-catalytic activity into a nanocatalyst for the determination of lipid kinase. *ACS Appl. Mater. Interfaces* **2018**, *10*, 59–65. [CrossRef] [PubMed]
183. Lee, J.O.; Kim, E.J.; Lim, B.; Kim, T.W.; Kim, Y.P. Rapid detection of protein phosphatase activity using Zn(II)-coordinated gold nanosensors based on His-tagged phosphopeptides. *Anal. Chem.* **2015**, *87*, 1257–1265. [CrossRef] [PubMed]
184. Kim, G.B.; Kim, K.H.; Park, Y.H.; Ko, S.; Kim, Y.P. Colorimetric assay of matrix metalloproteinase activity based on metal-induced self-assembly of carboxy gold nanoparticles. *Biosens. Bioelectron.* **2013**, *41*, 833–839. [CrossRef]
185. Lee, S.K.; Maye, M.M.; Zhang, Y.B.; Gang, O.; van der Lelie, D. Controllable g5p-protein-directed aggregation of ssDNA-gold nanoparticles. *Langmuir* **2009**, *25*, 657–660. [CrossRef] [PubMed]
186. Alsadig, A.; Vondracek, H.; Pengo, P.; Pasquato, L.; Posocco, P.; Parisse, P.; Casalis, L. Label-free, rapid and facile gold-nanoparticles-based assay as a potential spectroscopic tool for trastuzumab quantification. *Nanomaterials* **2021**, *11*, 3181. [CrossRef]
187. Swartz, J.D.; Gulka, C.P.; Haselton, F.R.; Wright, D.W. Development of a histidine-targeted spectrophotometric sensor using Ni(II)NTA-functionalized Au and Ag nanoparticles. *Langmuir* **2011**, *27*, 15330–15339. [CrossRef] [PubMed]
188. Cheng, W.; Chen, Y.L.; Yan, F.; Ding, L.; Ding, S.J.; Ju, H.X.; Yin, Y.B. Ultrasensitive scanometric strategy for detection of matrix metalloproteinases using a histidine tagged peptide-Au nanoparticle probe. *Chem. Commun.* **2011**, *47*, 2877–2879. [CrossRef]
189. Kaya, M.; Volkan, M. New approach for the surface enhanced resonance Raman scattering (SERRS) detection of dopamine at picomolar (pM) levels in the presence of ascorbic acid. *Anal. Chem.* **2012**, *84*, 7729–7735. [CrossRef]
190. Cao, X.M.; Qin, M.; Li, P.; Zhou, B.B.; Tang, X.H.; Ge, M.H.; Yang, L.B.; Liu, J.H. Probing catecholamine neurotransmitters based on iron-coordination surface-enhanced resonance Raman spectroscopy label. *Sens. Actuat. B Chem.* **2018**, *268*, 350–358. [CrossRef]
191. Li, P.; Zhou, B.; Ge, M.; Jing, X.; Yang, L. Metal coordination induced SERS nanoprobe for sensitive and selective detection of histamine in serum. *Talanta* **2022**, *237*, 122913–122920. [CrossRef] [PubMed]
192. Han, X.S.; Cao, M.D.; Zhou, B.C.; Yu, C.M.; Liu, Y.X.; Peng, B.; Meng, L.; Wei, J.F.; Li, L.; Huang, W. Specifically immobilizing His-tagged allergens to magnetic nanoparticles for fast and quantitative detection of allergen-specific IgE in serum samples. *Talanta* **2020**, *219*, 121301–121308. [CrossRef] [PubMed]
193. Filchakova, O.; Dossym, D.; Ilyas, A.; Kuanysheva, T.; Abdizhamil, A.; Bukasov, R. Review of COVID-19 testing and diagnostic methods. *Talanta* **2022**, *244*, 123409–123440. [CrossRef] [PubMed]
194. Davis, K.M.; Swartz, J.D.; Haselton, F.R.; Wright, D.W. Low-resource method for extracting the malarial biomarker histidine-rich protein ii to enhance diagnostic test performance. *Anal. Chem.* **2012**, *84*, 6136–6142. [CrossRef]
195. Bauer, W.S.; Gulka, C.P.; Silva-Baucage, L.; Adams, N.M.; Haselton, F.R.; Wright, D.W. Metal affinity-enabled capture and release antibody reagents generate a multiplex biomarker enrichment system that improves detection limits of rapid diagnostic tests. *Anal. Chem.* **2017**, *89*, 10216–10223. [CrossRef]
196. Yang, M.W.; Chen, D.J.; Hu, J.; Zheng, X.Y.; Lin, Z.J.; Zhu, H.M. The application of coffee-ring effect in analytical chemistry. *TrAC-Trend. Anal. Chem.* **2022**, *157*, 116752–116771. [CrossRef]
197. Trantum, J.R.; Wright, D.W.; Haselton, F.R. Biomarker-mediated disruption of coffee-ring formation as a low resource diagnostic indicator. *Langmuir* **2012**, *28*, 2187–2193. [CrossRef]
198. Gulka, C.P.; Swartz, J.D.; Trantum, J.R.; Davis, K.M.; Peak, C.M.; Denton, A.J.; Haselton, F.R.; Wright, D.W. Coffee rings as low-resource diagnostics: Detection of the malaria biomarker plasmodium falciparum histidine-rich protein-ii using a surface-coupled ring of Ni(II)NTA gold-plated polystyrene particles. *ACS Appl. Mater. Interfaces* **2014**, *6*, 6257–6263. [CrossRef]

biosensors

MDPI

Review

Recent Progress in Functional-Nucleic-Acid-Based Fluorescent Fiber-Optic Evanescent Wave Biosensors

Zheng Wang and Xinhui Lou *

Department of Chemistry, Capital Normal University, Xisanhuan North Road. 105, Beijing 100048, China
* Correspondence: xinhuilou@cnu.edu.cn; Tel.: +86-10-68902491 (ext. 808)

Abstract: Biosensors capable of onsite and continuous detection of environmental and food pollutants and biomarkers are highly desired, but only a few sensing platforms meet the "2-SAR" requirements (sensitivity, specificity, affordability, automation, rapidity, and reusability). A fiber optic evanescent wave (FOEW) sensor is an attractive type of portable device that has the advantages of high sensitivity, low cost, good reusability, and long-term stability. By utilizing functional nucleic acids (FNAs) such as aptamers, DNAzymes, and rational designed nucleic acid probes as specific recognition ligands, the FOEW sensor has been demonstrated to be a general sensing platform for the onsite and continuous detection of various targets ranging from small molecules and heavy metal ions to proteins, nucleic acids, and pathogens. In this review, we cover the progress of the fluorescent FNA-based FOEW biosensor since its first report in 1995. We focus on the chemical modification of the optical fiber and the sensing mechanisms for the five above-mentioned types of targets. The challenges and prospects on the isolation of high-quality aptamers, reagent-free detection, long-term stability under application conditions, and high throughput are also included in this review to highlight the future trends for the development of FOEW biosensors capable of onsite and continuous detection.

Keywords: functional nucleic acid; evanescent wave biosensors; optical fiber; aptamers; DNAzymes

Citation: Wang, Z.; Lou, X. Recent Progress in Functional-Nucleic-Acid-Based Fluorescent Fiber-Optic Evanescent Wave Biosensors. *Biosensors* **2023**, *13*, 425. https://doi.org/10.3390/bios13040425

Received: 16 February 2023
Revised: 20 March 2023
Accepted: 25 March 2023
Published: 27 March 2023

1. Introduction

Onsite continuous detection techniques are highly desired for real-time monitoring of pollutants in environmental waters [1] and food production processes [2,3]. They also are of central importance for the development of wearable medical devices to routinely measure biomarkers [4,5]. These technical advances are dramatically changing traditional lab-based strategies into more and more convenient, automatic, and labor-free means. To realize onsite continuous detection for daily use, a technology should be sensitive, specific, affordable, automated, rapid, and reusable, criteria referred to as "2-SAR". Numerous biosensors have been reported in recent years with the overall purpose to achieve high sensitivity or rapidity. Quite often, expensive and complicated signal amplification strategies, most commonly enzymatic reactions, are used to enhance the detection sensitivity. In addition, tedious sample processing steps prior to detection are required to avoid matrix interference. These offline processes greatly lengthen the assay time and complicate the operation, preventing their application for continuous detection, where the timely monitoring of the concentration of the target is required. Ideally, the detection should be reagent-free, where no reagents need to be added for signal amplification or sensor regeneration.

Of the existing sensing platforms, only a few meet the "2-SAR" criteria and are commercially available [6]. The most outstanding example is the wearable electrochemical sensor for the real-time detection of blood sugar levels [7,8]. The continuous detection is based on the electrochemical signals generated by the in situ oxidation reactions of glucose catalyzed by the enzymatic electrode. The technique is elegant, but only suitable for targets that can undergo specific redox reactions. Most pollutants or biomarkers do not have redox activity under mild conditions and the specific enzymes are also not available. Moreover,

the sensitivity of this technique is in the low millimole per liter (mM) concentration range, which does not meet the sensitivity requirements for most pollutants and biomarkers (typically in the picomole to nanomole per liter concentration range). Electrochemical devices are also commercially available for the onsite detection of heavy metal ions [9]. They are based on the redox reaction of metal ions, rendering high sensitivity and specificity. The limitation is the interference from the sample matrix resulting from the nonspecific absorption of various components on the electrode, which interferes with the current. Therefore, offline sample pretreatment is commonly required to ensure the reusability of the electrodes, leading to the long assay time and the high cost. Fluorescent evanescent wave sensors are another type of portable optical sensors that are suitable for continuous detection [6,10–13]. They are based on the evanescent wave generated on the surface of waveguide materials (chip or fiber) upon laser incidence from the light-dense medium to the light-sparse medium. Planar waveguide sensors are capable of the simultaneous detection of multiplex targets but require a much more sophisticated and expensive optical system than fiber optical evanescent wave (FOEW) sensors [14]. Fluorescent FOEW sensors are, therefore, more suitable for continuous detection merely from an affordability point of view. In fact, fluorescent FOEW sensors have attracted more attention than planar waveguide sensors in recent years. Over the past half-century, tremendous advances have been made in FOEW sensors, from the optical system, fluid system, to the modification chemistry of optical fiber and sensing mechanisms [6,10–13].

Functional nucleic acids (FNAs) include aptamers, DNAzymes, and rationally designed nucleic acids, which all have the ability to specifically recognize targets and are widely used in various types of biosensors [15]. Due to rapid advances in FNAs in the last thirty years, the application scope of FOEW sensors has been rapidly expanding from common water quality parameters including pH, temperature, oxygen, ions, refractive index, and (dissolved) gases and vapors to almost any type of target. FNA-FOEW sensors have been reported for the detection of all types of targets including metal ions, small molecules, proteins, nucleic acids, bacteria, and viruses with the promise of more affordable, durable, and flexible detection compared to antibody-based FOEW sensors. The sensitivity and dynamic range of all FNA-based sensors are strongly affected by the probe density on the sensor surface [16]. FNA-based electrochemical sensors are typically orders of magnitude more sensitive than FOEW, but they are difficult to regenerate. In contrast, FNA-FOEW sensors can be regenerated, enabling repeated measurements using the same sensor and, therefore, a higher accuracy.

After over 40 years of innovation, fluorescent FOEW biosensors are proceeding quickly and have found respective applications in highly diversified fields. Several excellent reviews on them have been published with different focuses on instrument configurations and patents [6], enzyme- or antibody-based biosensors [10,14], or a specific type of target such as viruses [17]. Recently, Loyez et al. published an excellent review on aptamer-based optical fiber sensors using all types of sensing strategies including surface plasmon resonance (SPR), localized SPR (LSPR), lossy mode resonance, fluorescence, and others [18]. The review covers a broad scope with less specific information for certain types of sensing strategy. There is no review with a focus on the functional-nucleic-acid-based fluorescent FOEW (FNA-FOEW) for diverse types of targets. In view of the significant difference of FNAs from antibodies, a comprehensive review of FNA-FOEW sensors would be a valuable complement to the reviews of fiber-optic sensing technology. The novelty of our review is to summarize the recent progress, challenges, and perspectives of FNA-FOEW sensors with a special focus on the probe immobilization chemistry and diverse sensing mechanisms for different types of targets. Please note that this review does not include SPR- or silicon-photonic-based FOEW biosensors. In those biosensors, the detection of targets is achieved by measuring the refractive index changes, instead of fluorescence intensity changes [19–21].

The major content of this review is summarized in Figure 1. Since the sensor optical and fluidic system is general for the optical fibers with different coating materials, the

above-mentioned reviews and many other books and articles are excellent resources for detailed information. This review focuses on the surface chemistry of the optical fiber and the sensing mechanisms, and the optical physics are briefly introduced. We started with an introduction of the recent advances in FNAs, which are responsible for specific target recognition in FNA-FOEW sensors. We then conducted a brief introduction of the major components of FOEW sensors and optical mechanisms for real-time fluorescence detection. The major methods for fiber modification and the representative sensing mechanisms for different types of targets are systemically reviewed according to the surface chemistry of the fiber. The challenges and prospects of fluorescent FNA-FOEW sensors are provided at the end of this review.

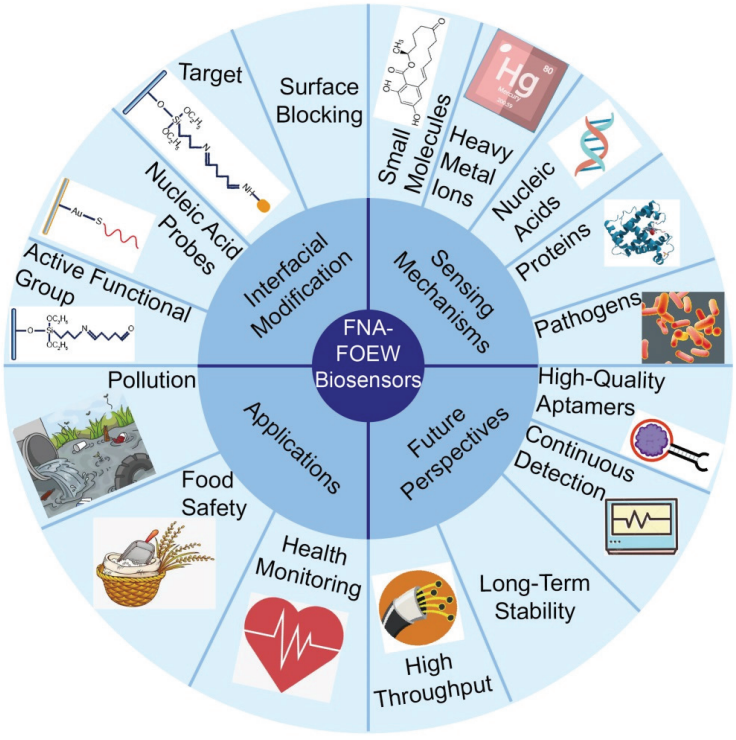

Figure 1. Scheme diagram of the content of this review.

2. Functional Nucleic Acids (FNAs)

Nucleic acids were initially defined as a hereditary substance that carries genetic information. Later, research clearly evidenced that some nucleic acids, called FNAs, also play many other important biological functions in vivo or in vitro [15,22–25]. FNAs with catalytic activity or specific molecular recognition capability have attracted tremendous attention in many fields. They are divided into two categories: natural and artificial FNAs. Natural FNAs are found in vivo and include ribozymes and riboswitches. Artificial FNAs are obtained by in vitro screening or engineering, and include rationally designed nucleic acid probes, aptamers, DNAzymes, and aptazymes (Figure 2). Artificial FNAs are attractive synthetic probes because of their low cost, ease of synthesis and modification, high stability, and biocompatibility. They have been extensively used for sensing detection [26,27], drug delivery [28] and disease therapy [22], molecular imaging [29], and self-assembly of nanomaterials [30,31]. Among these applications, their applications in fluorescent, colorimetric, and electrochemical sensors are dominant and have shown the greatest potentials for practical uses.

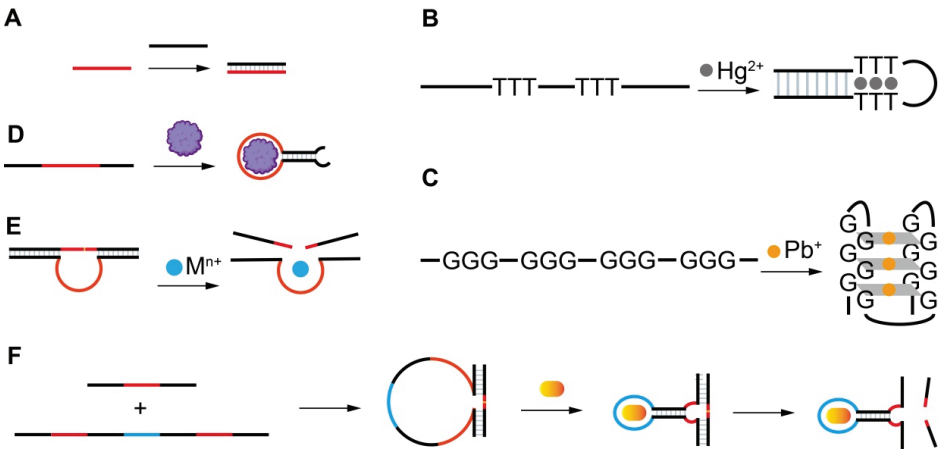

Figure 2. The artificial FNAs most popularly used in biosensors including FNA-FOEW sensors. (**A**) Complementary DNA probe (cDNA); (**B**) rationally designed thymine (T)-rich probe for highly specific Hg^{2+} detection; (**C**) rationally designed guanine (G)-rich probe for highly specific Pb^{2+} detection; (**D**) aptamers; (**E**) DNAzymes specific to various metal ions; (**F**) aptazymes for nonmetal ion targets.

The different types of FNAs enable the specific recognition of different types of targets. The first groups of FNAs are short complementary DNA probes (cDNAs) (Figure 2A), typically 10–25 mer in length, which are rationally designed to be completely or partially complementary to the target DNA or RNA sequences. The hybridization reactions between cDNAs and target sequences cause the formation of duplex structures in a solution or on the sensor surface, allowing the specific detection of target sequences by various signal transformation means. The hybridization reaction has also been extended for the indirect detection of other types of targets beyond nucleic acids by incorporating the following FNAs. Another type of rationally designed FNA sequence is metal-ion-specific DNA probes. The most applied ones are thymine (T)-rich probes highly specific to Hg^{2+} [32–34] (Figure 2B) and guanine (G)-rich probes highly specific to Pb^{2+} [35–38] (Figure 2C). The two types of probes respectively undergo a large conformation change from random coil to duplex or G-quadruplex structures upon binding to Hg^{2+} or Pb^{2+}. Rationally designed probes have also been reported for other metal ions, such as Ag^{+} [39] and K^{+} [40,41], but are much less applied because they are not the most common pollutants of concern in the environment or food.

Both aptamers and DNAzymes are in vitro isolated nucleic acids from a nucleic acid library by SELEX (Systematic Evolution of Ligands by Exponential Enrichment) technology [27,42,43]. Aptamers are specific binding ligands without catalytic activity (Figure 2D). Since the invention of SELEX, more than one thousand aptamers have been isolated, targeting all types of targets from metal ions, small molecules, and proteins to complex targets such as bacteria and viruses [44–47]. The specific binding event can be signally transformed in diverse sensing platforms. DNAzymes are FNAs with diverse enzymatic activities. DNAzymes with cleavage activity catalyzed by a wide spectrum of metal ions as cofactors have been reported in recent years [27,48] (Figure 2E). Among them, the most popularly used are those specific to Pb^{2+}. The DNAzyme forms two duplex segments with its substrate, leaving the central loop region as the metal ion recognition pocket. In the presence of the right metal ion, the cleavage activity is activated due to the binding between the metal ion and the loop, and the phosphodiester bond next to the RNA nucleotide in the substrate sequence is cleaved. The catalytic cleavage of the substrate sequence lays the basis for various sensing mechanisms. Due to their catalytic property, one metal ion can

trigger multiple cycles of cleavage, leading to high sensitivity and negating the use of protein enzymes for signal amplification.

Aptazymes are a type of FNA with both catalytic activity and specific binding capability, in which the binding pocket in DNAzymes for metal ions is designed through engineering to include aptamer sequences [49] (Figure 2F). Even though the design is elegant, tedious optimization is required and their extended applications are limited. So far, no aptazymes have been used in FOEW sensors.

In FOEW sensors, the above-described FNAs are either functionalized on the fiber surface or added into the test sample. The fluorescent group is typically modified on the FNAs or their complementary sequences for signal transduction of the specific molecular recognition event that occur on the fiber surface. The representative designs are illustrated in the following sections.

3. The Major Components of Fluorescent FOEW Sensors and Optical Mechanisms for Real-Time Fluorescence Detection

A typical fluorescent FOEW sensor consists of an optical system (laser, optical fiber coupler, filter, photodiode, and signal amplifier), a mechanic fluidic system (peristaltic pump, tubes, reaction chamber), and a data analysis system (software and computer) (Figure 3A) [6]. The optical fiber is installed inside the reaction chamber. The inlet and outlet tubes are connected to the chamber for automatic sample injection and waste elution with controlled flow rate and time [50]. For the purpose of portability, the FOEW sensors have been miniaturized and several portable FOEW sensors have been commercialized for in situ applications [10]. Continuous onsite measurements are realized by the regeneration of the sensor surface by simply rinsing with sodium dodecyl sulfate solution (0.5% SDS, pH 1.9) after each measurement [51]. Very recently, the miniaturized all-fiber-optical system and microfluidic system have been integrated with smartphones for onsite real-time quantitative detection of bisphenol A and norfloxacin in 15 min with high sensitivity and reusability, and automated interpretation of reporting results [52].

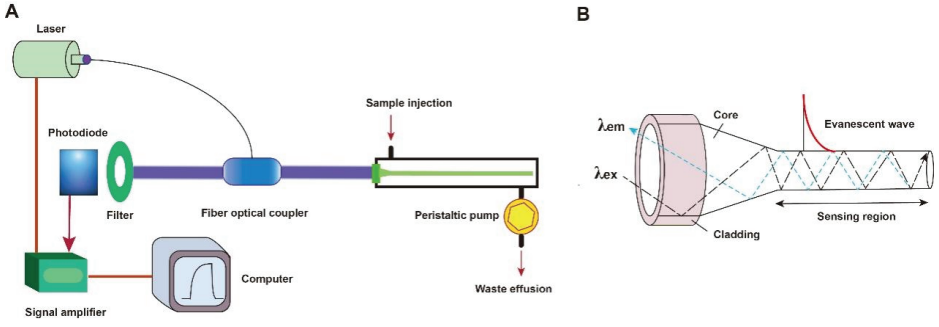

Figure 3. (**A**) The components of a typical fluorescent FOEW sensor; (**B**) the structure of the tapered fiber and the evanescent wave generated vertical to the fiber surface.

The optical fiber is the core element of an FOEW sensor for real-time fluorescence sensing. It usually consists of the inside core and the outside cladding. The refractive index (RI) of the fiber core is higher than that of the fiber cladding. Light travels through the fiber via total internal reflection. The material of the core is usually transparent glass (SiO_2) or plastic with excellent laser transport capability and ease of surface modification. With the purpose of improving sensitivity, optical fibers with diverse shapes have been reported. They can be roughly divided into two categories, fiber gratings (FGs) and structured optical fibers (SOFs) [11]. FGs are optical fibers that have periodic gratings, which change the refractive index (RI) of the core. Common SOFs include D-shaped, U-shaped, tapered, and biconical fibers (Figure 4). The SOFs, especially the tapered fiber, are much easier to fabricate than FGs. Optical fibers for the preparation of tapered fibers are commercially

available at quite a low price (approximately USD 1–2 per probe). For this reason, tapered fibers are the most widely used fibers in FOEW sensors.

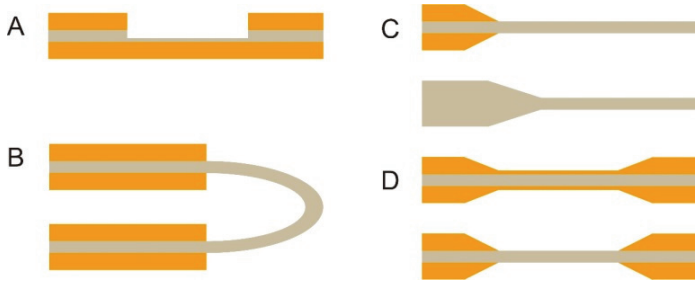

Figure 4. The most common optical fiber structures. (**A**) D-shaped fibers; (**B**) U-shaped fibers; (**C**) tapered fibers; (**D**) biconical fibers. The gray part is the core, and the orange part is the cladding. The section without the cladding is the sensing region, where the surface modification is typically performed prior to the sensing.

Taking the tapered fiber as an example, the generation of the optical phenomenon inside and on the surface of the fiber was illustrated (Figure 3B). For other shapes of optical fibers, an excellent review has introduced them in detail [11]. When the laser incidence from the light-dense medium (such as SiO_2) to the light-sparse medium (such as an aqueous sample) and the angle of incidence is greater than the critical angle, the refracted light disappears, and total reflection occurs. The total reflection of the incident laser inside the fiber leads to the formation of the evanescent wave field propagated vertical to the surface of the fiber. The distance is called the depth of penetration (d_p) when the intensity of the evanescent wave decays to 1/e of the original light wave intensity [53]. The d_p is a function of several parameters as shown in the following equation and is typically in the 100–200 nm range.

$$d_p = \frac{\lambda}{2\pi\left(n_1^2 \sin^2\theta - n_2^2\right)^{1/2}}$$

where λ represents the wavelength of the incident light; n_1 represents the refractive index of the fiber core medium; n_2 represents the refractive index of the surrounding solution medium; and θ is the angle of incidence of the fiber at the interface. A large d_p is the key to achieve high sensitivity for FOEW sensors. The tapering, launch angle, and taper length of the fiber strongly affect the sensitivity and can be easily optimized.

The evanescent wave excites the fluorescence emission of fluorophores inside the evanescent wave field. The intensity of the emission fluorescence is then real-time measured by the photodiode detector after the filter. It is worth pointing out that FOEW sensors tend to show a higher signal-to-noise (or lower background interference) ratio compared to the fluorescence measurements conducted in solution because only the fluorophores within the evanescent wave field can be effectively excited [6].

In order to realize the simultaneous detection of multiple targets, Long et al. designed and manufactured a compact dual-color FOEW sensor installed with two lasers for the simultaneous excitation of two fluorophores at distinct wavelengths. The simultaneous detections of aflatoxin M1 (AFM1) and ochratoxin A (OTA) [54], *Escherichia coli* (*E. coli*) O157:H7 and *Salmonella typhimurium* [55], or acetamiprid and fipronil [56] were respectively achieved. The group further simplified the optical structure, where a single-multi mode fiber optic coupler was employed to replace the sophisticated confocal optical system for the transmission of two excitation lights and dual-color fluorescence [57,58]. A photodiode detector was used instead of a photomultiplier for the simultaneous detection of dual-color fluorescence.

Besides the solid fibers described above, a hollow-core fiber has also been used in fluorescent FNA-FOEW sensors [59]. Wang et al. recently demonstrated that hollow-core

microstructured antiresonant fibers (HARFs) can stringently confine light in the fiber core, ensuring a high signal and sensitivity. The hollow-hole fiber or capillary serving as a waveguide was first invented in 2000 by Liger et al., and has been commercialized. Those seeking more information on the progress of the systems using the hollow-hole fiber can refer to the excellent review [10].

4. Optical Fiber Interfacial Modification Methods

Optical fibers can be chemically modified at the interface before use or left unmodified, depending on the different sensing mechanisms. Unmodified optical fibers have been used for the detection of diverse types of targets including bacteria and metal ions [60]. Taking advantage of the large size of bacteria (at least submicron in diameter) and the short evanescent wave depth (typically less than 100 nm), an unmodified bare SiO_2 fiber has been used for the detection of *E. coli* O157:H7. A bare fiber etched with a nanoporous layer was used and better sensitivity was achieved, which not only separates *E. coli* O157:H7 from the aptamer, but also enhances the performance of the evanescent wave [55,61]. The benefits for using the unmodified fiber include no need for surface modification, easy surface regeneration, and low cost. However, the sensitivity is commonly much lower than those using modified fibers. To overcome the sensitivity limitation, offline signal amplifications are required to improve the detection sensitivity.

The well-controlled surface modification of fiber optics is critical for sensor performance including sensitivity, specificity, dynamic range, binding kinetics, long-term stability, reproducibility, and surface regeneration. Many different chemical reactions have been used for surface modification. Among them, the silanization and the mild crosslinking reactions compatible with aqueous solutions are the most popularly used. In the following, we summarized the most popularly used methods for the interfacial modification of SiO_2 fibers according to different purposes including modification to introduce active functional groups, nucleic acid probes, and targets, or to block the surface.

4.1. Modification to Introduce Active Functional Groups on Fiber Surface

Through silanization reactions and the following one- or two-step crosslinking reactions, various functional groups can be facilely introduced on the SiO_2 fiber surface. The most popularly used silanization reaction is the reaction between the hydroxyl groups and 3-aminopropyltriethoxysilane (APTS), by which the fiber is functionalized with amino groups (Figure 5A) [62]. The hydroxyl groups are generated by soaking the fiber in piranha solution.

The amino-group-modified fiber surface can be further converted into other active function groups such as the carboxylic acid group (Figure 5B) and aldehyde group (Figure 5C) by soaking the fiber in different crosslinkers. The crosslinker with dual-amino groups is commonly used to lengthen the spacer (Figure 5D). Very recently, a single-stranded binding protein (SSB) was immobilized on the fiber surface using the same EDC/NHS-mediated reaction for the capture of the free aptamer [63]. The dethiobiotin groups bind to streptavidin or streptavidin-modified molecules with weaker affinity than biotin, rendering easier interruption of the binding for surface regeneration [64–66]. They can be modified on the fiber through the highly efficient coupling reaction between the amino group on the fiber and the ECD/NHS-activated carboxylic acid group on dethiobiotin (Figure 5D). Very recently, a single-stranded binding protein (SSB) was immobilized on the fiber surface using the same EDC/NHS-mediated reaction for the capture of the free aptamer [63]. By using 3-mercaptopropyl-trimethoxysilane (MTS), the sulfhydryl groups are introduced to the fiber surface [67]. One maleimide group in the bifunctional crosslinking reagent N-(4-maleimidobuty-ryloxy) succinimide (GMBS) reacts specifically with sulfhydryl groups and forms a stable thioether linkage. The other maleimide group further reacts with the amino group in streptavidin to covalently immobilize streptavidin on the fiber surface (Figure 5E). Streptavidin can be used for immobilization of any target labeled with the biotin group via the strong binding between streptavidin and biotin [63].

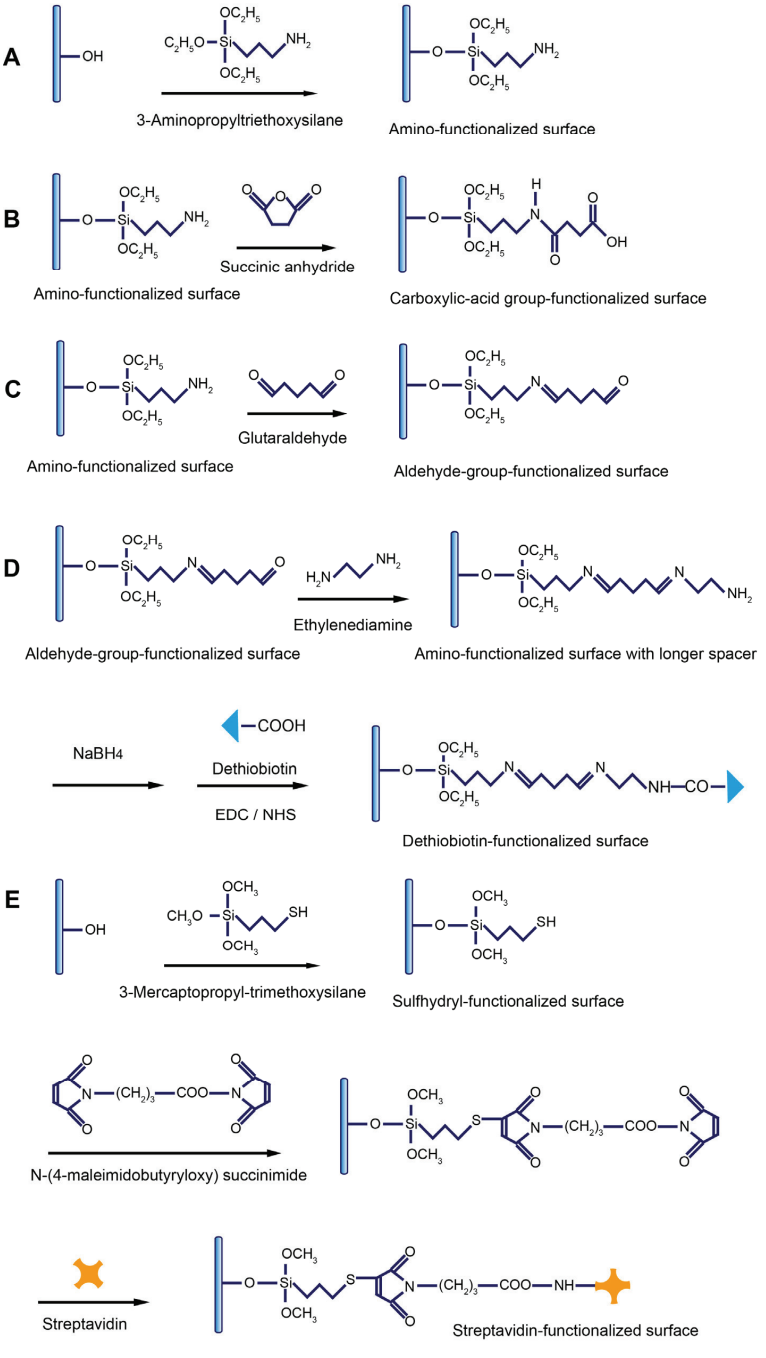

Figure 5. The representative methods to modify the fiber with active functional groups: (**A**) amino-group-functionalized surface; (**B**) carboxylic-acid-group-functionalized surface; (**C**) aldehyde-group-functionalized surface; (**D**) dethiobiotin-group-functionalized surface; and (**E**) sulfhydryl, NHS ester, or streptavidin-group-functionalized surface. EDC: 1-ethyl-3-(3-dimethylaminopropyl)carbodiimide; NHS: N-hydroxysuccinimide.

4.2. Immobilization of Nucleic Acid Probes on Fiber Surface

Three types of immobilization chemistry are used for the immobilization of nucleic acid probes on the fiber including gold-thiol (Au-S) coordinate interaction (Figure 6A), covalent coupling (Figure 6B), and noncovalent binding (Figure 6C). To be compatible with these modification strategies, the nucleic acid probes are respectively modified with the thiol, amino, or biotin group at either end of the terminals.

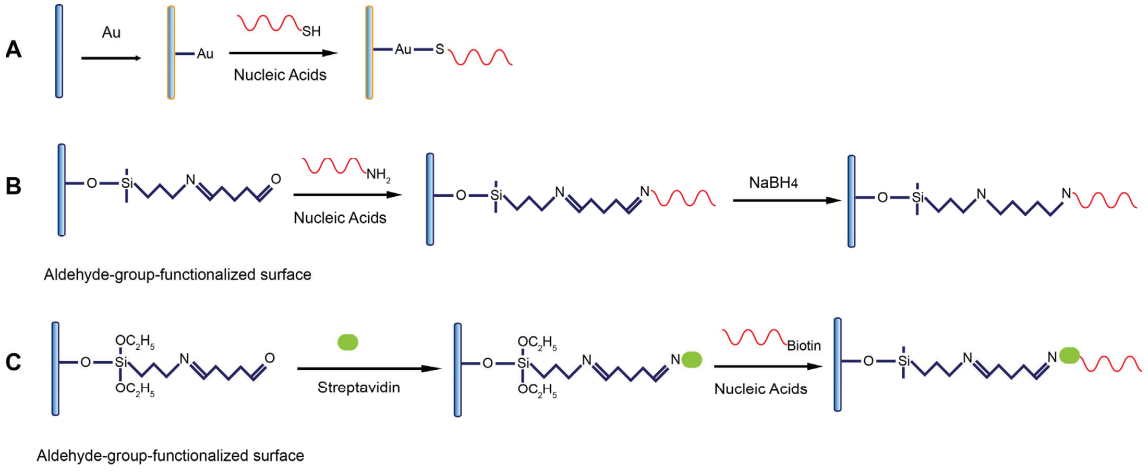

Figure 6. The representative methods to functionalize the fiber with nucleic acids modified with (**A**) thiol; (**B**) amino; and (**C**) biotin groups.

The coating of a thin layer of gold film is typically used to enhance the evanescent wave and, therefore, the sensing sensitivity in various types of waveguide sensors including FOEW sensors, but is not often used in fluorescent FOEW sensors. Gold nanoparticles are a universal fluorescence quencher and widely used in biosensors. They have been recently used in FNA-FOEW sensors for the detection of exosomes in blood samples from breast cancer patients [56]. The gold film is compatible with several commonly used surface characterization techniques such as SPR [65], quartz crystal microbalance (QCM) [66], and electrochemical sensors [67]. Thus, multiple characterization techniques can be simultaneously used to investigate the complicated surface effects on sensor performance. The thiolated nucleic acids are the most popularly used for the immobilization on the gold surface due to the well-controlled formation of the self-assembled monolayer. However, the Au-S bond is prone to be auto-oxidized in air, resulting in quite a limited surface stability (typically within one to two weeks) [68,69]. Therefore, the Au-S-based nucleic acid immobilization method is more suitable for theoretical study, but not robust enough for practical uses.

The immobilization of nucleic acid probes via the covalent bond can overcome the stability limitation of the Au-S-based immobilization strategy. Our experiments showed that fibers functionalized with DNA probes retain stable hybridization signals over several months when they are stored at 4 °C in a humid environment. The high stability has also been demonstrated by other research groups [68–70]. The drawback of this covalent immobilization method is its multiple-step process and the difficulty to quantitatively monitor each modification step on the surface. The most popularly used route consists of several steps: (1) oxidation to form hydroxyl groups, (2) silanization to convert the hydroxyl groups into an amino group, (3) the transformation of the amino to an aldehyde group by amine aldehyde condensation reaction, (4) covalently coupling the amino-modified nucleic acid probes, and (5) reduction of the less-stable imine bond into a C-N single bond and the unreacted aldehyde groups into hydroxyl groups by $NaBH_4$ reduction [50]. Many works use a similar approach to immobilize amino aptamers on the fiber surface with slight

differences [51,71–78]. For examples, glycine [60,79] and $NaCNBH_3$ [60,80] were used to deplete the remaining aldehyde sites after the coupling of aptamers. A similar route has also been used for the attachment of nucleic acid probes on PMMA fibers [81].

Another strategy for nucleic acid probe immobilization is via the strong noncovalent binding between biotin and streptavidin. The whole process is largely the same as the covalent route described above except for the final noncovalent binding step, where the biotin-labeled nucleic acid probes are attached to the surface via the strong noncovalent binding between streptavidin (or avidin) and biotin [82–84]. The advantage of the use of noncovalent binding to immobilize the nucleic acid probes might be its better antifouling property. However, the long-term surface stability of the sensor is not as good as the covalent one, besides the high cost of streptavidin. Therefore, this immobilization strategy is not often used for continuous detection.

4.3. Immobilization of Target Molecules

The immobilization of targets (most commonly small molecules and their protein complexes) on the fiber is most widely performed when antibodies are used as recognition elements. Thus, the targets in the testing samples and those bound on the surface competitively bind with the antibodies added in the testing samples, enabling the signal-off detection of targets. In FNA-FOEW sensors, targets, complementary probes to FNAs, and FNAs all can be immobilized on the fiber surface for different sensing mechanisms. The following two processes are most utilized to immobilize the targets according to their available function groups on the optical fiber. For a target with at least one primary amino group, such as kanamycin [50], it is covalently immobilized on the fiber through the crosslinking reaction between the aldehyde group pre-functionalized on the fiber and the amino group of the target (Figure 7A). This method is also used for the immobilization of the target–protein complex when a target itself has no amino group. For example, to construct an FOEW sensor for the detection of 17β-estradiol, a complex of 17β-estradiol and bovine serum albumin (BSA) was immobilized on the surface of an optical fiber via the reaction of an amino group of BSA with an aldehyde group on the fiber surface [85]. For a target with at least one carboxylic acid group, such as dethiobiotin (Figure 5D) and ochratoxin A [86], the carboxylic acid group is activated by EDC/sulfo-NHS or NHS in solution, followed by the highly efficient reaction between the activated carboxyl group with the amino group on the fiber.

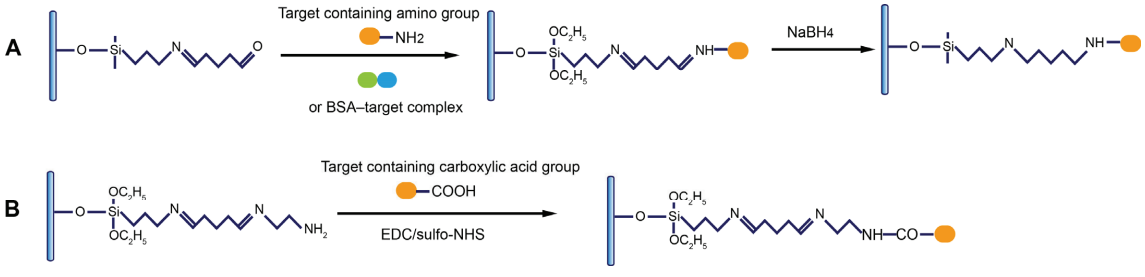

Figure 7. The representative methods to modify the fiber with targets containing (**A**) amino or (**B**) carboxylic acid groups.

4.4. Surface Blocking of Optical Fiber

After the immobilization of nucleic acid probes or targets, it is necessary to block the fiber surface to quench the remaining active groups or to minimize the nonspecific absorption of fluorescent probes and other components in the sample matrix. Quenching the unreacted active function groups is easy. For example, the remaining aldehyde groups can be depleted by the small-molecule reagents containing the amino group, such as Tris or ethanolamine. The minimization of the nonspecific absorption on the sensor surface remains one of the most challenging issues for biosensors, including FNA-FOEW sensors.

In recent years, several types of antifouling reagents have been reported, such as thiolated oligo(ethylene glycol) [87–89], mercaptohexanol [90], zwitterionic moieties [91,92], polyethylene glycol [93], and BSA [94]. The oligo(ethylene glycol) moiety, zwitterionic moieties, and BSA are well known for their capability to prevent the nonspecific absorption of proteins. Mercaptohexanol can prevent the nonspecific absorption of nucleic acids [90]. Unfortunately, the most widely reported thiolated passivation reagents are only used for the gold surface, and are not compatible with the SiO_2 fiber, where the well-controlled self-assembly of the passivation monolayer is formed by Au-S interactions. BSA has been used to block all types of surfaces ranging from microplates, nitrocellulose membranes, to electrodes and glass surfaces. So far, BSA is the most popularly used blocking agent in FNA-FOEW sensors due to its low cost and chemical compatibility [60,66,75,80,85,86].

Even though the specific mechanisms are unclear, the antifouling capability of the oligo(ethylene glycol) moiety and zwitterionic moieties has been related to the formation of an aqueous layer [87–89,91–93]. Quite differently, the mechanism of BSA for the minimization of nonspecific absorption is due to the physical coverage of the active binding sites of the surfaces. Therefore, the complete coating of the surface is essential. One important advance is the formation of the passivation layer using denatured BSA at pH near its isoelectric point (4.6), instead of the routine neutral pH. At the isoelectric point, the BSA is neutral, allowing the formation of a more uniform passivation layer on the fiber. The iep-BSA-blocked FNA-FOEW sensor showed a 10-fold-improved limit of detection (LOD, S/N = 3, 125 pM) for the detection of target DNA and the highest number of regeneration cycles (120 cycles) [95]. Even though the BSA layer minimized the nonspecific absorption of nucleic acids, its capability to resist the interference from the complex sample matrix is still not satisfactory.

5. Sensing Mechanisms

FNA-FOEW sensors have been utilized for the detection of all types of targets after Krull et al. demonstrated their capability for the detection of DNA in 1995 (Figure 8). In the following, we summarized the progress of the sensing mechanisms according to the types of targets. We drew the core sensing mechanisms in the literature in the same style to highlight the differences among different strategies. We also summarized the important progresses in the tables to facilitate the direct comparison of the performance (LOD, dynamic range, reusability, et al.) of each method for the detection of small molecules, heavy metal ions, and nucleic acids, respectively (Tables 1–3).

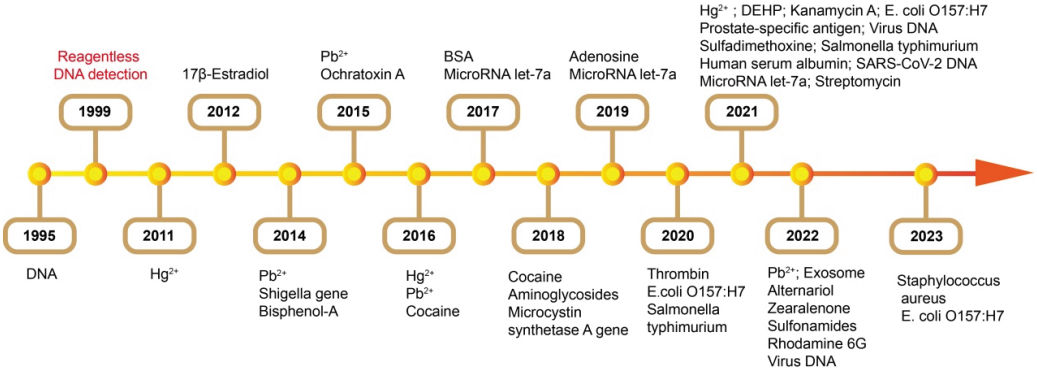

Figure 8. The major progress of FNA-FOEW sensors according to the target scope.

5.1. Separation-Free Detection of Small Molecules Using Aptamers

Small molecules are the most diverse type of environmental and food pollutants including antibiotics, toxins, hormones, etc. In recent years, the number of small-molecule-binding aptamers has been rapidly increasing, which lays the basis for the development

of aptamer-based FOEW sensors. Different from antibodies, aptamers not only bind with their targets, but also bind with the complementary sequences. In addition, some aptamers, called split aptamers, can be split into two fragments, which are assembled upon target binding [96]. Thus, aptamer-based sensing mechanisms for the detection of small-molecule targets are more diverse than the antibody-based ones (Figure 9). We classified the current reported methods into the separation-free and offline-separation-based methods. According to the different surface modifications of the fiber, we divided the first category methods into five different sensing mechanisms.

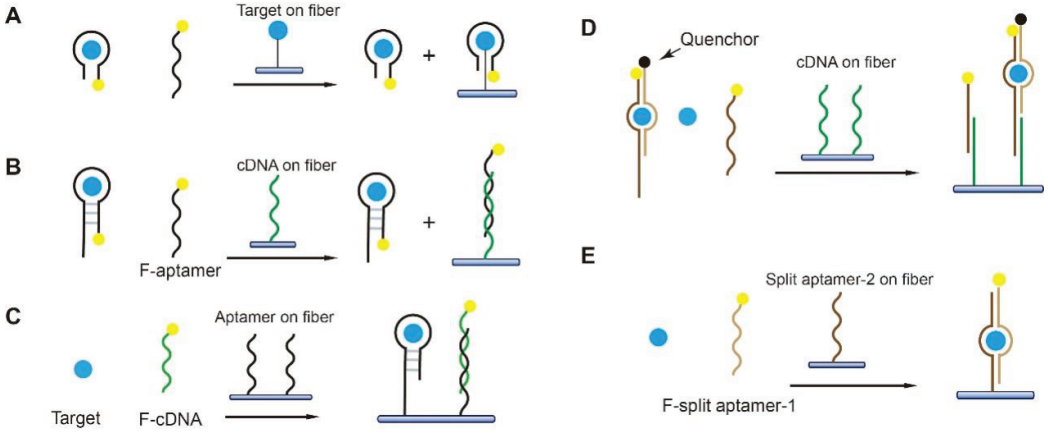

Figure 9. The separation-free detection of small-molecule targets using FNA-FOEW sensors installed with fibers functionalized by (**A**) target [85,86]; (**B**) cDNA [75]; (**C**) aptamer [71,72,77]; (**D**) cDNA complementary to one of the split aptamer fragments [73]; or (**E**) one fragment of the split aptamer [76,80].

The first aptamer-based FOEW sensor for small molecule detection was reported in 2012 for the detection of 17β-estradiol, a frequently detected endocrine-disrupting compound (EDC) in environmental waters (Figure 10) [85]. The sensing mechanism is an analogue of the most popularly used, indirect competitive binding immunoassays for small-molecule targets, in which 17β-estradiol 6-(o-carboxy-methyl)oxime-BSA is covalently immobilized on the surface (Figures 9A and 10). The 17β-estradiol molecules in the water sample and immobilized on the surface competitively bind with the fluorophore-labeled aptamer in the water sample, enabling the signal-off detection of 17β-estradiol in the water sample with an LOD of 2.1 nM. The same strategy was also used for the development of an FOEW sensor for the detection of mycotoxin ochratoxin A (OTA, LOD = 0.97 nM) in wheat samples [86]. The advantage of this type of sensing method is high accuracy because the dynamic range is typically only within two orders of magnitude. The sensors also possessed excellent reusability (>100 times) and quite a short assay time (within 10 min). The limitations included low sensitivity and the difficulty of target immobilization for the targets lack of functional groups.

To avoid the complication of target immobilization, the cDNA was immobilized on the fiber instead of the target (Figure 9B) for the detection of bisphenol A (BPA) with an LOD of 1.86 nM [75]. BPA is a known endocrine disruptor and one of the most serious environmental contaminants. The sensors retain excellent reusability (>100 times) and quite a short assay time (within 10 min). However, the LODs are typically in the low nanomole per liter (nM) concentration range for the targets when the dissociation constants (K_D) of their aptamers are 10–100 nM (Table 1). The sensitivity is not high enough for practical applications because the samples have to be diluted to minimize the matrix interference.

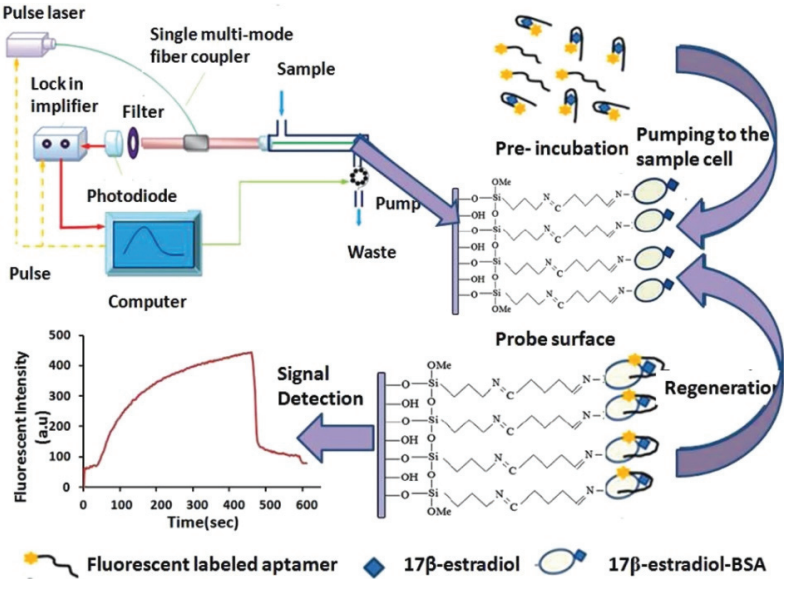

Figure 10. Aptamer-based FOEW sensor for rapid and sensitive detection of 17β-estradiol in water samples. Reprinted from Yildirim et al. (2012) [85], Copyright (2018), with permission from American Chemical Society.

Table 1. Detection of small molecules.

Target	Sensing Mechanism	LOD (nM)	Linear Range (nM)	Real Sample	Reusability (Times)	Time [a] (min)	Selectivity	Ref.
Bisphenol A	Figure 9B	1.86	2–100	Wastewater	100	10	Estriol; 17β-estradiol; 2,4-dichlorophenol; bromophenol blue; phenol; phenol red	[75]
Ochratoxin A	Figure 10A	3	6–500	Oat samples	300	5	Aflatoxin B1; aflatoxin B2; deoxynivalenol; chloramphenicol	[66]
Ochratoxin A	Figure 9A	0.97	1.81–31.0	Wheat sample	100	10 [b]	Aflatoxin B1; deoxynivalenol	[86]
Cocaine	Figure 9D	165.2	200–2 × 10^5	Human serum	40	7.5 [b]	Kanamycin; amikacin; sulfadimethoxine; ibuprofen	[73]
Aminoglycoside [c]	Figure 10C	26	0–1 × 10^3	Milk	60	N/A	Tetracycline; terramycin; chlortetracycline; ibuprofen; bisphenol A; sulfadimethoxine	[78]
Cocaine	Figure 9B	1.05 × 10^4	1 × 10^4–5 × 10^6	N/A	50	16.5	Neomycin; sulfadimethoxine; ampicillin; kanamycin	[74]
Adenosine	Figure 9E	2.5 × 10^4	5 × 10^4–3.5 × 10^6	N/A	N/A	N/A	N/A	[76]
Streptomycin	Figure 9D	33	60–526	Waters [d]	100	5	Penicillin G; tetracycline; tobramycin; neomycin; kanamycin A	[80]
Zearalenone	Figure 9C	2.31 × 10^{-6}	1 × 10^{-6}–0.1	Corn flour extract	28	6	Deoxynivalenol; aflatoxin B1, B2, G1, G2, M1; ochratoxin A; fumonisin B1, B2	[77]
Sulfonamides	Figure 9C	0.2 × 10^{-6} [e] 0.5 × 10^{-6} [f] 4.8 × 10^{-3} [g]	1 × 10^{-7}–1 × 10^{-3} [e] 1 × 10^{-7}–1 × 10^{-2} [f] 1 × 10^{-3}–10 [g]	Lake water	40	5	Kanamycin A; ampicillin; doxycycline; diethylhexyl phthalate; tobramycin	[71]
Alternariol	Figure 9C	42 × 10^{-6} [h] 6 × 10^{-6} [i] 2 × 10^{-6} [j]	1 × 10^{-4}–0.1 [h] 1 × 10^{-5}–1 × 10^{-2} [i] 1 × 10^{-6}–0.1 [j]	Wheat powder	35	5	Vomitoxin; zearalenone; patulin; altenuene; tenuazonic acid; tentoxin	[72]

[a] Detection time only; [b] including incubation time; [c] kanamycin A, kanamycin B, amikacin, gentamycin; [d] mineral spring water, bottled purified water, tap water, surface water, wastewater; [e] for sulfaguanidine; [f] for sulfamethizole; [g] for sulfamethoxazole; [h] original truncated aptamer; [i] bivalent aptamer; [j] trivalent aptamer.

Recently, our group devised an ultrasensitive FNA-FOEW sensing platform to overcome the sensitivity limitation, named the nanoscale affinity double layer (NADL)-FOEW sensor, for the detection of small-molecule targets regardless of their hydrophobicity (Figure 11) [50]. In the NADL-FOEW sensor, the aptamer is covalently immobilized on the fiber along with a nonspecifically absorbed Tween 80 thin layer (Figures 9C and 11). The fluorophore-labeled cDNA and target competitively bind with the immobilized aptamer, enabling the signal-off detection of targets. Different from the target or cDNA-immobilized strategies, the NADL-FOEW sensor enables in situ target enrichment, purification, and sensing on the same surface simultaneously, therefore dramatically improving the LOD down to the unprecedented femtomolar ranges. So far, we have demonstrated the ultrasensitive and specific detection of kanamycin [50], sulfadimethoxine [50], di-(2-ethylhexyl) phthalate [50], zearalenone [77], sulfonamides [71], and alternariol [72] in diverse matrices including environmental water, fresh milk, wine, wheat, and corn extracts. Both the detection sensitivity and the dynamic range all meet the practical applications. The reusability (around 30 times for different targets) is not as good as the FOEW sensors shown in Figure 9A,B, but is much higher than typical electrochemical biosensors (commonly less than three times). We also demonstrated the first class-specific detection of sulfonamides, where the total concentration of 14 sulfonamides spiked in the environmental water was continuously detected [71]. Due to the rapid increase in the numbers of synthetic structure analogues, the total concentration of structure analogues is commonly used for the evaluation of pollution levels. This is the first example to demonstrate the applicability of the FOEW sensor for the detection of the total concentration of multiple structure analogues. The broad dynamic range is a benefit for the detection of targets with a broad concentration distribution in real samples such as industrial waste. However, it also limits applications for the detection of targets, such as immunosuppressive drugs, with a narrow effective concentration range. This is an important issue.

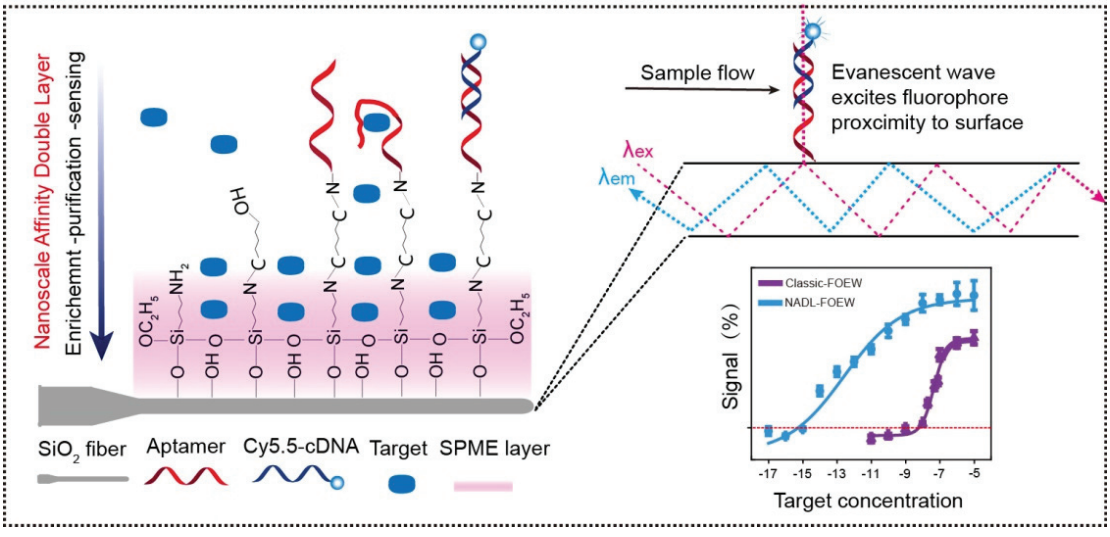

Figure 11. NADL-FOEW for rapid and ultrasensitive detection of small-molecule targets in environmental water, fresh milk, wine, and urine samples. Reprinted from Zhao et al. (2021) [50], Copyright (2021), with permission from American Chemical Society.

Enzymatic signal amplification has also been used to improve the sensitivity of FNA-FOEW sensors. Li et al. reported a portable chemiluminescent FNA-FOEW sensor for the ultrasensitive onsite detection of four mycotoxins in food samples. The SSB was immobilized on the fiber surface and the unbound biotin-labeled free aptamer was captured

by the SSB, while the target-bound aptamer was not captured by the SSB. The streptavidin–biotinylated horseradish peroxidase (SA-Bio-HRP) complex was then employed as a signal amplification tag to catalyze the oxidation of luminol into a chemiluminescent product [63]. The sensors possess low LODs in the range of 0.015–0.423 pg/mL for different mycotoxins. The limitation of this method is the high cost since both SSB and SA-Bio-HRP are expensive. The reusability of the sensor would also be limited since SSB is protein, which tends to be denatured.

Split aptamers enable novel sensing mechanisms that are not suitable for monolithic aptamers. He et al. reported the first split-aptamer-based FOEW sensor for the detection of cocaine in serum, in which the cDNA complementary to one fragment of the split aptamer was immobilized on the fiber (Figure 9D). The flow sample contains cocaine and the two split aptamer fragments, one labeled with fluorophore and the other labeled with a quencher. The binding between cocaine and the pair of fragments not only allows the fluorescence quenching, but also prohibits the hybridization of the fluorophore-labeled fragment with the cDNA. Thus, only the free fluorophore-labeled fragment hybridizes with the cDNA immobilized on the fiber, enabling the signal-off detection of cocaine (LOD = 165.2 nM) [73]. The advantage of this sensing mechanism is that it is a separation-free process. The limitations of this design include its low sensitivity and the signal-off detection mode.

Later on, a signal-on sensing mechanism was reported by immobilizing one of the split aptamers on the fiber (Figure 9E). The fluorophore-labeled single fragment of the spilt aptamer and the target, adenosine, are assembled with the other fragment of the split aptamer attached to the surface, enabling the detection of adenosine (LOD = 25 μM) [76]. The same sandwich strategy has also been used for the continuous detection of streptomycin (LOD = 25 μM) [80]. The signal-on detection is attractive, while the split aptamers sacrifice binding affinity compared to the original aptamer, resulting in unsatisfactory sensitivity.

5.2. Offline-Separation-Based Detection of Small Molecules Using Aptamers

Offline separation using magnetic beads or graphene oxide has been coupled with FOEW sensors for the detection of small molecules (Figure 12). It not only helps to minimize the matrix interference on the fiber, but also enables the new surface regeneration method [66], signal-on detection [66,74], or novel sensing mechanisms [78]. The limitation is a relatively longer assay time and less convenient operation compared to the separation-free strategies described above.

The first offline magnetic-bead-based detection strategy was reported by Shi et al. for the signal-on detection of OTA (LOD = 3 nM) [66]. In their method, the OTA-binding aptamer is immobilized on the magnetic beads and the cDNA probe is dual-labeled with fluorophore and streptavidin. The cDNA is immobilized on the magnetic beads via the hybridization with the aptamer. The cDNA probe is displaced from the magnetic bead when OTA binds with the aptamer. The released cDNA in the supernatant after magnetic separation is captured by dethiobiotin functionalized on the fiber via the strong dethiobiotin–streptavidin interaction. The sensor can be easily regenerated over 300 times without losing sensitivity. Later, the same group used a similar strategy for the signal-on detection of cocaine (LOD = 10.5 μM) [74]. The major difference is the use of a fiber coated with the capture probe complementary to the fluorophore-labeled cDNA to quantitate the amount of replaced cDNA via hybridization.

Graphene oxide is an effective fluorescence-quenching material and a widely used absorption material. Taking advantage of its selective absorption capability to single-stranded DNA over G-quadruplex, He et al. used graphene oxide as both quencher and separation matrix to realize the continuous detection of aminoglycoside antibiotics with an LOD of 26 nM [78]. Specifically, the fluorophore-labeled aptamers fold into an interstrand G-quadruplex in the absence of aminoglycosides. The fluorescence is partially quenched due to the photo-induced electron transfer (PET) when the aptamer binds with aminoglycoside. The fluorescence of the aptamer–aminoglycoside complex is further quenched by graphene

oxide when it absorbs on graphene oxide. The remaining free aptamer forms the G-quadruplex with the surface-attached aptamer, enabling the signal-off detection of several aminoglycosides. The limitation of this sensing mechanism is its limited generality. Only the aptamers that can form multiple strand complexes may possibly be compatible with this sensing mechanism.

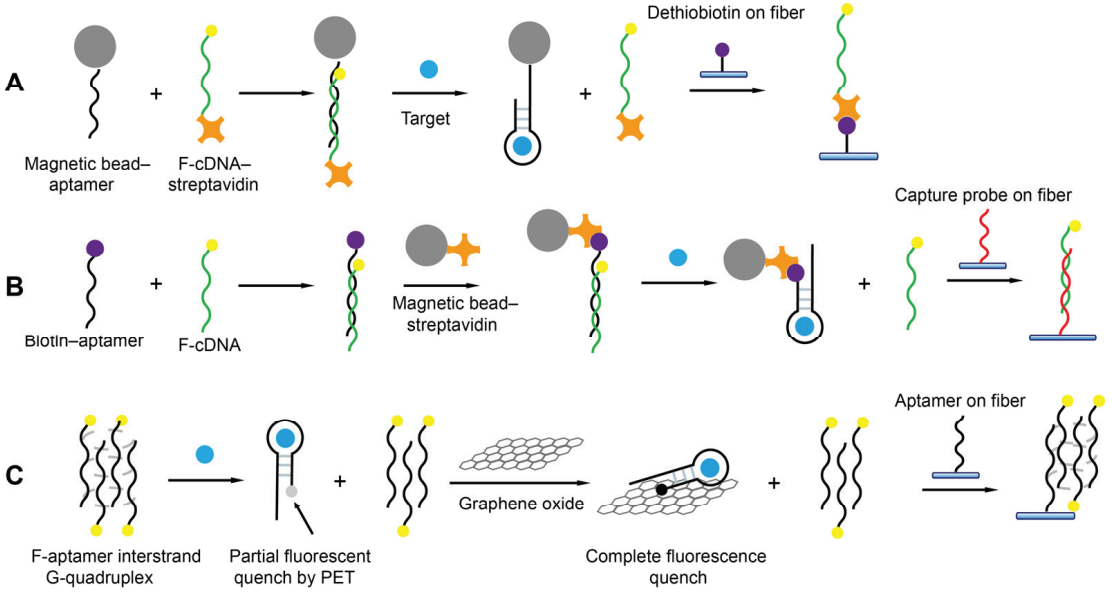

Figure 12. The offline-separation-based detection of small-molecule targets using FOEW sensors installed with fibers functionalized by (**A**) dethiobiotin [66]; (**B**) capture probe complementary to cDNA of aptamer [74]; and (**C**) aptamer [78].

5.3. Detection of Heavy Metal Ions Using DNAzyme and T-Rich Probes

Heavy metal ions are extremely harmful to both the ecosystem and human health. The sensitive and specific detection of heavy metal ions in the environment and food is of paramount importance. The rapid development of FNAs specific to certain metal ions has provided valuable chances for the development of biosensors. Even though numerous FNA-based biosensors have been reported in recent years, most of them are only suitable for a one-time test and not capable of continuous detection [97,98]. Several FNA-FOEW sensors have been reported for the onsite continuous detection of Pb^{2+} and Hg^{2+}, which show great potential for real applications (Table 2).

The first detection of Pb^{2+} using FNA-FOEW was reported by Long et al. in 2014 [99]. They used the fluorophore-labeled G-rich aptamer as a molecular probe (Figure 2C), which forms a stabilized G-quadruplex structure upon binding with Pb^{2+}. The G-quadruplex cannot hybridize with the cDNA attached to the fiber, enabling the signal-off detection of Pb^{2+} (Figure 13A). The good regeneration of the sensor in the absence of Pb^{2+} was demonstrated (50 times). The sensing mechanism is simple; however, the sensor may suffer from difficulty in surface regeneration after Pb^{2+} detection due to the nonspecific binding of Pb^{2+} on the fiber.

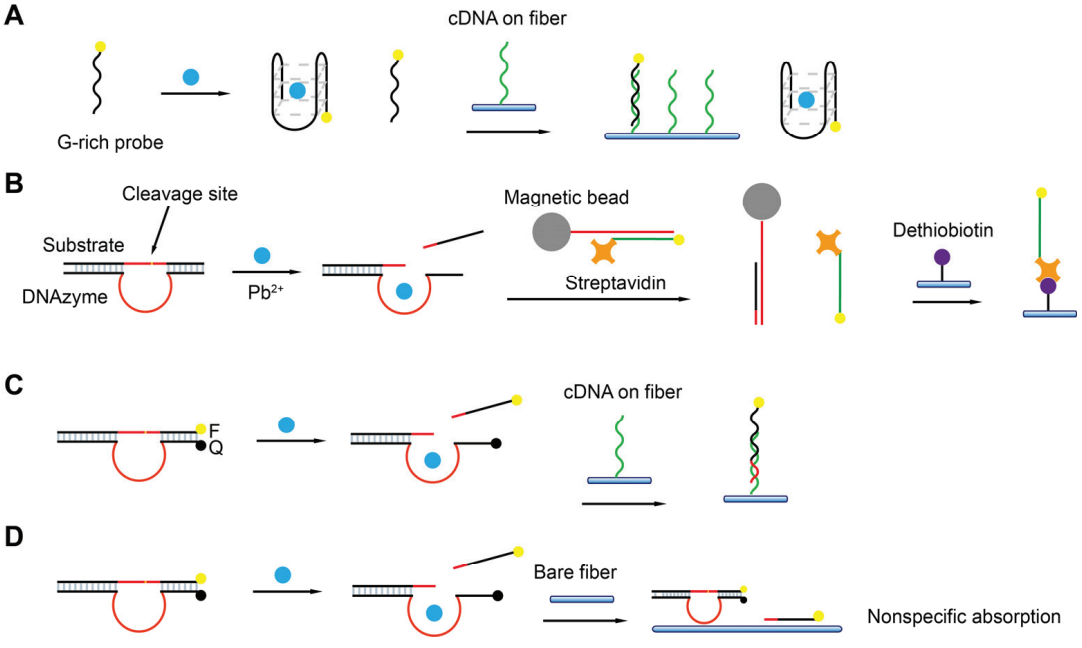

Figure 13. Schematic diagrams of FOEW sensors for Pb^{2+} detection using (**A**) G-rich probe [99] or DNAzymes via (**B**) offline magnetic-separation-based strategy [65] and (**C**,**D**) separation-free means enabled by cDNA functionalized fiber [79] or bare fiber [100].

Later, Shi et al. reported the first DNAzyme-FOEW sensor for the detection of Pb^{2+} with a greatly improved reusability (>300 times) and long-term stability (over one month at room temperature) [65]. The Pb^{2+}-specific DNAzyme 8–17 is so far the most popularly used DNAzyme in all types of Pb^{2+} biosensors [101]. In their method, the sensor was constructed using DNAzyme 8–17 in an offline-separation-based mode (Figure 13B). The magnetic beads are immobilized with the duplexes, which are formed by the streptavidin and fluorophore dual-modified signal probe and the strand complementary to the substrate of 8–17. Pb^{2+} catalyzes the cleavage of the substrate of 8–17 and the released fragment hybridizes with the above complementary strand on the magnetic bead. The dual-labeled signal probe is replaced and subsequently detected by the dethiobiotin-modified fiber. The signal-on detection of Pb^{2+} was then realized with an LOD of 1 nM and the linear range was from 20 nM to 800 nM. The limitation of this method is the requirement of offline operation (1 h), which complicates the detection process and lengthens the total detection time.

The DNAzyme 8–17 and GR-5 were respectively used to construct the separation-free FOEW sensors by direct detection of the fluorophore-labeled cleaved substrate (LOD = 20 nM) either using the cDNA functionalized fiber (Figure 13C) [79] or the bare fiber (Figure 13D) [100]. The hybridization and the nonspecific absorption were respectively utilized to capture the cleaved substrate. LODs of 20 nM and 9.34 nM were respectively achieved by both methods. The detection time was similar for both sensors (approximately 13 min per test). The use of bare fiber for the detection of Pb^{2+} provides several advantages including low cost and better reusability. The nonspecific absorption-based sensing methods are prone to be strongly affected by the presence of nontargets. Therefore, the limitation is the hard-to-predict matrix interference from different samples.

Table 2. Detection of heavy metal ions.

Target	Sensing Mechanism	LOD (nM)	Linear Range (nM)	Real Sample	Reusability (Times)	Time (min)	Selectivity	Ref.
Pb^{2+}	Figure 13A	0.22	1–300	Bottled water; tap water; lake water; wastewater	50	10	Hg^{2+} Ni^{2+} Co^{2+} Cd^{2+} Ca^{2+} Cu^{2+} Fe^{3+} Ag^{+} K^{+}	[99]
Pb^{2+}	Figure 13B	1	20–800	Bottled water; tap water; mineral spring water	250	60 + 5 [a]	Hg^{2+} Ni^{2+} Co^{2+} Cd^{2+} Ca^{2+} Cu^{2+}	[65]
Pb^{2+}	Figure 13C	20	0–1×10^4	Dan Jiang Kou reservoir water	18	13	Ag^{+} Ca^{2+} Zn^{2+} Fe^{2+} Cu^{2+} Cd^{2+} Co^{2+} Mn^{2+} Mg^{2+} Pb^{2+} Hg^{2+} Fe^{3+} Al^{3+}	[79]
Pb^{2+}	Figure 13D	9.34	N/A	Tap water; underground water; bottled purified water; human serum	N/A	13	Zn^{2+} Mg^{2+} Ca^{2+} Cu^{2+} Cd^{2+} Hg^{2+}	[100]
Hg^{2+}	Figure 14C	2.2×10^{-2}	2.2×10^{-2}–10	Dan Jiang Kou reservoir water	18	7	Ag^{+} Ca^{2+} Zn^{2+} Fe^{2+} Cu^{2+} Cd^{2+} Co^{2+} Mn^{2+} Mg^{2+} Pb^{2+} Hg^{2+} Fe^{3+} Al^{3+}	[79]
Hg^{2+}	Figure 14A	2.1	N/A	Tap water; pinery wastewater plant; bottled water	100	6	Ca^{2+} Zn^{2+} Fe^{2+} Cu^{2+} Sn^{2+} Cr^{2+} Mn^{2+} Ni^{2+} Pb^{2+}	[51]
Hg^{2+}	Figure 14B	1.06	75–1×10^3	Bottled water; tap water; pond water	200	N/A	Ni^{2+} Co^{2+} Cd^{2+} Pb^{2+} Ca^{2+}	[64]
Hg^{2+}	Figure 14D	1	7–1200	Effluent of wastewater treatment plants	31	30	Ni^{2+} Co^{2+} Cd^{2+} Pb^{2+} Ca^{2+} Mg^{2+}	[60]
Hg^{2+}	Figure 14E	8.5	N/A	Tap water; bottled water; lake water; underground water	N/A	10	Ca^{2+} Zn^{2+} Cu^{2+} Mg^{2+} Cd^{2+} Pb^{2+}	[60]

[a]: offline incubation time + online detection time.

The T-rich probes have been widely used for the specific detection of Hg^{2+} [102] since the finding of the specific coordination binding between T-Hg^{2+}-T [32]. Five different strategies have been developed to realize the detection of Hg^{2+} and are all in the separation-free modes (Figure 14). The sensing mechanisms are very similar to those used for the detection of Pb^{2+} except the molecular probes are different. The advantages and limitations of each method are not repeatedly discussed. The first Hg^{2+}-FOEW sensor was reported in 2011 by A.Z. Gu et al. (Figure 14A) [51]. In their method, the T-rich probe is immobilized on the optical fibers. Hg^{2+} and the fluorophore-labeled cDNA probe compete for the T-rich sequence on the fiber, realizing the signal-off detection of Hg^{2+} (LOD = 2.1 nM). The sensing mechanism is simple, but the signal-on sensing mechanism is preferred, and the sensitivity is not high enough to meet the requirements.

Later, a signal-on method was developed by adopting a strand-displacement-based method with slightly improved sensitivity (LOD = 1.06 nM), where the T-rich probe is dual-labeled with fluorophore and streptavidin and the cDNA is labeled with a quencher (Figure 14B). The cDNA and the T-rich probe are separated upon the binding of Hg^{2+} with the T-rich probe. The released T-rich probe is then captured by the dethiobiotin-coated fiber, enabling the signal-on detection of Hg^{2+} [64]. The LOD was further improved to 22 pM when a different pair of T-rich probe and cDNA are used, and they are respectively labeled with quencher and fluorophore (Figure 14C). The displaced cDNA upon the binding of Hg^{2+} with T-rich probe is detected by the capture probe immobilized on the fiber [79].

The sensing mechanism was further simplified by only using the fluorophore-labeled T-rich probe (LOD = 1 nM) (Figure 14D) [60]. The T-rich probe forms a hairpin structure upon binding to Hg^{2+} and is unable to bind to the cDNA on the fiber. The sensing mechanism was also simplified by using a bare fiber and the quencher-labeled T-rich probe/fluorophore-labeled cDNA pair (LOD = 8.5 nM) (Figure 14E) [60]. The signal-on detection of Hg^{2+} is realized by the fluorescence increase caused by the adsorption of the released cDNA on the bare fiber. The method avoids the surface modification of the fiber, while the limitation is its lower sensitivity compared to the above modified-fiber-based methods.

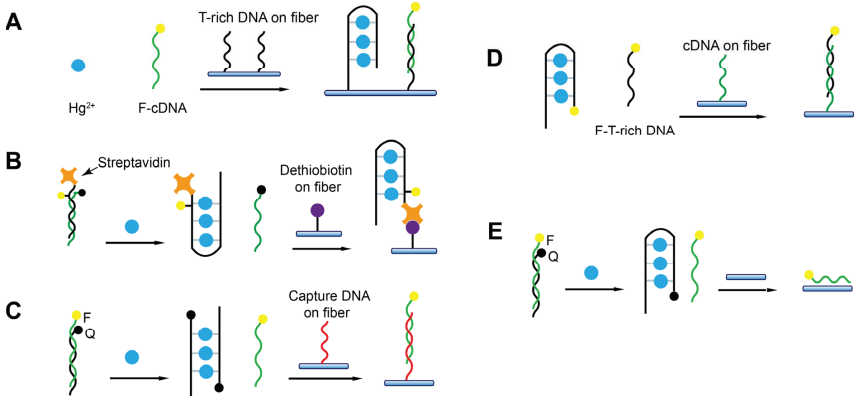

Figure 14. Schematic diagrams of T-rich probe-based FOEW sensors for Hg^{2+} detection using fibers functionalized by (**A**) T-rich DNA [51]; (**B**) dethiobiotin [64]; (**C**) capture DNA [79]; (**D**) cDNA [60]; or (**E**) nothing (bare fiber) [60].

5.4. Detection of Nucleic Acids

FOEW sensors have been used for the detection of all types of nucleic acids including DNA and miRNA since its first report in 1995 (Table 3) [103]. In the first demonstration, the 20 mer cDNA probes (dT20) were in situ-synthesized on the surfaces of derivatized quartz optical fibers, and the hybridization on optical fibers was detected by the use of the fluorescent DNA stain ethidium bromide (EB). One year later, a more facile streptavidin–biotin-based strategy similar to what we introduced in Section 4.2 (Figure 5E) was utilized for cDNA immobilization [82]. Different shapes of fibers have been used for the detection of nucleic acids. However, the sensitivity for most FOEW sensors is in the micromolar to low nanomolar range [104], which is too low for practical applications. Therefore, different from the above sensing mechanisms for small-molecule targets and metal ions, the sensing mechanisms for nucleic acids commonly involve signal amplifications, as we summarized below, to improve the sensing sensitivity. The signal amplification strategies can be roughly divided into three categories (Figure 15): (1) using more sensitive optical labels such as gold nanoparticles or quantum dots (QDs); (2) introducing multiple optical labels via synthesis, hybridization chain reaction, or polymerase chain reaction; and (3) other enzymatic reactions. The gold nanoparticles are typically used in the SPR-based FOEW sensors [81,105,106]. In the following, we only summarize the progress of fluorescent FOEW sensors using organic fluorophore or QDs for the detection of nucleic acid targets.

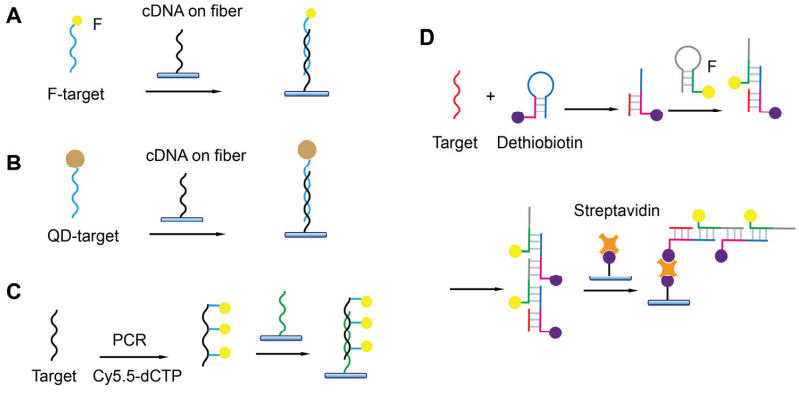

Figure 15. Schematic diagrams of FOEW sensors for detection of nucleic acids via hybridization with (**A**) single-fluorophore Cy5.5-labeled target [107]; (**B**) quantum-dots-labeled target [67]; (**C**) multiple-

fluorophore-labeled target synthesized by PCR [108]; or (**D**) multiple-fluorophore-labeled duplex formed via hybridization reaction (HCR) [109].

The use of more sensitive optical labels is the easiest way to improve detection sensitivity. For example, the LOD for the detection of Cy5.5-labeled Shigella DNA was 100 pM [107]. In their method, the cDNA was immobilized on the fiber and the signal on detection of target DNA was then realized due to the specific hybridization on the fiber (Figure 15A). The three-strand sandwich detection mode has also been used for the detection of nucleic acid. For example, Zhang et al. realized the detection of miRNA let-7a by using a cDNA probe immobilized on the fiber and a Cy5.5-labeled signal probe complementary to the target (LOD = 24 pM). They also used a "locker" strand to partially hybridize with the target to reduce the false-negative results at the high target concentration [110].

Compared with organic dyes, quantum dots are 20 times brighter and several orders of magnitude more photostable. The LOD was improved to 1 pM when the target was labeled with quantum dots and hybridized with the cDNA on the fiber for 30 min (Figure 15B) [67]. The lower LOD can be achieved by lengthening the hybridization time.

The multiple-fluorophore-labeled target was used for the detection of the microcystin synthetase A gene (LOD = 10 pM) [108]. Cy5.5-labeled deoxycytidine triphosphate (dCTP) was used in the polymerase chain reaction (PCR) to introduce multiple Cy5.5 labels on one target sequence (Figure 15C). The sensitivity was greatly improved by the combination of the CRISPR-Cas13a system and hybridization chain reaction (HCR) (Figure 15D) [109]. Specifically, CRISPR-Cas13a was activated upon binding of the target gene to crRNA. The reporter DNA was subsequently cleaved, and the generated fragment triggered the HCR. The formed duplex contained multiple biotin labels for its immobilization on the fiber and multiple Cy5.5 labels for signal transduction. The LODs of S genes, N genes, and Orf1ab genes were 10, 100, and 10 aM, respectively. The HCR-based multiple Cy5.5 and biotin label strategy has also been used for ultrasensitive detection of miRNA let-7a (LOD = 0.8 fM) [111].

As shown above, all the methods rely on the labeled analyte or intercalation reagents or other reagents for signal amplification and transduction. In 1999, Tan et al. reported the first reagent-free FOEW sensor for the detection of DNA, in which a biotin, fluorophore, and quencher tri-modified molecular beacon DNA probe (MB) was used to replace the cDNA probe. MBs were immobilized on the optical fiber surface via biotin–avidin or biotin–streptavidin interactions. The MBs become fluorescent upon hybridization with target DNA/RNA molecules. The sensor can be used to directly detect, in real-time, target DNA/RNA molecules without using competitive assays. The limitation of the sensor is its low sensitivity (LOD = 1.1 nM) and that the offline PCR amplification of targets is needed. The development of reagent-free FOEW sensors for continuous detections is highly desired, but quite challenging, as we discuss in Section 6.

Table 3. Detection of nucleic acids.

Target	Sensing Mechanism	LOD (nM)	Linear Range (nM)	Reusability (Times)	Time (min)	Ref.
DNA	Figure 15B	1×10^{-3}	0.1–2.5	30	N/A	[67]
Shigella DNA	Figure 15A	0.1	0–2.5	30	5	[107]
dsDNA	N/A	N/A	5×10^{3}–400×10^{3}	N/A	0.5	[112]
ssDNA	Figure 15B (AuNP)	0.2×10^{-3}	N/A	N/A	7	[81]
Let-7a	Fluorescent-labeled signal probes	2.4×10^{-2}	N/A	N/A	4	[110]

Table 3. *Cont.*

Target	Sensing Mechanism	LOD (nM)	Linear Range (nM)	Reusability (Times)	Time (min)	Ref.
ssDNA	Transmission spectroscopy	10	N/A	N/A	N/A	[104]
Let-7a	Shift in the interference spectrum	0.212	2–2 × 10^4	N/A	N/A	[113]
Microcystin synthetase A	Figure 15C	10×10^{-3}	0.05–5	150	7.25	[108]
Let-7a	Figure 15D	0.8×10^{-6}	1×10^{-6}–7.1×10^{-2}	100	N/A	[111]
Let-7a; mRNA 141; let-7c; mRNA 21; mRNA 200	Gold triangular nanoprisms	103×10^{-9}–261×10^{-9}	1×10^{-6}–100	2	N/A	[106]
Three genes of SARS-CoV-2	Figure 15D	10×10^{-9} [a] 100×10^{-9} [b] 10×10^{-9} [c]	0–1	100	60	[109]
Chilli Leaf Curl Virus	LSPR of AuNP [d]	179.3	N/A	N/A	N/A	[114]
Prostate-specific antigen	Figure 15B (AuNP)	0.54×10^{-6}	N/A	N/A	N/A	[105]

[a] S, [b] N, and [c] Orf1ab of SARS-CoV-2; [d] local surface plasmon resonance.

5.5. Detection of Proteins Using Aptamers

Most biomarkers that are currently tested in clinics are proteins in nature. The major sensing platforms for protein biomarker detection are immunoassays, especially the chemiluminescence immunoassay and electroluminescence immunoassay, due to the high sensitivity, specificity, and reliability. The use of FNA-FOEW sensors for the detection of proteins is rather limited. In most applications, the continuous detection of protein biomarkers may not be necessary. In addition, FOEW sensors have low throughput, which cannot meet the high throughput requirement typically needed for hospital applications. However, an FOEW sensor is a low-cost instrument and is quite suitable for small clinics when the number of samples is not large. The current major effort for the detection of proteins is to improve detection sensitivity. Our group recently isolated several high-affinity DNA aptamers specific to human serum albumin (HSA) [115,116] and used one of the aptamers to construct an NADL-FOEW sensor [50]. The ultrasensitive detection of HSA in urine was realized with an LOD of 0.14 fM. Even though the sensitivity meets the practical requirement, the dynamic range is too broad, which results in a precision issue.

Exosomes are regarded as a promising biomarker for the noninvasive diagnosis and treatment of diseases. A sandwich-based sensing mechanism was developed for exosome detection (Figure 16) [117]. In their method, an exosome fluorescence probe/aptamer sandwich structure was formed based on both types of interactions: (1) hydrophobic interaction between the cholesteryl on the fluorescent probe and phospholipid bilayer membrane; and (2) CD63 on the surface of the exosome and aptamer attached to the fiber surface. The LOD was 7.66 particles/mL and the linear range was 47.5–4.75 × 10^6 particles/mL. The detection time was 1 h and the sensor can be regenerated for 60 cycles. The good surface regeneration should be attributed to the surface passivation using BSA.

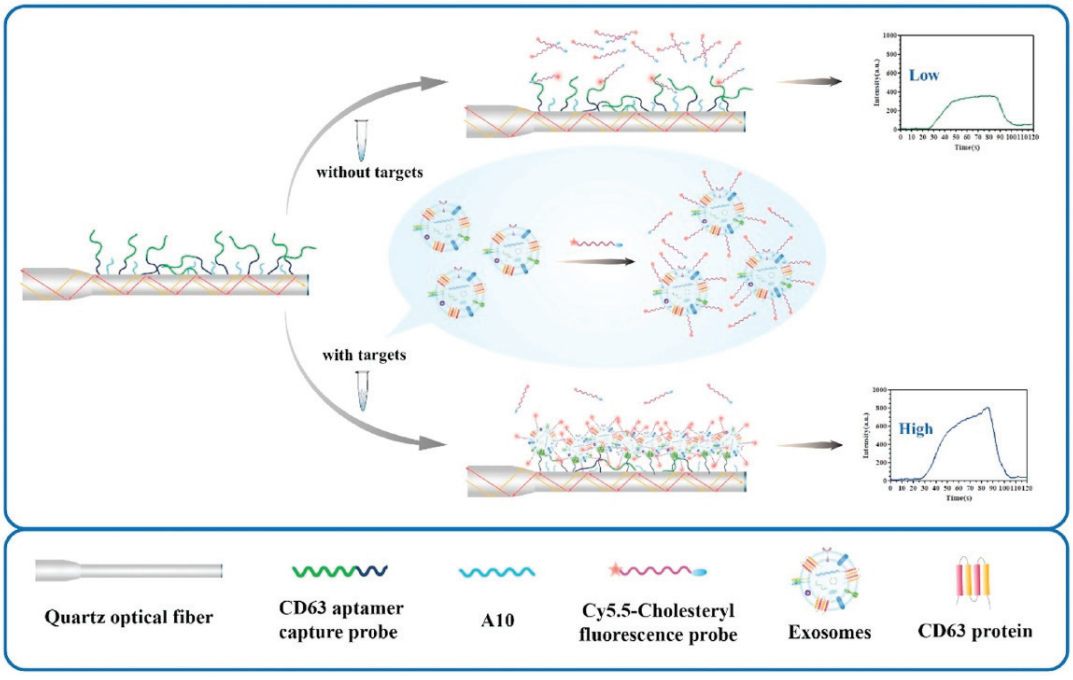

Figure 16. A sandwich-based sensing mechanism for exosome detection using FNA-FOEW sensor. Reprinted from Li et al. (2022) [117], Copyright (2022), with permission from Elsevier.

5.6. Detection of Pathogens

Pathogens are microorganisms such as bacteria and viruses that can cause diseases in humans or animals and plants. The development of rapid and low-cost methods for pathogen detection has been a hot topic in recent years. Recent progress on optical biosensors developed for nucleic acid detection related to infectious viral diseases has been recently reviewed [17]. Numerous methods have been reported with a focus on real-time PCR detection kits and immune test strips. Aptamers have also been used for pathogen detections on diverse sensing platforms.

Very recently, a few aptamer-FOEW sensors for the detection of pathogens were reported by Long's group. The detection of *E. coli* O157:H7 was realized by using the fluorophore-labeled aptamer and bare optical fiber (LOD = 610 CFU/mL) [118]. The nonspecific adsorption of the aptamer on the fiber decreased with the increase in the *E. coli* concentration in the sample. They further improved the sensitivity by using a fiber with an in situ etched nanoporous layer to effectively prohibit the entrance of the pathogen-bound Cy5.5 aptamer into the nanopores and to enhance the fluorescence intensity [61]. The LODs for the detection of *E. coli* O157:H7 and *Salmonella typhimurium* were 110 and 210 CFU/mL, respectively. They further realized the simultaneous detection of *E. coli* O157:H7 and *Salmonella typhimurium* using a dual-color FOEW sensor [55]. In their method, the two aptamers were respectively labeled with Cy5.5 and Cy3. The LODs for the detection of *E. coli* O157:H7 and *Salmonella typhimurium* were 340 CFU/mL and 180 CFU/mL, respectively. They also used hybridization chain reaction and CRISPR/Cas12a to detect *E. coli* O157:H7 with an LOD of 17.4 CFU/ mL [119]. An evanescent wave fluorescence nanobiosensing platform based on CRISPR/Cas12a was developed for the ultrasensitive detection of Staphylococcus aureus. (LOD = 13.2 CFU/mL) (Figure 17) [120].

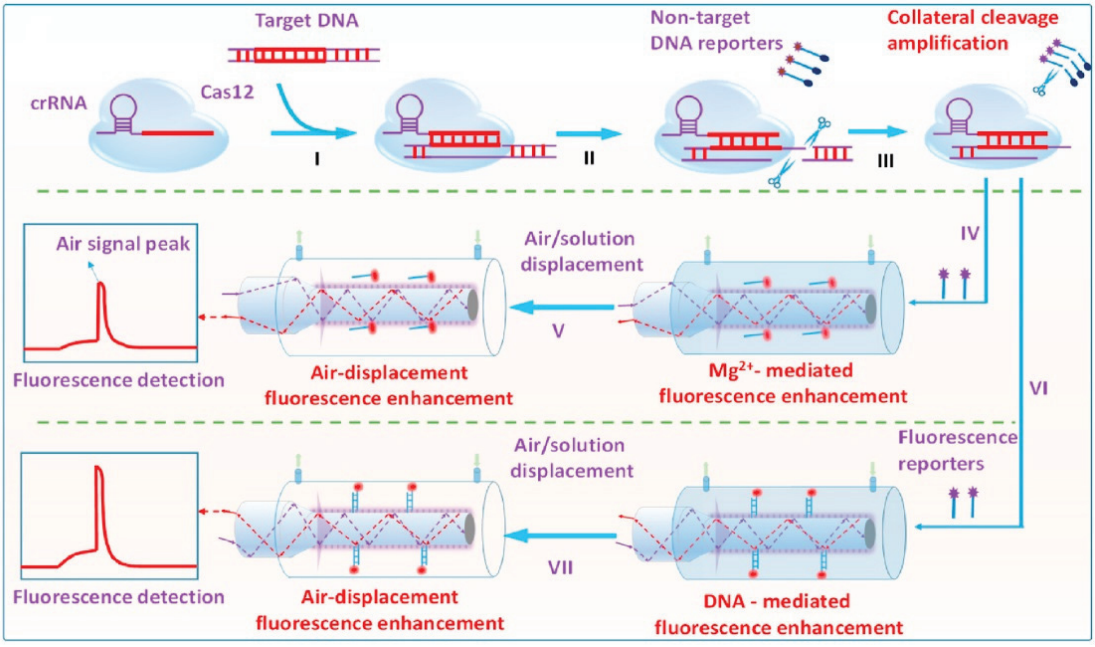

Figure 17. A CRISPR/Cas12a-powered FOEW sensor for nucleic acid amplification-free detection of Staphylococcus aureus with multiple signal enhancements. Reprinted from Song et al. (2023) [120], Copyright (2023), with permission from Elsevier.

6. Challenges and Perspectives

With the improvement of people's living standard, there is an increasing demand for green environment and food and healthy life. To achieve these goals, intelligent technologies including biosensors are highly desired and the market is rapidly growing. Biosensors with continuous monitoring capability are going to be one of the major types of products for environment protection, food safety, and point-of-care applications. Although some FOEW sensors, such as those used for the measurement of temperature, pH, oxygen, and refractive index, are now commercially available [12], FOEW sensors for the detection of heavy metal ions, small molecules, proteins, nucleic acids, and microorganisms are still at the laboratory research stage. There are some major challenges that need to be overcome to realize the commercial applications of FNA-FOEW sensors.

6.1. High-Quality Small-Molecule-Binding Aptamers

Compared to other biosensors, FNA-FOEW sensors are most attractive for the continuous detection of small-molecule targets. One of the major challenges is the availability of high-quality small-molecule-binding aptamers. Even though hundreds of them have been reported in the last 30 years, aptamers with satisfactory affinity (e.g., nanomolar range dissociation constant) and specificity (low crossreactivity required for the detection of a specific target; high crossreactivity for the detection of class-specific targets) are still limited [121]. Aptamers suitable for clinical uses are even rarer due to the presence of numerous structural analogues in vivo. To speed up the discovery of high-quality small-molecule-binding aptamers, the following fields need to be developed first. First, new strategies are needed for the isolation of small-molecule-binding aptamers since the current methods have been demonstrated to be insufficient. Second, crossreactivity tests are either missing or rather limited in many original aptamer isolation papers, which impedes the wide acceptance of aptamers. More systematic characterization of the specificity and crossreactivity is required to push the aptamer field for practical uses. Third, standard

affinity characteristic methods are lacking for small-molecule-binding aptamers, causing conflicting results in the literature [122,123]. More general affinity characteristic methods are urgently needed.

6.2. Reagent-Free and Continuous Detection

Achieving continuous and reagent-free detection of trace amounts of targets is difficult for biosensors, including FNA-FOEW sensors. Even though extremely low LODs have been achieved by many methods, almost all of them rely on multiple-step signal amplification and/or advanced and expensive instruments. For example, we recently developed NADL-FOEW sensing platforms enabling femtomolar LODs for small-molecule targets without the need for multiple-step signal amplification, but the samples still need to be 1000- to 10,000-fold diluted to minimize the matrix interference. Clearly, the method cannot be used for the direct detection of biomarkers in a reagent-free form like wearable blood sugar electrochemical sensors. To solve this problem, several challenging issues need to be solved. First, the reagent-less detection mode requires target-induced structure switching to realize signal transduction, instead of competitive sensing modes. Aptamers with structure-switching capability are rare, and the rational design of structure-switching aptamers are challenging [124]. Second, continuous and reagent-less detection requires that FNAs can rapidly respond to changes in target concentration. Therefore, both the association and disassociation kinetics need to be fast. However, the study of the kinetic performance of aptamers is quite limited. Third, regenerating the sensor surface without the need for chemicals is quite challenging. So far, the surface regeneration is completely carried out by chemical regeneration [125]. Novel surface modification strategies, especially biomimic layers, are expected to be more effective than the current BSA or nonionic liquid layers. So far, the fundamental studies in this direction are rather limited compared to the development of new sensing mechanisms.

6.3. Long-Term Stability under Application Conditions

The long-term stability of FNA-FOEW sensors is critical for continuous detection. Many previous works have demonstrated the successful regeneration of the sensor surface up to 300 times and a storage time of more than one month at 4 °C. However, these tests are typically performed using buffer samples, not real samples, and at low temperatures. The stability tests of FNAs and FNA-FOEW sensors at an outdoor temperature (such as ~40 °C) and in real samples that might contain nucleases have not been reported. These conditions might cause a shortening of the storage time of FNA-functionalized fibers. Modified nucleic acids might be needed to improve the long-term stability and the nuclease-resistance capability.

6.4. Throughput

The limitation of the FOEW sensor is its low throughput compared to planar array sensors. Fiber bundles are the future direction to realize the simultaneous detection of multiple targets. The technical challenges are the design and fabrication of the compact optical and signal transduction systems.

7. Conclusions

FNA-FOEW sensors have great potential for in situ continuous detection of environmental and food pollutants and biomarkers, with attractive features including low cost, reusability, and portability. We reviewed the recent progress of FNA-FOEW sensors with a focus on the fluorescent FOEW sensors. We sequentially introduced FNAs, the major components of FOEW sensors, and the optical mechanism for real-time fluorescence detection, and the optical fiber interfacial modification methods. The progresses of the sensing mechanisms were then reviewed according to the types of targets, small molecules, heavy metal ions, proteins, nucleic acids, and pathogens. We finally discussed the challenges faced by FNA-FOEW sensors and future directions. FNA-FOEW sensors are a multidisciplinary

research field. Technical advances from aptamer isolation, surface modification, organic synthesis chemistry, optics, electrical, and manufacturing engineering are all required. With progressing technical advances, we believe that FNA-FOEW sensors will gradually broaden their application scope from lab benchtop use to onsite practical applications.

Author Contributions: Writing—original draft preparation, Z.W.; writing—review and editing, X.L.; funding acquisition, X.L. All authors have read and agreed to the published version of the manuscript.

Funding: This research was funded by the National Natural Science Foundation of China [21675112], Natural Science Foundation of Beijing Municipality [L182046].

Institutional Review Board Statement: Not applicable.

Informed Consent Statement: Not applicable.

Data Availability Statement: Data are contained within the article.

Conflicts of Interest: The authors declare no conflict of interest.

References

1. Hui, Y.; Huang, Z.; Alahi, M.E.E.; Nag, A.; Feng, S.; Mukhopadhyay, S.C. Recent advancements in electrochemical biosensors for monitoring the water quality. *Biosensors* **2022**, *12*, 551. [CrossRef] [PubMed]
2. Faraji Rad, Z. Microneedle technologies for food and crop health: Recent advances and future perspectives. *Adv. Eng. Mater.* **2022**, *25*, 2201194. [CrossRef]
3. Medina, S.; Perestrelo, R.; Silva, P.; Pereira, J.A.M.; Câmara, J.S. Current trends and recent advances on food authenticity technologies and chemometric approaches. *Trends Food Sci. Technol.* **2019**, *85*, 163–176. [CrossRef]
4. Chung, M.; Fortunato, G.; Radacsi, N. Wearable flexible sweat sensors for healthcare monitoring: A review. *J. R. Soc. Interface* **2019**, *16*, 20190217. [CrossRef] [PubMed]
5. Teymourian, H.; Parrilla, M.; Sempionatto, J.R.; Montiel, N.F.; Barfidokht, A.; Van Echelpoel, R.; De Wael, K.; Wang, J. Wearable electrochemical sensors for the monitoring and screening of drugs. *ACS Sens.* **2020**, *5*, 2679–2700. [CrossRef]
6. Taitt, C.R.; Anderson, G.P.; Ligler, F.S. Evanescent wave fluorescence biosensors. *Biosens. Bioelectron.* **2005**, *20*, 2470–2487. [CrossRef]
7. Adeel, M.; Rahman, M.M.; Caligiuri, I.; Canzonieri, V.; Rizzolio, F.; Daniele, S. Recent advances of electrochemical and optical enzyme-free glucose sensors operating at physiological conditions. *Biosens. Bioelectron.* **2020**, *165*, 112331. [CrossRef]
8. Zafar, H.; Channa, A.; Jeoti, V.; Stojanovic, G.M. Comprehensive review on wearable sweat-glucose sensors for continuous glucose monitoring. *Sensors* **2022**, *22*, 638. [CrossRef]
9. Ding, Q.; Li, C.; Wang, H.; Xu, C.; Kuang, H. Electrochemical detection of heavy metal ions in water. *Chem. Commun.* **2021**, *57*, 7215–7231. [CrossRef]
10. Taitt, C.R.; Anderson, G.P.; Ligler, F.S. Evanescent wave fluorescence biosensors: Advances of the last decade. *Biosens. Bioelectron.* **2016**, *76*, 103–112. [CrossRef]
11. Jiao, L.; Zhong, N.; Zhao, X.; Ma, S.; Fu, X.; Dong, D. Recent advances in fiber-optic evanescent wave sensors for monitoring organic and inorganic pollutants in water. *TrAC Trends Anal. Chem.* **2020**, *127*, 115892. [CrossRef]
12. Wang, X.D.; Wolfbeis, O.S. Fiber-optic chemical sensors and biosensors (2013–2015). *Anal. Chem.* **2016**, *88*, 203–227. [CrossRef] [PubMed]
13. Wang, X.D.; Wolfbeis, O.S. Fiber-optic chemical sensors and biosensors (2008–2012). *Anal. Chem.* **2013**, *85*, 487–508. [CrossRef] [PubMed]
14. Benito-Pena, E.; Valdes, M.G.; Glahn-Martinez, B.; Moreno-Bondi, M.C. Fluorescence based fiber optic and planar waveguide biosensors. A review. *Anal. Chim. Acta* **2016**, *943*, 17–40. [CrossRef] [PubMed]
15. Liu, J.; Cao, Z.; Lu, Y. Functional nucleic acid sensors. *Chem. Rev.* **2009**, *109*, 1948–1998. [CrossRef] [PubMed]
16. Ravan, H.; Kashanian, S.; Sanadgol, N.; Badoei-Dalfard, A.; Karami, Z. Strategies for optimizing DNA hybridization on surfaces. *Anal. Biochem.* **2014**, *444*, 41–46. [CrossRef]
17. Eksin, E.; Erdem, A. Recent progress on optical biosensors developed for nucleic acid detection related to infectious viral diseases. *Micromachines* **2023**, *14*, 295. [CrossRef]
18. Loyez, M.; DeRosa, M.C.; Caucheteur, C.; Wattiez, R. Overview and emerging trends in optical fiber aptasensing. *Biosens. Bioelectron.* **2022**, *196*, 113694. [CrossRef]
19. Huertas, C.S.; Calvo-Lozano, O.; Mitchell, A.; Lechuga, L.M. Advanced evanescent-wave optical biosensors for the detection of nucleic acids: An analytic perspective. *Front. Chem.* **2019**, *7*, 724. [CrossRef]
20. Mao, Z.; Peng, X.; Zhou, Y.; Liu, Y.; Koh, K.; Chen, H. Review of interface modification based on 2D nanomaterials for surface plasmon resonance biosensors. *ACS Photonics* **2022**, *9*, 3807–3823. [CrossRef]
21. Puumala, L.S.; Grist, S.M.; Morales, J.M.; Bickford, J.R.; Chrostowski, L.; Shekhar, S.; Cheung, K.C. Biofunctionalization of multiplexed silicon photonic biosensors. *Biosensors* **2022**, *13*, 53. [CrossRef] [PubMed]

22. Peng, T.; Deng, Z.; He, J.; Li, Y.; Tan, Y.; Peng, Y.; Wang, X.-Q.; Tan, W. Functional nucleic acids for cancer theranostics. *Coord. Chem. Rev.* **2020**, *403*, 213080. [CrossRef]
23. Alsaafin, A.; McKeague, M. Functional nucleic acids as in vivo metabolite and ion biosensors. *Biosens. Bioelectron.* **2017**, *94*, 94–106. [CrossRef] [PubMed]
24. Liu, R.; McConnell, E.M.; Li, J.; Li, Y. Advances in functional nucleic acid based paper sensors. *J. Mater. Chem. B* **2020**, *8*, 3213–3230. [CrossRef]
25. Li, Y.; Yi, L. *Functional Nucleic Acids for Analytical Applications*; Springer: Berlin/Heidelberg, Germany, 2009.
26. Mok, W.; Li, Y. Recent progress in nucleic acid aptamer-based biosensors and bioassays. *Sensors* **2008**, *8*, 7050–7084. [CrossRef]
27. Zhou, W.; Saran, R.; Liu, J. Metal sensing by DNA. *Chem. Rev.* **2017**, *117*, 8272–8325. [CrossRef]
28. Zhao, H.; Yuan, X.; Yu, J.; Huang, Y.; Shao, C.; Xiao, F.; Lin, L.; Li, Y.; Tian, L. Magnesium-stabilized multifunctional DNA nanoparticles for tumor-targeted and pH-responsive drug delivery. *ACS Appl. Mater. Interfaces* **2018**, *10*, 15418–15427. [CrossRef]
29. Wu, Y.; Yang, Z.; Lu, Y. Photocaged functional nucleic acids for spatiotemporal imaging in biology. *Curr. Opin. Biotechnol.* **2020**, *57*, 95–104. [CrossRef]
30. Lu, Y.; Liu, J. Functional DNA nanotechnology: Emerging applications of DNAzymes and aptamers. *Curr. Opin. Biotechnol.* **2006**, *17*, 580–588. [CrossRef]
31. Zhang, J.; Lan, T.; Lu, Y. Molecular engineering of functional nucleic acid nanomaterials toward in vivo applications. *Adv. Healthcare Mater.* **2019**, *8*, 1801158. [CrossRef]
32. Ono, A.; Togashi, H. Highly selective oligonucleotide-based sensor for mercury (II) in aqueous solutions. *Angew. Chem. Int. Ed. Engl.* **2004**, *43*, 4300–4302. [CrossRef]
33. Du, J.; Liu, M.; Lou, X.; Zhao, T.; Wang, Z.; Xue, Y.; Zhao, J.; Xu, Y. Highly sensitive and selective chip-based fluorescent sensor for mercuric ion: Development and comparison of turn-on and turn-off systems. *Anal. Chem.* **2012**, *84*, 8060–8066. [CrossRef]
34. Lou, X.; Zhao, T.; Liu, R.; Ma, J.; Xiao, Y. Self-assembled DNA monolayer buffered dynamic ranges of mercuric electrochemical sensor. *Anal. Chem.* **2013**, *85*, 7574–7580. [CrossRef] [PubMed]
35. Peng, D.; Li, Y.Q.; Huang, Z.C.; Liang, R.P.; Qiu, J.D.; Liu, J.W. Efficient DNA-catalyzed porphyrin metalation for fluorescent ratiometric Pb^{2+} detection. *Anal. Chem.* **2019**, *91*, 11403–11408. [CrossRef] [PubMed]
36. Xu, L.; Shen, X.; Hong, S.; Wang, J.; Zhang, Y.; Wang, H.; Zhang, J.; Pei, R. Turn-on and label-free fluorescence detection of lead ions based on target-induced G-quadruplex formation. *Chem. Commun.* **2015**, *51*, 8165–8168. [CrossRef]
37. Li, T.; Dong, S.J.; Wang, E.K. A lead(II)-driven DNA molecular device for turn-on fluorescence detection of lead(II) ion with high selectivity and sensitivity. *J. Am. Chem. Soc.* **2010**, *132*, 13156–13157. [CrossRef] [PubMed]
38. Li, T.; Wang, E.K.; Dong, S.J. Lead(II)-induced allosteric G-quadruplex DNAzyme as a colorimetric and chemiluminescence sensor for highly sensitive and selective Pb^{2+} detection. *Anal. Chem.* **2010**, *82*, 1515–1520. [CrossRef]
39. Ono, A.; Cao, S.; Togashi, H.; Tashiro, M.; Fujimoto, T.; Machinami, T.; Oda, S.; Miyake, Y.; Okamoto, I.; Tanaka, Y. Specific interactions between silver(I) ions and cytosine-cytosine pairs in DNA duplexes. *Chem. Commun.* **2008**, *39*, 4825–4827. [CrossRef]
40. He, F.; Tang, Y.L.; Wang, S.; Li, Y.L.; Zhu, D.B. Fluorescent amplifying recognition for DNA G-quadruplex folding with a cationic conjugated polymer: A platform for homogeneous potassium detection. *J. Am. Chem. Soc.* **2005**, *127*, 12343–12346. [CrossRef]
41. Zheng, D.; Zou, R.; Lou, X. Label-free fluorescent detection of ions, proteins, and small molecules using structure-switching aptamers, SYBR gold, and exonuclease I. *Anal. Chem.* **2012**, *84*, 3554–3560. [CrossRef]
42. Wang, T.; Chen, C.; Larcher, L.M.; Barrero, R.A.; Veedu, R.N. Three decades of nucleic acid aptamer technologies: Lessons learned, progress and opportunities on aptamer development. *Biotechnol. Adv.* **2019**, *37*, 28–50. [CrossRef]
43. Willner, I.; Shlyahovsky, B.; Zayats, M.; Willner, B. DNAzymes for sensing, nanobiotechnology and logic gate applications. *Chem. Soc. Rev.* **2008**, *37*, 1153–1165. [CrossRef]
44. Yu, H.; Alkhamis, O.; Canoura, J.; Liu, Y.; Xiao, Y. Advances and challenges in small-molecule DNA aptamer isolation, characterization, and sensor development. *Angew. Chem. Int. Ed. Engl.* **2021**, *60*, 16800–16823. [CrossRef] [PubMed]
45. Guo, W.; Zhang, C.; Ma, T.; Liu, X.; Chen, Z.; Li, S.; Deng, Y. Advances in aptamer screening and aptasensors' detection of heavy metal ions. *J. Nanobiotechnol.* **2021**, *19*, 166. [CrossRef] [PubMed]
46. Majdinasab, M.; Hayat, A.; Marty, J.L. Aptamer-based assays and aptasensors for detection of pathogenic bacteria in food samples. *TrAC Trends Anal. Chem.* **2018**, *107*, 60–77. [CrossRef]
47. Lou, B.; Liu, Y.; Shi, M.; Chen, J.; Li, K.; Tan, Y.; Chen, L.; Wu, Y.; Wang, T.; Liu, X.; et al. Aptamer-based biosensors for virus protein detection. *TrAC Trends Anal. Chem.* **2022**, *157*, 116738. [CrossRef]
48. Lake, R.J.; Yang, Z.; Zhang, J.; Lu, Y. DNAzymes as activity-based sensors for metal Ions: Recent applications, demonstrated advantages, current challenges, and future directions. *Acc. Chem. Res.* **2019**, *52*, 3275–3286. [CrossRef]
49. Liu, J.W.; Lu, Y. Adenosine-dependent assembly of aptazyme-functionalized gold nanoparticles and its application as a colorimetric biosensor. *Anal. Chem.* **2004**, *76*, 1627–1632. [CrossRef] [PubMed]
50. Zhao, J.; Lu, Z.; Wang, S.; Wei, Z.; Zhou, J.; Ren, S.; Lou, X. Nanoscale affinity double layer overcomes the poor antimatrix interference capability of aptamers. *Anal. Chem.* **2021**, *93*, 4317–4325. [CrossRef]
51. Long, F.; Gao, C.; Shi, H.C.; He, M.; Zhu, A.N.; Klibanov, A.M.; Gu, A.Z. Reusable evanescent wave DNA biosensor for rapid, highly sensitive, and selective detection of mercury ions. *Biosens. Bioelectron.* **2011**, *26*, 4018–4023. [CrossRef]
52. Cheng, Y.; Wang, H.; Zhuo, Y.; Song, D.; Li, C.; Zhu, A.; Long, F. Reusable smartphone-facilitated mobile fluorescence biosensor for rapid and sensitive on-site quantitative detection of trace pollutants. *Biosens. Bioelectron.* **2022**, *199*, 113863. [CrossRef]

53. Ahmad, M.; Hench, L.L. Effect of taper geometries and launch angle on evanescent wave penetration depth in optical fibers. *Biosens. Bioelectron.* **2005**, *20*, 1312–1319. [CrossRef]
54. Song, D.; Yang, R.; Fang, S.; Liu, Y.; Long, F. A FRET-based dual-color evanescent wave optical fiber aptasensor for simultaneous fluorometric determination of aflatoxin M1 and ochratoxin A. *Microchim. Acta* **2018**, *185*, 508. [CrossRef] [PubMed]
55. Fang, S.; Song, D.; Zhuo, Y.; Chen, Y.; Zhu, A.; Long, F. Simultaneous and sensitive determination of *Escherichia coli* O157:H7 and Salmonella Typhimurium using evanescent wave dual-color fluorescence aptasensor based on micro/nano size effect. *Biosens. Bioelectron.* **2021**, *185*, 113288. [CrossRef] [PubMed]
56. Song, D.; Liu, J.; Xu, W.; Han, X.; Wang, H.; Zhuo, Y.; Li, C.; Long, F. On-site rapid and simultaneous detection of acetamiprid and fipronil using a dual-fluorescence lab-on-fiber biosensor. *Microchim. Acta* **2022**, *189*, 234. [CrossRef] [PubMed]
57. Song, D.; Yang, R.; Wang, H.; Fang, S.; Liu, Y.; Long, F.; Zhu, A. Development of dual-color total internal reflection fluorescence biosensor for simultaneous quantitation of two small molecules and their affinity constants with antibodies. *Biosens. Bioelectron.* **2019**, *126*, 824–830. [CrossRef]
58. Song, D.; Yang, R.; Fang, S.; Liu, Y.; Liu, J.; Xu, W.; Long, F.; Zhu, A. A novel dual-color total internal reflection fluorescence detecting platform using compact optical structure and silicon-based photodetector. *Talanta* **2019**, *196*, 78–84. [CrossRef]
59. Liu, Z.; Zhang, W.; Zhang, X.; Wang, S.; Xia, Z.; Guo, X.; Zhao, Y.; Wang, P.; Wang, X.-H. Microstructured optical fiber-enhanced light-matter interaction enables highly sensitive exosome-based liquid biopsy of breast cancer. *Anal. Chem.* **2023**, *95*, 1095–1105. [CrossRef]
60. Zhou, Y.; Wang, H.; Song, D.; Li, Z.; Han, S.; Long, F.; Zhu, A. Simple, rapid, and sensitive on-site detection of Hg^{2+} in water samples through combining portable evanescent wave optofluidic biosensor and fluorescence resonance energy transfer principle. *Anal. Chim. Acta* **2021**, *1155*, 338351. [CrossRef]
61. Fang, S.; Song, D.; Zhu, A.; Long, F. Nanoporous layer fiber biosensing platform for real time culture- and separation-free detecting bacterial pathogens and measuring their susceptibility to antibiotics. *Sens. Actuators B* **2020**, *325*, 128748. [CrossRef]
62. Tran, N.H.T.; Kim, J.; Phan, T.B.; Khym, S.; Ju, H. Label-free optical biochemical sensors via liquid-cladding-induced modulation of waveguide modes. *ACS Appl. Mater. Interfaces* **2017**, *9*, 31478–31487. [CrossRef]
63. Jia, Y.; Zhao, S.; Li, D.; Yang, J.; Yang, L. Portable chemiluminescence optical fiber aptamer-based biosensors for analysis of multiple mycotoxins. *Food Control* **2023**, *144*, 109361. [CrossRef]
64. Wang, R.; Zhou, X.; Shi, H.; Luo, Y. T-T mismatch-driven biosensor using triple functional DNA-protein conjugates for facile detection of Hg2+. *Biosens. Bioelectron.* **2016**, *78*, 418–422. [CrossRef]
65. Wang, R.; Zhou, X.; Shi, H. Triple functional DNA-protein conjugates: Signal probes for Pb(2+) using evanescent wave-induced emission. *Biosens. Bioelectron.* **2015**, *74*, 78–84. [CrossRef]
66. Wang, R.; Xiang, Y.; Zhou, X.; Liu, L.H.; Shi, H. A reusable aptamer-based evanescent wave all-fiber biosensor for highly sensitive detection of Ochratoxin A. *Biosens. Bioelectron.* **2015**, *66*, 11–18. [CrossRef] [PubMed]
67. Long, F.; Wu, S.; He, M.; Tong, T.; Shi, H. Ultrasensitive quantum dots-based DNA detection and hybridization kinetics analysis with evanescent wave biosensing platform. *Biosens. Bioelectron.* **2011**, *26*, 2390–2395. [CrossRef] [PubMed]
68. Baliyan, A.; Sital, S.; Tiwari, U.; Gupta, R.; Sharma, E.K. Long period fiber grating based sensor for the detection of triacylglycerides. *Biosens. Bioelectron.* **2016**, *79*, 693–700. [CrossRef]
69. Kumar, P.; Gupta, A.; Dhakate, S.R.; Mathur, R.B.; Nagar, S.; Gupta, V.K. Covalent immobilization of xylanase produced from Bacillus pumilus SV-85S on electrospun polymethyl methacrylate nanofiber membrane. *Biotechnol. Appl. Biochem.* **2013**, *60*, 162–169. [CrossRef]
70. Mahmoudifard, M.; Soudi, S.; Soleimani, M.; Hosseinzadeh, S.; Esmaeili, E.; Vossoughi, M. Efficient protein immobilization on polyethersolfone electrospun nanofibrous membrane via covalent binding for biosensing applications. *Mater. Sci. Eng. C* **2016**, *58*, 586–594. [CrossRef] [PubMed]
71. Wei, Z.; Cheng, X.; Li, J.; Wang, G.; Mao, J.; Zhao, J.; Lou, X. Ultrasensitive evanescent wave optical fiber aptasensor for online, continuous, type-specific detection of sulfonamides in environmental water. *Anal. Chim. Acta* **2022**, *1233*, 340505. [CrossRef]
72. Wang, S.; Gao, H.; Wei, Z.; Zhou, J.; Ren, S.; He, J.; Luan, Y.; Lou, X. Shortened and multivalent aptamers for ultrasensitive and rapid detection of alternariol in wheat using optical waveguide sensors. *Biosens. Bioelectron.* **2022**, *196*, 113702. [CrossRef]
73. Tang, Y.; Long, F.; Gu, C.; Wang, C.; Han, S.; He, M. Reusable split-aptamer-based biosensor for rapid detection of cocaine in serum by using an all-fiber evanescent wave optical biosensing platform. *Anal. Chim. Acta* **2016**, *933*, 182–188. [CrossRef] [PubMed]
74. Qiu, Y.; Tang, Y.; Li, B.; He, M. Rapid detection of cocaine using aptamer-based biosensor on an evanescent wave fibre platform. *R. Soc. Open Sci.* **2018**, *5*, 180821. [CrossRef] [PubMed]
75. Yildirim, N.; Long, F.; He, M.; Shi, H.C.; Gu, A.Z. A portable optic fiber aptasensor for sensitive, specific and rapid detection of bisphenol-A in water samples. *Environ. Sci. Process. Impacts* **2014**, *16*, 1379–1386. [CrossRef] [PubMed]
76. Zhu, X.; Wang, R.; Xia, K.; Zhou, X.; Shi, H. Nucleic acid functionalized fiber optic probes for sensing in evanescent wave: Optimization and application. *RSC Adv.* **2019**, *9*, 2316–2324. [CrossRef]
77. Zhao, H.; Ren, S.; Wei, Z.; Lou, X. Evanescent wave optical-fiber aptasensor for rapid detection of zearalenone in corn with unprecedented sensitivity. *Biosensors* **2022**, *12*, 438. [CrossRef]

78. Tang, Y.; Gu, C.; Wang, C.; Song, B.; Zhou, X.; Lou, X.; He, M. Evanescent wave aptasensor for continuous and online aminoglycoside antibiotics detection based on target binding facilitated fluorescence quenching. *Biosens. Bioelectron.* **2018**, *102*, 646–651. [CrossRef]
79. Han, S.; Zhou, X.; Tang, Y.; He, M.; Zhang, X.; Shi, H.; Xiang, Y. Practical, highly sensitive, and regenerable evanescent-wave biosensor for detection of Hg(2+) and Pb(2+) in water. *Biosens. Bioelectron.* **2016**, *80*, 265–272. [CrossRef]
80. Zhu, Q.; Liu, L.; Wang, R.; Zhou, X. A split aptamer (SPA)-based sandwich-type biosensor for facile and rapid detection of streptomycin. *J. Hazard. Mater.* **2021**, *403*, 123941. [CrossRef]
81. Baldini, F.; Homola, J.; Lieberman, R.A.; A, G.; Sai, V.V.R. U-bent plastic optical fiber based plasmonic biosensor for nucleic acid detection. In *Optical Sensors*; Proc. of SPIE: Prague, Czech Republic, 2017; p. 1023113.
82. Abel, A.P.; Weller, M.G.; Duveneck, G.L.; Ehrat, M.; Widmer, H.M. Fiber-optic evanescent wave biosensor for the detection of oligonucleotides. *Anal. Chem.* **1996**, *68*, 2905–2912. [CrossRef]
83. Kleinjung, F.; Klussmann, S.; Erdmann, V.A.; Scheller, F.W.; Furste, J.P.; Bier, F.F. High-affinity RNA as a recognition element in a biosensor. *Anal. Chem.* **1998**, *70*, 328–331. [CrossRef]
84. Liu, X.; Tan, W. A fiber-optic evanescent wave DNA biosensor based on novel molecular beacons. *Anal. Chem.* **1999**, *71*, 5054–5059. [CrossRef] [PubMed]
85. Yildirim, N.; Long, F.; Gao, C.; He, M.; Shi, H.C.; Gu, A.Z. Aptamer-based optical biosensor for rapid and sensitive detection of 17beta-estradiol in water samples. *Environ. Sci. Technol.* **2012**, *46*, 3288–3294. [CrossRef]
86. Liu, L.H.; Zhou, X.H.; Shi, H.C. Portable optical aptasensor for rapid detection of mycotoxin with a reversible ligand-grafted biosensing surface. *Biosens. Bioelectron.* **2015**, *72*, 300–305. [CrossRef] [PubMed]
87. Palegrosdemange, C.; Simon, E.S.; Prime, K.L.; Whitesides, G.M. Formation of self-assembled monolayers by chemisorption of derivatives of oligo(ethylene glycol) of structure $HS(CH_2)_{11}(OCH_2CH_2)$meta-OH on gold. *J. Am. Chem. Soc.* **1991**, *113*, 12–20. [CrossRef]
88. Feldman, K.; Hahner, G.; Spencer, N.D.; Harder, P.; Grunze, M. Probing resistance to protein adsorption of oligo(ethylene glycol)-terminated self-assembled monolayers by scanning force microscopy. *J. Am. Chem. Soc.* **1999**, *121*, 10134–10141. [CrossRef]
89. Lou, X.; He, L. Surface passivation using oligo(ethylene glycol) in ATRP-assisted DNA detection. *Sens. Actuators B Chem.* **2008**, *129*, 225–230. [CrossRef]
90. Herne, T.M.; Tarlov, M.J. Characterization of DNA probes immobilized on gold surfaces. *J. Am. Chem. Soc.* **1997**, *119*, 8916–8920. [CrossRef]
91. Chen, S.; Zheng, J.; Li, L.; Jiang, S. Strong resistance of phosphorylcholine self-assembled monolayers to protein adsorption: Insights into nonfouling properties of zwitterionic materials. *J. Am. Chem. Soc.* **2005**, *127*, 14473–14478. [CrossRef]
92. Erfani, A.; Seaberg, J.; Aichele, C.P.; Ramsey, J.D. Interactions between biomolecules and zwitterionic moieties: A review. *Biomacromolecules* **2020**, *21*, 2557–2573. [CrossRef]
93. Liu, B.; Huang, P.-J.J.; Zhang, X.; Wang, F.; Pautler, R.; Ip, A.C.F.; Liu, J. Parts-per-million of polyethylene glycol as a non-Interfering blocking agent for homogeneous biosensor development. *Anal. Chem.* **2013**, *85*, 10045–10050. [CrossRef] [PubMed]
94. Huang, T.T.; Sturgis, J.; Gomez, R.; Geng, T.; Bashir, R.; Bhunia, A.K.; Robinson, J.P.; Ladisch, M.R. Composite surface for blocking bacterial adsorption on protein biochips. *Biotechnol. Bioeng.* **2003**, *81*, 618–624. [CrossRef] [PubMed]
95. Wang, R.; Zhou, X.; Zhu, X.; Yang, C.; Liu, L.; Shi, H. Isoelectric bovine serum albumin: Robust blocking agent for enhanced performance in optical-Fiber based DNA sensing. *ACS Sens.* **2017**, *2*, 257–262. [CrossRef] [PubMed]
96. Chen, A.; Yan, M.; Yang, S. Split aptamers and their applications in sandwich aptasensors. *TrAC Trends Anal. Chem.* **2016**, *80*, 581–593. [CrossRef]
97. Khoshbin, Z.; Housaindokht, M.R.; Verdian, A.; Bozorgmehr, M.R. Simultaneous detection and determination of mercury (II) and lead (II) ions through the achievement of novel functional nucleic acid-based biosensors. *Biosens. Bioelectron.* **2018**, *116*, 130–147. [CrossRef]
98. Du, Z.-H.; Li, X.-Y.; Tian, J.-J.; Zhang, Y.-Z.; Tian, H.-T.; Xu, W.-T. Progress on detection of metals ions by functional nucleic acids biosensor. *Chin. J. Anal. Chem.* **2018**, *46*, 995–1004. [CrossRef]
99. Long, F.; Zhu, A.; Wang, H. Optofluidics-based DNA structure-competitive aptasensor for rapid on-site detection of lead(II) in an aquatic environment. *Anal. Chim. Acta* **2014**, *849*, 43–49. [CrossRef]
100. Yi, Z.; Zhou, Y.; Ren, Y.; Hu, W.; Long, F.; Zhu, A. A novel sensitive DNAzyme-based optical fiber evanescent wave biosensor for rapid detection of Pb(2+) in human serum. *Analyst* **2022**, *147*, 1467–1477. [CrossRef]
101. Yang, Y.; Li, W.; Liu, J. Review of recent progress on DNA-based biosensors for Pb(2+) detection. *Anal. Chim. Acta* **2021**, *1147*, 124–143. [CrossRef]
102. Li, L.; Wen, Y.; Xu, L.; Xu, Q.; Song, S.; Zuo, X.; Yan, J.; Zhang, W.; Liu, G. Development of mercury (II) ion biosensors based on mercury-specific oligonucleotide probes. *Biosens. Bioelectron.* **2016**, *75*, 433–445. [CrossRef]
103. Piunno, P.A.; Krull, U.J.; Hudson, R.H.; Damha, M.J.; Cohen, H. Fiber-optic DNA sensor for fluorometric nucleic acid determination. *Anal. Chem.* **1995**, *67*, 2635–2643. [CrossRef] [PubMed]
104. Wu, J.; Zhang, X.; Liu, B.; Zhang, H.; Song, B. Square-microfiber-integrated biosensor for label-free DNA hybridization detection. *Sens. Actuators B Chem.* **2017**, *252*, 1125–1131. [CrossRef]
105. Chauhan, A.; Dhenadhayalan, N.; Lin, K.-C. Evanescent wave cavity ring-down spectroscopy based interfacial sensing of prostate-specific antigen. *Sens. Actuators B Chem.* **2021**, *330*, 129284. [CrossRef]

106. Liyanage, T.; Lai, M.; Slaughter, G. Label-free tapered optical fiber plasmonic biosensor. *Anal. Chim. Acta* **2021**, *1169*, 338629. [CrossRef] [PubMed]
107. Xiao, R.; Rong, Z.; Long, F.; Liu, Q. Portable evanescent wave fiber biosensor for highly sensitive detection of Shigella. *Spectrochim. Acta Part A* **2014**, *132*, 1–5. [CrossRef] [PubMed]
108. Liu, J.; Zhou, X.; Shi, H. An optical biosensor-based quantification of the microcystin synthetase a gene: Early warning of toxic cyanobacterial blooming. *Anal. Chem.* **2018**, *90*, 2362–2368. [CrossRef]
109. Yang, Y.; Liu, J.; Zhou, X. A CRISPR-based and post-amplification coupled SARS-CoV-2 detection with a portable evanescent wave biosensor. *Biosens. Bioelectron.* **2021**, *190*, 113418. [CrossRef]
110. Zhu, X.; Wang, R.; Zhou, X.; Shi, H. Free-energy-driven lock/open assembly-based optical DNA sensor for cancer-related microRNA detection with a shortened time-to-result. *ACS Appl. Mater. Interfaces* **2017**, *9*, 25789–25795. [CrossRef] [PubMed]
111. Wang, R.; Zhu, X.; Xing, Y.; Memon, A.G.; Shi, H.; Zhou, X. Multitag-regulated cascade reaction: A generalizable ultrasensitive microRNA biosensing approach for cancer prognosis. *ACS Appl. Mater. Interfaces* **2019**, *11*, 36444–36448. [CrossRef]
112. Qiu, H.; Gao, S.; Chen, P.; Li, Z.; Liu, X.; Zhang, C.; Xu, Y.; Jiang, S.; Yang, C.; Huo, Y.; et al. Evanescent wave absorption sensor based on tapered multimode fiber coated with monolayer graphene film. *Opt. Commun.* **2016**, *366*, 275–281. [CrossRef]
113. Liang, L.; Jin, L.; Ran, Y.; Sun, L.-P.; Guan, B.-O. Interferometric detection of microRNAs using a capillary optofluidic sensor. *Sens. Actuators B Chem.* **2017**, *242*, 999–1006. [CrossRef]
114. Das, S.; Agarwal, D.K.; Mandal, B.; Rao, V.R.; Kundu, T. Detection of the chilli leaf curl virus using an attenuated total reflection-mediated localized surface-plasmon-resonance-based optical platform. *ACS Omega* **2021**, *6*, 17413–17423. [CrossRef] [PubMed]
115. Wan, Y.; Zhao, J.; He, J.; Lou, X. Nano-Affi: A solution-phase, label-free, colorimetric aptamer affinity assay based on binding-inhibited aggregation of gold nanoparticles. *Analyst* **2020**, *145*, 4276–4282. [CrossRef] [PubMed]
116. Qiao, N.; Li, J.; Wu, X.; Diao, D.; Zhao, J.; Li, J.; Ren, X.; Ding, X.; Shangguan, D.; Lou, X. Speeding up in vitro discovery of structure-switching aptamers via magnetic cross-linking precipitation. *Anal. Chem.* **2019**, *91*, 13383–13389. [CrossRef]
117. Li, S.; Zhu, L.; Zhu, L.; Mei, X.; Xu, W. A sandwich-based evanescent wave fluorescent biosensor for simple, real-time exosome detection. *Biosens. Bioelectron.* **2022**, *200*, 113902. [CrossRef]
118. Fang, S.; Song, D.; Liu, Y.; Xu, W.; Liu, J.; Han, X.; Long, F. Study on evanescent wave fluorescence aptasensor for direct and rapid detection of *Escherichia coli* O157:H7. *Biotechnol. Bull.* **2020**, *36*, 228–234.
119. Song, D.; Han, X.; Xu, W.; Liu, J.; Zhuo, Y.; Zhu, A.; Long, F. Target nucleic acid amplification-free detection of *Escherichia coli* O157:H7 by CRISPR/Cas12a and hybridization chain reaction based on an evanescent wave fluorescence biosensor. *Sens. Actuators B Chem.* **2023**, *376*, 133005–133013. [CrossRef]
120. Song, D.; Xu, W.; Han, X.; Wang, H.; Zhuo, Y.; Liu, J.; Zhu, A.; Long, F. CRISPR/Cas12a-powered evanescent wave fluorescence nanobiosensing platform for nucleic acid amplification-free detection of Staphylococcus aureus with multiple signal enhancements. *Biosens. Bioelectron.* **2023**, *225*, 115109. [CrossRef]
121. Qian, S.W.; Chang, D.R.; He, S.S.; Li, Y.F. Aptamers from random sequence space: Accomplishments, gaps and future considerations. *Anal. Chim. Acta* **2022**, *1196*, 339511. [CrossRef]
122. Jing, M.; Bowser, M.T. Methods for measuring aptamer-protein equilibria: A review. *Anal. Chim. Acta* **2011**, *686*, 9–18. [CrossRef]
123. McKeague, M.; De Girolamo, A.; Valenzano, S.; Pascale, M.; Ruscito, A.; Velu, R.; Frost, N.R.; Hill, K.; Smith, M.; McConnell, E.M.; et al. Comprehensive analytical comparison of strategies used for small molecule aptamer evaluation. *Anal. Chem.* **2015**, *87*, 8608–8612. [CrossRef] [PubMed]
124. Gao, H.; Zhao, J.; Huang, Y.; Cheng, X.; Wang, S.; Han, Y.; Xiao, Y.; Lou, X. Universal design of structure-switching aptamers with signal reporting functionality. *Anal. Chem.* **2019**, *91*, 14514–14521. [CrossRef] [PubMed]
125. Goode, J.A.; Rushworth, J.V.H.; Millner, P.A. Biosensor regeneration: A review of common techniques and outcomes. *Langmuir* **2015**, *31*, 6267–6276. [CrossRef] [PubMed]

biosensors

MDPI

Review

Biosensors for the Detection of Enzymes Based on Aggregation-Induced Emission

Fengli Gao [1], Gang Liu [1], Mingyi Qiao [1], Yingying Li [1] and Xinyao Yi [2,*]

[1] College of Chemistry and Chemical Engineering, Anyang Normal University, Anyang 455000, China
[2] College of Chemistry and Chemical Engineering, Central South University, Changsha 410083, China
* Correspondence: yixinyao@csu.edu.cn

Abstract: Enzymes play a critical role in most complex biochemical processes. Some of them can be regarded as biomarkers for disease diagnosis. Taking advantage of aggregation-induced emission (AIE)-based biosensors, a series of fluorogens with AIE characteristics (AIEgens) have been designed and synthesized for the detection and imaging of enzymes. In this work, we summarized the advances in AIEgens-based probes and sensing platforms for the fluorescent detection of enzymes, including proteases, phosphatases, glycosidases, cholinesterases, telomerase and others. The AIEgens involve organic dyes and metal nanoclusters. This work provides valuable references for the design of novel AIE-based sensing platforms.

Keywords: aggregation-induced emission; enzymes; fluorescent biosensors; organic dyes; metal nanoclusters

1. Introduction

Enzymes are a family of proteins or RNA with specific catalytic activities toward the substrates. They are involved in most of the complex biochemical processes, including gene expression, metabolic pathways, cell growth and differentiation, and signaling [1]. Abnormal manifestations of enzyme activities could be indicative of humans' health status. Thus, enzymes can be used as biomarkers for disease diagnosis [2–4]. For example, changes in the activity and content of proteases may cause some diseases, such as cancers, acquired immune deficiency syndrome, and neurodegenerative diseases [5,6]. Phosphatases have been considered important indicators for some diseases, including anemia, chronic nephritis, hypothyroidism, and hepatobiliary as well as bone diseases [7]. Evaluated concentrations of γ-glutamyltranspeptidase have been found in hepatocellular carcinoma as well as cervical and ovarian cancers [8]. Excessive use of organophosphorus pesticides can cause the inhibition of acetylcholinesterase (AChE) activity and the accumulation of neurotransmitter acetylcholine, eventually leading to the incidence of Alzheimer's and Parkinson's diseases [9]. In acute pancreatitis, lipase concentration in serum is at least three times the normal level [10]. Increased leucine aminopeptidase expression is closely related to many diseases, such as hepatic dysfunction and liver cancer [11].

Owing to the importance of enzymes in clinical diagnosis, various novel methods have been developed for the accurate and sensitive determination of enzymes, such as fluorescence, colorimetry, electrochemistry, electrochemiluminescence, and photoelectrochemistry [12,13]. Among them, fluorescent biosensors have attracted extensive attentions due to their excellent advantages of inexpensive equipment, rapid response, high sensitivity, and real-time and on-site detection [14,15]. However, traditional fluorophores with planar and intermolecular interaction may suffer from the aggregation-caused quenching (ACQ) problem at high concentrations or in the solid state [16], which will decrease the sensitivity and limit the applications of fluorescent biosensors in vivo detection and imaging of enzymes. Since Tang's group first introduced the concept of aggregation-induced emission (AIE) in 2001, AIE-based techniques have opened up the field with huge potential practical

Citation: Gao, F.; Liu, G.; Qiao, M.; Li, Y.; Yi, X. Biosensors for the Detection of Enzymes Based on Aggregation-Induced Emission. *Biosensors* **2022**, *12*, 953. https://doi.org/10.3390/bios12110953

Received: 12 October 2022
Accepted: 28 October 2022
Published: 1 November 2022

applications [17]. Unlike ACQ fluorophores, fluorogens with AIE features (AIEgens) exhibit a remarkable optical property and strong resistance toward photobleaching. Generally, AIEgens in the molecular state are non-emissive, because they can consume the excitation energy through the active intramolecular motion in a non-radiative decay manner. However, under the restrictions of intermolecular motion, AIEgens in the aggregate state will produce significantly enhanced and stable emission. Thus, versatile AIEgens have been used as functional components to prepare light-up probes. They have been used in a broad range of applications, including organic optoelectronic devices, biosensing, bioimaging, photodynamic therapy, photothermal therapy, and so on [18–21].

Within the continuous exploration of the new AIE systems, more mechanisms have been proposed as branches of AIE, including crystallization-induced emission, room-temperature phosphorescence, clusterization-triggered emission, and so on [22,23]. Besides tetraphenylsilols and tetraphenylethylene, versatile AIEgens with different structures have been innovatively synthesized for various applications under the guidance of these AIE mechanisms in recent years, such as tetraphenylpyrazines, perylene, organoboron or carborane complexes, cyclooctatetrathiophene, and so on [24,25]. Through modification of the π-conjugation systems with different functional groups, the absorption/emission wavelengths of AIEgens can cover the whole visible and near-infrared range. When the ACQ dyes were modified with AIEgens, the resulting probes may exhibit AIE characteristics. Moreover, some nanomaterials have also been reported to possess AIE properties, including quantum dots (QDs), copper nanoclusters (CuNCs), gold nanoclusters (AuNCs), silver nanoclusters (AgNCs) and carbon quantum dots [26,27]. The aggregation of AIEgens can be triggered by different stimuli, such as solubility change, hydrophobic assembly, hydrogen bonding, target-receptor binding, and electrostatic interactions. By linking AIEgens to the target ligands or reactive groups, many AIE light-up sensors have been developed for the signal-on detection of various targets, including ions, small molecules, microenvironment sensing (e.g., pH, temperature and viscosity), biological macromolecules (e.g., toxin, nucleic acids, proteins, enzymes), cellular processes and pathogens [28,29]. Thereby, the in vitro determination and in vivo monitoring of enzymes have been realized using AIEgens to label peptide probes due to their good biocompatibility, adjustable fluorescence wavelength, ultra-low background signal, and strong photobleaching resistance [30,31]. Moreover, peptides can improve the hydrophilicity of AIEgens, especially in imaging applications. In the presence of target enzymes, AIEgens-labeled peptide probes would be cleaved, causing the aggregation of AIEgens and thus generating a bright AIE luminescence for the in situ imaging of enzymes. Based on the approaches to activate the restriction of intramolecular motion and trigger the AIE process, the detection mechanisms of the works involved in this review could be classified into three categories: (i) the electrostatic interactions between AIEgens themselves or between AIEgens and other charged species (e.g., polymers and nanomaterials) cause the aggregation of AIEgens, (ii) enzyme catalysis adjusts the solubility of AIEgens and triggers the appearance of nanoaggregates, and (iii) enzyme catalysis induces the formation of intramolecular hydrogen bonds that can hamper the restriction of intramolecular motion and produce the effect of excited-state intramolecular proton transfer. These mechanisms have provided versatile approaches for the sensitive and selective detection of enzyme activity in vitro or in vivo.

Some excellent reviews have summarized the progresses in AIE-based applications, which mainly focus on the molecular design, detection mechanism, and AIEgens [32–36]. For instance, Liu et al. reported recent advances in AIE light-up probes for photodynamic therapy [37]. The achievements of tetraphenylethylene (TPE)-based AIE-active sensing probes have been reviewed by Bhosale's group [32]. Wang et al. summarized the development of Schiff base AIEgens for sensing applications [38]. In this work, we aimed to highlight the advances in AIEgens-based probes and sensing platforms for the detection of enzymes. According to the type of enzymes, AIE-based biosensors have been classified into six categories: proteases, phosphatases, glycosidases, cholinesterases, telomerase and oth-

ers. We mainly focus on the enzyme-responsive detection mechanisms and the analytical performances.

2. Proteases

With AIEgens-labeled peptide as the probe, the fluorescent detection and imaging of proteases has been achieved, including chymase, caspases, thrombin, metalloproteinase-2 (MMP-2), furin, carboxypeptidase Y (CPY), autophagy-related cysteine protease ATG4B, and so on (Table 1). The AIEgens involve the derivatives of TPE, PyTPA, (2-(2′-hydroxyphenyl)-4(3H)-quinazolinone (HPQ), pyrene and tetraphenylsilole (BATPS). Moreover, through the integration of AIE and excited-state intramolecular proton transfer (ESIPT) characteristics, some proteases such as aminopeptidase could be determined with leucine-conjugated TPE or tetraarylimidazole scaffolds [39,40]. In this section, we primarily summarized the AIEgen-labeled peptide probes for the detection and in vivo imaging of proteases. Meanwhile, applications of the AIE probes for monitoring apoptosis and tracking drug delivery were also discussed.

Among the different kinds of AIEgens, TPE is most the commonly used for the modification of protease substrates because of its advantages of easy synthesis and functionalization and excellent AIE characteristics [41]. Zhang et al. designed a fluorescent light-up probe for chymase detection. The probe contains the AIEgen TPE-thiophene (TPETH) with red emission in the aggregation state and two chymase-specific peptide (CFTER) sequences (Figure 1A) [42]. In order to improve the water-solubility and decrease the background, three aspartic acid residues (D_3) were introduced to the peptide sequence. The probe of TPETH-2(CFTERD_3) showed nearly no emission in buffer solution. After the enzymatic cleavage, the released hydrophobic TPETH segments could readily assemble into aggregates, lighting up the fluorescence. In order to promote the assembly of TPE and enhance the sensitivity of AIE biosensors, a self-assembly peptide could be incorporated into the probe. For example, Han et al. designed an AIEgen probe using a short self-assembly peptide GFFY to conjugate the protease-responsive peptide and AIEgen residue [43]. After responding to caspase-3, GFFY promoted the ordered assembly of AIEgen residues, substantially restricting the intramolecular motion of AIEgens and greatly improving the sensitivity. In addition, Li et al. designed an AIEgen probe named HPQF for the in situ detection and imaging of endogenous furin (Figure 1B) [44]. The probe consists of a furin-specific peptide (RVRR) and the fluorophore 6-chloro-2-(2-hydroxyphenyl) quinazolin-4(3H)-one (Cl-HPQ). The catalytic cleavage of peptide probes by furin caused the release of insoluble Cl-HPQ precipitates, turning on the fluorescence through the AIE effect.

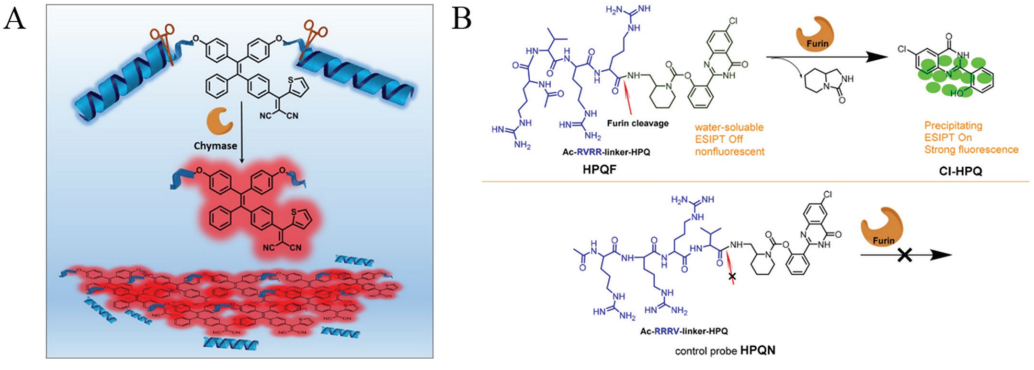

Figure 1. (**A**) Schematic illustration of the functional mechanism of the probe TPETH-2(CFTERD_n). n = 2 or 3 for chymase sensing. Reprinted with permission from ref. [42]. Copyright 2016, American Chemical Society. (**B**) Chemical structure of the activatable probe HPQF and its working mechanism with furin (top), and the molecular design strategy of the negative control non-cleavable probe HPQN (bottom). Reprinted with permission from ref. [44]. Copyright 2018, American Chemical Society.

In order to improve the sensitivity of AIE-based biosensors, Wu et al. developed a two-step sensing system for protease detection based on the peptide probe of RRRRRRGGPLGLAGPra (PyTPA)-NH_2 (MP), negatively charged nanoparticles (NPs) and slippery lubricant-infused porous substrates (SLIPS) (Figure 2) [45]. The water-soluble MP with an AIEgen of PyTPA showed weak fluorescence. Cleavage of MP by MMP-2 promoted the aggregation of the hydrophobic PyTPA-included residues. The aggregates were then electrostatically adsorbed onto the negatively charged NPs on SLIPS. With MMP-2 as the analytical example, the sensitivity was obviously improved in contrast to the previously reported AIE-based methods.

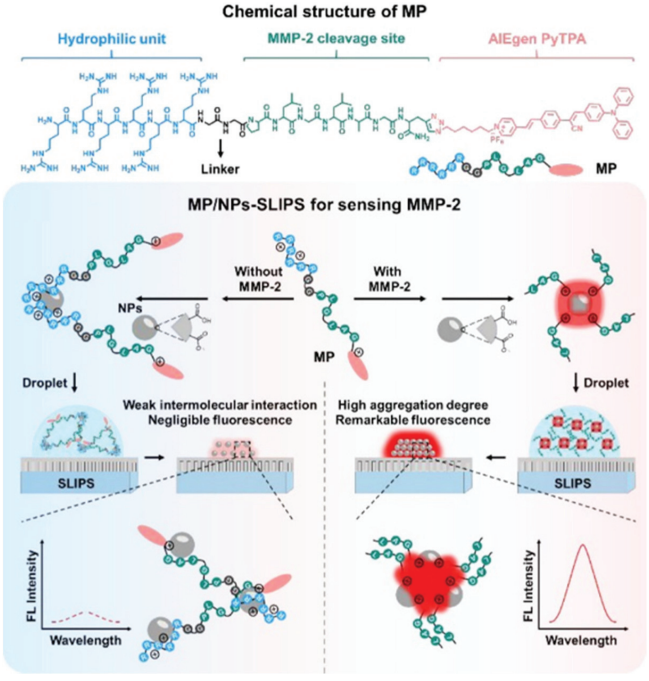

Figure 2. Design of modular peptide-conjugated AIEgen MP and development of the MP/NPs–SLIPS sensing system for sensitively detecting tumor marker MMP-2. Reprinted with permission from ref. [45]. Copyright 2021, American Chemical Society.

Real-time monitoring of apoptosis can provide valuable insights for the early detection of therapeutic effects and the evaluation of disease progress. Shi et al. designed an AIEgen probe for the real-time imaging of cell apoptosis by monitoring the caspase activity (Figure 3A) [46]. The probe consists of a hydrophilic caspase-specific peptide (DEVD) and a hydrophobic AIEgen of TPE unit. The water-soluble probe showed almost no fluorescence in the aqueous phase. Cleavage of the probe by caspase-3/7 led to the formation of hydrophobic TPE residues. The aggregation of TPE residues could restrict the intramolecular rotation of the TPE phenyl ring and populate the radiative decay channel, thus lighting up the fluorescence. Moreover, Ding et al. designed an AIEgen probe for the imaging of cell apoptosis by monitoring the activity of caspase-3 [47]. The probe (Ac-DEVD-TPS-cRGD) consists of a caspase-specific hydrophilic peptide (DEVD), a cell-binding cyclic peptide cRGD and an AIEgen of a tetraphenylsilole (TPS) unit. The two peptides were linked at both ends of the TPS unit. Cleavage of the probe by caspase-3 led to the release of TPS-cRGD. The aggregation of released TPS-cRGD residues lit up the fluorescence, enabling real-time imaging of cell apoptosis. Lately, Yuan et al. reported a dual-signal AIEgen probe for monitoring caspase activity. The probe (TPETH–DVEDIETD–TPS) includes three components: a hydrophilic peptide (DVEDIETD) specific to apoptosis initiator caspase-8 and

effector caspase-3 and two AIEgens with green (TPS) and red (TPETH) emission colors [48]. The probe could be cleaved into a TPETH–DVEDIETD and a TPS unit by caspase-8. The product of TPETH–DVEDIETD could be further cut into a TPETH unit and DVEDIETD by caspase-3. The aggregates of TPS and TPETH emitted green and red fluorescence, respectively.

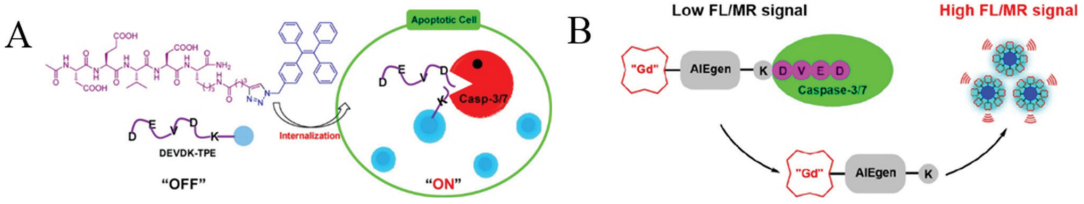

Figure 3. (**A**) Illustration of Ac-DEVDK-TPE for the study of caspase activities. Reprinted with permission from ref. [46]. Copyright 2012, American Chemical Society. (**B**) Schematic illustration of DPBP as a bioprobe for autophagy detection. Reprinted with permission from ref. [49]. Copyright 2019, American Chemical Society.

Effective methods for cancer treatment largely depend on inducing the apoptosis of cancer cells through chemotherapy and/or radiotherapy. Magnetic resonance (MR) imaging is one of the frontiers of experimental and clinical radiology. It has unlimited tissue penetration depth, excellent soft tissue contrast and time–space resolution, without the use of ionizing radiation. Recently, Meade's group reported a bimodal fluorescence–magnetic resonance (FL-MR) probe named CP1 for apoptosis imaging by monitoring the activity of caspase-3/7 (Figure 3B) [49]. The CP1 probe contains three parts: a DOTA-Gd(III) chelate for MR signal enhancement, an AIEgen of the TPE unit, and an enzyme-specific peptide, DEVD. In the presence of caspase-3/7, the water-soluble peptide DEVD was removed, and the resulting Gd(III)-AIEgen (Gad-AIE) conjugates tend to aggregate, thus inducing the increase of FL-MR signals. The dual-signal FL–MR probe was successfully used for the fluorescent imaging of cell apoptosis.

In addition, Yuan et al. designed a protease-responsive chemotherapeutic Pt(IV) prodrug with real-time in situ monitoring of drug release (Figure 4A) [50]. The chemotherapeutic Pt(IV) prodrug was modified with a cell-binding cyclic tripeptide, cRGD, and a TPS-labeled enzyme-specific peptide, DEVD. Pt(IV) could be reduced in active Pt(II) in cells and release the TPS-DEVD simultaneously. The cell apoptosis induced by Pt(II) activated the activity of caspase-3 to cleave TPS-DEVD. The released TPS residues tend to aggregate, thus causing fluorescence enhancement. Chen et al. designed a protease-responsive prodrug (DOX-FCPP-PyTPE, DFP) with AIE characteristics (Figure 4B) [51]. The drug delivery and release in living cells could be controlled and tracked. The DFP prodrug involved three parts: AIEgen PyTPE, functionalized cell-penetrating peptide (FCPP) with a cell-penetrating peptide (CPP) and a short MMP-2-specific peptide (LGLAG), and a therapeutic drug (doxorubicin, DOX). The prodrug itself cannot enter the cells. However, the prodrug could be cleaved by MMP-2 into two components: DOX-linked CPP and a PyTPE-containing peptide segment. The DOX-linked CPP could go inside the cells through the interaction of CPP with cell membrane, thus realizing controlled drug delivery. The hydrophobic PyTPE-containing peptide segments could self-assemble into aggregates to yield yellow fluorescence, thereby achieving the real-time tracking of drug release. Recently, Qin et al. prepared a self-assembly tracking micelle (TPR@DOX) by modifying the RGD peptide and TPE AIEgen on both ends of a caspase-responsive amphiphilic polymer (Figure 4C) [52]. The drug-induced apoptosis activated caspase to cut the DEVD-containing peptide in the polymer, thus releasing the hydrophobic TPE residues to form fluorescent aggregates. The turn-on of fluorescence indicated the successful delivery and release of DOX.

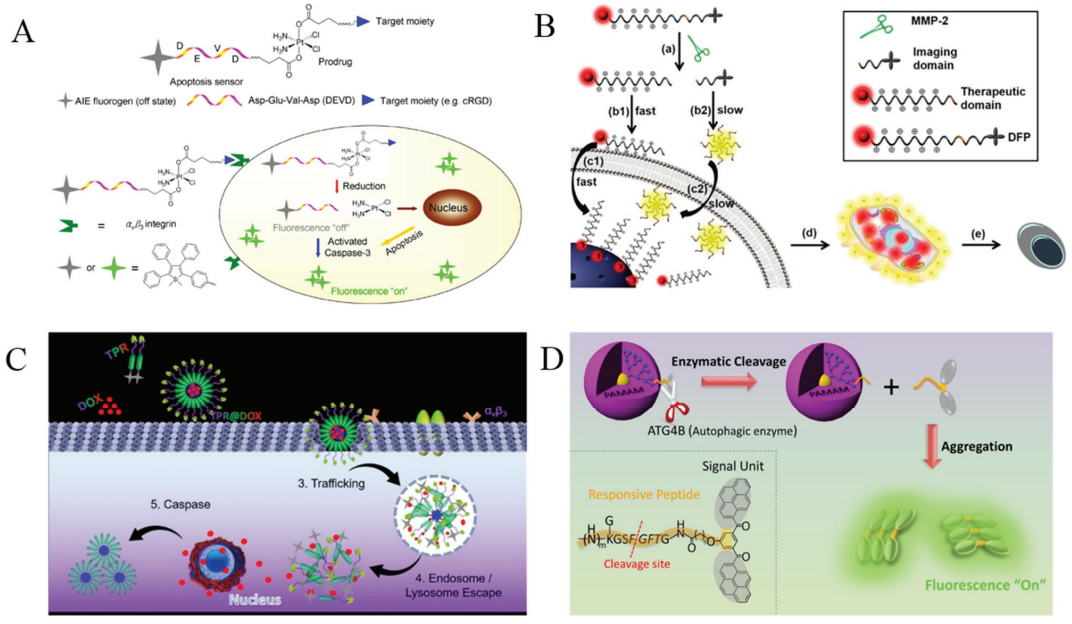

Figure 4. (**A**) Schematic illustration of the targeted theranostic platinum (IV) prodrug with a built-in aggregation-induced emission (AIE) light-up apoptosis sensor for noninvasive, in situ early evaluation of its therapeutic responses. Reprinted with permission from ref. [50]. Copyright 2014, American Chemical Society. (**B**) Schematic illustration showing the probe DFP for rapid drug delivery and drug release tracking in MMP-2 over-expression living cells. Reprinted with permission from ref. [51]. Copyright 2016, American Chemical Society. (**C**) Schematic illustration of TPR@DOX for tumor treatment and apoptosis monitoring. Reprinted with permission from Reference [52]. Copyright 2021, American Chemical Society. (**D**) Caspase-3/7-sensing mechanism of CP1. Reprinted with permission from ref. [53]. Copyright 2017, American Chemical Society.

Table 1. Overview on AIE-based methods for the detection and imaging of different proteases.

Targets	Probes	Linear Range	LOD	Ref.
LAP	DPA-TPE-Leu	–	8.9 ng/mL	[39]
LAP	ASSI-Leu	0~0.05 U/mL	2.983 mU/mL	[40]
CKII	TPE-GRRRADDSDDDD	0.1~80 mU/μL	0.05 mU/μL	[41]
chymase	TPETH-2(CFTERD$_3$)	0~9.0 ng/mL	0.1 ng/mL	[42]
caspase-3	TPE-GFFYK(DVEDEE-Ac)	0~70 pM	0.54 pM	[43]
Furin	Ac-RVRR-linker-HPQ	Imaging	–	[44]
MMP-2	RRRRRRGGPLGLAGPra(PyTPA)-NH$_2$	Imaging	–	[45]
caspase-3/7	Ac-DEVDK-TPE	Imaging	–	[46]
caspase-3	Ac-DEVD-TPS-cRGD	0~80 ng/mL	–	[47]
caspase-3/8	TPETH–DVEDLEHD–TPS	Imaging	–	[48]
caspase-3/7	DOTA-Gd(III)-TPE-KDEVD	Imaging	–	[49]
caspase-3	TPS-DEVD-Pt-cRGD	–	1 pM	[50]
MMP-2	DOX-FCPPs-PyTPE	Imaging	–	[51]
ATG4B	DPBP	Imaging	–	[53]
trypsin	TPE-2+/BSA	1~12.5 mU/mL	1.43 mU/mL	[54]
trypsin	TPE-2+	0.1~1 nM	0.02 nM	[55]
trypsin	PSMA-PhB+TPE/heparin	0~1.5 U/mL	0.02 U/mL	[56]
trypsin	SiNPs@GSH-AuNCs/protamine	0.15~3.0 μg/mL 10~100 ng/mL	0.07 μg/mL 4.50 ng/mL	[57]

Abbreviations: LAP, leucine aminopeptidase; DPA, diphenylamine; Leu, leucine; CKII, casein kinase; MMP-2, matrix metalloproteinase-2; TPS, tetraphenylsilole; PyTPE, tetraphenylethene derivative; DOX, doxorubicin; FCPPs, functionalized cell penetrating peptides; ATG4B, an autophagy-specific enzyme; PSMA, polystyrene-co-maleic anhydride; PhB, phloxine B; SiNPs, silicon nanoparticles; GSH, glutathione; AuNCs, gold nanoclusters.

Autophagy plays a crucial role in the metabolic process. ATG4B is an important autophagy-related protease, which can be used to regulate autophagy for cancer treatment. With a bis(pyrene)-derivative (BP)-labeled peptide (GKGSFGFTG) named DPBP as the AIE probe, Lin et al. proposed an effective strategy for the determination of autophagy in living objects by monitoring the activity of ATG4B (Figure 4D) [53]. The DPBP probe was modified onto the fourth-generation poly(amidoamine) dendrimer (PAMAM) as the carrier. The cleavage of DPBP led to the release of hydrophobic BP residues. The self-assembly of BP residues could enhance the fluorescence by AIE process, thus achieving the determination of autophagy in a living system.

Based on the electrostatic interaction-induced assembly of charged TPE derivatives, several groups have reported the detection of proteases with bovine serum albumin (BSA), protamine and heparin as the triggers. For example, Xu et al. demonstrated that BSA could trigger the assembly of positively charged TPE salts named TPE-2+ through electrostatic interactions, lighting up the fluorescence by AIE process [54]. The digestion of BSA by active trypsin limited the assembly of TPE-2+, thus depressing the fluorescence signal. Jiang's group reported the fluorescent assay of trypsin through the histone-controlled heparin-triggered aggregation of TPE-2+ by electrostatic interactions (Figure 5A) [55]. The cationic protein of histone could electrostatically bind with the anionic polymer of heparin, hindering the interaction between TPE-2+ and heparin. However, the cleavage of histone by trypsin allowed for the heparin-triggered aggregation of TPE-2+, thus enhancing the emission signal. Moreover, Zhao et al. reported the ratiometric fluorescence sensing of heparin and trypsin with phloxine B (PhB) and TPE-modified electrospun fibrous strips (Figure 5B) [56]. Protamine was attached to the modified fibers via electrostatic interactions, causing the static quenching of PhB fluorescence and the AIE-induced enhancement of TPE emission. The digestion of protamine by heparin or trypsin led to the increase of PhB emission at 574 nm, which was accompanied by the decrease of TPE emission at 472 nm.

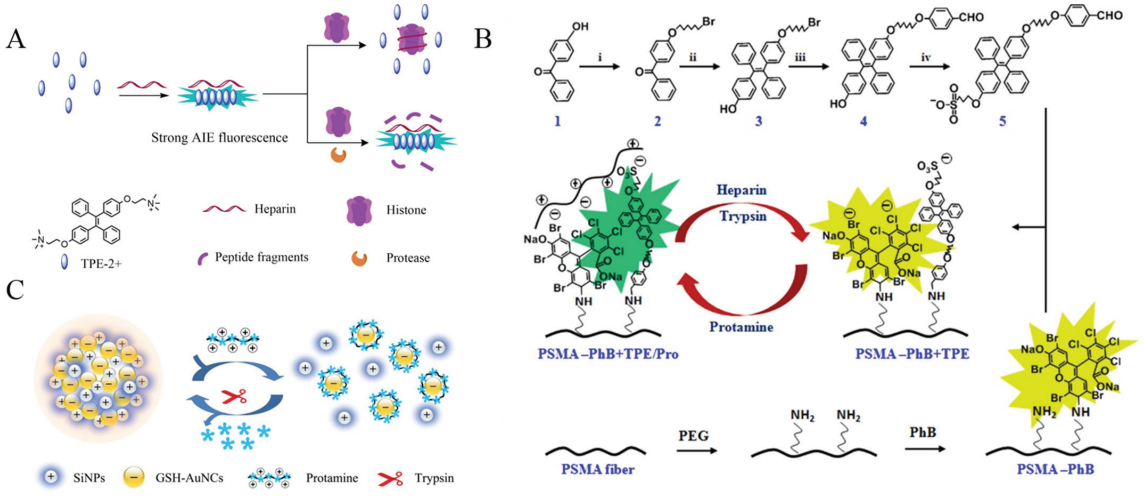

Figure 5. (**A**) Schematic illustration of the fluorometric assay for protease activity. Reprinted with permission from ref. [55]. Copyright 2018, Elsevier. (**B**) Synthetic route of TPE derivatives, schematic drawing of the ratiometric color changes of fibers, and grafting process of PhB on electrospun PSMA fibers. Reprinted with permission from ref. [56]. Copyright 2017, American Chemical Society. (**C**) Schematic illustration of the mechanism of the ratiometric detection of protamine and trypsin based on a nanohybrid probe. Reprinted with permission from ref. [57]. Copyright 2019, Elsevier.

With glutathione (GSH)-protected gold nanoclusters (GSH-AuNCs) as the AIEgens and positively charged silicon nanoparticles (SiNPs) as the triggers to induce the assembly of AuNCs, Xue et al. reported a ratiometric fluorescence sensing strategy for trypsin

detection (Figure 5C) [57]. Protamine could electrostatically adsorb onto the surface of GSH-AuNCs in order to disperse the assemblies, causing fluorescence quenching at 450 nm. In this process, the emission signal of SiNPs as the internal reference showed a negligible change. Subsequently, the trypsin-catalyzed hydrolysis of protamine dissociated the protamine/GSH-AuNCs complexes, facilitating self-assembly and recovering the fluorescence at 570 nm.

3. Phosphatases

Phosphatases widely existing in mammalian body fluids and tissues can catalyze the hydrolysis of phosphate ester during osteogenesis. The abnormal expression of phosphatases is closely related to many diseases, such as liver dysfunction, diabetes, bone tumors, and prostatic cancer [7]. As an important biomarker, alkaline phosphatase (ALP) is one of the most commonly used enzymes in medical diagnosis. Taking advantage of AIE−based biosensors, a series of AIEgens have been designed and synthesized for ALP detection, including phosphorylated TPE (TPE-PA, TPE-2PA and TPE-4PA) [58–60], phosphate-modified quinolone–malononitrile (QMTP), and tyrosine phosphate (pY)−included TPEPy-peptide (TPEPy-FpYGpYGpY and TPEPy-$^{D}F^{D}F_{P}Y^{D}EG^{D}K$) (Table 2). The AIE detection mechanism is based on the difference in the water solubility between substrates and products. After removing the phosphate group from TPE-phos by ALP−catalytic hydrolysis, the product emitted blue or green color due to the AIE effect (Figure 6A) [59]. This light-up probe could be used for the clinical analysis of ALP with high specificity. The auto-fluorescence from living cells may interfere with AIEgens emitting blue or green color. For this reason, several groups have designed fluorescent probes with red emission for ALP analysis [61–64]. ESIPT can induce redder emission by altering the conjugation system of fluorophores. For this reason, Song et al. designed a ratiometric strategy for ALP detection with greenish-yellow phosphorylated chalcone derivatives as the probes (Figure 6B) [63]. The enzymatic products could assemble into red fluorescent aggregates with ESIPT and AIE processes, realizing the visual and fluorescent detection of ALP in living cells.

Table 2. Analytical performances of AIE-based methods for the detection of phosphatases.

Targets	Probes	Linear Range	LOD	Ref.
ALP	TPE-PA	0~0.1 U/mL	18 mU/mL	[58]
ALP	TPE-2PA	3~526 U/L	0.2 U/L	[59]
ALP	TPE-4PA	10~50 mU/mL	–	[60]
ALP	THP	0~200 U/L	1.21228 U/L	[61]
ALP	QMTP	0~1200 U/L	5.36 U/L	[62]
ALP	HCAP	0~150 mU/mL	0.15 mU/mL	[63]
ALP	FAS-P	1~100 U/L	0.6 U/L	[64]
ALP	TPEPy-$^{D}F^{D}F_{P}Y^{D}EG^{D}K$	1~10^{6} CFU/mL	6.6 × 10^{-3} U/mL	[65]
ALP	TPE-Py-FpYGpYGpY	0~2 U/mL	–	[66]
ALP	PET-Flu-PO_4/TPE	0~100 mU/mL	5 mU/mL	[67]
ALP	BSPOTPE-PrS	0~36 mU/mL	28.7 μU/mL	[68]
ALP	H_4TCPE/SR101/Cu-GMP ICP	0.01~0.1 U/mL	0.0032 U/mL	[69]
ALP	GSH-capped CuNCs	0.5~25 mU/mL	0.15 mU/mL	[70]
ACP	CuNCs	2.2~100 U/L	0.8 U/L	[71]
ALP	P-Glu/CuNCs	0.56~30 U/L	0.17 U/L	[72]
ALP	PAH-AuNCs	0.5~100 U/L	0.2 U/L	[73]
ACP	GSH-AuNCs	0.005~2.4 U/L	0.001 U/L	[74]
PPase	AgNCs	2.1~35 U/L	0.7 U/L	[75]
PKM2	TEPC466	0~20 μg/mL	21.25 ng/mL	[76]

Abbreviations: ALP, alkaline phosphatase; TPE, tetraphenylethylene; PA, phosphate; THP, 2-(benzo[d]thiazol-2-yl)-4-(1,4,5-triphenyl-1H-imidazole-2-yl)phenyl dihydrogen phosphate; QMTP, the conjugate of quinolone–malononitrile and phosphate-modified thiophene; HCAP, phosphorylated conjugate of 2′-hydroxyacetophenone and 4-dimethylaminobenzaldehyde; FAS-P, (E)-2-(((9H-fluoren-9-ylidene) hydrazono)methyl) phenyl dihydrogen phosphate; BSPOTPE, 1,2-Bis[4-(3-sulfonatopropoxyl)phenyl]-1,2-diphenylethene; pY, tyrosine phosphate; PrS, protamine sulphate; H4TCPE, 1,1,2,2-tetra(4-carboxylphenyl)ethylene; SR101, sulforhodamine 101; GMP, guanosine-5-monophosphate; P-Glu, D-glucose 6-phosphate; CuNCs, copper nanoclusters; GSH, glutathione; PAH, polyallylamine hydrochloride; AuNCs, gold nanoclusters; ACP, acid phosphatase; PPase, inorganic pyrophosphatases; PKM2, pyruvate kinase.

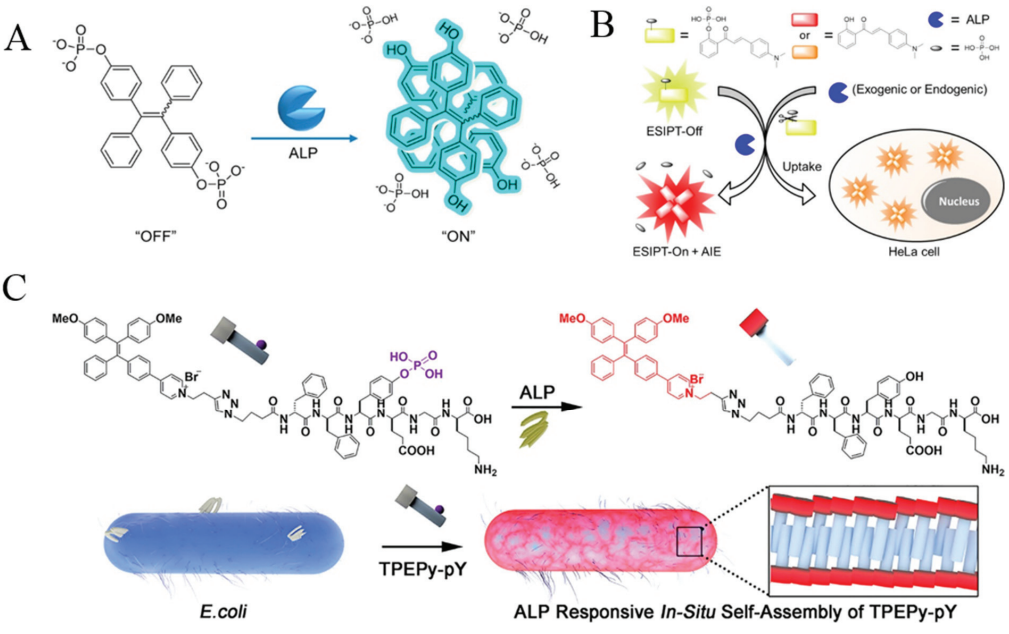

Figure 6. (**A**) Illustration of the design principles of ALP assay with a TPE-2PA probe. Reprinted with permission from ref. [59]. Copyright 2013, American Chemical Society. (**B**) Schematic illustration of HCAP for ALP activity assay in solution and in living cells. Reprinted with permission from ref. [63]. Copyright 2014, American Chemical Society. (**C**) Schematic illustration of the peptide self-assembly-controlled turn-on probe for sensing ALP activity. Reprinted with permission from ref. [65]. Copyright 2020, American Chemical Society.

The above AIE probes may suffer from complex design, low sensitivity and limited solubility in 100% aqueous solution. Compared to them, TPE-based peptide probes exhibited weak emission in a solution state and simple structure with easy synthetic modification. In addition, the ordered self-assembly of peptides can limit the intramolecular rotation of AIEgens, thus enhancing the luminescence. In this aspect, AIEgens−conjugated peptides have been used for the design of various AIE-based biosensors [65,66]. For example, Zhang et al. reported the detection of ALP activity in bacteria with a TPEPy-conjugated peptide probe TPEPy-$^{D}F^{D}F_{P}Y^{D}EG^{D}K$ (Figure 6C) [65]. To enhance the resistance of the probe to proteases, D-amino acids were used instead of natural L-amino acids in the peptide sequence. The dephosphorylated peptide probes could assemble into fibers on the bacterial surface due to their hydrophilicity, thus activating the AIE process and turning on the fluorescence.

Based on the self-assembly of anionic and cationic AIEgens mediated by phosphorylated products via electrostatic interactions, ALP could be determined with low background. For example, Zhao et al. found that the phosphorylation of fluorescein (Flu) on the polyethylene terephthalate (PET) fiber allowed for the attachment of bisquaternary ammonium salt of tetraphenylethylene (TPE-2N^{+}) through electrostatic interaction [67]. The assembled TPE-2N^{+} on the phosphorylated PET-Flu fiber (PET-Flu-PO_4) showed an emission peak at 471 nm. Compared to methods based on the absolute change of the fluorescence intensity, the ratiometric fluorescent assays exhibited minimized environmental fluctuation and enhanced sensitivity. Kaur et al. reported a sensing system for ALP detection involving the AIEgen of di-anionic 1,2-Bis[4-(3-sulfonatopropoxyl)phenyl]-1,2-diphenylethene salt (BSPOTPE) and polycationic protamine sulphate (PrS) [68]. The supramolecular complexes of BSPOTPE-PrS showed strong fluorescence. Hexametaphosphate (HMP) could compete with BSPOTPE to bind PrS, thus leading to the release of BSPOTPE from the supramolecu-

lar complexes and a decrease in fluorescence intensity. In contrary, the cleavage of HMP facilitated the formation of supramolecular BSPOTPE-PrS complexes, thus turning on the fluorescence. Moreover, Luo et al. reported the detection of ALP based on the stimulus response–regulated simultaneous ACQ and AIE effects from infinite coordination polymer (ICP) nanoparticles (Figure 7) [69]. The nanoparticles were formed by the self-assembly of 1,1,2,2-tetra(4-carboxylphenyl)ethylene (H_4TCPE), sulforhodamine 101 (SR101), Cu^{2+} ions, and guanosine-5-monophosphate (GMP). The encapsulation of Cu-GMP made the H_4TCPE/SR101/Cu-GMP nanoparticles emit blue fluorescence from the AIE of H_4TCPE at 450 nm, while the ACQ-induced red fluorescence emission of SR101 was inhibited. The enzymatic dephosphorylation of GMP to produce adenosine and PO_4^- destructed the networks of Cu-GMP hosts, leading to the separation of two guests (H_4TCPE and SR101). Consequently, the AIE of H_4TCPE with blue fluorescence was quenched, while the ACQ of SR101 with red fluorescence was recovered.

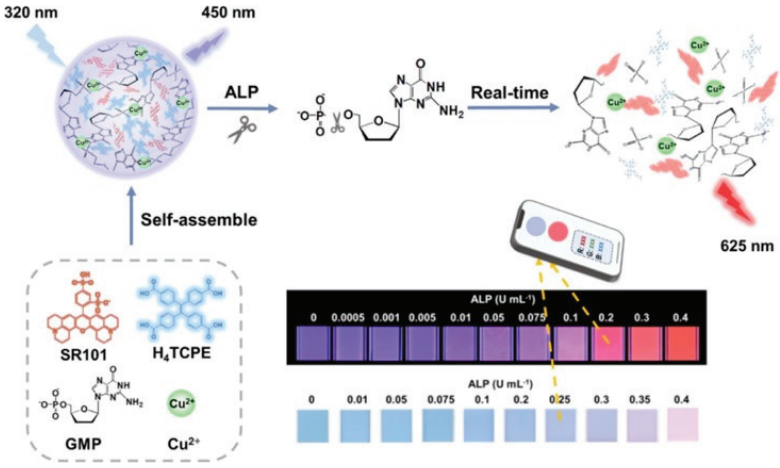

Figure 7. Schematic illustration of the real-time monitoring of ALP activity, based on the ratiometric fluorescence response of H_4TCPE/SR101/Cu-GMP ICP nanoparticles stemming from the AIE guest and the ACQ guest simultaneously, and its field application for algal bloom warning implanted with a smartphone. Reprinted with permission from ref. [69]. Copyright 2021, American Chemical Society.

Taking advantage of metal nanoclusters with AIE characteristics, several groups have reported the detection of ALP activity through the phosphorylated product-mediated assembly of CuNCs and AuNCs. Based on the competitive interaction between GSH-CuNCs and PPi with Al^{3+}, Geng et al. reported the signal-on detection of ALP [70]. The complexation of Al^{3+} by PPi prevented the Al^{3+}-induced aggregation of CuNCs. The enzymatic hydrolysis of PPi allowed for the formation of Al^{3+}/CuNCs nanoaggregates, thus activating the AIE process and turning on the fluorescence. Based on a similar sensing mechanism, acid phosphatase was analyzed using penicilamine-capped CuNCs as the AIEgens [71]. The AIE progress of CuNCs was activated by adjusting the pH. The bright red luminescence of the AIE of CuNCs could be quenched by Fe^{3+} ions but not PPi-Fe^{3+} complexes. The enzymatic hydrolysis of PPi released Fe^{3+} ions, thus quenching the fluorescence of CuNCs aggregates. Phenylboronic acids can form boronate ester bonds with the cis-diols of glucose (Glu) molecules. Based on the Glu-triggered assembly of p-mercaptophenylboronic acid, (MBA)-stabilized CuNCs to activate the AIE process. Huang et al. reported the detection of ALP using D-glucose 6-phosphate (P-Glu) to modify the CuNCs (Figure 8A) [72]. In this method, a part of the MBA groups on CuNPs reacted with the cis-diol on P-Glu molecules through the formation of boronate ester bonds. After dephosphorylation, P-Glu was converted into Glu, which triggered the assembly of CuNPs.

The method with dual recognitions (ALP/P-Glu and 5,6-diol/MBA) was applied for the in situ imaging of ALP activity in cells.

AuNCs have provided a series of platforms for various fluorescence assays. Han et al. reported a fluorescent and colorimetric dual-signal system for ALP assay through via 2, 6-dichlorophenolindophenol (DCIP)-mediated fluorescence resonance energy transfer (FRET) (Figure 8B) [73]. The positively charged polyallylamine hydrochloride (PAH)-capped AuNCs (PAH-AuNCs) with AIE characteristics showed an emission at 570 nm. The negatively charged DCIP could adsorb on the PAH-AuNCs via electrostatic interaction, thus quenching the fluorescence of PAH-AuNCs by fluorescence resonance energy transfer from PAH-AuNCs to DCIP. L-Ascorbic acid (AA), produced by ALP-catalytic hydrolysis of 2-phospho-L-ascorbic acid (AAP), reduced DCIP and can cause color change from blue to colorless, thereby recovering the quenched fluorescence from PAH-AuNCs. Moreover, it was found that Ce^{3+} but not Ce^{4+} ions could enhance the fluorescence of GSH-protected AuNCs via the AIE process [74]. The enzymatic product of AA could reduce Ce^{4+} into Ce^{3+}, thus turning on the fluorescence and achieving the detection of acid phosphatase.

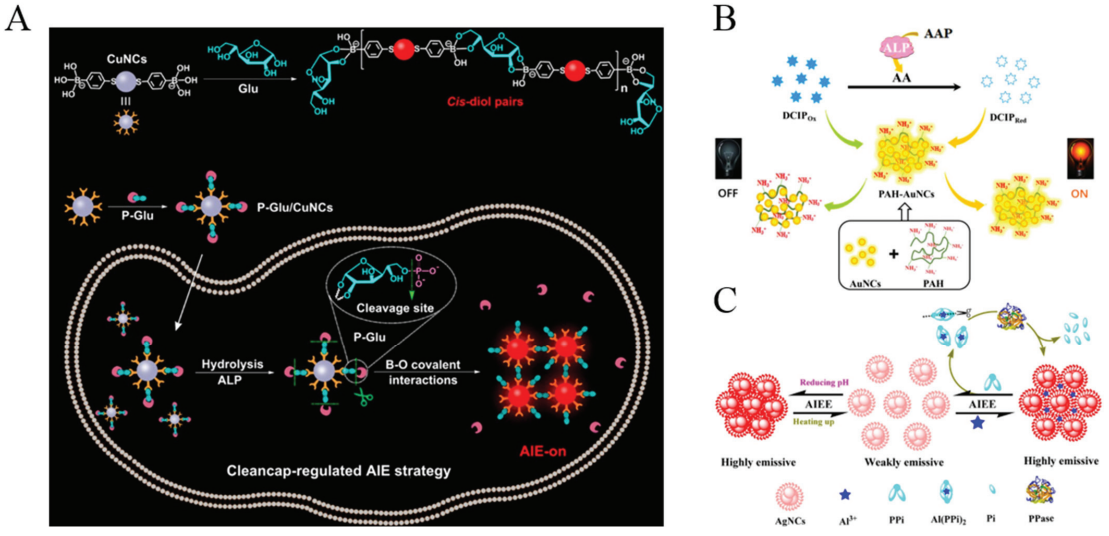

Figure 8. (**A**) Schematic illustration of (top) the proposed mechanism for specific recognition between MBA-stabilized CuNCs and glucose and (bottom) the cleancap-regulated AIE strategy for the imaging of ALP activity. Reprinted with permission from ref. [72]. Copyright 2020, American Chemical Society. (**B**) Schematic illustration of the detection strategy for ALP activity based on FRET. Reprinted with permission from ref. [73]. Copyright 2019, Elsevier. (**C**) Schematic illustration of AIEE-based AgNC nanoswitches in response to multiple stimuli and a detection strategy for PPase activity based on ion-triggered switch. Reprinted with permission from ref. [75]. Copyright 2017, American Chemical Society.

Inorganic pyrophosphatase (PPase) can catalyze the conversion of pyrophosphate (PPi) into phosphate (Pi) ions. It plays an important role in lipid synthesis and decomposition, calcium absorption, bone formation and DNA synthesis, and other biochemical transformations. With glutathione-capped silver nanoclusters (AgNCs) as the AIEgens, Tang et al. reported the assays of PPase by Al^{3+}-triggered luminescence switch (Figure 8C) [75]. The Al^{3+}/AgNCs aggregates showed bright red luminescence. Complexation of Al^{3+} by PPi but not Pi prevented the aggregation of AgNCs, while the decomposition of PPi by PPase facilitated the formation of Al^{3+}/AgNCs aggregates. Moreover, the AIE effect of AgNCs is dependent upon the change of solution pH and temperature.

4. Glycosidases

Glycosidases are responsible for removing the monosaccharide residues from glycoconjugates [2]. They are involved in many biological and pathological processes. For example, β-galactosidase is a key enzyme for monitoring gene transcription and transfection efficiency [77]. It is also an important biomarker of cell aging, ovarian cancer and other pathological processes. Several groups have reported the detection of β-galactosidase with AIE-active fluorescent probes, such as TPE-ETh-R-GFFY(gal)ERGD, TPE–DCM, HBTTPAG, TPh-PyBz-βgal, SA-βGal, and QM–βgal (Table 3) [78–82]. The enzymatic hydrolysis of the hydrophilic substrates could cause the release of hydrophobic fluorophores (e.g., TPE, SA or QM moieties), thus facilitating the formation of AIE aggregates with intensive emission. Some of the probes have been used for the on-site sensing and long-term imaging of β-galactosidase in living cells with low background interference. Moreover, the AIE luminogens (AIEgens) have been synthesized and used for the detection of other glycosidases. Typically, α-amylase can hydrolyze the α-1,4-glycosidic bonds in starch for the production of maltose, glucose, syrup, beer, rice wine, soy sauce, vinegar, juice, and so on. It can also be regarded as the biomarker for psychological stress (e.g., eustress, distress, anxiety, and depression) [83]. Shi et al. developed an AIE-based method for the assay of α-amylase with water-soluble TPE-labeled maltotriose as the probe (Figure 9A) [84]. The enzymatic cleavage of α-1,4 glycosidic bonds by α-amylase led to the release of maltotriose units and the production of insoluble TPE residues. Based on the AIE of TPE residues, the activity of α-amylase in a patient's body fluid has been determined.

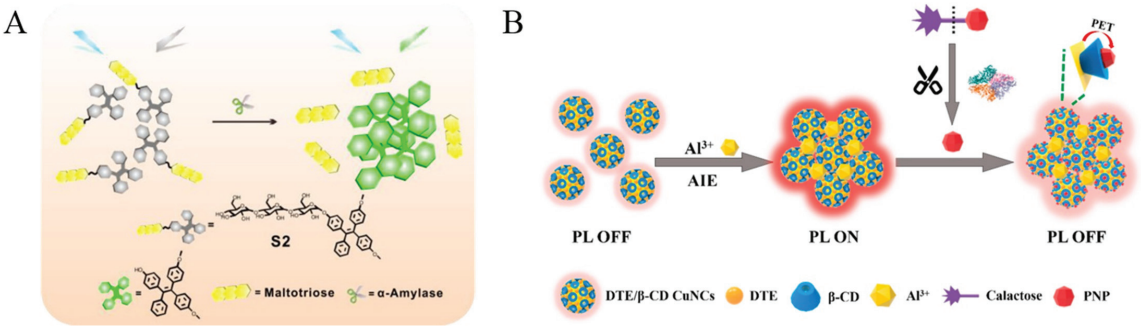

Figure 9. (**A**) Schematic illustration of the sensing mechanisms of the probe S2 in α-amylase activity sensing. Reprinted with permission from ref. [84]. Copyright 2018, American Chemical Society. (**B**) Schematic representation of the strategy for the determination of β-Gal. Reprinted with permission from ref. [87]. Copyright 2020, American Chemical Society.

Table 3. Analytical performances of AIE-based methods for the detection of glycosidases.

Targets	Probes	Linear Range	LOD	Ref.
β-gal	TPh-PyBz-βgal	0.2~2 U/mL	0.22 U/mL	[78]
β-gal	HBTTPAG	0~3.15 U/mL	3.7 mU/mL	[79]
β-gal	SA-βgal	0~0.1 U/mL	14 mU/mL	[80]
β-gal	QM-βgal	0~6 U	1 mU/mL	[81]
β-gal	TPE-DCM	0~7 U/mL	1.5 U/mL	[82]
α-amylase	TPE-maltotriose	0~45.5 U/L	0.14 U/L	[84]
β-gal	CuNCs	0~200 U/L	0.9 U/L	[85]
β-gal	CuNCs	2.3~96 U/L	0.7 U/L	[86]
β-gal	DTE/β-CD CuNCs	0~50 U/L	0.56 U/L	[87]
GUS	BTBP-Gluc	0~7 U/mL	–	[88]

Abbreviations: β-gal, β-galactosidase; SA, salicylaldehyde azines; QM, qnoline-malononitrile; TPE, tetraphenylethene; DCM, dicyanomethylene-4H-pyran; CuNCs, copper nanoclusters; DTE, dithioerythritol; β-CD, β-cyclodextrin; GUS, β-glucuronidase.

In contrast to organic AIEgens, it has been found that some metal nanoclusters show unique AIE properties with longer wavelength emission, which may decrease the interference of fluorescent proteins in biological systems. For example, Zhao et al. found that CuNCs with weak emission could assemble into particles with bright luminescence through hydrophobic interactions [85]. Unlike the thiolated CuNCs, the intense red luminescence of the 4-methylthiophenol protected CuNCs AIE particles and remained stable in neutral and alkaline solution. β-Galactosidase could trigger the substrate hydrolysis to produce galactose and 4-nitrophenol. The resulting 4-nitrophenol could adsorb on the surface of CuNC particles, thus quenching the luminescence and achieving the quantification of β-galactosidase. Qian's group found that Al^{3+} could induce the aggregation of GSH-capped CuNCs to activate the AIE process [86]. 4-Nitrophenol produced from the enzymatic hydrolysis of 4-nitrophenyl-β-D-galactopyranoside by β-galactosidase quenched of the emission of CuNCs aggregates. The method could be applied for the assay of β-galactosidase activity under physiological condition. However, CuNCs-based assays only show one function, which may limit the detection sensitivity to a certain extent. Recently, Huang et al. developed an on-off-on fluorescent method for the detection of β-galactosidase with multi-functional dithioerythritol (DTE) and β-cyclodextrin (β-CD)-covered CuNCs as the probes (Figure 9B) [87]. Al^{3+} cations caused the aggregation of CuNCs through the formation of Al-O bonds, thus triggering the AIE property. The product of p-nitrophenol from the enzymatic hydrolysis of 4-nitrophenyl-β-D-galactopyranoside could bind with β-CD to quench the fluorescence of aggregated CuNPs through photoelectron transfer. This is the first report integrating AIE and host–guest interaction in one system.

5. Cholinesterases

Cholinesterases are a class of key enzymes for biological nerve transmission. Typically, AChE can degrade acetylcholine between cholinergic synapses, prevent the excitatory effect of neurotransmitters on the postsynaptic membrane, and ensure the normal transmission of neural signals in the organism [9]. Organophosphorus pesticides (OPs) are widely used in agricultural production because of their advantages of effectively controlling pests and improving crop yield. Unfortunately, the abuse of OPs has caused the pollution of water resources, fruits, vegetables and processed food, thus causing great damage to the ecological environment and human health. Serine on AChE can be phosphorylated by OPs, thus inhibiting the enzyme activity and preventing the decomposition of neurotransmitters. Based on the AChE substrate or product-induced aggregation of AIEgens, three TPE derivatives have been designed and used for the evaluation of AChE activity and the detection of OPs content (Table 4), including sulfonated TPE, maleimide-functionalized TPE (TPE-M) and leucine–conjugated TPE (TPE-Leu). In the first report, myristoylcholine was used as the AChE substrate, which can assemble into an aggregate or heteroaggregation complex in the presence of sulfonated TPE through electrostatic interactions (Figure 10A) [89]. The formation of TPE assemblies turned on the fluorescence. However, the AChE-catalytic hydrolysis of myristoylcholine limited the formation of assembles, thus causing the decrease in the fluorescence signal. The method could be used for screening of AChE inhibitors in a signal-on detection format. In the second work, acetylthiocholine (ATCh) was used as the AChE substrate [90]. The hydrolysis product of thiocholine could react with the maleimide ring of TPE-M to form an AIE molecule named TPE-M-S. The resulting TPE-M-S on a paper-based fluorescent sensor significantly enhanced the fluorescence. Additionally, a pH-responsive AIE probe of TPE-Leu has also been used for the assay of AChE [91]. The protonated TPE-Leu was water-soluble under basic conditions, showing poor fluorescence. However, the AIEgen would exhibit strong fluorescence in an acidic environment due to its hydrophobic properties. The AChE-catalytic hydrolysis of acetylcholine into choline and acetic acid decreased the pH value of the solution, thus promoting the formation of TPE-Leu aggregates and turning on the fluorescence.

Gold nanoparticles (AuNPs) show excellent fluorescence quenching efficiency. By integrating AIE with nanotechnology, AChE has been detected with AIE nanoparticles and

AuNPs as the sensing platforms [92]. The AIE-Au nanoconjugates showed weak fluorescence due to the fluorescence resonance energy transfer from AIE (QAU-1) nanoparticles to AuNPs. The hydrolysis product of thiocholine could interact with AuNPs by the Au-S interaction to separate AIE nanoparticles from the nanoconjugates, thus recovering the fluorescence. Cai et al. reported a metal−organic framework (MOF)-based system for the detection of AChE with AuNCs as the AIEgens (Figure 10B) [93]. The encapsulation of AuNCs on the ZIF-8 MOF to form AuNCs@ZIF-8 nanocomposites triggered the AIE effect and turned on the fluorescence. In the presence of choline oxidase (CHO), H_2O_2 was produced during the enzymatic oxidation of choline. The produced H_2O_2 decomposed ZIF-8 and destroyed the AuNCs aggregates on MOF, thus reducing the fluorescence. Moreover, the released AuNCs could be used as peroxidase mimics to catalyze the oxidization of 3,3′,5,5′-tetramethylbenzidine (TMB), thus achieving the visual detection of AChE activity in parallel.

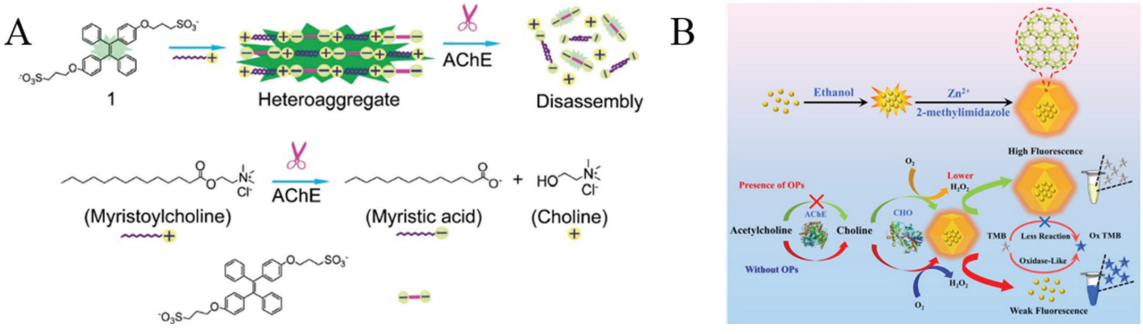

Figure 10. (**A**) Illustration of the formation of heteroaggregate between myristoylcholine and tetraphenylethylene 1 and the disassembly of the aggregate in the presence of AChE. Reprinted with permission from ref. [89]. Copyright 2009, American Chemical Society. (**B**) Schematic diagram of the mechanism for the detection of OPs. Reprinted with permission from ref. [93]. Copyright 2021, American Chemical Society.

Butyrylcholinesterase (BChE) is an important cholinesterase in the process of metabolism and regulation. It is associated with various diseases, such as liver disease, diabetes and Alzheimer's disease [94]. Recently, Xiang et al. designed a ratiometric fluorescent probe (TB-BChE) for imaging of BChE based on AIE mechanisms [95]. The TB-BChE probe showed a low intramolecular charge transfer effect because of the poor electron-donating ability of the ester group. Once the cyclopropyl group in TB-BChE was removed by BChE, the resulting tricyanofuranyl iminosalicylaldehyde (TCFIS) showed strong intramolecular charge transfer and caused the blue-shifted enhanced fluorescence. The probe was further employed for the ratiometric imaging of endogenous BChE in a nonalcoholic fatty liver mouse model.

Table 4. Analytical performances of AIE-based methods for the detection of cholinesterases.

Targets	Probes	Linear Range	LOD	Ref.
AChE	Sulfonated TPE	0.5~2 U/mL	0.5 U/mL	[89]
AChE	TPE-Maleimide	0.3~3 mU/mL	2.5 mU/mL	[90]
AChE	TPE-Leu	0~100 mU	–	[91]
AChE	AIE-AuNPs	0~8 mU/mL	0.015 mU/mL	[92]
BChE	TB-BChE	0~70 μg/mL	39.24 ng/mL	[95]

Abbreviations: AChE, acetylcholinesterase; TPE, tetraphenylethylene; Leu, leucine; AuNPs, gold nanoparticles; BChE, butyrylcholinesterase.

6. Telomerase

Telomerase is a basic nuclear protein reverse transcriptase responsible for telomere elongation in cells [3]. It can add telomere DNA $(TTAGGG)_n$ to the chromosome ends of eukaryotic cells, fill in the telomeres lost in DNA replication, and extend telomere repair. Telomerase plays an important role in maintaining chromosome stability and cell activity in different kinds of cells. Its activity in normal human tissues is inhibited, but it can be reactivated in tumors and participates in malignant transformation. Therefore, telomerase is believed to be a tumor biomarker for the early diagnosis, treatment and monitoring of cancers. Based on the electrostatic interactions between positively charged fluorogens and negatively charged extended DNA sequences, Lou and co-workers developed a series of AIE-based sensing systems for telomerase detection [96–100]. In their first study, a water-soluble tetraphenylethene salt (TPE-Z) with two positive charges was used as the AIEgen (Figure 11A) [97]. The fluorescence signal of TPE-Z was poor in the presence of telomerase substrate oligonucleotides (TS primers). When the repeated $(TTAGGG)_n$ stands were added to the end of TS primers by telomerase, TPE-Z molecules were bound to the extended DNA backbone, resulting in the increase of fluorescence intensity. Based on the same sensing principle, they reported a more specific strategy for telomerase detection using Silole-R as the AIE indicator (Figure 11B) [98]. In contrast to TPE-Z, Silole-R shows a higher fluorescence quantum yield. Thus, the sensitivity and specificity have been remarkably improved for the detection of telomerase extracted from different cell lines.

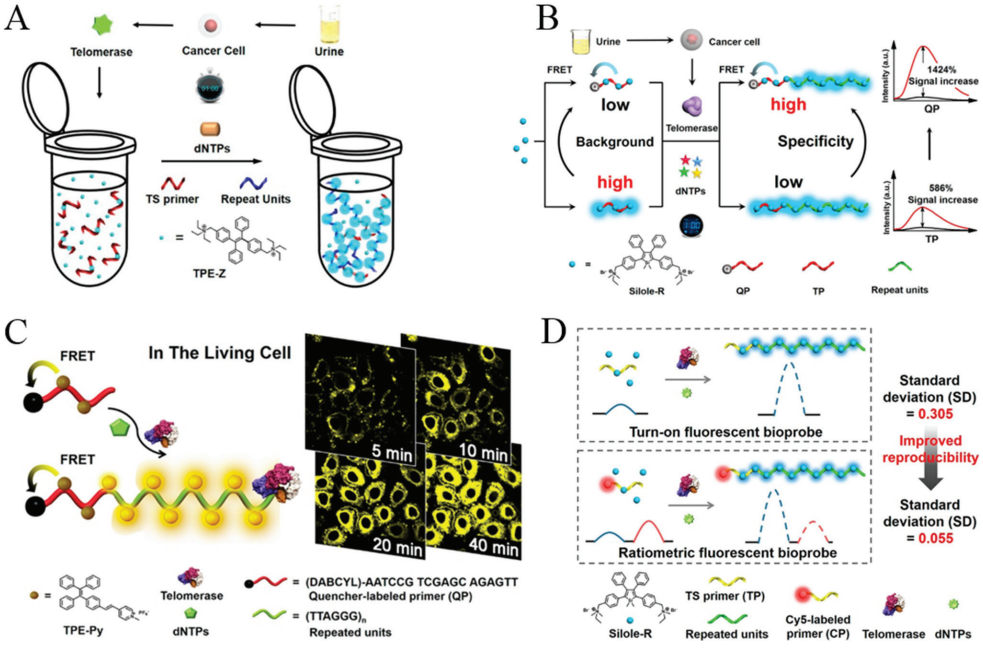

Figure 11. (**A**) Schematic illustration of the AIE-based simple one-pot technique for telomerase activity detection. Reprinted with permission from ref. [97]. Copyright 2015, American Chemical Society. (**B**) Schematic illustration of the quencher group-induced high specificity fluorescence strategy for the detection of telomerase activity. Reprinted with permission from ref. **[98]**. Copyright 2015, American Chemical Society. (**C**) Schematic Illustration of the AIE-based in situ telomerase activity detection and imaging. Reprinted with permission from ref. [99]. Copyright 2016, American Chemical Society. (**D**) Schematic illustration of the ratiometric fluorescent bioprobe for telomerase activity detection. Reprinted with permission from ref. [100]. Copyright 2016, American Chemical Society.

For the application of fluorescence probes in a complex biological environment, light-emitting dyes with long wavelengths are particularly popular due to their low background interference from optical self-absorption and autofluorescence. To overcome this limitation, Lou's group proposed an AIE sensing system for the fluorescent analysis and in situ imaging of telomerase in normal and tumor cells with yellow-emissive AIE dyes (Figure 11C) [99]. The AIEgen (TPE-Py) was synthesized by coupling a pyridinium unit to TPE with vinyl functionality. The positively charged TPE-Py could bind with the free TS primer or quencher-labeled primer (QP) via electrostatic interactions. Without the extension reaction, the emission of TPE-Py aggregates in the primer backbone was quenched due to the fluorescence–resonance energy transfer from TPE-Py to quencher. After the extension reaction, TPE-Py aggregates bound to the repeat units of $(TTAGGG)_n$ which are relatively far away from the quencher, thus producing a distance-dependent fluorescence emission. Furthermore, Lou's group reported an AIE-based ratiometric fluorescent probe for telomerase detection by using Cy5-labeled TS primer and AIEgen Silole-R (Figure 11D) [100]. When the Silole-R molecules were attached onto the extended primer to form the aggregates, a strong blue emission was observed, while the red emission from the internal reference (Cys5) had no change. In the contrast to previous methods, the ratiometric probe showed higher reproducibility and positive result rate for urine samples from bladder cancers.

7. Others

γ-Glutamyltranspeptidase (GGT) is believed to be a biomarker of hepatocellular carcinoma (HCC). Its imaging is of great significance for the early monitoring of precise medicine and intraoperative navigation. Based on the enzymatic generation of hydrophobic products, GGT has been determined with TPE derivatives functionalized with γ-glutamyl amide residues. The substrates dispersed in aqueous solution exhibited no or a poor fluorescence peak. When the γ-glutamyl amide group was removed through enzymatic cleavage, the hydrophobic TPE derivatives were assembled into aggregates with blue fluorescence. The probe could be used to determine GGT in serum samples and image endogenous GGT in living cells [101]. In addition, Zeng's group reported a near-infrared fluorescence probe for GGT imaging by combining AIE and ESIPT (Figure 12A) [102]. The glutamic acid-conjugated ABTT, named ABTT-Glu, is water-soluble and showed almost no fluorescence emission. The GGT-mediated cleavage of ABTT-Glu caused the formation of ABTT aggregates via intramolecular hydrogen interactions, thereby enhancing the fluorescence emission. The probe was further used to detect GGT in HepG2 cells for precision medicine in surgery. Moreover, fluorophores with AIE and ESIPT characteristics have been designed and synthesized for the fluorescent sensing of other enzymes such as lactamase esterases (Table 5) [103–105]. For example, esterases are a kind of hydrolase enzyme which participate in a variety of biochemical reactions, depending on the receptors and protein structures and functions; several AIEgen probes have been prepared for esterase detection with the combination of AIE and ESIPT effects by the hydrolysis of esters into acids and alcohols (Figure 12B) [104,105].

Additionally, AIEgen probes have been synthesized for the detection and imaging of other enzymes such as lipase [106,107], fucosidase [108], cyclooxygenase-2 (COX-2) [109] and β-N-acetylhexosaminidase (Hex) [110]. For example, lipase plays an important role in industrial catalysis, drug discovery and disease diagnosis; two AIEgens have been designed and used for the detection of lipase, including TPE and benzophenone derivatives [106,107]. It has been documented that COX-2 is an effective biomarker for the early diagnosis of some cancers. It is overexpressed in cancer cells but not in normal tissues. Xie et al. reported an AIEgen with COX-2 binding ability using the modification of rofecoxib (Figure 12C) [109]. The rofecoxib analogues showed good AIE properties due to the introduction of a phenyl ring. β-N-acetylhexosaminidase (Hex) is a kind of glucoside hydrolase which participates in the catalytic release of N-acetylhexose at the non-reducing end of the substrate. Human Hex (HsHex) plays a key role in lysosomal storage disorders, which can mediate the degradation of GM2 ganglioside in neuronal lysosome [111]. The dysfunction of HsHex

can lead to severe neurodegenerative lipid storage disorders. Wang et al., for the first time, designed a lysosome-targeting Hex-lighting-up AIE-active probe (GlcNAc-TPE) for Hex detection (Figure 12D) [110]. The Hex-catalyzed hydrolysis of GlcNAc-TPE produced hydrophobic Py-TPE with poor water solubility. The Py-TPE aggregates boosted the bright emission with large Stokes shift and excellent photostability.

Based on the electrostatic interactions, methyltransferases (MTase) and hyaluronidase (HAase) have also been determined by the AIE mechanism. For example, DNA MTase is a type of enzyme involved in the regulation of gene expression. It can lead to aberrant DNA methylation of tumor-suppressor genes, thus becoming highly methylated and transcriptional silenced in some blood cancers. With the combination of AIE and target-initiated template-free DNA polymerization, Nie et al. designed an AIE probe of TPE-Z to detect MTase [112]. The positively charged TPE-Z bound with single-stranded DNA through electrostatic interactions. Then, DNA MTase catalyzed the polymerization of a sequence-specific hairpin DNA, thus turning on the fluorescence through the AIE effect. The method was used to detect DNA MTase activity in serum samples and evaluate the inhibition efficiency of 5-fluorouracil inhibitor. HAase can catalyze the hydrolysis of hyaluronic acid (HA) into small pieces. It can reduce the activity of hyaluronic acid in the body, thus improving the liquid permeability of tissues. HAase is associated with a variety of physiological and pathological processes, including embryogenesis, inflammation, and wound healing. It has been demonstrated that HAase was overexpressed in some cancer patients, such as those with cancers of the bladder, colon, and prostate [113]. Thus, the evaluation of HAase activity has attracted much attention. Li et al. reported the detection of HAase through the HA-triggered assembly of TPE-$4N^+$ compounds via electrostatic interactions [114]. The resulting assemblies showed a yellow-greenish emission. The enzymatic digestion of HA was limited the assembly of TPE-$4N^+$, causing the fluorescence quenching. Moreover, based on the quenching ability of AuNPs, Wang et al. reported the detection of HAase with AIE-dot-based nanoprobes (AIEDs) [115]. In this method, the negatively charged HA stabilized AuNPs and promoted their assembly on AIEDs to form HA-AuNPs@AIEDs, thus quenching the fluorescence through fluorescence resonance energy transfer. HAase-induced degradation of HA to small pieces caused the dissociation of AuNPs and thus recovered the fluorescence. Moreover, the HA-AuNPs@AIEDs assemblies could specifically recognize the HA receptors on the cells, thus facilitating endogenous detection and in vitro imaging of HAase.

Table 5. Analytical performances of AIE-based methods for the detection of other enzymes.

Targets	Probes	Linear Range	LOD	Ref.
GGT	ABTT-Glu	10~90 U/L	2.9 U/L	[101]
GGT	TPE	0~80 U/L	0.59 U/L	[102]
β-lactamase	DNBS-CSA	0~10 mU/mL	0.5 mU/mL	[103]
Lyso	AIE-Lyso-1	0.1~0.5 U/mL	2.4 mU/mL	[104]
esterase	probe 4	0.01~0.15 U/mL	5 mU/mL	[105]
lipase	TPE−$COOC_6H_{13}$	0.1~1.3 mg/mL	0.1 mg/mL	[106]
lipase	benzophenone	0.1~4 U/mL	50 mU/mL	[107]
α-fuc	QM-NHαfuc	0~1.75 U/mL	10 mU/mL	[108]
Hex	GlcNAc-TPE	0~0.2 U/mL	3 mU/mL	[110]
MTase	TPE-Z	0.5~100 U/mL	0.16 U/mL	[112]
HAase	TPE-$4N^+$	0.05~2 U/mL	20 mU/mL	[114]
HAase	HA-AuNPs@AIEDs	0.01~60 U/mL	7.2 mU/mL	[115]

Abbreviations: GGT, γ-glutamyltranspeptidase; Glu, γ-glutamate; Lyso, lysosomal esterase; CSA, salicylaldehyde azine derivative; α-fuc, α-L-fucosidase; QM, quinoline malononitrile; Hex, β-N-acetylhexosaminidase; MTase, methyltransferases; TPE-Z, tetraphenylethene salt; HAase, hyaluronidase; HA, hyaluronic acid; AuNPs, gold nanoparticles.

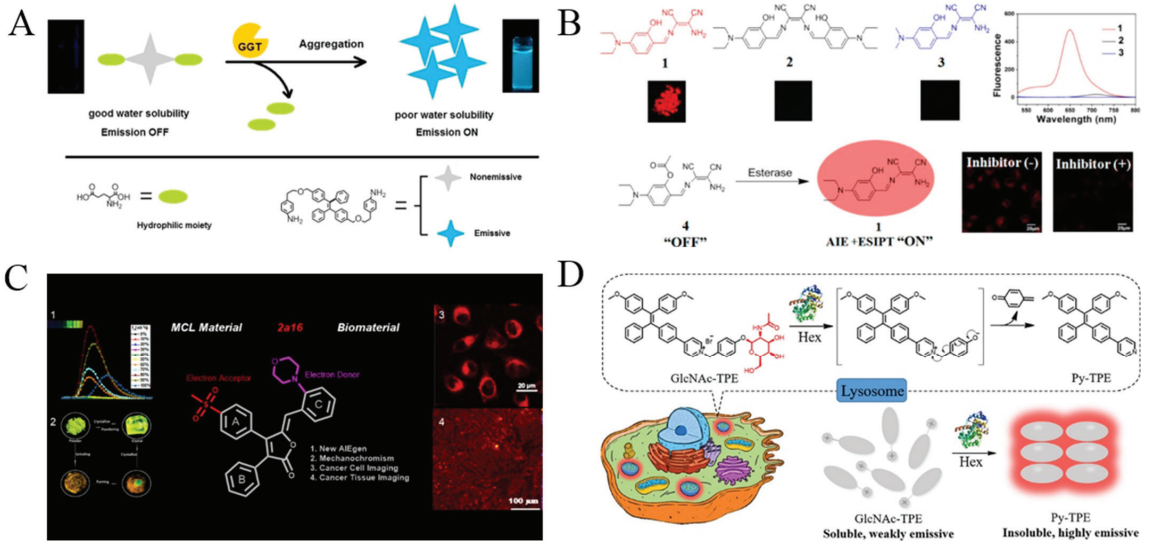

Figure 12. (**A**) Schematic illustration of the probe's fluorescent detection for GGT. Reprinted with permission from ref. [102]. Copyright 2016, Elsevier. (**B**) Schematic illustration of red-emissive fluorophore with AIE and ESIPT characteristics for light-pp sensing of esterase. Reprinted with permission from ref. [105]. Copyright 2014, American Chemical Society. (**C**) Schematic illustration of rofecoxib-based fluorescent probes for COX-2-targeted bioimaging. Reprinted with permission from ref. [109]. Copyright 2021, American Chemical Society. (**D**) Detection mechanism of GlcNAc-TPE towards Hex. Reprinted with permission from ref. [110]. Copyright 2019, American Chemical Society.

8. Conclusions

This review has summarized the recent advances in AIEgen-based biosensors for the detection and imaging of enzymes. When triggered by certain stimulus, the well-designed AIEgens in aggregate state exhibit the unique advantages of excellent signal-to-noise ratio, strong photostability and large Stokes' shift. By simply adjusting the molecule structures, the optical properties of AIEgens can be easily modulated to meet the requirement of enzyme sensing. By selecting the corresponding substrate probes to conjugate with AIEgens, different enzymes have been sensitively detected in vitro and in vivo, including proteases, phosphatases, β-galactosidases, cholinesterases, telomerase, and others. However, there are still some shortcomings and challenges in the AIE-based detection and imaging of enzymes. For example, in order to decrease the back fluorescence from proteins in cells, AIEgens with far-red or near-infrared emission and multiphoton excitation characteristics should be extensively explored for the in vivo sensing and monitoring of enzymatic processes. Second, more detection mechanisms should be proposed in order to detect other types of enzymes, such as redox enzymes and isomerases. Third, aiming to monitor the dynamic enzymatic process, it is necessary to explore reversible enzyme-responsive AIE probes. Lastly, the undefined degradation and cell toxicity of AIEgens-based probes in cells and tissues needs more detailed assessments.

Author Contributions: Writing—original draft preparation, F.G., G.L., M.Q. and Y.L.; writing—review and editing, X.Y.; project administration, X.Y.; funding acquisition, X.Y. All authors have read and agreed to the published version of the manuscript.

Funding: This research was funded by the National Natural Science Foundation of China (21705166) and the Central South University Innovation-Driven Research Programme (2023CXQD022).

Conflicts of Interest: The authors declare no conflict of interest.

References

1. Kwek, G.; Do, T.C.; Lu, X.; Lin, J.; Xing, B. Scratching the surface of unventured possibilities with in situ self-assembly: Protease-activated developments for imaging and therapy. *ACS Appl. Bio. Mater.* **2021**, *4*, 2192. [CrossRef] [PubMed]
2. Yao, Y.; Zhang, Y.; Yan, C.; Zhu, W.H.; Guo, Z. Enzyme-activatable fluorescent probes for beta-galactosidase: From design to biological applications. *Chem. Sci.* **2021**, *12*, 9885. [CrossRef] [PubMed]
3. Luo, S.; Zhang, Y.; Situ, B.; Zheng, L. Fluorescence sensing telomerase activity: From extracellular detection to in situ imaging. *Sens. Actuat. B Chem.* **2018**, *273*, 853. [CrossRef]
4. Feng, G.; Liao, S.; Liu, Y.; Zhang, H.; Luo, X.; Zhou, X.; Fang, J. When AIE meets enzymes. *Analyst* **2022**, *147*, 3958. [CrossRef]
5. Hu, Z.; Li, Y.; Hussain, E.; Huang, X.; Zhang, Y.; Niu, N.; Shahzad, S.A.; Yu, C. Black phosphorus nanosheets based sensitive protease detection and inhibitor screening. *Talanta* **2019**, *197*, 270. [CrossRef]
6. Oliveira-Silva, R.; Sousa-Jeronimo, M.; Prazeres, D.M.F. Monitoring proteolytic activity in real time: A new world of opportunities for biosensors. *Trends Biochem. Sci.* **2020**, *45*, 604. [CrossRef]
7. Balbaied, T.; Moore, E. Overview of optical and electrochemical alkaline phosphatase (ALP) biosensors: Recent approaches in cells culture techniques. *Biosensors* **2019**, *9*, 102. [CrossRef]
8. Park, S.; Lim, S.Y.; Bae, S.M.; Kim, S.Y.; Myung, S.J.; Kim, H.J. Indocyanine-based activatable fluorescence turn-on probe for γ-glutamyltranspeptidase and its application to the mouse model of colon cancer. *ACS Sens.* **2016**, *1*, 579. [CrossRef]
9. Xia, N.; Wang, Q.; Liu, L. Nanomaterials-based optical techniques for the detection of acetylcholinesterase and pesticides. *Sensors* **2015**, *15*, 499. [CrossRef]
10. Hameed, A.M.; Lam, V.W.T.; Pleass, H.C. Significant elevations of serum lipase not caused by pancreatitis: A systematic review. *HPB* **2015**, *17*, 99. [CrossRef]
11. Hata, R.; Nonaka, H.; Takakusagi, Y.; Ichikawa, K.; Sando, S. Design of a hyperpolarized molecular probe for detection of aminopeptidase N activity. *Angew. Chem. Int. Ed.* **2016**, *55*, 1765. [CrossRef] [PubMed]
12. Niu, N.; Zhou, H.; Liu, N.; Jiang, H.; Hussain, E.; Hua, Z.; Yu, C. A smart perylene derived photosensitizer for lysosome-targeted and self-assessed photodynamic therapy. *Chem. Commun.* **2019**, *55*, 1036. [CrossRef] [PubMed]
13. Eivazzadeh-Keihan, R.; Saadatidizaji, Z.; Maleki, A.; de la Guardia, M.; Mahdavi, M.; Barzegar, S.; Ahadian, S. Recent progresses in development of biosensors for thrombin detection. *Biosensors* **2022**, *12*, 767. [CrossRef] [PubMed]
14. Hori, Y.; Kikuchi, K. Chemical tools with fluorescence switches for verifying epigenetic modifications. *Acc. Chem. Res.* **2019**, *52*, 2849. [CrossRef]
15. Suzuki, Y.; Yokoyama, K. Development of functional fluorescent molecular probes for the detection of biological substances. *Biosensors* **2015**, *5*, 337. [CrossRef]
16. Hu, Z.; Chen, J.; Li, Y.; Wang, Y.; Zhang, Q.; Hussain, E.; Yang, M.; Shahzad, S.A.; Yu, D.; Yu, C. Nucleic acid-controlled quantum dots aggregation: A label-free fluorescence turn-on strategy for alkaline phosphatase detection. *Talanta* **2017**, *169*, 64. [CrossRef]
17. Yan, Y.; Zhang, J.; Yi, S.; Liu, L.; Huang, C. Lighting up forensic science by aggregation-induced emission: A review. *Anal. Chim. Acta* **2021**, *1155*, 238119. [CrossRef]
18. Cai, X.; Liu, B. Aggregation-induced emission: Recent advances in materials and biomedical applications. *Angew. Chem. Int. Ed.* **2020**, *59*, 9868. [CrossRef]
19. Suzuki, S.; Sasaki, S.; Sairi, A.S.; Iwai, R.; Tang, B.Z.; Konishi, G.I. Principles of aggregation-induced emission: Design of deactivation pathways for advanced AIEgens and applications. *Angew. Chem. Int. Ed.* **2020**, *59*, 9856. [CrossRef]
20. Wang, X.; Hu, J.; Zhang, G.; Liu, S. Highly selective fluorogenic multianalyte biosensors constructed via enzyme-catalyzed coupling and aggregation-induced emission. *J. Am. Chem. Soc.* **2014**, *136*, 9890–9893. [CrossRef]
21. Gao, Y.; He, Z.; He, X.; Zhang, H.; Weng, J.; Yang, X.; Meng, F.; Luo, L.; Tang, B.Z. Dual-color emissive AIEgen for specific and label-free double-stranded DNA recognition and single-nucleotide polymorphisms detection. *J. Am. Chem. Soc.* **2019**, *141*, 20097–20106. [CrossRef]
22. Shi, J.; Li, Y.; Li, Q.; Li, Z. Enzyme-responsive bioprobes based on the mechanism of aggregation-induced emission. *ACS Appl. Mater. Interfaces* **2018**, *10*, 12278. [CrossRef] [PubMed]
23. Gao, M.; Tang, B.Z. Fluorescent sensors based on aggregation-induced emission: Recent advances and perspectives. *ACS Sens.* **2017**, *2*, 1382. [CrossRef] [PubMed]
24. Li, Y.; Zhou, H.; Chen, J.; Shahzad, S.A.; Yu, C. Controlled self-assembly of small molecule probes and the related applications in bioanalysis. *Biosens. Bioelectron.* **2016**, *76*, 38. [CrossRef]
25. Shellaiah, M.; Sun, K.-W. Pyrene-based AIE active materials for bioimaging and theranostics applications. *Biosensors* **2022**, *12*, 550. [CrossRef] [PubMed]
26. Dai, D.; Yang, J.; Yang, Y.W. Supramolecular assemblies with aggregation-induced emission properties for sensing and detection. *Chem. Eur. J.* **2022**, *28*, e202103185. [PubMed]
27. Li, X.; Zha, M.; Li, Y.; Ni, J.; Min, T.; Kang, T.; Yang, G.; Tang, H.; Li, K.; Jiang, X. Sub-10 nm aggregation-induced emission quantum dots assembled by microfluidics for enhanced tumor targeting and reduced retention in the liver. *Angew. Chem. Int. Ed.* **2020**, *59*, 21899. [CrossRef]
28. Mao, L.; Liu, Y.; Yang, S.; Li, Y.; Zhang, X.; Wei, Y. Recent advances and progress of fluorescent bio-/chemosensors based on aggregation-induced emission molecules. *Dyes Pigments* **2019**, *162*, 611. [CrossRef]

29. Wei, W.; Qiu, Z. Diagnostics and theranostics of central nervous system diseases based on aggregation-induced emission luminogens. *Biosens. Bioelectron.* **2022**, *217*, 114670. [CrossRef]
30. Yang, J.; Wei, J.; Luo, F.; Dai, J.; Hu, J.J.; Lou, X.; Xia, F. Enzyme-responsive peptide-based AIE bioprobes. *Top. Curr. Chem.* **2020**, *378*, 47. [CrossRef]
31. Chen, B.; Yuan, H.; Zhang, W.; Hu, J.; Lou, X.; Xia, F. AIEgen-peptide bioprobes for the imaging of organelles. *Biosensors* **2022**, *12*, 667. [CrossRef] [PubMed]
32. La, D.D.; Bhosale, S.V.; Jones, L.A.; Bhosale, S.V. Tetraphenylethylene-based AIE-active probes for sensing applications. *ACS Appl. Mater. Interfaces* **2018**, *10*, 12189. [CrossRef] [PubMed]
33. Mei, J.; Huang, Y.; Tian, H. Progress and trends in AIE-based bioprobes: A brief overview. *ACS Appl. Mater. Interfaces* **2018**, *10*, 12217. [CrossRef] [PubMed]
34. Würthner, F. Aggregation-induced emission (AIE): A historical perspective. *Angew. Chem. Int. Ed.* **2020**, *59*, 14192. [CrossRef]
35. Zhao, Z.; Zhang, H.; Lam, J.W.Y.; Tang, B.Z. Aggregation-induced emission: New vistas at the aggregate level. *Angew. Chem. Int. Ed.* **2020**, *59*, 9888. [CrossRef]
36. Kang, X.Y.; Li, Y.; Yin, S.; Li, W.; Qi, J. Reactive species-activatable AIEgens for biomedical applications. *Biosensors* **2022**, *12*, 646. [CrossRef]
37. Liu, S.; Feng, G.; Tang, B.Z.; Liu, B. Recent advances of AIE light-up probes for photodynamic therapy. *Chem. Sci.* **2021**, *12*, 6488. [CrossRef]
38. Wang, J.; Meng, Q.; Yang, Y.; Zhong, S.; Zhang, R.; Fang, Y.; Gao, Y.; Cui, X. Schiff base aggregation-induced emission luminogens for sensing applications: A review. *ACS Sens.* **2022**, *7*, 2521. [CrossRef]
39. Huang, S.; Wu, Y.; Zeng, F.; Chen, J.; Wu, S. A turn-on fluorescence probe based on aggregation-induced emission for leucine aminopeptidase in living cells and tumor tissue. *Anal. Chim. Acta* **2018**, *1031*, 169. [CrossRef]
40. Huang, X.; Lei, Q.; Huang, S.; Zeng, H.; Feng, B.; Zeng, Q.; Hu, Y.; Zeng, W. Construction of a novel asymmetric imidazole-cored AIE probe for ratiometric imaging of endogenous leucine aminopeptidase. *Chem. Commun.* **2021**, *57*, 6608. [CrossRef]
41. Luan, Z.; Zhao, L.; Liu, C.; Song, W.; He, P.; Zhang, X. Detection of casein kinase II by aggregation-induced emission. *Talanta* **2019**, *201*, 450. [CrossRef] [PubMed]
42. Zhang, R.; Zhang, C.J.; Feng, G.; Hu, F.; Wang, J.; Liu, B. Specific light-up probe with aggregation-induced emission for facile detection of chymase. *Anal. Chem.* **2016**, *88*, 9111. [CrossRef] [PubMed]
43. Han, A.; Wang, H.; Kwok, R.T.; Ji, S.; Li, J.; Kong, D.; Tang, B.Z.; Liu, B.; Yang, Z.; Ding, D. Peptide-induced AIEgen self-assembly: A new strategy to realize highly sensitive fluorescent light-up probes. *Anal. Chem.* **2016**, *88*, 3872. [CrossRef] [PubMed]
44. Li, K.; Hu, X.X.; Liu, H.W.; Xu, S.; Huan, S.Y.; Li, J.B.; Deng, T.G.; Zhang, X.B. In situ imaging of furin activity with a highly stable probe by releasing of precipitating fluorochrome. *Anal. Chem.* **2018**, *90*, 11680. [CrossRef]
45. Wu, F.; Huang, Y.; Yang, X.; Hu, J.J.; Lou, X.; Xia, F.; Song, Y.; Jiang, L. Tunning intermolecular interaction of peptide-conjugated AIEgen in nano-confined space for quantitative detection of tumor marker secreted from cells. *Anal. Chem.* **2021**, *93*, 16257. [CrossRef]
46. Shi, H.; Kwok, R.T.; Liu, J.; Xing, B.; Tang, B.Z.; Liu, B. Real-time monitoring of cell apoptosis and drug screening using fluorescent light-up probe with aggregation-induced emission characteristics. *J. Am. Chem. Soc.* **2012**, *134*, 17972. [CrossRef]
47. Ding, D.; Liang, J.; Shi, H.; Kwok, R.T.K.; Gao, M.; Feng, G.; Yuan, Y.; Tang, B.Z.; Liu, B. Light-up bioprobe with aggregation-induced emission characteristics for real-time apoptosis imaging in target cancer cells. *J. Mater. Chem. B* **2014**, *2*, 231. [CrossRef]
48. Yuan, Y.; Zhang, C.J.; Kwok, R.T.K.; Mao, D.; Tang, B.Z.; Liu, B. Light-up probe based on AIEgens: Dual signal turn-on for caspase cascade activation monitoring. *Chem. Sci.* **2017**, *8*, 2723. [CrossRef]
49. Li, H.; Parigi, G.; Luchinat, C.; Meade, T.J. Bimodal fluorescence-magnetic resonance contrast agent for apoptosis imaging. *J. Am. Chem. Soc.* **2019**, *141*, 6224. [CrossRef]
50. Yuan, Y.; Kwok, R.T.; Tang, B.Z.; Liu, B. Targeted theranostic platinum(IV) prodrug with a built-in aggregation-induced emission light-up apoptosis sensor for noninvasive early evaluation of its therapeutic responses in situ. *J. Am. Chem. Soc.* **2014**, *136*, 2546. [CrossRef]
51. Cheng, Y.; Huang, F.; Min, X.; Gao, P.; Zhang, T.; Li, X.; Liu, B.; Hong, Y.; Lou, X.; Xia, F. Protease-responsive prodrug with aggregation-induced emission probe for controlled drug delivery and drug release tracking in living cells. *Anal. Chem.* **2016**, *88*, 8913. [CrossRef] [PubMed]
52. Qin, W.; Wu, Y.; Hu, Y.; Dong, Y.; Hao, T.; Zhang, C. TPE-Based Peptide Micelles for Targeted Tumor Therapy and Apoptosis Monitoring. *ACS Appl. Bio Mater.* **2021**, *4*, 1038. [CrossRef]
53. Lin, Y.X.; Qiao, S.L.; Wang, Y.; Zhang, R.X.; An, H.W.; Ma, Y.; Rajapaksha, R.P.; Qiao, Z.Y.; Wang, L.; Wang, H. An in situ intracellular self-assembly strategy for quantitatively and temporally monitoring autophagy. *ACS Nano* **2017**, *11*, 1826. [CrossRef] [PubMed]
54. Xu, J.P.; Fang, Y.; Song, Z.G.; Mei, J.; Jia, L.; Qin, A.J.; Sun, J.Z.; Ji, J.; Tang, B.Z. BSA-tetraphenylethene derivative conjugates with aggregation-induced emission properties: Fluorescent probes for label-free and homogeneous detection of protease and alpha1-antitrypsin. *Analyst* **2011**, *136*, 2315. [CrossRef] [PubMed]
55. Zhang, Y.; Li, Y.; Yang, N.; Yu, X.; He, C.; Niu, N.; Zhang, C.; Zhou, H.; Yu, C.; Jiang, S. Histone controlled aggregation of tetraphenylethene probe: A new method for the detection of protease activity. *Sens. Actuat. B Chem.* **2018**, *257*, 1143. [CrossRef]

56. Zhao, L.; Wang, T.; Wu, Q.; Liu, Y.; Chen, Z.; Li, X. Fluorescent strips of electrospun fibers for ratiometric sensing of serum heparin and urine trypsin. *ACS Appl. Mater. Interfaces* **2017**, *9*, 3400. [CrossRef]
57. Xue, F.; Qu, F.; Han, W.; Xia, L.; You, J. Aggregation-induced emission enhancement of gold nanoclusters triggered by silicon nanoparticles for ratiometric detection of protamine and trypsin. *Anal. Chim. Acta* **2019**, *1046*, 170. [CrossRef]
58. Gu, X.; Zhang, G.; Wang, Z.; Liu, W.; Xiao, L.; Zhang, D. A new fluorometric turn-on assay for alkaline phosphatase and inhibitor screening based on aggregation and deaggregation of tetraphenylethylene molecules. *Analyst* **2013**, *138*, 2427. [CrossRef]
59. Liang, J.; Kwok, R.T.; Shi, H.; Tang, B.Z.; Liu, B. Fluorescent light-up probe with aggregation-induced emission characteristics for alkaline phosphatase sensing and activity study. *ACS Appl. Mater. Interfaces* **2013**, *5*, 8784. [CrossRef]
60. Cao, F.Y.; Long, Y.; Wang, S.B.; Li, B.; Fan, J.X.; Zeng, X.; Zhang, X.Z. Fluorescence light-up AIE probe for monitoring cellular alkaline phosphatase activity and detecting osteogenic differentiation. *J. Mater. Chem. B* **2016**, *4*, 4534. [CrossRef]
61. Huang, L.; Cao, X.; Gao, T.; Feng, B.; Huang, X.; Song, R.; Du, T.; Wen, S.; Feng, X.; Zeng, W. A novel aggregation-induced dual emission probe for in situ light-up detection of endogenous alkaline phosphatase. *Talanta* **2021**, *225*, 121950. [CrossRef] [PubMed]
62. Zhao, M.; Gao, Y.; Ye, S.; Ding, J.; Wang, A.; Li, P.; Shi, H. A light-up near-infrared probe with aggregation-induced emission characteristics for highly sensitive detection of alkaline phosphatase. *Analyst* **2019**, *144*, 6262. [CrossRef] [PubMed]
63. Song, Z.; Kwok, R.T.; Zhao, E.; He, Z.; Hong, Y.; Lam, J.W.; Liu, B.; Tang, B.Z. A ratiometric fluorescent probe based on ESIPT and AIE processes for alkaline phosphatase activity assay and visualization in living cells. *ACS Appl. Mater. Interfaces* **2014**, *6*, 17245. [CrossRef] [PubMed]
64. Li, Y.; Xie, R.; Pang, X.; Zhou, Z.; Xu, H.; Gu, B.; Wu, C.; Li, H.; Zhang, Y. Aggregation-induced emission fluorescent probe for monitoring endogenous alkaline phosphatase in living cells. *Talanta* **2019**, *205*, 120143. [CrossRef] [PubMed]
65. Zhang, X.; Ren, C.; Hu, F.; Gao, Y.; Wang, Z.; Li, H.; Liu, J.; Liu, B.; Yang, C. Detection of bacterial alkaline phosphatase activity by enzymatic in situ self-assembly of the AIEgen-peptide conjugate. *Anal. Chem.* **2020**, *92*, 5185. [CrossRef]
66. Ji, S.; Gao, H.; Mu, W.; Ni, X.; Yi, X.; Shen, J.; Liu, Q.; Bao, P.; Ding, D. Enzyme-instructed self-assembly leads to the activation of optical properties for selective fluorescence detection and photodynamic ablation of cancer cells. *J. Mater. Chem. B* **2018**, *6*, 2566. [CrossRef]
67. Zhao, L.; Xie, S.; Song, X.; Wei, J.; Zhang, Z.; Li, X. Ratiometric fluorescent response of electrospun fibrous strips for real-time sensing of alkaline phosphatase in serum. *Biosens. Bioelectron.* **2017**, *91*, 217. [CrossRef]
68. Kaur, J.; Singh, P.K. An AIEgen–protamine assembly/disassembly based fluorescence turn-on probe for sensing alkaline phosphatase. *Sens. Actuat. B Chem.* **2021**, *346*, 130517. [CrossRef]
69. Luo, Y.; Li, J.; Li, Y.; Yang, B.; Zhou, T.; Deng, J. Lanthanide-Free Infinite Coordination Polymer Nanoparticles for Real-Time Monitoring of Alkaline Phosphatase and Its Application for Digital Algal Bloom Detection. *ACS Appl. Nano Mater.* **2021**, *4*, 11134. [CrossRef]
70. Geng, F.; Zou, C.; Liu, J.; Zhang, Q.; Guo, X.; Fan, Y.; Yu, H.; Yang, S.; Liu, Z.; Li, L. Development of luminescent nanoswitch for sensing of alkaline phosphatase in human serum based onAl3+-PPi interaction and Cu NCs with AIE properties. *Anal. Chim. Acta* **2019**, *1076*, 131. [CrossRef]
71. Zhao, M.; Feng, H.; Han, J.; Ao, H.; Qian, Z. Multi-stimuli responsive copper nanoclusters with bright red luminescence for quantifying acid phosphatase activity via redox-controlled luminescence switch. *Anal. Chim. Acta* **2017**, *984*, 202. [CrossRef] [PubMed]
72. Huang, Y.; Zhu, L.; Ji, J.; Li, Y.; Liu, T.; Lei, J. Cleancap-regulated aggregation-induced emission strategy for highly specific analysis of enzyme. *Anal. Chem.* **2020**, *92*, 4726. [CrossRef] [PubMed]
73. Han, X.; Han, M.; Ma, L.; Qu, F.; Kong, R.M.; Qu, F. Self-assembled gold nanoclusters for fluorescence turn-on and colorimetric dual-readout detection of alkaline phosphatase activity via DCIP-mediated fluorescence resonance energy transfer. *Talanta* **2019**, *194*, 55. [CrossRef] [PubMed]
74. Pan, T.; Zhou, T.; Tu, Y.; Yan, J. Turn-on fluorescence measurement of acid phosphatase activity through an aggregation-induced emission of thiolate-protected gold nanoclusters. *Talanta* **2021**, *227*, 122197. [CrossRef] [PubMed]
75. Tang, C.; Feng, H.; Huang, Y.; Qian, Z. Reversible luminescent nanoswitches based on aggregation-induced emission enhancement of silver nanoclusters for luminescence turn-on assay of inorganic pyrophosphatase activity. *Anal. Chem.* **2017**, *89*, 4994. [CrossRef]
76. Wang, D.; Li, C.; Zhu, Y.; Song, Y.; Lu, S.; Sun, H.; Hao, H.; Xu, X. TEPP-46-Based AIE Fluorescent Probe for Detection and Bioimaging of PKM2 in Living Cells. *Anal. Chem.* **2021**, *93*, 12682. [CrossRef]
77. Gao, Z.; Gao, H.; Zheng, D.; Xu, T.; Chen, Y.; Liang, C.; Wang, L.; Ding, D.; Yang, Z. β-galactosidase responsive AIE fluorogene for identification and removal of senescent cancer cells. *Sci. China Chem.* **2020**, *63*, 398. [CrossRef]
78. Zhang, S.; Wang, X.; Wang, X.; Wang, T.; Liao, W.; Yuan, Y.; Chen, G.; Jia, X. A novel AIE fluorescent probe for beta-galactosidase detection and imaging in living cells. *Anal. Chim. Acta* **2022**, *1198*, 339554. [CrossRef]
79. Gao, T.; Li, H.; Wu, Y.; Deng, C.; Xie, Y.; Wang, J.; Yang, Y.; Lv, Q.; Jin, Q.; Chen, Y.; et al. First aggregation-induced emission-active probe for species-specific detection of beta-galactosidase. *Talanta* **2021**, *235*, 122659. [CrossRef]
80. Peng, L.; Gao, M.; Cai, X.; Zhang, R.; Li, K.; Feng, G.; Tong, A.; Liu, B. A fluorescent light-up probe based on AIE and ESIPT processes for beta-galactosidase activity detection and visualization in living cells. *J. Mater. Chem. B* **2015**, *3*, 9168. [CrossRef]
81. Gu, K.; Qiu, W.; Guo, Z.; Yan, C.; Zhu, S.; Yao, D.; Shi, P.; Tian, H.; Zhu, W.H. An enzyme-activatable probe liberating AIEgens: On-site sensing and long-term tracking of beta-galactosidase in ovarian cancer cells. *Chem. Sci.* **2019**, *10*, 398. [CrossRef] [PubMed]

82. Dong, L.; Zhang, M.Y.; Han, H.H.; Zang, Y.; Chen, G.R.; Li, J.; He, X.P.; Vidal, S. A general strategy to the intracellular sensing of glycosidases using AIE-based glycoclusters. *Chem. Sci.* **2021**, *13*, 247. [CrossRef] [PubMed]
83. Mandal, N.; Bhattacharjee, M.; Chattopadhyay, A.; Bandyopadhyay, D. Point-of-care-testing of alpha-amylase activity in human blood serum. *Biosens. Bioelectron.* **2019**, *124*, 75. [CrossRef] [PubMed]
84. Shi, J.; Deng, Q.; Li, Y.; Zheng, M.; Chai, Z.; Wan, C.; Zheng, Z.; Li, L.; Huang, F.; Tang, B. A rapid and ultrasensitive tetraphenylethylene-based probe with aggregation-induced emission for direct detection of alpha-amylase in human body fluids. *Anal. Chem.* **2018**, *90*, 13775. [CrossRef]
85. Zhao, M.; Qian, Z.; Zhong, M.; Chen, Z.; Ao, H.; Feng, H. Fabrication of stable and luminescent copper nanocluster-based AIE particles and their application in beta-galactosidase activity assay. *ACS Appl. Mater. Interfaces* **2017**, *9*, 32887. [CrossRef]
86. Huang, Y.; Feng, H.; Liu, W.; Zhang, S.; Tang, C.; Chen, J.; Qian, Z. Cation-driven luminescent self-assembled dots of copper nanoclusters with aggregation-induced emission for beta-galactosidase activity monitoring. *J. Mater. Chem. B* **2017**, *5*, 5120. [CrossRef]
87. Huang, X.; Lan, M.; Wang, J.; Guo, L.; Lin, Z.; Sun, N.; Wu, C.; Qiu, B. A fluorescence signal amplification and specific energy transfer strategy for sensitive detection of beta-galactosidase based on the effects of AIE and host-guest recognition. *Biosens. Bioelectron.* **2020**, *169*, 112655. [CrossRef]
88. Wei, X.; Wu, Q.; Feng, Y.; Chen, M.; Zhang, S.; Chen, M.; Zhang, J.; Yang, G.; Ding, Y.; Yang, X.; et al. Off-on fluorogenic substrate harnessing ESIPT and AIE features for in situ and long-term tracking of β-glucuronidase in Escherichia coli. *Sens. Actuat. B Chem.* **2020**, *304*, 127242. [CrossRef]
89. Wang, M.; Gu, X.; Zhang, G.; Zhang, D.; Zhu, D. Convenient and continuous fluorometric assay method for acetylcholinesterase and inhibitor screening based on the aggregation-induced emission. *Anal. Chem.* **2009**, *81*, 4444. [CrossRef]
90. Chang, J.; Li, H.; Hou, T.; Li, F. Paper-based fluorescent sensor for rapid naked-eye detection of acetylcholinesterase activity and organophosphorus pesticides with high sensitivity and selectivity. *Biosens. Bioelectron.* **2016**, *86*, 971. [CrossRef]
91. Shi, L.; Liu, Y.; Wang, Q.; Wang, T.; Ding, Y.; Cao, Y.; Li, Z.; Wei, H. A pH responsive AIE probe for enzyme assays. *Analyst* **2018**, *143*, 741. [CrossRef]
92. Wang, C.; Wang, X.; Gai, P.; Li, H.; Li, F. Target-responsive AIE-Au nanoconjugate for acetylcholinesterase activity and inhibitor assay with ultralow background noise. *Sens. Actuat. B Chem.* **2019**, *284*, 118. [CrossRef]
93. Cai, Y.; Zhu, H.; Zhou, W.; Qiu, Z.; Chen, C.; Qileng, A.; Li, K.; Liu, Y. Capsulation of AuNCs with AIE effect into metal-organic framework for the marriage of a fluorescence and colorimetric biosensor to detect organophosphorus pesticides. *Anal. Chem.* **2021**, *93*, 7275. [CrossRef] [PubMed]
94. Holas, O.; Musilek, K.; Pohanka, M.; Kuca, K. The progress in the cholinesterase quantification methods. *Expert Opin. Drug Dis.* **2012**, *7*, 1207. [CrossRef] [PubMed]
95. Xiang, C.; Xiang, J.; Yang, X.; Li, C.; Zhou, L.; Jiang, D.; Peng, Y.; Xu, Z.; Deng, G.; Zhu, B.; et al. Ratiometric imaging of butyrylcholinesterase activity in mice with nonalcoholic fatty liver using an AIE-based fluorescent probe. *J. Mater. Chem. B* **2022**, *10*, 4254. [CrossRef] [PubMed]
96. Ou, X.; Hong, F.; Zhang, Z.; Cheng, Y.; Zhao, Z.; Gao, P.; Lou, X.; Xia, F.; Wang, S. A highly sensitive and facile graphene oxide-based nucleic acid probe: Label-free detection of telomerase activity in cancer patient's urine using AIEgens. *Biosens. Bioelectron.* **2017**, *89*, 417. [CrossRef]
97. Lou, X.; Zhuang, Y.; Zuo, X.; Jia, Y.; Hong, Y.; Min, X.; Zhang, Z.; Xu, X.; Liu, N.; Xia, F.; et al. Real-time, quantitative lighting-up detection of telomerase in urines of bladder cancer patients by AIEgens. *Anal. Chem.* **2015**, *87*, 6822. [CrossRef]
98. Zhuang, Y.; Zhang, M.; Chen, B.; Duan, R.; Min, X.; Zhang, Z.; Zheng, F.; Liang, H.; Zhao, Z.; Lou, X.; et al. Quencher group induced high specificity detection of telomerase in clear and bloody urines by AIEgens. *Anal. Chem.* **2015**, *87*, 9487. [CrossRef]
99. Zhuang, Y.; Huang, F.; Xu, Q.; Zhang, M.; Lou, X.; Xia, F. Facile, fast-responsive, and photostable imaging of telomerase activity in living cells with a fluorescence turn-on manner. *Anal. Chem.* **2016**, *88*, 3289. [CrossRef]
100. Zhuang, Y.; Xu, Q.; Huang, F.; Gao, P.; Zhao, Z.; Lou, X.; Xia, F. Ratiometric fluorescent bioprobe for highly reproducible detection of telomerase in bloody urines of bladder cancer patients. *ACS Sens.* **2016**, *1*, 572. [CrossRef]
101. Liu, Y.; Feng, B.; Cao, X.; Tang, G.; Liu, H.; Chen, F.; Liu, M.; Chen, Q.; Yuan, K.; Gu, Y.; et al. A novel "AIE + ESIPT" near-infrared nanoprobe for the imaging of gamma-glutamyl transpeptidase in living cells and the application in precision medicine. *Analyst* **2019**, *144*, 5136. [CrossRef] [PubMed]
102. Hou, X.; Zeng, F.; Wu, S. A fluorescent assay for gamma-glutamyltranspeptidase via aggregation induced emission and its applications in real samples. *Biosens. Bioelectron.* **2016**, *85*, 317. [CrossRef] [PubMed]
103. Peng, L.; Xiao, L.; Ding, Y.; Xiang, Y.; Tong, A. A simple design of fluorescent probes for indirect detection of beta-lactamase based on AIE and ESIPT processes. *J. Mater. Chem. B* **2018**, *6*, 3922. [CrossRef]
104. Gao, M.; Hu, Q.; Feng, G.; Tang, B.Z.; Liu, B. A fluorescent light-up probe with "AIE + ESIPT" characteristics for specific detection of lysosomal esterase. *J. Mater. Chem. B* **2014**, *2*, 3438. [CrossRef] [PubMed]
105. Peng, L.; Xu, S.; Zheng, X.; Cheng, X.; Zhang, R.; Liu, J.; Liu, B.; Tong, A. Rational design of a red-emissive fluorophore with AIE and ESIPT characteristics and its application in light-up sensing of esterase. *Anal. Chem.* **2017**, *89*, 3162. [CrossRef] [PubMed]
106. Shi, J.; Zhang, S.; Zheng, M.; Deng, Q.; Zheng, C.; Li, J.; Huang, F. A novel fluorometric turn-on assay for lipase activity based on an aggregation-induced emission (AIE) luminogen. *Sens. Actuat. B Chem.* **2017**, *238*, 765. [CrossRef]

107. Guan, P.; Liu, Y.; Yang, B.; Wu, Y.; Chai, J.; Wen, G.; Liu, B. Fluorometric probe for the lipase level: Design, mechanism and biological imaging application. *Talanta* **2021**, *225*, 121948. [CrossRef]
108. Koo, S.; Won, M.; Li, H.; Kim, W.Y.; Li, M.; Yan, C.; Sharma, A.; Guo, Z.; Zhu, W.H.; Sessler, J.L.; et al. Harnessing alpha-l-fucosidase for in vivo cellular senescence imaging. *Chem. Sci.* **2021**, *12*, 10054. [CrossRef]
109. Xie, L.; Li, R.; Zheng, B.; Xie, Z.; Fang, X.; Wang, Y.; Cuny, G.D.; Li, Z.; Lin, B.; Chen, X.; et al. Development of rofecoxib-based fluorescent probes and investigations on their solvatochromism, AIE activity, mechanochromism, and COX-2-targeted bioimaging. *Anal. Chem.* **2021**, *93*, 11991. [CrossRef]
110. Wang, Q.; Li, C.; Chen, Q.; Zhang, P.; Wang, D.; Kang, M.; Jiang, G.; Wang, J. Lysosome-targeting red-emitting aggregation-induced emission probe with large Stokes shift for light-up in situ visualization of beta-N-acetylhexosaminidase. *Anal. Chem.* **2019**, *91*, 12611. [CrossRef]
111. Horsch, M.; Mayer, C.; Sennhauser, U.; Rast, D.M. beta-N-acetylhexosaminidase: A target for the design of antifungal agents. *Pharmacol. Therapeut.* **1997**, *76*, 187. [CrossRef]
112. Niu, S.; Bi, C.; Song, W. Detection of DNA methyltransferase activity using template-free DNA polymerization amplification based on aggregation-induced emission. *Anal. Biochem.* **2020**, *590*, 113532. [CrossRef]
113. Mio, K.; Stern, R. Inhibitors of the hyaluronidases. *Matrix Biol.* **2002**, *21*, 31. [CrossRef]
114. Li, X.; Zhou, Z.; Tang, Y.; Cheng Zhang, C.; Zheng, Y.; Gao, J.; Wang, Q. Modulation of assembly and disassembly of a new tetraphenylethene based nanosensor for highly selective detection of hyaluronidase. *Sens. Actuat. B Chem.* **2018**, *276*, 95. [CrossRef]
115. Wang, S.; Zhang, C.H.; Zhang, P.; Chen, S.; Song, Z.L.; Chen, J.; Zeng, R. Rational design of a HA-AuNPs@AIED nanoassembly for activatable fluorescence detection of HAase and imaging in tumor cells. *Anal. Methods* **2021**, *13*, 2030. [CrossRef] [PubMed]

biosensors

MDPI

Review

An Overview of the Design of Metal-Organic Frameworks-Based Fluorescent Chemosensors and Biosensors

Ning Xia, Yong Chang, Qian Zhou, Shoujie Ding and Fengli Gao *

College of Chemistry and Chemical Engineering, Anyang Normal University, Anyang 455000, China
* Correspondence: flgao@aynu.edu.cn

Abstract: Taking advantage of high porosity, large surface area, tunable nanostructures and ease of functionalization, metal-organic frameworks (MOFs) have been popularly applied in different fields, including adsorption and separation, heterogeneous catalysis, drug delivery, light harvesting, and chemical/biological sensing. The abundant active sites for specific recognition and adjustable optical and electrical characteristics allow for the design of various sensing platforms with MOFs as promising candidates. In this review, we systematically introduce the recent advancements of MOFs-based fluorescent chemosensors and biosensors, mainly focusing on the sensing mechanisms and analytes, including inorganic ions, small organic molecules and biomarkers (e.g., small biomolecules, nucleic acids, proteins, enzymes, and tumor cells). This review may provide valuable references for the development of novel MOFs-based sensing platforms to meet the requirements of environment monitoring and clinical diagnosis.

Keywords: metal-organic frameworks; fluorescence; chemosensors; biosensors

Citation: Xia, N.; Chang, Y.; Zhou, Q.; Ding, S.; Gao, F. An Overview of the Design of Metal-Organic Frameworks-Based Fluorescent Chemosensors and Biosensors. *Biosensors* **2022**, *12*, 928. https://doi.org/10.3390/bios12110928

Received: 10 October 2022
Accepted: 24 October 2022
Published: 26 October 2022

1. Introduction

Metal organic frameworks (MOFs), a class of porous-crystalline materials, are self-assembled from metal ions/clusters and organic ligands. They have been popularly applied in different fields, such as adsorption and separation, heterogeneous catalysis, drug delivery, light harvesting and chemical/biological sensing [1–4]. Various strategies have been proposed for the synthesis of MOFs, including hydrothermal/solvothermal reaction, solvent volatilization, and microwave-assisted, sonochemical and electrochemical methods. The influence of experimental parameters on the properties of MOFs have been investigated, such as metal ions, ligands, solvent, temperature, and reactant ratio. Many groups have summarized the progress in the advantages and disadvantages of different methods for the synthesis of MOFs [5–10]. Recently, MOFs have received special attention due to their versatile optical properties. Because some metal ions and organic ligands show adjustable fluorescence properties, a series of multi-dimensional MOFs with inherent fluorescence have been prepared and successfully implemented as fluorescent platforms for a wide range of applications, such as photocatalysis, chemical/biological sensing and biomedical imaging [11–15].

For the MOFs with intrinsic fluorescence, the emitting mechanisms can be classified into four subtypes: ligand-centered emission, metal ion-centered emission, ligand-to-metal charge transfer (LMTC)-based metal-centered emission, and metal-to-ligand charge transfer (MLCT)-based ligand-centered emission [16]. The resulting emission depends on the structure of MOFs, such as the spacing and orientation between linkers, the energy gap between linkers and metal units, the electronic configuration of metal ions and the bonding geometry. In addition, the aggregation-induced emission (AIE) luminogens (AIEgens) have been used as ligands to synthesize luminescent MOFs with AIE properties for various applications [17]. Moreover, the morphology and size of MOFs (e.g., spherical, wheat ear-like, and flower-like nanostructures) have a significant impact on

the optical properties [18,19]. Fluorescent dyes and nanomaterials (e.g., quantum dots (QDs), carbon dots (CDs), and metal nanoclusters) can be integrated with MOFs as additional emission units by the ways of physical adsorption, covalent coupling and in-situ encapsulation [20–23]. For example, Rhodamine 6G (Rh6G) could be encapsulated into Zn-MOFs to form dual-emitting MOFs for the detection of 2,4,6-trinitrophenol (TNP) [24]. CdSe/ZnS core/shell QDs could be immobilized on porphyrin-based MOFs with the amine−Zn coordination interaction for enhancing light harvesting by energy transfer from QDs to MOFs [25]. Fluorescent CDs could be embedded into MOFs with molecularly imprinted polymers for the detection of quercetin [26]. Moreover, Ln^{3+} ions could bound with the functional groups of ligands in MOFs for emitting the characteristic fluorescence via the antenna effect [27].

During the past decades, MOFs-based fluorescent sensing platforms have been developed for the detection of various targets, including metal ions, small organic molecules and biomolecules [28–32]. Besides their unique optical properties, the high porosity and the abundant active sites of MOFs provide the spatial environment and multiple recognition sites and facilitate the adsorption of analyte in the pores, leading to the preconcentration of target and the enhancement of detection sensitivity. Recently, a few review papers have summarized the applications of MOFs-based materials in chemical/biological sensing [33–39]. For example, Wu's group and Wang's group reviewed the recent progress in fluorescence biosensors based on DNA–MOF hybrids [36,37]. Jia's group discussed the post-synthetic modification methods for MOFs-based fluorescent sensors [38]. Li et al. summarized the achievements of CDs@MOFs-based sensors [39]. In this context, we systematically introduce the recent advancements of MOFs-based fluorescent chemosensors and biosensors, mainly focusing on the detection mechanisms and analytes. First, the common detection mechanisms in MOFs-based fluorescent sensing platforms are briefly introduced. Then, MOFs-based sensors for the detection of inorganic ions (i.e., metal ions cations and inions) are summarized. Next, the assays of small organic molecules using MOFs as fluorescence probes are reviewed. Last, most efforts were put into the summarization of recent advances in the field of MOFs-based sensing of biological species, such as small biomolecules, nucleic acids, enzymes, proteins and tumor cells. Additionally, the outlook and several issues of MOFs-based fluorescent sensing platforms are discussed. The aim of this review is to provide an extensive overview of a wide range of fluorescent MOF-based sensing methods.

2. Detection Mechanisms of MOFs-Based Fluorescent Sensing Platforms

Through a judicious selection of linkers and metal ions, functional groups, Lewis basic/acidic sites, and metal ions in MOFs can be used as the specific recognition sites for preferential responses toward targets. For example, MOFs with free-base porphyrin as the linker can bind to metal ions with high affinity, leading to the change of optical properties of porphyrinic MOFs [40]. Fluorescent MOFs containing pyridyl could be utilized for Cu^{2+} detection because of the strong affinity between pyridyl and Cu^{2+} ions [41]. Meanwhile, the quenching or increasing of the ligand fluorescence by extra metal ions can be used as a switch mode for target analysis. The general detection modes in fluorescence assays can be divided into three categories: signal-on, signal-off, and ratio analysis. MOFs can also be used as fluorescent sensing platforms to act as fluorescent probes or fluorescent modulators. The specific receptor–target interaction can induce the change in the fluorescence of MOFs via different mechanisms [42]. Herein, we briefly introduced four common detection mechanisms involved in most works, including photoelectron transfer (PET), Forster resonance energy transfer (FRET), inner filter effect (IFE), and target-induced chemical or structural change of MOFs (Figure 1) [43].

PET is an excited-state charge-transfer process in which the excited electron in the lowest unoccupied molecular orbital (LUMO) of the photo-excited donor can be transferred to the LUMO of acceptor, leading to the fluorescence quenching (Figure 1A) [44,45]. FRET with a distance-dependent non-radiative energy transfer process is the mostly common

mechanism for fluorescence sensing. When the emission spectrum of donor partially overlaps with the absorption spectrum of acceptor, the energy is transferred from the donor to the acceptor through FRET process (Figure 1B) [46]. The FRET efficiency depends on several factors, including the spectral overlap extent, the distance between the donor and the acceptor, and the dipole–dipole interaction. Thus, when the excitation spectrum of targets overlaps with the emission spectrum of MOFs, the presence of targets (acceptors) can induce the change of the fluorescence of MOFs (donors). IFE involves the competitive absorption of the excitation light between analyte and MOFs or the adsorption of the fluorescent emission of MOFs, resulting in the obvious fluorescence quenching (Figure 1B) [46]. In this method, the adsorption spectrum of analyte always overlaps with the emission or adsorption of MOFs. Unlike PET and FRET, this process is independent on the distance between two species. Moreover, appropriate functional groups on ligands can influence the fluorescence properties of MOFs. They can act as the active sites for specific recognition of targets through coordination or covalent interaction, thus leading to the change of the fluorescence of MOFs. Furthermore, during the detection process, a target can induce the destruction of the skeleton of MOFs-based composites by interacting with the metal nodes or the ligands in MOFs, resulting in the change of fluorescence signal [47,48].

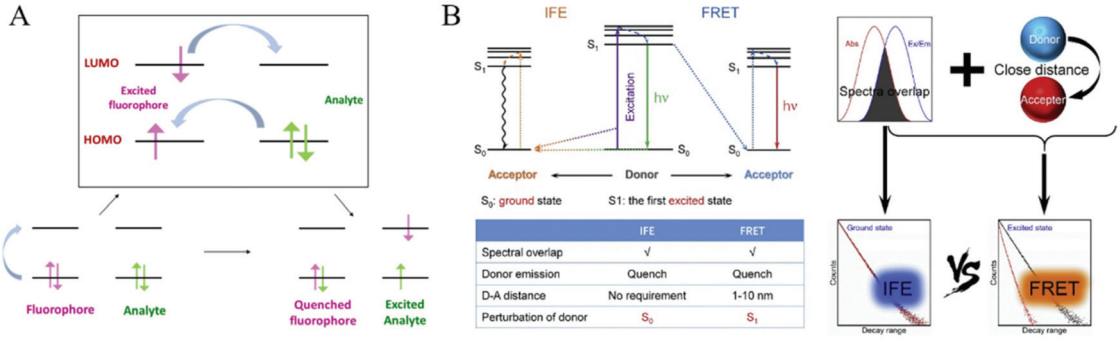

Figure 1. (**A**) Schematic illustration of the process of PET. Reproduced with permission [45]. Copyright 2020, Elesvier. (**B**) Schematic illustration of the process of IFE and FRET. Reproduced with permission [46]. Copyright 2019, Elsevier.

3. Chemosensors

Chemosensors based on the analyte-induced signal change are the most direct and convenient methods for sensing of ions, pollutants, pesticides, volatile organic compounds and drugs. Currently, a wide range of fluorescent chemosensors have been extensively exploited, including small organic molecules, semiconductor QDs, metal nanomaterials, CDs, and AIEgens-based chemosensors [49–53]. Compared to those fluorescent materials, MOFs exhibited several excellent advantages in the field of fluorescent assays. First, the tunable pore sizes of MOFs can act as the sieves to control the entry of analytes into the pores, resulting in the increased selectivity. Second, the large surface area of MOFs can adsorb and concentrate targets to high levels, leading to the enhanced sensitivity. Third, the versatile functional sites (e.g., open metal sites, functional groups in ligands and Lewis acidic/basic sites) can realize the specific recognition through different chemical reaction. Four, the tunability in optical properties of MOFs facilitates the development of fluorescent sensors with multiplex emissions. We do not discuss these topics here since many excellent reviews about the adsorption and separation of targets with porous MOFs are available elsewhere [54–57]. In this part, we mainly discussed the recently advancements of chemosensors for the direct detection of inorganic ions and small organic molecules.

3.1. Inorganic Ions

3.1.1. Metal Ions

Inorganic metal ions, including heavy metal ions and transition metal ions, have an important role in environmental and ecological systems. Heavy metal ions (e.g., Cu^{2+}, Fe^{3+}, Hg^{2+} and Cr^{3+}) can cause serious harm to the water and soil resources. Several transition metal ions are essential trace elements in biological metabolism. As a result, a large number of MOFs-based fluorescent sensors have been developed for the detection of metal ions in recent past years (Table 1). Due to the abundant functional groups of ligands in MOFs (e.g., carboxyl, amino, and phenolic hydroxyl group), metal ions with the unfilled *d* orbital can bind to the groups with the lone-pair of electrons to result in the quenched fluorescence of MOFs by PET. Several excellent reviews have been reported to summarize the progress of MOFs-based fluorescent assays for metal ions [58–62]. In this section, we mainly summarized the recently reported and representative literatures.

Copper is a fundamental metal element in biological systems due to its enzymatic property. Exposure to excessive concentrations of Cu^{2+} may cause neurodegenerative disorders such as Wilson's disease and Parkinson's disease. Several fluorescent MOFs-based Cu^{2+} sensors have been developed in a signal-off mode based on the excellent fluorescence quenching ability of Cu^{2+}. For example, Chen et al. designed a ratiometric fluorescent probe for Cu^{2+} detection by integrating UiO-66$(OH)_2$ with porphyrin-based MOF PCN-224 (Figure 2A) [63]. The green-emission UiO-66$(OH)_2$ acted as the internal reference, while Cu^{2+} quenched the red emission of PCN-224 by binding to the porphyrin ligand with strong affinity. Cheng et al. applied fluorescent porphyrinic MOF-525 as the probe for signal-off detection of Cu^{2+} ions [64]. Because the sensitivity of "turn-off" sensors may be lower than that of "turn-on" sensors. Chen et al. reported "turn-on" fluorescent sensing of Cu^{2+} ions based on the porphyrinic MOFs-catalyzed Heck reaction [65]. As displayed in Figure 2B, porphyrin in PCN-222 was pre-inserted with Pb^{2+} ions. Cu^{2+} ions could replace Pb^{2+} ions due to the stronger binding affinity. Then, the released Pb^{2+} ions were in-situ reduced into PbNPs in MOFs and catalyzed the transformation of non-fluorescent aniline into fluorescent product via Heck cross-coupling reaction. More interestingly, ratiometric fluorescence MOFs-based sensors have been widely constructed because they can overcome the shortcomings of single-emission fluorescence methods. Xia et al. prepared dual-emission MOFs with dual ligands and used them for the ratiometric detection of Cu^{2+} ions in human serum [66]. As shown in Figure 2C, the ligand terephthalic acid (H_2BDC) was used to sensitize Eu^{3+} ions via the antenna effect. 2,5-Diaminoterephthalic acid (H_2DATA) with the emission at 465 nm could selectively identify the target. Cu^{2+} was coordinated with the -NH_2 group of DATA, thus quenching the fluorescence of DATA via PET. For simultaneously monitoring of Cu^{+} and Cu^{2+} ions in biological samples, Zhang et al. reported a dual-channel fluorescence method for the speciation of both Cu^{+} and Cu^{2+} ions based on CDs-encapsulated Eu-MOFs (Figure 2D) [67]. In this work, fluorescent CDs were prepared from folic acid through a hydrothermal method and then in-situ encapsulated in Eu-MOFs. Cu^{2+} could quench the fluorescence of Eu-MOFs at $\lambda_{ex}/\lambda_{em}$ = 380/454 nm by replacing Eu^{3+} in the frameworks. Cu^{+} was interacted with bathocuproine disulfonate (BCS) and the product (BCS−Cu^{+}) to quench the fluorescence of CDs at $\lambda_{ex}/\lambda_{em}$ = 275/615 nm via the IFE mechanism.

Aluminum is widely used in aluminum tableware, food packaging, and other production products. An excessive intake of aluminum in the body will disrupt the activities of the central nervous system, cause human dysfunction, and hinder the normal metabolism of calcium and phosphorus. Zhong et al. prepared two types of fluorescent curcumin@MOF-5 composites through post-adsorption and one-pot synthesis and applied them to detect Al^{3+} ions [68]. In this method, the fluorescence was quenched by the PET process, and Al^{3+} could inhibit the PET process between curcumin and MOFs-5, resulting in the restoration of curcumin fluorescence. Li et al. applied an AIE-active MOFs for sensing of Al^{3+} in a "turn-on" mode (Figure 3A) [69]. The fluorescence of Zn-MOF containing AIE ligands was

quenched by the auxiliary ligand of 4,4′-bypyridine (Bpy) through the exciton migration. Al^{3+} was competitively coordinated with Bpy to recovery the fluorescence.

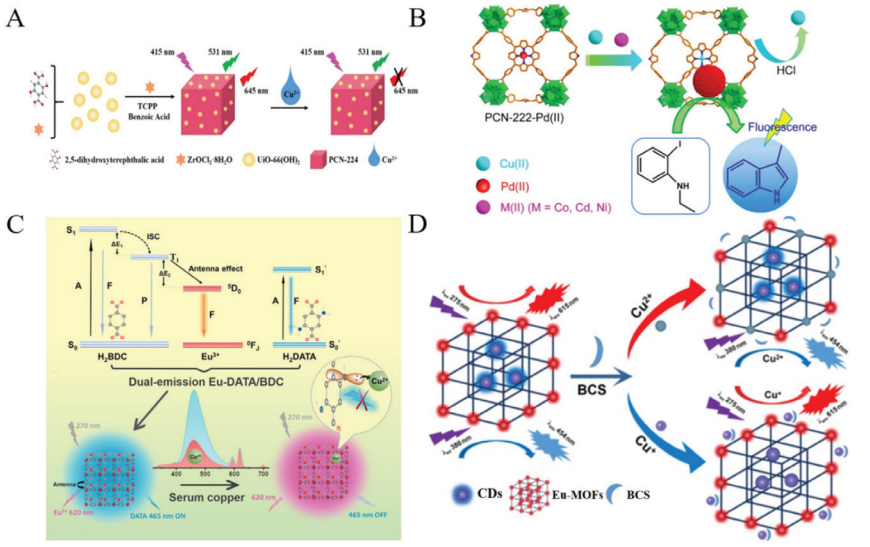

Figure 2. (**A**) Schematic illustration of process for encapsulating the UiO-66$(OH)_2$ into the porphyrin MOFs (PCN-224) and concept for sensing Cu^{2+}. Reproduced with permission [63]. Copyright 2019, American Chemical Society. (**B**) Schematic illustration of the fluorescence "turn-on" sensing of Cu^{2+} ions based on the porphyrinic MOFs-catalyzed Heck reaction. Reproduced with permission [65]. Copyright 2016, American Chemical Society. (**C**) Schematic illustration of the design principle of dual-emission Eu-DATA/BDC MOFs and the ratiometric sensing and visible detection of Cu^{2+} ions in human serum. Reproduced with permission [66]. Copyright 2022, Elsevier. (**D**) Schematic illustration of the detection mechanisms for Cu^{+} ions and Cu^{2+} ions with the dual fluorescence Eu-MOFs@CDs. Reproduced with permission [67]. Copyright 2022, American Chemical Society.

Fe^{3+} is an essential trace element in human nutrition. However, the abnormal level of Fe^{3+} may cause many health problems, such as anemia, diabetes, cardiovascular failure, liver laceration and so on. Due to the half-filled *d* orbits and the light absorption ability, MOFs (e.g., NTU-9 nanosheets, Tb-MOFs and dye@Zr-MOFs) were used to develop fluorescence Fe^{3+} sensor in which Fe^{3+} ions could quench the fluorescence of MOFs through the PET and/or IFE process [70–73]. For example, Qi et al. demonstrated that Fe^{3+} could quench the fluorescence of Tb-MOF via the IFE process and the inhibition of the energy transfer between linker and Tb^{3+} [74]. Recently, Yin et al. developed a fluorescent sensor for Fe^{3+} and HCHO detection based on the mixed-ligand MOFs [75]. As shown in Figure 3B, the prepared Zn-MOFs exhibited dual emission at 450 and 550 nm and the relative intensity was controlled by adjusting the ligand ratio and the excitation wavelength. Fe^{3+} could be coordinated with the amino group of the ligand 2-aminoterephthalic acid (BDC-NH_2), thus quenching the fluorescence via the PET and IFE mechanism. HCHO could react with the amino group of BDC-NH_2 to form a Shiff base, leading to the decrease of the fluorescence. Consequently, the yellow emission of the ligand of 2,5-dihydroxylterephthalic acid [BDC-$(OH)_2$] at 550 nm increased. Additionally, Fe^{3+} ions can cause the collapse of the structure of Tb-MOFs and disturb the energy transfer from the ligand to Tb^{3+}, resulting in the quenching of the fluorescence of Tb-MOFs [76].

As one of the most toxic heavy metals, mercury exists extensively in the ecosystem by the format of inorganic ion (HgX_2, X = halide) or organic mercury [77]. Guo et al. prepared Eu^{3+}-functionalized Ca-MOF through the post-synthesis modification and applied it for the detection of Hg^{2+} [78]. In this study, Hg^{2+} chelated with the soft Lewis base S in the ligand

and inhibited the LMCT, leading to the decrease of the fluorescence signal of Eu^{3+} and the recovery of the emission of the ligand. Wang et al. reported the detection of Hg^{2+} and CH_3Hg^+ ions by using boric acid (BA)-functionalized Eu-MOF as the dual-signal probe (Figure 3C) [79]. The BA-Eu-MOF was prepared with 5-boronobezene-1,3-dicarboxylic acid (5-bop) as the ligand. The 5-bop ligands can sensitize the red emission of Eu^{3+} and provide the binding sites for Hg^{2+} and CH_3Hg^+. The electron-withdrawing effect of BA could passivate the antenna effect of 5-bop. Hg^{2+} and CH_3Hg^+ ions could replace the BA groups in the framework by transmetalation reaction, thus activating the antenna effect of 5-bop and resulting in the increase of red emission.

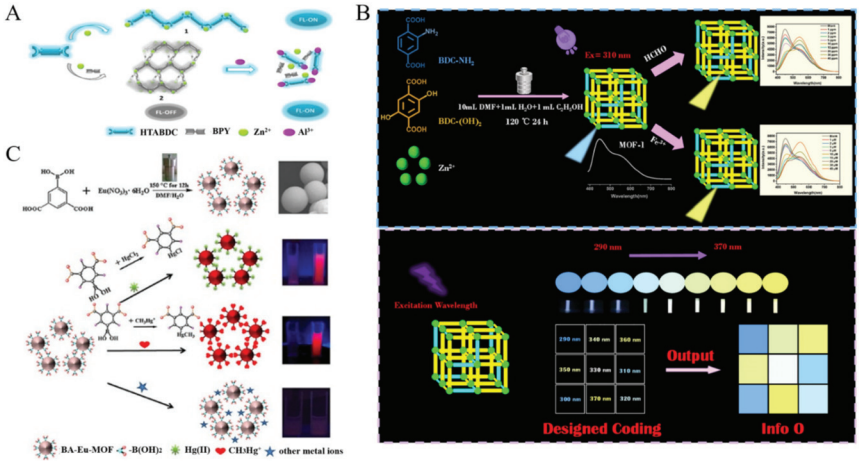

Figure 3. (**A**) Schematic illustration of the AIE-active MOFs-based sensor for the detection of Al^{3+}. Reproduced with permission [69]. Copyright 2018, American Chemical Society. (**B**) Schematic illustration of BA-Eu-MOF synthesis and the sensing process of BA-Eu-MOF toward Hg^{2+} and CH_3Hg^+ ions based on transmetalation. Reproduced with permission [75]. Copyright 2016, American Chemical Society. (**C**) Schematic illustration of the design principle of dual-emission Eu-DATA/BDC MOFs and the ratiometric sensing and visible detection of Cu^{2+} ions in human serum. Reproduced with permission [79]. Copyright 2022, Elsevier.

Furthermore, Li et al. developed a Cd(II)-MOFs-based signal-on fluorescence sensor for Cr^{3+} detection [80]. Cr^{3+} could be chelated by the –COOH group on the ligand, improving the rigidity of the framework and resulting in the increased fluorescence. Liu's prepared NH_3 plasma-functionalized UiO-66-NH_2 for the detection of U(VI) [81]. The functionalized UiO-66-NH_2 showed high fluorescence intensity due to the large number of electron-donating groups. U(VI) could quench the fluorescence of MOFs through the static quenching effect by binding to the amino group.

pH plays an important regulatory role in physiological/pathologic processes. The abnormal intracellular pH is related to many diseases, such as cancer, stroke, and Alzheimer's disease [82]. Several fluorescent MOFs have been reported to exhibit response toward different pH values, such as PCN-225(Zn), Y(III)-MOFs and Dy-MOF [83–87]. Typically, Chen et al. reported a dual-emission fluorescent MOF for monitoring the change of pH value with an excitation wavelength (Figure 4) [88]. In this work, the DBI-PEG-NH_2-functionalized Fe_3O_4 NPs were first embedded to the MOF PCN-224. Then, rhodamine B isothiocyanate (RBITC) was conjugated onto the surface of Fe_3O_4 to form the RBITC-PCN nanoprobe. The covalent coupling of RBITC with DBI-PEG-NH_2 prevented the leaching of RBITC. Under single excitation, the core-shell-like nanoprobe showed dual-emission from porphyrin of PCN and RBITC. H^+ ions could enter into the pores rapidly to open the channels of MOFs. The RB-PCN nanoprobe could detect the pH change over a wide range.

In the acidic pH (1.7 − 7.0), the nanoprobe showed two emissions from RBITC at 575 nm. However, it showed an emission at 641 nm for PCN-224 in the pH ranging from 7.0 to 11.3.

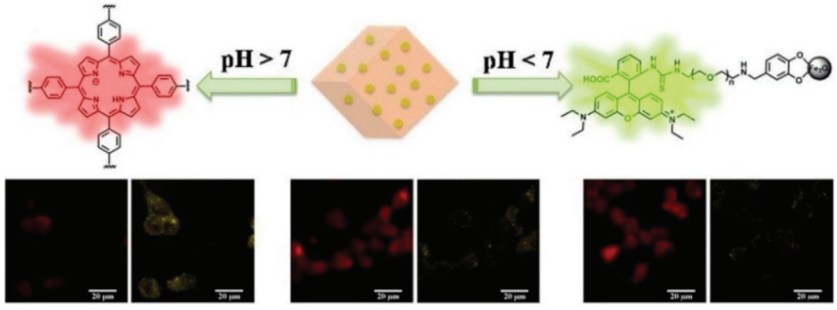

Figure 4. Schematic illustration of the dual-emission fluorescent MOF for monitoring the change of pH value with an excitation wavelength. Reproduced with permission [88]. Copyright 2018, American Chemical Society.

3.1.2. Anions

Anions (e.g., Cl^-, Br-, I^-, SCN^- and $NO_3{}^-$) can replace the free counterions in MOFs via anion-exchange, thus changing the optical properties of MOFs. In addition, anions can restore the fluorescence of MOFs quenched by metal ions based on different interactions, such as high affinity interaction and chemical reaction, achieving a fluorescence "on-off-on" switch. A lot of MOFs-based fluorescence sensors have been fabricated to determine anions with satisfactory results (Table 1). Herein, we summarized only the recent advancement since several excellent reviews have been reported to discuss MOFs-based fluorescent anions sensors [89,90].

Fluoride ion (F^-) is one of the most harmful elements in drinking water. Over-intake of F^- can result in dental fluorosis, kidney failure, or DNA damage. According to the Pearson hard−soft acid−base (HSAB) classification, F^- as a hard Lewis base can bind to Ln^{3+} ions as hard Lewis acids with high affinity. Thus, Ln-MOFs can be used to develop fluorescent sensors for F^- detection [91]. Zeng et al. synthesized a series of mixed Ln-MOFs with triazine-based planar 4,4,4"-s-triazine-2,4,6-triyltribenzoate (TATB) as the ligand and Tb/Eu ions as the centers (Figure 5A) [92]. The luminescent wavelength of Tb/Eu(TATB) MOFs could be regulated by adjusting the ratio of the two lanthanide metal ions. The host−guest interaction between F^- and MOF induced the signal change in color and luminescence intensity of MOFs, thus realizing the visual and ratiometric luminescent detection of F^-. Che et al. reported a portable logic detector based on Eu-MOF for the detection of Eu^{3+} and F^- in groundwater [93]. In this study, Eu^{3+} combined with the amino groups on MOFs, leading to the aggregation of MOFs and the fluorescence quenching. F^- ions could replace Eu^{3+} to bind with the amino groups, resulting in the recovery of the fluorescence. Dalapati et al. prepared the pyrene-tagged UiO-66-NH_2 through the post-synthetic modification and used it to detect F^- and $H_2PO_4{}^-$ based on "turn-on" fluorescence mechanism [94]. In this work, the hydrogen bonding interactions between anions and pyrene units made the two π-stacked pyrene moieties closer and formed static pyrene excimers, resulting in the enhancement and blue shift of the fluorescence.

Hypochlorous acid (HClO) is a typical reactive oxygen species. Excessive endogenous HClO may cause oxidative stress, tissue damage and diseases. With dual ligands of BDC-NH_2 and dipicolinic acid (DPA) and metal node Eu^{3+} ions as the precursors, a ratiometric fluorescent MOF probe was prepared (Figure 5B) [95]. The Eu-BDC-NH_2/DPA MOF with exposed amino groups could be used to determine hypochlorous (ClO^-) ions due to the formation of hydrogen bonds [95]. In this process, the blue fluorescence from BDC-NH_2 was reduced, while the antenna effect emission from Eu^{3+} remained stable. Moreover, Tan et al. used MOFs as the scaffolds to develop a FRET system for the ratiometric detection

of ClO^- ions [96]. In this work, CDs as the donor and curcumin as the acceptor were entrapped into MOFs for the construction of the FRET system. In the presence of ClO^-, curcumin was oxidized and the FRET was blocked, resulting in the increase of the CDs fluorescence at 410 nm and the decrease of the curcumin (CCM) fluorescence at 585 nm.

Phosphate (PO_4^{3-}) plays an important role in many biological functions. An excessive content of PO_4^{3-} in the human body is harmful to blood vessels and may accelerate aging [97]. PO_4^{3-} has a significant quenching effect on the fluorescence of Ln-MOF or Ln-functionalized MOFs [98]. For example, Fan et al. used a Tb(III)-functionalized Zn-MOFs for fluorometric detection of PO_4^{3-} [99]. In this work, the binding between PO_4^{3-} and Tb^{3+} inhibited the antenna effect, leading to the decrease of Tb^{3+} emission. Recently, Shi et al. prepared dual-ligands Eu-MOF with dual emissions for the ratiometric/visual determination of PO_4^{3-} [100]. As illustrated in Figure 5C, Eu-MOFs with benzene-1,3,5-tricarboxylate (BTC) and BDC-NH_2 as ligands exhibited two emissions at 425 nm and 617 nm. PO_4^{3-} could replace a part of the ligand to coordinate with Eu^{3+} and weakened the antenna effect, causing a reduced intensity at 617 nm and an enhanced signal at 425 nm.

Other anions can also be sensitively determined by fluorescent MOFs. For instance, Zhang et al. demonstrated that bromate could oxidize Fe^{2+} into Fe^{3+} in Eu-MOFs@Fe^{2+}, thus quenching the fluorescence [101]. Karmakar et al. modified ZIF-90 with the dicyanovinyl (DCV) group for the specific recognition of CN^- (Figure 5D) [102]. The nucleophilic addition reaction between cyanide and DCV group resulted in the loss of conjugation and the decrease of fluorescence intensity. Jain et al. reported a boric-acid-functionalized Eu-MOFs-based sensor for $Cr_2O_7^{2-}$ detection [103]. The red fluorescence of dual-emission MOFs was quenched and the blue emission was enhanced. Zhang et al. reported that $Cr_2O_7^{2-}$ could quench the fluorescence of Zn-MOFs via the IFE mechanism [104].

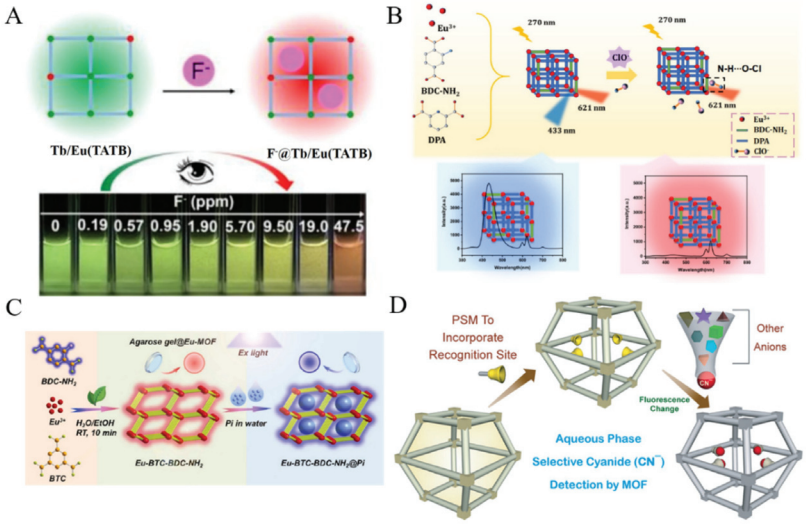

Figure 5. (**A**) Schematic illustration of visual detection of F^- using mixed Ln-MOFs with a smartphone. Reproduced with permission [92]. Copyright 2020, American Chemical Society. (**B**) Schematic illustration of the preparation of Eu-BDC-NH_2/DPA and fluorescence spectra and photographs in the absence and presence of HClO. Reproduced with permission [95]. Copyright 2021, American Chemical Society. (**C**) Schematic illustration of the detection of PO_4^{3-} based on Eu-BTC-BDC-NH_2. Reproduced with permission [100]. Copyright 2022, Elsevier. (**D**) Schematic illustration of the post-synthetic modification in MOF leading to selective sensing of CN^-. Reproduced with permission [102]. Copyright 2016, Wiley.

H_2S is one of the reactive sulfur species that is generated from the decomposition of sulfur-containing organic molecules by microbes. Ma et al. prepared a Cu(II)-contained 3D porous nanoscale MOF (denoted as nano-MOF PAC) by using meso-tetrakis (4-carboxylphenyl)porphyrin (TCPP) as the ligand (Figure 6A) [105]. The reactive Cu(II) ions were introduced into the framework as the responding sites of H_2S. The fluorescence of ligand in PAC was quenched by Cu(II) due to its paramagnetic characteristics. H_2S could sequester Cu(II) from the porphyrin center to form CuS, thus turning on the fluorescence. With the nano-MOF as fluorescent probe, the signal-on in-situ detection of H_2S in living cells was achieved. Gao et al. reported the detection of H_2S with the ratiometric fluorescent MOF (rhodamine B (RhB)/UiO-66-N_3) (Figure 6B) [106]. The nanoprobe exhibited dual emissions (425 nm and 575 nm) with a single excitation wavelength. The red fluorescence at 575 nm as the internal reference is attributed to RhB. The H_2S-mediated biorthogonal reduction of azide to amine caused the increase in the blue fluorescence at 425 nm. The signal-on ratiometric sensing strategy could be used to image H_2S in live cells.

Table 1. Performances of MOFs-based fluorescent chemosensors for the detection of inorganic ions.

MOFs	Targets	Linear Range	LOD	Ref.
Cd-MOFs	Cr^{3+}	0~3 mM	0.164 μM	[80]
UiO-66-NH_2	U(VI)	0~1.2 μM	0.08 μM	[81]
UiO-66$(OH)_2$@PCN-224	Cu^{2+}	0~10 μM	0.068 nM	[63]
Porphyrinic Zr-MOF-525	Cu^{2+}	1~250 nM	220 pM	[64]
Porphyrinic PCN-222-Pd(II)	Cu^{2+}	0.05~2 μM	50 nM	[65]
Eu-MOF	Cu^{2+}	1~40 μM	0.15 μM	[66]
CDs@Eu-MOF	Cu^{+} and Cu^{2+}	0.5~20 μM and 0.5~20 μM	0.22 and 0.14 μM	[67]
CCM@MOF-5	Al^{3+}	0~0.33 mM	2.84 μM	[68]
AIE-active Zn-MOFs	Al^{3+}	Not reported	3.73 ppb	[69]
Tb-MOFs	Fe^{3+}	0.33~33 μM	0.936 μM	[74]
Tb-MOFs	Fe^{3+}	0~100 μM	0.35 μM	[71]
Zn-MOFs	Fe^{3+} and HCHO	1~40 μM and 1~40 ppm	0.58 μM and 370 ppb	[75]
RhB@Zr-MOF	Fe^{3+} and $Cr_2O_7^{2-}$	0.01~1 mM and 1~100 μM	Not reported	[72]
Eu-modified Ga-MOFs	Hg^{2+}	0.02~200 μM	2.6 nM	[78]
BA-Eu-MOF	Hg^{2+} and CH_3Hg^{+}	1~60 μM and 2~80 μM	220 and 440 nM	[79]
BODIPY@Eu-MOF	F^{-}, H_2O_2 and glucose	0~30 μM, 0~6 μM and 0~6 μM	0.1737 μM, 6.22 nM and 6.92 nM	[91]
Tb^{3+} and Eu^{3+}-MOFs	F^{-}	0~1.9 ppm	96 ppb	[92]
Eu-MOFs	Eu^{3+} and F^{-}	0~7.4 μM and 0~515 μM	0.2481 μM and 1.145 μM	[93]
Eu-MOFs	HClO	1~20 μM and 20~40 μM	37 nM	[95]
CDs/CCM@ZIF-8	HClO	0.1~50 μM	67 nM	[96]
Eu-MOFs	PO_4^{3-}	0.1~10 μM and 10~50 μM	0.07 μM	[100]
M-ZIF-90	CN^{-}	0~0.1 mM	2 μM	[102]
UiO-66@COFs	PO_4^{3-}	0~30 μM	0.067 μM	[97]
Tb-modified Zn-MOFs	PO_4^{3-}	0.01~200 μM	4 nM	[99]
Eu-MOF@Fe^{2+}	BrO_4^{-}	0~0.2 mM	3.7 μM	[101]
BA-Eu-MOFs	$Cr_2O_7^{2-}$	0.1~3 μM	0.58 μM	[103]
Zn-MOFs	$Cr_2O_7^{2-}$	0.3~20 μM	0.09 μM	[104]
RhB/UiO-66-N_3	H_2S	0.1~4 mM	82.4 μM	[106]

Abbreviation: CDs, carbon dots; CCM, curcumin; AIE, aggregation-induced emission; RhB, rhodamine B; BA, boric acid; BODIPY, boron-dipyrromethene; COFs, covalent organic frameworks.

3.2. Small Organic Molecules

Organic molecules with functional groups can coordinate with metal nodes or react with the linkers, finally changing the emission properties of MOFs. In addition, metal ions-mediated fluorescence "turn-off-on" switch can be utilized to detect small organic molecules. Based on these principles, many MOFs-based fluorescence sensors have been

reported for the detection of a wide range of analytes, including nitro explosives, pesticides, antibiotics and other small molecules (Table 2) [107].

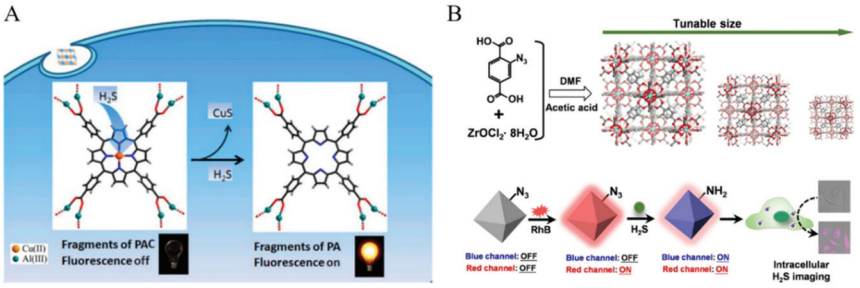

Figure 6. (**A**) Schematic illustration of structural fragment of nano-MOF PAC and the proposed strategy for fluorescent variation of PAC upon reactive Cu(II) ions as the H_2S-responding site. Reproduced with permission [105]. Copyright 2014, American Chemical Society. (**B**) Schematic illustration of one-step hydrothermal synthesis of UiO-66-N_3 in acetic acid/DMF with tunable size, the principle of H_2S detection on the basis of RhB/UiO-66-N_3 and their applications for intracellular H_2S imaging. Reproduced with permission [106]. Copyright 2021, Elsevier.

For homeland security, environmental and humanitarian implications, various fluorescent methods have been developed for explosive substances detection. Explosives with electron-deficient $–NO_2$ groups are good electron acceptors that can interact with the electron-rich aromatic rings and functional groups with lone-pair electrons, leading to decreased fluorescence [108–110]. For this view, Zhang et al. prepared a 2D MOF (NENU-503) for the detection of nitroaromatic molecules with different numbers of $–NO_2$ groups [111]. Wang et al. introduced a cationic dye into MOFs through ion-exchange process and used the fluorescent dye@bio-MOFs as the dual-emitting platforms for the detection of different kinds of nitro-explosive substances [112]. In this work, nitroaromatics could quench the fluorescence of MOFs, and aliphatic nitro-organics could increase the fluorescence via confinement-induced enhancement. Sun et al. in-situ encapsulated RhB molecules into Cd-MOFs and used the dual-emission of MOFs to detect 4-nitroaniline [113]. Sharma et al. synthesized a hydroxyl-functionalized indium MOF for the fluorescent detection of nitro-aromatic compounds [114]. The fluorescence was quenched due to the PET effect. With tetraphenylethylene, γ-cyclodextrin (γ-CD) and metal ion (K^+) as the precursors, Qiu et al. synthesized γ-CD-MOF-K and used it to encapsulate the AIE molecules of tetraphenylethylene (Figure 7A) [115]. The resulting TPE@γ-CD-MOF-K composites exhibited a strong fluorescence emission. Attachment of nitro-aromatic compounds on the surface of TPE@γ-CD-MOF-K caused solid-state fluorescence quenching.

Chemical pesticides have been widely used around the world, including organophosphate pesticides and dinotefuran. When entering the surrounding environment, they may show an important influence on human health and life quality. MOFs have been used as fluorescent probes to detect various pesticides [116–118]. For example, Jiao et al. reported a fluorescent method for the detection of dinotefuran with Cd-MOFs, in which dinotefuran quenched the fluorescence of MOFs via the IFE and static quenching process [119]. Based on the host–guest interaction, Yu et al. reported the detection of pesticide glyphosate with tetra-pyridyl calix [4]arene decorated ultrathin 2D MOF nanosheet as the fluorescence probe (Figure 7B) [120]. Glyphosate could interact with the calix [4]arene (Calix) group on the surface of 3D layered MOF nanosheets, thus causing fluorescence enhancement. Dyes-encapsulated MOFs can also be used to detect pesticides. Zhang et al. used methylene blue (MB)-loaded Cd-MOF as the dual-emission probe for the detection of carbaryl that could enhance the fluorescence through the energy transfer and PET mechanisms [121]. Wei et al. prepared eosin Y (EY)-embedded Zr-MOFs for the ratiometric detection of nitenpyram (Figure 7C) [122]. In this study, the dual-emissive characteristics of EY@Zr-MOFs could

be tuned by changing the loading quantity of EY. The FRET between EY@Zr-MOFs and nitenpyram blocked the energy transfer from pristine MOFs to EY, resulting in the decrease of the emission at 430 nm and 560 nm.

Aldehydes are one of the typical volatile organic compounds (VOCs), which can cause serious health problems. Wang et al. reported the detection of formaldehyde (FA) with N-propyl-4-hydrazine-naphthalimide (PHN)-embedded UiO-66-NH_2 (PHN@MOF) as the ratiometric fluorescent probe (Figure 7D) [123]. The intrinsic fluorescence of UiO-66-NH_2 offered a reference signal. FA was reacted with the hydrazine group of PHN through the surrounding confinement space provided by MOF.

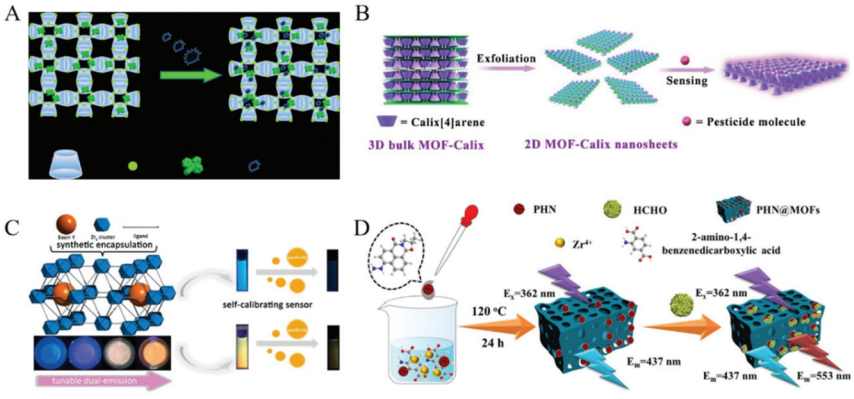

Figure 7. (**A**) Schematic illustration of the AIE-active MOFs for sensitive detection of explosives in liquid and solid phases. Reproduced with permission [115]. Copyright 2020, American Chemical Society. (**B**) Schematic illustration of the fabrication of 2D MOF-Calix nanosheets and sensitive detection of pesticide through host-guest chemistry. Reproduced with permission [120]. Copyright 2020, Elsevier. (**C**) Schematic illustration of EY-embedded Zr-MOFs as a dual-emitting built-in self-calibrating platform for nitenpyram detection. Reproduced with permission [122]. Copyright 2020, American Chemical Society. (**D**) Schematic illustration of the PHN@MOF probe for the detection of FA. Reproduced with permission [123]. Copyright 2021, American Chemical Society.

Antibiotics have been widely used in the treatment of infectious diseases by killing a variety of bacteria and parasites. The misuse of antibiotics seriously threaten the safety of water resources, food, and humans. Thus, many MOFs-based fluorescent sensing platforms have been constructed for the detection of antibiotics, including tetracycline antibiotics (TCs), nitrofuran and fluoroquinolone [124–131]. For instance, Chen et al. employed Zn-MOFs as fluorescent probes for the detection of TCs and NH^{4+} [132]. Qin et al. prepared two-dimensional ultrathin Cd-MOF/Tb^{3+} fluorescent nanosheets and applied them to detect cefxime antibiotic [133]. In this work, cefxime quenched the fluorescence of Cd-MOF/Tb^{3+} via the PET and IFE effects. To reduce environmental interferences, Gan et al. reported a ratiometric fluorescence sensor for visual detection of TC based on the nanohybrid of MOFs and lanthanide the coordination polymers [134]. As shown in Figure 8A, the coordination polymers assembled by Eu^{3+} and guanosine monophosphate (GMP) were in-situ synthesized on the surface of fluorescein-encapsulated MOF-5 (FSS@MOF-5). The resulting FSS@MOF-5/GMP-Eu composites exhibited two fluorescence (yellowish-green and red). In the presence of TC, the red emission from Eu^{3+} was enhanced due to the antenna effect between TC and Eu^{3+}. The yellowish-green emission from FSS@MOF-5 kept constant as an internal reference. Under a UV lamp (365 nm), the fluorescence color of FSS@MOF-5/GMP-Eu changed from yellowish-green to red. Dual MOFs-based heterostructure composites (ZIF-8@PCN-128Y) were used to detect TC in milk and beef samples [135]. In this work, TC enriched by ZIF-8 quenched the fluorescence of PCN-128Y, attributing to the IFE and PET processes. To improve the selectivity of sensors toward TC antibiotics,

Yu et al. found that the AIE effect of chlortetracycline (CTC) could be enhanced by binding with the zinc/pyromellitic acid-based MOF (Zn-BTEC) (Figure 8B) [136]. The CTC molecules were embedded into the porous Zn-BTEC to form assemblies or aggregates. The nanoprobe showed high sensitivity for CTC detection by discriminating it from other antibiotics with high specificity.

There are many toxic and cancerogenic substances in crops and food. For example, gossypol, a natural toxin existing in cottonseeds, shows a great risk to the safe consumption of cottonseed products. Rosi's group found that Yb^{3+}-based MOF (Yb-3,3″-diamino-1,1′:4′,1″-terphenyl-4,4″-dicarboxylic acid) could be used to detect gossypol with a low detection limit (Figure 8C) [137]. In this method, gossypol could sensitize Yb^{3+} and turn on its photoluminescence by facilitating the energy transfer and/or reacting with the amine-functionalized aromatic linker in MOF. The resulting Schiff base compounds caused the red shift of the wavelength. The proposed method could be further used for the design of novel probes for the detection of other aromatic molecules.

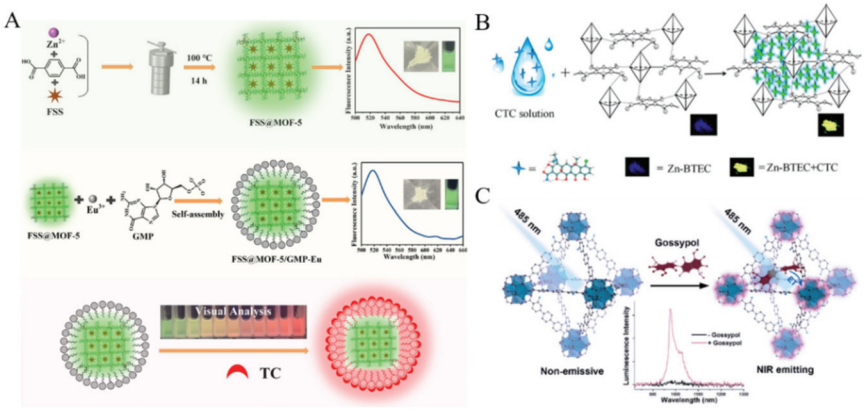

Figure 8. (**A**) Schematic illustration of the synthesis process of FSS@MOF-5/GMP-Eu for rapid and visual detection of TC. Reproduced with permission [134]. Copyright 2021, Elsevier. (**B**) Schematic illustration of sensing process for CTC using MOF Zn-BTEC as a fluorescent probe based on AIE mechanism. Reproduced with permission [136]. Copyright 2019, American Chemical Society. (**C**) Schematic illustration of fluorescent "turn-on" detection of gossypol using Ln^{3+}-based MOFs and Ln^{3+} salts. Reproduced with permission [137]. Copyright 2020, American Chemical Society.

Biological molecules playing an important role in the pathophysiology can be recognized as the biomarkers for disease diagnosis. MOFs have been used to construct fluorescent sensors for the direct determination of biological molecules, such as hypoxanthine, uric acid, histidine and 3-nitrotyrosine [138–143]. For example, Zhang et al. used the mixed-crystal Ln-MOF as a fluorescent indicator for the detection of lysophosphatidic acid, a biomarker for ovarian cancer [144]. Wang et al. reported a UiO-66-NH_2 MOF-based ratiometric fluorescent sensor for the detection of dopamine and reduced glutathione [145]. In this work, dopamine was reacted with polyethyleneimine to form copolymer, and it quenched the fluorescence of MOF via FRET. However, glutathione could inhibit the formation of copolymer and block the FRET, leading to the recovery of the fluorescence of MOFs. Reversibly, MOFs can also act as the acceptor to quench the fluorescent dye-labeled probes. Bhardwaj et al. reported a Tb-MOFs-based sensor for fluorescent detection of DPA, a biomarker for bacteria in feces [146]. In this work, the competitive interaction between Tb^{3+} ions and DPA inhibited the sensitization of Tb^{3+} ions in MOFs, leading to the decrease of the fluorescence. Li et al. reported a ratiometric fluorescent system for monitoring the main component of bacterial spore, DPA with CdS QDs-loaded ZIF-8 MOF as the sensing platform [147]. As shown in Figure 9A, Rhodamine 6G (Rho 6G) was encapsulated in the QDs/MOF nanocrystal as the internal reference. The

fluorescence from QDs could be quenched by the capture of Eu^{3+} ions. Once the Eu^{3+} ions were sequestered by DPA, the fluorescence of QDs would be restored, while no signal change was observed for Rho 6G. The method showed a high sensitivity and excellent anti-interference ability for monitoring spore germination. Qu et al. reported the detection of creatinine by using 8-hydroxy-2-quinoline-carboxaldehyde (HQCA) and Al^{3+}-modified MOFs (UiO-66-NH_2) (Figure 9B) [148]. In this method, the formed creatinine-Al^{3+} Lewis acid-base complexes turned on the fluorescence by interrupting the energy transfer and electron transfer from UiO-HQCA to Al^{3+}. With the rhodamine B (RhB)-encapsulated porous Zn(II)-MOF (DiCH_3MOF-5) composite as the sensing platform, Guo et al. reported an "on-off-on" fluorescent switching method for the determination of Fe^{3+} and ascorbic acid (Figure 9C) [149]. The fluorescence of RhB@DiCH_3MOF-5 could be quenched by Fe^{3+} due to the synergism of IFE and PET. However, addition of ascorbic acid to the quenched solution would recover the fluorescence due to the oxidation−reduction reaction. Benzene is one of the ubiquitous environmental pollutants. The trans,trans-muconic acid (tt-MA) is a suitable urinary biomarker for benzene at high levels. Qu and co-workers found that the bi-metal-loaded Eu(III)/Tb(III)@MOF-SO_3^- showed a Tb(III)-induced luminescence of Eu(III) (Figure 9D) [150]. Based on the fluorescence quenching effect, the lanthanide-based MOF hybrids were used for the signal-off detection of tt-MA in urine.

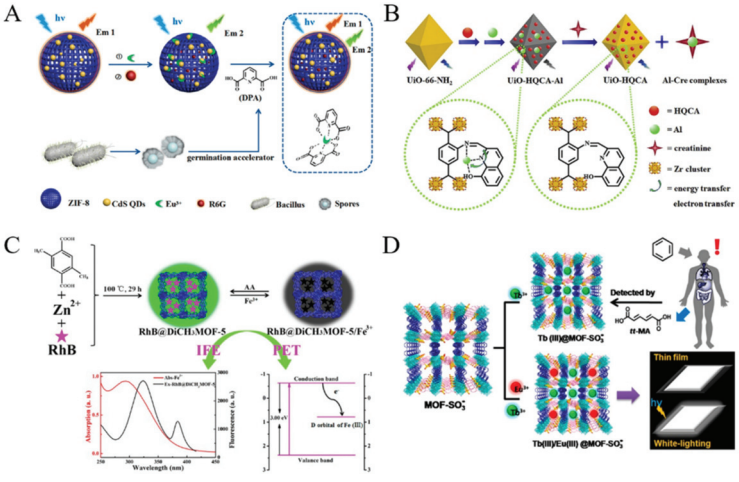

Figure 9. (**A**) Schematic illustration of the preparation of R6G/Eu-CdS@ZIF-8 and its application for DPA detection. Reproduced with permission [147]. Copyright 2020, American Chemical Society. (**B**) Schematic illustration of the HQCA and Al^{3+}-modified MOFs-based fluorescent sensor for the detection of creatinine. Reproduced with permission [148]. Copyright 2020, Elsevier. (**C**) Schematic illustration of synthesis of fluorescent RhB@DiCH_3MOF-5 composites and their application in Fe^{3+} and ascorbic acid detection. Reproduced with permission [149]. Copyright 2019, American Chemical Society. (**D**) Schematic illustration of the design principle of Tb(III)@MOF-SO^{3-} as a fluorescent probe for tt-MA. Reproduced with permission [150]. Copyright 2018, American Chemical Society.

For some solid pharmaceuticals and chemical products, water may be a contaminant and impurity. Trace water may affect the stability and efficacy of drugs. Several MOFs-based fluorescent sensors have been developed for water determination. For instance, Yin et al. reported the ratiometric fluorescence detection of water in organic solvents based on $Ru(bpy)_3^{2+}$-encapsulated MIL-101(Al)−NH_2 [151]. Water facilitated the protonation of the ligand BDC-NH_2, resulting in the shift of the fluorescence of MOFs. Zhou et al. presented a ratiometric and turn-on fluorescence method for water detection by using Eu-MOFs as the probes [152]. Water could switch on the intramolecular charge transfer from the electron donating amino group to the electron-withdrawing carboxyl group, leading

to the enhancement of the fluorescence from ligand. However, these sensors are limited to the determination of water in organic solvents. To realize the analysis of water in solid samples, Yu et al. designed a portable analytical device based on Eu-dipicolinic acid/2-aminophthalic acid (Eu-DPA/PTA-NH_2) [153] MOFs. As shown in Figure 10, a one-to-two logic gate was developed for determining water content and the two fluorescence signals as the input and output signals. MOFs were deposited on the fiber paper to prepare a microsensor. When the water content increased, the fluorescence of PTA-NH_2 increased and the fluorescence of Eu^{3+} declined. Under the illustration of 254 nm UV light, the color of paper changed from red to blue. Furthermore, Chen et al. developed a ratiometric fluorescent and colorimetric method for the detection of methanol using bimetallic Ln-MOFs [154]. In this work, methanol could improve the LMCT efficiency from the ligand to Tb^{3+}, resulting in the increase of the fluorescence of Tb^{3+} ions.

Table 2. Performances of MOFs-based fluorescent chemosensors for the detection of small organic molecules.

MOFs	Targets	Linear Range	LOD	Ref.
NH_2–Cu-MOF	TNP	0.5~30 μM	80 nM	[108]
RhB@Cd-MOFs	4-nitroaniline	0~0.054 mM	43.06 μM	[113]
2D MOF-Calix	glyphosate	2.5~45 μM	2.25 μM	[120]
EY-Zr-MOF	nitenpyram	0~0.1 mM	0.94 μM	[122]
PHN@UiO-66-NH_2	FA	1~3 and 3~4 μM	0.173 μM	[123]
UiO-67/Ce-PC	glyphosate	0.02~30 μg/mL	0.0062 μg/mL	[116]
Cd-MOFs	dinotefuran	0~130 μM	2.09 ppm	[119]
MB@Cd-MOF	carbaryl	0~90 μM	6.7 ng/mL	[121]
Zn-MOF	DOX, TET, OTC and CTC	0.001~46.67 μM for DOX, 0.001~53.33 μM for TET, OTC and CTC	0.56, 0.53, 0.58 and 0.86 nM	[124]
Zn-MOFs	ofloxacin	0~0.0215 mM	0.52 μM	[125]
Cd-MOFs	NFT and NFZ	4~18 nM	0.15 and 0.29 nM	[126]
Eu-MOFs	BRH and TET	0.5~320 μM and 0.05~160 μM	78 nM and 17 nM	[128]
Zn-MOFs	TEA, TET and NB	5~35 μM, 1~7.5 μM and 2~15 μM	1.07 μM, 0.1 μM and 0.2 μM	[129]
Zn-MOFs	OTC	0.02~13 μM	0.017 μM	[132]
Tb^{3+}-modified Cd-MOFs	CFX	0~6 μM	26.7 nM	[133]
FSS@MOF-5/GMP-Eu	TET	0~20 μM	18.5 nM	[134]
ZIF-8@PCN-128Y	TET	0.4~200 μM	60 nM	[135]
Zn-BTEC MOFs	CTC	0~8 μM	28 nM	[136]
Yb-NH_2-TPDC MOFs	gossypol	25~100 μg/mL	25 μg/mL	[137]
NH_2-Cu-MOF	hypoxanthine	10~2000 μM	3.93 μM	[138]
Pyrene-modified Hf-UiO-66	UA	0~30 μM	1.4 μM	[139]
Eu^{3+}-modified Mn-MOFs	histidine	0~30 μM	0.23 μM	[140]
Eu/Bi-MOF	histidine	0.001~10 mM	0.18 μM	[141]
Zn-MOFs	3-nitrotyrosine	0~4 μM	0.3099 μM	[142]
GNR and QD-embeded MOFs	BA	0.002~5 ppm	1.2 ppb	[143]
Tb-MOFs	DPA	0.001~5 μM	0.04 nM	[146]
CdS QDs@ZIF-8	DPA	0.1~150 μM	67 nM	[147]
HQCA-modified UiO-66-NH_2	creatinine	0.05~200 μM	4.7 nM	[148]
RhB@Di-MOF	Fe^{3+} and AA	1~10 μM and 1~25 μM	0.36 μM and 0.31 μM	[149]
Eu(III)/Tb(III)@MOF-SO_3^-	*tt*-MA	0~20 μg/mL	0.1 μg/mL	[150]

Abbreviation: TNP, 2,4,6-trinitrophenol; RhB, rhodamine B; Calix, calix [4]arene; EY, eosin Y; PHN, N-propyl-4-hydrazinenaphthalimide; FA, formaldehyde; Ce-PC, porous carbon materials derived from Ce-MOF; MB, methylene blue; DOX, doxycycline; TET, tetracycline; OTC, oxytetracycline; CTC, chlortetracycline; NFT, nitrofurantoin; NFZ, nitrofurancillin; BRH, berberine hydrochloride; TEA, triethylamine; CFX, cefxime; FSS, fluorescein; GMP, guanosine monophosphate; BTEC, pyromellitic acid; NH_2-TPDC, 3,3″-diamino-1,1′:4′,1″-terphenyl-4,4″-dicarboxylic acid; UA, uric acid; BA, benzaldehyde; GNR, gold nanorod; QD, quantum dot; DPA, dipicolinic acid; HQCA, 8-hydroxy-2-quinolinecarboxaldehyde; tt-MA, trans,trans-muconic acid.

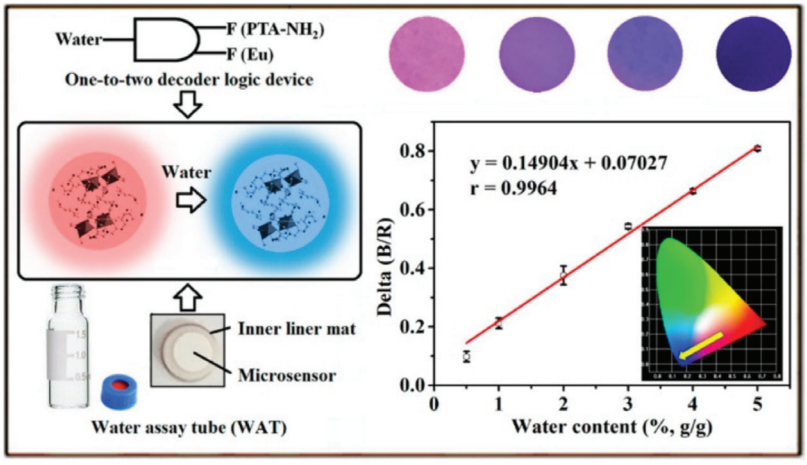

Figure 10. Schematic illustration of Eu-DPA/PTA-NH_2-based portable analytical device for water analysis in solid samples. Reproduced with permission [153]. Copyright 2020, American Chemical Society.

4. Biosensors

Chemicals and metabolites can provide important information about human healthy. Thus, it is meaningful to monitor their contents from the biological samples. Biomarkers can reflect the relationship between biological systems and external chemical, physical and biological factors. Thus, considerable effort has been devoted to develop fluorescent MOFs-based biosensors for the determination of biomarkers (Table 3) [155–159]. Among them, a variety of DNA-based switch fluorescent biosensors have been extensively developed for the detection of various biomarkers because of the intrinsic specificity and predictability, including small biomolecules, nucleic acids, enzymes, proteins and tumor cells. In common switch fluorescent DNA/MOFs-based biosensors, dye-labeled DNA/aptamers are adsorbed on the surface of MOFs through the π–π stacking, electrostatic, coordination, and hydrogen bonding interactions. Then, the fluorescence was efficiently quenched by MOFs via PET or FRET process in a "turn-off" mode [160]. In the presence of a target, the higher affinity between target and DNA/aptamer may result in the release of DNA/aptamer from the surface of MOFs, thus recovering the fluorescence. In this part, we highlighted the MOFs-based for the detection of biomarkers including small biomolecules, nucleic acids, enzymes, proteins and others.

4.1. Small Biomolecules

Nucleotides as the energy supply for human body have a critical influence on the regulation of various cellular metabolic processes. Extensive efforts have been focused on the fabrication of MOFs-based fluorescent biosensors for the detection of nucleotides [161–163]. For example, Qu et al. developed a fluorometric aptasensor for adenosine triphosphate (ATP) detection [164]. In this method, AuNPs were used to quench the emission of Tb-MOF by FRET. Under the condition of high concentration of salts, AuNPs would assembly into aggregates, thus losing the fluorescence quenching ability. In the presence of ATP, the aptamer specifically bound to ATP, and the complex was adsorbed onto the AuNPs to prevent the formation of aggregates, resulting in the decrease of the fluorescence. However, due to the similar structure and binding mode of ATP with its analogues, it is difficult to selectively respond to certain nucleotides with this method. To further improve the discrimination ability, Wang et al. synthesized a series of bimetallic Co_xZn_{100-x}-ZIF (x = 0~100) MOFs and investigated their interactions with different nucleoside triphosphates (Figure 11A) [165]. It was found that $Co_{50}Zn_{50}$-ZIF and $Co_{80}Zn_{20}$-ZIF could recognize guanosine triphosphate (GTP) and ATP with high specificity. However, $Co_{65}Zn_{35}$-

ZIF and $Co_{20}Zn_{80}$-ZIF could bind with both ATP and GTP. The resulting MOFs could quench the fluorescence of dye-labeled DNA. The target nucleoside triphosphate was then determined by displacing the attached DNA probe from the MOF surface to recover the fluorescence.

Due to its simplicity and specificity, aptamers against different molecules have been designed and used to develop fluorescent biosensors by combining with MOFs [166]. For example, Lu et al. reported a bimetallic MOFs-based fluorescent aptasensor for the detection of chloramphenicol [167]. Amalraj et al. developed a dual-mode MOFs-based fluorescent aptasensor for simultaneous determination of 17β-estradiol and chloramphenicol using two different dyes-labeled aptamers [168]. Ochratoxin A (OTA) is primarily generated through the consumption of improperly stored food products and uptake of OTA may cause organ damage. Recently, Li et al. developed a Zr-MOFs-based fluorescent and electrochemical dual-channel biosensor for OTA detection [169]. As displayed in Figure 11B, in the presence of OTA, its aptamer was released from the surface of Zr-MOFs due to the specific interaction between them. Thus, the fluorescence of dye-labeled aptamer was enhanced and the decreased amount of aptamer on the electrode surface resulted in a reduced electrochemical signal.

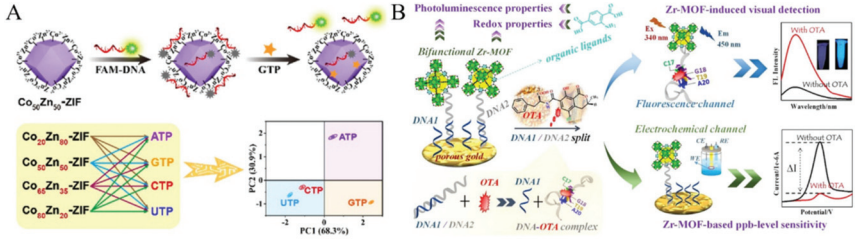

Figure 11. (**A**) Schematic illustration of DNA coated CoZn-ZIF MOFs for fluorescent sensing GTP. Reproduced with permission [165]. Copyright 2022, Elsevier. (**B**) Schematic illustration of the dual-channel Zr-MOFs-based detection strategy of OTA. Reproduced with permission [169]. Copyright 2022, American Chemical Society.

4.2. Nucleic Acids

Based on the canonical Watson–Crick model, DNA is a type of natural probe for selective detection of nucleic acids. MOFs can selectively adsorb ssDNA against dsDNA due to the difference in the adsorption affinity, thus quenching the fluorescence of dye-labeled ssDNA via PET or FRET [170,171]. For example, Chen et al. for the first time reported a Cu-MOF-based biosensor for the fluorescent detection of duplex DNA (HIV 16-bp oligopyrimidine oligopurine proviral DNA) [172]. In this study, the duplex DNA target could preferentially bind to the dye-labeled probe triplex-forming oligonucleotide (TFO), leading to the release of TFO from MOFs and the restoration of the fluorescence. Zhao et al. prepared ultrathin 2D Zn-TCPP MOF nanosheets through a surfactant-assisted synthetic method and used them to construct a fluorescent biosensor for the detection of DNA [173]. In this work, Zn-TCPP MOF with a π-electron conjugated system could adsorb the dye-labeled ssDNA and quench the fluorescence via FRET. The influenza A virus subtype H5N1 gene hybridized with ssDNA to form dsDNA, thus recovering the fluorescence. Recently, Zhang et al. investigated the interaction between ultrathin 2D Zr-BTB MOF nanosheets and fluorophore-labeled dsDNA as well as ssDNA by molecular dynamics simulations (Figure 12A) [174]. The nanosheets composed of Zr-O clusters and 1,3,5-benzenetribenzoate were prepared by a bottom-up method. Based on the difference in the affinity of dsDNA and ssDNA toward the Zr-BTB MOF nanosheets, the target DNA could be determined with high sensitivity and specificity. Besides the direct adsorption, dye-labeled DNA was covalently immobilized on MOFs, leading to the quenching of the fluorescence. Han et al. developed a fluorescent biosensor for the ratiometric detection of miRNAs based on UiO-66-NH_2 and triple helix molecular switch (THMS) [175]. As shown

in Figure 12B, the pre-formed THMS was modified on the amino-functionalized MOFs. The emission from UiO-66-NH_2 at 440 nm was selected as the internal reference and that from FAM at 525 nm was related to the detection of target miRNA-203. The target miRNA-203 could hybridize with the dye-labeled probe, causing it to move away from MOFs to restore the quenched fluorescence.

By using different dye-labeled DNA probes, multiplex detection of DNA can be realized by monitoring the corresponding emission at different wavelengths [176]. For instance, Ye et al. developed a Cu-MOFs-based fluorescent biosensor for multiplexed detection of DNA with two carboxyfluorescein (FAM) and 5(6)-carboxyrhodamine triethylammonium salt (ROX)-modified probes [177]. Yang et al. synthesized a 3D zwitterionic Cu-MOFs for the selective fluorescent detection of human immunodeficiency virus 1 (HIV 1) ds-DNA and Sudan virus RNA [178].

MOFs with intrinsic fluorescence can be used as the electron or energy donor to develop biosensor for DNA detection. Afzalinia et al. developed a fluorescent miRNA biosensor by using Ln-MOFs as the donors and silver nanoparticles (AgNPs) as the acceptors [179]. As shown in Figure 12C, fluorescent Ln-MOFs and AgNPs were modified with two DNA probes that were partially complementary to target miRNA-155. In the presence of miRNA-155, the energy donor−acceptor probes were linked and the fluorescence of Ln-MOFs were quenched through FRET. G-Quadruplexes (G4s), a typical noncanonical conformation of guanine-rich DNA and RNA fragments, can regulate the transcriptional functions of the genome. Kouzegaran et al. reported the detection of human telomeric G4s DNA based on a hemin-modified fluorescent Ce-MOFs [180]. In this work, the hemin molecules were adsorbed on the pores and surface of Ce-MOF to quench the fluorescence. The target H-Telo G4s bound to hemin with the high affinity, resulting in the recovery of the fluorescence.

Due to their excellent properties of large specific surface area with well-defined porosity, MOFs can be employed as nanocarriers to load a large number of dyes and release the guest molecules under certain stimulus (e.g., targets, hypoxia and acidic pH). For this view, Wu et al. reported a fluorescent biosensor for the multicolor detection of DNA by using MOFs to load different dyes (Figure 12D) [181]. In this study, different DNA hairpins were used to cap the pores, preventing the leakage of dyes due to the steric-hindrance effect. In the presence of targets, the DNA hairpins hybridized with its complementary DNA targets to release the fluorophores from the MOFs' pores, producing an enhanced fluorescence signal. However, the single signal mode may suffer from the interference of other substances in complex samples. To improve sensitivity and selectivity, Han et al. reported a DNA/MOF-based ratiometric fluorescent system for miRNA detection by FRET [182]. In this work, UiO-66-NH_2 MOFs were used as the carriers to encapsulate RhB and capture DNA via the formation of Zr-O-P bonds. The DNA-modified MOFs could further encapsulate Thiazole Orange (TO) to form DNA-RhB@UiO-66-NH_2. The target miRNA could bind with the ratiometric fluorescent DNA-RhB@UiO-66-NH_2 probe by strand displacement reaction, thus restoring the fluorescence of TO.

Dysregulated expression of miRNAs is associated with different diseases including cancers. Real-time imaging of miRNAs with low expression level in vivo would provide valuable information for disease diagnosis and evaluation of drug efficiency. MOFs can be used as the carriers to fabricate the stimuli-responsive cargo delivery nanosystems and efficiently deliver nucleases and detection probes to cytoplasm [183]. For example, Zhang et al. reported an enzymatic amplification strategy for the detection of miRNA in living cells by using pH-sensitive MOF (ZIF-8) nanoparticles to deliver ϕ29 DNA polymerase and detection probes (Figure 13A) [184]. After entering cells, the ZIF-8 nanoparticles could be dissolved due to the low pH environment, which led to the release of ϕ29DP and DNA probes. Then, the target miRNA triggered a rolling circle amplification (RCA) with the aid of ϕ29DP. The autonomously produced Mg^{2+}-dependent DNAzymes could cleave the fluorogenic substrates, thus generating a readout fluorescence signal. Meng et al. reported the in vivo detection of aberrant miRNA by using a hypoxia-responsive Cu-MOF

to load the signal strand block Cu-specific DNAzyme precursors and substrate strands (Figure 13B) [185]. The tumor microenvironment promoted the dissolution of DNA@Cu-MOF, leading to the release of extensive Cu^{2+} ions, DNAzyme precursors, and substrate strands. The aberrant target miRNA could displace the signal strand by toehold-mediated strand displacement hybridization, thus recovering the fluorescence signal of Cy3-labeled block DNA. More importantly, this reaction would trigger the Cu-specific DNAzyme signal amplification and cause the release of an increasing number of Cy3-labeled DNA stands. Thus, the work proposed a novel method for aberrant miRNA-related hypoxic tumor diagnosis.

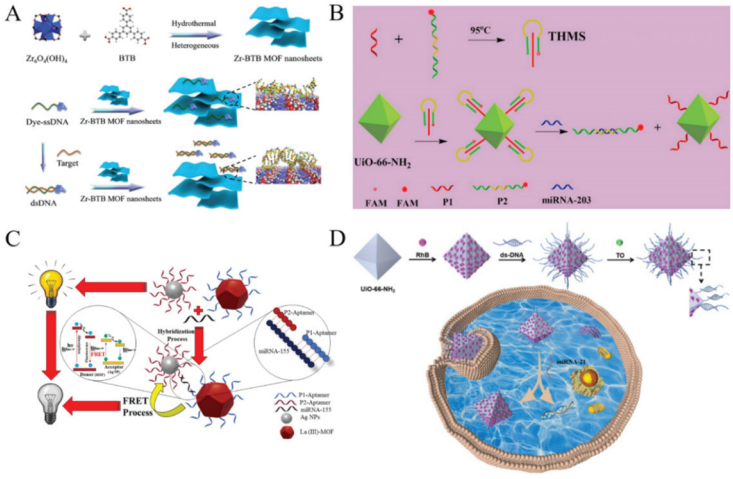

Figure 12. (**A**) Schematic illustration of preparation of Zr-BTB MOF nanosheets and projected interaction between nanosheets with ssDNA and dsDNA. Reproduced with permission [174]. Copyright 2020, American Chemical Society. (**B**) Schematic illustration of UiO-66-integrated programmable DNA triple-helix molecular switch for tumor-related miRNA-203 ratiometric detection. Reproduced with permission [175]. Copyright 2021, Elsevier. (**C**) Schematic illustration of fluorescence quenching-based detection of miRNA-155 by the FRET process. Reproduced with permission [179]. Copyright 2020, American Chemical Society. (**D**) Schematic illustration of fabrication of the probe (DNA-RhB@UiO-66-NH_2 + TO) and reaction mechanism. Reproduced with permission [182]. Copyright 2022, Elsevier.

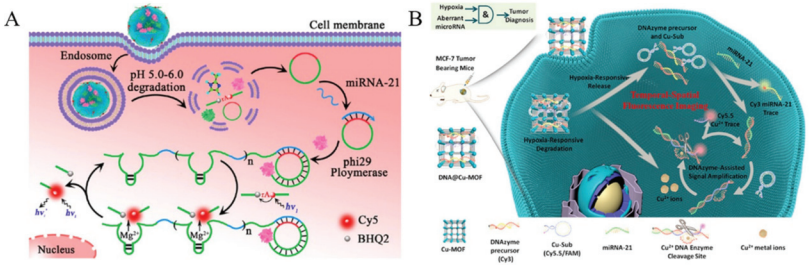

Figure 13. (**A**) Schematic illustration of the intracellular RCA by Using ZIF-8 NPs as a nanocarrier for codelivery of ϕ29 DNA polymerase and DNA probes for miRNA-21 imaging in vivo. Reproduced with permission [184]. Copyright 2019, American Chemical Society. (**B**) Schematic illustration of hypoxia-responsive DNA@Cu-MOF nanoprobes for aberrant miRNA and hypoxic tumor imaging using Cu^{2+} self-powered DNAzyme-assisted amplification. Reproduced with permission [185]. Copyright 2020, American Chemical Society.

4.3. Enzymes

Enzymes play an important role in almost all organs by participating in different biological processes. Overexpressed enzymes are closely related to various diseases. Therefore, the development of effective methods for enzyme activities is of great importance for the early diagnosis of diseases. The fluorescence of MOFs can be modulated by enzyme catalysis in which the substrate or the product can quench the fluorescence of MOFs via different mechanisms. For example, Yu et al. used the dual-emission Ln-MOFs for the detection of alkaline phosphatase (ALP) and demonstrated that ALP-based enzymatic products of phosphate ions (PO_4^{3-}) could quench the emission of Tb^{3+} ions and enhance the fluorescence of ligands by blocking the energy transfer from ligand to Tb^{3+} [186]. Guo et al. found that the RhB-encapsulated porous crystalline Zn(II)-MOF (RhB@MOF-5) could be used to detect β-Glucuronidase (β-GCU) (Figure 14A) [187]. In this work, the RhB@MOF-5 nanoprobe showed a yellow-green emission of RhB at 552 nm. Based on the synergistic effect of IFE and static quenching effect (SQE), the fluorescence of RhB could be quenched by 4-nitrophenyl-β-D-glucuronide (PNPG), the substrate of β-GCU. The enzymatic hydrolysis of PNPG into p-nitrophenol caused the recovery of fluorescence, thus achieving the signal-on detection of β-GCU in human serum.

Taking advantage of the quenching ability of metal ions, enzyme activities can be determined through the capture of metal ions from MOFs by their products or substrates. For example, Chen et al. reported the detection of glutathione S-transferase (GST) with brightly red emissive ZIF-8@QDs (Figure 14B) [188]. The nanoprobes exhibited the advantages of MOFs, and the assembly of Hg-ZnSe QDs and ZIF-8 MOFs enhanced the fluorescence of QDs. Cu^{2+} ions were attached onto the surface of ZIF-8@QDs, thus leading to the fluorescence quenching. The addition of glutathione (GSH) recovered the fluorescence of ZIF-8@QDs by the interaction of Cu^{2+} and GSH. However, GST could catalyze the reaction between GSH and 1-chloro-2,4-dinitrobenzene (CDNB), thus preventing the release of Cu^{2+} ions from the ZIF-8@QDs.

Enzymatic products can further react with other reagents to in-situ form complexes that can change the fluorescence of MOFs. Yu et al. reported a dual-response biosensor, the detection of tyrosinase (TYR) monophenolase activity by integration of fluorescent polymer dots and luminescent lanthanide MOF (Ln-MOF) (Figure 14C) [189]. In this study, monoaromatic ligand DPA was used as the linker for the preparation of Eu^{3+}-based Ln-MOF. In alkaline boric acid buffer, L-tyrosine was converted into boric acid-levodopa by TYR monophenolase. With the aid of Eu-DPA, BA-levodopa was initiated by diethylaminepropyltrimethoxysilane (DAMO), thus promoting the formation of BA-levodopa polymer dots. This reaction could turn on a strong blue fluorescence and quench the red fluorescence of Eu-DPA via enhanced PET.

Moreover, enzyme products can regulate the surface, chemical and structure properties of MOFs by tuning the formation of chemical bonds [190,191]. Li et al. reported a luminescent MOFs-based label-free assay of polyphenol oxidase (PPO) [192]. In this study, the fluorescence of La-based MOFs was quenched by the enzymatic product of *o*-benzoquinone through the Michael-type addition reaction between o-quinone and the free amino group of MOFs. Wang et al. proposed a strategy for monitoring apyrase activity by mediating the catalytic and fluorescence quenching abilities of nanoscale MOFs through coordination-driven self-assembly (Figure 14D) [193]. Platinum nanoparticles (PtNPs) were loaded onto the commonly used MIL-88B-NH_2 Fe-MOF. The catalytic activity of Pt/MIL-88B-NH_2 nanozyme was enhanced due to the binding of ATP. Meanwhile, the fluorophore-labeled DNA could adsorb onto the surface of Pt/MIL-88B-NH_2, thus quenching the fluorescence signal. Enzymatic products, such as phosphates, small DNA strands and H_2O_2, could lead to the release of ATP and fluorophore-labeled DNA, thus allowing for the detection of apyrase and alkaline phosphatase. Cai et al. encapsulated gold nanoclusters (AuNCs) into MOFs and used the fluorescent MOFs to detect organophosphorus pesticides with the aid of acetylcholinesterase (AChE) and choline oxidase (CHO) [194]. In this study, AuNCs were confined in MOFs to show an enhanced fluorescence due to the AIE effect. Under

the sequential catalysis of AChE and CHO in the presence of acetylcholine, the produced H_2O_2 could destroy the structure of MOFs and weaken the restraint on AuNCs, resulting in decreased fluorescence. However, pesticides could inhibit the enzyme activity, thus protecting MOFs from the decomposition and leading to the unchanged fluorescence.

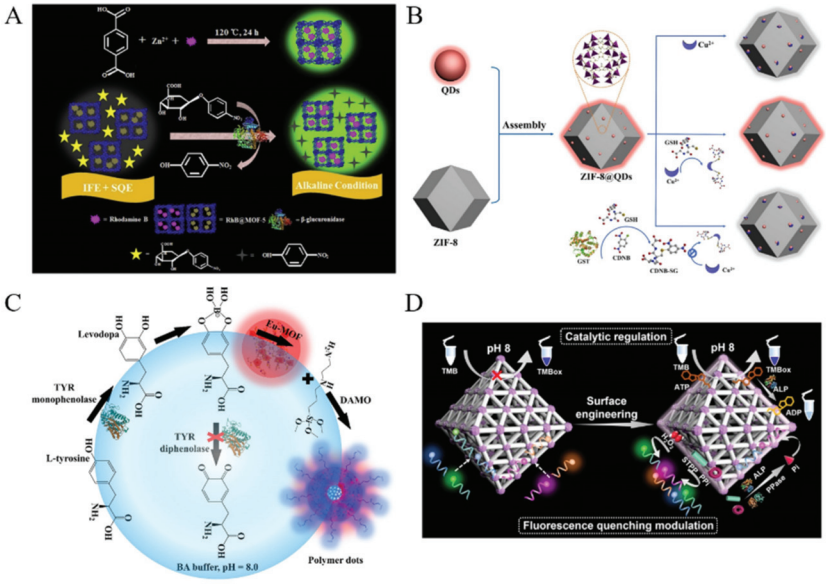

Figure 14. (**A**) Schematic illustration of the preparation procedure of RhB@MOF-5 by one-pot synthesis approach and the mechanism for β-GCU detection based on the synergistic effect of IFE and SQE. Reproduced with permission [187]. Copyright 2019, Elsevier. (**B**) Schematic illustration of the preparation of ZIF-8@QDs nanoprobe and its detection principle for GST activity. Reproduced with permission [188]. Copyright 2022, Elsevier. (**C**) Schematic illustration of fluorescence on/off dual-response sensing of TYR monophenolase activity based on Eu-MOF-assisted boric acid-levodopa polymer dots. Reproduced with permission [189]. Copyright 2022, Elsevier. (**D**) Schematic illustration of enzyme-modulated catalytic and fluorescence quenching of nanoscale MOFs. Reproduced with permission [193]. Copyright 2022, American Chemical Society.

4.4. Proteins

Sensitive and specific determination of proteins is of great importance in early diagnosis, prognosis and therapeutic evaluation. MOFs-based fluorescent aptasensors have also been developed for protein detection. For example, Zhang et al. reported a fluorescence proximity assay for the detection of prostate specific antigen (PSA) by using MOFs as the platforms [195]. Huang et al. reported a no-wash fluorescence biosensor for ratiometric detection of PSA with the nanohybrid of MOF@AuNP@graphene oxide as the nanoquencher [196]. Zhang et al. reported the fluorescent detection and imaging of phosphorylation and glycosylation based on the Zr(IV)-phosphate and boronic acid-diol interactions, respectively (Figure 15) [197]. Phosphate could interact with the metal node Zr(IV) of UIO-66-NH_2 to interrupt the metal-ligand charge transfer, restoring the fluorescence. Boronic acid anchored on the framework could react with alizarin red by the formation of borate ester bonds. The embedded alizarin red showed poor fluorescence. The release of alizarin red from the framework by the competitive reaction with glycosyl turned on the fluorescence. In addition, Wei et al. developed a MOFs-based fluorescent biosensor for H_5N_1 antibody detection [198]. In the absence of a target, exonuclease I (Exo I) catalyzed the hydrolysis of the DNA probe at the 3′-terminus and the fluorophore was released from the MOF, resulting in the recovery of the fluorescence. H_5N_1 antibody could bind with the

antigen conjugating at the end of the DNA, and it protected the DNA from the hydrolysis, leading to the adsorption of DNA on MOFs and the quenching of the fluorescence.

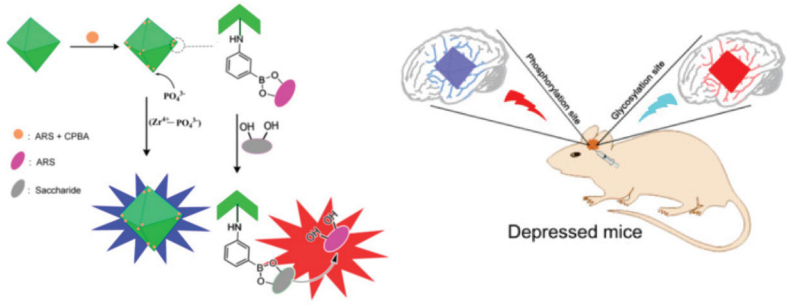

Figure 15. Schematic illustration of the proposed mechanism of MOFs-based detection of the levels of glycosylation and phosphorylation (left) and in-situ fluorescence imaging of the levels of glycosylation and phosphorylation in depressed mice (right). Reproduced with permission [197]. Copyright 2020, American Chemical Society.

4.5. Others

Exosomes derived from tumor cells carry important molecular information from parent tumor cells. Thus, increasing levels of exosomes are closely related to the occurrence and progress of tumors. Exosomes could be detected by using magnetic bead-modified MOFs, such as UiO-66 to extract the target [199]. As shown in Figure 16A, the fluorescent probe of UiO-66-NH_2 modified with anti-epithelial cell adhesion molecule (anti-EpCAM) was used as the signal reporter to recognize the EpCAM-positive exosome. Circulating tumor cells are shed from metastatic sites or primary tumors to peripheral blood and travel in the blood vessels, which is regarded as the main reason of metastatic spread. Circulating tumor cells from the blood of cancer patients could be determined with rhodamine 6G (Rho 6G)-entrapped MOF probe [200]. The probe denoted as MOF-Rho 6G-DNA was prepared by connecting sulfhydrylated DNA (Arm-DNA), entrapping Rho 6G and modifying EpCAM hairpin DNA onto the MOF. The binding of CTCs with hairpin DNA opened the hairpin structure and thus induced its conformational change, causing the release of entrapped Rho 6G molecules. Moreover, BA-functionalized MOF named Zr-UiO-66-$B(OH)_2$ has been used for fluorescence detection of bacteria (Figure 16B) [201]. Zr-UiO-66-$B(OH)_2$ was attached onto the bacteria surface by the interaction of BA and glycolipid outside the bacteria, in the presence of which the fluorescence of Zr-UiO-66-$B(OH)_2$ was intensified by converting -$B(OH)_2$ group into -OH group.

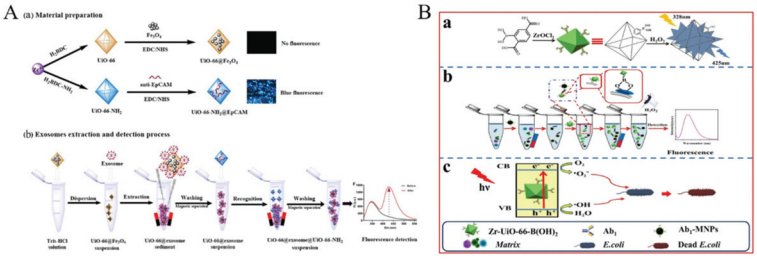

Figure 16. (**A**) Schematic illustration of the fluorescence detection method for cancer cell-derived exosomes based on Zr-MOFs. Reproduced with permission [199]. Copyright 2022, Elsevier. (**B**) Schematic illustration of (a) preparation of Zr-UiO-66-$B(OH)_2$ and its fluorescence "turn-on" mechanism by H_2O_2; (b) the immunoassay process for detection of *E. coli* through fluorescence signal; (c) Mechanism underlying the photocatalytic elimination of *E. coli* by the Zr-UiO-66-$B(OH)_2$. Reproduced with permission [201]. Copyright 2021, Elsevier.

Table 3. Performances of different MOFs-based fluorescent biosensors.

Probes	Targets	Linear Range	LOD	Ref.
Tb-MOFs and aptamer-modified AuNPs	ATP	0.5~10 μM	0.32 μM	[161]
ZIF-67 and FAM-aptamer	ATP	0.03~30 μM	29 nM	[162]
Cr-MIL-101 and FAM-aptamer	ATP	5~400 μM	1.7 μM	[163]
Tb-MOFs, aptamer and AuNPs	ATP	0.05~10 μM	23 nM	[164]
Co_xZn_{100-x}-ZIF (x = 0–100) and FAM-aptamer	GTP	0~50 μM	0.13 μM	[165]
UiO-66-NH_2 and TAMRA-aptamer	AFB1	0~180 ng/mL	0.35 ng/mL	[166]
Cu/UiO-66 and ROX-aptamer	CAP	0.2~10 nM	0.09 nM	[167]
MOF−MoS_2 and ROX/TAMRA-aptamer	CAP and 17E	0~5 nM	200 and 180 pM	[168]
Zr-MOFs and aptamer	OTA	0.10~160 pg/mL	0.051 pg/mL	[169]
Cu-MOFs and FAM-aptamer	H5N1 antibody	0.005~1 μM	1.6 nM	[198]
Cu-MOFs and FAM-aptamer	dsDNA	4~200 nM	1.3 nM	[172]
UiO-66-NH_2 and FAM-DNA	miRNA	1~160 nM	400 pM	[175]
DNA-modified Ln-MOFs and DNA-modified AgNPs	miRNA-155	0.0027~0.01 pM	5.2 fM	[179]
Tb-MOFs	ALP	0~8 mU/mL	0.002 mU/mL	[186]
RhB@MOF-5	β-glucuronidase	0.1~10 U/L	0.03 U/L	[187]
Cu@Eu-BTC MOFs	ALP	0.3~24 mU/mL	0.02 mU/mL	[190]
Ln-MOFs	PPO	0.001~0.1 mU/mL	0.12 mU/mL	[192]
EpCAM-modified UiO-66-NH_2	exosomes	168~1 × 10^6 particles/μL	16.72 particles/μL	[199]
Zr-UiO-66-B$(OH)_2$	*E. coli*	5~2.5 × 10^4 CFU/mL	1 CFU/mL	[201]

Abbreviation: ATP, adenosine triphosphate; AuNPs, gold nanoparticles; FAM, 5-carboxyfluorescein; GTP, guanosine triphosphate; TAMRA, tetramethylrhodamine; AFB1, aflatoxin B1; ROX, 6-carboxy-x-rhodamine; CAP, chloramphenicol; 17E, 17β-estradiol; OTA, ochratoxin A; ALP, alkaline phosphatase; RhB, rhodamine B; QD, quantum dot; BTC, 1,3,5-benzenetricarboxylic acid; PPO, polyphenol oxidase; *E. coli*, *Escherichia coli*.

5. Conclusions

In summary, we presented a brief overview of the current status of MOFs-based fluorescent sensing platforms via diverse sensing mechanisms. MOFs exhibiting intrinsic emission or encapsulated with fluorescent species can be used as fluorescent probes for the detection of various targets. The excellent results of MOFs-based sensing platforms can be attributed to their distinguished characters of large surface area, high porosity and tunable optical properties. However, MOF-based fluorescent chemosensors and biosensors are still limited by several bottlenecks. For example, some MOFs involved in this review show low stability against moisture/aqueous conditions and prone to breakdown under certain harsh conditions. Modifying the linker with water-repelling (hydrophobic) functional groups may be an effective way to improve stability. Second, the poor solubility and inadequate dispersiveness may decrease sensitivity and limit the applications of MOFs in portable sensing devices. Third, for the detection of anions and cations, the sensitivity and selectivity depending on the binding affinity between inorganic ions and MOFs should be improved. Although highly selective sensors have been proposed by careful selection and design, the ability to specifically differentiate analytes with their similar structures is still weak. Finally, the fluorescence quenching mechanism for some MOFs should be systematically investigated and the quenching efficiency for biosensing should be further improved in MOFs-based biosensors. Additionally, the combination of MOFs with other materials and signal amplification strategies is helpful to achieve a higher sensitivity under the synergistic enhancement effect. It can be expected that MOFs-based fluorescent sensing platforms will possess broader application prospects under continuous efforts and in-depth investigation.

Author Contributions: Conceptualization, N.X.; writing—original draft preparation, N.X., Y.C., Q.Z. and S.D.; writing—review and editing, N.X. and F.G.; project administration, F.G.; funding acquisition, N.X. All authors have read and agreed to the published version of the manuscript.

Funding: This research was funded by the Program for Innovative Research Team of Science and Technology in the University of Henan Province (21IRTSTHN005).

Conflicts of Interest: The authors declare no conflict of interest.

References

1. Mohan, B.; Kumar, S.; Kumar, V.; Jiao, T.; Sharma, H.K.; Chen, Q. Electrochemiluminescence metal-organic frameworks biosensing materials for detecting cancer biomarkers. *TrAC Trends Anal. Chem.* **2022**, *157*, 116735–116750. [CrossRef]
2. Karmakar, A.; Li, J. Luminescent MOFs (lmofs): Recent advancement towards a greener wled technology. *Chem. Commun.* **2022**, *58*, 10768–10788. [CrossRef] [PubMed]
3. Campbell, M.G.; Dinca, M. Metal-organic frameworks as active materials in electronic sensor devices. *Sensors* **2017**, *17*, 1108. [CrossRef] [PubMed]
4. Liu, L.; Zhou, Y.; Liu, S.; Xu, M. The applications of metal−organic frameworks in electrochemical sensors. *ChemElectroChem* **2018**, *5*, 6–19. [CrossRef]
5. He, T.; Kong, X.-J.; Li, J.-R. Chemically stable metal-organic frameworks: Rational construction and application expansion. *Acc. Chem. Res.* **2021**, *54*, 3083–3094. [CrossRef]
6. Wang, J.; Li, N.; Xu, Y.; Pang, H. Two-dimensional MOF and cof nanosheets: Synthesis and applications in electrochemistry. *Chem. Eur. J.* **2020**, *26*, 6402–6422. [CrossRef]
7. Ma, Y.J.; Jiang, X.X.; Lv, Y.K. Recent advances in preparation and applications of magnetic framework composites. *Chem. Asian J.* **2019**, *14*, 3515–3530. [CrossRef]
8. Wang, S.; McGuirk, C.M.; d'Aquino, A.; Mason, J.A.; Mirkin, C.A. Metal-organic framework nanoparticles. *Adv. Mater.* **2018**, *30*, e1800202. [CrossRef]
9. Liu, B.; Vellingiri, K.; Jo, S.-H.; Kumar, P.; Ok, Y.S.; Kim, K.-H. Recent advances in controlled modification of the size and morphology of metal-organic frameworks. *Nano Res.* **2018**, *11*, 4441–4467. [CrossRef]
10. Tranchemontagne, D.J.; Mendoza-Cortes, J.L.; O'Keeffe, M.; Yaghi, O.M. Secondary building units, nets and bonding in the chemistry of metal-organic frameworks. *Chem. Soc. Rev.* **2009**, *38*, 1257–1283. [CrossRef]
11. Yu, X.; Wang, L.; Cohen, S.M. Photocatalytic metal–organic frameworks for organic transformations. *CrystEngComm* **2017**, *19*, 4126–4136. [CrossRef]
12. Kolobov, N.; Goesten, M.G.; Gascon, J. Metal-organic frameworks: Molecules or semiconductors in photocatalysis? *Angew. Chem. Int. Ed.* **2021**, *60*, 26038–26052. [CrossRef] [PubMed]
13. Sohrabi, H.; Javanbakht, S.; Oroojalian, F.; Rouhani, F.; Shaabani, A.; Majidi, M.R.; Hashemzaei, M.; Hanifehpour, Y.; Mokhtarzadeh, A.; Morsali, A. Nanoscale metal-organic frameworks: Recent developments in synthesis, modifications and bioimaging applications. *Chemosphere* **2021**, *281*, 130717–130751. [CrossRef] [PubMed]
14. Liu, Y.; Jiang, T.; Liu, Z. Metal-organic frameworks for bioimaging: Strategies and challenges. *Nanotheranostics* **2022**, *6*, 143–160. [CrossRef]
15. Zhao, Y.; Zeng, H.; Zhu, X.W.; Lu, W.; Li, D. Metal-organic frameworks as photoluminescent biosensing platforms: Mechanisms and applications. *Chem. Soc. Rev.* **2021**, *50*, 4484–4513. [CrossRef]
16. Karmakar, A.; Samanta, P.; Dutta, S.; Ghosh, S.K. Fluorescent "turn-on" sensing based on metal-organic frameworks (MOFs). *Chem. Asian J.* **2019**, *14*, 4506–4519. [CrossRef]
17. Asad, M.; Imran Anwar, M.; Abbas, A.; Younas, A.; Hussain, S.; Gao, R.; Li, L.-K.; Shahid, M.; Khan, S. AIE based luminescent porous materials as cutting-edge tool for environmental monitoring: State of the art advances and perspectives. *Coord. Chem. Rev.* **2022**, *463*, 214539–214564. [CrossRef]
18. Liu, K.; You, H.; Zheng, Y.; Jia, G.; Song, Y.; Huang, Y.; Yang, M.; Jia, J.; Guo, N.; Zhang, H. Facile and rapid fabrication of metal–organic framework nanobelts and color-tunable photoluminescence properties. *J. Mater. Chem.* **2010**, *20*, 3272–3279. [CrossRef]
19. Liu, K.; You, H.; Jia, G.; Zheng, Y.; Song, Y.; Yang, M.; Huang, Y.; Zhang, H. Coordination-induced formation of one-dimensional nanostructures of europium benzene-1,3,5-tricarboxylate and its solid-state thermal transformation. *Cryst. Growth Des.* **2009**, *9*, 3519–3524. [CrossRef]
20. Sun, M.; Zhang, L.; Xu, S.; Yu, B.; Wang, Y.; Zhang, L.; Zhang, W. Carbon dots-decorated hydroxyapatite nanowires-lanthanide metal-organic framework composites as fluorescent sensors for the detection of dopamine. *Analyst* **2022**, *147*, 947–955. [CrossRef]
21. Xu, O.; Wan, S.; Yang, J.; Song, H.; Dong, L.; Xia, J.; Zhu, X. Ni-MOF functionalized carbon dots with fluorescence and adsorption performance for rapid detection of Fe (III) and ascorbic acid. *J. Fluoresc.* **2022**, *32*, 1743–1754. [CrossRef] [PubMed]
22. Yan, F.; Wang, X.; Wang, Y.; Yi, C.; Xu, M.; Xu, J. Sensing performance and mechanism of carbon dots encapsulated into metal-organic frameworks. *Microchim. Acta* **2022**, *189*, 379–395. [CrossRef] [PubMed]
23. Li, J.; Zhang, N.; Yang, X.; Yang, X.; Wang, Z.; Liu, H. Rhb@MOF-5 composite film as a fluorescence sensor for detection of chilled pork freshness. *Biosensors* **2022**, *12*, 544. [CrossRef] [PubMed]
24. Chen, D.M.; Zhang, N.N.; Liu, C.S.; Du, M. Dual-emitting dye@MOF composite as a self-calibrating sensor for 2,4,6-trinitrophenol. *ACS Appl. Mater. Interfaces* **2017**, *9*, 24671–24677. [CrossRef] [PubMed]

25. Jin, S.; Son, H.J.; Farha, O.K.; Wiederrecht, G.P.; Hupp, J.T. Energy transfer from quantum dots to metal-organic frameworks for enhanced light harvesting. *J. Am. Chem. Soc.* **2013**, *135*, 955–958. [CrossRef]
26. Xu, L.; Pan, M.; Fang, G.; Wang, S. Carbon dots embedded metal-organic framework@molecularly imprinted nanoparticles for highly sensitive and selective detection of quercetin. *Sens. Actuators B Chem.* **2019**, *286*, 321–327. [CrossRef]
27. Zhao, Y.; Li, D. Lanthanide-functionalized metal-organic frameworks as ratiometric luminescent sensors. *J. Mater. Chem. C* **2020**, *8*, 12739–12754. [CrossRef]
28. Liu, Y.; Xie, X.-Y.; Cheng, C.; Shao, Z.-S.; Wang, H.-S. Strategies to fabricate metal-organic framework (MOF)-based luminescent sensing platforms. *J. Mater. Chem. C* **2019**, *7*, 10743–10763. [CrossRef]
29. Dong, J.; Zhao, D.; Lu, Y.; Sun, W.-Y. Photoluminescent metal-organic frameworks and their application for sensing biomolecules. *J. Mater. Chem. A* **2019**, *7*, 22744–22767. [CrossRef]
30. Li, J.; Yao, S.-L.; Liu, S.-J.; Chen, Y.-Q. Fluorescent sensors for aldehydes based on luminescent metal-organic frameworks. *Dalton Trans.* **2021**, *50*, 7166–7175. [CrossRef]
31. Shi, L.; Li, N.; Wang, D.; Fan, M.; Zhang, S.; Gong, Z. Environmental pollution analysis based on the luminescent metal organic frameworks: A review. *TrAC Trends Anal. Chem.* **2021**, *134*, 116131–116150. [CrossRef]
32. Kukkar, D.; Vellingiri, K.; Kim, K.-H.; Deep, A. Recent progress in biological and chemical sensing by luminescent metal-organic frameworks. *Sens. Actuators B Chem.* **2018**, *273*, 1346–1370. [CrossRef]
33. Carrasco, S. Metal-organic frameworks for the development of biosensors: A current overview. *Biosensors* **2018**, *8*, 92. [CrossRef] [PubMed]
34. Yan, B. Photofunctional MOF-based hybrid materials for the chemical sensing of biomarkers. *J. Mater. Chem. C* **2019**, *7*, 8155–8175. [CrossRef]
35. Diamantis, S.A.; Margariti, A.; Pournara, A.D.; Papaefstathiou, G.S.; Manos, M.J.; Lazarides, T. Luminescent metal-organic frameworks as chemical sensors: Common pitfalls and proposed best practices. *Inorg. Chem. Front.* **2018**, *5*, 1493–1511. [CrossRef]
36. Wu, F.; Ye, J.; Cao, Y.; Wang, Z.; Miao, T.; Shi, Q. Recent advances in fluorescence sensors based on DNA-MOF hybrids. *Luminescence* **2020**, *35*, 440–446. [CrossRef]
37. Huo, Y.; Liu, S.; Gao, Z.; Ning, B.; Wang, Y. State-of-the-art progress of switch fluorescence biosensors based on metal-organic frameworks and nucleic acids. *Microchim. Acta* **2021**, *188*, 168–196. [CrossRef]
38. Yu, Q.; Li, Z.; Cao, Q.; Qu, S.; Jia, Q. Advances in luminescent metal-organic framework sensors based on post-synthetic modification. *TrAC Trends Anal. Chem.* **2020**, *129*, 115939–115955. [CrossRef]
39. Li, B.Z.; Suo, T.Y.; Xie, S.Y.; Xia, A.Q.; Ma, Y.J.; Huang, H.; Zhang, X.; Hu, Q. Rational design, synthesis, and applications of carbon dots@metal-organic frameworks (cd@MOF) based sensors. *TrAC Trends Anal. Chem.* **2021**, *135*, 116163–116174. [CrossRef]
40. Wang, X.S.; Chrzanowski, M.; Wojtas, L.; Chen, Y.S.; Ma, S. Formation of a metalloporphyrin-based nanoreactor by postsynthetic metal-ion exchange of a polyhedral-cage containing a metal-metalloporphyrin framework. *Chem. Eur. J.* **2013**, *19*, 3297–3301. [CrossRef]
41. Yang, L.-Z.; Wang, J.; Kirillov, A.M.; Dou, W.; Xu, C.; Fang, R.; Xu, C.-L.; Liu, W.-S. 2D lanthanide MOFs driven by a rigid 3,5-bis(3-carboxy-phenyl)pyridine building block: Solvothermal syntheses, structural features, and photoluminescence and sensing properties. *CrystEngComm* **2016**, *18*, 6425–6436. [CrossRef]
42. Yan, B. Luminescence response mode and chemical sensing mechanism for lanthanide-functionalized metal-organic framework hybrids. *Inorg. Chem. Front.* **2021**, *8*, 201–233. [CrossRef]
43. Goshisht, M.K.; Tripathi, N. Fluorescence-based sensors as an emerging tool for anion detection: Mechanism, sensory materials and applications. *J. Mater. Chem. C* **2021**, *9*, 9820–9850. [CrossRef]
44. De Silva, A.P.; Gunaratne, H.Q.; Gunnlaugsson, T.; Huxley, A.J.; McCoy, C.P.; Rademacher, J.T.; Rice, T.E. Signaling recognition events with fluorescent sensors and switches. *Chem. Rev.* **1997**, *97*, 1515–1566. [CrossRef] [PubMed]
45. Shakya, S.; Khan, I.M. Charge transfer complexes: Emerging and promising colorimetric real-time chemosensors for hazardous materials. *J. Hazard. Mater.* **2021**, *403*, 123537. [CrossRef] [PubMed]
46. Zhang, J.; Zhou, R.; Tang, D.; Hou, X.; Wu, P. Optically-active nanocrystals for inner filter effect-based fluorescence sensing: Achieving better spectral overlap. *TrAC Trends Anal. Chem.* **2019**, *110*, 183–190. [CrossRef]
47. Chen, L.; Liu, D.; Zheng, L.; Yi, S.; He, H. A structure-dependent ratiometric fluorescence sensor based on metal-organic framework for detection of 2,6-pyridinedicarboxylic acid. *Anal. Bioanal. Chem.* **2021**, *413*, 4227–4236. [CrossRef]
48. Sousaraei, A.; Queiros, C.; Moscoso, F.G.; Lopes-Costa, T.; Pedrosa, J.M.; Silva, A.M.G.; Cunha-Silva, L.; Cabanillas-Gonzalez, J. Subppm amine detection via absorption and luminescence turn-on caused by ligand exchange in metal organic frameworks. *Anal. Chem.* **2019**, *91*, 15853–15859. [CrossRef]
49. Cao, D.; Liu, Z.; Verwilst, P.; Koo, S.; Jangjili, P.; Kim, J.S.; Lin, W. Coumarin-based small-molecule fluorescent chemosensors. *Chem. Rev.* **2019**, *119*, 10403–10519. [CrossRef]
50. Raymo, F.M.; Yildiz, I. Luminescent chemosensors based on semiconductor quantum dots. *Phys. Chem. Chem. Phys.* **2007**, *9*, 2036–2043. [CrossRef]
51. Zheng, P.; Wu, N. Fluorescence and sensing applications of graphene oxide and graphene quantum dots: A review. *Chem. Asian J.* **2017**, *12*, 2343–2353. [CrossRef] [PubMed]
52. Shellaiah, M.; Sun, K. Luminescent metal nanoclusters for potential chemosensor applications. *Chemosensors* **2017**, *5*, 36. [CrossRef]

53. Chua, M.H.; Shah, K.W.; Zhou, H.; Xu, J. Recent advances in aggregation-induced emission chemosensors for anion sensing. *Molecules* **2019**, *24*, 2711. [CrossRef] [PubMed]
54. Zhang, Y.; Yuan, S.; Day, G.; Wang, X.; Yang, X.; Zhou, H.-C. Luminescent sensors based on metal-organic frameworks. *Coord. Chem. Rev.* **2018**, *354*, 28–45. [CrossRef]
55. Lakshmi, P.R.; Nanjan, P.; Kannan, S.; Shanmugaraju, S. Recent advances in luminescent metal-organic frameworks (lmofs) based fluorescent sensors for antibiotics. *Coord. Chem. Rev.* **2021**, *435*, 213793–213819. [CrossRef]
56. Hao, Y.; Chen, S.; Zhou, Y.; Zhang, Y.; Xu, M. Recent progress in metal-organic framework (MOF) based luminescent chemodosimeters. *Nanomaterials* **2019**, *9*, 974. [CrossRef] [PubMed]
57. Fang, X.; Zong, B.; Mao, S. Metal-organic framework-based sensors for environmental contaminant sensing. *Nano-Micro Lett.* **2018**, *10*, 64–82. [CrossRef] [PubMed]
58. Kanan, S.M.; Malkawi, A. Recent advances in nanocomposite luminescent metal-organic framework sensors for detecting metal ions. *Comments Inorg. Chem.* **2021**, *41*, 1–66. [CrossRef]
59. Shayegan, H.; Ali, G.A.M.; Safarifard, V. Recent progress in the removal of heavy metal ions from water using metal-organic frameworks. *ChemistrySelect* **2020**, *5*, 124–146. [CrossRef]
60. Samanta, P.; Let, S.; Mandal, W.; Dutta, S.; Ghosh, S.K. Luminescent metal-organic frameworks (lmofs) as potential probes for the recognition of cationic water pollutants. *Inorg. Chem. Front.* **2020**, *7*, 1801–1821. [CrossRef]
61. Razavi, S.A.A.; Morsali, A. Metal ion detection using luminescent-MOFs: Principles, strategies and roadmap. *Coord. Chem. Rev.* **2020**, *415*, 213299–213343. [CrossRef]
62. Gomez, G.E.; Dos Santos Afonso, M.; Baldoni, H.A.; Roncaroli, F.; Soler-Illia, G. Luminescent lanthanide metal organic frameworks as chemosensing platforms towards agrochemicals and cations. *Sensors* **2019**, *19*, 1260. [CrossRef] [PubMed]
63. Chen, J.; Chen, H.; Wang, T.; Li, J.; Wang, J.; Lu, X. Copper ion fluorescent probe based on Zr-MOFs composite material. *Anal. Chem.* **2019**, *91*, 4331–4336. [CrossRef] [PubMed]
64. Cheng, C.; Zhang, R.; Wang, J.; Zhang, Y.; Wen, C.; Tan, Y.; Yang, M. An ultrasensitive and selective fluorescent nanosensor based on porphyrinic metal-organic framework nanoparticles for Cu^{2+} detection. *Analyst* **2020**, *145*, 797–804. [CrossRef] [PubMed]
65. Chen, Y.-Z.; Jiang, H.-L. Porphyrinic metal–organic framework catalyzed heck-reaction: Fluorescence "turn-on" sensing of Cu(ii) ion. *Chem. Mater.* **2016**, *28*, 6698–6704. [CrossRef]
66. Xia, Y.D.; Sun, Y.Q.; Cheng, Y.; Xia, Y.; Yin, X.B. Rational design of dual-ligand eu-MOF for ratiometric fluorescence sensing Cu^{2+} ions in human serum to diagnose wilson's disease. *Anal. Chim. Acta.* **2022**, *1204*, 339731–339740. [CrossRef]
67. Zhang, Q.; Zhang, X.; Shu, Y.; Wang, J. Metal-organic frameworks encapsulating carbon dots enable fast speciation of mono- and divalent copper. *Anal. Chem.* **2022**, *94*, 2255–2262. [CrossRef]
68. Zhong, T.; Li, D.; Li, C.; Zhang, Z.; Wang, G. Turn-on fluorescent sensor based on curcumin@MOF-5 for the sensitive detection of Al3+. *Anal. Methods* **2022**, *14*, 2714–2722. [CrossRef]
69. Li, Q.; Wu, X.; Huang, X.; Deng, Y.; Chen, N.; Jiang, D.; Zhao, L.; Lin, Z.; Zhao, Y. Tailoring the fluorescence of AIE-active metal-organic frameworks for aqueous sensing of metal ions. *ACS Appl. Mater. Interfaces* **2018**, *10*, 3801–3809. [CrossRef]
70. Xu, H.; Gao, J.; Qian, X.; Wang, J.; He, H.; Cui, Y.; Yang, Y.; Wang, Z.; Qian, G. Metal–organic framework nanosheets for fast-response and highly sensitive luminescent sensing of Fe^{3+}. *J. Mater. Chem. A* **2016**, *4*, 10900–10905. [CrossRef]
71. Zhao, Y.; Zhai, X.; Shao, L.; Li, L.; Liu, Y.; Zhang, X.; Liu, J.; Meng, F.; Fu, Y. An ultra-high quantum yield Tb-MOF with phenolic hydroxyl as the recognition group for a highly selective and sensitive detection of Fe^{3+}. *J. Mater. Chem. C* **2021**, *9*, 15840–15847. [CrossRef]
72. Zhang, Z.; Wei, Z.; Meng, F.; Su, J.; Chen, D.; Guo, Z.; Xing, H. Rhb-embedded zirconium-naphthalene-based metal-organic framework composite as a luminescent self-calibrating platform for the selective detection of inorganic ions. *Chem. Eur. J.* **2020**, *26*, 1661–1667. [CrossRef] [PubMed]
73. Puglisi, R.; Pellegrino, A.L.; Fiorenza, R.; Scire, S.; Malandrino, G. A facile one-pot approach to the synthesis of gd-eu based metal-organic frameworks and applications to sensing of Fe^{3+} and $CR_2O_7^{2-}$ ions. *Sensors* **2021**, *21*, 1679. [CrossRef] [PubMed]
74. Qi, C.; Xu, Y.-B.; Li, H.; Chen, X.-B.; Xu, L.; Liu, B. A highly sensitive and selective turn-off fluorescence sensor for Fe^{3+} detection based on a terbium metal-organic framework. *J. Solid State Chem.* **2021**, *294*, 121835–121841. [CrossRef]
75. Yin, X.B.; Sun, Y.Q.; Yu, H.; Cheng, Y.; Wen, C. Design and multiple applications of mixed-ligand metal-organic frameworks with dual emission. *Anal. Chem.* **2022**, *94*, 4938–4947. [CrossRef]
76. Dang, S.; Wang, T.; Yi, F.; Liu, Q.; Yang, W.; Sun, Z.M. A nanoscale multiresponsive luminescent sensor based on a terbium(III) metal-organic framework. *Chem. Asian. J.* **2015**, *10*, 1703–1709. [CrossRef]
77. Shin, W.-J.; Jung, M.; Ryu, J.-S.; Hwang, J.; Lee, K.-S. Revisited digestion methods for trace element analysis in human hair. *J. Anal. Sci. Technol.* **2020**, *11*, 1. [CrossRef]
78. Hao Guo, N.W.; Peng, L.; Chen, Y.; Liu, Y.; Li, C.; Zhang, H.; Yang, W. A novel ratiometric fluorescence sensor based on lanthanide-functionalized MOF for Hg^{2+} detection. *Talanta* **2022**, *250*, 123710–123717. [CrossRef]
79. Wang, H.; Wang, X.; Liang, M.; Chen, G.; Kong, R.M.; Xia, L.; Qu, F. A boric acid-functionalized lanthanide metal-organic framework as a fluorescence "turn-on" probe for selective monitoring of Hg^{2+} and CH_3Hg^+. *Anal. Chem.* **2020**, *92*, 3366–3372. [CrossRef]
80. Li, H.; Li, D.; Qin, B.; Li, W.; Zheng, H.; Zhang, X.; Zhang, J. Turn-on fluorescence in a stable Cd(ii) metal-organic framework for highly sensitive detection of Cr^{3+} in water. *Dye. Pigment.* **2020**, *178*, 108359–108364. [CrossRef]

81. Liu, J.; Wang, X.; Zhao, Y.; Xu, Y.; Pan, Y.; Feng, S.; Liu, J.; Huang, X.; Wang, H. Nh3 plasma functionalization of UiO-66-NH^2 for highly enhanced selective fluorescence detection of u(vi) in water. *Anal. Chem.* **2022**, *94*, 10091–10100. [CrossRef] [PubMed]
82. Steinegger, A.; Wolfbeis, O.S.; Borisov, S.M. Optical sensing and imaging of pH values: Spectroscopies, materials, and applications. *Chem. Rev.* **2020**, *120*, 12357–12489. [CrossRef] [PubMed]
83. Jiang, H.L.; Feng, D.; Wang, K.; Gu, Z.Y.; Wei, Z.; Chen, Y.P.; Zhou, H.C. An exceptionally stable, porphyrinic Zr metal-organic framework exhibiting pH-dependent fluorescence. *J. Am. Chem. Soc.* **2013**, *135*, 13934–13938. [CrossRef]
84. Qiao, J.; Liu, X.; Zhang, L.; Eubank, J.F.; Liu, X.; Liu, Y. Unique fluorescence turn-on and turn-off-on responses to acids by a carbazole-based metal-organic framework and theoretical studies. *J. Am. Chem. Soc.* **2022**, *144*, 17054–17063. [CrossRef] [PubMed]
85. Chen, F.G.; Xu, W.; Chen, J.; Xiao, H.P.; Wang, H.Y.; Chen, Z.; Ge, J.Y. Dysprosium(III) metal-organic framework demonstrating ratiometric luminescent detection of pH, magnetism, and proton conduction. *Inorg. Chem.* **2022**, *61*, 5388–5396. [CrossRef]
86. Harbuzaru, B.V.; Corma, A.; Rey, F.; Jorda, J.L.; Ananias, D.; Carlos, L.D.; Rocha, J. A miniaturized linear pH sensor based on a highly photoluminescent self-assembled europium(III) metal-organic framework. *Angew. Chem. Int. Ed.* **2009**, *48*, 6476–6479. [CrossRef]
87. Wang, J.; Li, D.; Ye, Y.; Qiu, Y.; Liu, J.; Huang, L.; Liang, B.; Chen, B. A fluorescent metal-organic framework for food real-time visual monitoring. *Adv. Mater.* **2021**, *33*, 2008020–2008027. [CrossRef]
88. Chen, H.; Wang, J.; Shan, D.; Chen, J.; Zhang, S.; Lu, X. Dual-emitting fluorescent metal-organic framework nanocomposites as a broad-range pH sensor for fluorescence imaging. *Anal. Chem.* **2018**, *90*, 7056–7063. [CrossRef]
89. Jin, J.; Xue, J.; Liu, Y.; Yang, G.; Wang, Y.-Y. Recent progresses in luminescent metal-organic frameworks (lmofs) as sensors for the detection of anions and cations in aqueous solution. *Dalton Trans.* **2021**, *50*, 1950–1972. [CrossRef]
90. Yi, F.-Y.; Chen, D.; Wu, M.-K.; Han, L.; Jiang, H.-L. Chemical sensors based on metal-organic frameworks. *Chempluschem* **2016**, *81*, 675–690. [CrossRef]
91. Li, Y.; Li, J.-J.; Zhang, Q.; Zhang, J.-Y.; Zhang, N.; Fang, Y.-Z.; Yan, J.; Ke, Q. The multifunctional bodipy@eu-MOF nanosheets as bioimaging platform: A ratiometric fluorescencent sensor for highly efficient detection of F^-, H_2O_2 and glucose. *Sens. Actuators B Chem.* **2022**, *354*, 131140–131153. [CrossRef]
92. Zeng, X.; Hu, J.; Zhang, M.; Wang, F.; Wu, L.; Hou, X. Visual detection of fluoride anions using mixed lanthanide metal-organic frameworks with a smartphone. *Anal. Chem.* **2020**, *92*, 2097–2102. [CrossRef] [PubMed]
93. Che, H.; Li, Y.; Zhang, S.; Chen, W.; Tian, X.; Yang, C.; Lu, L.; Zhou, Z.; Nie, Y. A portable logic detector based on eu-MOF for multi-target, on-site, visual detection of eu3+ and fluoride in groundwater. *Sens. Actuators B Chem.* **2020**, *324*, 128641–128650. [CrossRef]
94. Dalapati, R.; Biswas, S. Post-synthetic modification of a metal-organic framework with fluorescent-tag for dual naked-eye sensing in aqueous medium. *Sens. Actuators B Chem.* **2017**, *239*, 759–767. [CrossRef]
95. Sun, Y.Q.; Cheng, Y.; Yin, X.B. Dual-ligand lanthanide metal-organic framework for sensitive ratiometric fluorescence detection of hypochlorous acid. *Anal. Chem.* **2021**, *93*, 3559–3566. [CrossRef]
96. Tan, H.; Wu, X.; Weng, Y.; Lu, Y.; Huang, Z.Z. Self-assembled FRET nanoprobe with metal-organic framework as a scaffold for ratiometric detection of hypochlorous acid. *Anal. Chem.* **2020**, *92*, 3447–3454. [CrossRef]
97. Wang, X.Y.; Yin, H.Q.; Yin, X.B. MOF@cofs with strong multiemission for differentiation and ratiometric fluorescence detection. *ACS Appl. Mater. Interfaces* **2020**, *12*, 20973–20981. [CrossRef]
98. Wang, Y.M.; Yang, Z.R.; Xiao, L.; Yin, X.B. Lab-on-MOFs: Color-coded multitarget fluorescence detection with white-light emitting metal-organic frameworks under single wavelength excitation. *Anal. Chem.* **2018**, *90*, 5758–5763. [CrossRef]
99. Fan, C.; Lv, X.; Tian, M.; Yu, Q.; Mao, Y.; Qiu, W.; Wang, H.; Liu, G. A terbium(III)-functionalized zinc(ii)-organic framework for fluorometric determination of phosphate. *Microchim. Acta* **2020**, *187*, 84–90. [CrossRef]
100. Shi, W.; Zhang, S.; Wang, Y.; Xue, Y.D.; Chen, M. Preparation of dual-ligands eu-MOF nanorods with dual fluorescence emissions for highly sensitive and selective ratiometric/visual fluorescence sensing phosphate. *Sens. Actuators B Chem.* **2022**, *367*, 132008–132015. [CrossRef]
101. Zhang, X.; Ma, Q.; Liu, X.; Niu, H.; Luo, L.; Li, R.; Feng, X. A turn-off eu-MOF@Fe^{2+} sensor for the selective and sensitive fluorescence detection of bromate in wheat flour. *Food Chem.* **2022**, *382*, 132379–132386. [CrossRef] [PubMed]
102. Karmakar, A.; Kumar, N.; Samanta, P.; Desai, A.V.; Ghosh, S.K. A post-synthetically modified MOF for selective and sensitive aqueous-phase detection of highly toxic cyanide ions. *Chem. Eur. J.* **2016**, *22*, 864–868. [CrossRef] [PubMed]
103. Jain, S.; Nehra, M.; Dilbaghi, N.; Kumar, R.; Kumar, S. Boric-acid-functionalized luminescent sensor for detection of chromate ions in aqueous solution. *Mater. Lett.* **2022**, *306*, 130933–130936. [CrossRef]
104. Zhang, Y.; Liu, Y.; Huo, F.; Zhang, B.; Su, W.; Yang, X. Photoluminescence quenching in recyclable water-soluble Zn-based metal–organic framework nanoflakes for dichromate sensing. *ACS Appl. Nano Mater.* **2022**, *5*, 9223–9229. [CrossRef]
105. Ma, Y.; Su, H.; Kuang, X.; Li, X.; Zhang, T.; Tang, B. Heterogeneous nano metal-organic framework fluorescence probe for highly selective and sensitive detection of hydrogen sulfide in living cells. *Anal. Chem.* **2014**, *86*, 11459–11463. [CrossRef]
106. Gao, X.; Sun, G.; Wang, X.; Lin, X.; Wang, S.; Liu, Y. Rhb/UiO-66-n3 MOF-based ratiometric fluorescent detection and intracellular imaging of hydrogen sulfide. *Sens. Actuators B Chem.* **2021**, *331*, 129448–129457. [CrossRef]
107. Rasheed, T.; Nabeel, F. Luminescent metal-organic frameworks as potential sensory materials for various environmental toxic agents. *Coord. Chem. Rev.* **2019**, *401*, 213065–213086. [CrossRef]

108. Chen, J.; Zhang, Q.; Dong, J.; Xu, F.; Li, S. Amino-functionalized Cu metal-organic framework nanosheets as fluorescent probes for detecting tnp. *Anal. Methods* **2021**, *13*, 5328–5334. [CrossRef]
109. Firuzabadi, F.D.; Alavi, M.A.; Zarekarizi, F.; Tehrani, A.A.; Morsali, A. A pillared metal-organic framework with rich π-electron linkers as a novel fluorescence probe for the highly selective and sensitive detection of nitroaromatics. *Colloids Surf. A* **2021**, *622*, 126631–126637. [CrossRef]
110. Gu, P.; Wu, H.; Jing, T.; Li, Y.; Wang, Z.; Ye, S.; Lai, W.; Ferbinteanu, M.; Wang, S.; Huang, W. (4,5,8)-connected cationic coordination polymer material as explosive chemosensor based on the in situ generated AIE tetrazolyl-tetraphenylethylene derivative. *Inorg. Chem.* **2021**, *60*, 13359–13365. [CrossRef]
111. Zhang, S.R.; Du, D.Y.; Qin, J.S.; Bao, S.J.; Li, S.L.; He, W.W.; Lan, Y.Q.; Shen, P.; Su, Z.M. A fluorescent sensor for highly selective detection of nitroaromatic explosives based on a 2D, extremely stable, metal-organic framework. *Chem. Eur. J.* **2014**, *20*, 3589–3594. [CrossRef] [PubMed]
112. Wang, C.; Tian, L.; Zhu, W.; Wang, S.; Wang, P.; Liang, Y.; Zhang, W.; Zhao, H.; Li, G. Dye@bio-MOF-1 composite as a dual-emitting platform for enhanced detection of a wide range of explosive molecules. *ACS Appl. Mater. Interfaces* **2017**, *9*, 20076–20085. [CrossRef] [PubMed]
113. Sun, Z.; Li, J.; Wang, X.; Zhao, Z.; Lv, R.; Zhang, Q.; Wang, F.; Zhao, Y. Rhb-encapsulated MOF-based composite as self-calibrating sensor for selective detection of 4-nitroaniline. *J. Lumin.* **2022**, *241*, 118480–118487. [CrossRef]
114. Sharma, A.; Kim, D.; Park, J.-H.; Rakshit, S.; Seong, J.; Jeong, G.H.; Kwon, O.-H.; Lah, M.S. Mechanistic insight into the sensing of nitroaromatic compounds by metal-organic frameworks. *Commun. Chem.* **2019**, *2*, 39–46. [CrossRef]
115. Qiu, Z.J.; Fan, S.T.; Xing, C.Y.; Song, M.M.; Nie, Z.J.; Xu, L.; Zhang, S.X.; Wang, L.; Zhang, S.; Li, B.J. Facile fabrication of an AIE-active metal-organic framework for sensitive detection of explosives in liquid and solid phases. *ACS Appl. Mater. Interfaces* **2020**, *12*, 55299–55307. [CrossRef]
116. Qiang, Y.; Yang, W.; Zhang, X.; Luo, X.; Tang, W.; Yue, T.; Li, Z. UiO-67 decorated on porous carbon derived from ce-MOF for the enrichment and fluorescence determination of glyphosate. *Microchim. Acta* **2022**, *189*, 130–140. [CrossRef]
117. Zhao, D.; Yu, S.; Jiang, W.-J.; Cai, Z.-H.; Li, D.-L.; Liu, Y.-L.; Chen, Z.-Z. Recent progress in metal-organic framework based fluorescent sensors for hazardous materials detection. *Molecules* **2022**, *27*, 2226. [CrossRef]
118. Mukherjee, S.; Dutta, S.; More, Y.D.; Fajal, S.; Ghosh, S.K. Post-synthetically modified metal-organic frameworks for sensing and capture of water pollutants. *Dalton Trans.* **2021**, *50*, 17832–17851. [CrossRef]
119. Jiao, Z.H.; Hou, S.L.; Kang, X.M.; Yang, X.P.; Zhao, B. Recyclable luminescence sensor for dinotefuran in water by stable cadmium-organic framework. *Anal. Chem.* **2021**, *93*, 6599–6603. [CrossRef]
120. Yu, C.-X.; Hu, F.-L.; Song, J.-G.; Zhang, J.-L.; Liu, S.-S.; Wang, B.-X.; Meng, H.; Liu, L.-L.; Ma, L.-F. Ultrathin two-dimensional metal-organic framework nanosheets decorated with tetra-pyridyl calix[4]arene: Design, synthesis and application in pesticide detection. *Sens. Actuators B Chem.* **2020**, *310*, 127819–127825. [CrossRef]
121. Zhang, Y.; Gao, L.; Ma, S.; Hu, T. Porous MB@Cd-MOF obtained by post-modification: Self-calibrated fluorescent turn-on sensor for highly sensitive detection of carbaryl. *Cryst. Growth Des.* **2022**, *22*, 2662–2669. [CrossRef]
122. Wei, Z.; Chen, D.; Guo, Z.; Jia, P.; Xing, H. Eosin y-embedded zirconium-based metal-organic framework as a dual-emitting built-in self-calibrating platform for pesticide detection. *Inorg. Chem.* **2020**, *59*, 5386–5393. [CrossRef] [PubMed]
123. Wang, X.; Rehman, A.; Kong, R.M.; Cheng, Y.; Tian, X.; Liang, M.; Zhang, L.; Xia, L.; Qu, F. Naphthalimide derivative-functionalized metal-organic framework for highly sensitive and selective determination of aldehyde by space confinement-induced sensitivity enhancement effect. *Anal. Chem.* **2021**, *93*, 8219–8227. [CrossRef] [PubMed]
124. Li, C.; Yang, W.; Zhang, X.; Han, Y.; Tang, W.; Yue, T.; Li, Z. A 3D hierarchical dual-metal–organic framework heterostructure up-regulating the pre-concentration effect for ultrasensitive fluorescence detection of tetracycline antibiotics. *J. Mater. Chem. C* **2020**, *8*, 2054–2064. [CrossRef]
125. Li, C.P.; Long, W.W.; Lei, Z.; Guo, L.; Xie, M.J.; Lu, J.; Zhu, X.D. Anionic metal-organic framework as a unique turn-on fluorescent chemical sensor for ultra-sensitive detection of antibiotics. *Chem. Commun.* **2020**, *56*, 12403–12406. [CrossRef]
126. Liang, Y.; Li, J.; Yang, S.; Wu, S.; Zhu, M.; Fedin, V.P.; Zhang, Y.; Gao, E. Self-calibrated FRET fluorescent probe with metal-organic framework for proportional detection of nitrofuran antibiotics. *Polyhedron* **2022**, *226*, 116080–116087. [CrossRef]
127. Yue, X.; Zhou, Z.; Li, M.; Jie, M.; Xu, B.; Bai, Y. Inner-filter effect induced fluorescent sensor based on fusiform Al-MOF nanosheets for sensitive and visual detection of nitrofuran in milk. *Food Chem.* **2022**, *367*, 130763– 130770. [CrossRef]
128. Xiong, J.; Yang, L.; Gao, L.X.; Zhu, P.P.; Chen, Q.; Tan, K.J. A highly fluorescent lanthanide metal-organic framework as dual-mode visual sensor for berberine hydrochloride and tetracycline. *Anal. Bioanal. Chem.* **2019**, *411*, 5963–5973. [CrossRef]
129. Wang, L.-B.; Wang, J.-J.; Yue, E.-L.; Li, J.-F.; Tang, L.; Wang, X.; Hou, X.-Y.; Zhang, Y.; Ren, Y.-X.; Chen, X.-L. Luminescent Zn (ii) coordination polymers for highly selective detection of triethylamine, nitrobenzene and tetracycline in water systems. *Dye. Pigment.* **2022**, *197*, 109863–109871. [CrossRef]
130. Liu, X.; Zhang, X.; Li, R.; Du, L.; Feng, X.; Ding, Y. A highly sensitive and selective "turn off-on" fluorescent sensor based on sm-MOF for the detection of tertiary butylhydroquinone. *Dye. Pigment.* **2020**, *178*, 108347–108354. [CrossRef]
131. Guo, G.; Wang, T.; Ding, X.; Wang, H.; Wu, Q.; Zhang, Z.; Ding, S.; Li, S.; Li, J. Fluorescent lanthanide metal-organic framework for rapid and ultrasensitive detection of methcathinone in human urine. *Talanta* **2022**, *249*, 123663–123670. [CrossRef] [PubMed]
132. Chen, J.; Xu, F.; Zhang, Q.; Li, S.; Lu, X. Tetracycline antibiotics and NH_4^+ detection by Zn-organic framework fluorescent probe. *Analyst* **2021**, *146*, 6883–6892. [CrossRef] [PubMed]

133. Qin, G.; Wang, J.; Li, L.; Yuan, F.; Zha, Q.; Bai, W.; Ni, Y. Highly water-stable Cd-MOF/Tb3+ ultrathin fluorescence nanosheets for ultrasensitive and selective detection of cefixime. *Talanta* **2021**, *221*, 121421–121428. [CrossRef] [PubMed]
134. Gan, Z.; Zhang, W.; Shi, J.; Xu, X.; Hu, X.; Zhang, X.; Wang, X.; Arslan, M.; Xiao, J.; Zou, X. Collaborative compounding of metal-organic frameworks and lanthanide coordination polymers for ratiometric visual detection of tetracycline. *Dye. Pigment.* **2021**, *194*, 109545–109554. [CrossRef]
135. Wang, X.; Zhang, L.; Ye, N.; Xiang, Y. Synthesis of a dual metal–organic framework heterostructure as a fluorescence sensing platform for rapid and sensitive detection of tetracycline in milk and beef samples. *Food Anal. Methods* **2022**, *15*, 2801–2809. [CrossRef]
136. Yu, L.; Chen, H.; Yue, J.; Chen, X.; Sun, M.; Tan, H.; Asiri, A.M.; Alamry, K.A.; Wang, X.; Wang, S. Metal-organic framework enhances aggregation-induced fluorescence of chlortetracycline and the application for detection. *Anal. Chem.* **2019**, *91*, 5913–5921. [CrossRef] [PubMed]
137. Luo, T.Y.; Das, P.; White, D.L.; Liu, C.; Star, A.; Rosi, N.L. Luminescence "turn-on" detection of gossypol using Ln^{3+}-based metal-organic frameworks and Ln^{3+} salts. *J. Am. Chem. Soc.* **2020**, *142*, 2897–2904. [CrossRef]
138. Hu, S.; Yan, J.; Huang, X.; Guo, L.; Lin, Z.; Luo, F.; Qiu, B.; Wong, K.-Y.; Chen, G. A sensing platform for hypoxanthine detection based on amino-functionalized metal organic framework nanosheet with peroxidase mimic and fluorescence properties. *Sens. Actuators B Chem.* **2018**, *267*, 312–319. [CrossRef]
139. Dalapati, R.; Biswas, S. A pyrene-functionalized metal-organic framework for nonenzymatic and ratiometric detection of uric acid in biological fluid via conformational change. *Inorg. Chem.* **2019**, *58*, 5654–5663. [CrossRef]
140. Xiao, J.; Song, L.; Liu, M.; Wang, X.; Liu, Z. Intriguing pH-modulated luminescence chameleon system based on postsynthetic modified dual-emitting Eu^{3+}@Mn-MOF and its application for histidine chemosensor. *Inorg. Chem.* **2020**, *59*, 6390–6397. [CrossRef]
141. Song, L.; Xiao, J.; Cui, R.; Wang, X.; Tian, F.; Liu, Z. Eu^{3+} doped bismuth metal-organic frameworks with ultrahigh fluorescence quantum yield and act as ratiometric turn-on sensor for histidine detection. *Sens. Actuators B Chem.* **2021**, *336*, 129753–129760. [CrossRef]
142. Geng, J.; Li, Y.; Lin, H.; Liu, Q.; Lu, J.; Wang, X. A new three-dimensional zinc(ii) metal-organic framework as a fluorescence sensor for sensing the biomarker 3-nitrotyrosine. *Dalton Trans.* **2022**, *51*, 11390–11396. [CrossRef] [PubMed]
143. Xia, Z.; Li, D.; Deng, W. Identification and detection of volatile aldehydes as lung cancer biomarkers by vapor generation combined with paper-based thin-film microextraction. *Anal. Chem.* **2021**, *93*, 4924–4931. [CrossRef] [PubMed]
144. Zhang, S.Y.; Shi, W.; Cheng, P.; Zaworotko, M.J. A mixed-crystal lanthanide zeolite-like metal-organic framework as a fluorescent indicator for lysophosphatidic acid, a cancer biomarker. *J. Am. Chem. Soc.* **2015**, *137*, 12203–12206. [CrossRef] [PubMed]
145. Wang, N.; Xie, M.; Wang, M.; Li, Z.; Su, X. UiO-66-NH2 MOF-based ratiometric fluorescent probe for the detection of dopamine and reduced glutathione. *Talanta* **2020**, *220*, 121352–121358. [CrossRef] [PubMed]
146. Bhardwaj, N.; Bhardwaj, S.; Mehta, J.; Kim, K.H.; Deep, A. Highly sensitive detection of dipicolinic acid with a water-dispersible terbium-metal organic framework. *Biosens. Bioelectron.* **2016**, *86*, 799–804. [CrossRef]
147. Li, X.; Luo, J.; Deng, L.; Ma, F.; Yang, M. In situ incorporation of fluorophores in zeolitic imidazolate framework-8 (ZIF-8) for ratio-dependent detecting a biomarker of anthrax spores. *Anal. Chem.* **2020**, *92*, 7114–7122. [CrossRef] [PubMed]
148. Qu, S.; Cao, Q.; Ma, J.; Jia, Q. A turn-on fluorescence sensor for creatinine based on the quinoline-modified metal organic frameworks. *Talanta* **2020**, *219*, 121280–121286. [CrossRef]
149. Guo, L.; Liu, Y.; Kong, R.; Chen, G.; Liu, Z.; Qu, F.; Xia, L.; Tan, W. A metal-organic framework as selectivity regulator for Fe^{3+} and ascorbic acid detection. *Anal. Chem.* **2019**, *91*, 12453–12460. [CrossRef]
150. Qu, X.L.; Yan, B. Ln(III)-functionalized metal-organic frameworks hybrid system: Luminescence properties and sensor for trans, trans-muconic acid as a biomarker of benzene. *Inorg. Chem.* **2018**, *57*, 7815–7824. [CrossRef]
151. Yin, H.Q.; Yang, J.C.; Yin, X.B. Ratiometric fluorescence sensing and real-time detection of water in organic solvents with one-pot synthesis of Ru@MIL-101(Al)-NH_2. *Anal. Chem.* **2017**, *89*, 13434–13440. [CrossRef] [PubMed]
152. Zhou, Y.; Zhang, D.; Xing, W.; Cuan, J.; Hu, Y.; Cao, Y.; Gan, N. Ratiometric and turn-on luminescence detection of water in organic solvents using a responsive europium-organic framework. *Anal. Chem.* **2019**, *91*, 4845–4851. [CrossRef] [PubMed]
153. Yu, L.; Zheng, Q.; Wang, H.; Liu, C.; Huang, X.; Xiao, Y. Double-color lanthanide metal-organic framework based logic device and visual ratiometric fluorescence water microsensor for solid pharmaceuticals. *Anal. Chem.* **2020**, *92*, 1402–1408. [CrossRef] [PubMed]
154. Chen, D.-M.; Sun, C.-X.; Peng, Y.; Zhang, N.-N.; Si, H.-H.; Liu, C.-S.; Du, M. Ratiometric fluorescence sensing and colorimetric decoding methanol by a bimetallic lanthanide-organic framework. *Sens. Actuators B Chem.* **2018**, *265*, 104–109. [CrossRef]
155. Pashazadeh-Panahi, P.; Belali, S.; Sohrabi, H.; Oroojalian, F.; Hashemzaei, M.; Mokhtarzadeh, A.; de la Guardia, M. Metal-organic frameworks conjugated with biomolecules as efficient platforms for development of biosensors. *TrAC Trends Anal. Chem.* **2021**, *141*, 116285–116304. [CrossRef]
156. Zhang, Q.; Wang, C.-F.; Lv, Y.-K. Luminescent switch sensors for the detection of biomolecules based on metal-organic frameworks. *Analyst* **2018**, *143*, 4221–4229. [CrossRef]
157. Wang, H.S.; Wang, Y.H.; Ding, Y. Development of biological metal-organic frameworks designed for biomedical applications: From bio-sensing/bio-imaging to disease treatment. *Nanoscale Adv.* **2020**, *2*, 3788–3797. [CrossRef]

158. Lin, Y.; Huang, Y.; Chen, X. Recent advances in metal-organic frameworks for biomacromolecule sensing. *Chemosensors* **2022**, *10*, 412. [CrossRef]
159. Udourioh, G.A.; Solomon, M.M.; Epelle, E.I. Metal organic frameworks as biosensing materials for COVID-19. *Cell. Mol. Bioeng.* **2021**, *14*, 535–553. [CrossRef]
160. Hu, P.P.; Liu, N.; Wu, K.Y.; Zhai, L.Y.; Xie, B.P.; Sun, B.; Duan, W.J.; Zhang, W.H.; Chen, J.X. Successive and specific detection of Hg^{2+} and I^{-} by a DNA@MOF biosensor: Experimental and simulation studies. *Inorg. Chem.* **2018**, *57*, 8382–8389. [CrossRef]
161. Sun, C.; Zhao, S.; Qu, F.; Han, W.; You, J. Determination of adenosine triphosphate based on the use of fluorescent terbium(III) organic frameworks and aptamer modified gold nanoparticles. *Microchim. Acta* **2019**, *187*, 34–42. [CrossRef] [PubMed]
162. Wang, Z.; Zhou, X.; Li, Y.; Huang, Z.; Han, J.; Xie, G.; Liu, J. Sensing ATP: Zeolitic imidazolate framework-67 is superior to aptamers for target recognition. *Anal. Chem.* **2021**, *93*, 7707–7713. [CrossRef] [PubMed]
163. Yao, J.; Yue, T.; Huang, C.; Wang, H. A magnified aptamer fluorescence sensor based on the metal organic frameworks adsorbed DNA with enzyme catalysis amplification for ultra-sensitive determination of ATP and its logic gate operation. *Bioorganic Chem.* **2021**, *114*, 105020–105027. [CrossRef] [PubMed]
164. Qu, F.; Sun, C.; Lv, X.; You, J. A terbium-based metal-organic framework@gold nanoparticle system as a fluorometric probe for aptamer based determination of adenosine triphosphate. *Microchim. Acta* **2018**, *185*, 359–365. [CrossRef]
165. Wang, Z.; Zhou, X.; Han, J.; Xie, G.; Liu, J. DNA coated cozn-ZIF metal-organic frameworks for fluorescent sensing guanosine triphosphate and discrimination of nucleoside triphosphates. *Anal. Chim. Acta.* **2022**, *1207*, 339806–339813. [CrossRef]
166. Jia, Y.; Zhou, G.; Wang, X.; Zhang, Y.; Li, Z.; Liu, P.; Yu, B.; Zhang, J. A metal-organic framework/aptamer system as a fluorescent biosensor for determination of aflatoxin b1 in food samples. *Talanta* **2020**, *219*, 121342–121349. [CrossRef]
167. Lu, Z.; Jiang, Y.; Wang, P.; Xiong, W.; Qi, B.; Zhang, Y.; Xiang, D.; Zhai, K. Bimetallic organic framework-based aptamer sensors: A new platform for fluorescence detection of chloramphenicol. *Anal. Bioanal. Chem.* **2020**, *412*, 5273–5281. [CrossRef]
168. Amalraj, A.; Perumal, P. Dual-mode amplified fluorescence oligosensor mediated MOF-MoS_2 for ultra-sensitive simultaneous detection of 17β -estradiol and chloramphenicol through catalytic target- recycling activity of exonuclease i. *Microchem. J.* **2022**, *173*, 106971–106980. [CrossRef]
169. Li, W.; Zhang, X.; Hu, X.; Shi, Y.; Liang, N.; Huang, X.; Wang, X.; Shen, T.; Zou, X.; Shi, J. Simple design concept for dual-channel detection of ochratoxin a based on bifunctional metal-organic framework. *ACS Appl. Mater. Interfaces* **2022**, *14*, 5615–5623. [CrossRef]
170. Wang, H.S.; Liu, H.L.; Wang, K.; Ding, Y.; Xu, J.J.; Xia, X.H.; Chen, H.Y. Insight into the unique fluorescence quenching property of metal-organic frameworks upon DNA binding. *Anal. Chem.* **2017**, *89*, 11366–11371. [CrossRef]
171. Wang, X.Z.; Du, J.; Xiao, N.N.; Zhang, Y.; Fei, L.; LaCoste, J.D.; Huang, Z.; Wang, Q.; Wang, X.R.; Ding, B. Driving force to detect alzheimer's disease biomarkers: Application of a thioflavine t@er-MOF ratiometric fluorescent sensor for smart detection of presenilin 1, amyloid beta-protein and acetylcholine. *Analyst* **2020**, *145*, 4646–4663. [CrossRef]
172. Chen, L.; Zheng, H.; Zhu, X.; Lin, Z.; Guo, L.; Qiu, B.; Chen, G.; Chen, Z.N. Metal-organic frameworks-based biosensor for sequence-specific recognition of double-stranded DNA. *Analyst* **2013**, *138*, 3490–3493. [CrossRef] [PubMed]
173. Zhao, M.; Wang, Y.; Ma, Q.; Huang, Y.; Zhang, X.; Ping, J.; Zhang, Z.; Lu, Q.; Yu, Y.; Xu, H.; et al. Ultrathin 2D metal-organic framework nanosheets. *Adv. Mater.* **2015**, *27*, 7372–7378. [CrossRef] [PubMed]
174. Zhang, H.; Luo, B.; An, P.; Zhan, X.; Lan, F.; Wu, Y. Interaction of nucleic acids with metal-organic framework nanosheets by fluorescence spectroscopy and molecular dynamics simulations. *ACS Appl. Bio Mater.* **2022**, *5*, 3500–3508. [CrossRef] [PubMed]
175. Han, Y.; Zou, R.; Wang, L.; Chen, C.; Gong, H.; Cai, C. An amine-functionalized metal-organic framework and triple-helix molecular beacons as a sensing platform for miRNA ratiometric detection. *Talanta* **2021**, *228*, 122199–122205. [CrossRef]
176. Qiu, G.H.; Weng, Z.H.; Hu, P.P.; Duan, W.J.; Xie, B.P.; Sun, B.; Tang, X.Y.; Chen, J.X. Synchronous detection of ebolavirus conserved rna sequences and ebolavirus-encoded miRNA-like fragment based on a zwitterionic copper (ii) metal-organic framework. *Talanta* **2018**, *180*, 396–402. [CrossRef]
177. Ye, T.; Liu, Y.; Luo, M.; Xiang, X.; Ji, X.; Zhou, G.; He, Z. Metal-organic framework-based molecular beacons for multiplexed DNA detection by synchronous fluorescence analysis. *Analyst* **2014**, *139*, 1721–1725. [CrossRef]
178. Yang, S.P.; Chen, S.R.; Liu, S.W.; Tang, X.Y.; Qin, L.; Qiu, G.H.; Chen, J.X.; Chen, W.H. Platforms formed from a three-dimensional Cu-based zwitterionic metal-organic framework and probe ss-DNA: Selective fluorescent biosensors for human immunodeficiency virus 1 ds-DNA and sudan virus rna sequences. *Anal. Chem.* **2015**, *87*, 12206–12214. [CrossRef]
179. Afzalinia, A.; Mirzaee, M. Ultrasensitive fluorescent miRNA biosensor based on a "sandwich" oligonucleotide hybridization and fluorescence resonance energy transfer process using an ln(III)-MOF and Ag nanoparticles for early cancer diagnosis: Application of central composite design. *ACS Appl. Mater. Interfaces* **2020**, *12*, 16076–16087. [CrossRef]
180. Javan Kouzegaran, V.; Farhadi, K.; Forough, M.; Bahram, M.; Persil Cetinkol, O. Highly-sensitive and fast detection of human telomeric g-quadruplex DNA based on a hemin-conjugated fluorescent metal-organic framework platform. *Biosens. Bioelectron.* **2021**, *178*, 112999–113007. [CrossRef]
181. Wu, S.; Li, C.; Shi, H.; Huang, Y.; Li, G. Design of metal-organic framework-based nanoprobes for multicolor detection of DNA targets with improved sensitivity. *Anal. Chem.* **2018**, *90*, 9929–9935. [CrossRef]
182. Han, Q.; Zhang, D.; Zhang, R.; Tang, J.; Xu, K.; Shao, M.; Li, Y.; Du, P.; Zhang, R.; Yang, D.; et al. DNA-functionalized metal-organic framework ratiometric nanoprobe for MicroRNA detection and imaging in live cells. *Sens. Actuators B Chem.* **2022**, *361*, 131676–131683. [CrossRef]

183. Chen, J.; Oudeng, G.; Feng, H.; Liu, S.; Li, H.W.; Ho, Y.P.; Chen, Y.; Tan, Y.; Yang, M. 2D MOF nanosensor-integrated digital droplet microfluidic flow cytometry for in situ detection of multiple miRNAs in single ctc cells. *Small* **2022**, *18*, 2201779–2201791. [CrossRef] [PubMed]
184. Zhang, J.; He, M.; Nie, C.; He, M.; Pan, Q.; Liu, C.; Hu, Y.; Yi, J.; Chen, T.; Chu, X. Biomineralized metal-organic framework nanoparticles enable enzymatic rolling circle amplification in living cells for ultrasensitive MicroRNA imaging. *Anal. Chem.* **2019**, *91*, 9049–9057. [CrossRef]
185. Meng, X.; Zhang, K.; Yang, F.; Dai, W.; Lu, H.; Dong, H.; Zhang, X. Biodegradable metal-organic frameworks power DNAzyme for in vivo temporal-spatial control fluorescence imaging of aberrant MicroRNA and hypoxic tumor. *Anal. Chem.* **2020**, *92*, 8333–8339. [CrossRef] [PubMed]
186. Yu, L.; Feng, L.; Xiong, L.; Li, S.; Xu, Q.; Pan, X.; Xiao, Y. Rational design of dual-emission lanthanide metal-organic framework for visual alkaline phosphatase activity assay. *ACS Appl. Mater. Interfaces* **2021**, *13*, 11646–11656. [CrossRef]
187. Guo, L.; Liu, Y.; Kong, R.; Chen, G.; Wang, H.; Wang, X.; Xia, L.; Qu, F. Turn-on fluorescence detection of β-glucuronidase using rhb@MOF-5 as an ultrasensitive nanoprobe. *Sens. Actuators B Chem.* **2019**, *295*, 1–6. [CrossRef]
188. Chen, J.; Wang, G.; Su, X. Fabrication of red-emissive ZIF-8@QDs nanoprobe with improved fluorescence based on assembly strategy for enhanced biosensing. *Sens. Actuators B Chem.* **2022**, *368*, 132188–132196. [CrossRef]
189. Yu, L.; Gao, Z.; Xu, Q.; Pan, X.; Xiao, Y. A selective dual-response biosensor for tyrosinase monophenolase activity based on lanthanide metal-organic frameworks assisted boric acid-levodopa polymer dots. *Biosens. Bioelectron.* **2022**, *210*, 114320–114327. [CrossRef] [PubMed]
190. Xiong, L.; Yu, L.; Li, S.; Feng, L.; Xiao, Y. Multifunctional lanthanide metal-organic framework based ratiometric fluorescence visual detection platform for alkaline phosphatase activity. *Microchim. Acta* **2021**, *188*, 236–246. [CrossRef]
191. Guo, J.; Liu, Y.; Mu, Z.; Wu, S.; Wang, J.; Yang, Y.; Zhao, M.; Wang, Y. Label-free fluorescence detection of hydrogen peroxide and glucose based on the Ni-MOF nanozyme-induced self-ligand emission. *Microchim. Acta* **2022**, *189*, 219–229. [CrossRef] [PubMed]
192. Li, Y.; Guo, A.; Chang, L.; Li, W.J.; Ruan, W.J. Luminescent metal-organic-framework-based label-free assay of polyphenol oxidase with fluorescent scan. *Chem. Eur. J.* **2017**, *23*, 6562–6569. [CrossRef] [PubMed]
193. Wang, M.; Zhao, Z.; Gong, W.; Zhang, M.; Lu, N. Modulating the biomimetic and fluorescence quenching activities of metal-organic framework/platinum nanoparticle composites and their applications in molecular biosensing. *ACS Appl. Mater. Interfaces* **2022**, *14*, 21677–21686. [CrossRef] [PubMed]
194. Cai, Y.; Zhu, H.; Zhou, W.; Qiu, Z.; Chen, C.; Qileng, A.; Li, K.; Liu, Y. Capsulation of auncs with AIE effect into metal-organic framework for the marriage of a fluorescence and colorimetric biosensor to detect organophosphorus pesticides. *Anal. Chem.* **2021**, *93*, 7275–7282. [CrossRef] [PubMed]
195. Zhang, G.; Dong, H.; Zhang, X. Fluorescence proximity assay based on a metal-organic framework platform. *Chem. Commun.* **2019**, *55*, 8158–8161. [CrossRef] [PubMed]
196. Huang, X.; He, Z.; Guo, D.; Liu, Y.; Song, J.; Yung, B.C.; Lin, L.; Yu, G.; Zhu, J.J.; Xiong, Y.; et al. "Three-in-one" nanohybrids as synergistic nanoquenchers to enhance no-wash fluorescence biosensors for ratiometric detection of cancer biomarkers. *Theranostics* **2018**, *8*, 3461–3473. [CrossRef]
197. Zhang, W.; Liu, X.; Li, P.; Zhang, W.; Wang, H.; Tang, B. In situ fluorescence imaging of the levels of glycosylation and phosphorylation by a MOF-based nanoprobe in depressed mice. *Anal. Chem.* **2020**, *92*, 3716–3721. [CrossRef]
198. Wei, X.; Zheng, L.; Luo, F.; Lin, Z.; Guo, L.; Qiu, B.; Chen, G. Fluorescence biosensor for the H_5N_1 antibody based on a metal-organic framework platform. *J. Mater. Chem. B* **2013**, *1*, 1812–1817. [CrossRef]
199. Wang, X.; Wu, Y.; Shan, J.; Pan, W.; Pang, S.; Chu, Y.; Ma, X.; Zou, B.; Li, Y.; Wu, H.; et al. Lipid membrane anchoring and highly specific fluorescence detection of cancer-derived exosomes based on postfunctionalized zirconium-metal-organic frameworks. *Biochem. Biophys. Res. Commun.* **2022**, *609*, 69–74. [CrossRef]
200. Li, C.; Feng, X.; Yang, S.; Xu, H.; Yin, X.; Yu, Y. Capture, detection, and simultaneous identification of rare circulating tumor cells based on a rhodamine 6g-loaded metal-organic framework. *ACS Appl. Mater. Interfaces* **2021**, *13*, 52406–52416. [CrossRef]
201. Zuo, W.; Liang, L.; Ye, F.; Zhao, S. An integrated platform for label-free fluorescence detection and inactivation of bacteria based on boric acid functionalized Zr-MOF. *Sens. Actuators B Chem.* **2021**, *345*, 130345–130352. [CrossRef]

MDPI AG
Grosspeteranlage 5
4052 Basel
Switzerland
Tel.: +41 61 683 77 34

Biosensors Editorial Office
E-mail: biosensors@mdpi.com
www.mdpi.com/journal/biosensors

Academic Open
Access Publishing

mdpi.com

ISBN 978-3-7258-2596-7